

Advances in Polymer Science 267

Susheel Kalia
Yuvaraj Haldorai *Editors*

Organic- Inorganic Hybrid Nanomaterials

 Springer

Editorial Board:

- A. Abe, Tokyo, Japan
A.-C. Albertsson, Stockholm, Sweden
G.W. Coates, Ithaca, NY, USA
J. Genzer, Raleigh, NC, USA
S. Kobayashi, Kyoto, Japan
K.-S. Lee, Daejeon, South Korea
L. Leibler, Paris, France
T.E. Long, Blacksburg, VA, USA
M. Möller, Aachen, Germany
O. Okay, Istanbul, Turkey
V. Percec, Philadelphia, PA, USA
B.Z. Tang, Hong Kong, China
E.M. Terentjev, Cambridge, UK
M.J. Vicent, Valencia, Spain
B. Voit, Dresden, Germany
U. Wiesner, Ithaca, NY, USA
X. Zhang, Beijing, China

Aims and Scope

The series *Advances in Polymer Science* presents critical reviews of the present and future trends in polymer and biopolymer science. It covers all areas of research in polymer and biopolymer science including chemistry, physical chemistry, physics, material science.

The thematic volumes are addressed to scientists, whether at universities or in industry, who wish to keep abreast of the important advances in the covered topics.

Advances in Polymer Science enjoys a longstanding tradition and good reputation in its community. Each volume is dedicated to a current topic, and each review critically surveys one aspect of that topic, to place it within the context of the volume. The volumes typically summarize the significant developments of the last 5 to 10 years and discuss them critically, presenting selected examples, explaining and illustrating the important principles, and bringing together many important references of primary literature. On that basis, future research directions in the area can be discussed. *Advances in Polymer Science* volumes thus are important references for every polymer scientist, as well as for other scientists interested in polymer science - as an introduction to a neighboring field, or as a compilation of detailed information for the specialist.

Review articles for the individual volumes are invited by the volume editors. Single contributions can be specially commissioned.

Readership: Polymer scientists, or scientists in related fields interested in polymer and biopolymer science, at universities or in industry, graduate students.

Special offer:

For all clients with a standing order we offer the electronic form of *Advances in Polymer Science* free of charge.

More information about this series at
<http://www.springer.com/series/12>

Susheel Kalia · Yuvaraj Haldorai
Editors

Organic-Inorganic Hybrid Nanomaterials

With contributions by

A.C.S. Alcântara · P. Aranda · A. Celli · Q. Chen ·
M. Darder · A. Fahmi · M.L. Focarete · M. Gallei ·
C. Gualandi · Y. Haldorai · K. Haraguchi · R.Y. Hong ·
E. Ionescu · S. Kalia · S. Kango · S. Kaur · B. Kumari ·
B. Lund · D. Pathania · R. Reit · E. Ruiz-Hitzky · J.-J. Shim ·
P. Thakur · W. Voit · B. Wicklein · A. Zucchelli

 Springer

Editors

Susheel Kalia
Department of Chemistry
Bahra University
Waknaghat, Dist. Solan (H.P.)
India

Yuvaraj Haldorai
Yeungnam University
School of Chemical Engineering
Gyeongbuk
Korea, Republic of (South Korea)

ISSN 0065-3195

ISBN 978-3-319-13592-2

DOI 10.1007/978-3-319-13593-9

Springer Cham Heidelberg New York Dordrecht London

ISSN 1436-5030 (electronic)

ISBN 978-3-319-13593-9 (eBook)

Library of Congress Control Number: 2014956549

© Springer International Publishing Switzerland 2015

This work is subject to copyright. All rights are reserved by the Publisher, whether the whole or part of the material is concerned, specifically the rights of translation, reprinting, reuse of illustrations, recitation, broadcasting, reproduction on microfilms or in any other physical way, and transmission or information storage and retrieval, electronic adaptation, computer software, or by similar or dissimilar methodology now known or hereafter developed. Exempted from this legal reservation are brief excerpts in connection with reviews or scholarly analysis or material supplied specifically for the purpose of being entered and executed on a computer system, for exclusive use by the purchaser of the work. Duplication of this publication or parts thereof is permitted only under the provisions of the Copyright Law of the Publisher's location, in its current version, and permission for use must always be obtained from Springer. Permissions for use may be obtained through RightsLink at the Copyright Clearance Center. Violations are liable to prosecution under the respective Copyright Law.

The use of general descriptive names, registered names, trademarks, service marks, etc. in this publication does not imply, even in the absence of a specific statement, that such names are exempt from the relevant protective laws and regulations and therefore free for general use.

While the advice and information in this book are believed to be true and accurate at the date of publication, neither the authors nor the editors nor the publisher can accept any legal responsibility for any errors or omissions that may be made. The publisher makes no warranty, express or implied, with respect to the material contained herein.

Printed on acid-free paper

Springer is part of Springer Science+Business Media (www.springer.com)

Preface

Organic–inorganic hybrid nanomaterials made up of inorganic nanoparticles and organic polymers represent a new class of materials that exhibit improved performance compared with their individual constituents. These hybrid materials combine the unique properties of organic and inorganic components in one material and are used in sensors and in photocatalytic, antibacterial, electronic, and biomedical applications. Inorganic nanoparticles have a strong tendency to form aggregates; therefore, to improve the stability of dispersions and compatibility of inorganic nanofiller with organic solvents or polymer matrices, the surfaces of inorganic nanofiller should be modified either by grafting polymers onto them or by absorption of small molecules such as silane coupling agents. Surface modification improves the interfacial interactions between inorganic nanofiller and polymer matrix, which results in unique properties such as very high mechanical properties, even at low loadings of inorganic reinforcement, and other optical and electronic properties. This volume provides full information about the fabrication of hybrid nanomaterials, surface functionalization of inorganic nanoparticles, and applications of organic–inorganic nanocomposite materials in various fields.

The various review articles in this volume were contributed by prominent researchers from industry, academia, and research laboratories across the world. This interesting book will prove to be a very useful tool for undergraduate and post-graduate students, scientists, academics, research scholars, materials engineers, and for industry. This volume covers the following topics in the area of hybrid nanomaterials:

In the chapter “Dispersion of Inorganic Nanoparticles in Polymer Matrices: Challenges and Solutions,” the synthesis, properties, and applications of nanoparticles; their surface modification; and preparation of polymer–inorganic nanocomposites are reviewed in detail. The chapter “Recent Advances on Fibrous Clay-Based Nanocomposites” reviews recent results on nanocomposite materials derived from the fibrous clay silicates sepiolite and palygorskite and combined with diverse types of polymers, from typical thermoplastics to biopolymers such as polysaccharides, proteins, lipids, and nucleic acids. The chapter “Nanohybrid Materials by Electrospinning” highlights recent progress and current issues in the production of

hybrid nanofibers using the electrospinning technique. Hybrid nanomaterials based on polymer–ceramic are discussed in the chapter “Polymer–Ceramic Nanohybrid Materials.” Some advanced applications of polymer–ceramic hybrid nanomaterials are also addressed and compared with those of their polymeric counterparts.

Soft nanohybrid materials with novel organic–inorganic network structures, such as nanohydrogels, soft nanocomposites (solid), and their derivatives are described in the chapter “Soft Nanohybrid Materials Consisting of Polymer–Clay Networks.” Synthesis of polymer hybrids based on metal-oxide nanoparticles are discussed in “Fabrication of Metal Oxide–Polymer Hybrid Nanocomposites.” Some properties and applications of these hybrid nanocomposites are also discussed in this chapter.

The chapter “Semiconductor-Polymer Hybrid Materials” deals with the synthesis, properties, and applications of semiconductor nanoparticles and semiconductor polymer nanocomposites. Synthesis of semiconductor polymer nanocomposites by melt blending and in situ polymerization is discussed in detail. The properties and some applications of these nanocomposites are also discussed. The chapter “Shape Memory Polymer–Inorganic Hybrid Nanocomposites” discusses methods of preparing shape memory polymer inorganic nanocomposites as well as the effects of fillers on the biological, electromagnetic, and mechanical properties of the resulting nanocomposites. “Frontiers in Nanofabrication via Self-Assembly of Hybrid Materials into Low Dimensional Nanostructures” reviews the different concepts for fabrication of one-dimensional nanostructures based on hybrid materials via directed self-assembly. The concepts describe how different types of self-assembled organic phases drive the unidirectional assembly of the inorganic moieties.

The Editors would like to express their gratitude to all contributors of this book, who have provided excellent contributions.

Susheel Kalia would like to thank his students, who helped him in the editorial work. Finally, we gratefully acknowledge permissions to reproduce copyrighted materials from a number of sources.

Shimla Hills, India
Gyeongsan, Republic of Korea

Susheel Kalia
Yuvaraj Haldorai

Contents

Dispersion of Inorganic Nanoparticles in Polymer Matrices: Challenges and Solutions	1
R.Y. Hong, and Q. Chen	
Recent Advances on Fibrous Clay-Based Nanocomposites	39
Eduardo Ruiz-Hitzky, Margarita Darder, Ana C.S. Alcântara, Bernd Wicklein, and Pilar Aranda	
Nanohybrid Materials by Electrospinning	87
Chiara Gualandi, Annamaria Celli, Andrea Zucchelli, and Maria Letizia Focarete	
Polymer–Ceramic Nanohybrid Materials	143
Sarabjeet Kaur, Markus Gallei, and Emanuel Ionescu	
Soft Nanohybrid Materials Consisting of Polymer–Clay Networks	187
Kazutoshi Haraguchi	
Fabrication of Metal Oxide–Polymer Hybrid Nanocomposites	249
Yuvaraj Haldorai, and Jae-Jin Shim	
Semiconductor–Polymer Hybrid Materials	283
Sarita Kango, Susheel Kalia, Pankaj Thakur, Bandna Kumari, and Deepak Pathania	
Shape Memory Polymer–Inorganic Hybrid Nanocomposites	313
Radu Reit, Benjamin Lund, and Walter Voit	

Frontiers in Nanofabrication via Self-Assembly of Hybrid Materials into Low Dimensional Nanostructures	351
Amir Fahmi	
Index	381

Dispersion of Inorganic Nanoparticles in Polymer Matrices: Challenges and Solutions

R.Y. Hong and Q. Chen

Abstract Recently, nanoparticles with remarkable physical and chemical properties have attracted intense attention. Many techniques have been developed to synthesize nanoparticles. The introduction of nanoparticles into organic polymers offers an effective way to improve properties such as electrical conductivity, mechanical properties, thermal stability, flame retardancy, and resistance to chemical reagents. The properties of polymer composites depend on the nanoparticles that are incorporated, including their size, shape, concentration, and interactions with the polymer matrix. However, the lack of compatibility between inorganic particles and polymer matrix limits the applications of nanoparticles in composites. As a result of incompatibility, the dispersion of synthesized inorganic nanoparticles in polymer matrices is very difficult, and particles with specific surface area and volume effects can form aggregates. Therefore, it is necessary to modify the particles to overcome their tendency to aggregate and improve their dispersion in polymer matrices. Two ways are used to modify the surface of inorganic particles: modification of the surface by chemical treatment and the grafting of functional polymeric molecules to the hydroxyl groups existing on the particles. By surface modification of nanoparticles the dispersion of inorganic nanoparticles in organic solvents and polymer matrices is improved.

Keywords Nanoparticles · Organic–inorganic nanocomposites · Surface modification

R.Y. Hong (✉)

School of Chemical Engineering, Fuzhou University, Fuzhou 350108, China

College of Chemistry, Chemical Engineering and Materials Science & Key Laboratory of Organic Synthesis of Jiangsu Province, Soochow University, SIP, Suzhou 215123, China
e-mail: rhong@suda.edu.cn

Q. Chen

College of Chemistry, Chemical Engineering and Materials Science & Key Laboratory of Organic Synthesis of Jiangsu Province, Soochow University, SIP, Suzhou 215123, China

Contents

1	Introduction	3
2	Synthesis of Nanoparticles	5
2.1	Solid-State Reaction	5
2.2	Molten Salt Synthesis	5
2.3	Sol–Gel Processing	6
2.4	Hydrothermal Method	7
2.5	Co-precipitation	7
2.6	Thermal Evaporation	7
2.7	Plasma Methods	8
2.8	Other Methods	8
3	Modification of Nanoparticles	9
3.1	Chemical Treatments	9
3.2	Grafting Functional Polymeric Molecules	10
4	Preparation of Polymer/Inorganic Nanocomposites	12
4.1	Solution Blending	12
4.2	Melt Blending	13
4.3	In Situ Polymerization	14
5	Preparation of Polymer/Inorganic Nanocomposites	15
6	Synthesis, Characterization, and Application of Nanoparticles	16
6.1	Magnetic Suspensions	17
6.2	ZnFe ₂ O ₄ Nanoparticles	19
6.3	BST Nanoparticles	19
6.4	ZnO Nanoparticles	22
6.5	Antimony-Doped Tin Oxide	25
6.6	Silica Nanoparticles	26
6.7	Multiwalled Carbon Nanotubes	27
6.8	Carbon Black Nanoparticles	30
6.9	ABS/EPDM Composites Filled with Carbon Black	32
7	Conclusions and Prospects	34
	References	35

Abbreviations

ABS	Acrylonitrile-butadiene-styrene
ATO	Antimony-doped tin oxide
ATRP	Atom transfer radical polymerization
BADCy	Bisphenol-A dicyanate [2,2-bis (4-cyanatophenyl) isopropylidene]
BFN	BaFe _{0.5} Nb _{0.5} O ₃
BST	Ba _x Sr _{1-x} TiO ₃
BSTO	Barium strontium titanyl oxalate [Ba _{1-x} Sr _x TiO(C ₂ O ₄) ₂ ·4H ₂ O]
CB	Carbon black
CE	Cyanate ester
CNF	Carbon nanofiber
CNT	Carbon nanotube
CTAB	Hexadecyltrimethyl-ammonium bromide
DBP	Dibutyl phthalate
DSC	Differential scanning calorimetry

EPDM	Ethylene-propylene-diene rubber
FF	Ferrofluid
FTIR	Fourier transform infrared spectroscopy
GMA	Glycidyl methacrylate
h-BaTiO ₃	Hydroxylated BaTiO ₃
HBP	Hyperbranched aromatic polyamide
IAAT	Isopropyl tris(<i>N</i> -amino-ethyl aminoethyl)titanate
iPP	Isotactic polypropylene
KH550	3-Aminopropyl triethoxysilane
KH570	γ -Methacryloxypropyltrimethoxysilane
MAH	Maleic anhydride
MF	Magnetic fluid
MMA	Methyl methacrylate
MMT	Montmorillonite
MRF	Magnetorheological fluid
MWCNT	Multiwalled carbon nanotube
PA6	Nylon 6
PC	Polycarbonate
PCL	Poly(caprolactone)
PLA	Poly(lactic acid)
PMMA	Poly(methyl methacrylate)
PP	Polypropylene
PP-g-MA	Poly(propylene- <i>graft</i> -maleic anhydride) copolymer
PPS	Polyphenylene sulfide
PS	Polystyrene
PU	Polyurethane
PVDF	Poly(vinylidene fluoride)
PVDF-HFP	Poly(vinylidene fluoride- <i>co</i> -hexafluoropropylene)
PVP	Polyvinylpyrrolidone
SEM	Scanning electron microscopy
SWNT	Single-walled carbon nanotube
TBP	Tributyl phosphate
TEM	Transmission electron microscopy
TESPT	Bis(triethoxysilylpropyl)tetrasulfane
TG	Thermogravimetric
T_g	Glass transition temperature
XRD	X-ray powder diffraction
ZnFe ₂ O ₄	Zinc ferrite

1 Introduction

Recently, polymer-based nanocomposites have become incredibly important due to their unique properties and numerous applications in modern technology. The properties of polymer composites are mostly a simple combination of the properties

of incorporated inorganic fillers and the polymer matrix. The properties of conventional polymers such as electrical conductivity, dielectric and mechanical properties, thermal stability, flame retardancy, and resistance to chemical reagents are improved by the addition of a certain amount of the fillers.

However, a homogeneous distribution of inorganic fillers in the polymer resin is not always obtained due to the poor compatibility between inorganic filler and polymer matrix. There is no chemical bonding between the nanoparticles and the polymer matrices, which may restrict the application of these nanocomposites in many fields. To take advantage of the properties of nanoparticles, the surface of the nanoparticles must be modified. Surface modification not only improves the inherent characteristics of the nanoparticles, but also allows preparation of composite materials inexistent in nature. As a result, excellent integration and an improved interface between inorganic filler and the polymer matrix can be obtained. These modified nanoparticle/polymer nanocomposites exhibit good physical and chemical properties. Furthermore, surface modification can reduce the consumption of expensive master particles, thus lowering the production cost. For example, the hydrophilic nature of fibers often results in poor compatibility with hydrophobic polymer matrices. Therefore, it is necessary to modify the nanoparticle surface for better binding between nanoparticles and matrix. The modified fiber/polymer composites open the way towards intense and promising research, with an expanding area of potential applications that include nanocomposite materials, paper and paperboard additives, biomedical applications, and adsorbents [1–4].

Traditional surface modification of nanoparticles can be classified into chemical treatments and polymer grafting approaches. The latter includes “grafting-from” and “grafting-to” processes, and the coated polymer layer on the surface of nanoparticles is uniform. The traditional techniques have been used successfully in modifying nanoparticles, with the significant advantage that a covalent bond is formed by chemical reaction between the hydrophilic groups on the surface of the nanoparticles and the organic long-chained molecules or polymer.

Modification technology covers many research fields (including chemical engineering, physics, chemistry, material science, and engineering,) and complex processes. Although many studies have been discussed in this realm, there still lacks a systematic study. It is high time to make comprehensive use of the theories of chemical engineering, physics, and chemistry and make a systematic summary of the existing modification technologies so as to widen their application. This is a new field of chemical engineering and material science. A review of the modification technologies can help the research and application of nanocomposites.

In this work, we introduce nanoparticle/polymer matrix composites to the readers, in combination with our research experience. In order to fully describe the nanoparticle/polymer matrix composites, we will discuss the synthesis and modification of nanoparticles and the preparation, characterization, and applications of nanoparticle/polymer matrix composites.

2 Synthesis of Nanoparticles

Many techniques have been developed for the synthesis of nanoparticles, such as solid-state reactions [5–14], molten salt synthesis [15–21], hydrothermal methods [22–29], sol–gel processing [30–36], co-precipitation [37–46], thermal evaporation [47–50], plasma methods [51–54], chemical vapor deposition [55–60], pulsed laser deposition [61–66], and magnetron sputtering [67–72].

2.1 Solid-State Reaction

The solid-state reaction has the advantages of low cost and simple operability.

Wu et al. [73] prepared $\text{Ba}_x\text{Sr}_{1-x}\text{TiO}_3$ (BST) nanoparticles via solid-state techniques by heating stoichiometric amounts of the raw materials BaCO_3 , SrCO_3 , and TiO_2 . The BST ceramics showed good dielectric properties at both low frequencies and microwave frequency (2 GHz).

Shao et al. [74] prepared BaTiO_3 ceramic with a high piezoelectric coefficient by solid-state reaction, and found that the ceramic showed good dielectric properties.

However, the conventional method suffers from a variety of issues, such as chemical inhomogeneity, the formation of larger grain sizes, long ball milling (usually taking more than 12 h of high energy ball milling), and a high treating temperature.

2.2 Molten Salt Synthesis

Compared with the traditional sintering method, the molten salt method is one of the simplest methods for controlling the morphology of particles and obtaining highly reactive powders of a single phase at low temperatures in a short soaking time. This is because the molten salt can accelerate the reaction kinetics at this low temperature and facilitate the formation of ceramic particles.

Zhou et al. [75] prepared $\text{Ba}_5\text{Nb}_4\text{O}_{15}$ nanoparticles in molten salt with NaCl and KCl in a molar ratio of 1:1 at 650°C for 2 h. The success of this method was attributed to the enhanced diffusion coefficients in the molten chloride liquid phase. Furthermore, the ratios of precursor and NaCl - KCl salt had no influence on the phase formation of $\text{Ba}_5\text{Nb}_4\text{O}_{15}$.

$\text{K}_x\text{Na}_{1-x}\text{NbO}_3$ nanoparticles were synthesized by the molten-salt method in $\text{Na}_2\text{CO}_3/\text{K}_2\text{CO}_3$ flux at a low temperature of 650 – 900°C [76]. The morphology of $\text{K}_x\text{Na}_{1-x}\text{NbO}_3$ nanoparticles was affected by the synthesizing temperature and salt-to-oxide ratio. Because of the increased driving force of grain growth in the liquid state of the salts, the diffusion and transport rate of the mixed oxides was enhanced, which led to an increase in particle size with an increase in calcination temperature.

As the salt-to-oxide weight ratios increased, the molten flux was enough to separate the individual growing grains and agglomeration decreased. On the other hand, the large amount of molten liquid promoted the solubility and ion exchange rate of particles, which led to larger particle growth space and, as a result, the average particle size increased.

Compared with the conventional method, the ceramic prepared from the molten-salt route showed better dielectric properties. Tawichai et al. [77] reported $\text{BaFe}_{0.5}\text{Nb}_{0.5}\text{O}_3$ (BFN) ceramics that were obtained at 700°C . Because the ceramics prepared by the molten-salt method had a higher density (6.12 g/cm^3) than the ceramics prepared by the traditional sintering method (4.60 g/cm^3), a very high dielectric constant with low loss tangent was observed.

The type of molten salt plays an important role in controlling the phase composition and morphology of the resultant nanoparticles. Chen and Zhang [78] synthesized $\text{CaCu}_3\text{Ti}_4\text{O}_{12}$ ceramic nanoparticles by heating stoichiometric amounts of CaCO_3 , CuO , and TiO_2 in molten $\text{Na}_2\text{SO}_4/\text{K}_2\text{SO}_4$ or NaCl-KCl .

Pure perovskite phase $\text{Ba}_{0.7}\text{Sr}_{0.3}\text{TiO}_3$ nanoparticles were synthesized by the molten-salt method in NaCl-KCl flux at a low temperature of 850°C . The molten salts accelerated the formation of the $\text{Ba}_{0.7}\text{Sr}_{0.3}\text{TiO}_3$, and the calcination temperature played an important role in the development of BST particle morphology [79].

Li et al. [80] reported SrTiO_3 submicron crystallites and nanocrystals from a starting raw material of TiO_2 powder (submicron or nanosized) at 700°C by an eutectic NaCl-KCl molten-salt method, and found that TiO_2 played an important role in the morphology and size of the obtained SrTiO_3 .

2.3 Sol–Gel Processing

The wet chemistry methods have attracted increasing attention because homogeneous BST nanoparticles are necessary for the development of uniform microstructures with desired properties. Nanometer-scaled and well-dispersed BST powders have been successfully synthesized by wet chemistry methods.

Sol–gel processing is suitable for preparation of BST nanoparticles. Fuentes et al. [81] synthesized $\text{Ba}_{1-x}\text{Sr}_x\text{TiO}_3$ nanoparticles by the sol–gel hydrothermal process using different mole ratios of barium and strontium starting reactants and investigated the structure, morphology, and oxidation state of the samples. Chen et al. [82] synthesized $\text{Ba}_{0.75}\text{Sr}_{0.25}\text{Ti}_{0.95}\text{Zr}_{0.05}\text{O}_3$ nanoparticles with a uniform chemical composition and high surface area by the sol–gel process. Maensiri et al. [83] successfully produced $\text{Ba}_{0.6}\text{Sr}_{0.4}\text{TiO}_3$ nanoparticles using the sol–gel method and electrospinning techniques.

2.4 Hydrothermal Method

The raw material of the sol–gel method is expensive and sensitive to moisture; furthermore, the process is complex to handle and the power is normally amorphous. By contrast, the cost of the hydrothermal method is low, BST nanoparticles are synthesized at low temperature, and the agglomeration can be reduced. But, the shortcoming of this method is the unmanageable stoichiometry of the final particles.

Razak et al. [84] prepared $\text{Ba}_x\text{Sr}_{1-x}\text{TiO}_3$ nanoparticles using a hydrothermal route and discussed the effects of the Ba:Sr ratio, (Ba+Sr): TiO_2 ratio, and the reaction time on the resultant particles. In addition, Deshpande and Kholam [85] synthesized $\text{Ba}_{0.75}\text{Sr}_{0.25}\text{TiO}_3$ nanoparticles by a microwave–hydrothermal route with faster crystallization, shorter synthesis time, and higher purity compared with the conventional hydrothermal route.

2.5 Co-precipitation

The use of a large excess of barium and strontium precursors and low yield are the disadvantages of the hydrothermal method. The problems can be solved by a simple co-precipitation method. Using a simple one-step cation-exchange reaction, Kholam et al. [86] prepared barium strontium titanyl oxalate (BSTO) [$\text{Ba}_{1-x}\text{Sr}_x\text{TiO}(\text{C}_2\text{O}_4)_2-4\text{H}_2\text{O}$] precursor powder and then produced the BST nanoparticles by the pyrolysis of BSTO at 730°C for 4 h in air. They studied the ceramic by sintering BST pellets at $1,300^\circ\text{C}$ for 4 h and demonstrated a dielectric constant of 9,500 along with a dielectric loss of 0.0015 at the measurement frequency of 1 kHz.

Zuo et al. [87] prepared homogeneous 60–90 nm $\text{Ba}_{0.6}\text{Sr}_{0.4}\text{TiO}_3$ nanoparticles with fine characteristics at a low synthesis temperature of 650°C by a citrate method with ammonium nitrate addition.

2.6 Thermal Evaporation

Most of the synthesis methods for nanoparticles have the disadvantages of impurities, expensive raw materials, special conditions, tedious procedures, long reaction times, and not being environmentally friendly. The drawbacks limit the commercial use of nanoparticles; however, the simple synthesis and inexpensive method of thermal evaporation overcomes some of the shortcomings of previous methods. Pan et al. [88] prepared silicon-based nanostructures with different colors, morphologies, and microstructures over a wide temperature range of $890-1,320^\circ\text{C}$ by thermal evaporation of SiO_2 powder at $1,350^\circ\text{C}$ for 5 h.

2.7 *Plasma Methods*

In the last few years, the preparation and modification of inorganic powders via plasma methods have become increasingly important for engineering materials. Plasma can be generated by the glow discharge method, produced by exciting a gas with electrical energy to form a collection of charged particles containing positive and negative ions and a region filled with high-energy species such as electrons, radicals, and activated atoms. Plasma gases such as argon, helium, oxygen, nitrogen, and hydrogen can be used to produce nanoparticles with unique surface morphology, and the particles can be applied in various fields [89–92].

Iijima discovered carbon nanotubes (CNTs) in the soot of the arc-discharge method in 1991 [93]. CNTs synthesized with discharge plasma have attracted intense attention both theoretically and experimentally due to their wide range of potential applications [94–97]. Meanwhile, other carbon nanomaterials such as carbon nanoparticles [98], diamond-like carbon films [99], carbon nanofibers [100], and nano-onions [95, 101] have also been produced by the plasma method. However, the conventional plasma method has the serious drawback for commercial use of being a non-continuous process. Of all carbon materials, only the preparation of carbon black has been industrialized. The carbon black manufacturing processes can be classified into two routes: thermal decomposition and incomplete combustion of hydrocarbons. Although the furnace process has been used to produce carbon black for decades, it gives poor yields and serious environmental problems. Therefore, plasma technology has emerged and researchers have devoted themselves to improving the electrical conductivity of carbon black and to achieving a continuous and cleaner process in the arc discharge method. Liu et al. [102] reported that the diameter of carbon black particles could be improved and the reaction time prolonged from the stabilized AC arc by adjusting the electrical current.

2.8 *Other Methods*

Chemical vapor deposition has the advantage of allowing the scalable production of large-sized and high-quality graphene with controlled thickness. Furthermore, it can be used to design spatial structures for various applications [103]. Pulsed laser deposition is the most promising method for growing oxides such as high-quality ZnO because it is a high-speed deposition process under a high partial pressure of oxygen [104].

The use of reactive magnetron sputtering allows more control of the structure and properties of the films due to the ease of adjusting deposition conditions [105].

3 Modification of Nanoparticles

Inorganic nanoparticles have many amazing physical properties and novel polymer/inorganic nanocomposites can be achieved by adding functional nanoparticles into a polymer matrix using a small percentage of filler. However, the homogeneous dispersion of nanoparticle in composites is a challenge because of the immiscibility of polymer and nanoparticles. Single primary nanoparticles tend to aggregate; furthermore, their lipophobic properties result in performance loss of the composites. The ability to keep nanoparticles isolated and uniformly dispersed is crucial in creating composites that retain the fluidity of the host polymer while incorporating a high fraction of inorganic particles with their associated properties. In this system, competition between particle–particle, particle–matrix, and matrix–matrix associations have to be balanced. Therefore, it is necessary to modify the nanoparticles to avoid clustering of particles in polymer nanocomposites. Surface modification of inorganic particles is a popular technique because it produces excellent integration and an improved interface between inorganic filler and the polymer matrix [106].

There are two main approaches for modification of the surface of the nanoparticles: (i) modification of the surface of the inorganic particles by chemical treatment and (ii) grafting of functional polymeric molecules to the hydroxyl groups existing on the particles. By the two methods, nanoparticle agglomeration due to their large surface area and high surface energy is alleviated, and the dispersion stability of nanoparticles in polymer matrices is improved. Besides, plasma is also intensely reactive and can modify the surfaces of particles. Thus, the particle surfaces become more or less wettable, harder, rougher, and even more conducive to adhesion.

3.1 Chemical Treatments

For chemical treatment, different silane coupling agents are usually used, e.g., 3-aminopropyl triethoxysilane (KH550) and γ -methacryloxypropyltrimethoxysilane (KH570). By the hydrolytic process, the silane coupling agent molecule can react chemically with the acid anhydride groups of inorganic particles and bind strongly to particles. As the organic groups are introduced into the particles, the steric-hindrance effect of grafting of macromolecules reduces aggregation and allows better dispersion between the modified nanoparticles and polymer matrix.

Dang et al. [107] used a silane coupling agent (KH550) as a bridge-linked active agent between the high dielectric constant materials BaTiO_3 and polyvinylidene fluoride. The dispersion stability of BaTiO_3 particles in the nanocomposite was improved due to the introduction of KH550. In addition, the dielectric properties of the composites with KH550-modified BaTiO_3 were better than those of the composite with raw BaTiO_3 . Ma et al. [108] successfully accomplished the surface

modification of low-cost brucite with KH550 to enhance the compatibility of polypropylene (PP) and brucite. As a result, the susceptibility of the composite material to fire, the tensile strength, and the impact strength were significantly improved compared with unmodified PP/brucite.

Wang [109] reported org-attapulgit first modified by KH570 and then poly (butyl acrylate) grafted to polymerize. The silane coupling agent interacted with hydroxyl groups existing on the surface of the attapulgit, which improved the dispersion effect of inorganic filler in the polyolefin polymer.

The coupling mechanism of titanate coupling agent is similar to that of silane coupling agent; hydrolysable alkyl has the same effect as silane coupling agent. However, the coupling effect is better for thermoplastic polymers, and the best performance in terms of yield stress and flexural strength is observed in nanocomposites. Bose and Mahanwar [110] carried out surface modification of the ash by-product flyash with titanate coupling agent (tetra-isopropyl titanate) and found that the uniform dispersion of filler particles of flyash in the nylon 6 was enhanced.

3.2 Grafting Functional Polymeric Molecules

The surface modification of nanoparticles by grafting functional polymeric molecules is another promising approach for overcoming the incompatibility of the components of organic–inorganic nanocomposites. In contrast to physically coating the fabric, different molecular chains are grafted to the nanoparticle surface by means of strong covalent bonding. As a result, the modified nanoparticles become hydrophobic, and therefore the miscibility of the filler and nanoparticles is enhanced, which can be attributed to the covalent attachment of polymers. The polymers penetrate the particles and the further separation of nanoparticles also partially results from steric hindrance.

The methods for obtaining polymer chains grafted onto the surface of nanoparticles can be divided into two classes: “grafting-from” and “grafting-to” processes. In the former method, the nanoparticle surface is modified with functional groups by the reaction between molecules and particles, and then the molecules begin the polymerization processes via radical, cationic, or anionic polymerization. In the latter method, the groups at the end of preformed polymers react with the nanoparticle surface.

3.2.1 The “Grafting-from” Method

This method of surface graft polymerization usually includes two steps: surface activation and graft polymerization. Sites on the nanoparticle surface are first activated by high-energy electrons, plasma treatment, chemical reactions, etc. and, subsequently, the graft polymerization process is generated.

Hong et al. [111] modified ZnO nanoparticles by grafting polystyrene (PS) onto the surface of particles. This procedure contained two steps: first, the surface of ZnO nanoparticles was activated by KH570, and second, PS was grafted to the surface-activated ZnO nanoparticles through typical solution polymerization. Hong et al. [112] also investigated the radical polymerization of methyl methacrylate (MMA) on the surface of ZnO particles to which the functional double bond had first been introduced.

3.2.2 The “Grafting-to” Method

The “grafting-to” method (without involving elaborate synthetic procedures) involves a chemical reaction between (end)-functionalized polymers and complementary reactive groups on the surface of nanoparticles. The reactive polymers can be synthesized by controlled radical, anionic, or other polymerization techniques. Compared with other polymer attachment techniques, the (end)-functionalized polymer can be thoroughly characterized via various chemical and physical methods. However, the major shortcoming of this method is the low maximum thickness of the obtained polymer layers [113].

Qin et al. [114] prepared functionalized single-walled carbon nanotubes (SWNTs) through treatment of polystyrene via the “grafting-to” method. The results showed that the PS was covalently attached to the side walls of SWNTs. The poly(vinylidene fluoride-*co*-hexafluoropropylene) (PVDF-HFP) was functionalized with glycidyl methacrylate (GMA) via atom transfer-radical polymerization (ATRP) and the BaTiO₃ nanoparticles were modified by amino-terminated silane molecules. Then, the nanocomposites with high dielectric constant and high thermal conductivity were prepared by a “grafting to” method [115].

3.2.3 Plasma Surface Modification

The plasma method is also used to treat the nanoparticle surface. The main advantage of this treatment is in modifying the chemical and physical structure of the surface without influencing the bulk properties of the powder. However, the main limitation of plasma modification is that experimental environment requires a relatively complicated vacuum system. To date, much attention has been paid to low pressure plasma and nonthermal atmospheric pressure plasma methods [116, 117]. Atmospheric plasma has no need for expensive vacuum equipment; furthermore, its system is simple, efficient, and the operation is easy to study. The atmospheric pressure discharge methods include discharge jet, radio frequency discharge, and dielectric barrier discharge [118]. Compared with the traditional modification methods such as acid oxidation and polymer wrapping, the plasma method is environmentally benign and easy to scale up for industrial and

commercial use [119]. In conclusion, plasma treatment is the most versatile surface treatment technique and the surfaces of different materials can be readily and efficiently modified with plasma [120, 121]. In practical application in polymer materials, there are three ways of using plasma technology to modify the surface properties: plasma surface treatment, graft copolymerization, and polymerization [122, 123]. Researchers have also applied plasma techniques to treat the surface of carbon-based materials such as activated carbon, carbon fibers, and carbon nanotubes [124–126].

4 Preparation of Polymer/Inorganic Nanocomposites

The method of nanocomposite preparation has a great influence on the properties of the resulting composite. The methods mainly used are solution blending, melt blending, and in situ polymerization.

4.1 Solution Blending

First, the nanoparticles are added after the base resin is dissolved in solvent. The obtained mixture is agitated to prepare a uniform suspension. The nanocomposites are prepared by removing the solvent or polymerizing the monomer.

Manchado et al. [127] described the synthesis of layered silicate/natural rubber nanocomposites by mechanical and solution mixing. It was found that the filler and the polymer show good compatibility by solution blending. Addition of a coupling agent, namely bis(triethoxysilylpropyl)tetrasulfane (TESPT), could improve the adhesion between the filler and elastomer.

Chae and Kim [128] showed that the hydrophilic ZnO nanoparticles could be homogeneously dispersed in the hydrophobic PS matrix by solution blending.

Wu et al. [129] prepared biodegradable poly(lactic acid) (PLA)/organically modified montmorillonite (m-MMT) nanocomposites by solution blending, the most critical part of this process being the modification of the MMT. The MMT was first treated with hexadecyltrimethyl-ammonium bromide (CTAB) cations, and then modified with biocompatible and biodegradable chitosan. As the chemical similarity between m-MMT and PLA was improved, the m-MMT became well separated in the PLA matrix.

Shen et al. [130] prepared maleic anhydride grafted polypropylene (PP)/expanded graphite nanocomposites by solution blending. The conductive performance of PP was improved significantly.

4.2 Melt Blending

Melt blending and hot pressing processes are feasible and are more reproducible, economic, and environmentally benign methods for preparation of ceramic/polymer composites. Compared with the solution cast composites, the process is utilized to eliminate porosity and improve the uniformity of the composites. As a result, a dense composite could be obtained by modifying the ceramic filler. However, there is a danger of scalding during the operating process.

Thomas et al. [131] explored the possibility of obtaining a dielectric constant as high as 740 at 1 kHz for a composition of 50 vol% $\text{CaCu}_3\text{Ti}_4\text{O}_{12}$ and 50 vol% poly(vinylidene fluoride) by melt blending and hot pressing processes. Yang et al. [132] investigated the effect of nano- and microsized calcium copper titanate particles on the dielectric properties of composites obtained by hot pressing. Channal and Jog [133] prepared PVDF/ BaTiO_3 (10–30 wt%) nanocomposites using a simple melt blending method. Furthermore, the molecular relaxations in the nanocomposites were studied.

For nanoparticle/polymer composites using melt blending, the particles are difficult to disperse in the matrix due to strong van der Waals forces and the agglomeration of nanoparticles. The effect of different synthesis conditions (such as temperature, rotation, and time) on the mechanical properties has an impact on the dispersion of nanoparticles.

Pötschke et al. [134] discussed the different amounts of multiwalled carbon nanotube (MWNT)/polycarbonate (PC) composites obtained by melt blending. They emphasized the effects of blending conditions such as screw speed and blending time at percolation threshold. In addition, MWNTs were distributed uniformly in the PC matrix and significant agglomeration or clustering did not appear with long mixing (15 min) and low speed (50 rpm). Villmow et al. [135] studied poly(caprolactone) (PCL)/MWCT composites obtained at different rotations by melt blending. When the composites were filled with 0.5 wt% MWCTs under the selected processing temperature and blending time, the best dispersion was achieved at 75 rpm, which led to the lowest resistivity and optimum material properties. The “grafting to” approach was used to treat CNTs and, subsequently, MWNT/PMMA nanocomposites were produced; the mechanical properties were improved apparently due to high interfacial strength [136].

Haggenmueller et al. [137] demonstrated the preparation of SWNT/PMMA composites by two types of mixture methods. SWNTs were well distributed in the PMMA matrix by a combination of solvent casting and melt mixing.

In general, silane-coupling agent is used to modify the surface of nanoparticles to enhance the compatibility of nanoparticles and polymers and to improve the mechanical properties of the resulting nanocomposites. The results of melt blending are often ideal. Bikiaris et al. [138] studied the better dispersion of silica in isotactic polypropylene (iPP) matrix by adding poly(propylene-*graft*-maleic anhydride) copolymer (PP-*g*-MA) containing 0.6 wt% maleic anhydride as compatibility enhancer. This phenomenon could account for the reaction between the maleic

anhydride and the surface hydroxyl of SiO_2 , so the agglomeration of nanoparticles was reduced. Characterization by scanning electron microscopy (SEM), transmission electron microscopy (TEM), and mechanical analysis confirmed this conclusion.

Thermoplastic polymer polyphenylene sulfide (PPS)/BST composites were obtained with various BST contents. Particles were uniformly dispersed in PPS matrix using a twin-screw extruder, and composites with 70 wt% BST had a dielectric constant and dielectric loss of 13.5 and 0.0025, respectively, at 1 GHz [139]. Li et al. [140] embedded $\text{Ba}_{0.6}\text{Sr}_{0.4}\text{TiO}_3$ /silver core-shell nanoparticles into PVDF matrix. The silver-coated $\text{Ba}_{0.6}\text{Sr}_{0.4}\text{TiO}_3$ /PVDF nanocomposites showed 73% higher dielectric constant than composites of bare BST; meanwhile, the dielectric loss was still low (less than 0.2) at 55 vol% filler content.

Chao and Liang [141] investigated the effect of different weight fraction of KH550 on BaTiO_3 and BaTiO_3 /bisphenol-A dicyanate [2,2-bis(4-cyanatophenyl)isopropylidene] (BADCy) composites and discussed the dielectric properties of BaTiO_3 /BADCy composites at different frequencies. Wu et al. [142] reported novel permittivity gradient composites of MCNT/cyanate ester (CE) resin by the gravity sedimentation method. Compared with untreated MCNTs, the surface-treated nanotubes showed good compatibility with CE. Thus, the surface-treated MCNT/CE composites showed much lower dielectric loss than untreated MCNT/CE composites.

Sui et al. [143] studied the uniform dispersion of carbon nanofibers (CNFs) in PP matrix using a twin-screw extruder by means of the high shear compounding of melt blending. In addition, CNF/PP nanocomposites containing 5 wt% CNFs showed a surprisingly high dielectric constant and low dielectric loss at a wide range of frequencies.

4.3 In Situ Polymerization

Compared with other methods, the method of in situ polymerization has the advantage of better compatibility of the systems, and the composites show good dispersion and mechanical properties.

Potts et al. [144] investigated the morphology and thermomechanical properties of composites of poly(methyl methacrylate) (PMMA) and chemically modified graphene filler using an in situ polymerization method. The nylon-6 (PA6)/graphene composites were prepared by in situ polymerization of caprolactam in the presence of graphene oxide. The Young's modulus and tensile strength of the composite fibers were greatly improved at very low graphene content [145].

5 Preparation of Polymer/Inorganic Nanocomposites

Ferroelectric ceramics have extensive applications in tunable devices such as filters, varactors, phase shifters, and phase array antennas [146]. This is due to their high dielectric constant, low dielectric loss, and thermal stability. However, the conventional ceramics of large dielectric permittivity suffer from low electric breakdown strength, brittleness, and processing difficulty. On the other hand, the polymer matrix has the advantages of high flexibility, large breakdown strength, good processability, and great mechanical strength, but has a very low dielectric constant of less than 10. Therefore, the new composites have attracted attention by combining the merits of dielectric ceramic and polymer matrix.

For practical use, over 50 vol% of the ceramic powder is often required to be added into the polymer matrix, so the high ceramic powder loading spoils the superior properties of composites. Besides, at the high concentration of ceramic filler, due to the difference in the surface characteristics between the inorganic filler and organic matrix, the ceramic filler is difficult to distribute homogeneously in the polymer matrix and the agglomeration of nanoparticles in the matrix is inevitable. As a result, the resulting composites generally have the disadvantages of high dielectric loss and low dielectric constant, and thus show low energy density and low energy efficiency. The shortcomings have negative influences on the dielectric properties of the nanocomposites. Therefore, it is necessary to modify the particles to overcome the aggregation and improve the dispersion of nanoparticles in the polymer matrix [147]. Many useful approaches have been proposed for the fabrication of homogeneous ceramic/polymer nanocomposites.

Luo et al. [148] reported $\text{Ba}_{0.95}\text{Ca}_{0.05}\text{Zr}_{0.15}\text{Ti}_{0.85}\text{O}_3$ /poly(vinylidene fluoride) (PVDF) composite films by solution blending through the surface modification of $\text{Ba}_{0.95}\text{Ca}_{0.05}\text{Zr}_{0.15}\text{Ti}_{0.85}\text{O}_3$ nanoparticles with dopamine as a coupling agent, and investigated the microstructure and dielectric properties of the resulting composites.

Yu et al. [149] fabricated homogeneous ceramic/polymer composites comprising BaTiO_3 filler (treated with PVP as surface modifier) and PVDF polymer matrix by solution blending. The results showed that the dielectric constant of composite could be 77 (1 kHz) obtained at a BaTiO_3 content of 55 vol%. The breakdown strength of BaTiO_3 /PVDF composite was found to be enhanced significantly at a low BaTiO_3 content of 10 vol%.

Wang et al. [150] investigated the effect of isopropyl tris(*N*-amino-ethyl aminoethyl)titanate (IAAT) on the dielectric properties of BaTiO_3 /polyethersulfone composites. The obtained composite with 50 vol% BaTiO_3 showed a high dielectric constant of 22.6 with a low dielectric loss of 0.018 at 100 kHz. In addition, the matrix possessed high thermal stability, which was attributed to the enhancement of interaction between the polyethersulfone matrix and the BaTiO_3 particles that limited the segmental movement of the polymer matrix.

Xie et al. [151] developed a core–shell strategy to prepare composites in which a two-step polymerization method was used. Hyperbranched aromatic polyamide (HBP) was first grafted onto the BaTiO_3 core, and then PMMA shell was grown from the active groups of HBP via ATRP. Compared with the conventional solution-blended BaTiO_3 /PMMA composite, the BaTiO_3 /HBP/PMMA composite had higher dielectric constant, lower dielectric loss and higher energy density.

Yu et al. [152] prepared BaTiO_3 /PVDF composite through the surface functionalization of BaTiO_3 particles with tetrafluorophalic acid. Because of the passivation layers on the surface of BaTiO_3 filler, which enhanced the compatibility of the filler and polymer matrix, a composite with improved electric breakdown strength, high energy density, and low dielectric loss was fabricated.

Zhou et al. [153] investigated the dielectric properties of surface-hydroxylated BaTiO_3 (h- BaTiO_3)/PVDF composites. Compared with crude BaTiO_3 /PVDF composite, the h- BaTiO_3 /PVDF composite showed lower loss tangent, higher dielectric strength, and weaker temperature and frequency dependences. The dielectric properties of the composites were improved due to the strong interaction between h- BaTiO_3 fillers and PVDF matrix.

Tang and Sodano [154] developed a new synthesis method with fast discharge speed to prepare nanocomposites composed of high aspect ratio $\text{Ba}_{0.2}\text{Sr}_{0.8}\text{TiO}_3$ nanowires and PVDF. The highest breakdown strength (>450 MV/m) and maximum energy density (14.8 J/cc) were achieved by quenching the 7.5% nanowire/PVDF composite in ice water.

Sonoda et al. [155] observed an increase in relative permittivity of BST/polymer composites by introducing aliphatic carboxylic acids onto the BST surface. The modified nanoparticles with longer carboxylic acid chains had better compatibility with the polymer matrix. In addition, the mechanical properties of modified BST powder/polymer composites were not affected.

6 Synthesis, Characterization, and Application of Nanoparticles

Nanoparticles have been widely used in optical, resonant, electrical, and magnetic fields. The small size effect, large surface effect, and quantum tunnel effect demonstrate the unique properties of nanoparticles. It is necessary to study the techniques of nanoparticle preparation to meet the developments in nanotechnology and nanomaterials. In this section, we describe work carried out in our laboratory on the syntheses of several nanoparticles and nanocomposites and the study of their properties.

6.1 *Magnetic Suspensions*

Magnetic suspensions, as a class of smart magnetic materials, can be divided into two broad categories [156]: (i) magnetic fluid (MF) or ferrofluid (FF), which is a suspension of magnetic nanoparticles (1–15 nm) in a nonmagnetic liquid; and (ii) magnetorheological fluid (MRF), which is a suspension of soft-magnetic micron-sized particles (1–20 μm) and magnetic nanoparticles (1–15 nm) in a carrier liquid. Due to the significant difference in particle size, MFs and MRFs exhibit distinctive rheological behaviors in an applied magnetic field [157].

6.1.1 **Magnetic Fluids and Their Biological Applications**

MFs show small changes in viscosity and do not develop a yield stress under application of a high magnetic field. Their applications are limited to those where only a low magnetoviscous response is required.

Images of MFs based on kerosene and silicone oil are shown in Figs. 1 and 2, respectively. These kinds of MF can be used in lubrication, cooling, and damping. MF of high-boiling-point hydrocarbon has already been used in speakers.

Recently, the preparation of functional magnetic nanoparticles (MNPs) has attracted interest due to their biological application in magnetothermal therapy, magnetofection, magnetic separation, drug delivery, and in-vivo medical imaging. Furthermore, composite microspheres consisting of an iron oxide core and a polymer shell have attracted attention for their unique magnetic responsiveness, good stability, and chemically modifiable surface. At the same time, the polymer shell can protect the naked MNPs from oxidation and can magnetically isolate individual particles. A polymer shell with abundant functional groups (such as amino, hydroxyl, carboxyl, and thiol groups) is suited to further functionalization by the attachment of various biological molecules [158].

6.1.2 **Magnetorheological Fluid**

MRF is capable of being reversibly changed from a liquid fluid to a viscoelastic solid, and the viscosity changes by several orders of magnitude in response to a magnetic field within milliseconds. This phenomenon is also referred to as the magnetorheological effect [159]. MRFs possess outstanding rheological characteristics, such as high yield stress and shear viscosity, which can be altered by tuning an external magnetic field. Therefore, MRFs have a wide range of technological applications, mainly in semi-active damping devices, magnetorheological finishing, mechanical seals, and aerospace materials. MRFs also exhibit potential applications in biotechnology and medicine, such as for drug delivery and cancer therapy.

Fig. 1 Image of kerosene-based magnetic fluid

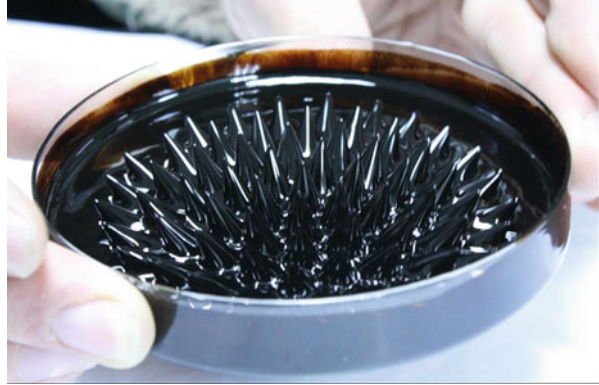
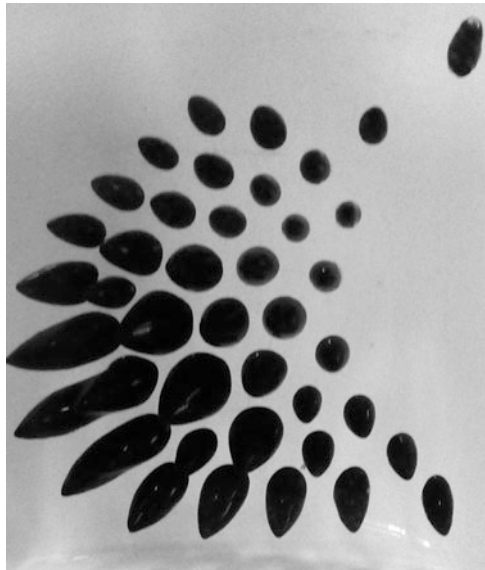


Fig. 2 Image of silicone oil-based magnetic fluid



Good MRFs should have certain features, including high magnetic saturation, stability against settling and aggregation, corrosion resistance, and temperature stability. High magnetic saturation mainly depends on the dispersed magnetic particles in the MRF. Carbonyl iron particles with relatively high saturation magnetization (2.1 T/212.7 emu/g) and low cost are more commonly used than other alloy and metal oxide powders. The temperature stability of MRF is closely related to carrier liquids. Typically, petroleum-based oils, silicone, mineral oils, polyesters, polyethers, and water are employed as carrier liquids.

6.2 $ZnFe_2O_4$ Nanoparticles

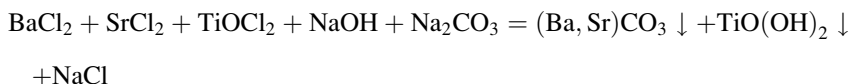
Zinc ferrite ($ZnFe_2O_4$) is of particular interest because of its remarkable magnetic [160], electrical [161], and optical properties [162]. These qualities make it a suitable material for high density magnetic recording, magnetic fluids, and hot-gas desulfurization. Moreover, $ZnFe_2O_4$, as a narrow band gap semiconductor (1.92 eV), is found to be a promising visible light photocatalyst [163]. The photocatalytic activity of the [110] crystal face of octahedral $ZnFe_2O_4$ nanoparticles is remarkable.

Octahedral $ZnFe_2O_4$ nanoparticles with size of about 50–150 nm were synthesized in our laboratory via a facile co-precipitation method. The crystal shape and morphology were determined by X-ray powder diffraction (XRD) and TEM techniques. Figure 3 shows the XRD patterns of $ZnFe_2O_4$ calcined at different temperatures, which indicate that the crystallization was complete at 800°C. The photocatalytic ability was characterized by the degradation rate of rhodamine-B solution with the addition of $ZnFe_2O_4$ nanoparticles. Figure 4 illustrates the UV-vis light absorption of pure rhodamine-B solution with and without zinc ferrite calcined at 800°C, showing that the nanoparticles calcined at 800°C had the best degradation rate.

6.3 *BST* Nanoparticles

6.3.1 Synthesis of *BST* Nanoparticles

Dielectric $Ba_{1-x}Sr_xTiO_3$ (*BST*) precursor was prepared by the co-precipitation of $TiOSO_4$, Ba^{2+} , and Sr^{2+} . $NaOH$ and $NaCO_3$ were used as precipitating agents to adjust the pH to 9. Inexpensive $TiOSO_4$ was used as the Ti source. After reaction for 180 min, the precipitate was washed with alcohol once, and then dried for about 12 h in an electric oven at 100°C to obtain the dried precursor powder. The dried powder was calcined at 950°C for 4 h. The residue solids were washed with deionized water to remove the remaining salts and dried in air at 100°C for 12 h. $Ba_{0.5}Sr_{0.5}TiO_3$ powder was obtained as follows:



At around 800°C, the melting of NaCl raised the local temperature and thus accelerated the kinetics and facilitated the formation of $Ba_{0.5}Sr_{0.5}TiO_3$ phase.

The obtained $Ba_{1-x}Sr_xTiO_3$ nanoparticles were characterized by thermogravimetric (TG) analysis, Fourier-transform infrared spectroscopy (FTIR), TEM, XRD, and SEM. The post-calcining treatment was at the low temperature of 950°C, which was about 200°C lower than that of the conventional solid-state

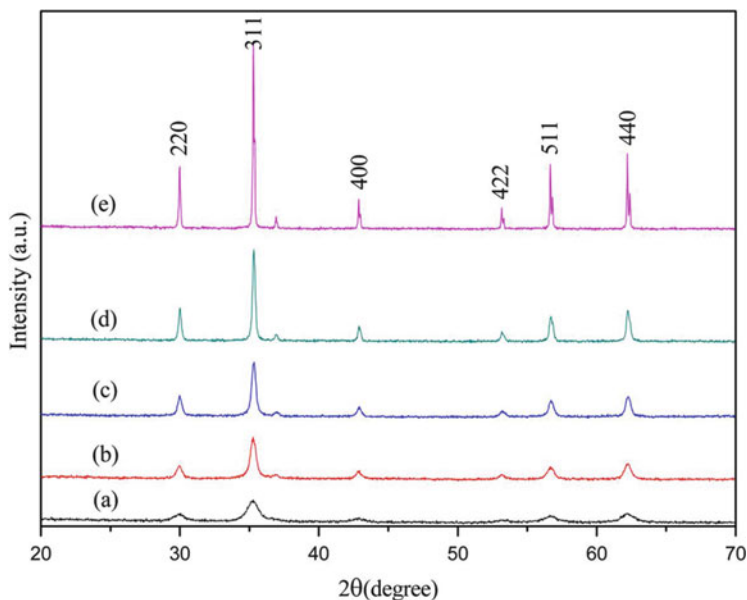


Fig. 3 X-ray diffraction patterns of ZnFe₂O₄ obtained at different calcinations temperatures: (a) 400°C, (b) 500°C, (c) 600°C, (d) 700°C, and (e) 800°C

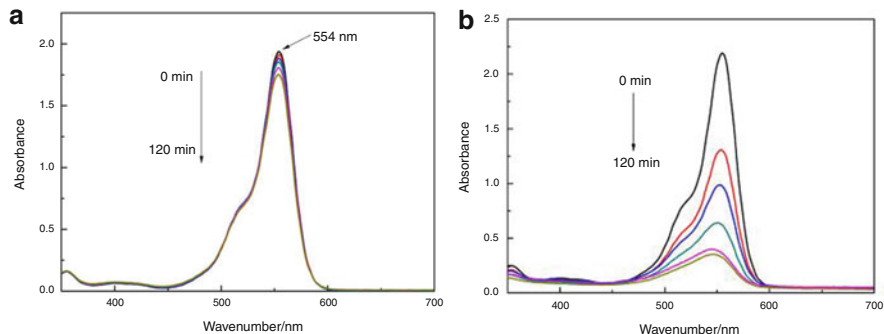
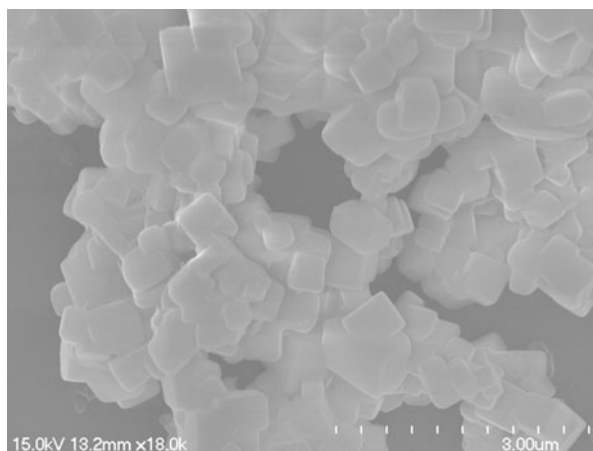


Fig. 4 UV-vis absorption spectrum of rhodamine-B without zinc ferrite (a) and with the addition of 10 mg zinc ferrite calcined at 800°C (b) after 120 min photocatalytic reaction

method. The precipitates of (Ba, Sr)CO₃ were calcined at 950°C for 4 h in air and the XRD analysis showed that the prepared Ba_{0.5}Sr_{0.5}TiO₃ nanoparticles had the finest crystallization with a larger crystal parameter α , which results in bigger unit cell volume and average crystal size. Figure 5 shows an SEM image of calcined nanoparticles, demonstrating that the molten salt synthesis could assist the formation of dispersive cubic morphologies.

Fig. 5 SEM micrograph of $\text{Ba}_{0.5}\text{Sr}_{0.5}\text{TiO}_3$ powder



6.3.2 Modification of BST Nanoparticles

For the BST nanoparticles, the poor compatibility between inorganic particles and polymer matrix does not always yield a homogeneous distribution of inorganic filler. Therefore, it is necessary to modify the particles to reduce the aggregation and improve the dispersion of nanoparticles in the polymer matrix.

The BST nanoparticles were modified by the “grafting from” approach. The nanoparticles were first activated by acrylic acid, so the nanoparticle surface was modified with functional groups by the reaction between the molecule and particles. Then, the PS molecule began the polymerization processes via radical polymerization, so PS was grafted onto $\text{Ba}_{0.5}\text{Sr}_{0.5}\text{TiO}_3$ nanoparticles. The mode of preparation of PS-grafted $\text{Ba}_{0.5}\text{Sr}_{0.5}\text{TiO}_3$ nanoparticles is shown in Fig. 6.

6.3.3 Preparation of BST/PS Nanocomposites

The BST powder was added into the PS matrix by solution blending. The modified BST powder was added after the PS resin was dissolved in tetrahydrofuran solvent. The obtained suspension mixture was stirred for 2 h by means of ultrasonic oscillation at 20°C. The nanocomposites were prepared after removing solvent completely. An SEM micrograph of the nanocomposite is shown in Fig. 7; because of the good compatibility between bare $\text{Ba}_{0.5}\text{Sr}_{0.5}\text{TiO}_3$ and PS matrix, few pores were observed. Furthermore, the PS-grafted $\text{Ba}_{0.5}\text{Sr}_{0.5}\text{TiO}_3$ show good distribution in the PS matrix.

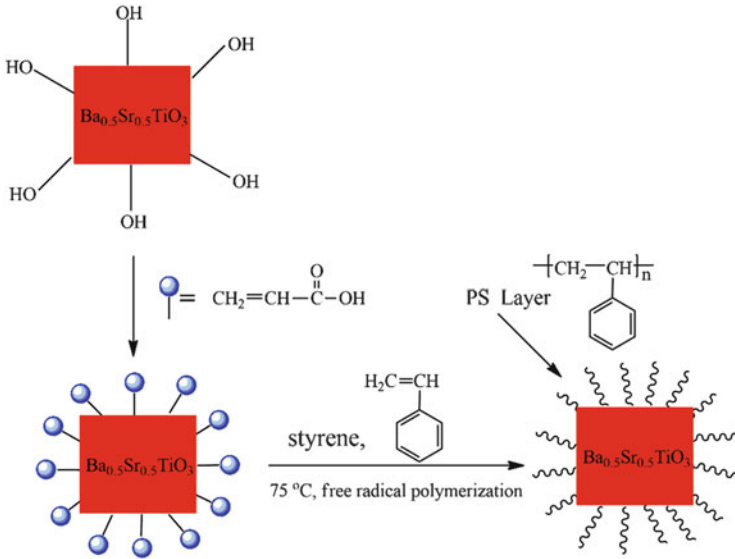
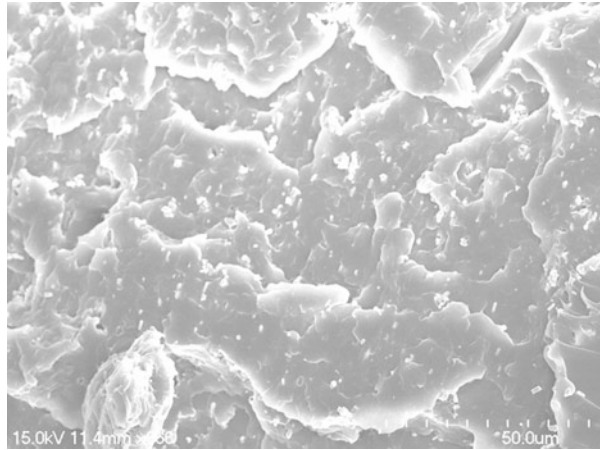


Fig. 6 Possible reaction mechanism for preparation of modified BST

Fig. 7 SEM micrograph of composite with 20 wt% BST powder

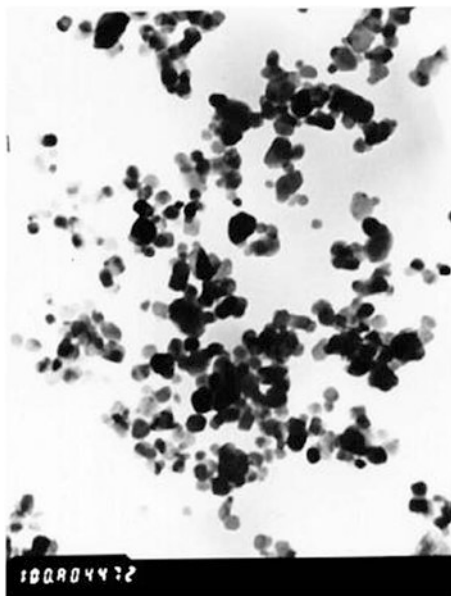


6.4 ZnO Nanoparticles

6.4.1 Synthesis of ZnO Nanoparticles

ZnO precursor was prepared by simple chemical co-precipitation [112]. ZnO precursors were synthesized by the precipitation method and then calcined to obtain ZnO nanoparticles. First, polyethylene glycol (PEG) solution was syringed into a

Fig. 8 TEM photograph of synthesized ZnO nanoparticles. Reprinted from Hong et al. [112], Copyright 2006, with permission from Elsevier



three-necked flask. Then, $\text{Zn}(\text{CH}_3\text{COO})_2 \cdot 2\text{H}_2\text{O}$ and $(\text{NH}_4)_2\text{CO}_3$ aqueous solutions were dropped into the flask at the same time with vigorous stirring. After reacting for 2 h at room temperature, the precipitates were washed and filtered with ammonia solution (pH 9) and anhydrous ethanol several times, and dried under vacuum for 12 h. Finally, the precursors were calcined in an oven at 450°C for 3 h and milled to obtain ZnO nanoparticles. A TEM image of the synthesized ZnO nanoparticles is shown in Fig. 8.

6.4.2 Surface Modification of ZnO Nanoparticles

The introduction of reactive groups onto the surface of ZnO nanoparticles was achieved through the reaction between KH570 and the hydroxyl groups on the nanoparticle surface. Similar to the preparation using KH570-treated ZnO with styrene monomer [111], the grafting polymerization was performed by the reaction of KH570-treated ZnO with MMA monomer [112]. The thermogravimetric analysis charts of ZnO nanoparticles grafted by PMMA are shown in Fig. 9. It can be seen that there was a remarkable difference in thermal behavior between the PMMA-grafted ZnO nanoparticles and the mixture of ZnO nanoparticles and PMMA. That is, the PMMA-grafted nanosized ZnO has much higher thermal stability than the simple mixture of PMMA and ZnO, which further verified a strong interaction between the grafting PMMA and ZnO nanoparticles.

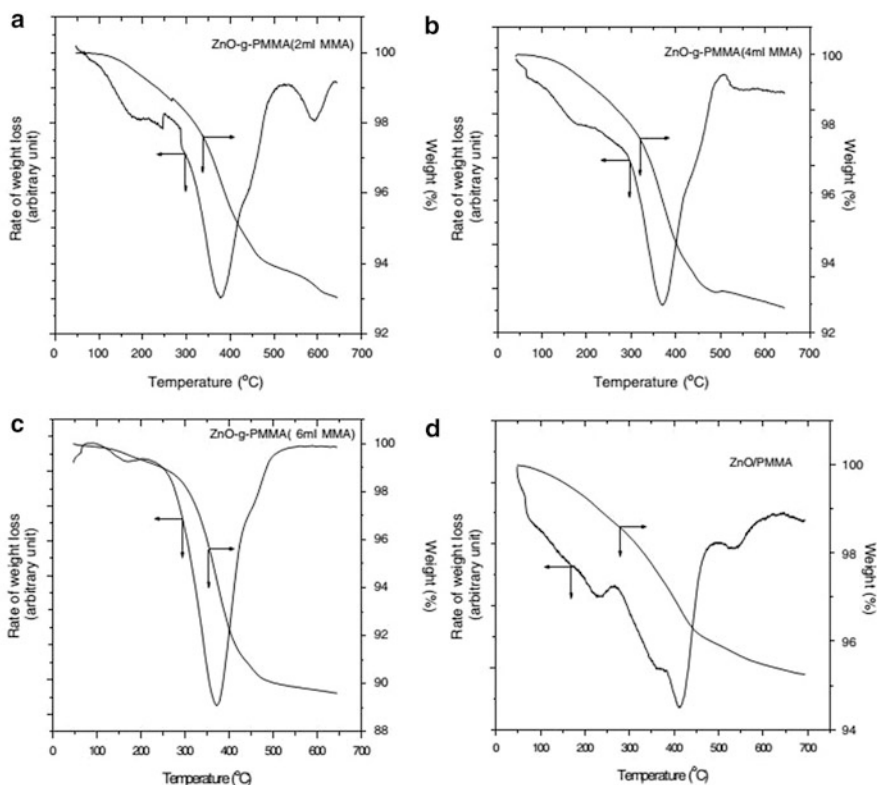


Fig. 9 Thermogravimetric charts of ZnO nanoparticles grafted by PMMA: (a) 2 mL MMA, (b) 4 mL MMA, (c) 6 mL MMA, and (d) mixture of ZnO nanoparticles and PMMA. Reprinted from Hong et al. [112], Copyright 2006, with permission from Elsevier

6.4.3 Preparation of ZnO/PS Nanocomposites

The preparation of ZnO/PS nanocomposites preceded as follows [112]: First, 110 mg bare ZnO or 110 mg PMMA-grafted ZnO were added into a three-necked bottle. Then, 10 mL styrene was added into the reactor. The mixture was stirred with the aid of ultrasonic oscillation until a uniform dispersion of the ZnO particles in styrene was attained. Afterwards, 36 mg azobisisobutyronitrile (AIBN) was added into the reactor as initiator. The subsequent polymerization was conducted at 85°C for 2.5 h. Then, the obtained composites were dried under vacuum for 24 h. The differential scanning calorimetry (DSC) heating curves of neat PS, PS/ZnO (bare), and PS/ZnO (PMMA grafted) are shown in Fig. 10. DSC traces in Fig. 10a show that neat PS has a lower glass transition temperature ($T_g = 87.7^\circ\text{C}$) than PS/ZnO (bare, $T_g = 97.9^\circ\text{C}$) and PS/ZnO (PMMA grafted, $T_g = 95.3^\circ\text{C}$). This behavior can be explained by the restricting effect of the nanoparticles in polymer. ZnO

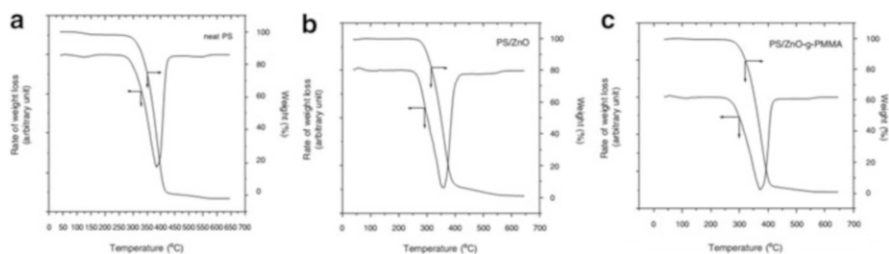


Fig. 10 Thermogravimetric charts of (a) neat PS, (b) PS/ZnO (bare), and (c) PS/ZnO (PMMA grafted). Reprinted from Hong et al. [112], Copyright 2006, with permission from Elsevier

nanoparticles were able to block the movement of PS polymer chains during DSC heating scans, resulting in the increase in the glass transition temperature of PS.

6.5 Antimony-Doped Tin Oxide

6.5.1 Synthesis of Antimony-Doped Tin Oxide

Antimony-doped tin oxide (ATO) with a tetragonal rutile structure was obtained by calcining co-precipitated precursors with sodium metasilicate nonahydrate and sodium chloride [164]. It was found that the amount of nanorods decreased and the length of the rods became shorter as the Sb-doping concentration increased, although the diameter changed little. Furthermore, the electrical resistivity of ATO showed a significant decrease after doping with a small amount of Sb. Figure 11 shows a TEM image of ATO nanorods with 1.5 mol% Sb.

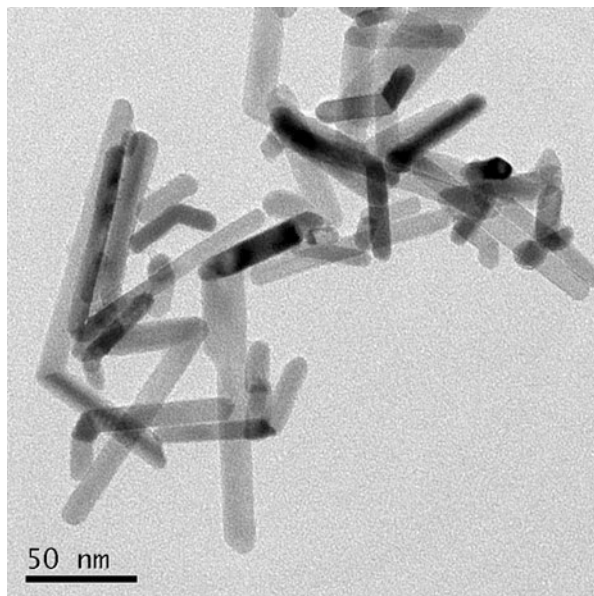
6.5.2 Surface Modification of ATO

The surface of ATO was modified by the “grafting-from” method; the specific steps were as follows: The ATO nanoparticles with 5 mol% of doped antimony were first activated by KH550. Then, PMMA was grafted onto the ATO nanoparticles via radical polymerization. The obtained modified nanoparticles were characterized by FTIR, TG, sedimentation test, SEM, and XRD. All results showed that the PMMA had been grafted onto the surface of ATO.

6.5.3 Preparation of ATO/PMMA Nanocomposites

The ATO powder was added into the PMMA matrix by solution blending. The PMMA-modified ATO nanoparticles were added into a tetrahydrofuran solution of PMMA to prepare ATO/PMMA nanocomposites. The composites showed high conductivity and good transparency.

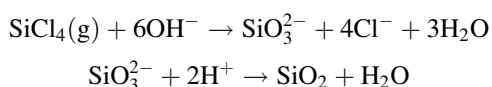
Fig. 11 TEM image of ATO nanorods with 1.5 mol% Sb



6.6 Silica Nanoparticles

6.6.1 Synthesis of Silica Nanoparticles

The silica nanoparticles were prepared by a facile co-precipitation using inexpensive silicon tetrachloride as raw material. The hydrolysis of silicon tetrachloride in alkaline solution was by the following reaction:



Compared with the ordinary chemical vapor deposition, this method has the advantages of inexpensive starting materials, being environmentally benign, and having large-scale production capability.

The effects of the type of alkali, alkali concentration, reaction time, surfactant, and post-processing on the properties of silica nanoparticles were investigated [165]. The TEM studies showed that the main factors influencing the morphology and particle size of silica were the type of alkali and alkali concentration. In addition, the main factor influencing the yield of silica was reaction time, while the main factor influencing the size distribution and high dibutyl phthalate (DBP)-absorption of silica nanoparticles was the PEG concentration. The above tests showed that the optimal preparation conditions were: Na_2CO_3 concentration of

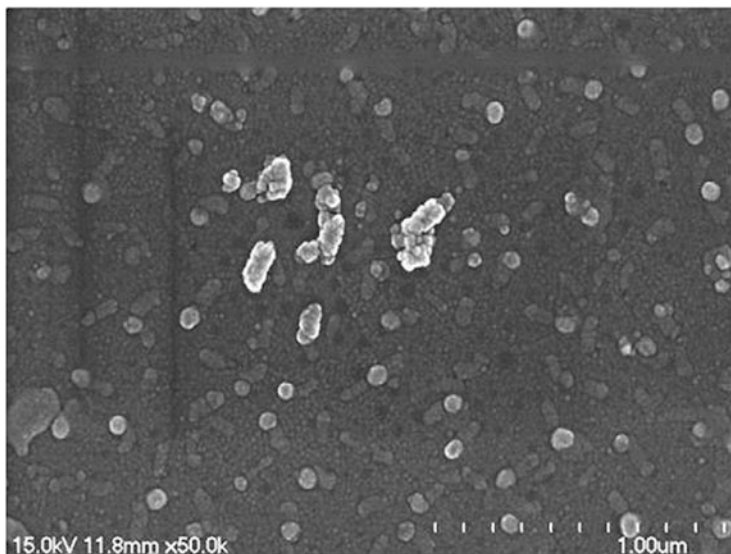


Fig. 12 SEM micrograph of silica nanoparticles prepared at optimal conditions. Reprinted from Luo et al. [165], Copyright 2012, with permission from Elsevier

10%, PEG concentration of 2.5%, reaction time 2 h, and use of a zeotropic distiller. The silica nanoparticles prepared at optimal conditions are shown in Fig. 12.

6.6.2 Surface Modification and Application of Silica Nanoparticles

The silica nanoparticles were modified by titanium coupling agent, and the mixture stirred vigorously and dispersed using a high-energy ball mill for 3 h. Silica/polyurethane (PU) composites were prepared by solution blending. The mechanical properties of PU films were improved by the addition of modified silica nanoparticles. Figure 13 shows the mechanical parameters of PU/silica films with different silica content. The results show that the optimum silica content was 2 wt% and that the tensile strength and Young's modulus of PU/silica films increased up to 64.2 and 2,535.9 MPa, respectively.

6.7 *Multiwalled Carbon Nanotubes*

CNTs have rapidly attracted interest because of their large aspect ratio, which presents unique mechanical, electrical, and thermal properties. Thus, CNT fillers in polymer-based composites present many potential applications in mechanical reinforcement, electron transport, energy storage, and so on. One of the most

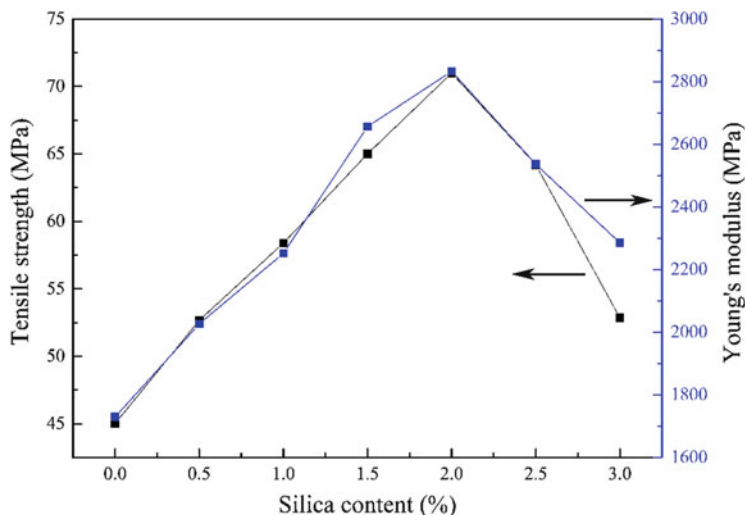


Fig. 13 Mechanical parameters of the PU/silica films prepared with different silica content. Reprinted from Luo et al. [165], Copyright 2012, with permission from Elsevier

straightforward methods for the incorporation of CNTs into a polymer matrix is by direct mixing. However, CNTs are easily aggregated, resulting in poor dispersion in the polymer matrix. Therefore, to improve the dispersion and compatibility it is necessary to modify the inorganic particles. The surface treatment of CNTs can be classified into two categories: (i) chemical treatment by oxidizing acids and (ii) - plasma-chemical treatment. In comparison with conventional chemical treatment, the plasma is used to modify CNTs in a facile and environmentally benign manner. Furthermore, plasma constitutes a little-explored medium for the surface treatment of materials. A set-up designed for plasma processing is shown in Fig. 14 [166].

6.7.1 Surface Modification of MWCNTs

MWCNTs were modified by grafting with PS using plasma polymerization of styrene monomer [166]. The modified MWCNTs were characterized by FTIR, dispersion test, TEM, SEM, and Raman analysis. TEM images of unmodified and modified MWCNTs are shown in Fig. 15. After plasma-induced grafting polymerization, the MWCNTs had a less-tangled organization, which demonstrated that the grafted styrene molecule efficiently promoted dispersal of the MWCNTs.

6.7.2 Preparation of MWCNT/PP Nanocomposites

MWCNT/PP nanocomposites were prepared by melt blending at 200°C with a rotor speed of 60 rpm using an internal batch mixer. SEM images of the fracture surface in the composites demonstrated that PS-grafted MWCNTs were dispersed well in

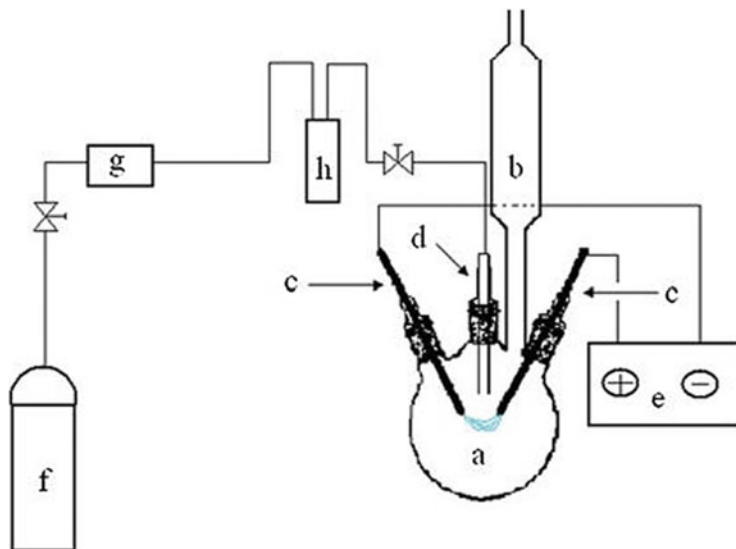


Fig. 14 Apparatus designed for plasma processing: (a) four-mouth flask, (b) custom-built fluidized bed reactor, (c) electrodes, (d) nozzle, (e) power supply, (f) argon gas cylinder, (g) monomer tank, and (h) surge tank. Reprinted from Luo et al. [166], Copyright 2012, with permission from Wiley Periodicals, Inc

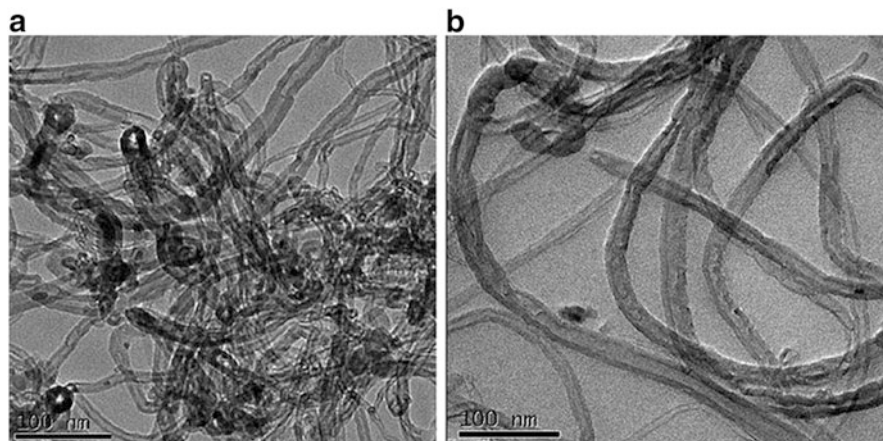


Fig. 15 TEM images of (a) untreated MWCNTs and (b) PS-grafted MWCNTs dispersed in toluene. Reprinted from Luo et al. [166], Copyright 2012, with permission from Wiley Periodicals, Inc

the PP matrix, and the strong interfacial bonding between the functionalized nanotubes and the resin led to an improvement in mechanical properties [166]. By contrast, in SEM images of untreated MWCNT/PP nanocomposites (as shown in Fig. 16), the aggregation of MWCNTs was obvious. The poor

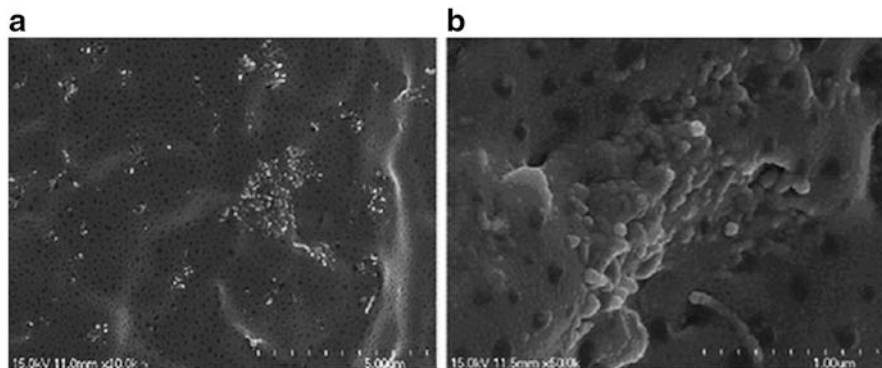


Fig. 16 SEM images of the fracture surface in composites containing 1 wt% of untreated MWCNTs: (a) 10,000 \times and (b) 50,000 \times (*white spots* indicate MWCNTs). Reprinted from Luo et al. [166], Copyright 2012, with permission from Wiley Periodicals, Inc

attachment between untreated MWCNTs and PP matrix led to the appearance of many holes, and a decrease in mechanical properties was observed.

6.8 Carbon Black Nanoparticles

6.8.1 Synthesis of Carbon Black Nanoparticles

The conventional method for production of carbon black (CB) has the disadvantages of low yield, large amount of polluting emissions, and limited reaction temperature. In this section, the environmentally benign plasma process for the preparation of CB is discussed. The effects of the flow rate of argon gas, propane gas, and the size of the current on the morphology of CB nanoparticles were investigated [167]. A schematic representation of the plasma apparatus is shown in Fig. 17. The microstructure and size of the carbon black particles were analyzed using SEM. Results demonstrated that spherical CB particles (see Fig. 18) with a narrow size distribution and a small average diameter of 50 nm, as well as a high oil absorption number of 1.14 mL/g, were produced by means of a gliding arc plasma process.

6.8.2 Surface Modification of Carbon Black

The prepared carbon black is hydrophobic and easily aggregated, so the dispersion in aqueous solution is poor. Consequently, modification of the surface of carbon black is a good method for achieving better performance in aqueous systems. The methods of oxidation, grafting, plasma treatment, and encapsulation modification

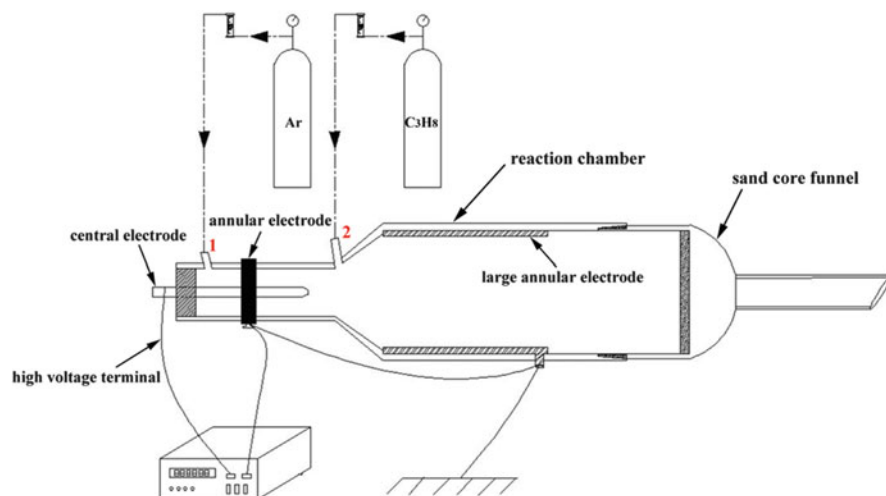


Fig. 17 Representation of the plasma apparatus. Reprinted from Yuan et al. [167], Copyright 2014, with permission from Elsevier

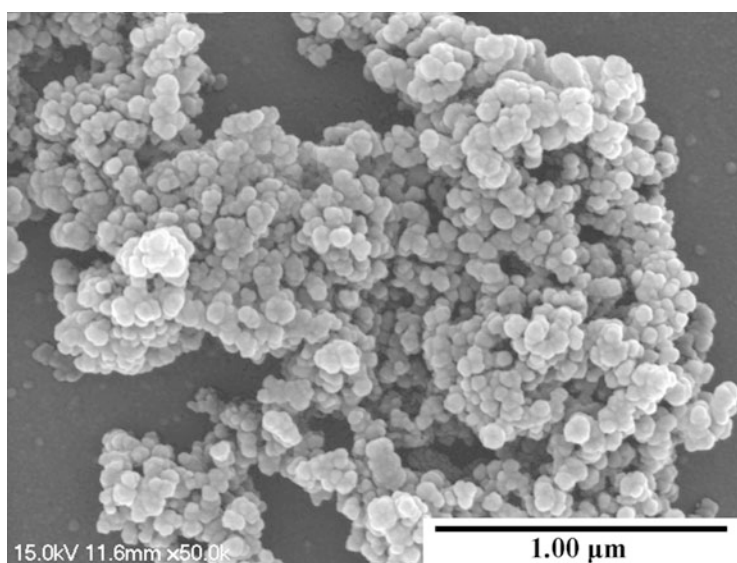


Fig. 18 SEM image of spherical CBs. Reprinted from Yuan et al. [167], Copyright 2014, with permission from Elsevier

have been reported for the surface modification of CB. Among these methods, acidic oxidation methods have attracted tremendous attention. The introduction of oxygen functional groups onto the CB surface not only brings desired hydrophilicity to the surface of nanoparticles, but also enables additional functionalization strategies to be carried out using such groups as anchoring sites.



Fig. 19 Printing qualities of (a) as-prepared ink and (b) purchased ink. Reprinted from Yuan et al. [167], Copyright 2014, with permission from Elsevier

The introduction of hydroxymethyl groups onto the CB surface was achieved by treatment of oxidized CB with formaldehyde solution in alkaline conditions [167]. The mixture of CB and 10% aqueous solution of HCHO at $\text{pH} \approx 10$ was stirred at 50°C for 3 h. After the reaction, the hydroxymethylated CB was filtered, repeatedly washed to neutral, and dried in vacuum drying oven.

6.8.3 Preparation of Printing Ink

Polyvinyl pyrrolidone (PVP)-modified CB nanoparticles were used as a pigment for the preparation of water-based ink-jet ink [167]. The physical properties of the as-prepared ink exhibited similar results to the purchased ink. Printing qualities were also investigated and the results were good, as shown in Fig. 19.

6.9 ABS/EPDM Composites Filled with Carbon Black

Acrylonitrile-butadiene-styrene (ABS) is one of the most important synthetic engineering resins because of its excellent properties of impact resistance, heat resistance, and chemical resistance along with being easy to fabricate, stable in finished size, and having good surface glossiness. ABS has wide application in machinery, vehicles, and electric products.

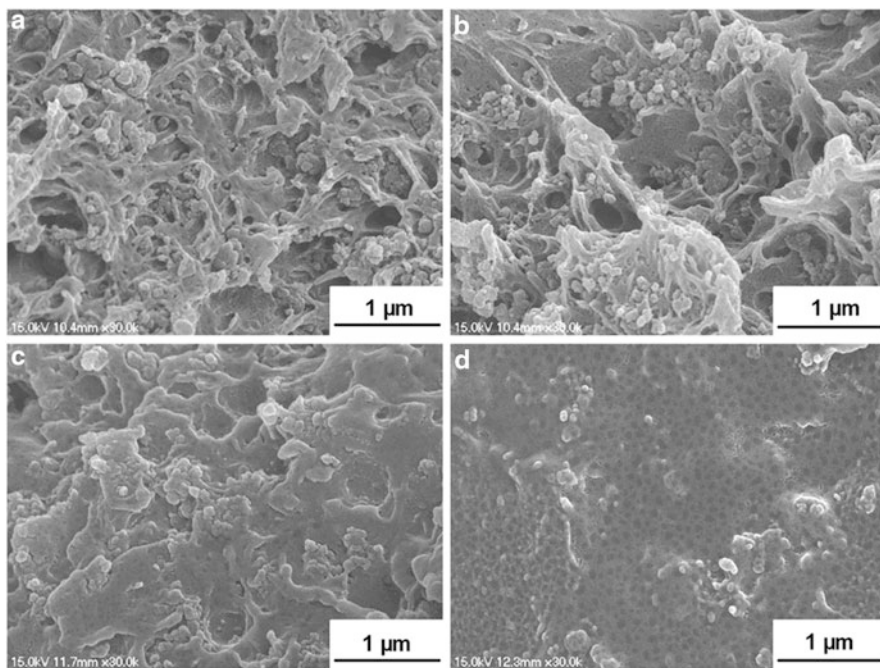


Fig. 20 SEM images of different ABS blends: (a) 85% ABS and 15% CB; (b) 47% ABS, 38% ABS-g-MAH, and 15% CB; (c) 65% ABS, 11% ABS-g-MAH, 9% EPDM-g-MAH, and 15% CB; and (d) 47% ABS-g-MAH, 38% EPDM-g-MAH, and 15% CB. Reprinted from Wang et al. [168], Copyright 2014, with permission from Elsevier

ABS was modified by maleic anhydride (MAH), and ethylene-propylene-diene rubber (EPDM) as compatibilizer could significantly improve the mechanical properties of ABS. To achieve good compatibility with the ABS-g-MAH matrix, EPDM was treated with MAH [168]. The CB particles as conductive filler were added into the composites to attain high conductivity while keeping the excellent mechanical properties. The SEM images in Fig. 20 show that ABS-g-MAH behaved as an excellent compatibilizer, which made EPDM-g-MAH and ABS domains miscible. This improved the tensile strength, impact strength, and elongation at break of composites compared with blends without ABS-g-MAH (Table 1). In addition, the resistivity was dramatically decreased by four orders of magnitudes when ABS was functionalized by MAH, as shown in Fig. 21.

Table 1 Mechanical properties of different ABS blends

Sample	ABS content (wt%)	ABS-g-MAH content (wt%)	EPDM-g-MAH content (wt%)	Carbon black (wt%)	Tensile strength (MPa)	Impact strength (kJ/m ²)	Tensile strength (MPa)	Impact strength (kJ/m ²)
1	100	–	–	–	27.42	81.18	27.42	81.18
2	85	–	–	15	17.89	40.31	17.89	40.31
3	–	47	38	15	5.52	179.38	5.52	179.38
4	47	–	38	15	17.56	95.03	17.56	95.03
5	63	11	9	17	18.76	30.74	18.76	30.74
6	65	11	9	15	21.74	44.20	21.74	44.20
7	68	11	9	12	27.37	60.13	27.37	60.13
8	71	11	9	9	26.51	67.19	26.51	67.19

Reprinted from Wang et al. [168], Copyright 2014, with permission from Elsevier

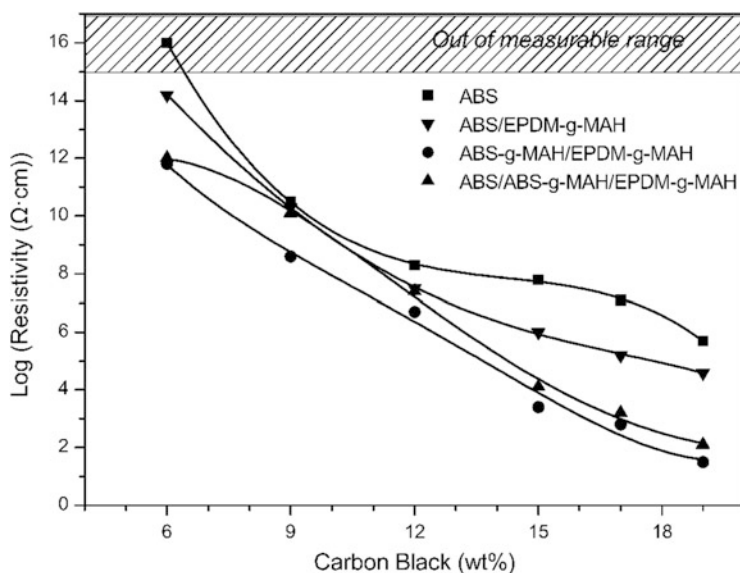


Fig. 21 Resistivity of ABS with or without modification, plotted versus carbon black content. Reprinted from Wang et al. [168], Copyright 2014, with permission from Elsevier

7 Conclusions and Prospects

Organic–inorganic nanocomposites not only exhibit the excellent properties of organic polymers, but also combine these with the unique properties of inorganic nanoparticles. However, the inorganic nanoparticles have a strong tendency to form aggregates and are hydrophilic. Therefore, to improve the dispersion stability and the compatibility of inorganic nanoparticles with organic solvents or polymer matrices, the surface modification of nanoparticles is indispensable. Such

modification improves the interfacial interaction between the nanoparticles and polymer matrix and can result in high performance composites with unique mechanical, optical, electric, dielectric, and other properties. The prospects of nanocomposites are attractive. During the past decade, many composites have been appearing either as prototypes or commercial products. Research in functional nanocomposites is mostly supported by the growing interest of chemists, physicists, biologists, and materials scientists in fully exploiting this opportunity for creating smart materials that benefit from the best of the three realms: inorganic, organic, and biological. Bio-inspired strategies are used to “mimic” the growth processes that occur during biomineralization and to design innovative multiscale structured hybrids (from nano- to millimeter scale), hierarchically organized in terms of structure and function. Several examples of “commercial hybrids” have been discussed in this review but only represent the tip of the iceberg. There is still much work to be done. For example, the large-scale synthesis of nanoparticles is difficult to achieve, which limits their application in industry. Control of the characteristics of synthesized nanoparticles makes it possible to prepare polymer/inorganic nanocomposites with specified properties. A substantial amount of work still needs to be carried out for practical application of nanoparticles.

Acknowledgments The project was supported by the National Natural Science Foundation of China (NSFC, No. 21246002), the National Basic Research Program of China (973 Program, No. 2009CB219904), the National Post-doctoral Science Foundation (No. 20090451176), the Jiangsu Provincial Key Laboratory of Environmental Materials and Engineering at Yangzhou University (No. K11025), the Technology Innovation Foundation of MOST (No. 11C26223204581), the Priority Academic Program Development of Jiangsu Higher Education Institutions (PAPD), the Natural Science Foundation of Jiangsu Province (No. BK2011328), and the Minjiang Scholarship of Fujian Province

References

1. Huang ZM, Zhang YZ, Kotaki M et al (2003) *Compos Sci Technol* 63:2223
2. Thakur VK, Thakur MK (2014) *Carbohydr Polym* 109:102
3. Kalia S, Boufi S, Celli A et al (2014) *Colloid Polym Sci* 292:5
4. Kalia S, Kaith BS, Inderjeet K (eds) (2011) *Cellulose fibers: bio- and nano-polymer composites*. Springer, Heidelberg
5. Babu B, Aswani T, Rao GT et al (2014) *J Magn Magn Mater* 355:76
6. Umadevi M, Parimaladevi R, Sangari M (2014) *Spectrochim Acta A* 120:365
7. Nogas-Cwikiel E, Suchanicz J (2013) *Arch Metall Mater* 58:1397
8. Choi D, Wang D, Bae IT et al (2010) *Nano Lett* 10:2799
9. Hsiang HI, Chang YL, Fang JS et al (2011) *J Alloys Compd* 509:7632
10. Chang CY, Huang CY, Wu YC et al (2010) *J Alloys Compd* 95:108
11. Siddiqui MA, Chandel VS, Azam A (2012) *Appl Surf Sci* 258:7354
12. Lee JH, Kim YJ (2008) *Mater Sci Eng B* 146:99
13. Li D, Sasaki Y, Kageyama M et al (2005) *J Power Sources* 148:85
14. Tan ETH, Ho GW, Wong ASW et al (2008) *Nanotechnology* 19:1
15. Yoon KH, Cho YS, Lee DH et al (1993) *J Am Ceram Soc* 76:1373
16. Wang X, Gao L, Zhou F et al (2004) *J Cryst Growth* 265:220

17. Yang Z, Chang Y, Li H (2005) *Mater Res Bull* 40:2110
18. Nie J, Xu G, Yang Y, Cheng C (2009) *Mater Chem Phys* 115:400
19. Chiu CC, Li CC, Desu SB (1991) *J Am Ceram Soc* 74:38
20. Reddy MV, Subba Rao GV, Chowdari BVR (2007) *J Chem Phys C* 111:11712
21. Kan Y, Jin X, Wang P et al (2003) *Mater Res Bull* 38:567
22. Thirumal M, Jain P, Ganguli AK (2001) *Mater Chem Phys* 70:7
23. Ohshima E, Ogino H, Niikura I et al (2004) *J Cryst Growth* 260:166
24. Tam KH, Cheung CK, Leung YH et al (2006) *J Chem Phys C* 110:20865
25. Kolen'ko YV, Churagulov BR, Kunst M et al (2004) *Appl Catal B* 54:51
26. Liu J, Ye X, Wang H et al (2003) *Ceram Int* 29:629
27. Kajiyoshi K, Ishizawa N, Yoshimura M (1991) *J Am Ceram Soc* 74:369
28. Xu H, Gao L, Guo J (2002) *J Eur Ceram Soc* 22:1163
29. Ishizawa N, Banno H, Hayashi M et al (1990) *Jpn J Appl Phys* 29:2467
30. Hu Y, Gu H, Sun X et al (2006) *Appl Phys Lett* 88:193210
31. Antonelli DM, Ying J (1995) *Angew Chem Int Ed* 34:2014
32. Lee JH, Ko KH, Park BO (2003) *J Cryst Growth* 247:119
33. Wang W, Serp P, Kalck P et al (2005) *J Mol Catal A* 235:194
34. Gu F, Wang SF, Lü MK et al (2004) *J Chem Phys C* 108:8119
35. Tahar RBH, Ban T, Ohya Y et al (1997) *Appl Phys Lett* 82:865
36. Ahmed MA, El-Katori EE, Gharni ZH (2013) *J Alloys Compd* 553:19
37. Kotobuki M, Koishi M (2014) *Ceram Int* 40:5043
38. Ding Y, Jiang Y, Xu F et al (2010) *Electrochem Commun* 12:10
39. Petcharoen K, Sirivat A (2012) *Mater Sci Eng B* 177:421
40. Muthukumaran S, Gopalakrishnan R (2012) *Opt Mater* 34:1946
41. Kripal R, Gupta AK, Srivastava RK et al (2011) *Spectrochim Acta A* 79:1605
42. Senthilkumar V, Senthil K, Vickraman P (2012) *Mater Res Bull* 47:1051
43. Kumar AP, Kumar BP, Kumar ABV et al (2013) *Appl Surf Sci* 265:500
44. Zhang M, Sheng G, Fu J et al (2005) *Mater Lett* 59:3641
45. Mahmoodi NM (2011) *Desalination* 279:332
46. Kripal R, Gupta AK, Mishra SK (2010) *Spectrochim Acta A* 76:52
47. Yang MR, Ke WH, Wu SH (2005) *J Power Sources* 146:539
48. Lin JM, Chen YC, Lin CP (2013) *J Nanomater* 2013:1
49. Dai ZR, Pan ZW, Wang ZL (2003) *Adv Funct Mater* 13:9
50. Chen Y, Li J, Dai J (2001) *Chem Phys Lett* 344:450
51. Cantalini C, Wlodarski W, Li Y et al (2000) *Sens Actuators B* 64:182
52. Kuai P, Liu C, Huo P (2009) *Catal Lett* 129:493
53. Yu B, Liu C (2012) *Plasma Chem Plasma Process* 32:201
54. Lin Y, Tang Z, Zhang Z et al (2000) *J Am Ceram Soc* 83:2869
55. Reina A, Jia X, Ho J et al (2009) *Nano Lett* 9:30
56. Chhowalla M, Teo KBK, Ducati C et al (2001) *J Appl Phys* 90:5308
57. Xia Y, Mokaya R (2004) *Adv Mater* 16:1553
58. Kumar M, Ando Y (2010) *J Nanosci Nanotechnol* 10:3739
59. Mattevi C, Kim H, Chhowalla M (2011) *J Chem Phys* 21:3324
60. Kim D, Yun I, Kim H (2010) *Curr Appl Phys* 10:5459
61. Sun L, He J, Kong H et al (2011) *Sol Energ Mater Sol Cell* 95:290
62. Vinodkumar R, Lethy KJ, Beena D et al (2010) *Sol Energ Mater Sol Cell* 94:68
63. Bdikin IK, Gracio J, Ayouchi R et al (2010) *Nanotechnology* 21:1
64. Gaur A, Singh P, Choudhary N et al (2011) *Physica B* 406:1877
65. Orlianges JC, Champeaux C, Dutheil P et al (2011) *Thin Solid Films* 519:7611
66. Scullin ML, Ravichandran J, Yu C et al (2010) *Acta Mater* 58:457
67. Hakoda T, Yamamoto S, Kawaguchi K et al (2010) *Appl Surf Sci* 257:1556
68. Cho HJ, Lee SU, Hong B et al (2010) *Thin Solid Films* 518:2941
69. Nam E, Kang YH, Jung D et al (2010) *Thin Solid Films* 518:6245

70. Wang X, Zeng X, Huang D et al (2013) *J Mater Sci* 23:1580
71. Sarakinos K, Alami J, Konstantinidis S (2010) *Surf Coat Technol* 204:1661
72. You ZZ, Hua GJ (2012) *J Alloys Compd* 530:11
73. Wu L, Chen YC, Chen LJ et al (1999) *Jpn J Appl Phys* 138:5612
74. Shao S, Zhang J, Zhang Z et al (2008) *J Phys D* 41:1
75. Zhou H, Chen X, Fang L et al (2010) *J Mater Sci* 21:939
76. Li Y, Wang J, Liao R et al (2010) *J Alloys Compd* 496:282
77. Tawichai N, Sittiyot W, Eitssayeam S et al (2012) *Ceram Int* 38S:S121
78. Chen K, Zhang X (2010) *Ceram Int* 36:1523
79. Mao C, Wang G, Dong X et al (2007) *Mater Chem Phys* 106:164
80. Li HL, Du ZN, Wang GL et al (2010) *Mater Lett* 64:431
81. Fuentes S, Chávez E, Padilla-Campos L et al (2013) *Ceram Int* 39:8823
82. Chen CF, Reagor DW, Russell SJ et al (2011) *J Am Ceram Soc* 94:3727
83. Maensiri S, Nuansing W, Klinkaewnarong J et al (2006) *J Colloid Interface Sci* 297:578
84. Razak KA, Asadov A, Gao W (2007) *Ceram Int* 33:1495
85. Deshpande SB, Kholam YB (2005) *Mater Lett* 59:293
86. Kholam YB, Deshpande SB, Potdar HS et al (2005) *Mater Charact* 54:63
87. Zuo XH, Deng XY, Chen Y et al (2010) *Mater Lett* 64:1150
88. Pan ZW, Dai ZR, Xu L et al (2001) *J Phys Chem* 105:2507
89. Choi S, Lee MS, Park DW (2014) *Curr Appl Phys* 14:433
90. Neamtu BV, Marinca TF, Chicinas I et al (2014) *J Alloys Compd* 600:1–7
91. Chaturvedi V, Ananthapadmanabhan PV, Chakravarthy Y et al (2014) *Ceram Int* 40:8273
92. Yuming W, Junjie H, Yanwei S (2013) *Rare Metal Mater Eng* 42:1810
93. Iijima S (1991) *Nature* 354:56
94. Anazawa K, Shimotani K, Manabe C et al (2002) *Appl Phys Lett* 81:739
95. Imasaka K, Kanatake Y, Ohshiro Y et al (2006) *Thin Solid Films* 506–507:250
96. Cui S, Scharff P, Siegmund C et al (2004) *Carbon* 42:931
97. Jong Lee S, Koo Baik H, Yoo J et al (2002) *Diamond Relat Mater* 11:914
98. Zhao S, Hong R, Luo Z et al (2011) *J Nanomater* 2011:6
99. Baba K, Hatada R, Flege S et al (2011) *Adv Mater Sci Eng* 2012:1
100. Liew PJ, Yan J, Kuriyagawa T (2013) *J Mater Process Technol* 213:1076
101. Borgohain R, Yang J, Selegue JP et al (2014) *Carbon* 66:272
102. Liu XY, Hong RY, Feng WG et al (2014) *Powder Technol* 256:158
103. Mattevi C, Kim H, Chhowalla M (2011) *J Mater Chem* 21:3324
104. Vinod Kumar R, Lethy KJ, Beena D et al (2010) *Sol Energ Mater Sol Cell* 94:68
105. Yu X, Shen Z (2011) *Vacuum* 85:1026
106. Kango S, Kalia S, Celli A et al (2013) *Prog Polym Sci* 38:1232
107. Dang ZM, Xu HP, Wang HY (2007) *Appl Phys Lett* 90:012901
108. Ma Z, Wang JH, Zhang XY (2008) *J Appl Polym Sci* 107:1000
109. Wang HL (2005) *Polymer* 46:6243
110. Bose S, Mahanwar PA (2006) *J Appl Polym Sci* 99:266
111. Hong RY, Li JH, Chen LL et al (2009) *Powder Technol* 189:426
112. Hong RY, Qian JZ, Cao JX (2006) *Powder Technol* 163:160
113. Zdyrko B, Luzinov I (2011) *Macromol Rapid Commun* 32:859
114. Qin S, Qin D, Ford WT et al (2004) *Macromolecules* 37:752
115. Xie L, Huang X, Yang K et al (2014) *J Mater Chem A* 2:5244
116. Baier M, Görgen M, Ehlbeck J et al (2014) *Innovat Food Sci Emerg Technol* 22:147
117. Ehlbeck J, Schnabel U, Polak M et al (2011) *J Phys D* 44:1
118. Okpalugo TIT, Papakonstantinou P, Murphy H et al (2005) *Carbon* 43:153
119. Yoon OJ, Lee HJ, Jang YM et al (2011) *Appl Surf Sci* 257:8535
120. Leroux F, Campagne C, Perwuelz A et al (2008) *Appl Surf Sci* 254:3902
121. Takada T, Nakahara M, Kumagai H et al (1996) *Carbon* 34:1087
122. Park JM, Matienzo LJ, Spencer DF (1991) *J Adhes Sci Technol* 5:153

123. Morent R, De Geyter N, Desmet T et al (2011) *Plasma Process Polym* 8:171
124. Yin CY, Aroua MK, Daud WMAW (2007) *Se Purif Technol* 52:403
125. Tashima D, Sakamoto A, Taniguchi M et al (2008) *Vacuum* 83:695
126. Xu T, Yang J, Liu J et al (2007) *Appl Surf Sci* 253:8945
127. López-Manchado MA, Herrero B, Arroyo M (2004) *Polym Int* 53:1766
128. Chae DW, Kim BC (2005) *Polym Adv Technol* 16:846
129. Wu TM, Wu CY (2006) *Polym Degrad Stab* 91:2198
130. Shen JW, Chen XM, Huang WY (2003) *J Appl Polym Sci* 88:1864
131. Thomas P, Varughese KT, Dwarakanath K et al (2010) *Compos Sci Technol* 70:539
132. Yang W, Yu S, Sun R et al (2011) *Acta Mater* 59:5593
133. Chanmal CV, Jog JP (2008) *Express Polym Lett* 2:294
134. Pötschke P, Bhattacharyya AR, Janke A (2004) *Carbon* 42:965
135. Villmow T, Kretzschmar B, Pötschke P (2010) *Compos Sci Technol* 70:2045
136. Spitalsky Z, Tasis D, Papagelis K et al (2010) *Prog Polym Sci* 35:357
137. Hagenmueller R, Gommans HH, Rinzler AG et al (2000) *Chem Phys Lett* 330:219
138. Bikiaris DN, Vassiliou A, Pavlidou E et al (2005) *Eur Polym J* 41:1965
139. Hu T, Juuti J, Jantunen H (2009) *J Eur Ceram Soc* 27:2923
140. Li K, Wang H, Xiang F et al (2009) *Appl Phys Lett* 95:202904
141. Chao F, Liang G (2009) *J Mater Sci* 20:560
142. Wu H, Gu A, Liang G et al (2011) *J Mater Chem* 21:14838
143. Sui G, Jana S, Zhong WH et al (2008) *Acta Mater* 56:2381
144. Potts JR, Lee SH, Alam TM et al (2011) *Carbon* 49:2615
145. Xu Z, Gao C (2010) *Macromolecules* 43:6716
146. Cava RJ (2001) *J Mater Chem* 11:54
147. Balazs AC, Emrick T, Russell TP (2006) *Science* 314:1107
148. Luo B, Wang X, Wang Y et al (2014) *J Mater Chem* 2:510
149. Yu K, Niu Y, Zhou Y et al (2013) *J Am Ceram Soc* 96:2519
150. Wang FJ, Li W, Xue MS et al (2011) *Compos B* 42:87
151. Xie L, Huang X, Huang Y et al (2013) *J Phys Chem C* 117:22525
152. Yu K, Niu Y, Xiang F et al (2003) *Appl Phys Lett* 114:174107
153. Zhou T, Zha JW, Hou Y et al (2011) *ACS Appl Mater Interfaces* 3:2184
154. Tang H, Sodano HA (2013) *Nano Lett* 13:1373
155. Sonoda K, Juuti J, Moriya Y et al (2010) *Compos Struct* 92:1052
156. Vékás L (2008) *Adv Sci Technol* 54:127
157. Hong RY (2009) *Nanoparticles and magnetic fluid: preparation and application*. Chem. Ind. Press, China
158. Liu XY, Zheng SW, Hong RY et al (2014) *Colloids Surf A* 443:425
159. Kordonsky WI (1993) *J Magn Magn Mater* 122:395
160. Hong RY, Li JH, Zheng SW et al (2009) *J Alloys Compd* 480:947
161. Hong R, Pan T, Qian J et al (2006) *Chem Eng J* 119:71
162. Xu Y, Liang YT, Jiang LJ et al (2011) *J Nanomater* 1:1
163. Zhou ZH, Xue JM, Chan HSO et al (2002) *Mater Chem Phys* 75:181
164. Lu HF, Hong RY, Wang LS et al (2012) *Mater Lett* 68:237
165. Luo Z, Cai X, Hong RY et al (2012) *Chem Eng J* 187:357
166. Luo Z, Cai X, Hong RY et al (2013) *J Appl Polym Sci* 1:4756
167. Yuan JJ, Hong RY, Wang YQ, Feng WG (2014) *Chem Eng J* 253:107–120
168. Wang F, Hong RY, Feng WG et al (2014) *Mater Lett* 125:48

Recent Advances on Fibrous Clay-Based Nanocomposites

Eduardo Ruiz-Hitzky, Margarita Darder, Ana C.S. Alcântara, Bernd Wicklein, and Pilar Aranda

Abstract This review critically introduces recent results on nanocomposite materials derived from the fibrous clay silicates sepiolite and palygorskite and combined with diverse types of polymers, from typical thermoplastics to biopolymers such as polysaccharides, proteins, lipids, and nucleic acids. First, the main features of both silicates are described, emphasizing the structural and textural characteristics that determine the interaction mechanisms with organic compounds and particularly with polymers, which define the final properties of the resulting materials. The crucial role of the clay–silicate interface governing the terminal properties of the nanocomposites is especially considered. Second, this work reports and discusses different experimental approaches and preparative procedures adopted for the nanofabrication and conformation (powders, films, monoliths, foams, etc.) of nanocomposites, comparing in certain cases with analogous materials derived from layered clays instead of sepiolite or palygorskite. Selected examples of fibrous clay-based nanocomposites are discussed to show the broad versatility of these materials in application fields as diverse as structural materials, conducting nanocomposites, biomaterials, environmental remediation, and sensor devices.

Keywords Bionanocomposites · Bioplastics · Biopolymers · Clays · DNA · Nanocomposites · Organoclays · Palygorskite · Phospholipids · Polymers · Polysaccharides · Proteins · Sepiolite

E. Ruiz-Hitzky (✉), M. Darder, and P. Aranda
Instituto de Ciencia de Materiales de Madrid, CSIC, c/Sor Juana Inés de la Cruz 3, 28049
Madrid, Spain
e-mail: eduardo@icmm.csic.es

A.C.S. Alcântara
Department of Chemistry, Federal University of Rio Grande do Norte, UFRN, Lagoa Nova,
59072-970 Natal-RN, Brazil

B. Wicklein
Arrhenius Laboratory, Stockholm University, 10691 Stockholm, Sweden

Contents

1	Introduction	40
2	Interaction Mechanisms Between Fibrous Clays and Organic Compounds	42
3	Synthetic Polymers/Fibrous Clays Nanocomposites	45
3.1	Fibrous Clays as Nanofillers of Thermoplastic Polymers	45
3.2	Fibrous Clays as Nanofillers for Thermosetting Polymers	48
3.3	Fibrous Clay Nanocomposites Based on Hydrogel Polymers	49
4	Biopolymer–Fibrous Clay Nanocomposites	51
4.1	Polylactic Acid and Other Biodegradable Polyesters	51
4.2	Polysaccharides	53
4.3	Proteins	60
4.4	Lipids	65
4.5	Nucleic Acids	67
5	Conducting Fibrous Clay Nanocomposites	67
5.1	Conducting Polymer–Fibrous Clay Nanocomposites	68
5.2	Conducting Carbon–Fibrous Clay Nanocomposites	70
6	Conclusion	73
	References	74

1 Introduction

It could be considered that the polymer–clay nanocomposite era started in 1987 after the first publication by Fukushima and other researchers at the Toyota Central Laboratory describing their discovery regarding delamination of smectite layered clays during assembly with a polyamide (Nylon-6) matrix [1, 2]. Since this seminal work, impressive development of the topic has taken place, which at this moment includes more than 12,000 publications on polymer–clay nanocomposites, according to the ISI Web of Science data. A huge majority of these publications correspond to clays showing a layered structure, mainly smectites such as montmorillonite and other 2:1 charged and swelling phyllosilicates of natural origin (beidellites, saponites, hectorites, etc.) or synthetic materials (e.g., laponite and fluor-taenolite). Excellent reviews on these nanocomposites offer an actualized perspective from theoretical studies and preparative aspects to considerations on their current applications (see for instance [3–10]).

On a minor level, but not of lesser significance than smectites, fibrous clays such as sepiolite and palygorskite (also known as attapulgite) have been used as fillers in the preparation of polymer–clay nanocomposites [7, 11–15]. The high aspect ratio of the silicate fibers (typically up to 100) can a priori be favorable for the mechanical reinforcement of polymer matrices. The individual elastic properties of a single sepiolite nanofiber have been recently measured using atomic force microscopy (AFM) strategies (Fig. 1). The modulus values measured in bending mode are around 8 GPa, indicating the potential of fibrous clays as reinforcement for polymer matrices [16].

Both, sepiolite and palygorskite exhibit an elevated specific surface area, as measured from nitrogen adsorption isotherms, with BET values that are in the order

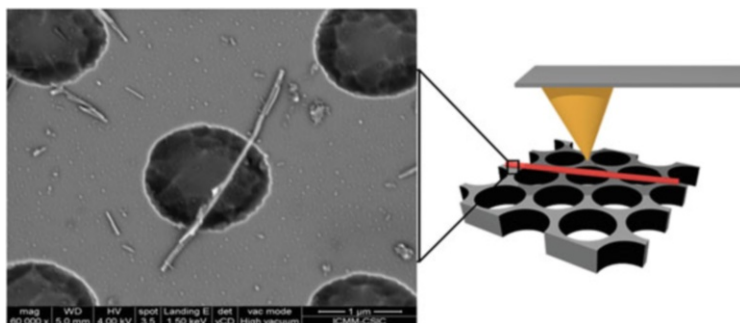


Fig. 1 Measurement of the elastic properties of a single clay sepiolite nanofiber using atomic force microscopy (AFM) strategies. Reproduced from [16] with permission from The Royal Society of Chemistry

of 300 and 200 m²/g, respectively [17]. This feature is potentially significant in the interactions between these clay surfaces and polymer matrices. In “conventional” polymer–clay nanocomposites involving layered silicates, the maximum surface area theoretically available in the interaction with polymers is in the order of 750 m²/g for entirely delaminated silicates, taking into account the total (internal plus external) surface of montmorillonite and other smectites [18]. This value is much greater than the value of the accessible area offered by the fibrous clays and, therefore, at first glance a larger degree of interaction in the layered clay could be expected. However, the delamination level reached by smectites is actually quite limited and only a partial exfoliation of the layered clay particles can be produced in smectite–polymer nanocomposites.

In contrast to smectites, fibrous clays are non-swelling materials and therefore are not susceptible to delamination by polymer inclusion. Sepiolite and palygorskite clays naturally occur as microfiber aggregates, forming bundles that can be defibrillated to give rise to fine powders that are of great interest for diverse applications including polymer reinforcement [13]. Currently, commercial xerogels consisting of “defibrillated sepiolite” (e.g., Pangel and Pansil marketed by TOLSA, S.A, Madrid, Spain) can offer high-quality nanodispersions of particles in diverse polymer matrices [13]. Of particular relevance are the nanocomposites resulting from the assembly of these fibrous clays and a wide range of polymers of natural origin (green polymers) such as polylactic acid (PLA) and gelatin, with a large choice of polysaccharides and other biopolymers [11, 12, 19–21].

In this contribution, we intend to introduce recent work dedicated to polymer–clay nanocomposites based on sepiolite and palygorskite fibrous silicates. We will consider as a priority the role of the interface between the mineral surface and the polymer matrix. In fact, this type of clay is markedly hydrophilic because their surface is covered by hydroxyl groups, mainly silanol groups ($\equiv\text{Si-OH}$) [17, 22], and therefore they are compatible with many polar polymers. However, chemical modification of the silicate surface could be necessary for adjusting their

compatibility with polymers of low-polar character, in a similar way to smectites where treatment with surfactants (e.g., cetyltrimethylammonium bromide – CTAB – and other alkylammonium salts) results in “organoclays,” facilitating their dispersion in low-polar matrices.

2 Interaction Mechanisms Between Fibrous Clays and Organic Compounds

Sepiolite and palygorskite are naturally occurring clays of fibrous morphology with a crystalline structure consisting of talc-like ribbons arranged parallel to the fiber direction (*c*-axis). It can be assimilated to discontinuous phyllosilicate layers, present as structural blocks alternating with structural cavities (tunnels) that grow in the *c*-axis direction (Fig. 2). The structural blocks contain two tetrahedral silica sheets and a central sheet of magnesium hydroxide that can contain isomorphous substitutions of trivalent cations (mainly Al^{3+}), particularly significant in the case of the palygorskite mineral [23, 24]. Usually, a fraction of the structural hydroxyls in the octahedral layers are substituted by fluorine, as occurs in sepiolite deposits in the Taxus basin, Spain [25]. The tunnel dimensions of both fibrous clays are in the nanometer range with cross-section values of $1.06 \times 0.37 \text{ nm}^2$ and $0.64 \times 0.37 \text{ nm}^2$ for sepiolite and palygorskite, respectively [17].

Typically, fiber length dimensions of sepiolite from the Taxus basin deposits are in the micrometer range (1–5 μm), with diameters varying between 50 and 100 nm [13]. Apparently contact with fibers of such dimensions does not represent any health risk. However, longer fibers of sepiolite and palygorskite of different origin are suspected of being a potential risk for diverse pulmonary and pleura diseases [27]. The reports from the International Agency for Research on Cancer (IARC) indicate that there is “inadequate evidence” in animals and humans to determine the carcinogenicity of sepiolite fibers of length inferior to 5 μm , whereas there is “limited evidence” in experimental animals for the carcinogenicity of longer sepiolite fibers [28].

A noteworthy characteristic of fibrous clays is that their external surface is covered by silanol groups ($\equiv\text{Si-OH}$) and, therefore, this represents an approach to silica chemistry, allowing the preparation of organic derivatives of these silicates. In this way, the surface of sepiolite can be easily modified by reaction with organosilanes and other reagents such as epoxides and isocyanates [29]. Similarly to 2:1 charged phyllosilicates, the negative electrical charge due to isomorphous substitutions is compensated by cations that can be exchanged by treatment with alkylammonium salts in solution. In this manner, organoclays derived from sepiolite and palygorskite can be prepared that show compatibility towards low-polymer matrices.

The presence of tunnels inherent to the structure of fibrous clays, as well as defects in their microcrystalline structure, allows the access of small molecules

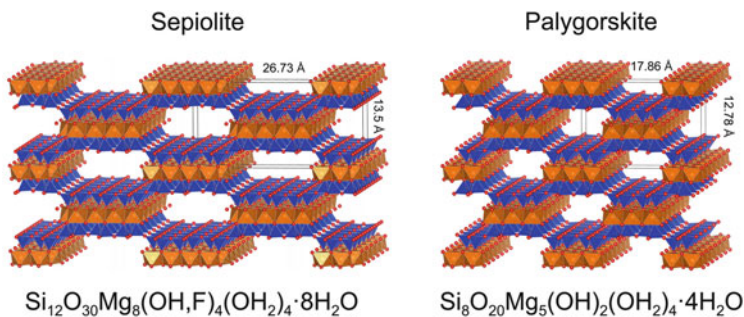


Fig. 2 Structural models and ideal formulae of sepiolite and palygorskite fibrous clays [26]

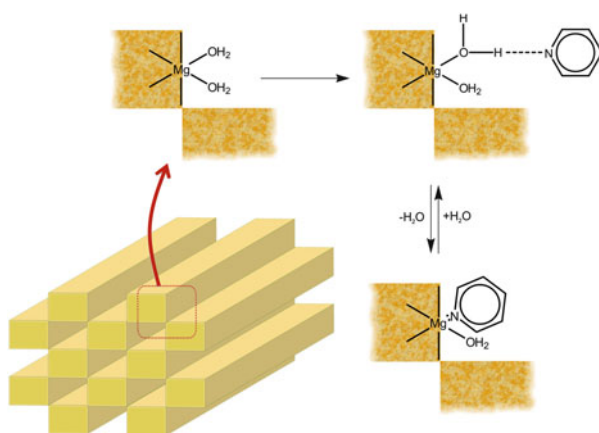


Fig. 3 Interaction mechanisms between pyridine and coordinated water located in the tunnels and channels of fibrous clays

such as water, methanol, acetone, and pyridine. Water molecules are located in the interior of the crystals, filling the structural tunnels with the so-called “zeolitic water”, which is reversibly adsorbed and desorbed by heating or by vacuum exposure. Another type of water (“coordinated water”) is located at the border of the structural blocks coordinated to magnesium cations facing the tunnels. This latter type of water is only eliminated by heating at high temperature ($>250^\circ\text{C}$) and complete rehydration is extremely slow, being considered an irreversible process. Small polar molecules such as ammonia, methanol, acetone, ethylene glycol, and pyridine can penetrate into the structural tunnels and interact with the coordinated water molecules, which can be completely replaced depending on the experimental conditions [17, 30–34]. For instance, pyridine is adsorbed in the microporous tunnels of sepiolite and palygorskite, giving rise to pyridine–clay nanohybrids of high stability. According to the scheme in Fig. 3, the nitrogen heteroatom of pyridine interacts in a first step by hydrogen bonding with the H_2O coordinated to

Mg²⁺ ions at the edge of the structural blocks (“talc-like ribbons”). By heating this intermediate material (>150°C) the water molecules are eliminated and the pyridine molecule becomes directly coordinated to the Mg²⁺ ions, in agreement with spectroscopic results [32].

Molecular dyes with appropriate dimensions can also penetrate into the structural cavities of sepiolite and palygorskite. The paradigmatic case of Maya Blue refers to a pigment prepared several centuries ago on the Yucatan peninsula, and in general in the Mesoamerica region, that consists of a very stable complex between palygorskite and indigo [35]. This organic–inorganic hybrid material shows a remarkable stability as it has preserved its blue color even though exposed for a long time to weathering and microbiological degradation. Diverse authors have claimed that encapsulation of the dye inside the clay tunnels provides a protective effect. However, there are controversial interpretations about the penetration of indigo in palygorskite as the size of these molecules appears to be too big to enter into the structural tunnels [36], although various authors have proposed a partial penetration into this clay [37]. It is probable that indigo molecules remain strongly assembled at the tunnel entrances, avoiding further penetration of other species [38, 39]. A similar situation could be proposed for related dyes such as methylene blue that show adsorption isotherms in sepiolite that correspond to a high affinity in the clay–dye nanohybrid formation [40, 41]. From spectroscopic techniques and adsorption microcalorimetry experiments, a partial penetration of this dye into the sepiolite tunnels or its blockage at the tunnel entrances can be inferred based on the observation of an obstruction to further access of these molecules [17]. Incorporation of sepiolite-dye nanohybrids into polymer matrices allows the introduction of encapsulated pigments, leading to coloration that is stable against degradation by sun exposure, showing a recent application of the ancient Mayan technology [42, 43].

It also appears that small-sized monomers such as isoprene [44], ethylene, and polyethylene [45] as well as acrylonitrile [46] can penetrate into the tunnels of sepiolite, allowing further polymerization. Certain polymers such as poly(ethylene oxide), PEO, can be directly inserted, producing at least a partial penetration into the nanopores of sepiolite [17]. However, the most frequent situation corresponds to the interaction of the fibrous clays with polymers involving the external surface of the silicates. The silanol groups at the clay surface are very effective adsorption centers for strong interaction with polar polymers through hydrogen bonding. On the other hand, the tunnels in sepiolite and palygorskite facing the external surface of the fibers (channels) contain coordinated water molecules, which are also available as adsorption centers (hydrogen bonding and/or water bridges).

As indicated above, the hydrophilic character of sepiolite and palygorskite can be modified in a controlled manner by grafting of organophilic groups after reaction with the external silanol groups. Also, treatment with neutral or cationic surfactants (e.g., long-chain alkylammonium salts) [47, 48] allows a molecular coverage, making this type of nanofiller compatible with low-polar matrices. Novel routes of surface modification include the treatment of sepiolite with alkyl and functional silanes in the form of aqueous gels [49]. More recently, Wicklein et al. [50] have

developed biohybrids based on the coverage of the sepiolite surface by phospholipids of natural origin, giving rise to bio-organoclays, which can be considered ecofriendly and nontoxic materials.

3 Synthetic Polymers/Fibrous Clays Nanocomposites

Fibrous clays are attractive nanofillers for the reinforcement of thermoplastics and other conventional polymers due to their high aspect ratio and specific surface area, which may be favorable for the improvement of certain properties when used instead of layered clays. Although their high hydrophilicity is an important drawback when combined with many of those polymers (e.g., polyethylene, polypropylene, etc.), diverse strategies have been applied to promote an adequate compatibility with the polymer matrix for reaching a good dispersion of the fibers in it. Thus, much work has been done in the last 10 years, with an increasing number of publications referring to the use of sepiolite and palygorskite as nanofillers (see for instance reviews published by Ruiz-Hitzky et al. [13, 14]). A large number of the reported references focus on the modification of the clay to reach compatibility with the polymer or to procure its assembly with monomeric species that can be further used in copolymerization reactions. It should be noted that the strategies of synthesis in many cases have to be adapted for incorporation into an existing process for large scale production of the involved polymer. In more recent years, research has tried to address other interesting issues, such as the use of fibrous clays in nanocomposites involving various polymers or in their incorporation in the presence of other nanoparticles (e.g., carbon nanotubes, magnetic nanoparticles) in view of new applications.

3.1 *Fibrous Clays as Nanofillers of Thermoplastic Polymers*

Typical thermoplastic polymers [polyethylene (PE), polypropylene (PP), polybutylene (PB), polystyrene (PS), polymethylmethacrylate (PMMA), polyvinyl chloride (PVC), polyethylene terephthalate (PET), polytetrafluoroethylene (Teflon or PTFE), and polyamides (e.g., Nylon)] are highly hydrophobic polymers. The preparation of nanocomposites based on these polymers requires the previous incorporation of adequate functionalities in the chosen nanofillers to reach their required compatibility for procuring good dispersions in the continuous phase. The methods for incorporating organophilicity and specific functionalities in palygorskite and sepiolite in order to tune their compatibility with this type of polymer are relatively easy. So, a variety of organoclays have been tested in the preparation of nanocomposites in which the presence of the fibrous clay improves the thermal stability and certain mechanical properties [13, 14]. Recent investigations have looked at ways to improve compatibilization between both components

as well as alternative processes for nanocomposite preparation. Besides, the incorporation of other nanoparticles, separately or assembled with the fibrous clay, opens the way to the development of new functional plastics. In this section, various examples of these last advances are described.

Sepiolite and palygorskite have been used as nanofillers for polyamides, with special relevance in the preparation of polyamide-6 (PA-6) resin. There are two main synthetic methods: in situ polymerization in the presence of organically modified clays [51] and dispersion in the already formed polymeric matrix of either the neat clay [52] or nanofibers previously modified with appropriate organosilanes [53]. Modification of palygorskite with *N*- β -aminoethyl-aminopropyltrimethoxy silane coupling agent allows its compatibilization with PA-6 for the preparation of composite fibers by melt spinning. By controlling the experimental conditions it is possible to obtain good orientation of the nanofillers and the PA-6 along the drawing direction, which improves tensile properties [54].

The incorporation of sepiolite and palygorskite into PE enhanced mechanical properties and thermostability while reducing the thermo-oxidation of the polymer [55]. It has also been found that the processing methodology can affect the final characteristic of the prepared nanocomposites. Thus, dynamic packing injection molding produces better dispersions of the nanofiller than conventional injection molding. Application of the former results in high density PE (HDPE)–palygorskite nanocomposites endowed with better inorganic–organic interfacial nucleation effect, and orientation of the polymer chains/crystallization induced by the shearing force [56]. Comparison of methodologies for modification of the nanofiller (e.g., sepiolite modified with vinyltriethoxysilane) before heat mixing (*ex situ*) and modification during heat mixing (*in situ*) reveals that the latter results in PE–sepiolite nanocomposites exhibiting higher thermal stability and improved tensile strength and modulus whereas elongation at break was reduced [57]. The nanofiller has also been used as support for a catalyst for polymerization in methodologies that combine in situ blending and in situ polymerization of ethylene to produce low density PE (LDPE)–sepiolite nanocomposites [58]. The presence of the clay is also favorable when certain flame retardant additives (e.g., magnesium hydroxide) and vinyltriethoxysilane as crosslinking agent are added to PE. In this way, the incorporation of sepiolite results in synergistic effects that improve flame retardancy, thermal stability, and the mechanical properties of PE nanocomposites, which have been ascribed to an increase in the crosslinking degree associated with the presence of the clay [59]. The use of gamma irradiation improves even further the mechanical properties of the resulting magnesium hydroxide–sepiolite–PE nanocomposites by reducing the presence of OH functionalities [60]. The use of sepiolite incorporating Au or Ag nanoparticles in the preparation by injection or compression molding of nanocomposites based on PE (and also on PS) results in the formation of plasmonic plastics (Fig. 4), which could be of interest in new functional applications of this type of plastics [61].

The use of palygorskite with grafted octadecyl acrylate, a cationic surfactant, and atactic polypropylene favors its further compatibilization with PP, giving rise to nanocomposites with improved mechanical properties (e.g., 123% and 23% higher

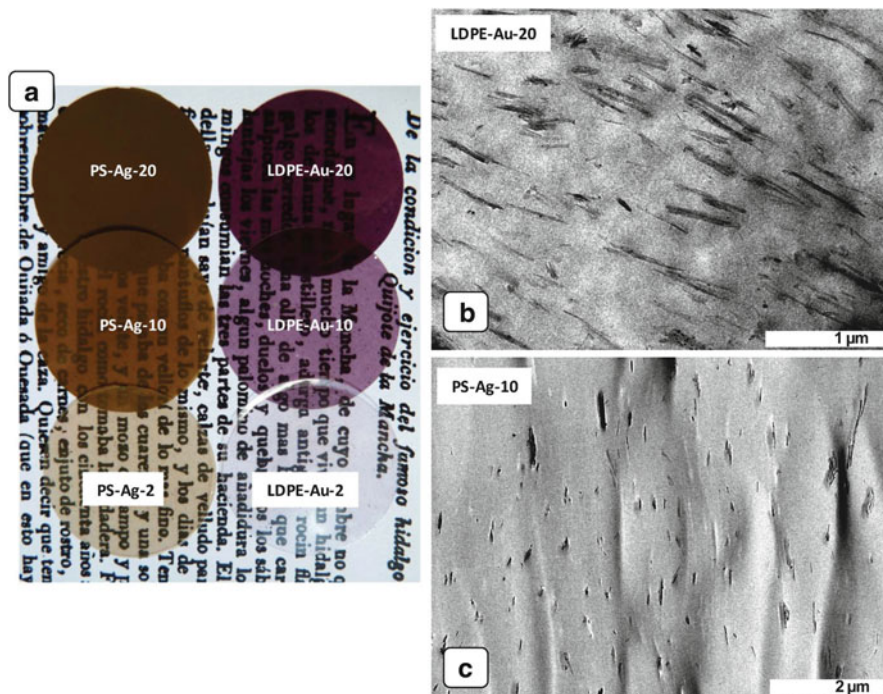


Fig. 4 (a) Image of low density polyethylene (*LDPE*) and polystyrene (*PS*) nanocomposite films incorporating sepiolite modified with Ag and Au nanoparticles. (b, c) Representative TEM images of those nanocomposites. Reproduced from [61] with permission of The Royal Society of Chemistry

values for the impact strength and tensile strength, respectively, compared with pure PP [62]. As reported for PE nanocomposites, the incorporation of fibrous clays together with fire-retardant additives results in improved properties in the ternary systems based on other polyolefins. For instance, the use of sepiolite modified with cethyltrimethylammonium ions and zinc borate results in synergistic effects in the fire retardancy properties of PP nanocomposites [63]. In the same way, PP nanocomposites incorporating neat sepiolite and multiwalled carbon nanotubes (MWCNTs) show improved thermal degradation and flammability properties favored by the char formation [64].

As indicated above, PS has been used as a matrix for sepiolites incorporating Au and Ag nanoparticles to produce plastics endowed with plasmonic properties, using methodologies of synthesis that allow easy up-scaling of the process [61]. In the same way, sepiolite with embedded FeCo nanoparticles and modified with methyltrimethoxysilane was used as nanofiller of PS to produce highly transparent nanocomposite films exhibiting magneto-optical Faraday activity [65]. In the same way, styrene was polymerized in the presence of palygorskite modified with magnetite nanoparticles, giving rise to magnetic PS nanocomposites in which the

presence of the magnetic nanoparticles assembled in the clay prevents their aggregation [66].

PMMA is a classic thermoplastic polymer and so the formation of PMMA–fibrous clay nanocomposites requires the use of organically modified clays. In situ modification of the clay, for instance by treatment of palygorskite with toluene-2,4-di-isocyanate, significantly improved the compatibility with PMMA giving rise to nanocomposites with improved mechanical and thermal properties [67]. Melt-compounding of PMMA also requires the use of organoclays that, once dispersed in the melt, act to a certain degree as crosslinking agents, reducing the motion of the polymer chains and improving thermal stability of the resulting nanocomposites [68]. Soapless polymerization of methacrylate in the presence of organopalygorskite results in the formation of polymeric matrices in which the fibrous clay becomes encapsulated [69]. The incorporation of Fe(III) favors the UV initiation of the polymerization reaction, allowing the preparation of bead-string shaped nanocomposites of controlled morphology [70]. The use of methacrylate monomers provided with two sites of polymerization (e.g., ethylene glycol dimethacrylate) and organoclays drives the formation of hydrophobic polymeric networks that can be used, for instance, in the absorption of oil [71]. The use of methacrylate monomers allows the application of copolymerization reactions that could give rise to diverse types of functional materials. In this way, 2-(2-methoxyethoxy) ethyl methacrylate, oligo (ethylene glycol) methacrylate, and acrylic acid have been prepared by free radical in situ polymerization in the presence of palygorskite, producing stimuli-responsive nanocomposite hydrogels [72]. The incorporation of palygorskite modified with Fe_3O_4 nanoparticles produces the formation of hydrogels with good mechanical properties that are sensitive to temperature and pH changes and also show magnetic properties [73, 74].

3.2 Fibrous Clays as Nanofillers for Thermosetting Polymers

Reinforcement of epoxy, polyurethane (PU), and other thermosetting resins [75] is of major interest for improving the mechanical properties and light-mass characteristics of these versatile materials of technological interest in diverse areas such as aviation and construction. Sepiolite and palygorskite nanofillers could have a double role, improving both mechanical and thermal properties, because fibers could act as crosslinking agents retarding the motion of the polymer chains [13].

Assays of the incorporation of commercial organosepiolite in glassy bisphenol A-based epoxy resin revealed good dispersion of the clay in the epoxy matrix and enhanced storage modulus in flexion, but only slight improvement in thermal stability [76]. In fact, the presence of organically modified (e.g., glycidyl silane) nanofiller may also contribute to the improved toughness, but above certain concentrations the clay agglomerates, affecting the mechanical properties [77]. In the search for improved compatibility between the fibrous clay and the polymeric matrix, diverse types of organic modifiers have been tested, including surfactants

of natural origin conveniently modified with epoxy functionalities that allow further grafting of epoxy monomers to improve the compatibility and enhance the properties of the resulting nanocomposites [78]. Actually, both unmodified and organically modified sepiolite can be used as nanofiller, although only the latter drives the formation of physical gels strongly influencing the rheology of the nanocomposite systems [79]. Results comparing the use of sepiolites with assembled SiO₂ nanoparticles reveal a more effective adhesion between the dispersed and the continuous phases when the surfactant used to template the growth of the silica was not removed from the nanofiller. This feature has been ascribed to a weaker interaction between filler and matrix in the absence of the interfacial agent [80]. In the same way, a systematic study on the characteristics of epoxy resins filled with neat palygorskite and organically modified clay, either using surfactant molecules (cetyltrimethylammonium ions) or grafted groups (3-aminopropyltriethoxysilane, APTES), reveals that organically modified palygorskites procure a better distribution and stronger interfacial adhesion. This results in enhanced mechanical and thermal properties of the final nanocomposites, although the optimum effect is reached at low loadings (ca. 2 wt%) in the case of palygorskite with grafted amino groups. In contrast, palygorskite modified with surfactant ions can be incorporated at higher loadings without severe degradation of the mechanical properties [81]. Epoxy-based nanocomposites incorporating highly dispersed palygorskite and graphite oxide nanoparticles have been prepared under ultrasound irradiation. The incorporation of both types of nanoparticles results in nanocomposites with improved properties compared with those prepared with individual nanoparticles [82].

One of the major interests in the development of PU nanocomposites is the improvement of thermal properties, especially in view of the strict regulations in the construction building sector, which is one of the main application fields of these materials. The use of sepiolite and palygorskite as nanofillers also procures nanocomposites with improved tensile strength and other mechanical properties [83–87]. In spite of the insolubility, lower thermal stability, and mechanical properties of water-borne polyurethanes (WPU) compared with organic solvent-borne PU, WPU are attracting increasing interest because they are nontoxic, nonflammable, and do not pollute the air. Thus, WPU nanocomposites filled with neat palygorskite [88], or palygorskite together with carbon black for introducing electrical properties [89], have been reported.

3.3 Fibrous Clay Nanocomposites Based on Hydrogel Polymers

Hydrophilic polymers such as polyvinyl alcohol (PVA) exhibit high affinity for association with sepiolite and palygorskite via interaction with the silanol groups at the external surface of the fibrous clays. Thus, a simple mixture of both components

results in formation of the nanocomposite [90]. The use of freeze-drying techniques for removal of the solvent used for the PVA–sepiolite suspension and crosslinking with other biocompatible polymers, such as polyacrylic acid, result in the formation of macroporous nanocomposites of potential interest as scaffolds in tissue regeneration [91].

The incorporation of sepiolite and palygorskite in hydrogels generated by polymerization (or copolymerization) of acrylic acid (AA) and/or acrylamide (AM) and other related monomers is driving a generation of a new family of low production cost superadsorbent materials of interest for diverse applications in agriculture and horticulture, sanitary goods, drug-delivery systems, and water remediation. The presence of the silanol groups of sepiolite and palygorskite in combination with the use of crosslinking agents (e.g., *N,N'*-methylenebisacrylamide) and an initiator of polymerization (e.g., ammonium persulfate) favors the growth of the AA or AM polymers (or copolymers) linked to the clay, which results in the generation of superadsorbent materials [92, 93]. The amount of clay, crosslinker content, initiator dosage, nature of monomer, ratio of monomers in AA/AM copolymer systems, and other parameters in the synthesis all affect the final characteristics of the materials regarding water absorbency properties in the presence of pure water, saline solutions, or mixtures of solvents [93, 94].

Recently, alternative routes for the preparation of this type of nanocomposite have been proposed, for instance using freeze–thaw–extrusion cycles to improve the dispersion of the clay, which allows the incorporation of higher amounts of clay [95]. Other approaches allow the incorporation of even larger amounts of clay in the hydrogel (approx. 90%). In this way, palygorskite modified with APTES is polymerized with AA in the presence of palygorskite modified with 3-methacryloxypropyltrimethoxysilane (APTMS), the first clay-hybrid acting as initiator and the second as crosslinker in the polymerization reaction [96]. Other proposed routes employ the use of the “one-pot” inverse suspension radical polymerization of AA, incorporating palygorskite previously modified with APTMS in the presence of paraffin and an emulsifier, which results in the formation of microgels [97]. Hydrogels with improved mechanical properties have been prepared by using palygorskite with grafted vinyl groups copolymerized with 2-acrylamido-2-methylpropane-sulfonic acid to produce a nanocomposite network. Polymerization of acrylamide in the presence of this network gives rise to a double network hydrogel [98].

Examples of applications of polyacrylamide-based nanocomposites refer mainly to improved superabsorbents with water absorption capacities higher than 1,000 g H₂O/g of solid [92]. Other uses of this type of material address the removal of pollutants, such as Pb(II) and Cu(II) [97, 99], methylene blue (Fig. 5), and other dyes [100]. Other examples related to environmental applications are reported in Sect. 4.2.2 as the nanocomposites may also incorporate biopolymers such as psyllium gum [101].

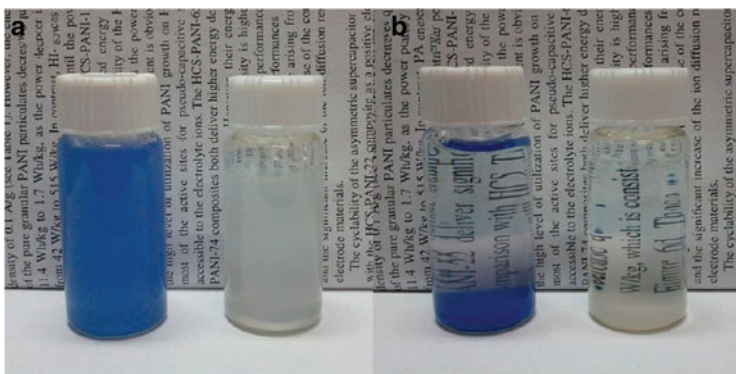


Fig. 5 (a, b) Images of water dispersions of poly(acrylic acid)-palygorskite hydrogels combined with (left) or without (right) methylene blue dye before (a) and after (b) freely settling. Reprinted with permission from [96]. Copyright (2014) American Chemical Society

4 Biopolymer-Fibrous Clay Nanocomposites

Bionanocomposites are an ecological alternative to conventional nanocomposites based on petroleum-derived polymers, as they are based on biodegradable polymers obtained from renewable resources. Biomass is the source of agropolymers like starch and cellulose and also of monomers used to chemically synthesize polymers like polylactic acid (PLA). Other kinds of biopolymers, e.g., xanthan gum and poly(hydroxyalkanoates), are produced by microorganisms. Even though most of the bionanocomposites reported in the literature are based on layered silicates, the number of examples illustrating the use of fibrous clays in the preparation of new bionanocomposites is growing rapidly.

Bionanocomposites based on sepiolite and palygorskite involving different types of water-soluble polysaccharides (starch, chitosan, alginate, etc.), proteins (gelatin, collagen, wheat gluten), and other biomolecules have been reported [15], as well as the development of biomimetic interfaces based on phospholipids as immobilization hosts for biological species [50, 102]. These bionanocomposites are usually processed as films or as hierarchical porous structures (cellular structures) by means of solvent casting or freeze-drying processes, respectively. In certain cases, these materials can exhibit enhanced mechanical properties compared with analogous materials based on layered silicates. This could be relevant in numerous applications, e.g., thermal and acoustic insulation, as well as in the packaging industry.

4.1 Polylactic Acid and Other Biodegradable Polyesters

Polylactic acid (PLA), which is derived from fermentation of agricultural by-products, is a very promising sustainable alternative to conventional polymers

within the packaging industry due to its biodegradable character when composted. However, similarly to other biopolymers, certain properties of PLA such as brittleness, slow crystallization rate, and high gas permeability, limit its adoption as a main raw material for bioplastic production. Therefore, nanoclays have been extensively used to improve some of these characteristics while attempting to not adversely affect some inherent properties of PLA [103]. Within this perspective, the use of sepiolite as reinforcing agent of this polymer demonstrated an easy dispersion and high compatibility with the PLA matrix, without the need for organic modifiers or compatibilizers, as well as a high thermo-mechanical improvement of the obtained bionanocomposites [11]. In addition, it was recently noticed that sepiolite could modify the crystallinity of PLA, affecting both gas barrier and mechanical properties of the resulting nanocomposite films [104]. On the other hand, PLA–palygorskite bionanocomposites prepared via melt blending are a promising material for agricultural packaging purposes, according to a study carried out by Jiang et al. [105]. In this case, Fourier transform infrared spectroscopy (FTIR) and X-ray photoelectron spectroscopy (XPS) measurements indicated strong interactions through hydrogen bonds between the fibrous clay and PLA. In addition, SEM and TEM images revealed that palygorskite fibrils are very well integrated in the PLA matrix, which could be the reason for the significant enhancement in tensile properties.

Polycaprolactone (PCL), another biodegradable polyester, was also evaluated as matrix in the synthesis of sepiolite-reinforced films [11, 106]. The effect of sepiolite on the biodegradation rate of both PLA and PCL films was studied, and a significant level of degradation in compost at 40°C, together with evidence of erosion after 35 days could be shown. PLA films loaded with sepiolite showed significant changes in their biodegradation compared with pure PLA film. In this case, it was postulated that the use of sepiolite as filler could limit polymer chain mobility in the bulk material and/or reduce the PLA/enzyme miscibility, causing a possible preventative effect in the bionanocomposite film. Conversely, PCL–sepiolite nanocomposite showed a preferential surface mechanism of degradation, whereby the fibrous silicate does not have an important effect on PCL degradation. Hydrolytic degradation of PLA–sepiolite films in phosphate buffer at pH 7.0 was also evaluated by Fukushima et al. [107], and it was shown that the presence of sepiolite favors a delay in degradation at 37°C, probably due to the increase in PLA crystallization induced by the clay mineral.

Other biodegradable polyesters of great interest in the plastics industry have been combined with sepiolite or palygorskite in order to improve certain specific properties of the polymer. This is the case for poly(3-hydroxybutyrate-*co*-3-hydroxyvalerate) (PHBV), a polyester widely used in disposable goods, where the assembly with organophilic palygorskite led to significant changes in PHBV properties [108]. In this study, all the PHBV–palygorskite films showed an improved crystallization ability of PHBV, which can be ascribed to a nucleation effect of the clay in the polymer matrix during the non-isothermal crystallization process. However, it was reported that the addition of organo-palygorskite in PHBV provoked a decrease in thermal stability compared to pure polymer. This behavior

is likely to be associated with the presence of quaternary alkylammonium compounds used as modifier agents in the clay.

Pristine palygorskite was also used as a nucleating agent and filler in poly (butylene succinate) (PBS), employing 1,2-octanediol as co-monomer to synthesize branched PBS copolymers [109]. The salient feature of this research was that thanks to hydrogen bonding interactions established between the components, palygorskite was found to be uniformly dispersed in the PBS matrix, resulting in an elongation at break of 550% for the clay-reinforced branched PBS containing as little as 3 wt% of silicate. Furthermore, the palygorskite fibrils played an important role as nucleating agent, improving the thermal stability and the crystallization temperature of the PBS matrix, which makes these nanocomposites very attractive as reinforced bioplastics.

4.2 *Polysaccharides*

Polysaccharides are polymeric carbohydrates composed of long chains of sugar units that are joined by glycosidic linkages. This class of natural polymers is the most abundant found in Nature, making them very attractive raw materials that could replace synthetic polymers in the development of biodegradable nanocomposite materials (bionanocomposites) and providing benefits originating from their low cost and positive ecological impact.

4.2.1 **Bioplastics**

In general, polysaccharides have the ability to form films or to be molded into objects [110]. However, these biopolymer materials have the tendency to show poor mechanical and barrier properties and high water solubility, which limits their use in a wide range of applications. In this sense, inorganic solids such as clays have been extensively used in order to improve some properties of these polysaccharides. In this context, it is important to mention that since the first study reported by Lynch et al. [111], which showed a decrease in the degradation of cellulose dextrin by soil microorganisms due to the presence of palygorskite fibrils in the biopolymer matrix, several studies on the association of fibrous clays and polysaccharides have emerged [13, 15, 112–114]. Assorted strategies have been employed using neutral or charged polysaccharides associated with both sepiolite and palygorskite for the preparation of functional reinforced bionanocomposites.

Focusing on reinforced polysaccharide films, positively charged chitosan (a linear polysaccharide mainly extracted from shrimp and other crustacean shells) was assembled with sepiolite clay, giving rise to self-supported bionanocomposite films with interesting structural and functional properties. In this study, Darder and co-authors [113] revealed that the association of sepiolite and chitosan resulted in a threefold improvement in the mechanical properties as compared with unmodified

biopolymer films, and at the same time exhibited interesting functional properties allowing their application as components in electrochemical devices. All these features were achieved thanks to the strong electrostatic interactions between the protonated amino groups of chitosan and the silanol groups located on the surface of the silicate. Moreover, these chitosan–sepiolite films proved to be very promising as membranes for N_2 separation, enlarging the scope of application of these materials [115].

More recently, sepiolite [116] and palygorskite [117] were incorporated into chitosan/PVA matrices yielding highly transparent bionanocomposite films. In both cases, it was observed that the presence of the fibrous clays in the polymer system induced an enhancement of the barrier and mechanical properties compared with neat polymer blend films. These improvements are mainly related to good interactions through hydrogen bonds between hydroxyl groups of the polymer matrix and the silicate, together with a very good integration and dispersion of the fibers in the polymer matrix.

Besides chitosan, other abundant polysaccharides like cellulose are good candidates for the preparation of bionanocomposites based on fibrous clays. Nevertheless, their application is limited due to the low solubility in water, which is caused by the numerous inter- and intra-molecular hydrogen bonds, forming close and stiffly packed chains. A novel strategy employed in order to overcome this problem is the use of ionic liquids as the main solvent in the preparation of materials based on cellulose [118, 119]. These types of compounds show desirable properties such as low toxicity, good chemical and thermal stability, near non-volatility, and recyclability, which make them attractive ecofriendly solvents in the synthesis of bionanocomposites. Within this context, bioregenerated cellulose films reinforced with microfibrillar sepiolite were prepared via ionic liquid using 1-butyl-3-methylimidazolium chloride (BMIMCl) as “green” solvent [120]. Among the different physico-chemical properties studied, the enhancement of thermal, mechanical, and water absorption properties with respect to pure cellulose films was highlighted as a consequence of the strong interactions and good affinity of the components. In addition, these nanocomposite films displayed interesting barrier properties toward O_2 , where the permeability values decrease gradually with increasing sepiolite content in the cellulose matrix, reaching values of 56% reduced permeability by addition of 8 wt% of clay. The use of ionic liquids as a novel route for the preparation of bionanocomposites and the interesting properties obtained for cellulose–sepiolite films make these materials very attractive for application in different sectors such as biomaterials and biomedicine, membrane processing, or food packaging.

Among the several cellulose derivatives are xylan-type hemicelluloses, which are the most abundant heteropolysaccharides derived as by-products from agricultural processes. Over the past few years their use in food packaging and other applications has increased considerably [121]. Hemicelluloses such as arabinoxylan are hydrophilic polysaccharides and their films tend to show high water uptake, becoming a drawback in the production of materials for the food sector. In order to improve both mechanical and barrier properties, Sárossy et al. [122] adopted the

incorporation of sepiolite clay as potential filler for arabinoxylan matrix obtained from rye flour. In addition to homogeneity and transparency, the bionanocomposites films prepared by the casting method showed a good distribution of sepiolite fibrils, which indicates better compatibility between the sepiolite and the polysaccharide matrix. The good compatibility between the components was reflected in the mechanical properties. Addition of sepiolite doubled the Young's modulus and tensile strength, giving higher values than in previous reports for xylan loaded with montmorillonite clay [123]. However, in this study the incorporation of sepiolite in the polysaccharide matrix did not reduce the water vapor or oxygen permeabilities, which makes an optimization of the system necessary in order to achieve better water and gas barrier properties for specific applications.

The reinforcement effect caused by the incorporation of fibrous clays in other carbohydrate matrices has been investigated by Chivrac and co-authors [114]. The potential strategy employed in order to obtain starch–sepiolite nanocomposites was the development of bio-organosepiolite as filler in plasticized starch films. In addition to good affinity between the biofiller and the biopolymer matrix, sepiolite modified with cationic starch produced a considerable improvement in Young's modulus by a factor of up to 2.5 compared with analogous materials based on montmorillonite. According to the authors, this behavior could be related to the high compatibility provided by the cationic starch located on the surface of the fibrous silicate and the polysaccharide matrix, which increases the material crystallinity and consequently leads to enhancement of the mechanical properties.

Polysaccharide-based nanocomposites can also be used in insulation and cushioning, and this type of application usually requires their processing as cellular solids [124]. Several techniques such as phase separation/emulsion freeze-drying, solvent casting followed by particle leaching, gas foaming, or fiber knitting can be applied in the preparation of this type of porous solid [124], but given that polysaccharide–fibrous clay materials are generally prepared from aqueous suspensions, freeze-drying is the most widely used technique for processing of low density foams [125]. In this process, the growth of ice crystals pushes the components of the aqueous suspension between adjacent crystals, and then the porous structure is generated by sublimation of the ice under vacuum. In some cases, the process can be carried out by unidirectional freezing, controlling the rate of immersion in a liquid nitrogen bath, to obtain a structure of well-aligned microchannels in the freezing direction, as shown for instance in a nanocomposite based on sepiolite previously modified with alkoxysilanes and titania nanoparticles [126]. Several works have reported the preparation of ultralightweight bionanocomposite foams incorporating polysaccharides and fibrous clays by means of freeze-drying [127, 128]. The resulting materials have a very low density, showing apparent density values below 0.20 g/cm^3 , but good mechanical properties reaching a compression modulus of up to 40 MPa in samples with a high content of sepiolite (50–75 wt%) [129]. In addition to enhancing the mechanical properties of the polysaccharide matrix, the assembly of fibrous clays also contributes to increase the fire resistance of the resulting materials. For instance, polysaccharide–sepiolite foams with clay content above 25 wt% behave as auto-extinguishable materials and

could have application as building materials [129]. A different application of these bionanocomposite foams is related to their use as a support for living species, for instance microalgae that are able to colonize foams based on chitosan–sepiolite [130]. Other techniques like supercritical drying with CO₂ [131] or foaming in a heated press in the presence of a blowing agent [132] have also been applied to prepare bionanocomposite foams based on smectites, and both technologies would also be applicable to fibrous clay-based systems.

4.2.2 Environmental Remediation

Polysaccharides and their derived bionanocomposites are also widely applied as low cost biosorbents in the removal of pollutants [133], as a green alternative to commonly used organoclays. Among this type of bionanocomposites, those based on fibrous clays show in some cases exceptional properties that combine the adsorption and absorption properties of both the inorganic and biological components. Their application in environmental remediation is a recent research topic and a huge number of the reported materials involve the polysaccharide chitosan. Its assembly with sepiolite and palygorskite proceeds by hydrogen bonding interaction between the silanol groups located at the external surface of the silicate fibers and the hydroxyl groups present in the polysaccharide chain, and partially through electrostatic interaction due to the protonated amino groups of chitosan [113]. Given that the cation-exchange capacity of these fibrous clays is much lower than that of smectites, chitosan–sepiolite and chitosan–palygorskite bionanocomposites usually present free protonated groups that provide these materials with good adsorption properties towards anionic species. For instance, this property was exploited to immobilize anionic dyes in a chitosan–palygorskite system for photoprotection of microbial biocontrol agents like the fungal conidia of the entomopathogen *Beauveria bassiana*, which are used for controlling insect pests [134]. The adsorption properties were also exploited for removal of organic pollutants like tannic acid, which is crucial in the treatment of drinking water [135]. In this last example, adsorption is attributed to the electrostatic interaction between the tannic acid molecules and the protonated amino groups of the bionanocomposite, together with hydrogen bonding and van der Waals interactions that could be established with the uncharged biopolymer chain [135]. Chitosan–palygorskite bionanocomposites were also applied in the removal of uranium from aqueous solutions [136]. In this case, the adsorption mechanism is attributed to the interaction of U(VI) cations with the –OH and –NH₂ groups of chitosan. The adsorption process is enhanced at pH 5.5, where the competing effect of protons at low pH or of carbonate and bicarbonate anions at high pH is minimized. Similarly, Fe(III) and Cr(III) cations were also removed from aqueous solution with chitosan–palygorskite materials, which showed higher adsorption than the components used individually [137].

Chitosan–sepiolite materials were also proposed for clarification of olive mill and winery wastewater effluents through a combination of coagulation and

flocculation processes [138]. In the case of winery wastewater, clarification is attributed to neutralization of the colloids with highly charged nanocomposites. In olive mill wastewater, van der Waals or OH interactions between specific organic colloids and the glucosamine units of the chitosan in low charge nanocomposites seem to be responsible for clarification. The efficient performance could also be related to the highly porous structure of the chitosan–sepiolite coagoflocculant materials [138]. In another interesting application, Pan et al. [139] proposed the use of chitosan-modified local soils with the aim of flocculating and removing harmful microalgal cells from the Taihu Lake, China. Previous studies were carried out in the laboratory using chitosan–sepiolite bionanocomposites as flocculants, which showed good removal efficiency with a reduced competing effect from humic acids.

In contrast to the materials mentioned above, in which chitosan was directly adsorbed on the silicate fibers, the preparation of bionanocomposites involving grafting of the polysaccharide to the clay has been reported as an alternative route. Thus, Peng et al. [140] reported the previous modification of the sepiolite fibers with 3-aminopropyltriethoxysilane, followed by soaking in glutaraldehyde as coupling agent, and finally by anchoring of the chitosan chains. This material was used for the adsorption of a reactive dye, reactive yellow 3RS, and showed a higher adsorption capacity than that of the pristine clay. In a related system, γ -glycidoxypropyltrimethoxysilane was added as a crosslinker of chitosan and palygorskite, but in this case the chitosan was previously mixed with a solution of a Co(II) salt in order to produce an ion-imprinted material that could be used as a selective extractant of Co(II) ions from aqueous solution [141]. Similarly, the use of crosslinking agents such as formaldehyde and glutaraldehyde in an emulsified chitosan–palygorskite suspension allowed the production of uniformly sized microspheres that were successfully applied for the removal of tannic acid [142].

Besides chitosan, other polysaccharides have been assembled with fibrous clays for application in environmental remediation, e.g., alginate, xanthan gum, carboxymethylcellulose (CMC), hydroxypropylmethylcellulose (HPMC), pectin, and starch [143]. The resulting materials showed enhanced stability in water, as well as good results in the uptake of heavy metal ions such as copper and lead from aqueous solution. A different application of alginate–palygorskite bionanocomposites processed as microspheres was the controlled release of an organophosphate insecticide, chlorpyrifos, with the aim of facilitating its safe handling and reducing the undesirable environmental impact [144]. Sacran, an anionic megamolecular polysaccharide recently extracted from the cyanobacteria *Aphanothece sacrum*, has also been assembled with sepiolite in order to exploit its ability to complex lanthanide ions for the development of biosorbent materials [145]. Controlling the composition of the bionanocomposite as well as the preparation conditions, it was possible to favor the arrangement of sacran chains as liquid crystals in the resulting sacran–sepiolite materials. The presence of such crystalline domains in materials of a given composition seems to be responsible for the high adsorption capacity of these materials towards neodymium ions in comparison with other tested lanthanide ions (Fig. 6).

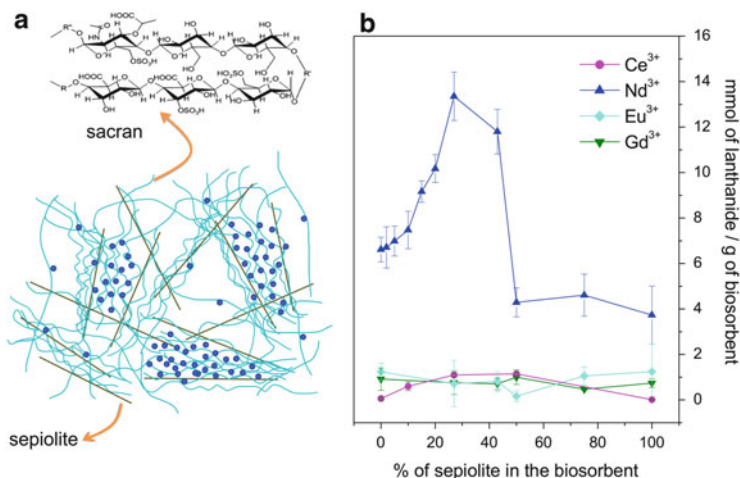


Fig. 6 (a) Possible arrangement of sacran chains as crystalline domains in sacran–sepiolite bionanocomposites and the adsorption of lanthanide(III) ions. (b) Uptake of diverse lanthanides by sacran–sepiolite materials with variable content of sepiolite

Superparamagnetic polysaccharide–fibrous clay materials can be prepared by previous modification of the silicate fibers with magnetic nanoparticles. A recent example describes the layer-by-layer deposition of chitosan and cysteine-modified β -cyclodextrin on Fe_3O_4 nanoparticle-decorated palygorskite fibers, and their application in the recovery of precious metal ions, showing a preferential adsorption towards Ag^+ and Pd^{2+} compared with Pt^{4+} [146]. In a similar material, chitosan was used as a bridge to assemble Au nanoparticles with the Fe_3O_4 -decorated palygorskite fibers by electrostatic interaction [147]. The resulting material showed catalytic activity and was applied for the rapid decoloration of a Congo Red solution. An additional advantage in both cases is the possibility of easy separation of the superparamagnetic bionanocomposites from the reaction medium by means of a magnet.

Other complex systems involving the combination of polysaccharide–fibrous clay materials with polymers like polyacrylic acid (PAA) or polyacrylamide (PAM) are commonly prepared as ecofriendly and biodegradable superabsorbents for different applications. Many of these materials are produced for application in agriculture and horticulture due to their high water absorbency that can be kept after several re-swelling cycles [148], but they also have other exceptional applications such as for control of the relative humidity in places like museums or galleries, as in the case of a composite system involving sepiolite, CMC, and a copolymer of PAA and PAM [149]. The presence of these polysaccharides provided with functional groups like carboxylates or sulfates also facilitates the use of these complex systems in environmental remediation. Some illustrative examples of this group of materials are CMC-*g*-PAA/palygorskite bionanocomposites applied in the uptake of heavy metal ions like $\text{Pb}(\text{II})$ [150], a κ -carrageenan-*g*-PAM/sepiolite

hydrogel used in the removal of crystal violet dye from water [151], and chitosan-*g*-PAA/palygorskite analogs that have been used for the removal of ammonium nitrogen ($\text{NH}_4^+\text{-N}$) (a primary indicator of water quality [152]), dyes like methylene blue [153], or heavy metal ions like Hg(II) [154]. It is also worth mentioning the possibility of applying this type of material for the slow release of fertilizers, which can contribute to reducing environmental pollution due to the excessive use of these compounds. An example of this application is the combination of alginate with palygorskite, urea, and KH_2PO_4 and coating of the mixture with an alginate-*g*-poly(acrylic acid-*co*-acrylamide)/humic acid system in order to prepare fertilizer granules [155].

4.2.3 Biomedical Applications

Nanomaterials have become interesting for drug delivery applications because of the high loading capacity of pharmacological molecules due to their large specific surface area and the possibility of directing these particles to the required site [156–158]. The combination of nanomaterials such as clays with biopolymers (e.g., polysaccharides) offers several advantages: (1) control over the drug release profile, (2) control over carrier assembly and its microstructure, and (3) improved biocompatibility and uptake [159, 160]. With the focus on fibrous clays in this context, Wang et al. reported the preparation of bionanocomposites based on chitosan–palygorskite for oral delivery of diclofenac sodium (DS) [161–163]. Chitosan–palygorskite crosslinked with glutaraldehyde or Ca^{2+} ions was processed into pH-sensitive microbeads of narrow size distribution of around 5 μm by employing the spray-drying method. The active species (i.e., the drug DS) remains entrapped within the crosslinked network after loading and can be released by changing the pH of the medium. This ensures that release of DS in gastric fluid (acidic pH) is avoided, but allows its complete and controlled delivery in intestinal fluid (neutral pH) through the increased isoelectric point of the microbeads brought about by the incorporated clay. The presence of palygorskite has also been observed to favor the production of small and uniform microbeads and has an important effect on the swelling ability of the system, a sensitive feature of drug release carriers.

Wound dressings are another type of interesting application for bionanocomposite materials showing drug release properties. This interest is kindled by specific features such as high water uptake and noncytotoxicity together with possible mucoadhesivity of specially tailored bionanocomposites. In this context, Salcedo et al. reported the successful assessment of chitosan–montmorillonite nanocomposites as wound-dressings [160], showing biocompatibility and the ability to stimulate cell proliferation and wound healing. These promising studies could trigger the future use of fibrous clays in bionanocomposites for this type of application.

Attributed to the demand for facile and low-risk vaccine administration, the needle-free, nasal delivery routes are sought and investigated [164]. Herein, bionanocomposites prepared by a combination of fibrous clay and polysaccharides

can contribute to improved delivery of antigenic material and, thus, may constitute a novel class of vaccine adjuvants addressed to nasal delivery. In this context, Ruiz-Hitzky et al. developed an influenza vaccine that showed high levels of seroprotection in mice and were based on the modification of the surface of sepiolite with the biopolymer xanthan for controlled immobilization of H1N1 influenza virions [165]. The reason for the choice of this biopolymer is its mimicry of the surface of nasal mucous, the natural adsorption site of the influenza virus during the entry into an organism. Mimicking this environment in terms of surface charge, water retention, and functional sugar groups is considered favorable for the interaction between carrier and virion and, thus, in determining the preservation of immunogenic activity of the antigen. Conversely, on unmodified inorganic carriers strong electrostatic interactions with highly polar surfaces can result in adsorption-induced alterations of the protein structure of antigens and subsequent diminishing of their immunogenicity, as observed for pristine sepiolite [165] and sometimes even in the case of standard aluminum-containing adjuvants [166, 167]. Another aspect of using microfibrinous clays such as sepiolite as vaccine adjuvants is connected with their needle-like texture that is thought to enhance mucosal immune responses provoked by irritation of the nasal mucous by fibers [165]. This can help to improve the efficacy of vaccination and, thus, reduce the necessary dose for immunization.

4.3 Proteins

Although less studied than polysaccharides, proteins have been traditionally used as raw materials in a wide range of non-food applications such as adhesives, glues, paints, textile fibers, paper coatings, and various molded plastic items. Proteins can be classified according to their shape and solubility as fibrous, globular, or membrane proteins, and among their possible source are included plants, animals, and bacteria [168].

4.3.1 Bioplastics

Due to the renewable and biodegradable properties of proteins, together with their good film-forming ability in some cases, proteins are attractive biopolymers in the synthesis of bionanocomposite materials. However, similarly to polysaccharides, protein-based materials show high water sensitivity and low mechanical properties. In order to improve such properties, various routes and strategies of synthesis have been explored, including the incorporation of clays such as sepiolite and palygorskite in the protein matrix. In this context, improved properties resulting from interactions between the structural proteins such as gelatin or collagen and the involved fibrous clay were explored in recent works [169–171]. This synergistic effect between the components was observed by Fernandes and co-authors in

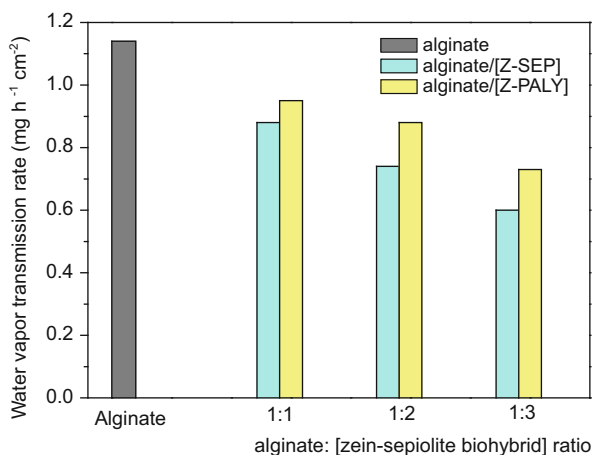
sepiolite-reinforced gelatin films [169, 170], where the good fitting of the triple helix of the re-naturalized gelatin along the external surface of the sepiolite channels resulted in a significant enhancement in the mechanical properties of the final bionanocomposite, reaching a 250% increase in the elastic modulus at 50% (w/w) clay loading. Analogously, the influence of the presence of palygorskite fibrils was evaluated in type I collagen films [171]. In this case, although fluorescence spectroscopy and FTIR analysis demonstrated that the presence of the fibrous clay promotes a contraction and aggregation of collagen chains, the triple-helix backbone of the protein was preserved throughout the process of synthesis. Additionally, collagen–palygorskite films showed enhanced thermal stability in comparison with pure collagen, where the increase in palygorskite content contributes to a better thermal behavior of the obtained bionanocomposite films.

Recently, Giménez et al. [172] reported the role of sepiolite fibers in the release of bioactive compounds from gelatin–egg white films containing clove essential oil. In this study, it was observed that the incorporation of sepiolite in the protein matrix resulted in an improvement in Young's modulus, whereas the increase in elongation at break and water vapor permeability (WVP) was influenced by the presence of clove essential oil in the bionanocomposite film, this latter compound acting as a plasticizer of the system. Moreover, the incorporation of fibrous nanoclay in gelatin–egg white films favored the release of protein components and eugenol from the matrix, contributing to the antioxidant and antimicrobial activities of the films.

Within the perspective of storage proteins, it is worth noting wheat gluten protein, a multicomponent agroproduct frequently employed as component in packaging film or edible coating materials [173]. The structure and biodegradable properties of homogeneous thermopressed wheat gluten films reinforced with palygorskite as nanofiller was studied in detail by Yuan et al. [174]. The good dispersion of palygorskite fibrils in the wheat gluten matrix was reflected by the increase in viscoelastic and mechanical properties, where 7% (w/w) clay loading showed the best results. In addition, the presence of palygorskite provoked an increase in the biodegradability, leading to the disaggregation and dwindling of wheat gluten/palygorskite films after 15 days of burial.

Zein, a storage protein extracted from corn, shows a hydrophobic character mainly due to the nonpolar amino acid residues in the structure. In addition to its zero-toxicity, its high hydrophobicity can be relevant in the preparation of materials in which zein can act as a barrier to moisture and oxygen. Based on this, Alcántara et al. [175–177] explored the assembly of zein in both sepiolite and palygorskite clays with the aim of developing bio-organoclays that could be used as green alternatives to conventional organoclays involving alkylammonium compounds. It was observed that the incorporation of zein–fibrous clays as biofillers in water-soluble polysaccharides increased the water resistance of these hydrophilic matrices, reducing the water uptake and water vapor permeabilities of the obtained films (Fig. 7). This behavior is probably related to the hydrophobic character introduced by the protein present in the biofillers, making the incorporation of water molecules difficult and leading to a consequent decrease in water adsorption and increase in

Fig. 7 Water vapor transmission rate of alginate-based bionanocomposite films incorporating zein–sepiolite (*Z-SEP*) and zein–palygorskite (*Z-PALY*) bio-organoclays at different loadings



the barrier properties. Indeed, the bionanocomposite films reinforced with zein–fibrous clays showed homogeneity, transparency, as well as interesting mechanical properties, therefore being promising as new ecofriendly materials with potential applications in food packaging.

4.3.2 Biomedical Applications

Fibrous clays are of great interest for biomedical purposes, as reviewed by Carretero and Pozo [178, 179]. A recent example reports the efficiency of pristine palygorskite in the healing of skin wounds in rats, as this silicate seems to provide better rehydration and topical anti-inflammatory action [180]. However, a few works have been reported in recent years on the application of protein–fibrous clays bionanocomposites for biomedical applications such as drug delivery or reparative medicine, which usually involves structural proteins like collagen or gelatin. The first works on this topic were carried out in the 1980s and 1990s and were focused on collagen–sepiolite complexes that showed biocompatibility in *in vitro* experiments, allowing the adhesion and proliferation of fibroblasts [181, 182]. On this basis, the same authors carried out *in vivo* experiments, implanting these bionanocomposites in surgically created rat calvaria defects [183]. Interestingly, the implanted materials did not produce any toxic effects and were fully resorbed, allowing healing through osseous regeneration. They also studied the behavior of collagen–sepiolite complexes crosslinked with 1% glutaraldehyde in order to slow down the rate of resorption after subcutaneous implantation [184]. In this case, the crosslinked implants showed 100% persistence for several months before resorption, in contrast to unmodified materials that began to be resorbed after few days of implantation. As mentioned above, new studies have been carried out in recent years with the aim of understanding how collagen and its derivative gelatin assemble with fibrous clays [170, 171], and there is also interest

in the processing of this type of material as hierarchically organized porous scaffolds. For instance, gelatin–sepiolite materials were processed by freeze-drying to produce macroporous foams with porosity of 98% and good mechanical properties, showing a Young's modulus close to 6 MPa for a sepiolite content of 9.1 wt% [185]. These preliminary works can be the basis for application of these bionanocomposite foams involving structural proteins and fibrous clays for relevant biomedical purposes including tissue regeneration, wound dressings, or drug delivery applications.

Biopolymer–clay nanocomposites offer interesting properties (such as swelling, bioadhesion, and cell uptake) for application as drug delivery systems [159], contributing to maintain a constant dose of the drug within the therapeutic dose throughout the treatment. Although most of the protein-based bionanocomposites reported for drug delivery applications involve layered silicates, a recent work confirms that fibrous clay minerals can also be useful for this purpose. In this case, silk fibroin, a natural protein created by spiders, the larvae of *Bombyx mori*, and many other insects, was assembled on the outer surface of palygorskite to form a core–shell structure [186]. The resulting bionanocomposites showed a slower release of diclofenac by about 50% in comparison with the pristine clay.

4.3.3 Biocatalytic Applications

Enzymes are globular proteins that have also been assembled with different silicates and other inorganic solids for the development of biosensors and bioreactors. Several works have reported the suitability of fibrous clays for that purpose because they can provide a protective support that may prevent the tertiary protein structure from unfolding. For instance, sepiolite and palygorskite were suitable for the immobilization of *Rhizomucor miehei* and *Candida cylindracea* lipases, which were assembled by ionic adsorption through the positively charged groups of the proteins and the silanol groups of the clay surface [187]. In this case, higher rates of hydrolysis of ethyl carboxylates were obtained when using fibrous silicates in comparison to analogous lipase-layered silicate complexes. In a similar example, an invertase–sepiolite system was used in a packed bed reactor profiting from the increased resistance to washing out as well as the higher thermal stability due to the clay support [188]. Assembly with the clay support usually enhances the thermal and storage stabilities of the enzymes, as in the case of catalase supported on sepiolite [189] or alcohol dehydrogenase on palygorskite [190], which allows recovery of the carrier and its repeated use in consecutive cycles. However, in some cases, the adsorption of the enzyme can provoke a partial loss of the enzymatic activity, as shown for a pig pancreatic lipase adsorbed on sepiolite [191]. The reduction of activity by up to 42% in comparison to the free enzyme was attributed to a steric effect of the supported lipase in the reaction and/or to the deactivation of its active sites due to the assembly. In spite of this, the high stability of the sepiolite-supported enzyme and the easy recyclability allowed its application in the continuous production of biofuel from sunflower oil [191]. In order to avoid

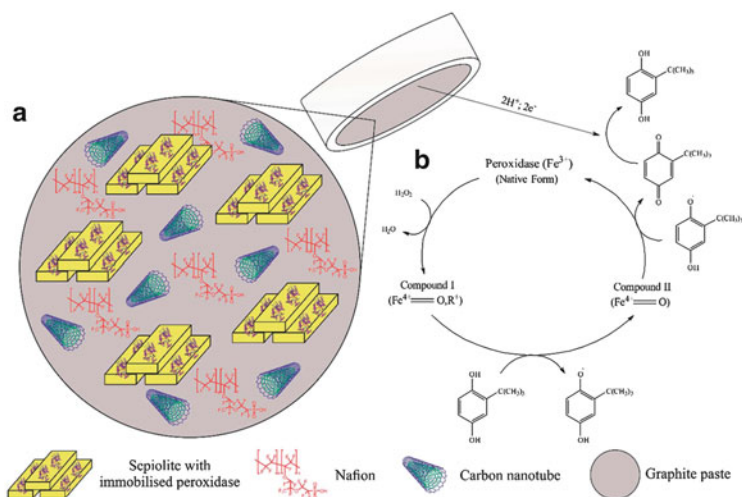


Fig. 8 (a) Sepiolite-immobilized peroxidase together with carbon nanotubes and Nafion within the graphite paste. (b) Electrocatalytic determination of *tert*-butylhydroquinone (TBHQ) with the peroxidase-based biosensor. Reproduced from [194] with permission from The Royal Society of Chemistry

enzyme denaturation, the surface of the fibrous clays can be first modified with a biocompatible molecule, e.g., phospholipids [102], as will be detailed in the next section.

Clay-supported enzymes are also useful in the construction of electrochemical biosensors. Palygorskite has been widely used as an immobilization matrix for numerous enzymes like tyrosinase [192] or glucose oxidase [193] on the electrode surface due to its excellent film-forming ability. In both cases, the enzymes preserved their bioactivity, allowing the development of electrochemical biosensors for the determination of phenol in the case of tyrosinase [192], or of glucose in blood and urine using the glucose oxidase biosensor [193]. In contrast to these surface-modified electrodes, a recent example reports the preparation of a bulk-modified biosensor based on peroxidase extracted from a fruit native to South America, which is then immobilized on sepiolite [194]. In this case, the clay-supported enzyme is dispersed in a mixture of graphite powder, MWCNTs, mineral oil, and Nafion perfluorinated resin, forming a biodeposited material that works as the sensing and conducting phase of the biosensor (Fig. 8). It was successfully applied in the determination of *tert*-butylhydroquinone (TBHQ), a food additive with antioxidant properties, in commercial salad dressings.

4.4 Lipids

The formation of organic mono- and multilayers on clay surfaces through adsorption of surfactant molecules like quaternary alkyl ammonium salts has been known and studied for many decades [7, 195]. The resulting so-called organoclays are hydrophobic and, thus, compatible for blending with many polymers and resins and find employment for instance as thickeners or nanofillers. An important drawback of this type of organoclay is connected with the toxicity of many quaternary alkylammonium components, which makes their extension into biological fields difficult [196]. Therefore, increased attention has been directed toward biosurfactants as biocompatible and ecofriendly alternatives [197, 198]. Naturally occurring biosurfactants are for instance glycolipids, fatty acids, phospholipids, lipopeptides, and polymeric biosurfactants [198]. There is also an increasing number of synthetically produced biosurfactants such as sugar-based surfactants, DNA surfactants, or full peptide surfactants [199–201]. From this library of molecules, interfaces with certain biomimetic features can be prepared via self-assembly routes [202] and find potential applications in biomedical or other biotechnological fields [203–205].

The opportunities of supported lipidic biomembranes have been investigated by Wicklein et al. through self-assembling different lipid structures on the surface of sepiolite [50, 206]. Lipid deposition was carried out either by liposome adsorption from aqueous media or by molecular adsorption from organic media [207]. In both cases, the adsorption isotherms show the characteristic shape of mono- and bilayer formation as function of the equilibrium phosphatidylcholine (PC) concentration. This study has also shown that liposomal deposition is more effective for the formation of a lipid membrane in this specific system. The reason is that in aqueous media PC adsorbs as aggregates (i.e., bilayered liposomes) whereas in ethanol single PC molecules adsorb on the clay. The molecular interaction between the lipid headgroup and the clay surface can be investigated by IR and NMR spectroscopy. These investigations strongly indicate hydrogen bonding between the ester and phosphatidyl groups of the lipid and the silanol groups located on the sepiolite surface [50]. The adsorption of phospholipids on sepiolite also has a marked influence on the surface hydrophilicity of the resultant material, as evidenced by contact angle measurements on cast sepiolite–PC films. The initially hydrophilic sepiolite turns more hydrophobic as the first monolayer is completed, which is in agreement with the presence of hydrocarbon chains at the surface of the material. With subsequent deposition of lipid molecules, the contact angle gradually decreases again as hydrophilic lipid headgroups accumulate at the external surface.

The self-assembly concept also allows for the preparation of mixed lipid membranes that can offer a larger variety of lipid-based membranes with diverse functionalities that can be of interest in different technological applications [208]. These hybrid layers are composed of individual membrane leaflets of different molecules [209–211]. Such a hybrid interface has been assembled on sepiolite and was composed of an inner phosphatidylcholine monolayer (ML-PC)

and an outer leaflet of *n*-octyl- β -D-galactoside (OGal) by subsequent monolayer deposition from the corresponding aqueous biosurfactant solutions [102]. It has been assumed that the PC monolayer serves as nucleation site for the growth of the OGal outer membrane leaflet by hydrophobic interaction between the hydrocarbon chains [212]. This assumption is also supported by Persson and co-workers who investigated adsorption of *n*-dodecyl- β -D-maltopyranoside on hydrophobized surfaces based on silane and concluded that insertion of the alkyl chains of the sugar-based surfactant into the hydrophobic silane layer acted as an anchoring mechanism [213]. The adsorption of OGal molecules causes an inversion of the surface hydrophilicity of the resultant material, as evidenced by water adsorption isotherms [102]. Nonionic sugar-based surfactants (SBSs) are particularly interesting for incorporation into these hybrid layers, e.g., for their antifouling properties [214, 215] or protein stabilization ability [216–218].

Related to their biocompatibility, clay–lipid hybrids are interesting materials for *in vivo* applications such as enterosorbents for mycotoxins. Infestation of crops and foodstuffs by mycotoxins (fungi-produced toxic compounds) has been a severe threat for millennia, with occasional catastrophic consequences for the lives and health of both animals and humans [219]. A convenient and efficient method for elimination of these compounds from animal alimentation is their *in vivo* adsorption and sequestration (i.e., enterosorption) by food additives like clay and soil minerals [220]. As many of these mycotoxins are rather hydrophobic (e.g., aflatoxins) the use of organophilic sorbents would increase their retention. In fact, bio-organoclays such as sepiolite–lipid hybrids demonstrated higher *in vitro* sequestration efficiencies for aflatoxin B1 than the neat clay analogue [50] and could thus be a promising candidate material for *in vivo* applications.

Another *in vivo* application of these hybrids is their employment as vaccine adjuvants, where they act as carrier for antigens of, for instance, Influenza A (i.e., whole virus particles, haemagglutinin protein) [167]. The bilayer lipid membrane supported on sepiolite fibers serves as accommodation site for these antigens in order to limit immunogenicity by compromising the support–antigen interactions that are frequently observed for inorganic vaccine adjuvants [166]. Functional studies in mice revealed that, in contrast to a standard aluminium hydroxide adjuvant, Influenza vaccines based on sepiolite–lipid induced high titres of specific antibodies with a Th1 profile that is often associated with efficient clearance of viral infections [221].

The biomimetic character of the clay-supported lipid interface is also beneficial for the immobilization of certain proteins, especially membrane-bound enzymes. The catalytic activity of such enzymes is very sensitive to the accommodating environment and easily compromised by protein structure deformations. It could be shown in electrochemical assays that, for instance, cholesterol oxidase (COx) maintained its catalytic activity when supported on sepiolite offering a bilayer lipid membrane [102]. However, the activity of COx was largely diminished after immobilization on sepiolite hybrids displaying cetyltrimethylammonium or hybrid lipid/octyl-galactoside layers, underlining the importance of biomimetic interfaces such as the bilayer lipid membrane for good stabilization of such enzymes. This

offers possibilities for the preparation of, for instance, selective biocatalysts [222] and sensitive biosensors [102] employing immobilized enzymes on sepiolite–lipid hybrids as active species.

4.5 Nucleic Acids

Fibrous clays are also of great interest in gene transfection, as they can be used as nonviral vectors. It can be assumed that the assembly mechanism of negatively charged nucleic acids to the silicate fibers proceeds through hydrogen-bonding interactions with the silanol groups located at the silicate surface. Short-chain DNA molecules show a high affinity towards sepiolite, being spontaneously assembled on the surface of this silicate [206]. In a similar way as reported for other types of clays such as smectites [223], adsorption of DNA chains on sepiolite protects against degradation by the action of DNase enzyme [206].

Interestingly, nonviral gene transfection using the supported DNA–sepiolite systems can be easily carried out following a remarkably simple approach. It consists of the simple mixing of a colloidal dispersion of DNA-modified mineral nanofibers with bacteria on agar plates, which are stimulated through sliding friction at their interface and subsequently take up the nanofibers. This is in short the so-called Yoshida effect [224], which leads to inoculation of the transfecting DNA previously adsorbed on the mineral nanofibers that are incorporated inside the cell and, therefore, the nucleic acid can be expressed therein [225, 226]. In this way, sepiolite fibers with diameters of around 50 nm have been evaluated for the transfer of exogenous plasmid DNA into bacterial cells such as *E. coli* and other bacteria using sepiolite [226]. Later, Wilharm and coworkers [227] confirmed Yoshida's observation and optimized this method for transfecting *E. coli*, *Y. enterocolitica*, and *A. baumannii*, and established a user-friendly protocol involving the use of sepiolite from Spanish deposits, which apparently has no carcinogenic potential and lower biological activity than sepiolite from other origins [228]. It should be interesting to prove whether this approach could also be operative for gene transfection involving eukaryotic cells.

5 Conducting Fibrous Clay Nanocomposites

Nanocomposites based on fibrous clays provided with electrical conductivity could be designed and prepared following approaches based on the assembly of conducting polymers with fibrous clays as well as on the combination of sepiolite and palygorskite with conducting carbonaceous materials. It can be expected that future research activities in this domain will consider the combination of both approaches with the aim of optimizing the mechanical behaviour and other properties with suitable ionic and/or electronic conductivity.

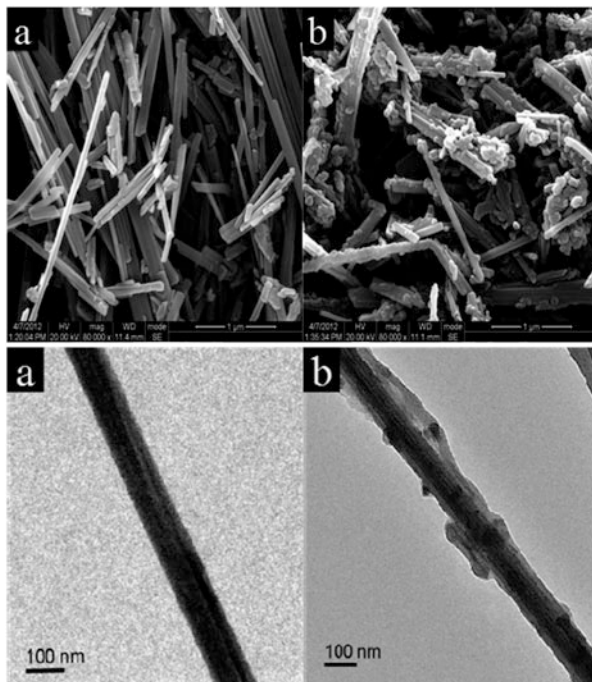
5.1 Conducting Polymer–Fibrous Clay Nanocomposites

The incorporation of palygorskite and sepiolite to conducting polymers has been scarcely investigated in comparison with the use of montmorillonite and other layered clays that can intercalate, giving rise in certain cases to delamination processes when they are assembled with typical electronically conducting polymers such as polyaniline (PANI), polypyrrole (PPy), and poly(3,4-ethylenedioxythiophene) (PEDOT) and ionically conducting polymers such as PEO [229–238]. The main advantage of assembling conducting polymers with layered clays is an improvement in stability based on the encapsulation by the clay layers, the anisotropy in the conducting behavior imposed by the 2D inorganic host arrangement, and the counterion effect because the smectites can act as negatively charged species compensating the cationic charge in ion-conducting nanocomposites, affording a quasi null contribution of the negative transport number ($t \approx 0$) [237, 239].

As indicated above, unsaturated monomers such as pyrrole, thiophene, and isoprene can be adsorbed and further polymerized inside the sepiolite tunnels [31, 44]. This is an interesting feature that can be used for preparation of polyunsaturated conducting polymers, using the tunnels of the fibrous clays for templating the preparation of clay nanocomposites. For instance, the *in situ* polymerization of pyrrole in the presence of iodine leads to I₂-doped PPy–sepiolite nanocomposites provided with conducting properties from polaron and bipolaron mechanisms as confirmed by electron paramagnetic resonance (EPR) signals and UV–Vis spectroscopic studies [240]. More recently, Chang and coworkers also reported the use of *in situ* oxidative polymerization for the preparation of one-dimensional core–shell conducting PPy–sepiolite nanocomposites (Fig. 9), which have been characterized by application of diverse techniques including electrochemical impedance spectroscopy (EIS) [241]. These authors emphasize the interfacial compatibility between PPy and the sepiolite when this inorganic substrate was previously modified by treatment with alkylammonium-based surfactants (e.g., CTAB). The resulting PPy nanocomposites compared to pure PPy electrodes appear to be more promising for application as electrode materials in supercapacitor devices due to their good electrical double-layer capacitance property, higher specific capacitance, and smaller resistance [241].

In the same way as sepiolite, palygorskite has also been used in the preparation of PPy nanocomposites, although no evidence of polymerization at the interior of the tunnels has been invoked in this last case. Wang and coworkers used rhodamine B (RhB) as an additive in the *in situ* oxidative polymerization of pyrrole with the aim of inducing the formation of RhB–palygorskite–PPy nanocomposites showing higher conductivity values and better electrochemical behavior than the same materials without the incorporation of the RhB dye [242]. These authors proposed the existence of π – π interactions and stacking between RhB molecules and the pyrrole rings to explain the observed behavior. In our opinion, related experiments involving diverse chromophores in PPy and PANI sepiolite and palygorskite

Fig. 9 (a, b) SEM (*top*) and TEM (*bottom*) images of sepiolite (a) and sepiolite–polypyrrole nanocomposite (b). Reprinted with permission from [241]. Copyright (2014) American Chemical Society



nanocomposites could open a way for development of novel photoconductor materials. Interestingly, another potential application of PPy–fibrous clays nanocomposites is the removal of anionic pollutants from industrial wastewater, which is attributed to the ion-exchange ability inherent to the PPy^+X^- entities assembled with the silicate support [243]. In this way, efficient chromate collectors from aqueous solution have been recently reported using PPy–palygorskite nanocomposites able to adsorb these anionic pollutant species in monolayer coverage [243].

In a similar way, PANI could be assembled with palygorskite and sepiolite [244, 245], although in these cases it seems that the polymer remains exclusively assembled at the external surface of the silicate framework. The role of the interphase is crucial for the final properties of the nanocomposites. For instance, treatment of palygorskite with APTES, after acid treatment of the clay to increase the amount of surface silanol groups, favors the assembly of PANI via grafting on the silicate framework through the APTES coupling agent. In this way, the conducting polymer cannot be extracted with absolute ethanol in a Soxhlet apparatus, whereas the samples untreated with APTES are completely removed by the Soxhlet extractions [244]. The electrical conductivity of palygorskite-based/PANI nanocomposites can reach better conductivity values (e.g., 2.21 S/cm) than pure PANI, which is thought to be because the polymer assembled with the silicate network adopts a more favorable conformation with more extended chains than pure PANI, leading to a greater conjugation length and therefore enhancing the

conductivity of the nanocomposite owing to the free motion of charge carriers [244]. On the other hand, sepiolite–PANI nanocomposites, prepared by slurry polymerization to produce PANI nanoparticles well adhered to the sepiolite surface, exhibit interesting electrorheological properties for samples containing 50% of conducting polymer [245].

Certain polymers of interest for potential use as ion-conductors, such as PEO, largely studied in layered clay nanocomposites [229, 232–235, 237], could also be assembled with sepiolite. Thus, PEO can be assembled with sepiolite either from solution in acetonitrile or from the melt by microwave irradiation, giving rise to nanocomposites in which a partial penetration of the polymer chains takes place [17, 237]. Further attempts recently reported focus on the modification of the physical characteristics of PEO–sepiolite composites by controlled modulation of the silicate interphase afforded by the incorporation of polyethylene glycol and other additives [246]. However, to our knowledge, no studies to date have addressed the use of PEO–fibrous clays as ion-conducting systems.

Proton-conducting membranes for fuel-cell applications have been developed based on fibrous clay nanocomposites. In this way, sepiolite or sepiolite modified with sulfonic groups incorporated to Nafion can be processed as membranes that show better performance than the pure polymer, especially at high temperature and low relative humidity [247]. In the same way, the preparation has been reported of proton conducting membranes based on sulfonated poly(ether sulfone) incorporating variable amounts of phosphotungstic acid and palygorskite for application in direct methanol fuel cells (DMFCs) [248]. Although membranes with palygorskite content >5% results in a decrease in the tensile strength of the membrane, the mechanical properties are still adequate for the intended application in membranes with up to 15% content. The incorporation of 10% palygorskite results in proton conductivity values of about 3×10^{-2} S/cm, which are about 60% of those of pure Nafion membranes, while its methanol permeability is still 25% of the Nafion membranes [248].

5.2 Conducting Carbon–Fibrous Clay Nanocomposites

The strategy based on the assembly of conducting carbonaceous nanomaterials to sepiolite and palygorskite is based on two approaches: (1) the development of carbonaceous materials from organic precursors adsorbed on the fibrous clays, and (2) the direct assembly of carbon nanotubes with the fibrous clays.

Polyacrylonitrile (PAN) is produced inside the sepiolite tunnels by in situ polymerization of previously adsorbed acrylonitrile molecules [46, 249]. Carbonization of PAN–sepiolite nanocomposites at temperatures superior to 500°C under inert gas flow give carbon–sepiolite nanocomposites showing electrical conductivity, probably associated with the formation of graphene-like species that remain strongly assembled with the silicate support. These materials have been studied to assess their suitability for applications in diverse electrochemical devices such as

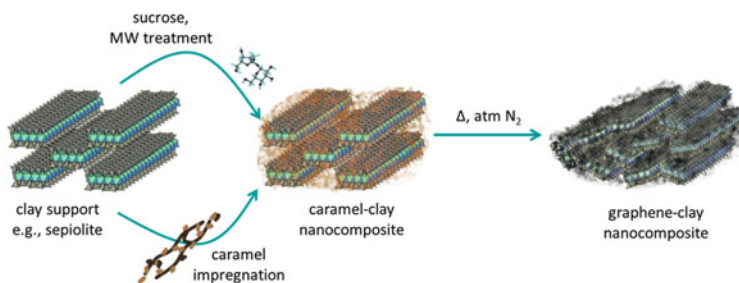


Fig. 10 Generation of graphene–sepiolite nanocomposites using sucrose or caramel as precursors. Reproduced from [252] with permission from The Royal Society of Chemistry

secondary battery electrodes and supercapacitors, as well as in ion-sensing electrodes [237, 250].

Polysaccharides and proteins assembled with diverse porous solids, including fibrous clays, act as precursors of graphene-based materials that result from thermal treatments at 700–800°C in complete absence of oxygen (e.g., under nitrogen flux) [251, 252]. For instance, sucrose and sepiolite mixtures give sepiolite–caramel nanocomposites after thermal treatment through conventional or microwave heating, which can be further transformed at ca. 800°C into graphene–sepiolite materials provided with electronic conductivity in the 10^{-2} to 1 S/cm range at room temperature (Fig. 10) with a low activation energy (0.15 eV), indicating its electronic character in agreement with the Raman spectra (sp^2 , G bands) [252, 253]. These conductivity values can be considered as elevated, taking into account that only a third of their mass corresponds to carbon and the rest to the insulating silicate backbone. The use of palygorskite instead of sepiolite gives comparable results in the formation of graphene-like species from caramel–silicate precursors (Zatitle et al. unpublished results).

The elevated specific surface area of the silicate substrate makes the graphene–sepiolite materials of interest for application in energy storage devices, being useful as electrodes for rechargeable Li-batteries with a specific capacity of ca. 400 mAh/g and excellent cyclability behavior [253, 254]. Preliminary tests as electrodes for double-layer supercapacitors indicate low specific capacity values (ca. 30 F/g), making further modifications of the protocol employed for these measurements necessary [254]. The inherent conductivity of these materials afforded by the graphene-like compounds, and the presence of the silicate backbone that allows further grafting reactions with functional organosilanes, make it possible to prepare electrodes for the selective detection of diverse ionic species in solution [255]. All these results point to the suitability of these carbon–clay materials for the development of low-cost and efficient components of electrochemical devices, although it seems that an additional deep study is necessary to optimize these applicative issues.

Other polymer–fibrous clay systems such as bionanocomposites combining gelatin and sepiolite are also efficient precursors that can be transformed into

conducting supported carbon materials at relatively low temperatures in similar conditions to those reported for caramel–sepiolite materials [251]. Freezing–drying procedures allow the processing of gelatin–sepiolite bionanocomposites as foams that can be further submitted to carbonization, leading to macroporous materials endowed with electrical conductivity in the range of around 10^{-2} S/cm, which can be of interest for application as electrocatalysts, biosensors, and bioreactors [256].

An alternative way to confer electronic conductivity to fibrous clays consists in its assembly with carbon nanotubes (CNTs). As is well known, CNTs represent a model for the structural reinforcement by nanofillers, holding the highest known elastic modulus ($E \sim 1$ TPa) and presenting a remarkable electronic conductivity together with a high aspect ratio [257]. Bilotti and coworkers reported that the incorporation of MWCNTs together with sepiolite in thermoplastic PU-based nanocomposites improved electrical percolation properties in the ternary systems. Extruded polymer nanocomposite filaments could be used for instance in the preparation of multifunctional strain sensors of interest in applications related to the development of smart textiles and other functional applications [258].

Carbon nanotubes show specific features, such as poor surface chemistry, in detriment to its wide potential application in the polymer nanocomposites field, mostly due to its extreme insolubility in water and in a wide range of liquid media. Recently, Fernandes and Ruiz-Hitzky [259] reported the assembly of CNTs and sepiolite nanofibers following a co-dispersion approach, which is based on a mechanism similar to steric stabilization. In this patented procedure, the combination is conducted under ultrasonic irradiation in the presence of the fibrous clay mineral and MWCNTs dispersed in aqueous media [260]. The presence of sepiolite nanofibers prevents re-aggregation of the MWCNTs and, thus, keeps them in stable aqueous suspension for long periods of time (>1 year). From these sepiolite–MWCNT aqueous dispersions, self-supported films were prepared by means of filtration. The resulting materials, showing a percolation threshold of around 1%, are termed hybrid buckypapers in relation to buckypapers previously prepared with the use of surfactants for dispersion of the MWCNTs (Fig. 11). The resulting buckypapers consist of a self-supported mesh of sepiolite and MWCNTs, where the CNT concentration can be varied from 0 to 16% [259]. Buckypapers, and therefore hybrid buckypapers, are of great interest for potential mechanical reinforcement of epoxy and other continuous matrices [261, 262]. The assembly of sepiolite and MWCNTs in the presence of PVA solution leads to homogeneous nanocomposites after casting processes. The nanocomposites show a Young's modulus that reaches a maximum value of 2.2 GPa, which represents a 280% increase, with contents of 10% sepiolite and 0.8% MWCNT.

Interestingly, the sepiolite–MWCNT hybrid buckypapers combine the adsorption properties of the fibrous silicate with the electrical conductivity characteristic of the CNTs, allowing functionalization of the system through reaction with the silanol groups at the external surface of sepiolite. In this way, a new amperometric biosensor based on immobilization of horseradish peroxidase (HRP) enzyme on sepiolite–MWCNT materials has been developed [259].

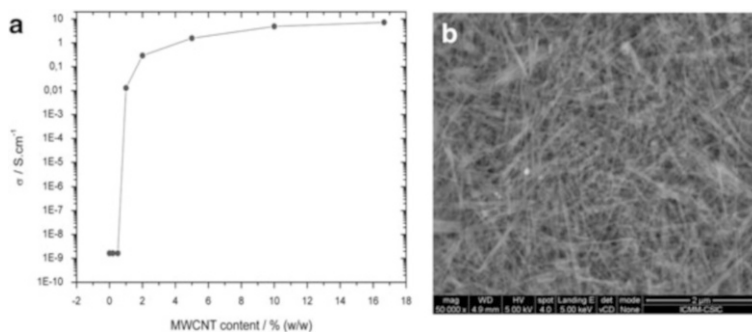


Fig. 11 Sepiolite–multiwalled carbon nanotubes (MWCNT) hybrid buckypapers: (a) electrical conductivity versus MWCNT loading; (b) Field emission SEM image of a buckypaper containing almost 6:1 (w/w) sepiolite/CNT. Reprinted from [259], Copyright (2014), with permission from Elsevier

In short, this innovative procedure has opened an easy pathway for the use of CNTs in aqueous media without the use of surfactants or commonly applied oxidative treatments responsible for extensively damaging the CNT outer walls, allowing an alternative preparation of fibrous clay materials provided with conducting properties and of great interest as nanofillers for diverse polymeric matrices.

6 Conclusion

In the present review we have introduced recent results on the main features of a remarkable class of nanocomposite materials based on the assembly of the microfibrillar silicates sepiolite and palygorskite with polymers. Polymer–clay nanocomposites are an outstanding example of nanostructured materials where synergy between the inorganic component and the polymer matrix represents the key to the amazing properties and derived applications of this class of hybrid materials. The crucial role of the interface between both components is directly related to the delamination ability of layered silicates belonging to the clay mineral family (montmorillonites, hectorites, saponites, etc.). However, sepiolite and palygorskite also belong to the clay family but show a different structural arrangement and morphology to the “conventional” (layered) clays, giving rise to advanced structural and functional nanocomposite materials with enhanced characteristics and potential significance in many applications. The nature of the silicate surface of fibrous clays with silanol groups and their surface electrical charge are decisive for the interfacial interactions with synthetic polymers as well as with biopolymers such as polysaccharides, proteins, lipids, and nucleic acids. Recent issues concerning sepiolite- and palygorskite-based nanocomposites and their application as nanofillers for thermoplastics, conducting polymers, bioplastics, hybrid

membranes, drug delivery systems, adjuvant of vaccines, tissue engineering, sensor devices, bioreactors, and conducting graphene and carbon nanotube composites have been reported here and critically discussed.

Acknowledgements This work was supported by the CICYT, Spain (project MAT2012-31759) and the EU COST Action MP1202. BW acknowledges the Swedish strategic foundation (SSF) (grant RMA11-0065). ACSA acknowledges the CNPq, Brazil (grant 406184/2013-5).

References

1. Fukushima Y, Inagaki S (1987) Synthesis of an intercalated compound of montmorillonite and 6-polyamide. *J Inclusion Phenom* 5:473–482
2. Fukushima Y, Okada A, Kawasumi M, Kurauchi T, Kamigaito O (1988) Swelling behavior of montmorillonite by poly-6-amide. *Clay Miner* 23:27–34
3. LeBaron PC, Wang Z, Pinnavaia TJ (1999) Polymer-layered silicate nanocomposites: an overview. *Appl Clay Sci* 15:11–29
4. Pinnavaia TJ, Beall G (2000) *Polymer-clay nanocomposites*. Wiley, New York
5. Alexandre M, Dubois P (2000) Polymer-layered silicate nanocomposites: preparation, properties and uses of a new class of materials. *Mat Sci Eng R* 28:1–63
6. Ray SS, Okamoto M (2003) Polymer/layered silicate nanocomposites: a review from preparation to processing. *Prog Polym Sci* 28:1539–1641
7. Ruiz-Hitzky E, Van Meerbeek A (2006) Clay mineral- and organoclay-polymer nanocomposite. In: Bergaya F, Theng BKG, Lagaly G (eds) *Handbook of clay science. Development in clay science*. Elsevier, Amsterdam, pp 583–621
8. Paul DR, Robeson LM (2008) Polymer nanotechnology: nanocomposites. *Polymer* 49:3187–3204
9. Pavlidou S, Papaspyrides CD (2008) A review on polymer-layered silicate nanocomposites. *Prog Polym Sci* 33:1119–1198
10. Lambert J-F, Bergaya F (2013) Smectite-polymer nanocomposites (CPN). In: Bergaya F, Lagaly G (eds) *Handbook of clay science*, 2nd edn. Elsevier, Amsterdam, pp 679–706
11. Fukushima K, Tabuani D, Camino G (2009) Nanocomposites of PLA and PCL based on montmorillonite and sepiolite. *Mater Sci Eng C Biomimetic Supramol Syst* 29:1433–1441
12. Darder M, Aranda P, Ruiz-Hitzky E (2007) Bionanocomposites: a new concept of ecological, bioinspired, and functional hybrid materials. *Adv Mater* 19:1309–1319
13. Ruiz-Hitzky E, Aranda P, Alvarez A, Santarén J, Esteban-Cubillo A (2011) Advanced materials and new applications of sepiolite and palygorskite. In: Galán E, Singer A (eds) *Developments in palygorskite-sepiolite research. A new outlook on these nanomaterials*. Elsevier, Oxford, pp 393–452
14. Ruiz-Hitzky E, Aranda P, Darder M, Fernandes FM (2013) Fibrous clay mineral-polymer nanocomposites. In: Bergaya F, Lagaly G (eds) *Handbook of clay science. Part A: fundamentals*, 2nd edn. Elsevier, Amsterdam, pp 721–741
15. Ruiz-Hitzky E, Darder M, Fernandes FM, Wicklein B, Alcantara ACS, Aranda P (2013) Fibrous clays based bionanocomposites. *Prog Polym Sci* 38:1392–1414
16. Fernandes FM, Vazquez L, Ruiz-Hitzky E, Carnicero A, Castro M (2014) Elastic properties of natural single nanofibres. *RSC Adv* 4:11225–11231
17. Ruiz-Hitzky E (2001) Molecular access to intracrystalline tunnels of sepiolite. *J Mater Chem* 11:86–91
18. Van Olphen H (1977) In: *An introduction to clay colloid chemistry. For clay technologists, geologists and soil scientists*, 2nd edn. Wiley, New York, pp 254–259

19. Ruiz-Hitzky E, Darder M, Aranda P (2008) An introduction to bio-nanohybrid materials. In: Ruiz-Hitzky E, Ariga K, Lvov YM (eds) *Bio-inorganic hybrid nanomaterials, strategies, syntheses, characterization and applications*. Wiley-VCH, Weinheim, pp 1–40
20. Ruiz-Hitzky E, Aranda P, Darder M, Rytwo G (2010) Hybrid materials based on clays for environmental and biomedical applications. *J Mater Chem* 20:9306–9321
21. Fernandes FM, Darder M, Ruiz AI, Aranda P, Ruiz-Hitzky E (2011) Gelatine-based bio-nanocomposites. In: Mittal V (ed) *Nanocomposites with biodegradable polymers. Synthesis, properties, and future perspectives*. Oxford University Press, New York, pp 209–233
22. Ahlrichs JL, Serna C, Serratos JM (1975) Structural hydroxyls in sepiolites. *Clays Clay Miner* 23:119–124
23. Brauner K, Pressinger A (1956) Struktur und entstehung des sepioliths. *Miner Petrol* 6:120–140
24. Bradley WF (1940) The structural scheme of attapulgite. *Am Miner* 25:405–410
25. Santarén J, Sanz J, Ruiz-Hitzky E (1990) Structural fluorine in sepiolite. *Clay Miner* 38:63–68
26. Momma K, Izumi F (2011) VESTA 3 for three-dimensional visualization of crystal, volumetric and morphology data. *J Appl Crystallogr* 44:1272–1276
27. López-Galindo A, Viseras C, Aguzzi C, Cerezo P (2011) Pharmaceutical and cosmetic uses of fibrous clays. In: Galán E, Singer A (eds) *Developments in palygorskite-sepiolite research. A new outlook on these nanomaterials*. Elsevier, Oxford, pp 299–324
28. International Agency for Research on Cancer (1997) Coal dust and para-aramid fibrils. In: *IARC monographs on the evaluation of carcinogenic risks to humans, silica, some silicates*, vol 68. World Health Organization, Lyon, pp 267–282
29. Ruiz-Hitzky E (2004) Organic-Inorganic materials: from intercalation chemistry to devices. In: Gómez-Romero P, Sanchez C (eds) *Functional hybrid materials*. Wiley-VCH, Weinheim, pp 15–49
30. Vanscoyoc GE, Serna CJ, Ahlrichs JL (1979) Structural-changes in palygorskite during dehydration and dehydroxylation. *Am Miner* 64:215–223
31. Inagaki S, Fukushima Y, Doi H, Kamigaito O (1990) Pore-size distribution and adsorption selectivity of sepiolite. *Clay Miner* 25:99–105
32. Kuang WX, Facey GA, Detellier C, Casal B, Serratos JM, Ruiz-Hitzky E (2003) Nano-structured hybrid materials formed by sequestration of pyridine molecules in the tunnels of sepiolite. *Chem Mater* 15:4956–4967
33. Kuang WX, Facey GA, Detellier C (2006) Organo-mineral nanohybrids. Incorporation, coordination and structuration role of acetone molecules in the tunnels of sepiolite. *J Mater Chem* 16:179–185
34. Ruiz-Hitzky E, Aranda P, Serratos JM (2004) Clay–organic interactions: organoclay complexes and polymer clay nanocomposites. In: Auerbach SM, Carrado KA, Dutta PK (eds) *Handbook of layered materials*. Marcel Dekker, New York, pp 91–154
35. Sánchez del Río M, Doménech A, Doménech-Carbó MT, Vázquez de Agredos Pascual ML, Suárez M, García-Romero E (2011) The Maya blue pigment. In: Galán E, Singer A (eds) *Developments in palygorskite–sepiolite research. A new outlook on these nanomaterials*. Elsevier, Oxford, pp 453–481
36. van Olphen H (1966) Maya blue – a clay–organic pigment. *Science* 154:645–646
37. Kleber R, Masschelein-Kleiner L, Thissen J (1967) Étude et identification du ‘Bleu Maya’. *Stud Conserv* 12:41–56
38. Hubbard B, Kuang WX, Moser A, Facey GA, Detellier C (2003) Structural study of Maya Blue: textural, thermal and solid state multinuclear magnetic resonance characterization of the palygorskite-indigo and sepiolite-indigo adducts. *Clays Clay Miner* 51:318–326
39. Sanchez del Rio M, Boccaleri E, Milanesio M, Croce G, van Beek W, Tsiantos C, Chyssikos GD, Gionis V, Kacandes GH, Suarez M, Garcia-Romero E (2009) A combined synchrotron powder diffraction and vibrational study of the thermal treatment of palygorskite-indigo to produce Maya blue. *J Mater Sci* 44:5524–5536

40. Aznar AJ, Casal B, Ruiz-Hitzky E, Lopez-Arbeloa I, Lopez-Arbeloa F, Santaren J, Alvarez A (1992) Adsorption of methylene-blue on sepiolite gels – spectroscopic and rheological studies. *Clay Miner* 27:101–108
41. Rytwo G, Nir S, Margulies L, Casal B, Merino J, Ruiz-Hitzky E, Serratos JM (1998) Adsorption of monovalent organic cations on sepiolite: experimental results and model calculations. *Clays Clay Miner* 46:340–348
42. Gándara F, Miyagawa K, Aranda P, Ruiz-Hitzky E, Cambor M (2009) On the Mayas' track: confinement of organic dyes into inorganic solids. In: Ruiz-Hitzky EPA (ed) *Jornada Científica Conmemorativa 50 Aniversario de la SEA*. FER Fotocomposición S.A., Madrid, pp 72–73
43. Volle N, Challier L, Burr A, Giullieri F, Pagnotta S, Chaze A-M (2011) Maya Blue as natural coloring fillers in a multi-scale polymer-clay nanocomposite. *Compos Sci Technol* 71:1685–1691
44. Inagaki S, Fukushima Y, Miyata M (1995) Inclusion polymerization of isoprene in the channels of sepiolite. *Res Chem Intermed* 21:167–180
45. Sandi G, Carrado KA, Winans RE, Johnson CS, Csencsits R (1999) Carbons for lithium battery applications prepared using sepiolite as an inorganic template. *J Electrochem Soc* 146:3644–3648
46. Fernández-Saavedra R, Aranda P, Ruiz-Hitzky E (2004) Templated synthesis of carbon nanofibers from polyacrylonitrile using sepiolite. *Adv Funct Mater* 14:77–82
47. Alvarez A, Santaren J, Perez-Castells R, Casal B, Ruiz-Hitzky E, Levitz P (1987) Surfactant adsorption and rheological behavior of surface modified sepiolite. In: Schultz LG, van Olphen H, Mumpton FA (eds) *Proceedings of the international clay conference Denver, 1985*. The Clay Minerals Society, Bloomington, pp 370–374
48. Li ZH, Willms CA, Kniola K (2003) Removal of anionic contaminants using surfactant-modified palygorskite and sepiolite. *Clays Clay Miner* 51:445–451
49. García N, Guzmán J, Benito E, Esteban-Cubillo A, Aguilar E, Santarén J, Tiemblo P (2011) Surface modification of sepiolite in aqueous gels by using methoxysilanes and its impact on the nanofiber dispersion ability. *Langmuir* 27:3952–3959
50. Wicklein B, Darder M, Aranda P, Ruiz-Hitzky E (2010) Bio-organoclays based on phospholipids as immobilization hosts for biological species. *Langmuir* 26:5217–5225
51. Shen L, Lin YJ, Du QG, Zhong W, Yang YL (2005) Preparation and rheology of polyamide-6/attapulgitic nanocomposites and studies on their percolated structure. *Polymer* 46:5758–5766
52. Xie SB, Zhang SM, Wang FS, Yang MS, Seguela R, Lefebvre JM (2007) Preparation, structure and thermomechanical properties of nylon-6 nanocomposites with lamella-type and fiber-type sepiolite. *Compos Sci Technol* 67:2334–2341
53. García-López D, Fernández JF, Merino JC, Pastor JM (2013) Influence of organic modifier characteristic on the mechanical properties of polyamide 6/organosepiolite nanocomposites. *Compos Part B Eng* 45:459–465
54. Tsai FC, Li P, Liu ZW, Feng G, Zhu P, Wang CK, Chen KN, Huang CY, Yeh JT (2012) Drawing and ultimate tenacity properties of polyamide 6/attapulgitic composite fibers. *J Appl Polym Sci* 126:1906–1916
55. García N, Hoyos M, Guzmán J, Tiemblo P (2009) Comparing the effect of nanofillers as thermal stabilizers in low density polyethylene. *Polym Degrad Stab* 94:39–48
56. Gao J, Zhang Q, Wang K, Fu Q, Chen Y, Chen H, Huang H, Rego JM (2012) Effect of shearing on the orientation, crystallization and mechanical properties of HDPE/attapulgitic nanocomposites. *Compos Part A Appl S* 43:562–569
57. Shafiq M, Yasin T, Saeed S (2012) Synthesis and characterization of linear low-density polyethylene/sepiolite nanocomposites. *J Appl Polym Sci* 123:1718–1723
58. Carrero A, van Grieken R, Suarez I, Paredes B (2012) Development of a new synthetic method based on in situ strategies for polyethylene/clay composites. *J Appl Polym Sci* 126:987–997

59. Gul R, Islam A, Yasin T, Mir S (2011) Flame-retardant synergism of sepiolite and magnesium hydroxide in a linear low-density polyethylene composite. *J Appl Polym Sci* 121:2772–2777
60. Shafiq M, Yasin T (2012) Effect of gamma irradiation on linear low density polyethylene/magnesium hydroxide/sepiolite composite. *Radiat Phys Chem* 81:52–56
61. Tiemblo P, Benito E, Garcia N, Esteban-Cubillo A, Pina-Zapardiel R, Pecharroman C (2012) Multiscale gold and silver plasmonic plastics by melt compounding. *RSC Adv* 2:915–919
62. Chen J, Chen J, Zhu S, Cao Y, Li H (2011) Mechanical properties, morphology, and crystal structure of polypropylene/chemically modified attapulgite nanocomposites. *J Appl Polym Sci* 121:899–908
63. He M, Cao WC, Wang LJ, Wilkie CA (2013) Synergistic effects of organo-sepiolite and zinc borate on the fire retardancy of polypropylene. *Polym Adv Technol* 24:1081–1088
64. Hapuarachchi TD, Peijs T, Bilotti E (2013) Thermal degradation and flammability behavior of polypropylene/clay/carbon nanotube composite systems. *Polym Adv Technol* 24:331–338
65. Fernández-García L, Pecharromán C, Esteban-Cubillo A, Tiemblo P, García N, Menéndez JL (2013) Magneto-optical Faraday activity in transparent FeCo-sepiolite/polystyrene nanocomposites. *J Nanopart Res* 15:1–6
66. Zhong W, Liu P, Wang A (2012) Facile approach to magnetic attapulgite-Fe₃O₄/polystyrene tri-component nanocomposite. *Mater Lett* 85:11–13
67. Chen F, Lou D, Yang J, Zhong M (2011) Mechanical and thermal properties of attapulgite clay reinforced polymethylmethacrylate nanocomposites. *Polym Adv Technol* 22:1912–1918
68. Huang N, Chen Z, Liu H, Wang J (2012) Thermal stability and degradation kinetics of poly(methyl methacrylate)/sepiolite nanocomposites by direct melt compounding. *J Macromol Sci Part B* 52:521–529
69. Liu Y, Liu P, Su Z (2008) Morphological characterization of attapulgite/poly(methyl methacrylate) particles prepared by soapless emulsion polymerization. *Polym Int* 57:306–310
70. Zhang H, Li C, Zang L, Luo J, Guo J (2012) Preparation of bead-string shaped attapulgite/poly(methyl methacrylate) particles by soapless emulsion polymerization based on uv irradiation in the presence of iron(III). *J Macromol Sci Part A* 49:154–159
71. Wang J, Wang Q, Zheng Y, Wang A (2013) Synthesis and oil absorption of poly(butylmethacrylate)/organo-attapulgite nanocomposite by suspended emulsion polymerization. *Polym Compos* 34:274–281
72. Wang Y, Chen D (2012) Preparation and characterization of a novel stimuli-responsive nanocomposite hydrogel with improved mechanical properties. *J Colloid Interface Sci* 372:245–251
73. Wang Y, Dong A, Yuan Z, Chen D (2012) Fabrication and characterization of temperature-, pH- and magnetic-field-sensitive organic/inorganic hybrid poly(ethylene glycol)-based hydrogels. *Colloid Surf A* 415:68–76
74. Yuan Z, Wang Y, Chen D (2014) Preparation and characterization of thermo-, pH-, and magnetic-field-responsive organic/inorganic hybrid microgels based on poly(ethylene glycol). *J Mater Sci* 49:3287–3296
75. Zhao L, Liu P, Liang G, Gu A, Yuan L, Guan Q (2014) The origin of the curing behavior, mechanical and thermal properties of surface functionalized attapulgite/bismaleimide/diallylbisphenol composites. *Appl Surf Sci* 288:435–443
76. Nohales A, Solar L, Porcar I, Vallo CI, Gomez CM (2006) Morphology, flexural, and thermal properties of sepiolite modified epoxy resins with different curing agents. *Eur Polym J* 42:3093–3101
77. Foix D, Rodríguez MT, Ferrando F, Ramis X, Serra A (2012) Combined use of sepiolite and a hyperbranched polyester in the modification of epoxy/anhydride coatings: a study of the curing process and the final properties. *Prog Org Coat* 75:364–372
78. Verge P, Fouquet T, Barrère C, Toniazzo V, Ruch D, Bomfim JAS (2013) Organomodification of sepiolite clay using bio-sourced surfactants: compatibilization and dispersion into epoxy thermosets for properties enhancement. *Compos Sci Technol* 79:126–132

79. Nohales A, López D, Culebras M, Gómez CM (2013) Rheological study of gel phenomena during epoxide network formation in the presence of sepiolite. *Polym Int* 62:397–405
80. Gomez-Aviles A, Aranda P, Fernandes FM, Belver C, Ruiz-Hitzky E (2013) Silica-sepiolite nanoarchitectures. *J Nanosci Nanotechnol* 13:2897–2907
81. Wang R, Li Z, Wang Y, Liu W, Deng L, Jiao W, Yang F (2013) Effects of modified attapulgite on the properties of attapulgite/epoxy nanocomposites. *Polym Compos* 34:22–31
82. Wang R, Li Z, Liu W, Jiao W, Hao L, Yang F (2013) Attapulgite–graphene oxide hybrids as thermal and mechanical reinforcements for epoxy composites. *Compos Sci Technol* 87:29–35
83. Chen H, Zheng M, Sun H, Jia Q (2007) Characterization and properties of sepiolite/polyurethane nanocomposites. *Mater Sci Eng a-Struct Mater Propert Microstruct Process* 445:725–730
84. Wang C-H, Auad ML, Marcovich NE, Nutt S (2008) Synthesis and characterization of organically modified attapulgite/polyurethane nanocomposites. *J Appl Polym Sci* 109:2562–2570
85. Lei Z, Yang Q, Wu S, Song X (2009) Reinforcement of polyurethane/epoxy interpenetrating network nanocomposites with an organically modified palygorskite. *J Appl Polym Sci* 111:3150–3162
86. Xu B, Huang WM, Pei YT, Chen ZG, Kraft A, Reuben R, De Hosson JTM, Fu YQ (2009) Mechanical properties of attapulgite clay reinforced polyurethane shape-memory nanocomposites. *Eur Polym J* 45:1904–1911
87. Chen H, Lu H, Zhou Y, Zheng M, Ke C, Zeng D (2012) Study on thermal properties of polyurethane nanocomposites based on organo-sepiolite. *Polym Degrad Stab* 97:242–247
88. Peng L, Zhou L, Li Y, Pan F, Zhang S (2011) Synthesis and properties of waterborne polyurethane/attapulgite nanocomposites. *Compos Sci Technol* 71:1280–1285
89. Bao Y, Li Q, Xue P, Wang J, Wu C (2012) Effect of electrostatic heterocoagulation of PVM/MA grafted carbon black and attapulgite nanorods on electrical and mechanical behaviors of waterborne polyurethane nanocomposites. *Colloid Polym Sci* 290:1527–1536
90. Alkan M, Benlikaya R (2009) Poly(vinyl alcohol) nanocomposites with sepiolite and heat-treated sepiolites. *J Appl Polym Sci* 112:3764–3774
91. Killeen D, Frydrych M, Chen B (2012) Porous poly(vinyl alcohol)/sepiolite bone scaffolds: preparation, structure and mechanical properties. *Mater Sci Eng C Biomimetic Supramol Syst* 32:749–757
92. Li A, Wang AQ, Chen JM (2004) Studies on poly(acrylic acid)/attapulgite superabsorbent composite. I. Synthesis and characterization. *J Appl Polym Sci* 92:1596–1603
93. Zhang FQ, Guo ZJ, Gao H, Li YC, Ren L, Shi L, Wang LX (2005) Synthesis and properties of sepiolite/poly (acrylic acid-co-acrylamide) nanocomposites. *Polym Bull* 55:419–428
94. Li A, Wang A, Chen J (2004) Studies on poly(acrylic acid)/attapulgite superabsorbent composites. II. Swelling behaviors of superabsorbent composites in saline solutions and hydrophilic solvent–water mixtures. *J Appl Polym Sci* 94:1869–1876
95. Chen J, Ding S, Jin Y, Wu J (2013) Semidry synthesis of the poly(acrylic acid)/palygorskite superabsorbent with high-percentage clay via a freeze–thaw–extrusion process. *J Appl Polym Sci* 128:1779–1784
96. Zhu L, Liu P, Wang A (2014) High clay-content attapulgite/poly(acrylic acid) nanocomposite hydrogel via surface-initiated redox radical polymerization with modified attapulgite nanorods as initiator and cross-linker. *Ind Eng Chem Res* 53:2067–2071
97. Liu P, Jiang L, Zhu L, Wang A (2014) Novel approach for attapulgite/poly(acrylic acid) (ATP/PAA) nanocomposite microgels as selective adsorbent for Pb(II) ion. *React Funct Polym* 74:72–80
98. Gao G, Du G, Cheng Y, Fu J (2014) Tough nanocomposite double network hydrogels reinforced with clay nanorods through covalent bonding and reversible chain adsorption. *J Mater Chem B* 2:1539–1548

99. Liu P, Jiang L, Zhu L, Wang A (2014) Novel covalently cross-linked attapulgite/poly(acrylic acid-co-acrylamide) hybrid hydrogels by inverse suspension polymerization: Synthesis optimization and evaluation as adsorbents for toxic heavy metals. *Ind Eng Chem Res* 53:4277–4285
100. Ekici S, Isikver Y, Saraydin D (2006) Poly(acrylamide-sepiolite) composite hydrogels: preparation, swelling and dye adsorption properties. *Polym Bull* 57:231–241
101. An J, Wang W, Wang A (2012) Preparation and swelling behavior of a pH-responsive psyllium-g-poly(acrylic acid)/attapulgite superabsorbent nanocomposite. *Int J Polym Mater Polymeric Biomater* 61:906–918
102. Wicklein B, Darder M, Aranda P, Ruiz-Hitzky E (2011) Phospholipid-sepiolite biomimetic interfaces for the immobilization of enzymes. *ACS Appl Mater Interfaces* 3:4339–4348
103. Ojijo V, Ray SS (2013) Processing strategies in bionanocomposites. *Prog Polym Sci* 38:1543–1589
104. Russo P, Cammarano S, Bilotti E, Peijs T, Cerruti P, Acierno D (2014) Physical properties of poly lactic acid/clay nanocomposite films: effect of filler content and annealing treatment. *J Appl Polym Sci* 131. doi:10.1002/app.39798
105. Jiang Y, Han S, Zhang S, Li J, Huang G, Bi Y, Chai Q (2014) Improved properties by hydrogen bonding interaction of poly(lactic acid)/palygorskite nanocomposites for agricultural products packaging. *Polym Compos* 35:468–476
106. Fukushima K, Tabuani D, Abbate C, Arena M, Ferreri L (2010) Effect of sepiolite on the biodegradation of poly(lactic acid) and polycaprolactone. *Polym Degrad Stab* 95:2049–2056
107. Fukushima K, Tabuani D, Dottori M, Armentano I, Kenny JM, Camino G (2011) Effect of temperature and nanoparticle type on hydrolytic degradation of poly(lactic acid) nanocomposites. *Polym Degrad Stab* 96:2120–2129
108. da Silva Moreira Thire RM, Arruda LC, Barreto LS (2011) Morphology and thermal properties of poly(3-hydroxybutyrate-co-3-hydroxyvalerate)/attapulgite nanocomposites. *Mater Res Ibero Am J Mater* 14:340–344
109. Qi Z, Ye H, Xu J, Peng J, Chen J, Guo B (2013) Synthesis and characterizations of attapulgite reinforced branched poly(butylene succinate) nanocomposites. *Colloid Surf A* 436:26–33
110. Sozer N, Kokini JL (2009) Nanotechnology and its applications in the food sector. *Trends Biotechnol* 27:82–89
111. Lynch DL, Wright LM, Cotnoir LJ (1957) Breakdown of cellulose dextrin and gelatin in presence of an attapulgite. *Nature* 179:1131
112. Chang SH, Ryan ME, Gupta RK (1991) Competitive adsorption of water-soluble polymers on attapulgite clay. *J Appl Polym Sci* 43:1293–1299
113. Darder M, Lopez-Blanco M, Aranda P, Aznar AJ, Bravo J, Ruiz-Hitzky E (2006) Microfibrous chitosan-sepiolite nanocomposites. *Chem Mater* 18:1602–1610
114. Chivrac F, Pollet E, Schmutz M, Averous L (2010) Starch nano-biocomposites based on needle-like sepiolite clays. *Carbohydr Polym* 80:145–153
115. Martínez-Frías P (2008) Estudio de la viabilidad del bio-nanocomposite quitosano-sepiolita como membrana para procesos de separación de gases. Thesis, Autonomous University of Madrid, Madrid
116. Huang D, Mu B, Wang A (2012) Preparation and properties of chitosan/poly (vinyl alcohol) nanocomposite films reinforced with rod-like sepiolite. *Mater Lett* 86:69–72
117. Huang D, Wang W, Xu J, Wang A (2012) Mechanical and water resistance properties of chitosan/poly(vinyl alcohol) films reinforced with attapulgite dispersed by high-pressure homogenization. *Chem Eng J* 210:166–172
118. Kosan B, Michels C, Meister F (2008) Dissolution and forming of cellulose with ionic liquids. *Cellulose* 15:59–66
119. Lan W, Liu C-F, Yue F-X, Sun R-C, Kennedy JF (2011) Ultrasound-assisted dissolution of cellulose in ionic liquid. *Carbohydr Polym* 86:672–677

120. Soheilmoghaddam M, Wahit MU, Yussuf AA, Al-Saleh MA, Whye WT (2014) Characterization of bio regenerated cellulose/sepiolite nanocomposite films prepared via ionic liquid. *Polym Test* 33:121–130
121. Ebringerová A, Heinze T (2000) Xylan and xylan derivatives – biopolymers with valuable properties, 1. Naturally occurring xylans structures, isolation procedures and properties. *Macromol Rapid Commun* 21:542–556
122. Sárossy Z, Blomfeldt TOJ, Hedenqvist MS, Koch CB, Ray SS, Plackett D (2012) Composite films of arabinoxylan and fibrous sepiolite: morphological, mechanical, and barrier properties. *ACS Appl Mater Interfaces* 4:3378–3386
123. Ünlü CH, Günister E, Atıcı O (2009) Synthesis and characterization of NaMt biocomposites with corn cob xylan in aqueous media. *Carbohydr Polym* 76:585–592
124. Gibson LJ, Ashby MF (1997) *Cellular solids: structure and properties*, 2nd edn. Cambridge University Press, Cambridge
125. Deville S, Saiz E, Nalla RK, Tomsia AP (2006) Freezing as a path to build complex composites. *Science* 311:515–518
126. Nieto-Suarez M, Palmisano G, Ferrer ML, Concepcion Gutierrez M, Yurdakal S, Augugliaro V, Pagliaro M, del Monte F (2009) Self-assembled titania-silica-sepiolite based nanocomposites for water decontamination. *J Mater Chem* 19:2070–2075
127. Ruiz-Hitzky E, Aranda P, Darder M, Fernandes FM, Matos CRS (2010) Espumas rígidas de tipo composite basadas en biopolímeros combinados con arcillas fibrosas y su método de preparación. Patent WO 2010081918 A1
128. Darder M, Aranda P, Ferrer ML, Gutiérrez MC, del Monte F, Ruiz-Hitzky E (2011) Progress in bionanocomposite and bioinspired foams. *Adv Mater* 23:5262–5267
129. Darder M, Matos CRS, Aranda P, Ruiz-Hitzky E (2010) Sepiolite-based nanocomposites foams. In: *Proceedings of the SEA-CSSJ-CMS trilateral meeting on clays*. Sevilla, pp 357–358. (<http://www.sea-arcillas.es/publicaciones/2010%20SEA-CSSJ-CMS%20Trilateral%20Meeting%20on%20Clays.pdf>)
130. Ruiz-Hitzky E, Darder M, Aranda P, Ariga K (2010) Advances in biomimetic and nanostructured biohybrid materials. *Adv Mater* 22:323–336
131. Okamoto M (2008) Biodegradable polymer-based nanocomposites: nanostructure control and nanocomposite foaming with the aim of producing nano-cellular plastics. In: Ruiz-Hitzky E, Ariga K, Lvov YM (eds) *Bio-inorganic hybrid nanomaterials. Strategies, syntheses, characterization and applications*. Wiley-VCH, Weinheim, pp 271–312
132. Chen M, Chen BQ, Evans JRG (2005) Novel thermoplastic starch-clay nanocomposite foams. *Nanotechnology* 16:2334–2337
133. Gupta VK, Suhas (2009) Application of low-cost adsorbents for dye removal – a review. *J Environment Manag* 90:2313–2342
134. Cohen E, Joseph T (2009) Photostabilization of *Beauveria bassiana* conidia using anionic dyes. *Appl Clay Sci* 42:569–574
135. Deng Y, Wang L, Hu X, Liu B, Wei Z, Yang S, Sun C (2012) Highly efficient removal of tannic acid from aqueous solution by chitosan-coated attapulgite. *Chem Eng J* 181:300–306
136. Pang C, Liu Y, Cao X, Hua R, Wang C, Li C (2010) Adsorptive removal of uranium from aqueous solution using chitosan-coated attapulgite. *J Radioanal Nucl Chem* 286:185–193
137. Zou X, Pan J, Ou H, Wang X, Guan W, Li C, Yan Y, Duan Y (2011) Adsorptive removal of Cr(III) and Fe(III) from aqueous solution by chitosan/attapulgite composites: equilibrium, thermodynamics and kinetics. *Chem Eng J* 167:112–121
138. Rytwo G, Lavi R, Rytwo Y, Monchase H, Dultz S, Koenig TN (2013) Clarification of olive mill and winery wastewater by means of clay-polymer nanocomposites. *Sci Total Environ* 442:134–142
139. Pan G, Zou H, Chen H, Yuan XZ (2006) Removal of harmful cyanobacterial blooms in Taihu Lake using local soils. III. Factors affecting the removal efficiency and an in situ field experiment using chitosan-modified local soils. *Environ Pollution* 141:206–212

140. Peng Y, Chen D, Ji J, Kong Y, Wan H, Yao C (2013) Chitosan-modified palygorskite: preparation, characterization and reactive dye removal. *Appl Clay Sci* 74:81–86
141. Li C, Pan J, Zou X, Gao J, Xie J, Yongsheng Y (2011) Synthesis and applications of novel attapulgite-supported Co(II)-imprinted polymers for selective solid-phase extraction of cobalt(II) from aqueous solutions. *Int J Environ Anal Chem* 91:1035–1049
142. Wu J, Chen J (2013) Adsorption characteristics of tannic acid onto the novel protonated palygorskite/chitosan resin microspheres. *J Appl Polym Sci* 127:1765–1771
143. Alcántara ACS, Darder M, Aranda P, Ruiz-Hitzky E (2014) Polysaccharide–fibrous clay bionanocomposites. *Appl Clay Sci* (in press) doi:10.1016/j.clay.2014.02.018
144. Zhou X, Liu Q, Ying G, Cui Y (2012) Chlorpyrifos-loaded attapulgite/sodium alginate hybrid microsphere and its release properties. In: Ji HB, Chen Y, Chen SZ (eds) *Advanced materials and processes II*, *Advance materials research*, vol 557–559. Trans Tech Publications, Zurich, pp 1528–1532
145. Alcántara ACS, Darder M, Aranda P, Tateyama S, Okajima MK, Kaneko T, Ogawa M, Ruiz-Hitzky E (2014) Clay-bionanocomposites with sacran megamolecules for the selective uptake of neodymium. *J Mater Chem A* 2:1391–1399
146. Mu B, Kang Y, Wang A (2013) Preparation of a polyelectrolyte-coated magnetic attapulgite composite for the adsorption of precious metals. *J Mater Chem A* 1:4804–4811
147. Wang W, Wang F, Kang Y, Wang A (2013) Facile self-assembly of Au nanoparticles on a magnetic attapulgite/Fe₃O₄ composite for fast catalytic decoloration of dye. *RSC Adv* 3:11515–11520
148. Wang W, Zheng Y, Wang A (2008) Syntheses and properties of superabsorbent composites based on natural guar gum and attapulgite. *Polym Adv Technol* 19:1852–1859
149. Yang H, Peng Z, Zhou Y, Zhao F, Zhang J, Cao X, Hu Z (2011) Preparation and performances of a novel intelligent humidity control composite material. *Energy Build* 43:386–392
150. Liu Y, Wang WB, Wang AG (2010) Adsorption of lead ions from aqueous solution by using carboxymethyl cellulose-g-poly (acrylic acid)/attapulgite hydrogel composites. *Desalination* 259:258–264
151. Mahdavinia GR, Asgari A (2013) Synthesis of kappa-carrageenan-g-poly(acrylamide)/sepiolite nanocomposite hydrogels and adsorption of cationic dye. *Polym Bull* 70:2451–2470
152. Zheng Y, Zhang J, Wang A (2009) Fast removal of ammonium nitrogen from aqueous solution using chitosan-g-poly(acrylic acid)/attapulgite composite. *Chem Eng J* 155:215–222
153. Wang L, Zhang J, Wang A (2011) Fast removal of methylene blue from aqueous solution by adsorption onto chitosan-g-poly (acrylic acid)/attapulgite composite. *Desalination* 266:33–39
154. Wang X, Wang A (2010) Adsorption characteristics of chitosan-g-poly(acrylic acid)/attapulgite hydrogel composite for Hg(II) ions from aqueous solution. *Sep Sci Technol* 45:2086–2094
155. Ni B, Liu M, Lue S, Xie L, Wang Y (2010) Multifunctional slow-release organic–inorganic compound fertilizer. *J Agric Food Chem* 58:12373–12378
156. Kievit FM, Zhang M (2011) Cancer therapy: cancer nanotheranostics: improving imaging and therapy by targeted delivery across biological barriers. *Adv Mater* 23:H217–H247
157. Doane TL, Burda C (2012) The unique role of nanoparticles in nanomedicine: imaging, drug delivery and therapy. *Chem Soc Rev* 41:2885–2911
158. Venkataraman S, Hedrick JL, Ong ZY, Yang C, Ee PLR, Hammond PT, Yang YY (2011) The effects of polymeric nanostructure shape on drug delivery. *Adv Drug Deliv Rev* 63:1228–1246
159. Viseras C, Aguzzi C, Cerezo P, Bedmar MC (2008) Biopolymer-clay nanocomposites for controlled drug delivery. *Mater Sci Technol* 24:1020–1026
160. Salcedo I, Aguzzi C, Sandri G, Bonferoni MC, Mori M, Cerezo P, Sanchez R, Viseras C, Caramella C (2012) In vitro biocompatibility and mucoadhesion of montmorillonite chitosan nanocomposite: a new drug delivery. *Appl Clay Sci* 55:131–137

161. Wang Q, Zhang JP, Wang AQ (2009) Preparation and characterization of a novel pH-sensitive chitosan-g-poly (acrylic acid)/attapulgitite/sodium alginate composite hydrogel bead for controlled release of diclofenac sodium. *Carbohydr Polym* 78:731–737
162. Wang Q, Wu J, Wang W, Wang A (2011) Preparation, characterization and drug-release behaviors of crosslinked chitosan/attapulgitite hybrid microspheres by a facile spray-drying technique. *J Biomater Nanobiotechnol* 2:250–257
163. Wang Q, Wang W, Wu J, Wang A (2012) Effect of attapulgitite contents on release behaviors of a pH sensitive carboxymethyl cellulose-g-poly(acrylic acid)/attapulgitite/sodium alginate composite hydrogel bead containing diclofenac. *J Appl Polym Sci* 124:4424–4432
164. Amrij J-P, Hinrichs WLJ, Frijlink HW, Wilschut JC, Huckriede A (2010) Needle-free influenza vaccination. *Lancet Infect Dis* 10:699–711
165. Ruiz-Hitzky E, Darder M, Aranda P, Martín del Burgo MÁ, del Real G (2009) Bionanocomposites as new carriers for influenza vaccines. *Adv Mater* 21:4167–4171
166. Clapp T, Siebert P, Chen D, Jones Braun L (2011) Vaccines with aluminum-containing adjuvants: optimizing vaccine efficacy and thermal stability. *J Pharm Sci* 100:388–401
167. Wicklein B, Martín del Burgo MÁ, Yuste M, Darder M, Escrig Llavata C, Aranda P, Ortín J, del Real G, Ruiz-Hitzky E (2012) Lipid-based bio-nanohybrids for functional stabilisation of influenza vaccines. *Eur J Inorg Chem* 2012:5186–5191
168. Avérous L, Pollet E (2012) Green nano-biocomposites. In: Avérous L, Pollet E (eds) *Environmental silicate nano-biocomposites*. Springer, London, pp 1–11
169. Fernandes FM, Ruiz AI, Darder M, Aranda P, Ruiz-Hitzky E (2009) Gelatin-clay bio-nanocomposites: structural and functional properties as advanced materials. *J Nanosci Nanotechnol* 9:221–229
170. Fernandes FM, Manjubala I, Ruiz-Hitzky E (2011) Gelatin renaturation and the interfacial role of fillers in bionanocomposites. *PCCP* 13:4901–4910
171. Su D, Wang C, Cai S, Mu C, Li D, Lin W (2012) Influence of palygorskite on the structure and thermal stability of collagen. *Appl Clay Sci* 62–63:41–46
172. Gimenez B, Gomez-Guillen MC, Lopez-Caballero ME, Gomez-Estaca J, Montero P (2012) Role of sepiolite in the release of active compounds from gelatin-egg white films. *Food Hydrocoll* 27:475–486
173. Mangavel C, Rossignol N, Perronnet A, Barbot J, Popineau Y, Gueguen J (2004) Properties and microstructure of thermo-pressed wheat gluten films: a comparison with cast films. *Biomacromolecules* 5:1596–1601
174. Yuan Q, Lu W, Pan Y (2010) Structure and properties of biodegradable wheat gluten/attapulgitite nanocomposite sheets. *Polym Degrad Stab* 95:1581–1587
175. Ruiz Hitzky E, Aranda P, Darder M, and Alcântara ACS (2010) Materiales composites basados en biohíbridos zeína-arcilla, su procedimiento de obtención y usos de estos materiales. Patent WO 2010146216 A1
176. Alcântara ACS, Darder M, Aranda P, Ruiz Hitzky E (2012) Zein–fibrous clays biohybrid materials. *Eur J Inorg Chem* 2012:5216–5224
177. Alcantara ACS, Aranda P, Darder M, Ruiz-Hitzky E (2011) Zein-clay biohybrids as nanofillers of alginate based bionanocomposites. *Abstr Pap Am Chem Soc* 241:114–115
178. Carretero MI, Pozo M (2009) Clay and non-clay minerals in the pharmaceutical industry: Part I. Excipients and medical applications. *Appl Clay Sci* 46:73–80
179. Carretero MI, Pozo M (2010) Clay and non-clay minerals in the pharmaceutical and cosmetic industries: part II. Active ingredients. *Appl Clay Sci* 47:171–181
180. da Silva MLD, Fortes AC, Tome AD, da Silva EC, de Freitas RM, Soares-Sobrinho JL, Leite CMD, Soares MFD (2013) The effect of natural and organophilic palygorskite on skin wound healing in rats. *Braz J Pharm Sci* 49:729–736
181. Perez-Castells R, Alvarez A, Gavilanes J, Lizarbe MA, Martínez Del Pozo A, Olmo N, Santaren J (1987) Adsorption of collagen by sepiolite. In: Schultz LG, van Olphen H, Mumpton FA (eds) *Proceedings of the international clay conference Denver, 1985*. The Clay Minerals Society, Bloomington, pp 359–362

182. Lizarbe MA, Olmo N, Gavilanes JG (1987) Adhesion and spreading of fibroblasts on sepiolite collagen complexes. *J Biomed Mater Res* 21:137–144
183. Herrera JI, Olmo N, Turnay J, Sicilia A, Bascones A, Gavilanes JG, Lizarbe MA (1995) Implantation of sepiolite-collagen complexes in surgically created rat calvaria defects. *Bio-materials* 16:625–631
184. Olmo N, Turnay J, Herrera JI, Gavilanes JG, Lizarbe MA (1996) Kinetics of in vivo degradation of sepiolite-collagen complexes: effect of glutaraldehyde treatment. *J Biomed Mater Res* 30:77–84
185. Frydrych M, Wan C, Stengler R, O’Kelly KU, Chen B (2011) Structure and mechanical properties of gelatin/sepiolite nanocomposite foams. *J Mater Chem* 21:9103–9111
186. Li W-Z, Li G-F, Wang J-L (2013) Core-shell assembly of natural polymers for adjusting release performance of diclofenac. *Int J Polym Mater Polym Biomater* 62:358–361
187. de Fuentes IE, Viseras CA, Ubiali D, Terreni M, Alcántara AR (2001) Different phyllosilicates as supports for lipase immobilisation. *J Mol Catal B Enzym* 11:657–663
188. Prodanovic RM, Simic MB, Vujcic ZM (2003) Immobilization of periodate oxidized invertase by adsorption on sepiolite. *J Serb Chem Soc* 68:819–824
189. Cengiz S, Çavaş L, Yurdaoç K (2012) Bentonite and sepiolite as supporting media: immobilization of catalase. *Appl Clay Sci* 65–66:114–120
190. Zhao Q, Hou Y, Gong G-H, Yu M-A, Jiang L, Liao F (2010) Characterization of alcohol dehydrogenase from permeabilized Brewer’s yeast cells immobilized on the derived attapulgite nanofibers. *Appl Biochem Biotechnol* 160:2287–2299
191. Caballero V, Bautista FM, Campelo JM, Luna D, Marinas JM, Romero AA, Hidalgo JM, Luque R, Macario A, Giordano G (2009) Sustainable preparation of a novel glycerol-free biofuel by using pig pancreatic lipase: partial 1,3-regiospecific alcoholysis of sunflower oil. *Process Biochem* 44:334–342
192. Chen J, Jin Y (2010) Sensitive phenol determination based on co-modifying tyrosinase and palygorskite on glassy carbon electrode. *Microchim Acta* 169:249–254
193. Xu J, Han W, Yin Q, Song J, Zhong H (2009) Direct electron transfer of glucose oxidase and glucose biosensor based on nano-structural attapulgite clay matrix. *Chin J Chem* 27:2197–2202
194. Regina de Oliveira T, Grawe GF, Moccelini SK, Terezo AJ, Castilho M (2014) Enzymatic biosensors based on inga-cipo peroxidase immobilised on sepiolite for TBHQ quantification. *Analyst* 139:2214–2220
195. Lagaly G (1986) Interaction of alkylamines with different types of layered compounds. *Solid State Ionics* 22:43–51
196. Abbate C, Arena M, Baglieri A, Gennari M (2009) Effects of organoclays on soil eubacterial community assessed by molecular approaches. *J Hazard Mater* 168:466–472
197. Lang S (2002) Biological amphiphiles (microbial biosurfactants). *Curr Opin Colloid Interface Sci* 7:12–20
198. Pacwa-Plociniczak M, Plaza GA, Piotrowska-Seget Z, Cameotra SS (2011) Environmental applications of biosurfactants: recent advances. *Int J Mol Sci* 12:633–654
199. Lu JR, Zhao XB, Yaseen M (2007) Biomimetic amphiphiles: biosurfactants. *Curr Opin Colloid Interface Sci* 12:60–67
200. Carnero Ruiz C (ed) (2008) Sugar-based surfactants. *Fundamentals and applications. Surfactant Science*, vol 143. CRC/Taylor & Francis, Boca Raton
201. Koutsopoulos S, Kaiser L, Eriksson HM, Zhang S (2012) Designer peptide surfactants stabilize diverse functional membrane proteins. *Chem Soc Rev* 41:1721–1728
202. Ariga K, Hill JP, Lee MV, Vinu A, Charvet R, and Acharya S (2008) Challenges and breakthroughs in recent research on self-assembly. *Sci Technol Adv Mater* 9:1–96
203. Sun T, Qing G (2011) Biomimetic smart interface materials for biological applications. *Adv Mater* 23:H57–H77
204. Zhang X, Zhao N, Liang S, Lu X, Li X, Xie Q, Zhang X, Xu J (2008) Facile creation of biomimetic systems at the interface and in bulk. *Adv Mater* 20:2938–2946

205. Mark K, Park J, Bauer S, Schmuki P (2010) Nanoscale engineering of biomimetic surfaces: cues from the extracellular matrix. *Cell Tissue Res* 339:131–153
206. Ruiz-Hitzky E, Darder M, Wicklein B, Fernandes FM, Castro-Smirnov FA, del Burgo MAM, del Real G, and Aranda P (2012) Advanced biohybrid materials based on nanoclays for biomedical applications. In: Choi SH, Choy JH, Lee U, Varadan VK (eds) *Nanosystems in engineering and medicine*, vol 8548. SPIE-Int Soc Optical Engineering, Bellingham
207. Wicklein B (2011) Bio-nanohybrid materials based on clays and phospholipids. Thesis, Autonomous University of Madrid, Madrid
208. Plant AL (1999) Supported hybrid bilayer membranes as rugged cell membrane mimics. *Langmuir* 15:5128–5135
209. Hubbard JB, Silin V, Plant AL (1998) Self assembly driven by hydrophobic interactions at alkanethiol monolayers: mechanism of formation of hybrid bilayer membranes. *Biophys Chem* 75:163–176
210. Hosseini A, Barile CJ, Devadoss A, Eberspacher TA, Decreau RA, Collman JP (2011) Hybrid bilayer membrane: a platform to study the role of proton flux on the efficiency of oxygen reduction by a molecular electrocatalyst. *J Am Chem Soc* 133:11100–11102
211. Xie H, Jiang K, Zhan W (2011) A modular molecular photovoltaic system based on phospholipid/alkanethiol hybrid bilayers: photocurrent generation and modulation. *PCCP* 13:17712–17721
212. Zhou Q, Somasundaran P (2009) Synergistic adsorption of mixtures of cationic gemini and nonionic sugar-based surfactant on silica. *J Colloid Interface Sci* 331:288–294
213. Persson CM, Claesson PM, Lunkenheimer K (2002) Interfacial behavior of *n*-decyl- β -D-maltopyranoside on hydrophobic interfaces and the effect of small amounts of surface-active impurities. *J Colloid Interface Sci* 251:182–192
214. Hederes M, Konradsson P, Liedberg B (2005) Synthesis and self-assembly of galactose-terminated alkanethiols and their ability to resist proteins. *Langmuir* 21:2971–2980
215. Fyrner T, Lee H-H, Mangone A, Ekblad T, Pettitt ME, Callow ME, Callow JA, Conlan SL, Mutton R, Clare AS, Konradsson P, Liedberg B, Ederth T (2011) Saccharide-functionalized alkanethiols for fouling-resistant self-assembled monolayers: synthesis, monolayer properties, and antifouling behavior. *Langmuir* 27:15034–15047
216. Stubbs GW, Smith HG, Litman BJ (1976) Alkyl glucosides as effective solubilizing agents for bovine rhodopsin – comparison with several commonly used detergents. *Biochim Biophys Acta* 426:46–56
217. Privé GG (2007) Detergents for the stabilization and crystallization of membrane proteins. *Methods* 41:388–397
218. Mukherjee D, May M, Khomami B (2011) Detergent–protein interactions in aqueous buffer suspensions of Photosystem I (PS I). *J Colloid Interface Sci* 358:477–484
219. Goldblatt L (1977) Mycotoxins-past, present and future. *J Am Oil Chem Soc* 54:A302–A309
220. Jaynes WF, Zartman RE, Hudnall WH (2007) Aflatoxin B1 adsorption by clays from water and corn meal. *Appl Clay Sci* 36:197–205
221. Moran TM, Park H, Fernandez-Sesma A, Schulman JL (1999) Th2 responses to inactivated influenza virus can be converted to Th1 responses and facilitate recovery from heterosubtypic virus infection. *J Infect Dis* 180:579–585
222. Wicklein B, Aranda P, Ruiz-Hitzky E, Darder M (2013) Hierarchically structured bioactive foams based on polyvinyl alcohol-sepiolite nanocomposites. *J Mater Chem B* 1:2911–2920
223. Paget E, Monrozier LJ, Simonet P (1992) Adsorption of DNA on clay minerals: protection against DNaseI and influence on gene transfer. *FEMS Microbiol Lett* 97:31–39
224. Yoshida N (2007) Discovery and application of the Yoshida effect: nano-sized acicular materials enable penetration of bacterial cells by sliding friction force. *Recent Patents Biotechnol* 1:194–201
225. Yoshida N, Ide K (2008) Plasmid DNA is released from nanosized acicular material surface by low molecular weight oligonucleotides: exogenous plasmid acquisition mechanism for

- penetration intermediates based on the Yoshida effect. *Appl Microbiol Biotechnol* 80:813–821
226. Yoshida N, Sato M (2009) Plasmid uptake by bacteria: a comparison of methods and efficiencies. *Appl Microbiol Biotechnol* 83:791–798
 227. Wilharm G, Lepka D, Faber F, Hofmann J, Kerrinns T, Skiebe E (2010) A simple and rapid method of bacterial transformation. *J Microbiol Methods* 80:215–216
 228. Bellmann B, Muhle H, Ernst H (1997) Investigations on health-related properties of two sepiolite samples. *Environ Health Perspect* 105:1049–1052
 229. Ruiz-Hitzky E, Aranda P (1990) Polymer-salt intercalation complexes in layer silicates. *Adv Mater* 2:545–547
 230. Mehrotra V, Giannelis EP (1991) Metal-insulator molecular multilayers of electroactive polymers – intercalation of polyaniline in mica-type layered silicates. *Solid State Commun* 77:155–158
 231. Mehrotra V, Giannelis EP (1992) Nanometer scale multilayers of electroactive polymers – intercalation of polypyrrole in mica-type silicates. *Solid State Ionics* 51:115–122
 232. Aranda P, Ruiz-Hitzky E (1992) Poly(ethylene oxide)-silicate intercalation materials. *Chem Mater* 4:1395–1403
 233. Ruiz-Hitzky E (1993) Conducting polymers intercalated in layered solids. *Adv Mater* 5:334–340
 234. Ruiz-Hitzky E, Aranda P, Casal B, Galvan JC (1995) Nanocomposite materials with controlled ion mobility. *Adv Mater* 7:180–184
 235. Vaia RA, Vasudevan S, Krawiec W, Scanlon LG, Giannelis EP (1995) New polymer electrolyte nanocomposites - melt intercalation of poly(ethylene oxide) in mica-type silicates. *Adv Mater* 7:154–156
 236. Giannelis EP (1996) Polymer layered silicate nanocomposites. *Adv Mater* 8:29–35
 237. Aranda P, Darder M, Fernandez-Saavedra R, Lopez-Blanco M, Ruiz-Hitzky E (2006) Relevance of polymer- and biopolymer-clay nanocomposites in electrochemical and electro-analytical applications. *Thin Solid Films* 495:104–112
 238. Letaief S, Aranda P, Fernandez-Saavedra R, Margeson JC, Detellier C, Ruiz-Hitzky E (2008) Poly(3,4-ethylenedioxythiophene)-clay nanocomposites. *J Mater Chem* 18:2227–2233
 239. Aranda P, Mosqueda Y, Perez-Cappe E, Ruiz-Hitzky E (2003) Electrical characterization of poly(ethylene oxide) – clay nanocomposites prepared by microwave irradiation. *J Polym Sci Part B Polym Phys* 41:3249–3263
 240. Kitayama Y, Katoh H, Kodama T, Abe J (1997) Polymerization of pyrrole in intracrystalline tunnels of sepiolite. *Appl Surf Sci* 121:331–334
 241. Chang Y, Liu Z, Fu Z, Wang C, Dai Y, Peng R, Hu X (2014) Preparation and characterization of one-dimensional core-shell sepiolite/polypyrrole nanocomposites and effect of organic modification on the electrochemical properties. *Ind Eng Chem Res* 53:38–47
 242. Wang Y, Liu P, Yang C, Mu B, Wang A (2013) Improving capacitance performance of attapulgite/polypyrrole composites by introducing rhodamine B. *Electrochim Acta* 89:422–428
 243. Yao C, Xu Y, Kong Y, Liu W, Wang W, Wang Z, Wang Y, Ji J (2012) Polypyrrole/palygorskite nanocomposite: a new chromate collector. *Appl Clay Sci* 67–68:32–35
 244. Shao L, Qiu J, Lei L, Wu X (2012) Properties and structural investigation of one-dimensional SAM-ATP/PANI nanofibers and nanotubes. *Synth Met* 162:2322–2328
 245. Marins JA, Giulieri F, Soares BG, Bossis G (2013) Hybrid polyaniline-coated sepiolite nanofibers for electrorheological fluid applications. *Synth Met* 185:9–16
 246. Mejia A, Garcia N, Guzman J, Tiemblo P (2013) Confinement and nucleation effects in poly(ethylene oxide) melt-compounded with neat and coated sepiolite nanofibers: modulation of the structure and semicrystalline morphology. *Eur Polym J* 49:118–129
 247. Beauger C, Lainé G, Burr A, Taguet A, Otazaghine B, Rigacci A (2013) Nafion[®]-sepiolite composite membranes for improved proton exchange membrane fuel cell performance. *J Memb Sci* 430:167–179

248. Wen S, Gong C, Shu Y-C, Tsai F-C, Yeh J-T (2012) Sulfonated poly(ether sulfone)/phosphotungstic acid/attapulgite composite membranes for direct methanol fuel cells. *J Appl Polym Sci* 123:646–656
249. Fernandez-Saavedra R, Aranda P, Carrado KA, Sandi G, Seifert S, Ruiz-Hitzky E (2009) Template synthesis of nanostructured carbonaceous materials for application in electrochemical devices. *Curr Nanosci* 5:506–513
250. Fernández-Saavedra R, Darder M, Gómez-Avilés A, Aranda P, Ruiz-Hitzky E (2008) Polymer-clay nanocomposites as precursors of nanostructured carbon materials for electrochemical devices: templating effect of clays. *J Nanosci Nanotechnol* 8:1741–1750
251. Ruiz-Hitzky E, Darder M, Fernandes FM, Zatile E, Palomares FJ, Aranda P (2011) Supported graphene from natural resources: easy preparation and applications. *Adv Mater* 23:5250–5255
252. Ruiz-García C, Darder M, Aranda P, Ruiz-Hitzky E (2014) Toward a green way for the chemical production of supported graphenes using porous solids. *J Mater Chem A* 2:2009–2017
253. Gómez-Avilés A, Darder M, Aranda P, Ruiz-Hitzky E (2010) Multifunctional materials based on graphene-like/sepiolite nanocomposites. *Appl Clay Sci* 47:203–211
254. Ruiz-García C, Jimenez R, Perez-Carvajal J, Berenguer-Murcia A, Darder M, Aranda P, Cazorla-Amoros D, Ruiz-Hitzky E (2014) Graphene-clay based nanomaterials for clean energy storage. *Sci Adv Mater* 6:151–158
255. Gómez-Avilés A, Darder M, Aranda P, Ruiz-Hitzky E (2007) Functionalized carbon-silicates from caramel-sepiolite nanocomposites. *Angew Chem Int Ed* 46:923–925
256. Ruiz-Hitzky E, Fernandes FM (2011) Composición de material carbonoso obtenible por carbonización de un biopolímero soportado sobre arcilla. Patent ES-P201130835
257. Salvetat JP, Bonard JM, Thomson NH, Kulik AJ, Forro L, Benoit W, Zuppiroli L (1999) Mechanical properties of carbon nanotubes. *Appl Phys a-Mater Sci Process* 69:255–260
258. Bilotti E, Zhang H, Deng H, Zhang R, Fu Q, Peijs T (2013) Controlling the dynamic percolation of carbon nanotube based conductive polymer composites by addition of secondary nanofillers: the effect on electrical conductivity and tuneable sensing behaviour. *Compos Sci Technol* 74:85–90
259. Fernandes FM, Ruiz-Hitzky E (2014) Assembling nanotubes and nanofibres: cooperativeness in sepiolite-carbon nanotube materials. *Carbon* 72:296–303
260. Ruiz-Hitzky E and Fernandes FM (2011) Use of fibrous clays as coadjuvants to improve the dispersion and colloidal stability of filamentous carbon materials in hydrophilic media. Patent WO 2011070208 A1
261. Wang Z, Liang Z, Wang B, Zhang C, Kramer L (2004) Processing and property investigation of single-walled carbon nanotube (SWNT) buckypaper/epoxy resin matrix nanocomposites. *Compos Part A Appl S* 35:1225–1232
262. Vohrer U, Kolaric I, Haque MH, Roth S, Detlaff-Weglikowska U (2004) Carbon nanotube sheets for the use as artificial muscles. *Carbon* 42:1159–1164

Nanohybrid Materials by Electrospinning

**Chiara Gualandi, Annamaria Celli, Andrea Zucchelli,
and Maria Letizia Focarete**

Abstract Organic-inorganic hybrid nanofibers obtained by electrospinning technology have experienced a growing interest in the last decade thanks to the versatility and the high productivity of the technique, compared to other technologies devoted to the fabrication of nanocomposites, and to the unique and numerous features displayed by the produced nanomaterials. In this review, we classify and highlight recent progress, as well as current issues, in the production of hybrid nanofibers by electrospinning and their related applications. In particular, the scientific literature has been classified by taking into account the different methodologies that have been developed to fabricate hybrid polymeric-inorganic nanofibers by making use of electrospinning technology in combination with additional specific synthetic and processing procedures. The following technological and synthetic strategies have been discussed in detail: (1) electrospinning of inorganic dispersions in polymer solutions, (2) post treatments of electrospun fibers, (3) electrospinning combined with sol–gel processes, (4) electrospinning combined with electrospraying, (5) coaxial electrospinning, and (6) electrospinning of hybrid polymers. The huge number of different fiber morphologies, structures, and properties that can be achieved by electrospinning is impressive. The power of this technology is even more evident if we take into account that innovative hybrid

C. Gualandi and M.L. Focarete (✉)

Department of Chemistry “G. Ciamician”, University of Bologna, via Selmi 2, 40126 Bologna, Italy

e-mail: marialetizia.focarete@unibo.it

A. Celli

Department of Civil, Chemical, Environmental and Materials Engineering, University of Bologna, Via Terracini 28, 40131, Bologna, Italy

A. Zucchelli

Department of Industrial Engineering (DIN) and Advanced Mechanics and Materials – Interdepartmental Center for Industrial Research (AMM ICIR), University of Bologna Viale Risorgimento 2, 40136, Bologna, Italy

nanofibers can be fabricated with a simple, versatile, extremely cheap, and scalable technology that makes electrospinning the most interesting currently available technique for the production of nanocomposites.

Keywords Electrospinning, Hybrid material, Nanofiber, Organic–inorganic nanocomposite, Review

Contents

1	Introduction	90
2	Electrospinning of Inorganic Dispersions in Polymer Solutions	92
2.1	Direct Dispersion Electrospinning	93
2.2	In Situ Generation of Inorganic Nanoparticles	101
3	Post-treatment of Electrospun Fibers	106
3.1	Liquid Phase Deposition	106
3.2	Atomic Layer Deposition	107
3.3	Hydrothermal Synthesis	108
3.4	Reduction of Metal Ions	109
3.5	Gas–Solid Reaction	111
3.6	Layer-by-Layer Assembly	111
3.7	Polymer Coating of Inorganic Fibers	113
4	Electrospinning Combined with the Sol–Gel Process	113
4.1	Preparation of SiO ₂ /Polymer Hybrid Fibers	115
4.2	Preparation of TiO ₂ /Polymer Hybrid Fibers	116
4.3	Preparation of ZnO/Polymer Hybrid Fibers	117
4.4	Properties and Applications of Hybrid Fibers from Electrospinning Combined with the Sol–Gel Process	118
5	Electrospinning Combined with Electrospaying	121
6	Coaxial Electrospinning	124
7	Hybrid Polymers	127
8	Conclusions	131
	References	132

Abbreviations

β -TCP	β -Tricalcium phosphate
1D	One-dimensional
Ac	Acetate
ALD	Atomic layer deposition
AOT	Diocetyl sulfosuccinate sodium salt
APTES	(3-Aminopropyl)triethoxysilane
ATRP	Atom transfer radical polymerization
BSA	Bovine serum albumine
BTESPTS	1,4-Bis(triethoxysilyl)propane tetrasulfide
CA	Cellulose acetate
Con-A	Concanavalin-A
COS	Chitosan oligomers

Ct	Cathecol
CTAB	Cetyltrimethyl ammonium bromide
DMF	<i>N,N</i> -Dimethyl formamide
DSC	Differential scanning calorimetry
FA	Formic acid
FESEM	Field emission scanning electron microscopy
FTIR	Fourier transform infrared spectroscopy
HA	Hydroxyapatite
HFIP	1,1,1,3,3,3-Hexafluoro-2-propanol
HSA	12-Hydroxystearic acid
LbL	Layer-by-layer
LPD	Liquid phase deposition
MPTMS	(3-Mercaptopropyl)trimethoxysilane
NEC	Neuro-microvascular endothelial cell
NIR	Near infrared
NP	Nanoparticle
P(LA- <i>co</i> -CL)	Poly(lactic acid- <i>co</i> -caprolactone)
P(VDF- <i>co</i> -CTFE)	Poly(vinylidene fluoride- <i>co</i> -chlorotrifluoroethylene)
PAA	Poly(acrylic acid)
PAN	Polyacrylonitrile
PANI	Polyaniline
PCL	Poly(ϵ -caprolactone)
PE	Polyethylene
PEDOT:PSS	Poly(3,4-ethylenedioxythiophene):poly(4-styrenesulfonate)
PEG	Poly(ethylene glycol)
PEO	Poly(ethylene oxide)
PET	Poly(ethylene terephthalate)
PHB	Poly(3-hydroxybutyric acid)
PHEMA	Poly(2-hydroxyethyl methacrylate)
PI	Polyimide
PLA	Poly(lactide)
PLLA	Poly(L-lactic acid)
PLGA	Poly(lactide- <i>co</i> -glycolide)
PMMA	Poly(methyl methacrylate)
POSS-NH ₃ ⁺	Octa(3-ammoniumpropyl) octasilsesquioxane octachloro ride
PPhe-GlyP	Polyphosphazenes with phenylalanine ethyl ester and glycine ethyl ester as co-substituents
PPV	Poly(<i>p</i> -phenylene vinylene)
PPy	Polypyrrole
PS	Polystyrene
PSEI	Poly(dimethylsiloxane- <i>b</i> -etherimide)
PSU	Polysulfone
PU	Polyurethane

PVA	Poly(vinyl alcohol)
PVAc	Poly(vinyl acetate)
PVC	Poly(vinyl chloride)
PVDF	Poly(vinylidene difluoride)
PVP	Poly(vinyl pyrrolidone)
QDs	Quantum dots
Rh-B	Rhodamine-B
RT	Room temperature
SEM	Scanning electron microscopy
SERS	Surface-enhanced Raman scattering
TEM	Transmission electron microscopy
TEOS	Tetraethyl orthosilicate
TESPSA	(3-Triethoxysilylpropyl)succinic anhydride
Triton X-100	4-(1,1,3,3-Tetramethylbutyl)phenyl-polyethylene glycol
UV	Ultraviolet
VA	Vinyl alcohol
Vis	Visible
XPS	X-ray photoelectron spectroscopy

1 Introduction

The interest in functional organic–inorganic nanocomposites has grown tremendously in the last two decades thanks to the development of nanotechnologies that allow the production of nanostructured components with unique physical properties and features such as superparamagnetism, ferromagnetism, size-dependent band-gap, and electron and photon transport.

Properties of organic–inorganic nanocomposites are not only the sum of the individual contributions of both phases but they are usually combined and improved. Indeed, the composite materials retain the advantageous features of both organic materials (such as light weight, versatility in tailoring chemical, physical and mechanical properties, low manufacturing cost, easy shaping and processability, etc.) and inorganic materials (such as high strength, heat stability, chemical resistance, and specific functionalities). Moreover, in most cases, the interface between the two phases plays a key role in determining the final material performances.

In this perspective, inorganic nanocomponents (such as nanoparticles) can be seen as “additives” to enhance polymer performance and thus they are also termed “nanofillers” or “nano-inclusions”. Organic–inorganic nanocomposites can be considered a form of hybrid material, even if the definition of “hybrid” nanomaterials typically refers to nanocomposites where the organic and the inorganic phases are

intimately mixed at the nanoscopic and molecular level. Typically, this particular type of nanocomposite is synthesized through sol–gel chemistry.

In this review we will cover the active research area of the design of hybrid organic–inorganic nanofibers obtained through the electrospinning technology, not limiting to nanomaterials obtained through sol–gel approaches but considering a broader set of combinations of polymers with inorganic components.

Challenges concerning the design of hybrid organic–inorganic nanocomposites are mainly related to (1) control of the compatibility between the organic and the inorganic phases, in order to avoid phase separation of the different components within the fibers; (2) control of the composition or the gradient of composition of the final material; and (3) control of structure and morphology.

Electrospinning is a polymer process technique that uses electrostatic forces to uniaxially stretch a viscoelastic jet derived from a polymer solution or melt, to produce continuous nanometric and micrometric fibers, typically assembled into nonwoven mats [1–3]. Advancements in proper material design, in controlling process parameters, and in the use of innovative spinning devices, have allowed a dramatic expansion of the potentialities of the technology.

Polymeric electrospun fibers are known to enhance the structural performance of composite polymeric materials [4]. Nanofibers made of materials other than polymers, such as metal oxides, carbon, ceramics, as well as composite organic–inorganic systems, have also been obtained and can be used advantageously in the field of nanocomposites, thus widening the spectrum of application of electrospun materials.

The great advantage of using the electrospinning technique to prepare hybrid nanomaterials lies in: (1) the possibility to process, through this technique, long and continuous fibers with incorporation of different functionalities and (2) the capability of controlling the morphology (from nano- to micrometer scales), the concentration, and the spatial dispersion of the components.

The electrospinning process enables to produce hybrid nanofibers characterized by: (1) one-dimensional (1D) confinement and a high aspect ratio that can induce and amplify strong anisotropic effects, (2) high orientations of structural elements along the fiber axis, and (3) high surface area as well as high porosities (up to 90%) of the electrospun nonwoven mats. Electrospun nanofibers are thus good candidates for numerous applications such as functional and protective coatings, catalytic and photocatalytic systems, sensing devices, energy storage systems (fuel cells, lithium ion batteries, solar cells), photonic and microelectronic applications, biotechnology.

Pure inorganic 1D nanostructures (nanofibers, nanotubes, nanorods, nanowires) can also be fabricated by using the electrospinning technique from the hybrid nanofibers through a calcination process at elevated temperature to remove the organic component. However, in this review we purposely have not considered the extremely wide literature concerning the design of pure inorganic electrospun nanofibers as well as of polymeric fibers loaded with carbon nanotubes, graphite

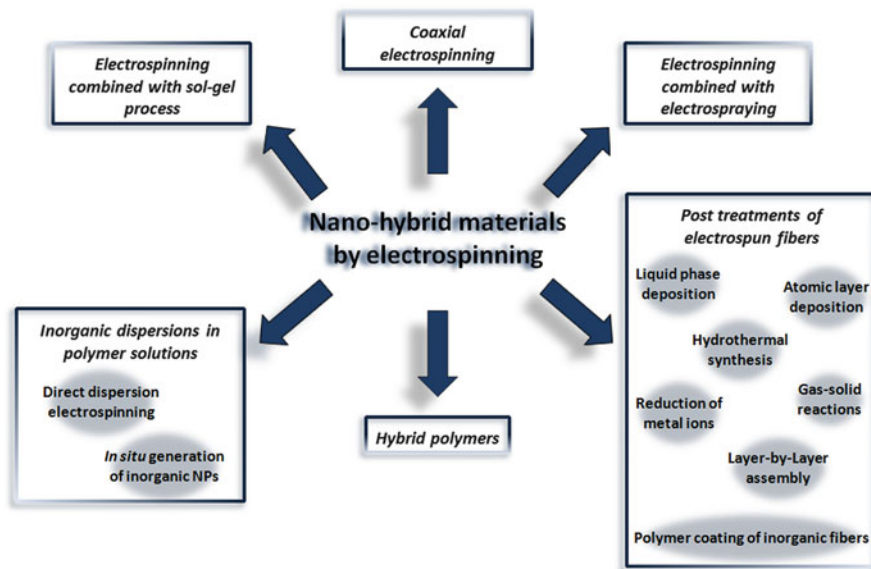


Fig. 1 Different methodologies that can be adopted to produce nanohybrid materials by electrospinning

and graphene, thus focusing only on the scientific literature dealing with polymeric fibers combined with inorganic components. In particular, this review presents the different methodologies that have been developed for fabrication of hybrid polymeric–inorganic nanofibers with advanced functionalities by making use of electrospinning technology in combination with additional specific synthetic and processing procedures, as illustrated in Fig. 1.

2 Electrospinning of Inorganic Dispersions in Polymer Solutions

Organic–inorganic hybrid nanofibers can be easily obtained by electrospinning polymer solutions containing inorganic fillers, such as metal salts or metal and metalloid oxide nanoparticles, minerals etc., on condition that the inorganic phase is soluble or well dispersed in the initial polymer solution. Therefore, the preparation of the starting dispersion to be electrospun requires great attention and is a relevant issue in the production of hybrid fibers. A homogeneous inorganic filler dispersion, the absence of nanoparticle aggregation, and a narrow particle size distribution represent key challenges since these conditions are required to achieve optimal interaction between the nanofiller and the polymer phase. Several examples

will be given to show different synthetic and processing strategies for achieving these goals.

It is well recognized that the complexity of the electrospinning process further increases with the introduction of colloids in the feeding solution, due to the presence of additional components in different phases that give rise to a broad spectrum of possible structures and morphologies [1].

In this section, literature will be discussed and analyzed on the basis of the following classification of the inorganic components:

- Metal, metal oxides and metal chloride
- Fluorescent and photoluminescent markers
- Minerals (such as hydroxyapatite, clays, carbonates)

The inorganic nanocomponents can be incorporated into polymer fibers by simply adding them into the spinning polymeric solution, according to a conventional direct dispersion approach, or they can be generated in situ by using suitable precursors, in order to prevent or limit their agglomeration. These two main methodologies are discussed in the following sections.

2.1 Direct Dispersion Electrospinning

The most straightforward methodology for incorporating inorganic nanoparticles into polymer fibers is to directly disperse them in the polymer solution before electrospinning. The simplest approach involves the addition of the inorganic nanoparticles to the polymer solution, followed by stirring or sonication to obtain a homogeneous suspension/mixture that is directly electrospun. Alternatively, the suspension containing the inorganic nanoparticles is prepared by ultrasonication or vigorous stirring and the polymer solution is subsequently added dropwise to obtain a hybrid organic–inorganic suspension that is then electrospun.

The simple direct dispersion strategy is, however, quite problematic when a high loading of nanoparticles is desired, due to the high viscosity of the resulting dispersion that eventually prevents fiber formation and to the tendency of the nanoparticles to agglomerate. Particle aggregation might cause formation of bead defects along the fiber axis, heterogeneity in the final composite fiber and, therefore, poor quality of the obtained nanofibrous mat, with adverse effects on its properties.

In order to facilitate uniform dispersion of the inorganic nanoparticles in polymer nanofibers, a surfactant is sometimes used. The nontoxic and cell-friendly surfactant 12-hydroxystearic acid (HSA) was used to incorporate the hydrophilic ceramic powder hydroxyapatite (HA), which presents low affinity for organic solvents and hydrophobic polymers, into polylactide (PLA) [5]. The surfactant stabilizes the dispersion that otherwise would settle within a few minutes. Other surfactants typically used are the anionic AOT [6–8] or the nonionic Triton-X-100 [9].

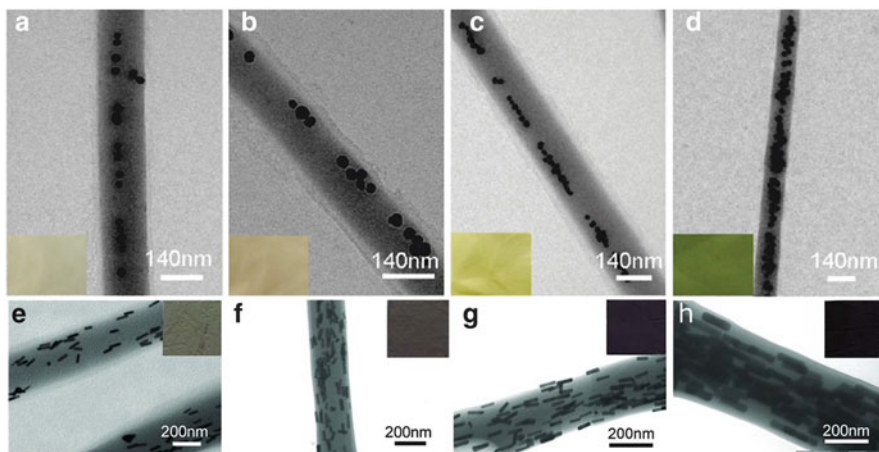


Fig. 2 (a–d) TEM images of Ag/PVA nanofibers with different molar ratios of PVA to Ag: (a) 530:1, (b) 530:2, (c) 530:3, and (d) 530:4. *Insets*: photographs of the corresponding Ag/PVA nanofiber mat. Adapted with permission from [10]. Copyright (2009) American Chemical Society. (e–h) TEM images of Au nanorods assembled within the PVA nanofibers with Au concentrations of (e) 50 nM, (f) 100 nM, (g) 150 nM, and (h) 200 nM. *Insets*: corresponding photographs of the nanofiber mats. Adapted with permission from [11]. Copyright (2012) American Chemical Society

2.1.1 Metal, Metal Oxides, and Metal Chloride Nanoparticles

Several metal nanoparticles (NPs) (such as silver, gold or cobalt NPs) were successfully incorporated into polymer fibers via direct dispersion electrospinning. However, we point out that metal NPs are more commonly generated through an in situ procedure (see Sect. 2.2) that allows to achieve a more uniform dispersion of small size particles.

Silver is typically incorporated within polymer fibers to confer antibacterial properties to the final fabric, for filtering applications or wound healing in the biomedical sector. In an interesting paper by He et al., Ag NPs were directly dispersed in a poly(vinyl alcohol) (PVA) solution, and assembled in an ordered linear chain-like structure along the fiber axis during the fiber stretching and thinning that occurs in the electrospinning process [10] (Fig. 2a–d). The electrospinning process was able to “freeze up” the alignment of the particles, preventing further aggregation, and allow fabrication of free-standing flexible surface-enhanced Raman scattering (SERS) substrates. The extent of aggregation and aggregate size were strongly dependent on the amount of Ag NPs added in the PVA solution and they were key factors in determining the magnitude of SERS signal enhancement and the sensitivity of detection. The same research group also obtained the free-standing SERS substrates by incorporating Au nanorods in PVA electrospun fibers [11]. The “sink-flow” effect and the shear forces that were exerted on the Au nanorods during the electrospinning process caused them to align along the flow path, i.e., the fiber axis direction (Fig. 2e–h).

It is noteworthy that self-assembly of anisotropic nanostructures, such as nanorods or nanowires, into well-controlled hierarchical arrangements represents a challenge in view of the integration of such nano-objects with unique properties within functional nanodevices for optoelectronic, information storage, catalysis, etc. that are frontier areas of research in chemistry and materials science.

In a very recent paper by Cheng et al. [12], gold nanorods were functionalized with poly(ethylene glycol) (PEG) chains and the PEG-modified Au nanorods were easily embedded in the biodegradable and biocompatible poly(lactide-*co*-glycolide) (PLGA) and PLA-*b*-PEG polymers to fabricate membranes that selectively killed the cancerous cells and inhibited cancer cell proliferation, thanks to the photothermal properties of PEG-Au nanorods. Indeed, the Au nanorods were released from the membrane and were taken up by the cancer cells that were killed upon heat generation caused by NIR irradiation of the Au nanorods. A homogeneous dispersion of gold nanoparticles with average diameter of around 20 nm and a narrow size distribution was successfully achieved in Poly(vinyl pyrrolidone) (PVP) fibers [13]. The good dispersion without particle aggregation was attributed to the steric effect exerted by the PVP chains and to the coordinative chemical bonding of the C–N and C=O moieties with Au atoms [13].

Other zero-valent nanoparticles that were incorporated in polymer nanofibers through direct dispersion electrospinning were transition metals such as superparamagnetic cobalt nanoparticles. Short hybrid fibers of the fluorescent poly(methylmethacrylate-*co*-vinylanthracene) copolymer containing cobalt nanoparticles were fabricated as magnetic micromanipulators of neurons [14].

A great number of metal oxide nanoparticles, such as silicon, titanium, magnesium, aluminum, iron, zinc, and other mixed metal oxides, were successfully incorporated into polymer solutions to obtain organic–inorganic nanofibers.

Silica nanoparticles were electrospun with synthetic polymers such as polyacrylonitrile (PAN) [15], poly(vinylidene difluoride) (PVDF) [16], poly(methyl methacrylate) (PMMA) [17], and PVA [18]. SiO₂ NPs were often embedded within electrospun polymer fibers to improve the mechanical properties of the obtained membranes, enhancing the tensile strength and Young's modulus [16] and thus causing a reinforcing effect. The NPs also reduce polymer crystallinity and increase the free volume for mobile lithium ions in applications such as Li-ion battery separators [16]. PMMA fibers containing photoluminescent SiO₂ NPs were prepared through physically adsorbing or chemically binding Rhodamine-B molecules to the surface of SiO₂ NPs [17]. In a very interesting paper by Jin et al. [18], SiO₂ NPs with different diameters (from 143 nm up to 910 nm) were used to fabricate fascinating necklace-like structures (Fig. 3a–c) through direct dispersion electrospinning with PVA. The weight ratio of the organic/inorganic components (Fig. 3d–f), as well as the diameter of SiO₂ NPs (Fig. 3g–i), influenced the morphology of the obtained electrospun fibers.

Addition of SiO₂ NPs into electrospun fibers was found to change fiber surface topography and roughness by creating wrinkles and nanoscaled protrusions on the surface of the nanofibers. Such fibers can find useful application as air filtration media with improved performances [15].

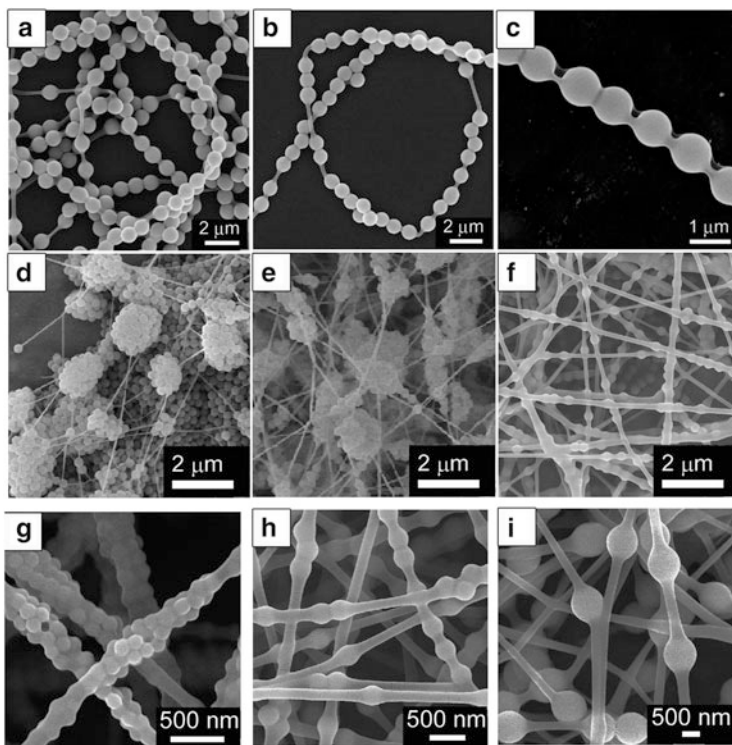


Fig. 3 (a–c) Necklace-like structures of PVA/SiO₂ (910 nm) electrospun mats obtained by removing part of the water in the solution (PVA:SiO₂ = 300:700). (d–f) PVA/SiO₂ (265 nm) electrospun mats with different PVA:SiO₂ volume ratios: (d) 400:600, (e) 600:400, and (f) 800:200. (g–i) PVA/SiO₂ fibers with different SiO₂ diameters: (g) 143 nm, PVA:SiO₂ = 500:500; (h) 265 nm, PVA:SiO₂ = 800:200; and (i) 910 nm, PVA:SiO₂ = 500:500. Adapted with permission from [18]. Copyright (2010) American Chemical Society

Titanium oxide nanoparticles are typically used as inorganic fillers capable of improving mechanical and thermal properties of the polymer, as bactericide additives, and as nanocomponents with photocatalytic activity. Depending on the type of crystalline phase (anatase, rutile, or brookite), TiO₂ can be used as photocatalyst (anatase), or as white pigment (rutile) in industry. TiO₂ NPs were electrospun in combination with both hydrophobic (such as polysulfone (PSU) [19], PVDF [20] and poly(ϵ -caprolactone) (PCL) [21]) and hydrophilic (PVA [22]) polymers. In particular, TiO₂ NPs incorporation increased the tensile strength of PSU membranes and their air permeability through the formation of micro- and nanoscale roughness on the fiber surface [16]. With the aim of fabricating nanocomposite membranes with enhanced ionic conductivity and electrochemical stability, as polymer electrolyte for Li-ion batteries, PVDF/PMMA-*g*-TiO₂ composite fibers were produced by electrospinning. TiO₂ NPs were modified by grafting PMMA onto the nanoparticle surface through Atom Transfer Radical Polymerization

(ATRP) in order to increase their compatibility with PVDF [20]. TiO₂ NPs were recently also proposed as attractive fillers for biodegradable polymer matrices such as PCL to enhance bioactivity of the fibrous composite [21].

Iron oxide nanoparticles, such as magnetite (Fe₃O₄), Fe₂O₃, or different mixed ferrite NPs, possessing magnetic and photoelectric properties were directly dispersed in PVP [23], poly(2-hydroxyethyl methacrylate) (PHEMA) [24], poly(L-lactic acid) (PLLA) [24], polyurethane (PU) [25], and PVDF [26] solutions. In all cases, a uniform distribution of iron oxide nanoparticles within the nanofibers was observed. In particular, superparamagnetic polymer nanofibers of biocompatible and biodegradable PHEMA and PLLA polymers containing magnetite were designed as drug carriers and drug release systems [24]. Flexible, elastomeric, and superparamagnetic substrates were obtained by electrospinning a polymer solution of an elastomeric PU, containing well dispersed NPs of a mixed ferrite of Mn–Zn–Ni [25]. When added to PVDF nanofibers, ferrite Ni_{0.5}Zn_{0.5}Fe₂O₄ NPs were found to enhance the ferroelectric phase content of PVDF fibers (β and γ phases) [26].

Organic–inorganic nanofibers containing zinc oxide nanoparticles embedded inside poly(ethylene oxide) PEO [27], PVA [28], and PU [29] polymeric components were successfully electrospun. The bactericide and the UV protection properties of ZnO NPs were exploited to deposit PU/ZnO nanofibers on cotton substrates to impart multifunctionalities to the textile [29]. Another interesting work by Sui et al. [27] investigated the photoluminescence properties of PEO/ZnO composite electrospun nanofibers to be used in nano-optoelectronic devices. The authors found that the presence of PEO enhanced the UV photoluminescence of ZnO. They proposed that, given the interactions between ZnO and PEO, the PEO molecules assembled on the surface of ZnO NPs that were, therefore, partly covered by long PEO chains. However, these ZnO–PEO interactions competed with interactions between ZnO NPs. According to the author's proposed model, large NP clusters initially form in the solution, but during electrospinning the applied high voltage might induce the polarization and orientation of ZnO NPs, that, given the interaction with PEO chains, are eventually embedded in and aligned along the polymer matrix fibers [27].

A novel nanofiller was recently developed, made up of zinc(II) octacarboxy phthalocyanine that was conjugated either with magnetic NPs [30] or with gold NPs [31]. These multiple conjugated systems showed heterogeneous photocatalytic activity for oxidizing organic pollutants, and their properties were investigated in the photodegradation of an azo-dye (Orange-G).

Nanoparticles of other metal oxides, such as MgO, Al₂O₃, MgAl₂O₄, and VO₂, were electrospun in different polymeric matrices. MgO NPs were used as inorganic fillers in polymers that are typically used to fabricate membranes (PVC, PVDF, PSU) in order to obtain nanocomposite membranes for protection against chemical warfare simulants [32].

Al₂O₃ is a heat-resistant ceramic filler that is usually employed to prevent dimensional changes caused by thermal deformation at high temperatures. Al₂O₃ powder treated with octylsilane was used as ceramic filler in P(VDF-*co*-CTFE)

nanofibers to coat a PE membrane to be used as separator in Li-ions batteries [33]. Similarly, magnesium aluminate (MgAl_2O_4) was incorporated into P (VDF-*co*-CTFE) nanofibers in order to develop a nanocomposite fibrous polymer electrolyte for Li-ions batteries [34]. $\text{Al}(\text{OH})_3$ as nanocomponent was inserted into PU nanofibers as a flame-retardant additive and to improve the thermal oxidation stability of PU fibers [35].

Very recently, vanadium dioxide hybrid fiber mats (PVP/ VO_2) were prepared for the first time and their diffuse reflectance was investigated [36].

Hafnium oxide is a fairly inert, inorganic compound with good chemical resistance to strong acids and bases, with potential applications in optical coatings and microelectronics [9]. HfO_2 shows a high dielectric constant and good thermal stability when in contact with silicon and is therefore a promising candidate to replace the SiO_2 currently used as a gate insulator in field-effect transistors. Cho et al. performed electrospinning of HfO_2 nanoparticles that were functionalized with acetate anions to be easily dispersible in water solution of PVA at high loadings. Strong hydrogen bonding between PVA and HfO_2 -acetate NPs resulted in a spinnable systems yielding smooth and bead-free fibers, even in the presence of high amounts of HfO_2 -acetate (up to 80 wt%) [9].

Among metal chloride nanoparticles, CoCl_2 is used for applications in humidity sensing, as well as catalysis, e.g., for hydrogen production. CoCl_2 was successfully electrospun by direct dispersion into nanofibers of PVDF [37] and PEO [38].

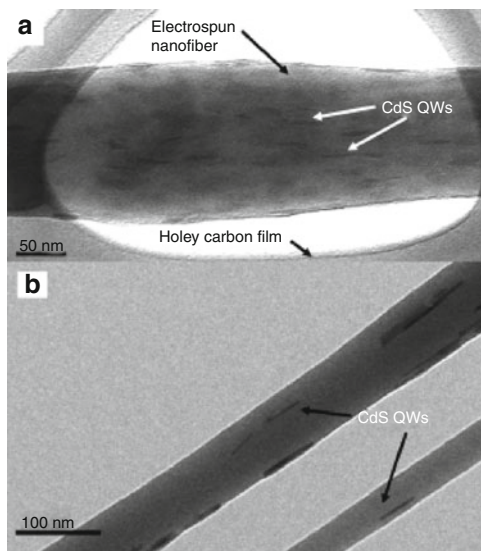
2.1.2 Fluorescent and Photoluminescent Markers

Fluorescent and photoluminescent nanofillers, such as CdTe, CdSe, CdS nanoparticles or quantum dots (QDs), ZnS and ZnSe QDs, and complexes of trivalent europium ion (Eu^{3+}), are promising inorganic materials with photoelectric, thermoelectric, and photoluminescent properties that find applications in optoelectronic devices, optical sensors, as photocatalysts for organic pollutants remediation [39] or hydrogen production [40], and as fluorescent biomaterials [41].

CdS QDs and quantum wires were successfully embedded in polymeric nanofibers of PEO [42], PAN [40], PMMA [43] and Zein [41], although a surface modification of the nanoparticles (e.g., capping with organic molecules) was in most cases applied to prevent nanoparticle agglomeration, thus improving the quality of the dispersion in the polymer solution [40, 42, 43].

When oleic acid-capped CdS quantum wires were embedded in electrospun PEO nanofibers, an unidirectional alignment of free-standing quantum wires was realized [42], which was attributed to the “sink-like” flow at the start of the electrospinning process (Fig. 4). Hydroxyl-coated CdS nanoparticles (CdS-OH) with a uniform size of 5 nm were embedded in PAN nanofibers by electrospinning and an even dispersion was obtained, due to effective protection of the CdS-OH nanoparticles by PAN macromolecules through hydrogen bonding interactions [40].

Fig. 4 (a, b) TEM images of aligned CdS quantum wires (*CdS QWs*) embedded in electrospun PEO polymer nanofibers. Reprinted with permission from [42]. Copyright (2006) Wiley Interscience



CdSe was incorporated in PVA [44] and PMMA [43] fibers, whereas CdTe NPs were successfully embedded within PVA nanofibers [8, 45]. Interestingly, a change in the photoluminescence characteristics of the obtained nanofibers, with respect to NP dispersed in solution, was found that was attributed to quantum confinement effects of CdTe embedded in nanofibers [45].

ZnS QDs with excellent fluorescent properties have been incorporated into PPV nanofibers by direct dispersion electrospinning, obtaining a good dispersion and limited particle aggregation [46]. Similarly, ZnSe QDs were embedded in polymer nanofibers using polystyrene (PS) and PLA as polymer matrices [47].

Europium ions are photoluminescent rare earth ions that exhibit a high yield of luminescence in the visible light region. Several Eu^{3+} -containing complexes were electrospun with synthetic polymers such as PVA [6], PMMA [48], PAN [49, 50], and PVP [51–53], in some cases in the presence of other functional inorganic particles. As an example, Fig. 5 shows bifunctional magnetic–photoluminescent nanofibers based on Fe_2O_3 nanoparticles and an europium complex [52].

2.1.3 Minerals

Clays (such as montmorillonite, laponite etc.) are usually employed as reinforcing filler to improve thermal stability as well as the stiffness and tensile strength of polymeric materials. Montmorillonite and organically modified montmorillonites – the latter showing an increased interfacial interaction between clay and polymer macromolecules – were incorporated into different polymeric materials such as PU [54], PCL [55], and chitosan/PVA [56]. The incorporated clays were well distributed, exfoliated and oriented along the fiber axis. It was reported that, during the

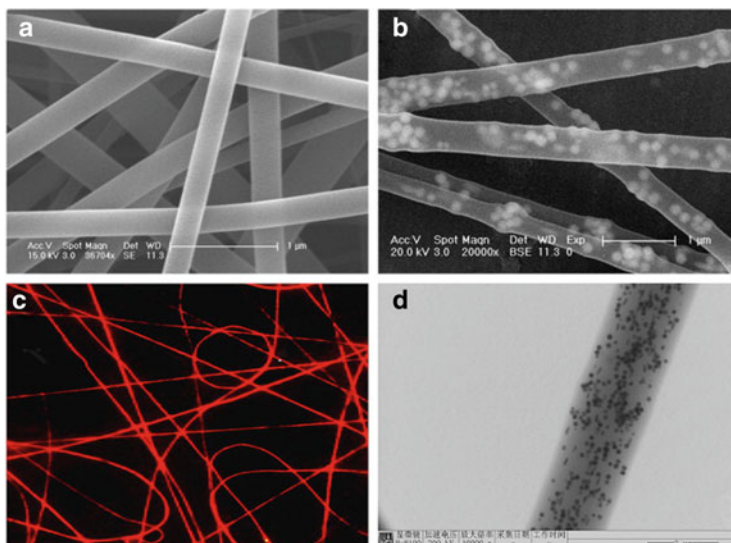


Fig. 5 Field emission SEM images of (a) PVP nanofibers and (b) $\text{Fe}_2\text{O}_3/\text{Eu}(\text{DBM})_3(\text{Bath})/\text{PVP}$ composite nanofibers. (c) Fluorescence microscopy image and (d) TEM image of $\text{Fe}_2\text{O}_3/\text{Eu}(\text{DBM})_3(\text{Bath})/\text{PVP}$ composite nanofibers. Adapted with permission from [52]. Copyright (2010) Elsevier

electrospinning process, the addition of montmorillonite in the spinning suspension increased its electric conductivity and viscosity. On the other hand, the high voltage and high extensional forces that are exerted on the suspension altered the structure of the initially prepared nanocomposite material, causing an increase in the interlayer spacing of the organo-modified montmorillonite clay [55]. Laponite clay was used to encapsulate the drug amoxicillin into PLGA nanofibers for biomedical applications [57].

Hydroxyapatite (HA) nanoparticles are osteoconductive bioactive ceramics that can support bone cell adhesion and proliferation and accelerate bone defects healing. HA is typically added to polymeric nanofibers to increase their mechanical strength. HA, often in the form of needle-like nanoparticles, was electrospun in the presence of synthetic biocompatible and biodegradable polymers such as PLA [5, 58–60] and PLA-PEG-PLA [61], natural polymers such as chitosan [62] and collagen [63, 64], and blends of natural and synthetic polymers such as PVA/chitosan [65] and PCL/gelatin [66].

β -Tricalcium phosphate (β -TCP) fillers were also used in PCL electrospun fibers [65, 67] to obtain bioactive nanocomposite fibers for applications in the bone tissue engineering field, as well as calcium carbonate (CaCO_3), which was incorporated in PCL membranes for guided bone regeneration [68].

2.2 *In Situ Generation of Inorganic Nanoparticles*

The second methodology used to obtain organic–inorganic hybrid nanofibers derives from the in situ generation of inorganic nanoparticles by using suitable precursors. Three main synthetic approaches can be identified:

1. In situ generation of NPs during the electrospinning process
2. In situ generation of NPs in the solution before the electrospinning process
3. Preparation of a hybrid organic–inorganic nanocomposite followed by its dissolution or dispersion and electrospinning

The literature discussion will be based on the three above-mentioned approaches.

We found only a few works dealing with in situ generation of silver nanoparticles during the electrospinning process. Ag NP formation was achieved starting from AgNO_3 solution in the presence of PVA and chitosan as the fiber-forming polymers [69]. It was reported that Ag NPs were spontaneously generated during the electrospinning process from the Ag^+ ions present in the polymer solution, even if only a partial conversion was achieved and Ag NPs coexisted with Ag^+ ions. Ag NPs were found both at the surface and inside the nanofibers. In addition, it was found that the dimensions of Ag NPs depended on the amount of chitosan in the solution. These results were ascribed to the presence of the amino and hydroxyl groups of chitosan that interact with Ag^+ ions in solution by chelating them [69]. A good nanoparticle dispersion was therefore obtained in the presence of chitosan. With the same approach and starting from the same PVA/chitosan fiber-forming polymeric system, Abdelgawad et al. generated Ag NPs with the addition of glucose into the spinning solution as reducing agent to increase the efficiency of the reduction power of chitosan [70].

Ag NPs were also obtained during the electrospinning process from AgNO_3 in a *N,N*-dimethyl formamide (DMF) solution of PVP polymer [71]. In this case, the DMF solvent was claimed to act as the reducing agent converting Ag^+ ions into Ag. It was also hypothesized that the polymer had a key role in the process. Indeed, the donated pair of electrons of oxygen and nitrogen atoms in the PVP monomer can form a coordinative complex with the Ag^+ ions that can stabilize them and decreases their chemical potential, thus facilitating their reduction. Therefore, PVP both promoted the formation of small sized Ag NPs and stabilized them, thus avoiding their aggregation [71].

A different example regards in situ generation of iron oxide (Fe_2O_3) nanoparticles on the surface of PEO fibers during the electrospinning process through reaction of the travelling jet with an active gaseous ammonia atmosphere [72].

A notable number of papers deal with the in situ formation of NPs in the solution before the electrospinning process. Many of them are related to Ag NP preparation.

Ag NPs were generated in situ through reduction of AgNO_3 by ethanol under refluxing conditions for 5 h at 360 K in PVP ethanol solution [73]. It was

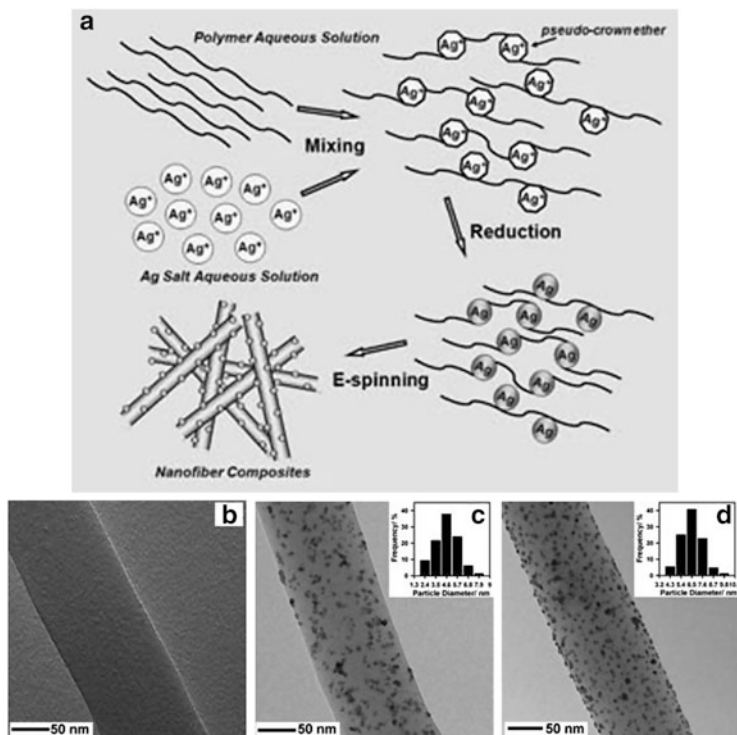


Fig. 6 (a) One-step process for fabricating PEO/Ag NPs composites via electrospinning. (b–d) TEM images of the mats fabricated from aqueous solution of 4 wt% PEO and AgNO₃ at concentrations of (b) 0, (c) 0.17, and (d) 0.26 wt%. Adapted with permission from [74]. Copyright (2009) Wiley Interscience

demonstrated that ethanol could reduce Ag⁺ ions into Ag under refluxing conditions in the absence of any external reducing agents. In addition, it was claimed that oxygen in the ethanol molecule could coordinate Ag⁺ ions, thus preventing nanoparticle aggregation and reducing particle size [73].

In a couple of very accurate and elegant studies, Ag NPs were generated in situ in the electrospinning solution by means of high molecular weight PEO in a true one-step process at ambient conditions and without the use of organic solvents [74, 75]. PEO and AgNO₃ were dissolved in deionized water at room temperature (RT) to effect reduction of the metal salt precursor by PEO. After reduction, the solution was electrospun. It was found that the reduction time of AgNO₃ played an important role in the size control of the Ag NPs [74, 75]. The paper by Saquing et al. was the first report on the use of a fiber-forming polymer that acted as both the reducing agent and the protecting agent for the resulting metal nanoparticles in solution. The formation of a pseudocrown ether holding the metal cations within the coiled polyether helix was proposed as the mechanism involved in the generation of Ag NPs [74] (Fig. 6).

NaBH_4 was used as reducing agent in a solution of AgNO_3 and chitosan in acetic acid to obtain Ag NPs. In this case, PEO was added to the solution in order to improve the spinnability of chitosan [76].

In another paper, the solvent for nylon-6, namely formic acid (FA), played the role of reducing agent for in situ synthesis of Ag NPs from AgNO_3 during the solution preparation, thus realizing a true one-step fabrication of composite fibers [77]. FA as reducing agent was also used by Penchew et al. [78]. They prepared water-insoluble nanofibers from chitosan/PEO/glutaraldehyde/Ag NPs and carboxyethyl-chitosan/PEO/glutaraldehyde/Ag NPs. This is a very interesting paper, showing a multiple use of concentrated FA: (1) to dissolve chitosan and carboxyethyl-chitosan, (2) to mildly reduce silver ions to Ag NPs, and (3) to slow down gel formation, thus allowing electrospinning to be carried out in the presence of a crosslinking agent (i.e., glutaraldehyde). The combination of the antibacterial properties of the chitosan matrix and of Ag NPs located at the surface of the electrospun nanofibers, coupled with the fibrous substrate stability in an aqueous environment, makes these new materials promising candidates for wound-healing and filtration applications [78].

An atmospheric plasma treatment was successfully applied to AgNO_3 /PAN solution in DMF to reduce AgNO_3 salt into Ag NPs within 5 min without the addition of adverse chemicals. Antibacterial electrospun Ag/PAN nanofibers were obtained and morphologically characterized [79].

Another interesting approach to obtaining Ag NPs from reduction of Ag^+ ions is the use of PVA polymer combined with hydroxypropyl- β -cyclodextrin. The former, due to the hydroxyl groups on the polymer backbone, stabilized the obtained Ag NPs by preventing their aggregation, and the latter was used as additional reducing and stabilizing agent to control the size and uniform dispersion of Ag NPs [80].

Ag_2S nanoparticles with photoelectric, thermoelectric, and photoluminescent properties were obtained starting from AgNO_3 precursor in a PVP ethanol solution after the addition of C_2S and stirring for 24 h in the dark to allow the sulfuration reaction to complete before the electrospinning process [81].

CdS NPs were easily prepared from the precursor CdAc in a solution of poly(vinyl acetate) (PVAc) in DMF, through the addition of ammonium sulfide with vigorous stirring in order to obtain a colloidal fine dispersion of CdS NPs [39, 82]. It was shown that CdS NPs were well embedded inside the fibers and formed a kind of self-assembled columnar structure with extensive close-packing, resembling a nematic-like structure [39, 82]. Similarly, a CdS/PdS alloy was obtained from the precursors CdAc and PdAc, dissolved in a solution of PVAc in DMF, through the addition of ammonium sulfide. The electrospinning process of the obtained colloidal solution led to a core-shell structure, possibly due to assembly of the wet nanoparticles so that the process resembles a kind of "emulsion" electrospinning (Fig. 7) [39].

Wang et al. reported the preparation of magnetite (Fe_3O_4) nanoparticles through an in situ method combined with electrospinning, starting from a mixed solution of Fe(II), Fe(III), and PVA [83]. In Fig. 8, the preparation procedure is shown. Briefly, NaOH was added to the mixed metal/polymer solution under vigorous stirring to

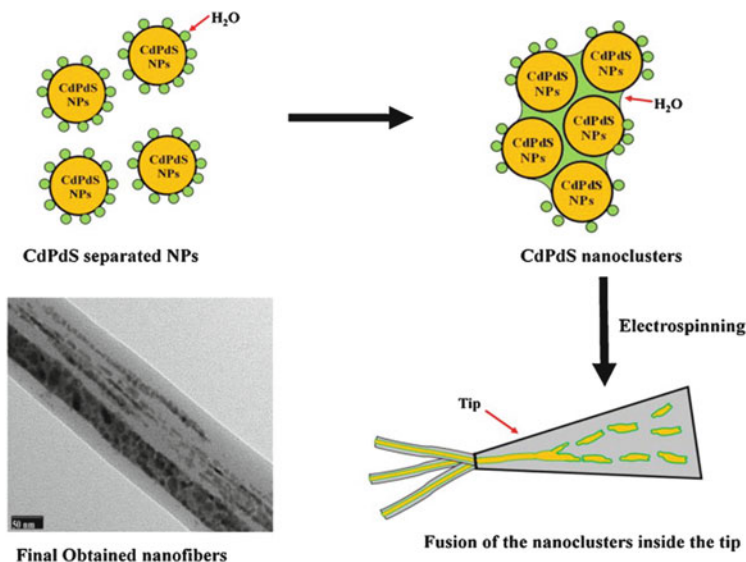


Fig. 7 Mechanism of formation of the core-shell structure. Reprinted with permission from [39]. Copyright (2012) Elsevier

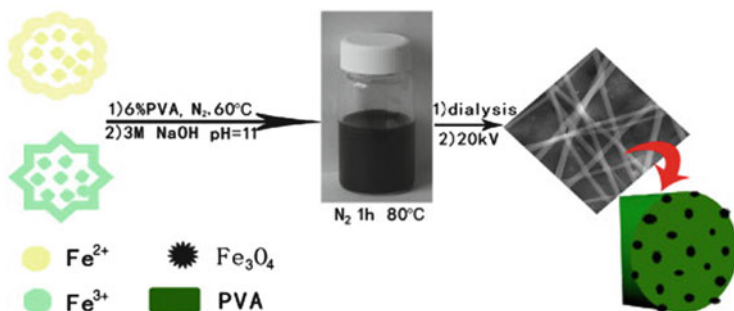
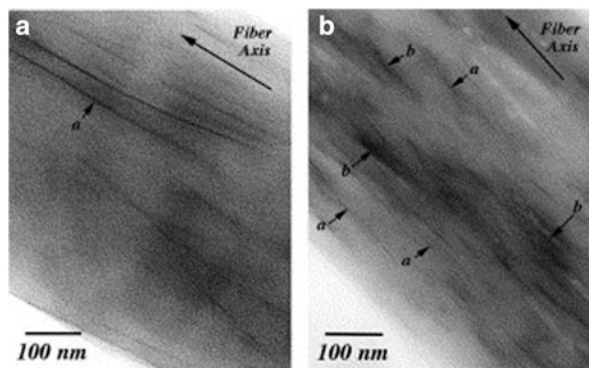


Fig. 8 Preparation route for Fe_3O_4/PVA nanofibers. Reprinted with permission from [83]. Copyright (2010) Elsevier

reach pH 11; after that the mixture was cooled at RT and dialyzed against deionized water in order to remove ions. The obtained dialyzed solution was used for electrospinning.

Cu nanoparticles were successfully incorporated within PVA nanofibers through an in situ deoxidization approach starting from $CuCl_2$ [7]. PVA-protected copper nanoparticles and copper nanowires were generated inside the electrospun fibers. It was found that the molar ratio of copper ions to VA units played an important role in the formation of the copper/PVA nanocables [7].

Fig. 9 Bright field TEM images of nylon-6/montmorillonite composite nanofibers from (a) pure HFIP solution and (b) a solution of 95% HFIP and 5% DMF (*a* single sheet, *b* stacked sheets/tactoids). Reprinted with permission from [87]. Copyright (2002) Elsevier



Deniz et al. showed a new method for obtaining gold nanoparticles embedded in PVP fibers. Au NPs were generated by laser ablation in the PVP solution of a solid gold block by focusing laser radiation on the cylindrical gold block via a lens and carrying out the ablation for about 15–30 min. Finally, the PVP/Au NP solution was electrospun. Spherical Au NPs with a uniform dispersion were obtained [84].

In situ formation of a hybrid organic–inorganic nanocomposite followed by its dissolution or dispersion and subsequent electrospinning was also used as a practical method to obtain organic–inorganic hybrid nanofibers. Electrospun chitosan/gelatin nanofibers containing Ag NPs were fabricated by dissolving a previously prepared Ag NP-chitosan nanocomposite in an acetic acid gelatin solution followed by electrospinning. The Ag NP-chitosan nanocomposite was previously prepared through reduction of AgNO_3 by microcrystalline chitosan, filtering the precipitate and then washing and air drying it [85].

Nylon-6/montmorillonite composite nanofibers were electrospun from a nanocomposite prepared by blending nylon-6 and montmorillonite in a twin-screw extruder. The obtained nanocomposite was then dissolved in FA and electrospun [86]. A similar procedure was used to fabricate electrospun nylon-6/montmorillonite nanofibers using 1,1,1,3,3,3-hexafluoro-2-propanol (HFIP) as solvent. It was demonstrated that the addition of a small amount of DMF in the electrospinning solution resulted in agglomeration of the dispersed montmorillonite layers and an overall mixed morphology was obtained, demonstrating that solvent plays a delicate role in maintaining good layer dispersion (Fig. 9) [87].

Nanocomposites of HA/chitosan were fabricated using a wet chemical co-precipitation approach from the Ca and P precursors and chitosan. The obtained HA/chitosan nanocomposite was filtered, dried and stored in a vacuum oven at RT before using in the electrospinning process to produce biomimetic nanocomposite nanofibers for bone tissue engineering [88]. The same procedure was used to prepare a HA/collagen nanocomposite that was then dissolved in HFIP for electrospinning [89]. A HA/gelatin nanocomposite was prepared by means of a similar method of chemical co-precipitation of Ca and P precursors, together with gelatin. The nanocomposite was then lyophilized and subsequently dissolved in the electrospinning solution [90].

An interesting and accurate study by Kim et al. [91] describes the fabrication of 1D arrangements of gold nanoparticle arrays within submicrometer PEO fibers through formation of a hybrid organic–inorganic nanocomposite. First, the Au NP/PEO nanocomposite was prepared from a PEO solution in chloroform, with the addition of dodecanethiol-capped Au dissolved in chloroform. The mixture was vigorously stirred, cast onto glass dishes, and the solvent subsequently evaporated. This nanocomposite was used to prepare the electrospinning solution. It was found that Au NPs were arranged in quite long 1D chain-like arrays within the electrospun fibers. In addition, Au NPs acted as nucleating sites during PEO crystallization and had an effect on PEO molecular conformation, causing transformation from a helix to *trans*-planar zigzag structure [91].

3 Post-treatment of Electrospun Fibers

In this section, we summarize the bibliographic literature concerning the production of organic–inorganic composite fibers where at least one of the two final phases is created by applying a specific post-treatment to the fibers obtained by electrospinning. Post-treatments can be applied: (1) to achieve the formation of the inorganic phase in polymeric fibers or (2) to cover inorganic fibers with an organic phase (polymer coating). In the following sub-sections, the most commonly employed post-treatments are described.

3.1 Liquid Phase Deposition

The first report on the production of composite fibers through the synthesis of the inorganic phase after electrospinning dates back to 2003 [92]. The authors used liquid phase deposition (LPD) to cover PAN electrospun fibers either with tin oxide or with titanium oxide. The LPD method is used to generate thin oxide films on several types of substrate through their immersion in the reactant solution. The metal oxide is synthesized from a metal-fluoro complex dissolved in water in the presence of either boric acid or aluminum metal. The complex is slowly hydrolyzed by water to generate a precipitate of metal oxide. The boric acid (or the aluminum) works as a fluoride scavenger, accelerating hydrolysis of the fluoro complex to get the corresponding oxide [93]. Accordingly, Drew et al. [92] immersed PAN fibers in a water solution of $\text{TiF}_6(\text{NH})_2$ and H_3BO_3 to generate TiO_2 coating, and in a water solution of $\text{SnF}_6(\text{NH}_4)_2$ and H_3BO_3 to generate SnO coating, envisioning that these new materials would provide highly reactive surfaces for catalysis, sensing, and photoelectric conversion applications.

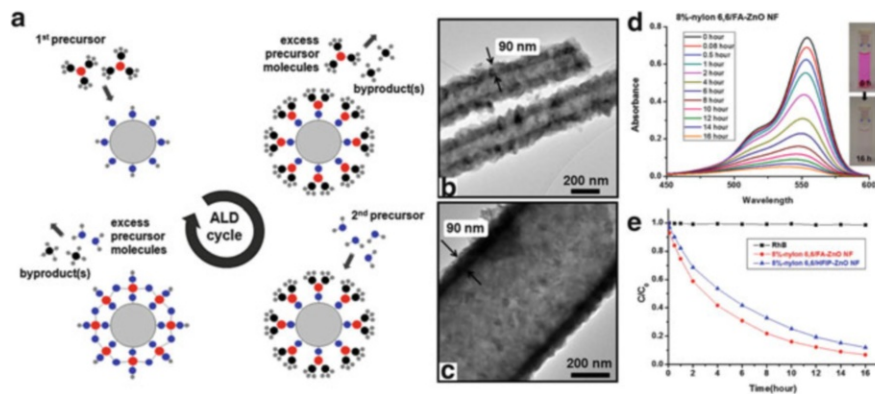


Fig. 10 (a) The atomic layer disposition (ALD) process. (b) TEM image of 8% nylon-6,6/FA-ZnO fiber (fiber diameter ~ 80 nm). (c) TEM image of 8% nylon-6,6/HFIP-ZnO fiber (fiber diameter ~ 650 nm). (d) UV-Vis spectra of the Rhodamine-B solution in contact with 8% nylon-6,6/FA-ZnO core-shell fiber as a function of the UV irradiation time. (e) The rate of Rhodamine-B degradation with and without core-shell fibers under UV light exposure. Adapted with permission from [96]. Copyright (2012) American Chemical Society

3.2 Atomic Layer Deposition

Atomic layer deposition (ALD) enables the deposition of very thin films of both polymeric and inorganic materials with a precise control of thickness at the atomic level on a variety of substrates. The ALD process is based on the use of two molecular precursors that react in sequence with the substrate, thus depositing a binary compound film. These reactions occur in a chamber where the molecular gaseous precursors are sequentially purged. Each reaction is self-limiting because there are only a finite number of substrate surface sites that can react with the precursor, thus the thickness increase is constant in each deposition cycle. Depending on the molecular precursors, a great variety of coatings can be synthesized by ALD such as oxides, nitrides, and sulfides [94].

The ALD process is mainly applied to produce hollow inorganic tubes and core-shell inorganic fibers by using organic fibers as templates that are calcinated in a second step. However, some authors have used this approach to produce composite fibers. Oldham et al. [95] produced nylon-6 fibers coated with either ZnO or Al_2O_3 and demonstrated that ALD coating could control the fiber wetting properties and chemical resistance.

More recently, Kayaci et al. [96] used the same technique to produce nylon-6,6 electrospun fibers with different diameters and covered with a homogeneous coating of ZnO (90 nm thick) and tested their photocatalytic activity against degradation of Rhodamine-B. By keeping the thickness of the ZnO layer constant, they demonstrated that the degradation of Rhodamine-B was more effective when thin fibers were used due to the higher surface area of the sample (Fig. 10).

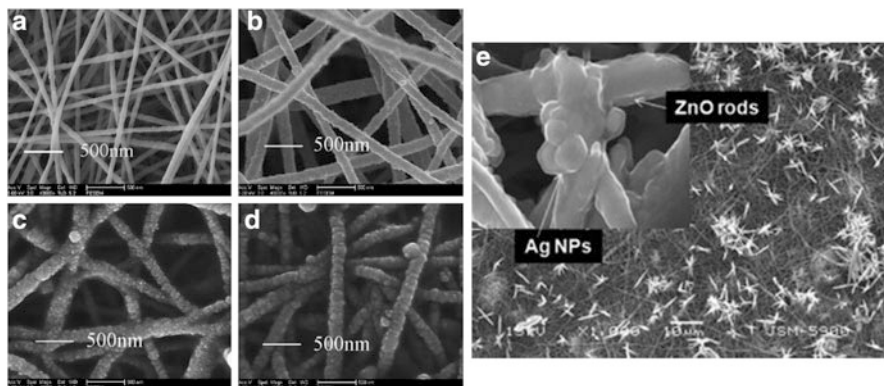


Fig. 11 (a) SEM image of poly(methacrylic acid-*co*-trifluoroethyl acrylate)/PVDF electrospun fiber mats. (b–d) SEM images of TiO₂–fluoropolymer fiber nanocomposites prepared at 150°C for (b) 3 h, (c) 6 h, and (d) 12 h. Reprinted with permission from [98]. Copyright (2009) Elsevier. (e) SEM image of ZnO/nylon-6 mat with ZnO and Ag precursors. Reprinted with permission from [100]. Copyright (2013) Elsevier

3.3 Hydrothermal Synthesis

Hydrothermal synthesis allows the generation of crystals of oxides and hydroxides by the chemical reaction of precursors in water solutions and by changes in the solubility of the products under controlled conditions of temperature and pressure [97]. The substrates over which the crystals grow must resist high temperature conditions, thus this kind of synthesis is limited to electrospun semicrystalline fibers having a high melting temperature or amorphous fibers having a high glass transition temperature.

Hydrothermal synthesis was used by He et al. [98] to cover the surface of PVDF fibers with grains of TiO₂. In order to favor the interaction between fiber surface and titanium ions, the authors introduced a small amount of poly(methacrylic acid-*co*-trifluoroethyl acrylate) copolymer bearing carboxylic groups in the fibers. After electrospinning, they immersed the fibers in an aqueous solution of titanium oxo-sulfate, sulfuric acid, and urea. The authors obtained TiO₂ nanocrystals on the fiber surface, their size and density being controlled by the reaction conditions (Fig. 11a–d), and demonstrated their photocatalytic activity against methylene blue.

Chang [99] produced polyimide (PI) fibers (obtained after thermal imidization of poly(amic acid) electrospun fibers) covered by rods of ZnO. First, the authors coated the PI nanofibers with ZnO NPs by immersion of the mat in an ethanol solution of zinc acetate and by performing a subsequent thermal treatment. These ZnO NPs acted as seeds for the growth of ZnO rods synthesized by hydrothermal synthesis, which occurred at 90°C in a mixture of zinc nitrate hexahydrate and hexamethylenetetramine. In order to improve the attachment of ZnO rods to the fiber surfaces, Kim et al. [100] incorporated the ZnO NPs seeds in the fiber by electrospinning a colloidal solution of polymer (nylon-6) and ZnO NPs.

Hydrothermal synthesis was then carried out in a solution of Zn nitrate and Ag nitrate to achieve simultaneous growth of ZnO nanorods and Ag nanoparticles with photocatalytic and antimicrobial properties (Fig. 11e).

3.4 Reduction of Metal Ions

The formation of a metallic inorganic phase is commonly achieved by introducing into the polymer fibers metal ions that turn into metallic nanoparticles as a consequence of a chemical reduction treatment. Two different approaches have been described in the literature for achieving metal ion insertion in polymeric fibers. The first method encompasses the use of fibers bearing functional groups able to coordinate the metal ions that come in contact with the fibers when the mat is immersed in a solution of their salt. Afterwards, the ions attached to the fibers are reduced by a chemical agent. The second approach consists in incorporating the metal ions in the polymeric fibers during electrospinning by processing a polymeric solution containing the corresponding salts. Similarly to the first approach, the metal is subsequently reduced to gain metallic particles.

By following the first approach, Xiao et al. synthesized iron NPs on electrospun fibers of PVA/PAA blend. The PAA conferred to the fibers the capability of immobilizing Fe^{3+} ions during the immersion of the crosslinked mat in an aqueous solution of FeCl_3 ; the ions were subsequently reduced by NaBH_4 [101, 102]. The same approach was used by the authors to immobilize Ag NPs on PVA fibers [103]. Dong et al. [104] produced fibers of PMMA and poly(4-vinylpyridine) and immersed the as-spun mat either in NaAuCl_4 or in AgNO_3 solution to obtain, after reduction with NaBH_4 , either gold or silver nanoparticles by exploiting the capability of pyridine rings to complex the corresponding ions. Fang et al. [105] synthesized gold nanoparticles on the surface of PVA fibers by blending the polymer with branched polyethyleneimine, thus taking advantage of the presence of amine groups for immobilizing AuCl_4^- ions. Amine groups were also employed by Gardella et al. [106] to immobilize Pd NPs on the surface of PLA fibers containing amino-functionalized silsesquioxane molecules.

In all the cited works, the reduction step was carried out after ion immobilization on fibers. By contrast, Liu et al. [107] and Son et al. [108] incorporated the reducing functional groups directly in the fibers during electrospinning, either by adding the reducing molecules to the electrospun solution [107] or by properly modifying the polymer to produce a redox-active material [108]. In these cases, metal ion reduction occurred in situ when the ion came in contact with the fiber, and the particle yield strictly depended on the redox group concentration in the fibers. For instance, PVA was grafted with catechol redox groups (PVA-*g*-ct) by taking inspiration from the adhesion mechanism of marine mussels, which facilitates binding and reduction of noble metal ions [108]. In this case, the reduction of silver ions to solid silver occurred spontaneously at RT, whereas gold and platinum ions were only partially

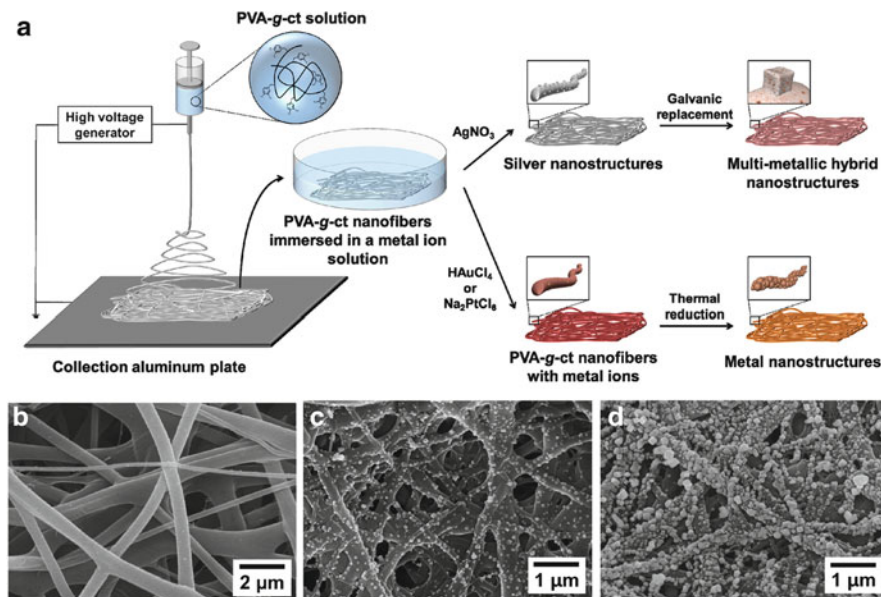


Fig. 12 (a) Mussel-inspired templating synthesis of noble metal nanostructures on the electrospun PVA-g-ct nanofibers. (b) SEM images of PVA nanofibers after incubation with a 0.2 mM AgNO_3 in methanol for 40 min. (c, d) SEM images of PVA-g-ct nanofibers after incubation in the same solution for (c) 20 and (d) 40 min. Adapted with permission from [108]. Copyright (2012) American Chemical Society

reduced by catechol groups and required an additional thermal treatment for achieving complete reduction into solid metal nanostructures (Fig. 12).

In other works, the metal ions were directly incorporated into the polymeric fibers during electrospinning. For instance, Demir et al. [109] electrospun a copolymer of acrylonitrile and acrylic acid with PdCl_2 and generated Pd NPs in the fibers by immersing the mat in hydrazine solution. They found that Pd particles size increased with the increase of acrylic acid amount in the polymer backbone. To explain this result, they hypothesized that acrylic acid groups interact with Pd cations and that nucleation of the metal particle takes place around acrylic acid units, whose amount and distribution along the polymeric chain regulate particle size and density [109].

Han et al. [110] electrospun PMMA with gold salt that was subsequently reduced to metallic Au by NaBH_4 . The authors also demonstrated that these Au particles can act as seeds for further growth of Au, which was achieved by immersing the composite PMMA/Au in a solution of Au salt and reducing agent. They also showed that the thickness of the gold layer can be regulated by the Au salt concentration in the solution [110]. A similar approach was used to generate Ag particles in cellulose acetate (CA) [111] and PAN [112] fibers. In these cases, the AgNO_3 salt was electrospun with the polymer and reduction of Ag^+ was achieved by exposing the nonwoven mats to UV light.

3.5 Gas–Solid Reaction

Gas–solid reaction was applied to electrospun fibers for the synthesis of metal sulfide nanoparticles. The synthetic strategy involves the electrospinning of a polymer solution containing the desired metal salt and the exposure of the nonwoven mats to H₂S gas as source of sulfide ions.

The Wang group has synthesized and characterized a variety of polymeric fibers containing metal sulfides that can be potentially applied in optoelectronic devices. For instance, they produced PVP fibers containing, cadmium acetate [113], lead acetate [114], or silver nitrate [115] that were converted into CdS, PbS, and Ag₂S, respectively, and they characterized the materials by XPS, SEM, TEM, and FTIR. Moreover, the group fabricated PVA fibers containing copper-doped zinc sulfide (ZnS:Cu) by loading the polymer solution with both zinc and copper acetate. They prepared ZnS:Cu/PVA nanofibers with different concentrations of Cu doping for modulating the luminescence properties of the composite fibers [116]. The optical properties were also tuned in PEO fibers containing CdS nanoparticles throughout the control of particle size by changing the CdS/PEO mass ratio [117].

A different approach for the synthesis of metal sulfides on a fiber surface was proposed by Ye et al. [118]. They electrospun a poly(methylmethacrylate-*co*-vinylbenzyl chloride) copolymer and carried out the ATRP synthesis of lead dimethacrylate that was subsequently treated with H₂S gas to obtain PbS particles.

3.6 Layer-by-Layer Assembly

The layer-by-layer (LbL) assembly technique is an easy and inexpensive process for generating multiple layers on a solid substrate from a variety of materials (e.g., polyelectrolytes, proteins, inorganic particles, small molecules). The LbL assembly is mainly driven by electrostatic interactions and is carried out by immersing the solid substrate in a solution of an oppositely charged substance at high concentration. The latter tends to neutralize the charge on the solid surface and is absorbed in excess, leading to charge reversion. The multilayer film is generated by depositing on the solid surface alternating layers of oppositely charged substances, with wash steps in between [119].

This technique has been applied by Ding et al. [120] to immobilize TiO₂ nanoparticles on the surface of CA fibers. They immersed the negatively charged CA nonwoven mat in an acid solution of positively charged TiO₂ NPs and subsequently in a water solution of the anionic PAA, repeating these steps sequentially several times. They demonstrated the successful attachment of TiO₂ and PAA by X-ray and FTIR measurements and visualized the formation of a new layer on the surface of the fibers by SEM and TEM.

Au negatively charged particles were immobilized on the surface of PS fibers [121]. The process consisted in inducing the negative charge on PS fibers through

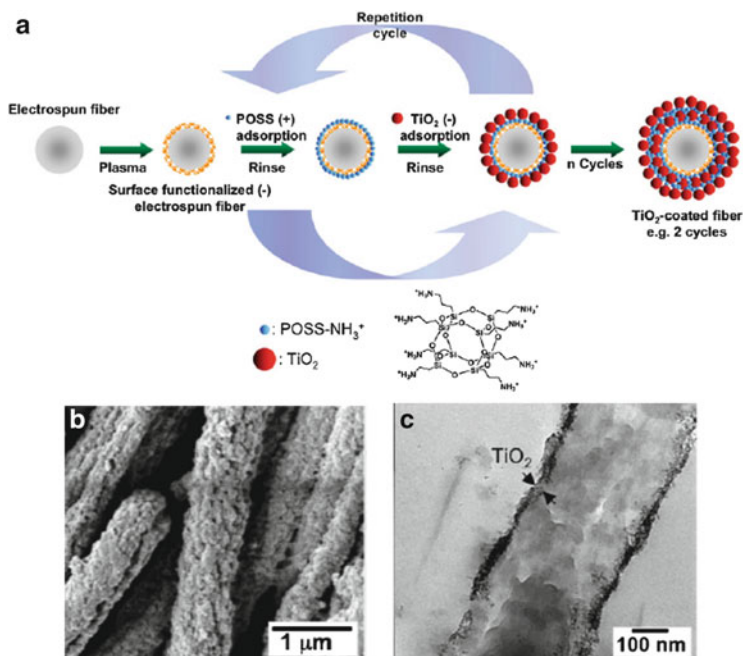


Fig. 13 (a) Preparation of TiO₂-coated electrospun polymer fibers using layer-by-layer deposition method. (b) SEM and (c) TEM images of TiO₂-coated poly(dimethylsiloxane-*b*-etherimide) fibers. Adapted with permission from [122]. Copyright (2009) Wiley Interscience.

sulfonation, immersing the modified PS fibers in a solution of positive polyelectrolyte and subsequently in a dispersion of 4-(dimethylamino)-pyridine-stabilized gold nanoparticles.

Lee et al. [122] introduced plasma treatment before carrying out the LbL process. The plasma treatment generated acidic groups on the surface of different kinds of polymers that acquired a negative charge in water. In particular the authors used PS, PAN, PSEI, and a blend of PMMA and PEO. The plasma-treated fibers were coated with alternating layers of positively charged POSS-NH₃⁺ and negatively charged TiO₂ nanoparticles. They obtained photocatalytically active TiO₂-decorated polymer fiber mats with enhanced stability against thermal, chemical, and UV degradation thanks to the use of POSS-NH₃⁺ molecules (Fig. 13).

The LbL assembly was exploited by Xiao et al. [123] to introduce carboxylic groups on the surface of CA fibers through the formation of polyelectrolyte multilayers containing PAA. These chemical groups were employed in a second step to adsorb Fe³⁺ ions that afterwards were reduced to metallic iron with NaBH₄.

3.7 Polymer Coating of Inorganic Fibers

The post-treatments described till now were applied to fibers mainly composed of organic phase and consisted in the generation of the inorganic phase. Some works have reported post-treatments that were applied to inorganic fibers with the intention of generating a conductive organic polymeric phase as a coating for the inorganic fibrous phase.

The first example is the work of Lu et al. [124] who fabricated polypyrrole (PPy)/TiO₂ coaxial nanocables, where the conductivity of PPy was integrated with the photocatalytic activity of TiO₂ for applications in electrochromic devices, nonlinear optical systems, and photoelectrochemical devices. The synthetic approach consisted in: (1) preparation of TiO₂ fibers by sol–gel electrospinning and calcination of the polymer (PVP in the specific case), (2) physical adsorption of Fe³⁺ oxidant on the surface of TiO₂ nanofibers, and (3) polymerization of pyrrole (from vapor) on the surface of TiO₂ nanofibers.

Similarly, PANI was synthesized on the surface of TiO₂ nanofibers [125] for developing a NH₃ gas sensor. In this case, the oxidizing agent (Mn₃O₄) required for the polymerization of aniline was incorporated into the TiO₂ fibers during the electrospinning process and its concentration regulated the PANI to TiO₂ ratio in the final composite fibers and thus the sensitivity of the sensor towards ammonia.

Zampetti et al. [126] developed PEDOT:PSS-coated titania nanofibers for NO₂ detection. The fabrication approach was rather easy and was based on: (1) preparation of TiO₂ fibers by sol–gel electrospinning and calcination of PVP and (2) -dip-coating of TiO₂ fibers in a aqueous dispersion of PEDOT:PSS.

4 Electrospinning Combined with the Sol–Gel Process

The main challenge in the fabrication of organic–inorganic nanomaterials is to control mixing between the two different phases. The drawbacks related to preparation routes based on suspensions, emulsions, or blends can be overcome either by forcing the two phases to grow simultaneously in intimate contact with each other or by applying a sequential process whereby one phase is synthesized in the presence of the second previously formed phase [127]. Such approaches enable the formation of nanocomposites in which the organic and inorganic components are intimately mixed over length scales ranging from a few Angstroms to a few tens of nanometers. On the basis of the nature of the interface, which plays a central role in defining hybrid properties, these kinds of materials are commonly classified into two classes: in Class I hybrids the two phases exchange weak interactions (such as van der Waals forces, hydrogen bonds, or electrostatic forces), whereas in Class II hybrids the organic and the inorganic components are linked by strong chemical bonds (i.e., covalent or ionic-covalent bonds).

In the case of electrospinning, the most effective strategy for the production of organic–inorganic hybrid fibers encompasses the *in situ* synthesis of the inorganic phase within a polymer that confers to the spinning solution the proper rheological properties to obtain continuous bead-free fibers. To this aim, the inorganic phase can be synthesized by a sol–gel process that involves the use of a molecular precursor [typically a metal or silicon alkoxide $M(\text{OR})_n$, $M = \text{Si, Ti, Zr, Al}$, etc. and $\text{OR} = \text{OC}_n\text{H}_{2n+1}$]. At mild temperatures the precursor reacts with water to form a hydroxide, $M(\text{OH})_4$, which condenses into a $M\text{--O--}M$ sequence with the formation of water and alcohol, generating an oxide framework. Overall, the process is very complex because hydrolysis and condensation reactions occur simultaneously and many chemical species are present in the solution. First, the reactions generate oligomers, polymers, and cyclic inorganic species resulting in a stable colloid (sol), then, during the condensation reaction a continuous solid network full of solvent is generated (gel). The kinetics are affected by several factors, such as the type of precursor, water-to-precursor ratio, pH, temperature, and solvent. The sol–gel process for the synthesis of inorganic materials has been known since the mid-1900s and the reader is referred to the literature cited for a more detailed description [127–130].

Larsen et al. combined for the first time electrospinning with sol–gel to design vesicles and nanofibers of pure inorganic oxides and organic–inorganic nanofibers [131]. In a typical electrospinning experiment, the production of organic–inorganic fibers assisted by sol–gel chemistry is carried out by: (1) preparing the solution to be electrospun by mixing the molecular precursors with the polymer in the desired proportions in order to achieve the proper rheological properties to successfully electrospin fibers of uniform diameter; (2) electrospinning the solution; and (3), if needed, hydrothermally treating the obtained fibers. The above-described approach is also carried out for the fabrication of pure inorganic metal oxide fibers. In this particular case, after electrospinning, the fibers are calcined to completely remove the organic phase. A literature review of inorganic fibers produced by coupling electrospinning with the sol–gel process and organic phase calcinations is out of the scope of this chapter and has been previously summarized by other authors [132–134].

The hybrid electrospun fibers that are most widely fabricated by the sol–gel approach and described in the literature are based either on a silica or titania inorganic phase. The composition of the sol to be electrospun is commonly defined by following the established knowledge of sol–gel processes. First of all, it is well known that silicon alkoxide precursors are much less reactive than their titanium counterparts, due to the higher electronegative character of Si compared with Ti, which makes the former less susceptible to nucleophilic attack during hydrolysis. From a practical point of view, the remarkably different reactivity of Si and Ti alkoxide precursors entails the use of different formulations in the phase of sol preparation for electrospinning.

4.1 Preparation of SiO₂/Polymer Hybrid Fibers

When Si alkoxides are used, a stoichiometric amount of water and a catalyst are normally required to ensure the hydrolysis of Si(OR)₄ in Si(OH)₄ and high yield of SiO₂ in the final material. Acid catalysis results in fast hydrolysis and slow condensation, which leads to linear chain growth of the organic phase. In contrast, slower hydrolysis and faster polycondensation were observed in the case of base catalysis, leading to spherical colloidal particles.

Sol formulations prepared for electrospinning generally contain water and an acid catalyst [135–138]. Alcohol is sometimes added to the solution [135] because it improves the solubility between Si(OR)₄ and water. However, alcohol is a by-product of hydrolysis, thus its use is not strictly necessary to obtain good SiO₂ yields.

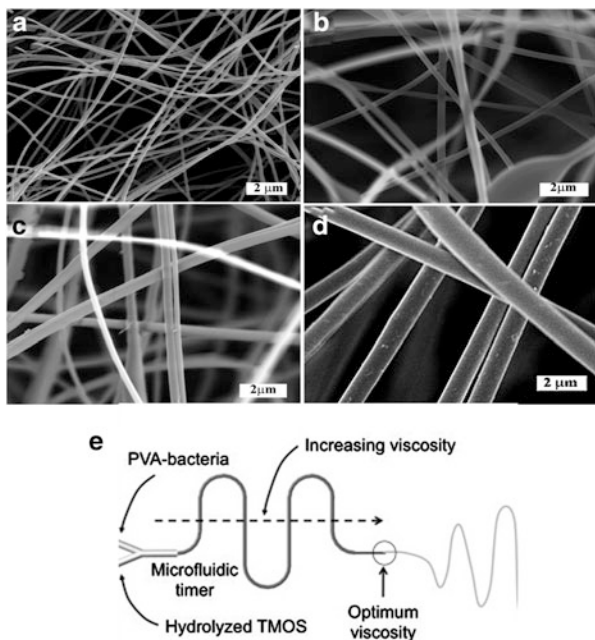
Given the slow reaction kinetics of silicon precursors, it is reasonable to hypothesize that sol aging time before electrospinning might have an effect on SiO₂ yield and on hybrid fiber morphology. This aspect was taken into account by Pirzada et al. [135], who prepared hybrid fibers of PVA and SiO₂ from TEOS sol aged for different times before electrospinning. Whether or not the PVA was present in the solution, they observed a progressive increase of viscosity over time, thus they investigated the effect of TEOS sol aging time rather than the temporal behavior of the mixed system (TEOS sol + PVA solution). Starting from an electrospun solution having the same TEOS:PVA ratio, the obtained fibers showed higher diameters with the increment of sol aging time (Fig. 14a–d). In addition, the obtained fibers had the same amount of inorganic phase, but the latter was characterized by the presence of an increment in the number of Si–O–Si bonds with increasing sol aging time since this factor has an influence on the progression of the condensation reaction.

By contrast, Tong et al. [139] observed a fast and progressive increase in viscosity when the Si precursor sol and PVA solution were mixed; they ascribed this behavior to the reaction of hydroxyl groups of PVA with silanol groups to generate covalent bonds between the inorganic and the organic phases. The changes in solution properties in such a system were solved by Tong et al. [139] by separating the TEOS sol and the PVA water solution in two different syringes and forcing the two solutions to mix for a controlled period of time before electrospinning through the use of a microfluidic timer (Fig. 14e). In this way the authors were able to maintain the optimum solution viscosity throughout the whole electrospinning process, thus achieving a controlled and continuous process.

The effect of aging time was also mentioned by Allo et al. [140], who qualitatively observed a continuous increment in solution viscosity during electrospinning of a sol containing TEOS and PCL, which highlighted the importance of finding the proper window of operation for spinnability.

The electrospinning of a reactive sol that changes its properties during time is a major problem when a reasonable amount of electrospun fibers must be produced. In addition, the factors that are known to influence the sol–gel process (such as

Fig. 14 Fibers spun from solutions containing the same amount of TEOS and PVA produced from solutions aged for different times: (a) 1 ($d_{\text{fiber}} = 150 \pm 30$ nm), (b) 2 ($d_{\text{fiber}} = 380 \pm 130$ nm), (c) 3 ($d_{\text{fiber}} = 470 \pm 130$ nm), and (d) 4 h ($d_{\text{fiber}} = 650 \pm 190$ nm). Reprinted with permission from [135]. Copyright (2012) American Chemical Society. (e) Formation of silica/PVA biocatalytic nanofibers using a microfluidic timer. Adapted with permission from [139]. Copyright (2013) Elsevier

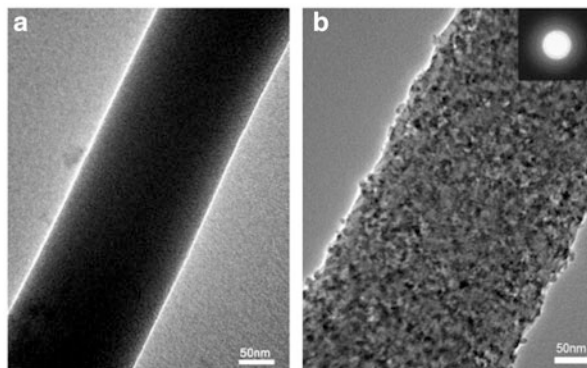


water-to-precursor ratio, type of catalyst, pH, temperature) have not yet been systematically taken into account in the context of electrospinning. Moreover, a systematic study that investigates the effect of these parameters on the morphology and distribution of the inorganic phase within the fibers as well as on SiO_2 yield and structure is still missing.

4.2 Preparation of TiO_2 /Polymer Hybrid Fibers

TiO_2 nanostructures are of primary interest for their established photocatalytic properties and their promising application in optoelectronic devices [141, 142]. Titanium alkoxide precursors, $\text{Ti}(\text{OR})_4$, are more reactive than $\text{Si}(\text{OR})_4$ and are quickly hydrolyzed by the traces of water present in the atmosphere and in the solvents. The reaction can be so fast that inhibitors are often necessary to prevent the uncontrolled precipitation of polydisperse TiO_2 nanopowders. Accordingly, titania-based hybrid electrospun fibers have been prepared by dissolving the precursor and the polymer in an organic solvent with the addition of inhibiting agents (e.g., acetic acid, acetylacetone, diethanolamine) that complex the Ti alkoxide, stabilizing its non-hydrolyzed form [143–147]. Obviously, the use of inhibitors to prevent the sudden and uncontrollable hydrolysis of Ti alkoxide is imperative when aqueous solvents are used for electrospinning [143–146]. However, inhibitors are

Fig. 15 Surface morphology of PET nanofibers containing TiO_2 precursors (a) before and (b) after hydrothermal treatment. *Inset*: selected-area electron diffraction pattern. Reprinted with permission from [148]. Copyright (2009) Elsevier



used also in the absence of water in the sol. In the latter cases, the formation of TiO_2 phase can be completed only by applying a subsequent hydrothermal treatment to the as-spun mats [147–149] (Fig. 15). Indeed, Su et al. [149] demonstrated that the mere electrospinning of a sol that contains Ti precursor, polymer, and inhibitor, without the presence of water, does not provide hybrid fibers. In their work, a subsequent hydrothermal treatment allowed the hydrolysis and condensation reactions to occur. They transformed the Ti precursor contained in as-spun fibers into TiO_2 nanoparticles clearly visible by TEM and exhibiting photocatalytic activity [149].

In the case of Ti precursor electrospinning, the need to understand the chemistry of the sol–gel process in order to control electrospinning process was discussed by Skotak and coworkers [144, 145]. They deeply analyzed a sol of Ti alkoxide, acetic acid, and PVP and monitored sol properties as a function of time. They investigated the effect of acetic acid and PVP concentration, type of Ti precursor, co-solvent addition, and type of chemical species on sol properties and stability in view of fabricating fibers with a controllable and reproducible diameter.

4.3 Preparation of ZnO/Polymer Hybrid Fibers

ZnO nanostructures have many applications in the field of gas sensors, photocatalysis, and optical devices [150, 151]. Given the high electropositivity of Zn, inhibiting agents are often used to avoid rapid precipitation of the metal hydroxides and allow stable solutions to be formed. ZnO can be obtained from several zinc precursors such as nitrate, chloride, and alkoxides, but the most often used is the acetate dihydrate [152]. The fabrication of 1D ZnO nanofibers by electrospinning followed by calcination of the organic phase is an established procedure [153–155]. Hybrid electrospun fibers have been produced starting from zinc acetate dihydrate [156, 157]. In the cited literature, ZnO particles embedded in polymeric fibers have been obtained by immersing the as-spun mat in a basic

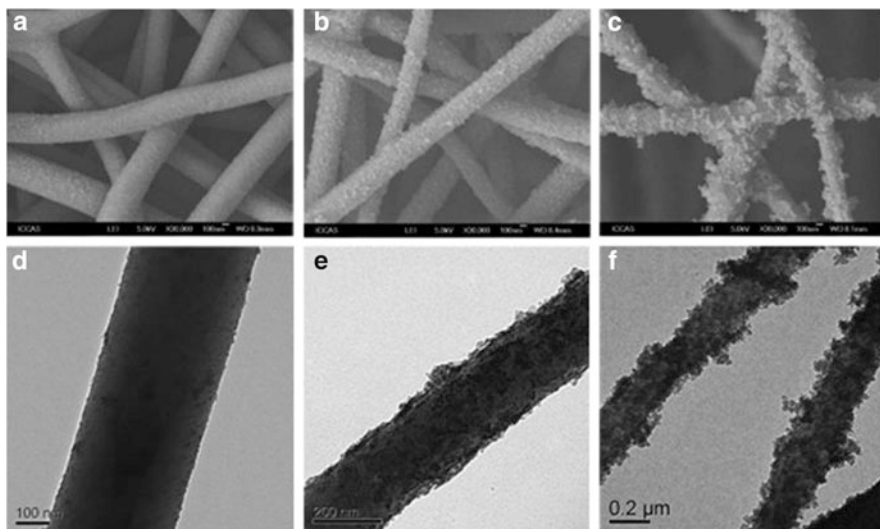


Fig. 16 (a–c) SEM images of ZnO/PET nanofibers from precursor nanofibers with different weight ratios of zinc acetate dihydrate to PET: (a) 1:7, (b) 3:7, and (c) 1:1. (d–f) Corresponding TEM images for a–c, respectively. Reprinted with permission from [158]. Copyright (2011) Wiley Interscience

solution at RT, which enabled the conversion of zinc acetate into ZnO [156–158]. In Fig. 16 it is shown that the final amount of ZnO in the fibers is strictly correlated to the zinc acetate concentration.

4.4 Properties and Applications of Hybrid Fibers from Electrospinning Combined with the Sol–Gel Process

In this kind of fiber, the inorganic phase is homogeneously dispersed in the organic phase and in intimate contact with it. The immediate advantage of this particular phase distribution is that the polymeric fiber can be loaded with high amounts of inorganic phase, avoiding issues of phase segregation and poor compatibility.

The nanometric distribution of the two phases has a direct effect on the polymer solid state, especially on the capability of chains to organize themselves in a regular crystal phase. Shao et al. [138] showed by DSC analysis and X-ray diffraction that the PVA crystal phase decreased with the increase of SiO₂ content in electrospun fibers (Fig. 17a). Similarly, a strong decrease in the enthalpy of fusion was observed in the DSC curve of PET fibers containing only 4 wt% of TiO₂ and it was found that PET crystallization was completely inhibited at higher TiO₂ content (Fig. 17b) [148]. In addition, the capability of PVDF and PCL to crystallize decreased through the addition of SiO₂ phase in the electrospun fibers [140, 159] (Fig. 17c).

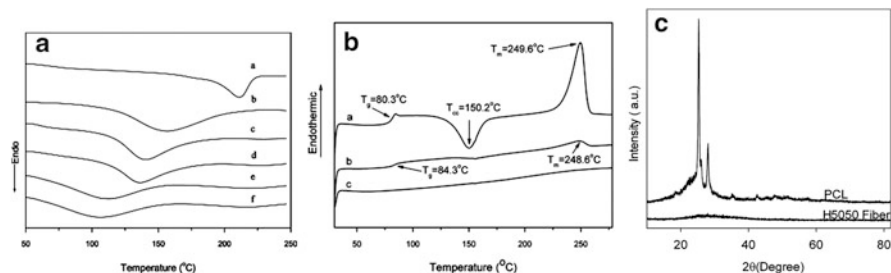


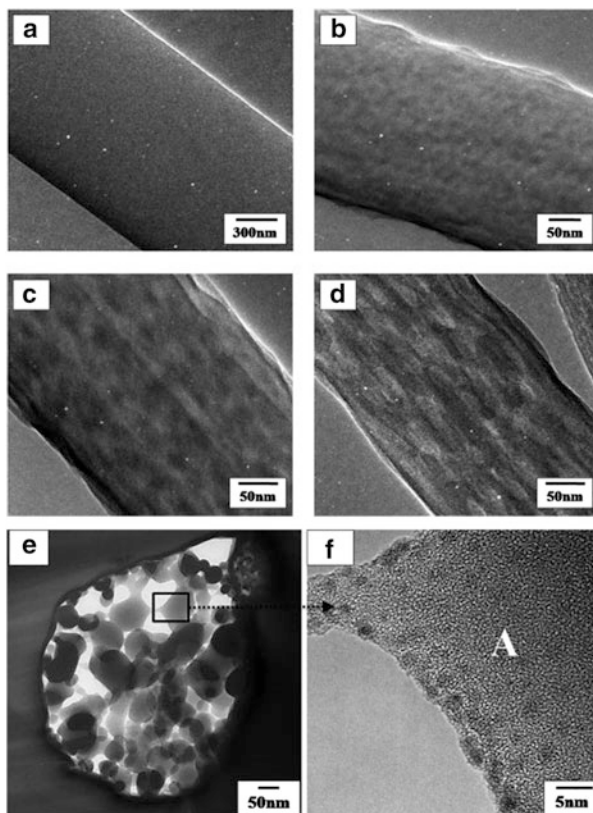
Fig. 17 (a) DSC curves of PVA/silica fibers with different SiO₂ content: (a) 0 (pure PVA), (b) 22, (c) 34, (d) 40, (e) 49, and (f) 59 wt% SiO₂. Reprinted with permission from [138]. Copyright (2003) Elsevier. (b) DSC curves of PET nanofibers containing (a) 0 (pure PET), (b) 4.0, and (c) 27.6 wt% TiO₂. Reprinted with permission from [148]. Copyright (2009) Elsevier. (c) X-ray diffraction pattern of pure PCL and PCL fibers containing 50 wt% of bioactive glass (*H5050 fiber*). Reprinted with permission from [140]. Copyright (2010) American Chemical Society.

The strong interaction between the organic and inorganic phases can also be exploited to increase the solvent resistance of the organic polymeric phase, particularly if this interaction is based on covalent bonds. This is the case for PVA that, when electrospun with a Si precursors, can participate in the condensation reaction with silanol groups. As a consequence, those chains covalently bonded with the inorganic phase are no longer soluble in water and the electrospun nonwoven material can maintain its fibrous morphology [135–138].

The advantages deriving from the intimate mixing of organic and inorganic phases at the nanoscale can be exploited for producing hybrid nanofibrous scaffolds for bone tissue engineering (Fig. 18). In this context, both natural [160–163] and synthetic biodegradable [137, 164] polymers have been used together with the SiO₂ phase and, in some cases, with the incorporation of calcium and phosphate ions to further enhance scaffold bioactivity [160, 162, 164]. When natural polymers (i.e., gelatin [160–162] and chitosan [163]) were used, the organic and inorganic phases were covalently linked (Class II hybrid materials) by means of organically modified Si alkoxide bearing an epoxy group. This group in acidic conditions can attack nucleophilic units in the polymer chains such as amines and carboxylic acids [161–163]. The presence of covalent bonds between the polymer chains and the SiO₂ phase limits polymer dissolution in water, thus preserving the scaffold fibrous structure [160, 162]. PCL was also used in combination with SiO₂ to generate hybrid materials of Class I with hydrogen bonds at the interface [137, 164]. In these cases, the introduction of the silica phase dramatically changed scaffold wettability by increasing fiber hydrophilicity (Fig. 19a) and improved scaffold mechanical properties by increasing elastic modulus and ultimate tensile strength (Fig. 19b).

The sol–gel approach coupled with dual-syringe reactive electrospinning was used by Poologasundarampillai et al. [165] to enrich PLLA–SiO₂ fibers with Ca²⁺ ions. To this aim they used a Ca alkoxide precursor. It is so reactive with water that, in order to avoid CaO precipitation, the authors used a modified electrospinning

Fig. 18 (a–d) TEM images of (a) pure poly(L-lactic acid) (PLLA) and its hybrid nanofibers with (b) 20, (c) 40, and (d) 60 wt% SiO₂ content. (e, f) Cross-sectional TEM images of the PLLA-40% SiO₂ xerogel electrospun nanofiber after heat treatment at 600°C for 3 h. Adapted with permission from [136]. Copyright (2012) Wiley Interscience



apparatus whereby the Ca precursor solution came in contact with the PLLA-Si sol immediately before the formation of the Taylor cone. Independently of the type of polymer of the organic phase, the introduction of homogeneously dispersed SiO₂ phase in the fibers was demonstrated to improve alkaline phosphatase activity and osteoblastic response [137, 160, 162–164], in vivo osteoconductivity [137], and scaffold bioactivity, especially when Ca⁺ ions were added to the starting electrospinning solution [162–164].

The sol–gel process combined with electrospinning was largely employed by the group of F. Li to produce functionalized hybrid nanofibers for the absorption of different chemical species from waste water [166–171]. The preparation procedure was always carried out using a porogen (such as CTAB) that created mesopores in the fibers with the aim of increasing membrane surface area for promoting substance absorption. Starting from TEOS, they prepared fibers with SiO₂ and PVA containing different chemical functionalities imparted by the addition of organically modified Si alkoxides to the sol. In particular, they used MPTMS to introduce mercapto groups for Cu²⁺ absorption [171], β -cyclodextrins for dye contaminants

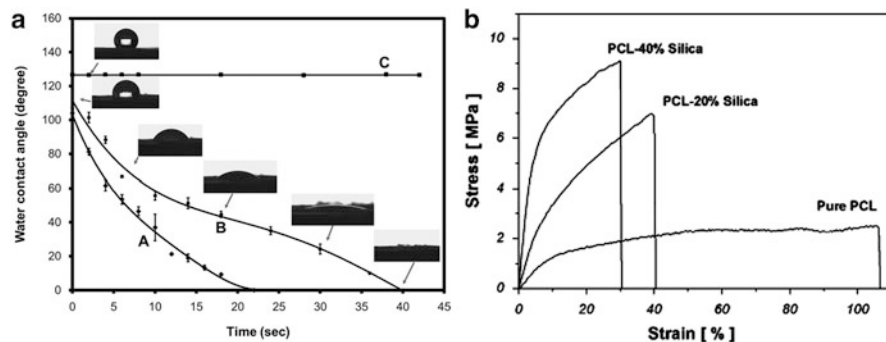


Fig. 19 (a) Water contact angle measurements as a function of time of (A) electrospun PCL/bioactive glass fibers with diameters of 260 ± 60 nm, (B) electrospun PCL/bioactive glass fibers with diameters of 600 ± 166 nm, and (C) electrospun PCL control scaffold. Reprinted with permission from [164]. Copyright (2013) American Chemical Society. (b) Representative stress–strain curves of PCL/SiO₂ electrospun membranes at different wt% compositions. Reprinted with permission from [137]. Copyright (2010) Elsevier

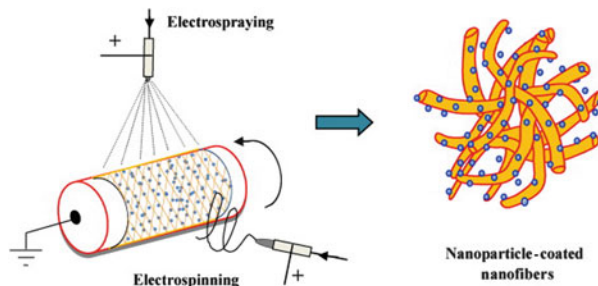
removal [170], and BTESPTS with thioether functional groups for Hg²⁺ absorption [169]. They also employed PAA to prepared hybrid nanofibers containing either mercapto groups [168] or vinyl groups [167] for absorption of dye contaminants. They demonstrated that membranes can be regenerated upon acidic treatment but, even if they used water-soluble polymers for membrane production (i.e., PVA and PAA), they did not take into account possible modifications of the nonwoven morphology upon water contact.

TiO₂-based fibers have been employed by exploiting the photocatalytic properties of TiO₂ for the production of antibacterial wound dressings [172] and of membranes capable of degrading toxic organic substances such as phenol [149]. Similarly, ZnO-based fibers were tested against the photodegradation of Rhodamine [157].

5 Electrospinning Combined with Electrospaying

The literature reports some examples of functional nanofiber mats prepared by simultaneously electrospinning a polymer solution and electrospaying a particle suspension on the same metallic collector. In electrospaying, when the electric force is higher than the surface tension of the liquid, the jets are atomized into fine droplets that are collected as solid particles. In electrospinning, the electric repulsion force cannot overcome the intermolecular forces in the liquid and, hence, the jet extends, bends and eventually reaches the collector, forming a solid fiber. The resulting nonwoven mat is composed of nanoparticles located on the fiber surface and within the pores of the nonwoven structure (Fig. 20).

Fig. 20 Electrospinning combined with electrospaying process. Reprinted with permission from [173]. Copyright (2013) Elsevier



The described methods of nanoparticle addition to the fibers (i.e., electrospinning of inorganic dispersions in polymer solutions, post-treatments, and sol-gel processes) determine in most cases an even distribution of the additive throughout the whole fiber section. This makes a fraction of particles ineffective when their function can be executed only in contact with the external environment. When nanoparticles are introduced into the nonwoven structure through electrospaying, they are completely and readily available for active reactions with the outside.

As a matter of fact, all the papers describing the combination of electrospinning and electrospaying techniques deal with the exploitation of hybrid specific surface properties.

Vitchuli et al. [174] used the combined technologies to prepare a multifunctional ZnO/nylon-6 nanofiber mat with antibacterial and detoxifying properties for use in protective applications. Nylon-6 polymer solution and a ZnO NP dispersion were loaded into two separate syringes and placed side-by-side on a two-syringe pump. In the resulting material, ZnO particles were attached to the nanofiber surface and were distributed throughout the entire mat.

Antibacterial properties have also been achieved in PLA electrospun nanofibers that were coated by TiO₂ particles using the electrospaying technique [173]. In this case, TiO₂ particles were synthesized in situ by hydrothermal treatment of the composite mat after electrospinning. In particular, a sol of a TiO₂ precursor was simultaneously electrospayed with a solution of PLA located in another syringe. The coated nanofibers were dried at 40°C and then hydrothermally treated at 120°C under 15 psi pressure in an autoclave for different times (30, 60, and 90 min). SEM micrographs of the hybrids show that hydrothermal treatment produced small globules of TiO₂ particles (in anatase and brookite crystalline phases), whose initial average size of 0.1–2 μm gradually decreased with increasing hydrothermal time.

Korina et al. [175] demonstrated that by combining electrospinning and electrospaying techniques and by appropriate selection of the dispersion stabilizing agent, the fabrication of hybrid materials with a desired surface design and bulk characteristics can be attained. The authors used Fe₃O₄ and TiO₂ NPs to prepare different nanostructures, using poly(3-hydroxybutyric acid) (PHB) as a matrix. TiO₂ was used for its photocatalytic properties while Fe₃O₄ was employed to impart magnetic properties to the mat. PHB, PHB/Fe₃O₄, and PHB/Fe₃O₄/TiO₂

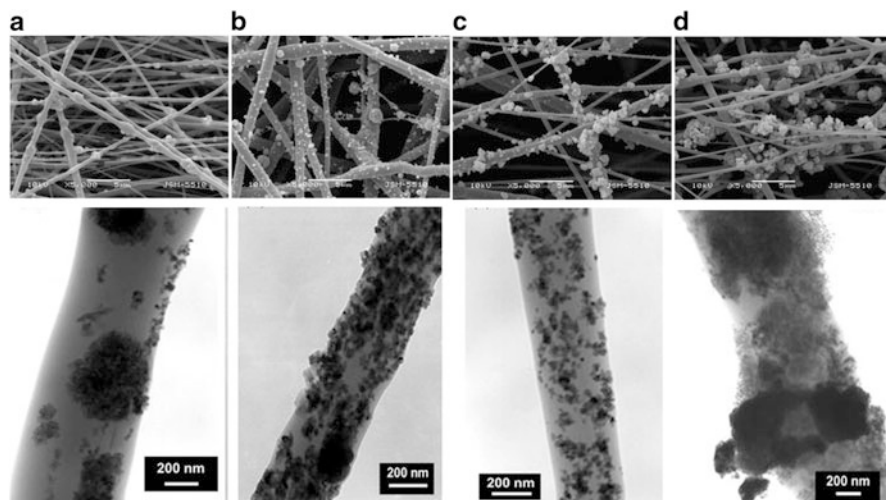


Fig. 21 SEM (top row) and TEM (bottom row) images of (a) $[\text{Fe}_3\text{O}_4/\text{TiO}_2\text{-in-PHB}]$, (b) $(\text{Fe}_3\text{O}_4/\text{chitosan})\text{-on-PHB}$, (c) $(\text{TiO}_2/\text{COS})\text{-on-}[\text{Fe}_3\text{O}_4\text{-in-PHB}]$, and (d) $(\text{Fe}_3\text{O}_4/\text{TiO}_2/\text{chitosan})\text{-on-PHB}$. Adapted with permission from [175]. Copyright (2014) Springer

suspensions were electrospun into fibers while $\text{Fe}_3\text{O}_4/\text{chitosan}$, TiO_2/COS , and $\text{Fe}_3\text{O}_4/\text{TiO}_2/\text{chitosan}$ suspensions were electrospayed into particles. The different combinations of electrospun and electrospayed suspensions produced different nonwoven materials where the NPs were located “on” the surface of the PHB fibers and/or “in” the bulk of the PHB fibers (Fig. 21).

The combination of electrospinning and electrospaying techniques also enables the preparation of materials with tunable wettability, from superhydrophobicity (static water contact angle $>150^\circ$) to hydrophilicity [176]. The obtained nanocomposite mats were comprised of hydrophobic PS nanofibers and hydrophilic TiO_2 nanoparticles, and the wetting properties were tuned by exposure to UV light. The mechanism behind the switching between superhydrophobicity to hydrophilicity is that UV light, reacting with TiO_2 , generated radicals, Ti^{3+} , and oxygen vacancies, which adsorbed water molecules at the defect sites, thus promoting mat hydrophilicity. The authors found that illumination time is the parameter that controls the gradual change of mat water contact angle from a maximum of 140° to a minimum of 26° .

For successful regeneration of damaged tissues, the simultaneous electrospaying of nano-HA on electrospun $\text{P(LA-co-CL)/gelatin}$ blend [177] and gelatin [178] was carried out to produce nanofibrous scaffolds for bone tissue regeneration. Blending of HA with polymers might reduce HA osteoinductivity because the HA particles are often completely embedded inside the polymer fiber. The deposition of HA nanoparticles on the surface of the fibers through electrospaying resulted in enhanced osteoconductive and osteoinductive effects on osteoblasts, thanks to the complete exposure of HA nanoparticles that easily interact with cells.

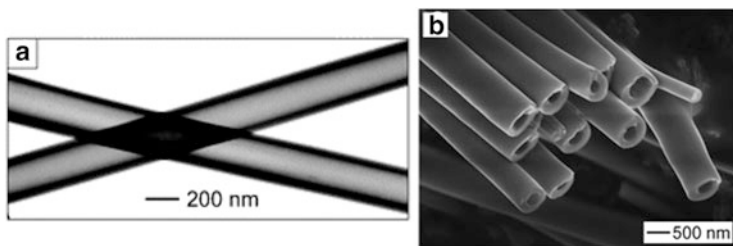


Fig. 22 (a) TEM and (b) SEM images of as-spun hollow fibers after the oily cores had been extracted with octane. The walls of these tubes were made of a composite containing amorphous TiO_2 and PVP. Adapted with permission from [180]. Copyright (2004) American Chemical Society

6 Coaxial Electrospinning

The basic spinneret for coaxial electrospinning is made by inserting an inner needle or capillary into a concentric outer needle. The internal needle is connected to the core fluid reservoir, while the outer needle is attached to the shell fluid one. The technique for generating coaxial jets of immiscible liquids using electrospinning was first developed by Loscertales et al. [179] in 2002. The authors demonstrated that, when a proper electrical potential and flow rate were used, a steady Taylor cone of the compound was formed at the exit of the spinneret, from which a liquid thread was generated. The varicose breakup of the generated compound jet produced monodisperse compound droplets with the outer liquid surrounding the inner one and diameters below the micrometer range.

In a subsequent paper, Larsen et al. [131] reported the combined use of sol-gel chemistry with coaxial electrospinning to produce vesicles and fibers made of inorganic oxides and hybrid (organic/inorganic) materials with diameters in the micrometer and submicrometer ranges. In 2004, Li et al. [180] used sol-gel electrospinning to produce a shell hybrid material made of PVP and TiO_2 , while the core material was mineral oil. The complete immiscibility of core and shell solutions enabled the formation of a regular core-shell structure along the fibers. The extraction of mineral oil by immersion in octane led to hollow hybrid fibers potentially useful as nanofluidic channels (Fig. 22).

Another group that exploited the combination of sol-gel and coaxial electrospinning was that of Yong L. Joo [181, 182]. The authors prepared a thermal resistant shell of silica by using TEOS as precursor that encapsulated a block copolymer, i.e., poly(styrene-*b*-isoprene), in the core of the fiber. They demonstrated that regular morphologies of nanometric dimensions could be created in the internal part of the fiber thanks to block copolymer self-assembly, depending on annealing conditions. Therefore, the thermally resistant shell enabled thermal annealing to the fiber core without compromising the fiber morphology [181] (Fig. 23a-d).

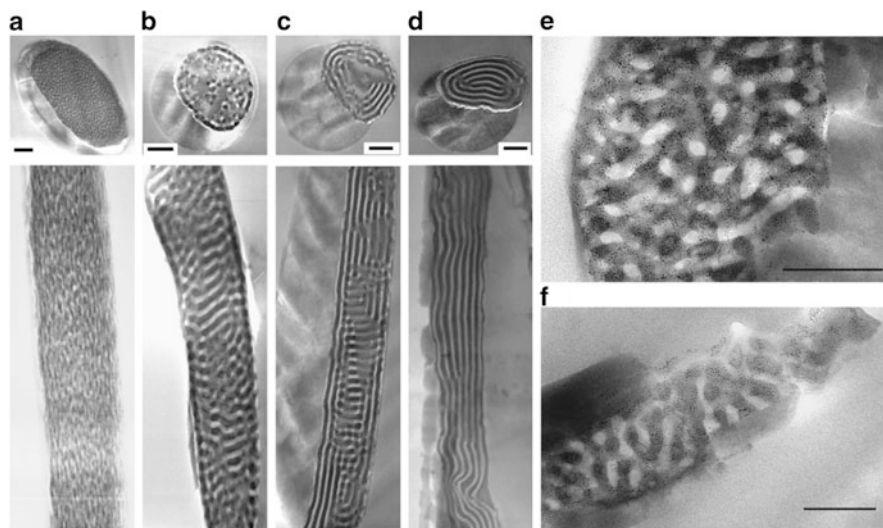


Fig. 23 (a–d) TEM images of poly(styrene-*b*-isoprene)/SiO₂ core-shell fibers: (a) as-spun fiber; (b) stacked polystyrene lamellar structure after annealing at 125°C for 24 h; (c) transition to alternating concentric-cylinder morphology after annealing at 175°C for 24 h; and (d) parallel morphology on annealing at 175°C for 50 h. The *top row* shows the cross-sections normal to the fiber axes, and the *bottom row* shows the cross-sections parallel to the fiber axes. Reprinted with permission from [181]. Copyright (2006) Wiley Interscience. (e, f) TEM images of poly(styrene-*b*-isoprene)/SiO₂ fibers with 10 wt% magnetite annealed at 175°C for 50 h: (e) cross-sectional cut of fiber and (f) fiber cut along the axis. *Grey shell region* is silica; in the core, *light regions* are polystyrene domains, *dark regions* are stained polyimide domains, and even *darker dots* are magnetite NPs. All *scale bars* are 200 nm. Reprinted with permission from [182]. Copyright (2008) Wiley Interscience

In a subsequent paper [182], the authors added to the polymeric core solution magnetite NPs that were surface-coated with oleyl groups. By applying thermal annealing, they were able to achieve a hierarchical spatial distribution of NPs that spontaneously migrated in the fiber nanodomains occupied by isoprene blocks (Fig. 23e, f).

Many papers dealing with the production of composite fibers by coaxial electrospinning describe the incorporation of nanoparticles in the core of the fiber with the aim of producing 1D nanoarrays with potential applications, mainly in magnetic nanodevices. In 2002, Song et al. [183] were able to encapsulate FePt NPs in a shell of PCL. TEM images demonstrated that they obtained discrete arrays of NPs that were as long as 3,000 nm along the fiber axis. Similarly, ferritin NPs were encapsulated in a shell of a polyelectrolyte polymer and generated uniform and continuous tubular core-shell nanostructures [184]. The authors were able to control the core diameter, and thus the width of a 1D array of ferritin, and achieved a nearly linear chain of individual ferritin particles encapsulated in a nanofiber of 40 nm diameter (Fig. 24).

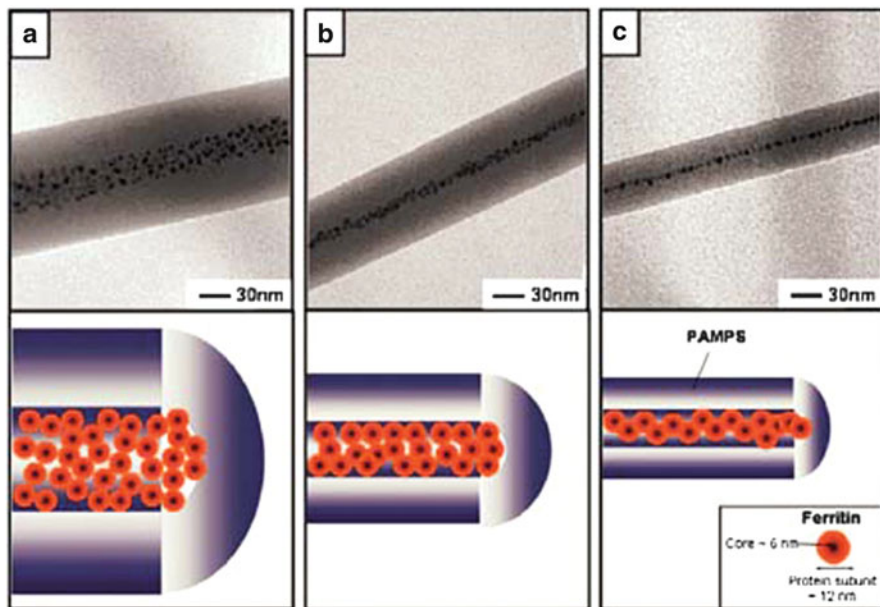


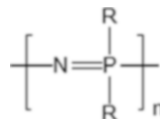
Fig. 24 (a–c) TEM images (*top row*) of different width ferritin 1D arrays in polyelectrolyte tubular nanostructures, formed by adjusting the concentration of the polymer solution. The illustrations (*bottom row*) indicate the different widths of the ferritin 1D arrays and polymer tubular nanostructures. Reprinted with permission from [184]. Copyright (2008) Wiley Interscience

The dependence of magnetic properties on fiber alignment was reported by Sharma et al. [185]. They prepared coaxial fibers of PEO incorporating Fe_2O_3 NPs that exhibited perpendicular magnetic anisotropy when collected as parallel fibers.

Sung et al. [186] incorporated Fe_2O_3 in a PET shell by using a ferrofluid colloidal suspension of NPs. The NPs were coated with an organic material to limit their agglomeration and the mobility of the NPs in the fluid was improved by adding mineral oil. The core–shell morphology depended on the mineral oil content in the core solution and on the relative solution feeds. The obtained fibers exhibited superparamagnetic behavior at RT. The authors also found an improvement in fiber mechanical properties in the presence of a magnetic field that was ascribed to strong dipole–dipole interactions between the magnetic NPs that easily aligned thanks to their high mobility in the core fluid.

Medina-Castillo et al. [187] fabricated a new multifunctional nonwoven mat made of tri-functional core–shell fibers prepared by coaxial electrospinning. A fluorescent pH-sensitive copolymer was used for the shell while the core contained magnetic NPs and a lipophilic indicator dye. Therefore, the fibers were magnetic, sensitive to O_2 , and able to change their optical properties upon pH change, thus enabling the optical monitoring of pH and O_2 in situ and in real time.

Fig. 25 General structure of polyphosphazenes



Multifunctional fibers were also prepared by Ma et al. [188] that incorporated magnetic Fe_2O_3 NPs in the core of PVP fibers and a photoluminescent europium complex in the shell.

In some cases, the NPs have been dispersed in the shell solution. This was the case for TiO_2 NPs [189] and silver NPs [190]. Here, the NPs were intentionally located in the shell of the fibers (i.e., very close to the fiber surface) to strengthen the effect that their photocatalytic and antimicrobial properties have on the fibers when they are positioned directly in contact with either the organic compound to be degraded or the bacteria.

7 Hybrid Polymers

The last section of this review is dedicated to the preparation of hybrid fibers made up of organic–inorganic polymers. In this case, the resulting fibers do not have two distinguishable organic and inorganic phases because the starting molecular chains contain both organic and inorganic atoms.

A relatively new family of hybrid organic–inorganic polymers consists of polyphosphazenes, which were first synthesized and developed by Allcock's group [191]. These hybrid polymers contain an inorganic backbone, made up of alternating phosphorus and nitrogen atoms, and organic or organometallic side groups attached to each phosphorous atom (Fig. 25). Therefore, polyphosphazenes have a very large number of possible chemical structures (depending on the nature of the side groups) and skeletal architectures (linear, branched, star, dendrimer, block copolymer, etc).

The presence of the phosphorus–nitrogen backbone confers to these kind of polymers thermo-oxidative stability, fire resistance, very high torsional mobility (low barrier to skeletal bond twisting), high refractive index, and hydrophilicity. On the other hand, the side groups in polyphosphazenes control other properties such as solubility, secondary reaction chemistry, thermal decomposition, and resistance to hydrolysis. The possibility of tuning the properties of polyphosphazenes thanks to their synthetic flexibility has led to enormous interest in their applications in several areas of research.

This class of polymer was first electrospun by Nair et al. [192] who evaluated the effect of process parameters such as the nature of the solvent, concentration of the polymer solution, effect of needle diameter, and applied potential on the diameter and morphology of poly[bis(*p*-methylphenoxy)phosphazene] fibers. A poly[(amino acid ester)phosphazene] has been electrospun in blend with gelatin [193] to

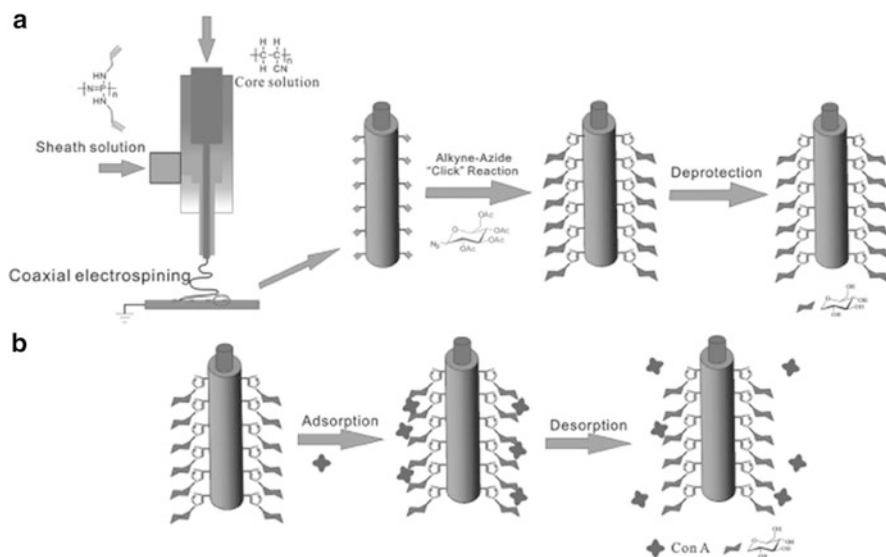


Fig. 27 (a) Preparation of a glycosylated polyphosphazene nanofibrous membrane via coaxial electrospinning and (b) its application in protein recognition. Reprinted with permission from [196]. Copyright (2013) Wiley Interscience

electrospinning of a highly fluorinated phosphazene generated nonwoven mats with high surface hydrophobicity, up to superhydrophobicity, depending on fiber diameter and morphology [197]. The advantage of using a fluorinated phosphazene, rather than, for example, poly(tetrafluoroethylene), is related to the solubility of polyphosphazenes in common organic solvents such as tetrahydrofuran, acetone, or methylethylketone.

Xu et al. [198] used a novel organic–inorganic hybrid copolymer, poly[styrene-co-3-(trimethoxysilyl) propyl-methacrylate], synthesized by free-radical copolymerization, to prepare nanofibrous membranes by the electrospinning technique. In order to obtain a crosslinked system, the as-prepared fibers were immersed in HCl aqueous solution for 3 days. The purpose was so that the methoxysilyl groups could be hydrolyzed to silanol groups and then condensed into crosslinkable polysilsesquioxanes. The prepared membranes showed a high resistance to different temperatures and typical solvents. Therefore, these hybrid mats can be used for applications involving surface chemistry, drug delivery, and multifunctional textiles. Schramm et al. [199] reported the preparation of PI nanofibers starting from TESPSA, APTES, and PAA, according to Fig. 28. The first step consisted in the hydrolysis of TESPSA. The subsequent addition of APTES resulted in the formation of a viscous solution of PAA, which could be subjected to an electrospinning process. The water-soluble fibers were then treated thermally at 110°C and at 220°C to form water-insoluble organic–inorganic polymeric fibers.

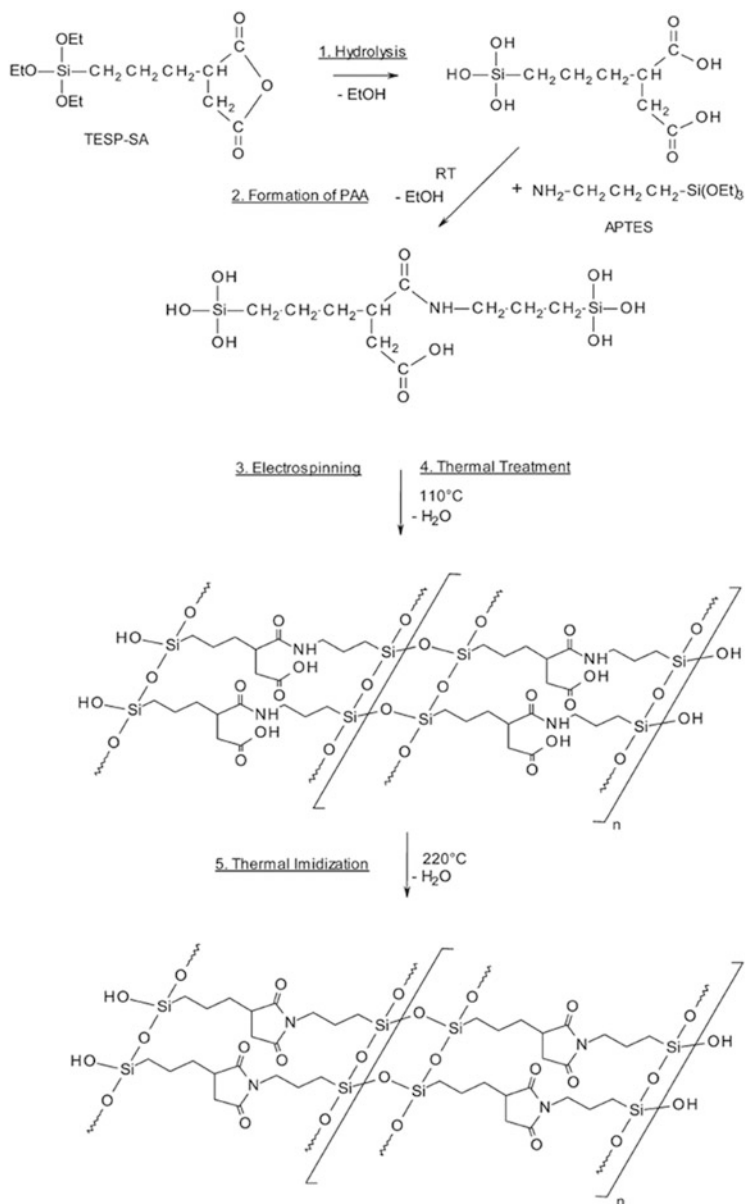


Fig. 28 Production of hybrid polyimide polymers. Reprinted with permission from [199]. Copyright (2013) Wiley Interscience

8 Conclusions

In this review we have attempted to classify and highlight the recent progress as well as current issues in hybrid organic–inorganic nanomaterials obtained by electrospinning. The literature papers were classified by taking into consideration the different methods for producing the electrospun nanohybrid materials with controlled structure and specific functionalities, and potential applications were evaluated. In particular, as illustrated in Fig. 1, the following main methodologies were described: (1) inorganic dispersion in polymer solution; (2) post-treatment of electrospun fibers; (3) electrospinning combined with the sol–gel process; (4) electrospinning combined with electrospraying; (5) coaxial electrospinning; and (6) formation of hybrid polymers. We have shown that the electrospinning technique, in combination with additional synthetic and processing procedures, is a suitable preparative method for combining inorganic nanocomponents into polymeric nanofibers, mainly thanks to its versatility. In particular, by means of the different synthetic and preparative methodologies described in this review, nanocomposite fibers with different levels of phase dispersion and homogeneity can be fabricated.

The electrospinning of inorganic dispersions in polymer solutions gives the possibility to incorporate in the fibers inorganic nanoparticles, nanorods, or quantum dots that maintain their morphology during the electrospinning process and, most importantly, that preserve their original functionalities in the final fibrous mats. Thus, in most cases, the unique inorganic material properties are transferred to the polymer nanofibrous substrate.

Another key aspect is related to the assembly of these inorganic nanostructures during the electrospinning process to generate ordered and controlled arrangements. This is a crucial step in the integration of nanocomponents within functional devices, and it is particularly interesting when anisotropic nanostructures such as nanorods and nanowires are used. 1D arrangements of inorganic nanocomponents within submicrometer polymer fibers can thus be obtained.

It is notable that 1D arrays of nanoparticles is still a great challenge for materials scientists. In this context, coaxial electrospinning is extremely effective and successful in achieving confined arrays of either nanoparticles or nanorods in the inner core of the nanofibers. The organic and inorganic phases are intentionally not mixed; instead, they must be well separated to display a distinct core–shell morphology.

Electrospinning has been combined with electrospraying in the production of nonwoven mats for those applications that require the presence of the functional nanocomponent at the surface of the fiber, and thus directly in contact with the external environment. Indeed, this methodology enables the nanoparticles to be placed only at the fiber surface, avoiding incorporation of the nanocomponent in the bulk of the fibers where it is masked by the surrounding organic phase.

A practical advantage of the use of electrospun substrates is represented by their high surface area and very high porosity and by the fact that the obtained nanofiber

mats are, in the majority of cases, flexible and easy to handle and can be incorporated in functional devices. These aspects are particularly important when the formation of the hybrid fiber is the result of post-treatments applied to the nonwoven mat. Generally the electrospun mats display mechanical properties that are good enough to resist the experimental conditions applied during the post-treatments, preserving their morphology and structure. Some examples are the high temperatures and pressures applied during the hydrothermal synthesis of the inorganic phase, the high vacuum required for the ALD process, and the numerous dipping and washing steps applied to achieve LbL assemblies.

Besides being a powerful technology for encapsulating nano-objects, either in the bulk or at the surface of polymeric fibers, electrospinning is even more interesting because it enables the production of hybrid nanofibers by means of the sol-gel process. The combination of electrospinning with sol-gel approaches is the obvious consequence of the fact that both processes are carried out in solution. Of course, the electrospinning of a reactive sol that changes its properties over time presents several issues that complicate the process and make control over final fiber morphology and structure difficult. However, the great benefit of this methodology is the possibility of producing hybrid nanofibers in which the organic and inorganic phases are mixed at a more intimate level than for composite nanofibers obtained by the other discussed methodologies.

Finally, electrospinning enables the production of fibers made of hybrid polymers, i.e., polymers that contain in the macromolecular chain both organic backbones and inorganic atoms (e.g., Si, P, Ti). In such fibers, the organic and inorganic phases are not separated or distinguishable and thus the maximum level of inorganic and organic combination is reached. The possibility of tuning the properties of these polymers thanks to their synthetic flexibility has led to enormous interest in their application in several areas of research.

The huge number of different fiber morphologies, structures, and properties that can be achieved by electrospinning is impressive. The power of this technology is even more evident if we take into account the fact that innovative hybrid nanofibers can be fabricated with a simple, versatile, extremely cheap, and scalable technology that makes electrospinning the most interesting currently available technique for the production of nanocomposites.

References

1. Crespy D, Friedemann K, Popa AM (2012) Colloid-electrospinning: fabrication of multicompartment nanofibers by the electrospinning of organic or/and inorganic dispersions and emulsions. *Macromol Rapid Commun* 33:1978–1995
2. Agarwal S, Greiner A, Wendorff JH (2013) Functional materials by electrospinning of polymers. *Progr Polym Sci* 38:963–991
3. Ramakrishna S, Fujihara K, Teo W-E, Lim T, Ma Z (2005) An introduction to electrospinning and nanofibers. World Scientific, Singapore

4. Zucchelli A, Focarete ML, Gualandi C, Ramakrishna S (2010) Electrospun nanofibers for enhancing structural performance of composite materials. *Polym Adv Technol* 22:339–349
5. Bianco A, Bozzo BM, Del Gaudio C, Cacciotti I, Armentano I, Dottori M, D'Angelo F, Martini S, Orlacchio A, Kenny JM (2011) Poly (L-lactic acid)/calcium-deficient nanohydroxyapatite electrospun mats for bone marrow stem cell cultures. *J Bioactive Compatible Polym* 26:225–241
6. Lu X, Liu X, Wang L, Zhang W, Wang C (2006) Fabrication of luminescent hybrid fibres based on the encapsulation of polyoxometalate into polymer matrices. *Nanotechnology* 17:3048–3053
7. Li Z, Huang H, Wang C (2006) Electrostatic forces induce poly(vinyl alcohol)-protected copper nanoparticles to form copper/poly(vinyl alcohol) nanocables via electrospinning. *Macromol Rapid Commun* 27:152–155
8. Li M, Zhang J, Zhang H, Liu Y, Wang C, Xu X, Tang Y, Yang B (2007) Electrospinning: a facile method to disperse fluorescent quantum dots in nanofibers without forster resonance energy transfer. *Adv Funct Mater* 17:3650–3656
9. Cho D, Bae WJ, Joo YL, Ober CK, Frey MW (2011) Properties of PVA/HfO₂ hybrid electrospun fibers and calcined inorganic HfO₂ fibers. *J Phys Chem C* 115:5535–5544
10. He D, Hu B, Yao QF, Wang K, Yu SH (2009) Large-scale synthesis of flexible free-standing sers substrates with high sensitivity: electrospun PVA nanofibers embedded with controlled alignment of silver nanoparticles. *ACS Nano* 3:3993–4002
11. Zhang CL, Lv KP, Cong HP, Yu SH (2012) Controlled assemblies of gold nanorods in PVA nanofiber matrix as flexible free-standing SERS substrates by electrospinning. *Small* 8:648–653
12. Cheng M, Wang H, Zhang Z, Li N, Fang X, Xu S (2014) Gold nanorod-embedded electrospun fibrous membrane as a photothermal therapy platform. *ACS Appl Mater Interfaces* 6:1569–1575
13. Wang Y, Li Y, Sun G, Zhang G, Liu H, Du J, Yang S, Bai J, Yang Q (2007) Fabrication of Au/PVP nanofiber composites by electrospinning. *J Appl Polym Sci* 105:3618–3622
14. Kriha O, Becker M, Lehmann M, Kriha D, Kriegelstein J, Yosef M, Schlecht S, Wehrspohn RB, Wendorff JH, Greiner A (2007) Connection of hippocampal neurons by magnetically controlled movement of short electrospun polymer fibers – a route to magnetic micromanipulators. *Adv Mater* 19:2483–2485
15. Wang N, Si Y, Wang N, Sun G, El-Newehy M, Al-Deyab SS, Ding B (2014) Multilevel structured polyacrylonitrile/silica nanofibrous membranes for high-performance air filtration. *Separation Purification Technol* 126:44–51
16. Kim YJ, Ahn CH, Lee MB, Choi MS (2011) Characteristics of electrospun PVDF/SiO₂ composite nanofiber membranes as polymer electrolyte. *Mater Chem Phys* 127:137–142
17. Hsu CY, Liu YL (2010) Rhodamine B-anchored silica nanoparticles displaying white-light photoluminescence and their uses in preparations of photoluminescent polymeric films and nanofibers. *J Colloid Interface Sci* 350:75–82
18. Jin Y, Yang D, Kang D, Jiang X (2009) Fabrication of necklace-like structures via electrospinning. *Langmuir* 26:1186–1190
19. Wan H, Wang N, Yang J, Si Y, Chen K, Ding B, Sun G, El-Newehy M, Al-Deyab SS, Yu J (2014) Hierarchically structured polysulfone/titania fibrous membranes with enhanced air filtration performance. *J Colloid Interface Sci* 417:18–26
20. Cui WW, Tang DY, Gong ZL (2013) Electrospun poly(vinylidene fluoride)/poly(methyl methacrylate) grafted TiO₂ composite nanofibrous membrane as polymer electrolyte for lithium-ion batteries. *J Power Sources* 223:206–213
21. Gupta KK, Kundan A, Mishra PK, Srivastava P, Mohanty S, Singh NK, Mishra A, Maiti P (2012) Polycaprolactone composites with TiO₂ for potential nanobiomaterials: tunable properties using different phases. *Phys Chem Chem Phys* 14:12844–12853
22. Ahmadpoor P, Nateri AS, Motaghtalab V (2013) The optical properties of PVA/TiO₂ composite nanofibers. *J Appl Polym Sci* 130:78–85

23. Xin Y, Huang ZH, Peng L, Wang DJ (2009) Photoelectric performance of poly(*p*-phenylene vinylene)/Fe₃O₄ nanofiber array. *J Appl Phys* 105:086106
24. Tan ST, Wendorff JH, Pietzonka C, Jia ZH, Wang GQ (2005) Biocompatible and biodegradable polymer nanofibers displaying superparamagnetic properties. *ChemPhysChem* 6:1461–1465
25. Gupta P, Asmatulu R, Claus R, Wilkes G (2006) Superparamagnetic flexible substrates based on submicron electrospun Estane[®] fibers containing MnZnFe-Ni nanoparticles. *J Appl Polym Sci* 100:4935–4942
26. Andrew JS, Clarke DR (2008) Enhanced ferroelectric phase content of polyvinylidene difluoride fibers with the addition of magnetic nanoparticles. *Langmuir* 24:8435–8438
27. Sui X, Shao C, Liu Y (2007) Photoluminescence of polyethylene oxide-ZnO composite electrospun fibers. *Polymer* 48:1459–1463
28. Sui XM, Shao CL, Liu YC (2005) White-light emission of polyvinyl alcohol/ZnO hybrid nanofibers prepared by electrospinning. *Appl Phys Lett* 87:113115
29. Lee S (2009) Multifunctionality of layered fabric systems based on electrospun polyurethane/zinc oxide nanocomposite fibers. *J Appl Polym Sci* 114:3652–3658
30. Modisha P, Nyokong T (2014) Fabrication of phthalocyanine-magnetic nanoparticles hybrid nanofibers for degradation of Orange-G. *J Mol Catal A Chem* 381:132–137
31. Tombe S, Antunes E, Nyokong T (2013) Electrospun fibers functionalized with phthalocyanine-gold nanoparticle conjugates for photocatalytic applications. *J Mol Catal A Chem* 371:125–134
32. Sundarajan S, Ramakrishna S (2007) Fabrication of nanocomposite membranes from nanofibers and nanoparticles for protection against chemical warfare stimulants. *J Mater Sci* 42:8400–8407
33. Lee YS, Jeong YB, Kim DW (2010) Cycling performance of lithium-ion batteries assembled with a hybrid composite membrane prepared by an electrospinning method. *J Power Sources* 195:6197–6201
34. Padmaraj O, Nageswara Rao B, Jena P, Venkateswarlu M, Satyanarayana N (2014) Electrochemical studies of electrospun organic/inorganic hybrid nanocomposite fibrous polymer electrolyte for lithium battery. *Polymer* 55:1136–1142
35. Im JS, Bai BC, Bae TS, In SJ, Lee YS (2011) Improved anti-oxidation properties of electrospun polyurethane nanofibers achieved by oxyfluorinated multi-walled carbon nanotubes and aluminum hydroxide. *Mater Chem Phys* 126:685–692
36. Li S, Li Y, Qian K, Ji S, Luo H, Gao Y, Jin P (2013) Functional fiber mats with tunable diffuse reflectance composed of electrospun VO₂/PVP composite fibers. *ACS Appl Mater Interfaces* 6:9–13
37. Chinnappan A, Kang HC, Kim H (2011) Preparation of PVDF nanofiber composites for hydrogen generation from sodium borohydride. *Energy* 36:755–759
38. Abiona AA, Ajao JA, Chigome S, Kana JB, Osinkolu GA, Maaza M (2010) Synthesis and characterization of cobalt chloride/poly(ethylene oxide) electrospun hybrid nanofibers. *J Sol Gel Sci Technol* 55:235–241
39. Unnithan AR, Barakat NAM, Abadir MF, Yousef A, Kim HY (2012) Novel CdPdS/PVAc core-shell nanofibers as an effective photocatalyst for organic pollutants degradation. *J Mol Catal A Chem* 363–364:186–194
40. Wang Q, Chen Y, Liu R, Liu H, Li Z (2012) Fabrication and characterization of electrospun CdS-OH/polyacrylonitrile hybrid nanofibers. *Compos Part A Appl Sci Manuf* 43:1869–1876
41. Dhandayuthapani B, Poulouse AC, Nagaoka Y, Hasumura T, Yoshida Y, Maekawa T, Kumar DS (2012) Biomimetic smart nanocomposite: in vitro biological evaluation of zein electrospun fluorescent nanofiber encapsulated CdS quantum dots. *Biofabrication* 4:025008
42. Bashouti M, Salalha W, Brumer M, Zussman E, Lifshitz E (2006) Alignment of colloidal cds nanowires embedded in polymer nanofibers by electrospinning. *ChemPhysChem* 7:102–106
43. Mthethwa TP, Moloto MJ, De Vries A, Matabola KP (2011) Properties of electrospun CdS and CdSe filled poly(methyl methacrylate) (PMMA) nanofibres. *Mater Res Bull* 46:569–575

44. Atabey E, Wei S, Zhang X, Gu H, Yan X, Huang Y, Shao L, He Q, Zhu J, Sun L, Kucknoor AS, Wang A, Guo Z (2013) Fluorescent electrospun polyvinyl alcohol/CdSe@ZnS nanocomposite fibers. *J Compos Mater* 47:3175–3185
45. Cho K, Kim M, Choi J, Kim K, Kim S (2010) Synthesis and characterization of electrospun polymer nanofibers incorporated with CdTe nanoparticles. *Synthetic Met* 160:888–891
46. Wang S, Sun Z, Yan E, Sun L, Huang N, Zang W, Ni L, Wang Q, Gao Y (2014) Spectrum-control of poly(*p*-phenylene vinylene) nanofibers fabricated by electrospinning with highly photoluminescent ZnS quantum dots. *Int J Electrochem Sci* 9:549–561
47. Schlecht S, Tan S, Yosef M, Dersch R, Wendorff JH, Jia Z, Schaper A (2005) Toward linear arrays of quantum dots via polymer nanofibers and nanorods. *Chem Mater* 17:809–814
48. Li M, Zhang Z, Cao T, Sun Y, Liang P, Shao C, Liu Y (2012) Electrospinning preparation and photoluminescence properties of poly(methyl methacrylate)/Eu³⁺ ions composite nanofibers and nanoribbons. *Mater Res Bull* 47:321–327
49. Tang S, Shao C, Liu Y, Mu R (2010) Electrospun nanofibers of poly(acrylonitrile)/Eu³⁺ and their photoluminescence properties. *J Phys Chem Solids* 71:273–278
50. Wang H, Yang Q, Sun L, Zhang C, Li Y, Wang S, Li Y (2009) Improved photoluminescence properties of europium complex/polyacrylonitrile composite fibers prepared by electrospinning. *J Alloys Comp* 488:414–419
51. Liu L, Li B, Zhang J, Qin R, Zhao H, Ren X (2009) Electrospinning preparation and characterization of a new kind of composite nanomaterials: one-dimensional composite nanofibers doped with TiO₂ nanoparticles and Ru(II) complex. *Mater Res Bull* 44:2081–2086
52. Wang H, Li Y, Sun L, Li Y, Wang W, Wang S, Xu S, Yang Q (2010) Electrospun novel bifunctional magnetic-photoluminescent nanofibers based on Fe₂O₃ nanoparticles and europium complex. *J Colloid Interface Sci* 350:396–401
53. Zhang H, Song H, Yu H, Bai X, Li S, Pan G, Dai Q, Wang T, Li W, Lu S, Ren X, Zhao H (2007) Electrospinning preparation and photoluminescence properties of rare-earth complex/polymer composite fibers. *J Phys Chem C* 111:6524–6527
54. Hong JH, Jeong EH, Lee HS, Baik DH, Seo SW, Youk JH (2005) Electrospinning of polyurethane/organically modified montmorillonite nanocomposites. *J Polym Sci B Polym Phys* 43:3171–3177
55. Marras SI, Kladi KP, Tsivintzelis I, Zuburtikudis I, Panayiotou C (2008) Biodegradable polymer nanocomposites: the role of nanoclays on the thermomechanical characteristics and the electrospun fibrous structure. *Acta Biomaterialia* 4:756–765
56. Park J, Lee H, Chae D, Oh W, Yun J, Deng Y, Yeum J (2009) Electrospinning and characterization of poly(vinyl alcohol)/chitosan oligosaccharide/clay nanocomposite nanofibers in aqueous solutions. *Colloid Polym Sci* 287:943–950
57. Wang S, Zheng F, Huang Y, Fang Y, Shen M, Zhu M, Shi X (2012) Encapsulation of amoxicillin within laponite-doped poly(lactic-co-glycolic acid) nanofibers: preparation, characterization, and antibacterial activity. *ACS Appl Mater Interfaces* 4:6393–6401
58. Deng XL, Sui G, Zhao ML, Chen CQ, Yang XP (2007) Poly(L-lactic acid)/hydroxyapatite hybrid nanofibrous scaffolds prepared by electrospinning. *J Biomater Sci Polym Ed* 18:117–130
59. Jeong SI, Ko EK, Yum J, Jung CH, Lee YM, Shin H (2008) Nanofibrous poly(lactic acid)/hydroxyapatite composite scaffolds for guided tissue regeneration. *Macromol Biosci* 8:328–338
60. Sui G, Yang X, Mei F, Hu X, Chen G, Deng X, Ryu S (2007) Poly-L-lactic acid/hydroxyapatite hybrid membrane for bone tissue regeneration. *J Biomed Mater Res Part A* 82A:445–454
61. Kutikov AB, Song J (2013) An amphiphilic degradable polymer/hydroxyapatite composite with enhanced handling characteristics promotes osteogenic gene expression in bone marrow stromal cells. *Acta Biomaterialia* 9:8354–8364
62. Shen K, Hu Q, Chen L, Shen J (2010) Preparation of chitosan bicomponent nanofibers filled with hydroxyapatite nanoparticles via electrospinning. *J Appl Polym Sci* 115:2683–2690

63. Teng SH, Lee EJ, Wang P, Kim HE (2008) Collagen/hydroxyapatite composite nanofibers by electrospinning. *Mater Lett* 62:3055–3058
64. Stanishevsky A, Chowdhury S, Chinoda P, Thomas V (2008) Hydroxyapatite nanoparticle loaded collagen fiber composites: microarchitecture and nanoindentation study. *J Biomed Mater Res Part A* 86A:873–882
65. Yang D, Jin Y, Ma G, Chen X, Lu F, Nie J (2008) Fabrication and characterization of chitosan/PVA with hydroxyapatite biocomposite nanoscaffolds. *J Appl Polym Sci* 110:3328–3335
66. Ba Linh NT, Min YK, Lee BT (2013) Hybrid hydroxyapatite nanoparticles-loaded PCL/GE blend fibers for bone tissue engineering. *J Biomater Sci Polym Ed* 24:520–538
67. Bianco A, Di Federico E, Cacciotti I (2011) Electrospun poly(ϵ -caprolactone)-based composites using synthesized β -tricalcium phosphate. *Polym Adv Technol* 22:1832–1841
68. Fujihara K, Kotaki M, Ramakrishna S (2005) Guided bone regeneration membrane made of polycaprolactone/calcium carbonate composite nano-fibers. *Biomaterials* 26:4139–4147
69. Hang AT, Tae B, Park JS (2010) Non-woven mats of poly(vinyl alcohol)/chitosan blends containing silver nanoparticles: fabrication and characterization. *Carbohydr Polym* 82:472–479
70. Abdelgawad AM, Hudson SM, Rojas OJ (2014) Antimicrobial wound dressing nanofiber mats from multicomponent (chitosan/silver-NPs/polyvinyl alcohol) systems. *Carbohydr Polym* 100:166–178
71. Jin WJ, Lee HK, Jeong EH, Park WH, Youk JH (2005) Preparation of polymer nanofibers containing silver nanoparticles by using poly(N-vinylpyrrolidone). *Macromol Rapid Commun* 26:1903–1907
72. Faridi-Majidi R, Sharifi-Sanjani N (2007) In situ synthesis of iron oxide nanoparticles on poly(ethylene oxide) nanofibers through an electrospinning process. *J Appl Polym Sci* 105:1351–1355
73. Wang Y, Li Y, Yang S, Zhang G, An D, Wang C, Yang Q, Chen X, Wei Y (2006) A convenient route to polyvinyl pyrrolidone/silver nanocomposite by electrospinning. *Nanotechnology* 17:3304–3307
74. Saquing CD, Manasco JL, Khan SA (2009) Electrospun nanoparticle-nanofiber composites via a one-step synthesis. *Small* 5:944–951
75. Tijting LD, Ruelo MT, Amarjargal A, Pant HR, Park CH, Kim CS (2012) One-step fabrication of antibacterial (silver nanoparticles/poly(ethylene oxide))-polyurethane bicomponent hybrid nanofibrous mat by dual-spinneret electrospinning. *Mater Chem Phys* 134:557–561
76. An J, Zhang H, Zhang J, Zhao Y, Yuan X (2009) Preparation and antibacterial activity of electrospun chitosan/poly(ethylene oxide) membranes containing silver nanoparticles. *Colloid Polym Sci* 287:1425–1434
77. Shi Q, Vitichuli N, Nowak J, Noar J, Caldwell JM, Breidt F, Bourham M, McCord M, Zhang X (2011) One-step synthesis of silver nanoparticle-filled nylon 6 nanofibers and their antibacterial properties. *J Mater Chem* 21:10330–10335
78. Penchev H, Paneva D, Manolova N, Rashkov I (2009) Electrospun hybrid nanofibers based on chitosan or *N*-carboxyethylchitosan and silver nanoparticles. *Macromol Biosci* 9:884–894
79. Shi Q, Vitichuli N, Nowak J, Caldwell JM, Breidt F, Bourham M, Zhang X, McCord M (2011) Durable antibacterial Ag/polyacrylonitrile (Ag/PAN) hybrid nanofibers prepared by atmospheric plasma treatment and electrospinning. *Eur Polym J* 47:1402–1409
80. Celebioglu A, Aytac Z, Umu OCO, Dana A, Tekinay T, Uyar T (2014) One-step synthesis of size-tunable Ag nanoparticles incorporated in electrospun PVA/cyclodextrin nanofibers. *Carbohydr Polym* 99:808–816
81. Lu X, Li L, Zhang W, Wang C (2005) Preparation and characterization of Ag₂S nanoparticles embedded in polymer fibre matrices by electrospinning. *Nanotechnology* 16:2233–2237
82. Afeesh R, Barakat NAM, Al-Deyab SS, Yousef A, Kim HY (2012) Nematic shaped cadmium sulfide doped electrospun nanofiber mat: highly efficient, reusable, solar light photocatalyst. *Colloids Surf A Physicochem Eng Asp* 409:21–29

83. Wang S, Wang C, Zhang B, Sun Z, Li Z, Jiang X, Bai X (2010) Preparation of Fe₃O₄/PVA nanofibers via combining in-situ composite with electrospinning. *Mat Lett* 64:9–11
84. Deniz AE, Vural HA, Ortac B, Uyar T (2011) Gold nanoparticle/polymer nanofibrous composites by laser ablation and electrospinning. *Mat Lett* 65:2941–2943
85. Zhuang X, Cheng B, Kang W, Xu X (2010) Electrospun chitosan/gelatin nanofibers containing silver nanoparticles. *Carbohydr Polym* 82:524–527
86. Li L, Bellan LM, Craighead HG, Frey MW (2006) Formation and properties of nylon-6 and nylon-6/montmorillonite composite nanofibers. *Polymer* 47:6208–6217
87. Fong H, Liu W, Wang CS, Vaia RA (2002) Generation of electrospun fibers of nylon 6 and nylon 6-montmorillonite nanocomposite. *Polymer* 43:775–780
88. Zhang Y, Venugopal JR, El-Turki A, Ramakrishna S, Su B, Lim CT (2008) Electrospun biomimetic nanocomposite nanofibers of hydroxyapatite/chitosan for bone tissue engineering. *Biomaterials* 29:4314–4322
89. Song JH, Kim HE, Kim HW (2008) Electrospun fibrous web of collagen-apatite precipitated nanocomposite for bone regeneration. *J Mater Sci Mater Med* 19:2925–2932
90. Kim HW, Song JH, Kim HE (2005) Nanofiber generation of gelatin-hydroxyapatite biomimetics for guided tissue regeneration. *Adv Funct Mater* 15:1988–1994
91. Kim GM, Wutzler A, Radosch HJ, Michler GH, Simon P, Sperling RA, Parak WJ (2005) One-dimensional arrangement of gold nanoparticles by electrospinning. *Chem Mater* 17:4949–4957
92. Drew C, Liu X, Ziegler D, Wang X, Bruno FF, Whitten J, Samuelson LA, Kumar J (2003) Metal oxide-coated polymer nanofibers. *Nano Lett* 3:143–147
93. Niesen TP, De Guire MR (2002) Review: deposition of ceramic thin films at low temperatures from aqueous solutions. *Solid State Ionics* 151:61–68
94. George SM, Ott AW, Klaus JW (1996) Surface chemistry for atomic layer growth. *J Phys Chem* 100:13121–13131
95. Oldham CJ, Gong B, Spagnola JC, Jur JS, Senecal KJ, Godfrey TA, Parsons GN (2011) Encapsulation and chemical resistance of electrospun nylon nanofibers coated using integrated atomic and molecular layer deposition. *J Electrochem Soc* 158:D549–D556
96. Kayaci F, Ozgit-Akgun C, Donmez I, Biyikli N, Uyar T (2012) Polymer–inorganic core–shell nanofibers by electrospinning and atomic layer deposition: flexible Nylon–ZnO core–shell nanofiber mats and their photocatalytic activity. *ACS Appl Mater Interfaces* 4:6185–6194
97. Shi W, Song S, Zhang H (2013) Hydrothermal synthetic strategies of inorganic semiconducting nanostructures. *Chem Soc Rev* 42:5714–5743
98. He T, Zhou Z, Xu W, Ren F, Ma H, Wang J (2009) Preparation and photocatalysis of TiO₂-fluoropolymer electrospun fiber nanocomposites. *Polymer* 50:3031–3036
99. Chang Z (2011) “Firecracker-shaped” ZnO/polyimide hybrid nanofibers viaelectrospinning and hydrothermal process. *Chem Commun* 47:4427–4429
100. Kim HJ, Pant HR, Amarjargal A, Kim CS (2013) Incorporation of silver-loaded ZnO rods into electrospun nylon-6 spider-web-like nanofibrous mat using hydrothermal process. *Colloids Surf A Physicochem Eng Asp* 434:49–55
101. Xiao S, Shen M, Guo R, Wang S, Shi X (2009) Immobilization of zerovalent iron nanoparticles into electrospun polymer nanofibers: synthesis, characterization, and potential environmental applications. *J Phys Chem C* 113:18062–18068
102. Xiao S, Shen M, Guo R, Huang Q, Wang S, Shi X (2010) Fabrication of multiwalled carbon nanotube-reinforced electrospun polymer nanofibers containing zero-valent iron nanoparticles for environmental applications. *J Mater Chem* 20:5700–5708
103. Xiao S, Xu W, Ma H, Fang X (2012) Size-tunable Ag nanoparticles immobilized in electrospun nanofibers: synthesis, characterization, and application for catalytic reduction of 4-nitrophenol. *RSC Adv* 2:319–327
104. Dong H, Fey E, Gandelman A, Jones WE (2006) Synthesis and assembly of metal nanoparticles on electrospun poly(4-vinylpyridine) fibers and poly(4-vinylpyridine) composite fibers. *Chem Mater* 18:2008–2011

105. Fang X, Ma H, Xiao S, Shen M, Guo R, Cao X, Shi X (2011) Facile immobilization of gold nanoparticles into electrospun polyethyleneimine/polyvinyl alcohol nanofibers for catalytic applications. *J Mater Chem* 21:4493–4501
106. Gardella L, Basso A, Prato M, Monticelli O (2013) PLA/POSS nanofibers: a novel system for the immobilization of metal nanoparticles. *ACS Appl Mater Interfaces* 5:7688–7692
107. Liu Z, Zhou C, Zheng B, Qian L, Mo Y, Luo F, Shi Y, Choi MMF, Xiao D (2011) In situ synthesis of gold nanoparticles on porous polyacrylonitrile nanofibers for sensing applications. *Analyst* 136:4545–4551
108. Son HY, Ryu JH, Lee H, Nam YS (2013) Bioinspired templating synthesis of metal–polymer hybrid nanostructures within 3D electrospun nanofibers. *ACS Appl Mater Interfaces* 5:6381–6390
109. Demir MM, Gulgun MA, Menciloglu YZ, Erman B, Abramchuk SS, Makhaeva EE, Khokhlov AR, Matveeva VG, Sulman MG (2004) Palladium nanoparticles by electrospinning from poly(acrylonitrile-co-acrylic acid)-PdCl₂ solutions. Relations between preparation conditions, particle size, and catalytic activity. *Macromolecules* 37:1787–1792
110. Han GY, Guo B, Zhang LW, Yang BS (2006) Conductive gold films assembled on electrospun poly(methyl methacrylate) fibrous mats. *Adv Mater* 18:1709–1712
111. Son WK, Youk JH, Lee TS, Park WH (2004) Preparation of antimicrobial ultrafine cellulose acetate fibers with silver nanoparticles. *Macromol Rapid Commun* 25:1632–1637
112. Li Z, Huang H, Shang T, Yang F, Zheng W, Wang C, Manohar S (2006) Facile synthesis of single-crystal and controllable sized silver nanoparticles on the surfaces of polyacrylonitrile nanofibers. *Nanotechnology* 17:917
113. Lu X, Zhao Y, Wang C, Wei Y (2005) Fabrication of CdS nanorods in PVP fiber matrices by electrospinning. *Macromol Rapid Commun* 26:1325–1329
114. Lu X, Zhao Y, Wang C (2005) Fabrication of PbS nanoparticles in polymer-fiber matrices by electrospinning. *Adv Mater* 17:2485–2488
115. Dong F, Li Z, Huang H, Yang F, Zheng W, Wang C (2007) Fabrication of semiconductor nanostructures on the outer surfaces of polyacrylonitrile nanofibers by in-situ electrospinning. *Mater Lett* 61:2556–2559
116. Wang H, Lu X, Zhao Y, Wang C (2006) Preparation and characterization of ZnS:Cu/PVA composite nanofibers via electrospinning. *Mater Lett* 60:2480–2484
117. Wang C, Yan E, Sun Z, Jiang Z, Tong Y, Xin Y, Huang Z (2007) Mass ratio of CdS/poly(ethylene oxide) controlled photoluminescence of one-dimensional hybrid fibers by electrospinning. *Macromol Mater Eng* 292:949–955
118. Ye J, Chen Y, Zhou W, Wang X, Guo Z, Hu Y (2009) Preparation of polymer@PbS hybrid nanofibers by surface-initiated atom transfer radical polymerization and acidolysis by H₂S. *Mater Lett* 63:1425–1427
119. Ariga K, Hill JP, Ji Q (2007) Layer-by-layer assembly as a versatile bottom-up nanofabrication technique for exploratory research and realistic application. *Phys Chem Chem Phys* 9:2319–2340
120. Ding B, Kim J, Kimura E, Shiratori S (2004) Layer-by-layer structured films of TiO₂ nanoparticles and poly(acrylic acid) on electrospun nanofibers. *Nanotechnology* 15:913
121. Muller K, Quinn JF, Johnston APR, Becker M, Greiner A, Caruso F (2006) Polyelectrolyte functionalization of electrospun fibers. *Chem Mater* 18:2397–2403
122. Lee JA, Krogman KC, Ma M, Hill RM, Hammond PT, Rutledge GC (2009) Highly reactive multilayer-assembled TiO₂ coating on electrospun polymer nanofibers. *Adv Mater* 21:1252–1256
123. Xiao S, Wu S, Shen M, Guo R, Huang Q, Wang S, Shi X (2009) Polyelectrolyte multilayer-assisted immobilization of zero-valent iron nanoparticles onto polymer nanofibers for potential environmental applications. *ACS Appl Mater Interfaces* 1:2848–2855
124. Lu X, Zhao Q, Liu X, Wang D, Zhang W, Wang C, Wei Y (2006) Preparation and characterization of polypyrrole/TiO₂ coaxial nanocables. *Macromol Rapid Commun* 27:430–434

125. Li Y, Gong J, He G, Deng Y (2011) Fabrication of polyaniline/titanium dioxide composite nanofibers for gas sensing application. *Mater Chem Phys* 129:477–482
126. Zampetti E, Macagnano A, Pantalei S, Bearzotti A (2013) PEDOT:PSS coated titania nanofibers for NO₂ detection: study of humidity effects. *Sensor Actuator B Chem* 179:69–73
127. Kickelbick G (2003) Concepts for the incorporation of inorganic building blocks into organic polymers on a nanoscale. *Progr Polym Sci* 28:83–114
128. Sanchez C, Julian B, Belleville P, Popall M (2005) Applications of hybrid organic–inorganic nanocomposites. *J Mater Chem* 15:3559–3592
129. Wen J, Wilkes GL (1996) Organic/inorganic hybrid network materials by the sol–gel approach. *Chem Mater* 8:1667–1681
130. Hench LL, West JK (1990) The sol–gel process. *Chem Rev* 90:33–72
131. Larsen G, Velarde-Ortiz R, Minchow K, Barrero A, Loscertales IG (2003) A method for making inorganic and hybrid (organic/inorganic) fibers and vesicles with diameters in the submicrometer and micrometer range via sol–gel chemistry and electrically forced liquid jets. *J Am Chem Soc* 125:1154–1155
132. Kim ID, Rothschild A (2011) Nanostructured metal oxide gas sensors prepared by electrospinning. *Polym Adv Technol* 22:318–325
133. Lu X, Wang C, Wei Y (2009) One-dimensional composite nanomaterials: synthesis by electrospinning and their applications. *Small* 5:2349–2370
134. Wu H, Pan W, Lin D, Li H (2012) Electrospinning of ceramic nanofibers: fabrication, assembly and applications. *J Adv Ceram* 1:2–23
135. Pirzada T, Arvidson SA, Saquing CD, Shah SS, Khan SA (2012) Hybrid silica-PVA nanofibers via sol–gel electrospinning. *Langmuir* 28:5834–5844
136. Jang TS, Lee EJ, Jo JH, Jeon JM, Kim MY, Kim HE, Koh YH (2012) Fibrous membrane of nano-hybrid poly-L-lactic acid/silica xerogel for guided bone regeneration. *J Biomed Mater Res* 100B:321–330
137. Lee EJ, Teng SH, Jang TS, Wang P, Yook SW, Kim HE, Koh YH (2010) Nanostructured poly (ε-caprolactone)-silica xerogel fibrous membrane for guided bone regeneration. *Acta Biomaterialia* 6:3557–3565
138. Shao C, Kim HY, Gong J, Ding B, Lee DR, Park SJ (2003) Fiber mats of poly(vinyl alcohol)/silica composite via electrospinning. *Mater Lett* 57:1579–1584
139. Tong HW, Mutlu BR, Wackett LP, Aksan A (2013) Silica/PVA biocatalytic nanofibers. *Mater Lett* 111:234–237
140. Allo BA, Rizkalla AS, Mequanint K (2010) Synthesis and electrospinning of ε-polycaprolactone-bioactive glass hybrid biomaterials via a sol–gel process. *Langmuir* 26:18340–18348
141. Rawolle M, Niedermeier MA, Kaune G, Perlich J, Lellig P, Memesa M, Cheng YJ, Gutmann JS, Muller-Buschbaum P (2012) Fabrication and characterization of nanostructured titania films with integrated function from inorganic–organic hybrid materials. *Chem Soc Rev* 41:5131–5142
142. Gaya UI, Abdullah AH (2008) Heterogeneous photocatalytic degradation of organic contaminants over titanium dioxide: a review of fundamentals, progress and problems. *J Photochem Photobiol C Photochem Rev* 9:1–12
143. Wu N, Shao D, Wei Q, Cai Y, Gao W (2009) Characterization of PVAc/TiO₂ hybrid nanofibers: from fibrous morphologies to molecular structures. *J Appl Polym Sci* 112:1481–1485
144. Larsen G, Skotak M (2008) Co-solvent mediated fiber diameter and fiber morphology control in electrospinning of sol–gel formulations. *J Non Crystal Solids* 354:5547–5554
145. Skotak M, Larsen G (2006) Solution chemistry control to make well defined submicron continuous fibres by electrospinning: the (CH₃CH₂CH₂O)₄Ti/AcOH/poly(*N*-vinylpyrrolidone) system. *J Mater Chem* 16:3031–3039
146. Wu N, Chen L, Wei Q, Liu Q, Li J (2011) Nanoscale three-point bending of single polymer/inorganic composite nanofiber. *J Text Inst* 103:154–158

147. Hong Y, Li D, Zheng J, Zou G (2006) Sol-gel growth of titania from electrospun polyacrylonitrile nanofibres. *Nanotechnology* 17:1986
148. Meng X, Luo N, Cao S, Zhang S, Yang M, Hu X (2009) In-situ growth of titania nanoparticles in electrospun polymer nanofibers at low temperature. *Mater Lett* 63:1401–1403
149. Su C, Tong Y, Zhang M, Zhang Y, Shao C (2013) TiO₂ nanoparticles immobilized on polyacrylonitrile nanofibers mats: a flexible and recyclable photocatalyst for phenol degradation. *RSC Adv* 3:7503–7512
150. Arafat MM, Dinan B, Akbar SA, Haseeb SMA (2012) Gas sensors based on one dimensional nanostructured metal-oxides: a review. *Sensors* 12:7207–7258
151. Udom I, Ram MK, Stefanakos EK, Hepp AF, Goswami DY (2013) One dimensional-ZnO nanostructures: synthesis, properties and environmental applications. *Mater Sci Semicond Process* 16:2070–2083
152. Znaidi L (2010) Sol-gel-deposited ZnO thin films: a review. *Mater Sci Eng B* 174:18–30
153. Liu H, Yang J, Liang J, Huang Y, Tang C (2008) ZnO nanofiber and nanoparticle synthesized through electrospinning and their photocatalytic activity under visible light. *J Am Ceram Soc* 91:1287–1291
154. Yang X, Shao C, Guan H, Li X, Gong J (2004) Preparation and characterization of ZnO nanofibers by using electrospun PVA/zinc acetate composite fiber as precursor. *Inorg Chem Commun* 7:176–178
155. Wu H, Pan W (2006) Preparation of zinc oxide nanofibers by electrospinning. *J Am Ceram Soc* 89:699–701
156. Hong Y, Li D, Zheng J, Zou G (2006) In situ growth of ZnO nanocrystals from solid electrospun nanofiber matrixes. *Langmuir* 22:7331–7334
157. Ye S, Zhang D, Liu H, Zhou J (2011) ZnO nanocrystallites/cellulose hybrid nanofibers fabricated by electrospinning and solvothermal techniques and their photocatalytic activity. *J Appl Polym Sci* 121:1757–1764
158. Zhang J, Wen B, Wang F, Ding Y, Zhang S, Yang M (2011) In situ synthesis of ZnO nanocrystal/PET hybrid nanofibers via electrospinning. *J Polym Sci B Polym Phys* 49:1360–1368
159. Park SH, Lee SM, Lim HS, Han JT, Lee DR, Shin HS, Jeong Y, Kim J, Cho JH (2010) Robust superhydrophobic mats based on electrospun crystalline nanofibers combined with a silane precursor. *ACS Appl Mater Interfaces* 2:658–662
160. Song JH, Yoon BH, Kim HE, Kim HW (2008) Bioactive and degradable hybridized nanofibers of gelatin-siloxane for bone regeneration. *J Biomed Mater Res Part A* 84A:875–884
161. Ren L, Wang J, Yang FY, Wang L, Wang D, Wang TX, Tian MM (2010) Fabrication of gelatin-siloxane fibrous mats via sol-gel and electrospinning procedure and its application for bone tissue engineering. *Mat Sci Eng C* 30:437–444
162. Gao C, Gao Q, Li Y, Rahaman MN, Teramoto A, Abe K (2013) In vitro evaluation of electrospun gelatin-bioactive glass hybrid scaffolds for bone regeneration. *J Appl Polym Sci* 127:2588–2599
163. Toskas G, Cherif C, Hund RD, Laourine E, Mahltig B, Fahmi A, Heinemann C, Hanke T (2013) Chitosan(PEO)/silica hybrid nanofibers as a potential biomaterial for bone regeneration. *Carbohydr Polym* 94:713–722
164. Allo BA, Lin S, Mequanint K, Rizkalla AS (2013) Role of bioactive 3D hybrid fibrous scaffolds on mechanical behavior and spatiotemporal osteoblast gene expression. *ACS Appl Mater Interfaces* 5:7574–7583
165. Poologasundarampillai G, Yu B, Jones JR, Kasuga T (2011) Electrospun silica/PLLA hybrid materials for skeletal regeneration. *Soft Matter* 7:10241–10251
166. Taha AA, Yn W, Wang H, Li F (2012) Preparation and application of functionalized cellulose acetate/silica composite nanofibrous membrane via electrospinning for Cr(VI) ion removal from aqueous solution. *J Environ Manag* 112:10–16

167. Xu R, Jia M, Zhang Y, Li F (2012) Sorption of malachite green on vinyl-modified mesoporous poly(acrylic acid)/SiO₂ composite nanofiber membranes. *Microporous Mesoporous Mater* 149:111–118
168. Xu R, Jia M, Li F, Wang H, Zhang B, Qiao J (2012) Preparation of mesoporous poly (acrylic acid)/SiO₂ composite nanofiber membranes having adsorption capacity for indigo carmine dye. *Appl Phys A* 106:747–755
169. Teng M, Wang H, Li F, Zhang B (2011) Thioether-functionalized mesoporous fiber membranes: sol–gel combined electrospun fabrication and their applications for Hg²⁺ removal. *J Colloid Interface Sci* 355:23–28
170. Teng M, Li F, Zhang B, Taha AA (2011) Electrospun cyclodextrin-functionalized mesoporous polyvinyl alcohol/SiO₂ nanofiber membranes as a highly efficient adsorbent for indigo carmine dye. *Colloids Surf A Physicochem Eng Asp* 385:229–234
171. Wu S, Li F, Wu Y, Xu R, Li G (2010) Preparation of novel poly(vinyl alcohol)/SiO₂ composite nanofiber membranes with mesostructure and their application for removal of Cu²⁺ from waste water. *Chem Commun* 46:1694–1696
172. Yan L, Si S, Chen Y, Yuan T, Fan H, Yao Y, Zhang Q (2011) Electrospun in-situ hybrid polyurethane/nano-TiO₂ as wound dressings. *Fibers Polym* 12:207–213
173. Gupta KK, Mishra PK, Srivastava P, Gangwar M, Nath G, Maiti P (2013) Hydrothermal in situ preparation of TiO₂ particles onto poly(lactic acid) electrospun nanofibres. *Appl Surface Sci* 264:375–382
174. Vitichuli N, Shi Q, Nowak J, Kay K, Caldwell JM, Breidt F, Bourham M, McCord M, Zhang X (2011) Multifunctional ZnO/Nylon-6 nanofiber mats by an electrospinning–electrospraying hybrid process for use in protective applications. *Sci Technol Adv Mater* 12:055004
175. Korina E, Stoilova O, Manolova N, Rashkov I (2014) Poly(3-hydroxybutyrate)-based hybrid materials with photocatalytic and magnetic properties prepared by electrospinning and electrospaying. *J Mater Sci* 49:2144–2153
176. Lee MW, An S, Joshi B, Latthe SS, Yoon SS (2013) Highly efficient wettability control via three-dimensional (3D) suspension of titania nanoparticles in polystyrene nanofibers. *ACS Appl Mater Interfaces* 5:1232–1239
177. Gupta D, Venugopal J, Mitra S, Giri Dev VR, Ramakrishna S (2009) Nanostructured biocomposite substrates by electrospinning and electrospaying for the mineralization of osteoblasts. *Biomaterials* 30:2085–2094
178. Francis L, Venugopal J, Prabhakaran MP, Thavasi V, Marsano E, Ramakrishna S (2010) Simultaneous electrospin-electrosprayed biocomposite nanofibrous scaffolds for bone tissue regeneration. *Acta Biomaterialia* 6:4100–4109
179. Loscertales IG, Barrero A, Guerrero I, Cortijo R, Marquez M, Ganan-Calvo AM (2002) Micro/nano encapsulation via electrified coaxial liquid jets. *Science* 295:1695–1698
180. Li D, Xia Y (2004) Direct fabrication of composite and ceramic hollow nanofibers by electrospinning. *Nano Lett* 4:933–938
181. Kalra V, Mendez S, Lee JH, Nguyen H, Marquez M, Joo YG (2006) Confined assembly in coaxially electrospun block copolymer fibers. *Adv Mater* 18:3299–3303
182. Kalra V, Lee J, Lee JH, Lee SG, Marquez M, Wiesner U, Joo YL (2008) Controlling nanoparticle location via confined assembly in electrospun block copolymer nanofibers. *Small* 4:2067–2073
183. Song T, Zhang Y, Zhou T, Lim CT, Ramakrishna S, Liu B (2005) Encapsulation of self-assembled FePt magnetic nanoparticles in PCL nanofibers by coaxial electrospinning. *Chem Phys Lett* 415:317–322
184. Kim MS, Shin KM, Kim SI, Spinks GM, Kim SJ (2008) Controlled array of ferritin in tubular nanostructure. *Macromol Rapid Commun* 29:552–556
185. Sharma N, Hassnain Jaffari G, Ismat Shah S, Pochan DJ (2010) Orientation-dependent magnetic behavior in aligned nanoparticle arrays constructed by coaxial electrospinning. *Nanotechnology* 21:085707

186. Sung YK, Ahn BW, Kang TJ (2012) Magnetic nanofibers with core (Fe_3O_4 nanoparticle suspension)/sheath (poly ethylene terephthalate) structure fabricated by coaxial electrospinning. *J Magn Magn Mater* 324:916–922
187. Medina-Castillo AL, Fernandez-Sanchez JF, Fernandez-Gutierrez A (2011) One-step fabrication of multifunctional core-shell fibres by co-electrospinning. *Adv Funct Mater* 21:3488–3495
188. Ma Q, Wang J, Dong X, Yu W, Liu G, Xu J (2012) Electrospinning preparation and properties of magnetic-photoluminescent bifunctional coaxial nanofibers. *J Mater Chem* 22:14438–14442
189. Bedford NM, Steckl AJ (2010) Photocatalytic self cleaning textile fibers by coaxial electrospinning. *ACS Appl Mater Interfaces* 2:2448–2455
190. Yu DG, Zhou J, Chatterton NP, Li Y, Huang J, Wang X (2012) Polyacrylonitrile nanofibers coated with silver nanoparticles using a modified coaxial electrospinning process. *Int J Nanomed* 7:5725–5732
191. Allcock HR (2002) Chemistry and applications of polyphosphazenes. Wiley, Hoboken
192. Nair LS, Bhattacharyya S, Bender JD, Greish YE, Brown PW, Allcock HR, Laurencin CT (2004) Fabrication and optimization of methylphenoxy substituted polyphosphazene nanofibers for biomedical applications. *Biomacromolecules* 5:2212–2220
193. Lin YJ, Cai Q, Li L, Li QF, Yang XP, Jin RG (2010) Co-electrospun composite nanofibers of blends of poly[(amino acid ester)phosphazene] and gelatin. *Polym Int* 59:610–616
194. Carampin P, Conconi MT, Lora S, Menti AM, Baiguera S, Bellini S, Grandi C, Parnigotto PP (2007) Electrospun polyphosphazene nanofibers for in vitro rat endothelial cells proliferation. *J Biomed Mater Res Part A* 80A:661–668
195. Deng M, Kumbar SG, Nair LS, Weikel AL, Allcock HR, Laurencin CT (2011) Biomimetic structures: biological implications of dipeptide-substituted polyphosphazene-polyester blend nanofiber matrices for load-bearing bone regeneration. *Adv Funct Mater* 21:2641–2651
196. Qian YC, Ren N, Huang XJ, Chen C, Yu AG, Xu ZK (2013) Glycosylation of polyphosphazene nanofibrous membrane by click chemistry for protein recognition. *Macromol Chem Phys* 214:1852–1858
197. Singh A, Steely L, Allcock HR (2005) Poly[bis(2,2,2-trifluoroethoxy)phosphazene] superhydrophobic nanofibers. *Langmuir* 21:11604–11607
198. Xu Y, Wen Y, Yn W, Lin C, Li G (2012) Hybrid nanofibrous mats with remarkable solvent and temperature resistance produced by electrospinning technique. *Mater Lett* 78:139–142
199. Schramm C, Rinderer B, Tessadri R (2013) Synthesis and characterization of novel ultrathin polyimide fibers via sol-gel process and electrospinning. *J Appl Polym Sci* 128:1274–1281

Polymer–Ceramic Nanohybrid Materials

Sarabjeet Kaur, Markus Gallei, and Emanuel Ionescu

Abstract This review is dedicated to nanohybrid materials consisting of a polymer-based matrix and a disperse nanoscaled ceramic phase. Different preparation techniques for the synthesis of polymer–ceramic nanohybrid materials will be presented, such as blending techniques, sol–gel processing, in-situ polymerization, and self-assembly methods. Selected structural and functional properties of polymer–ceramic nanohybrid materials will be highlighted and discussed within the context of their dependence on parameters such as the homogeneity of the dispersion of the ceramic throughout the polymer matrix, the particle size of the ceramic phase, and the polymer–ceramic interface. Moreover, some advanced applications of polymer–ceramic nanohybrid materials will be addressed and compared with their polymeric counterparts.

Keywords Functional properties · Multifunctional materials · Nanohybrid materials · Polymer–ceramic interface · Polymer–ceramic nanohybrids · Structural properties · Synthesis methods

Contents

1	Introduction	145
2	Synthesis of Polymer–Ceramic Nanohybrid Materials	146
2.1	Blending Techniques	146
2.2	Sol–Gel Processing	148
2.3	In-Situ Polymerization	152
2.4	Self-Assembly Techniques	154

S. Kaur and E. Ionescu (✉)
Institute for Materials Science, Technische Universität Darmstadt, Jovanka-Bontschits-Strasse 2,
64287 Darmstadt, Germany
e-mail: ionescu@materials.tu-darmstadt.de

M. Gallei
Ernst-Berl-Institute for Technical and Macromolecular Chemistry, Technische Universität
Darmstadt, Alarich-Weiss-Strasse 4, 64287 Darmstadt, Germany

3	Properties and Applications	156
3.1	Nanohybrid Structural Materials	156
3.2	Nanohybrid Functional Materials	160
4	Conclusions	168
	References	168

Abbreviations

APTES	Aminopropyl triethoxysilane
BMA	Butyl methacrylate
HEMA	2-Hydroxyethyl methacrylate
MAA	Methacrylic acid
MEH-PPV	Poly[2-methoxy-5(2'-ethyl)hexoxy]-phenylenevinylene
MMA	Methyl methacrylate
MPS	3-(Trimethoxysilyl)-propylmethacrylate
P2ClAn	Poly (2-chloroaniline)
PA	Polyamide
PAI	Poly(amide-imide)
PAN	Polyacrylonitrile
PANI	Polyaniline
PC	Polycarbonate
PCL	Poly(caprolactone)
PEEK	Poly(ether ether ketone)
PEG	Poly(ethylene glycol)
PEO	Poly(ethylene oxide)
PET	Poly(ethylene terephthalate)
PHEMA	Polyhydroxyethylmethacrylate
PI	Polyimide
PMMA	Poly(methyl methacrylate)
PMMA-g-	PMMA-grafted titanium dioxide
TiO ₂	
PP	Polypropylene
PP-g-SiO ₂	SiO ₂ nanoparticles grafted to terminally hydroxylated polypropylene
PS	Polystyrene
PTFE	Polytetrafluoroethylene
PTMSP	Poly(1-trimethylsilyl-1-propyne)
PU	Polyurethanes
PVA	Poly(vinyl alcohol)
PVAc	Polyvinylacetate
PVDF	Poly(vinylidene fluoride)
PVP	Poly(4-vinylpyridine)
PVPL	Polyvinylpyrrolidone
sPPEK	Sulfonated poly(phthalazinone ether ketone)
TEOS	Tetraethoxysilane, tetraethyl orthosilicate
TMOS	Tetramethoxysilane, tetramethyl orthosilicate

1 Introduction

Multifunctional materials are capable of providing two or more primary functions either in a simultaneous manner or sequentially. For instance, multifunctional structural materials exhibit additional functions beyond their basic mechanical strength or stiffness (which are typical attributes of structural materials). Thus, they can be designed to possess incorporated electrical, magnetic, optical, sensing, power generative, or other functionalities, which work in a synergistic manner [1].

The basic motivation for the development of multifunctional materials relies on their ability to address several mission objectives with only one structure; hence, they are capable of adapting on purpose their performance and response depending on the specific target application. Consequently, multifunctional materials represent the ultimate solution for addressing and providing multiple functions with one sole structure. They are usually (nano)composites or (nano)hybrids of several distinct (Gibbsian) phases, each of them providing a different but essential function. Optimized design of multifunctional materials allows no or little “no-function” volume (parasitic volume) and thus provides significant advantages over the traditional multicomponent “brassboard” systems: they are more weight and volume efficient, exhibit high flexibility with respect to their function(s) and performance, and are potentially less prone to maintenance issues [2].

Hybrid materials (such as polymer–ceramic hybrids) are not only a physical mixture of two phases, but are characterized by an intimate mixture of the organic and inorganic phases, with their interfaces consequently playing an important role in their properties and generating unusual features or improved performance of the hybrid materials [3–11]. The organic–inorganic hybrids are attracting much interest compared to other hybrid materials because they combine the flexibility of organic phases and the stiffness/strength of the inorganic part. Depending on the nature of the bonding between the organic and inorganic phases, two classes of organic–inorganic hybrids have been defined: Class I represents hybrid materials showing weak interactions between their phases (van der Waals, hydrogen bonding, weak electrostatic interactions). Class II consists of hybrid materials showing strong chemical interactions between the components [12].

This review addresses the class of organic–inorganic nanohybrid materials consisting of an organic matrix phase, which is a polymer, and an inorganic disperse phase, which is a nanoscaled ceramic material. Thus, general synthetic approaches for preparation of polymer–ceramic nanohybrid materials will be introduced and specific properties thereof will be highlighted. Additionally, various advanced and prospective applications of polymer–ceramic nanohybrids will be addressed and discussed within the context of the concept of multifunctionality.

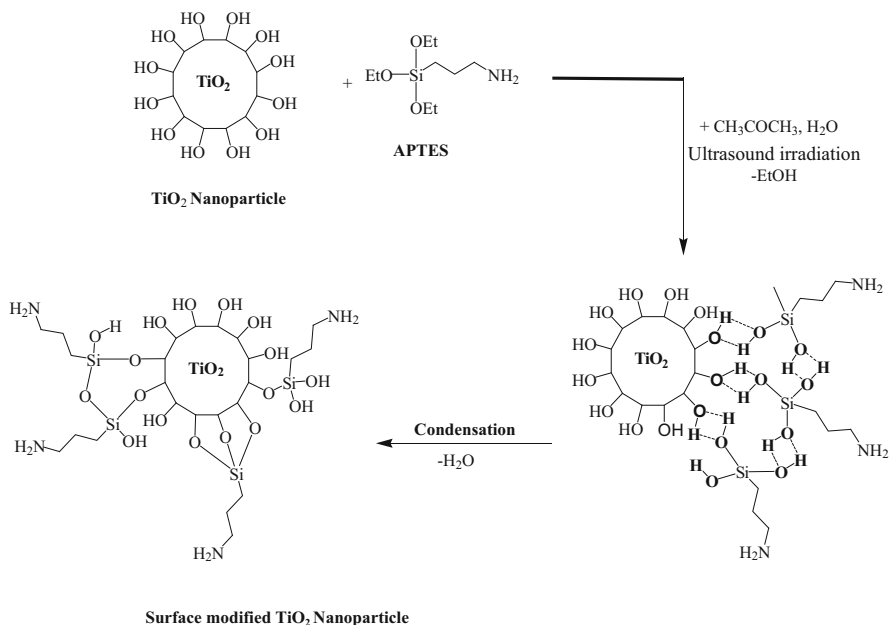


Fig. 1 Surface modification of TiO₂ nanoparticles for the preparation of PVA-titania nanohybrid materials (adapted after [21], with permission from Elsevier)

2 Synthesis of Polymer–Ceramic Nanohybrid Materials

2.1 Blending Techniques

One simple and straight-forward method for the preparation of polymer–ceramic nanohybrid materials is the direct mixing of the nanosized ceramic particles into the polymer matrix. Ceramic particles in the nanosize range are synthesized using various routes such as sol–gel, co-precipitation, ball milling, hydrothermal process, as well as gas-phase techniques or micro-emulsion methods [13–19]. However, preparation of a homogeneous dispersion of nanoparticles in a polymeric matrix is a challenging task due to the strong tendency of the nanoparticles to agglomerate. The nanoparticle-filled polymers sometimes suffer from clustering/agglomeration of the nanoparticles and, consequently, exhibit inferior properties compared to those of conventional microsized particle–polymer systems. In some of these cases, reagents to modify the properties of the interfaces between the nanoparticles and the polymer matrix have been used and significantly improved the dispersion of the nanoparticles [20], e.g., surface treatment of titania with aminopropyl triethoxysilane (APTES), as shown in Fig. 1.

Because surface modification helps in enhancing the properties of hybrid materials, much work has been reported on the surface modification of SiO₂ and

subsequent blending with different monomers, which finally convert into the respective polymers. For instance, hybrid materials based on polyimide (PI) and SiO₂ were prepared upon surface modification of the silica nanoparticles via APTES, 4'',4'''-(hexafluoro-*iso*-propylidene) bis (4-phenoxyaniline), 4,4'-(hexafluoro-*iso*-propylidene)diphenol), and oleic acid [22–25].

According to the methodology used during blending as well as to the features of the polymer and the nanoparticles, three categories of processes can be distinguished:

1. Solution blending processes, in which both the polymer and the nanoparticles (or their precursors) are dissolved in the solvent
2. Emulsion or suspension blending processes, used for cases in which either the nanoparticles or the polymer (or both) are not soluble in the solvent, or their solutions are not miscible [26].
3. Melt blending processes, which generally involve the melting of polymer pellets to form a viscous liquid and subsequent dispersion of the nanoparticles. Here, the samples can be fabricated upon compression molding, injection molding, or fiber melt spinning techniques [27]. Melt blending processes are most commonly used because they are efficient, easy to perform, and environmentally friendly. However, a homogeneous dispersion of ceramic nanoparticles within the polymeric matrix is difficult to achieve [28, 29]. In order to break down nanoparticle agglomerates, an irradiation grafting method has been applied, which provided an improved dispersion of the grafted nanoparticles upon their mechanical mixing [30].

Highly dispersed polypropylene (PP)-SiO₂ hybrid materials [31–39] were synthesized upon grafting *para*-vinylphenylsulfonylhydrazide (which is a polymerizable foaming agent) onto the silica nanoparticles [40]. Also, the use of poly(propylene maleic anhydride) copolymer was reported, which provided a higher adhesion between the PP matrix and SiO₂ nanoparticles [41].

A significant amount of work has been done to prepare silica-based hybrid materials using solution blending [42–48]. Poly(ethylene 2,6-naphthalate)-SiO₂ hybrid materials were prepared via melt blending using stearic-acid-modified silica [49, 50]. Poly(ethylene terephthalate) (PET)-SiO₂ [51], poly(caprolactone) (PCL)-SiO₂ [52–54], poly(3-hydroxybutyrate-*co*-3-hydroxyhexanoate)-SiO₂ [55], and poly(L-lactide)-SiO₂ [56] hybrid materials prepared upon melt compounding have been also reported. Polyamide (PA)-SiO₂ hybrid materials were prepared by blending of silica sols with solutions of nylon-6 in formic acid [57].

Proton exchange membranes (PEM) were also prepared by solution blending of sulfonated poly(phthalazinone ether ketone) (sPPEK) and various amounts of sulfonated silica nanoparticles (silica-SO₃H) [58]. The solution blending technique was also used in combination with compression molding; thus, poly(ether ether ketone) (PEEK)-based nanohybrids were fabricated by means of compression molding at 400°C under a pressure of 60 MPa using silica surface-modified with stearic acid and PEEK [59].

A similar technique was used for the preparation of polystyrene (PS)-SiO₂ nanohybrids, where colloidal silica solutions were mixed with PS solutions by means of ultrasonic homogenization [60]. Also, latex-silica nanohybrid films were synthesized upon mixing aqueous colloidal suspensions of silica and nanolatex polymer beads [61–63]. Other silica-based nanohybrid systems with poly(ethylene oxide) (PEO) [64, 65], poly(vinyl alcohol) (PVA) [66], PS [67], polybutylacrylate [68], or PMMA [69] can be prepared by using the same suspension blending method.

Solution blending is a liquid-state powder processing method that provides a good molecular level of mixing and is widely used in material preparation and processing. Solution-blending techniques were employed for the synthesis of titania-based hybrid materials, e.g., poly(vinylidene fluoride) (PVDF)-LiClO₄-TiO₂ [70] or PVA-TiO₂ [21]. The as-prepared TiO₂ particles were incorporated in polymers such as PI [71], PVA, partially hydrolyzed poly(vinyl acetate) (PVAc), polyvinylpyrrolidone (PVPL), and poly(4-vinylpyridine) (PVP). Nanohybrid PMMA-TiO₂ was also prepared by blending PMMA and TiO₂ nanowire powder in toluene [72].

Polymer-nanoparticle hybrid films based on TiO₂ nanoparticles dispersed within a poly(2-methoxy-5-(2'-ethyl)hexoxy)-phenylenevinylene (MEH-PPV) polymeric matrix were prepared upon dispersing the nanoparticles (either as neat nanoparticles or as a suspension in *p*-xylene) into a solution of MEH-PPV in *p*-xylene. Obviously, the use of nanoparticle suspension resulted in better dispersion of the nanoparticles within the resulting hybrid film [73].

Few reports concerning alumina-based hybrid systems are available due to the high reactivity of the alumina precursors. Acrylic resin-alumina hybrid materials were obtained by mixing acrylic resin and alumina sols (generated by the sol-gel process) and led to nanohybrids with improved homogeneity [74]. PET-alumina hybrid materials were synthesized by melt-mixing of PET with nanoalumina under inert atmosphere in a batch melt mixer [75]. Also, latex-alumina nanohybrid films were synthesized by mixing aqueous colloidal suspensions of alumina and nanolatex polymer beads. Prior to their mixing with the alumina sols, the latex nanoparticles were prepared via a semibatch emulsion polymerization of butyl methacrylate (BMA) in the presence of methacrylic acid (MAA). Small amounts of acrylic acid were incorporated into the latex in order to obtain a better interaction between the surface of the polymeric particles and the inorganic phase [76].

2.2 Sol-Gel Processing

For the synthesis of organic-inorganic hybrid materials, it is required that the inorganic component is generated at temperatures lower than those at which the organic polymers decompose. Although the decomposition temperature varies strongly from polymer to polymer (e.g., some polycarbonates (PC) decompose at temperatures of ca. 125°C; whereas the decomposition of PI or polyphenylenes

takes place at temperatures beyond 500°C), it is generally far lower than the temperatures used in the preparation of typical inorganic ceramics ($\geq 1,000^\circ\text{C}$). Consequently, the preparative techniques used for the synthesis of polymer–ceramic nanohybrid materials should work at mild temperatures, thus strongly restricting the number of methods available.

The sol–gel method is one highly explored chemical approach for nanomaterial synthesis and has the particular advantage that it can be performed at relatively low temperatures. The sol–gel method involves the preparation of a colloidal sol, which subsequently converts into a gel due to the occurrence of hydrolysis and polycondensation reactions. The sol–gel method has been explored for the synthesis of a wide variety of materials such as metal oxides, metal carbides, or metal nitrides, which can be prepared in high purity and under relatively mild conditions [77–80].

The sol–gel synthesis of hybrid materials involves the occurrence of hydrolysis and condensation reactions in the presence of an organic polymer. Obviously, the selection of suitable polymer is of fundamental importance for the synthesis of the hybrid materials, as it should exhibit good miscibility with typical sol–gel precursors. The presence of suitable functional groups can facilitate the linkage between the polymer and the inorganic component. Also, the nature of the polymeric matrix is important because different properties of the matrix and, consequently, of the resulting nanohybrid material can be addressed; for instance, the polymeric matrix can be an elastomer (as in the case of polydimethylsiloxane) or thermoplastic (e.g., polytetrahydrofuran), amorphous, or (partially) crystalline [81].

A serious challenge related to the sol–gel preparation of ceramic–polymer nanohybrids relates to the strong acidic or basic conditions needed to perform the hydrolysis/polycondensation reactions, which might strongly affect (for instance) the solubility of the polymeric component. Thus, numerous polymers that are soluble at the initial stage of the sol–gel process will precipitate or even degrade as hydrolysis and polycondensation reactions progress. This consequently strongly restricts the number of suitable polymers for the sol–gel preparation of polymer–ceramic nanohybrids. For instance, poly(2-vinylpyridine) (PVP), or polyacrylonitrile (PAN) were shown to remain soluble during the sol–gel process in aqueous tetraethyl orthosilicate (TEOS) or tetramethoxysilane (TMOS) solutions if organic acids were used as co-solvents [82].

Sol–gel processing of ceramic–polymer nanohybrid materials can be performed upon blending the polymer with the sol–gel precursor followed by the sol–gel process, as already mentioned. Alternatively, the sol–gel precursors can be chemically linked to the polymeric matrix material having suitable functional groups and the sol–gel process performed subsequently. This allows creation of novel materials with strong interface bonding that might exhibit properties being dictated by those interfaces [83].

An additional method for the preparation of ceramic–polymer nanohybrids relies on dispersing sol–gel-derived ceramic nanoparticles within a polymeric matrix. Because the properties of the hybrid materials depend on the content and dispersion of the nanoparticles, different approaches have been used to provide homogeneous dispersions. For instance, the homogeneity of the nanohybrid materials can be

improved by surface modification of the nanoparticles [84]. Within this context, amino- and epoxy-functionalized silanes, thiol, MAA etc. are some of the dispersants used to achieve good dispersion qualities of the ceramic nanoparticles within the polymer matrix [85–90]. An additional effective strategy is the use of polymers having suitable substituents that are able to attach to the ceramic nanoparticles and thus provide a good homogeneity of the nanohybrid materials [91, 92].

Extensive work has been done and reported on the preparation of silica-containing nanohybrid materials. Usually, TEOS is taken as inorganic precursor to deliver the silica nanoparticles used for preparing nanohybrids with different polymers such as PMA [93], polyacrylic acid [94, 95], poly(ether imide) [96], PA [97], PVAc [98, 99], PVPL [100], Nafion [99, 101], poly(amide-6-*b*-ethylene oxide) [102], and several other polymers. Among the large diversity of the currently available nanohybrid materials, PMMA-SiO₂-based materials have been intensively studied. However, the limited thermal stability of the polymer restricts the use of PMMA-SiO₂ hybrids, for instance in high-temperature optoelectronic devices [103]. Thus, PIs have been recognized as suitable high-temperature polymers and significant work has been done on the preparation of PI-SiO₂ nanohybrid materials.

One procedure for the synthesis of PI-SiO₂ hybrids is shown in Fig. 2. The PI was synthesized from pyromellitic dianhydride and *N,N*-dimethylacetamide. In order to allow for linkages between the PI and the silica particles (which were formed in situ, as the polymerization of PI and the sol-gel generation of the silica particles was done simultaneously), the PI was functionalized/capped with aminopropyl trimethoxysilyl groups (upon using APTES as coupling agent). These groups were able to participate in the sol-gel process for the generation of the silica nanoparticles, thus providing a homogeneous distribution within the PI matrix and, additionally, a strong bonding between the SiO₂ particles and PI. Furthermore, this synthesis method allowed reduction of the size of SiO₂ nanoparticles and an increase in the content of silica in the hybrid materials, without phase separation [104–112]. Also, the copolymerization of styrene and alkoxy silane-methacrylate was reported to deliver various SiO₂-based nanohybrid compositions [113].

Due to the photocatalytic activity, high refractive index, and low cost of TiO₂, a significant amount of work was reported on polymer-TiO₂ nanohybrid materials with different matrix polymers such as PEO [114], poly(amide-imide) (PAI) [115, 116], PMMA [117], poly(phenylenevinylene) [118–120], PCL [83], MEH-PPV [121, 122], or polyaniline (PANI) [123]. Titanium (IV) tetra-butoxide is used as common sol-gel precursor for the generation of TiO₂. In order to provide an increased bonding between the TiO₂ nanoparticles and the polymer matrix, a triethoxy silyl-capped trimercapto thioethyl amine has been used for the preparation of high-refractive-index nanohybrid materials [124, 125]. Also, PI-TiO₂ hybrid materials with excellent thermochemical resistance, outstanding mechanical properties, and low dielectric constants have been reported [126–129].

The synthesis of Al₂O₃ and ZrO₂ nanoparticles using the sol-gel process is relatively challenging because the respective metal alkoxides are highly reactive

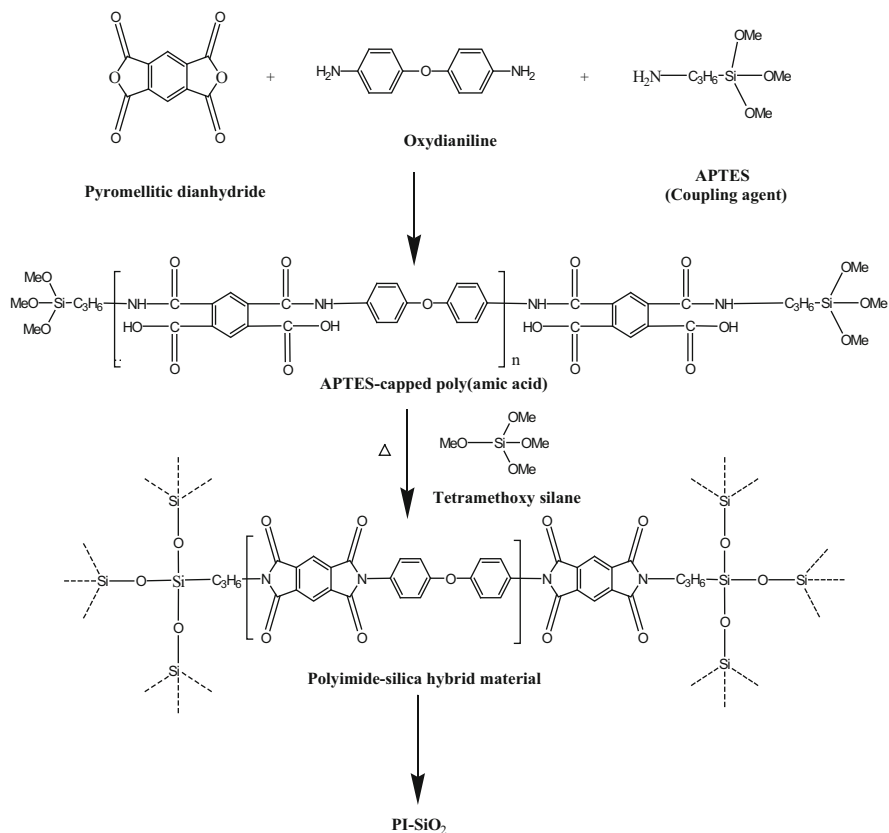


Fig. 2 Reaction scheme for preparing PI-silica hybrid materials (adapted after [103], with permission from the American Chemical Society)

and thus the sol-gel process is difficult to perform in a controlled manner [130]. Several studies have been reported in the literature, especially on the synthesis ZrO₂-based nanohybrid materials. For instance, highly water-dispersible silesqui-oxane/zirconium oxide hybrid nanoparticles were prepared by the following a two-step process: first, a mixture of a solution of APTES in methanolic HCl was reacted with a solution of zirconium tetra-*n*-butoxide in butanol; next, hydrolysis and polycondensation were performed in aqueous solution to obtain the hybrid nanoparticles [131–135]. Also, hybrid materials containing zirconia nanoparticles dispersed within an aromatic PA matrix have been prepared via sol-gel processing [136].

2.3 *In-Situ Polymerization*

In-situ polymerization to obtain polymer–ceramic nanohybrid materials involves three basic steps. First, the nanosized ceramic particles are pretreated with appropriate surface modifiers in order to improve the compatibility of the polymer with the ceramic nanoparticles. Subsequently, the surface-modified nanoparticles are dispersed into the monomer(s). The last step involves a bulk or solution polymerization in the presence of the ceramic nanoparticles.

A key feature of the design of hybrid materials relates to the development of specific interactions at the interface between the organic and inorganic components. Thus, the development of different grafting strategies for polymer immobilization of the surfaces of the ceramic nanoparticles with suitable agents is of great current interest in order to increase the polymer–ceramic compatibility. Two types of polymer–ceramic hybrid materials have been prepared by performing the polymerization process either in the presence of surface-modified ceramic nanoparticles (type I) or with the in-situ sol–gel-assisted growth of the ceramic nanoparticles (type II) [29, 137].

The synthesis of polymer–ceramic nanohybrid materials via in-situ polymerization techniques using different polymers (PA, PMMA, polyurethanes, etc.) and ceramics (SiO_2 , TiO_2 , ZrO_2 , etc.) was reported. For instance, PA6-silica-based nanohybrid materials were synthesized via in-situ polymerization of ϵ -caprolactam in the presence of surface-modified silica. The mixture was heated at relatively high temperatures (200°C) to form PA-6 through a ring-opening polymerization (ROP) mechanism using *n*-aminocaproic acid as initiator [104, 138–140]. PET- SiO_2 nanohybrids were successfully fabricated by in-situ polymerization of terephthalic acid and ethylene glycol in the presence silica nanoparticles having their surface modified with glycidoxypropyl-trimethoxysilane [141–143]. PMMA–silica nanohybrids were prepared via bulk or solution polymerization of methyl methacrylate (MMA) in the presence of colloidal silica [144–147].

A widely studied nanohybrid system is based on epoxy–silica [148, 149], which is generally prepared upon blending the epoxy monomer and silica nanoparticles, followed by the addition of a hardener to perform the curing reaction (e.g., diaminodiphenylmethane [150], diaminodiphenylsulfone [151], diethylphosphite [150], PA-amine [152, 153], or hexahydro-4-methylphthalic anhydride [154]). The compatibility between the epoxide compounds and the colloidal silica was optimized upon mixing the diglycidylether of bisphenol-A together with colloidal suspensions of silica nanoparticles dispersed in methylisobutylketone [150].

Photopolymerization was used as rapid polymerization technique in order to synthesize nanohybrid materials based on acrylate [155–163], epoxy acrylate polymers [164–169], or epoxy polymers [170, 171].

Also, numerous titania-based nanohybrid systems were synthesized by means of in-situ polymerization techniques. For instance, poly(phenylenevinylene) (PPV) was prepared from α,α -dichloro-*p*-xylene and tetrahydrothiophene by following the standard polyelectrolyte route. The polymerization process was carried out in

methanol in the presence of tetrabutylammonium hydroxide as a base catalyst and TiO₂ nanoparticles [118–120, 172].

PS-TiO₂ nanohybrid particles were synthesized in high yield via in-situ polymerization of styrene in the presence of TiO₂ nanoparticles surface-modified with 3-(trimethoxysilyl)-propylmethacrylate (MPS) [173]. The encapsulation of nano-TiO₂ by PS via mini-emulsion polymerization was also reported. In this case, polybutene-succinimide pentamine was used as stabilizer at the oil–water interface [174–176].

PMMA-TiO₂ nanohybrid materials have been obtained by encapsulating surface-modified TiO₂ nanoparticles into a PMMA network. PMMA was synthesized by in-situ radical polymerization of MMA initiated by 2,2'-azobisisobutyronitrile; whereas the surface modification of the TiO₂ nanoparticles was achieved by the formation of a charge transfer complex between the TiO₂ surface and 6-palmitate ascorbic acid [177].

Conventional emulsion polymerization was used to encapsulate TiO₂ within PMMA. Here, titanate-based coupling agents [isopropoxide 3-carboxylic acyl titanate (KR-TTS) and *iso*-propyldimethacryl-*iso*-stearoyl titanate (KR7)] were used to improve the interfacial interaction between TiO₂ and the surrounding polymeric matrix [178, 179]. “Emulsion”-polymerizations were carried out in aqueous dispersions of the TiO₂ nanoparticles, stabilized with an anionic surfactant [178] and polybutene-succinimide pentamine [180] to obtain PMMA-TiO₂-based [178] and PS-TiO₂ nanohybrid materials [136], respectively.

PMMA-TiO₂ and PS-TiO₂ nanohybrid systems were synthesized via pseudo-dispersion polymerization processes in supercritical carbon dioxide in the presence of MPS-modified TiO₂ nanoparticles [181].

Also, processes involving the in-situ formation of a titania-based polymeric gel in the presence of PCL lead to PCL-TiO₂ nanohybrids. Unlike in other systems, the inorganic component is in this case generated in-situ in the presence of the polymeric component [83]. Combinations of sol–gel and in-situ polymerization processes have also been reported. Thus, polybenzoxazine-TiO₂ nanohybrid systems were prepared from titanium *iso*-propoxide and bis(3-phenyl-3,4-dihydro-2H-1,3-benzoxazinyl)isopropane [182].

Epoxy-zirconia nanohybrid materials were synthesized from bisphenol A epoxy resin (diglycidyl ether of bisphenol A), zirconium(IV)-*n*-propoxide, and hexahydrophthalic anhydride using a combined sol–gel/polymerization process. The obtained materials exhibited nanosized zirconia particles uniformly dispersed within the epoxy matrix and, consequently, showed excellent optical transparency [183–185].

PMMA-ZrO₂ nanohybrid particles were synthesized via in-situ polymerization in the presence of surface-modified ZrO₂ (surface modification using a γ -methacryloxypropyl-trimethoxysilane [186, 187]).

Polyhydroxyethylmethacrylate (PHEMA)-ZrO₂ nanohybrid materials were prepared in a one-step process by mixing zirconium alkoxide and 2-hydroxyethyl methacrylate (HEMA) with or without benzoyl peroxide (BPO) [184]. Also, monolithic nanohybrid materials were prepared via in-situ polymerization of HEMA in

the presence of acetylacetonate-functionalized zirconium alkoxides [91, 188]. Furthermore, the synthesis of core-shell ZrO_2 -polyacetoacetoxyethylmethacrylate-PS nanohybrids was accomplished through a combined sol-gel and emulsion polymerization process [189]. For the synthesis of zirconia-polyurethane-acrylate nanohybrid materials, the ZrO_2 nanoparticles were functionalized with MPS and blended with UV-curable urethane-acrylate formulations [190–192].

2.4 Self-Assembly Techniques

The generation of well-defined periodic structures with dimensions below 100 nm has become realizable by established nanolithographic techniques. Novel and efficient protocols to overcome technical obstacles have been reported by combining “top-down” strategies with “bottom-up” approaches. This section focuses on two general “bottom-up” self-assembly techniques for building ceramic nanostructures from polymer-based (pre)ceramic materials: (1) the self-assembly of block copolymers and (2) colloidal crystallization of almost monodisperse organic/inorganic nanoparticles. Block copolymers, i.e., polymers consisting of two or more homogenous polymer fragments that are covalently connected, feature the intrinsic capability to undergo microphase separation yielding manifold fascinating structures ranging from spheres, cylinders, and lamella to co-continuous double gyroid or knitting pattern structures with domain sizes of 10–100 nm [193–195]. The phase separation is dependent on the volume fraction of the block segments, the overall molar mass of the chains, the chain constitution, and the presence of homopolymers, salts, or small organic molecules. Additionally, external parameters such as temperature, the presence of volatile solvents, or magnetic and electrical fields can be applied and varied.

The challenge here is to provide large-area ordering and well-defined orientation of nanodomains above the micron-scale, which is a basic prerequisite for industrial applications and still has issues to date. Improvements to overcome obstacles are based on applying external mechanical flow [196–198], an electric field [199–201], or a magnetic field [202, 203] during block copolymer self-assembly. Novel approaches are based on the concept of guiding the self-assembly on patterned substrates with spatial constraints [204–206] or different wetting properties [207–209]. Usually, most studies on ceramic precursors focus on self-assembly of organic/organic block copolymers followed by removal of one block segment, e.g., by exemplarily hydrolysis [210], UV degradation [211], or ozonolysis [212], while the second residual block segment acts as a place holder. The template nanochannels obtained from the removal of one block copolymer can be subsequently back-filled with inorganic metal particles or inorganic (sol-gel) precursors, followed by etching or calcination in order to remove the residual block segment and to produce void spaces. Besides such incorporation strategies, metals or metal oxides can be generated by various techniques such as electrochemical methods, electroless plating, sol-gel reactions, or seeded growth as mentioned in the previous

sections. As an example, fascinating metal foams featuring an excellent periodic order at the nanoscale can be obtained [213].

Evaporation-induced block copolymer self-assembly techniques in the presence of inorganic precursors or inorganic particles have gained significant attention for their ability to produce mesoporous ceramic materials after thermal removal of the structure-guiding organic segments [214–218]. For the preparation of non-oxide ceramics, di-block copolymers can be used as structure-directing agents for silazane-based pre-ceramic polymers to yield high temperature SiCN ceramic materials [219]. Recently, Wiesner and coworkers reported a general method for the production of templated mesoporous materials based on preformed nanocrystal building blocks. Thus, soluble di-block copolymers mixed with nanocrystals underwent an evaporation-induced self-assembly to yield, after subsequent thermal treatment, nanoporous metal oxides (e.g., manganese oxides [218]).

A further approach to obtaining built-up ceramic structures at the nanoscale focuses on the self-assembly of organic–inorganic block copolymers, with the inorganic block converting into ceramic after thermal treatment. Silicon-containing polymers and block copolymers have spurred much interest among researchers as potential ceramic precursors [220–223]. The self-assembly and pyrolysis of block copolymers comprising an organic and a decaborane segment to yield mesoporous boron nitride was first reported by Malenfant et al. [224].

Manners et al. reported the synthesis of ferrocene-containing polymers as suitable ceramic precursors featuring high ceramic yields after pyrolysis. These self-assembled organic–inorganic block copolymers attracted enormous attention for the preparation of nanostructured iron-based ceramics [225–231]. Tang and coworkers investigated the self-assembly and their template synthesis of tri-block copolymers featuring a polyferrocenyl methacrylate block-copolymer to yield ordered iron oxides [232]. Such metallo-polymers are also suitable for obtaining spherical iron oxide structures after thermal treatment [233].

A second approach for the generation of structured pre-ceramic polymer-based materials that will be briefly addressed here is based on the self-assembly of organic–inorganic core–shell particles, also referred to as colloidal crystallization. The self-assembly of almost monodisperse colloidal micro- and nanoparticles is a feasible method for gaining access to ceramic functional materials for various applications, especially if the final materials feature an optical band gap [234–238]. In general, colloidal crystals can be prepared from their dispersions by various techniques of deposition or spin coating, which are depicted in Fig. 3 [239, 240].

Moreover, the precise arrangement of polymer-based pre-ceramic particles can be improved in flow fields by, e.g., combinations of melting and shear-ordering methods [241–243].

To sum up, the self-assembly technique for preparation of organic or inorganic block copolymers and/or nanoparticles is unambiguously a powerful tool for generating various nanostructured next-generation materials. Such materials are promising candidates for emerging applications in the fields of micro-electronics, energy conversion, optoelectronics, catalysis, and data storage.

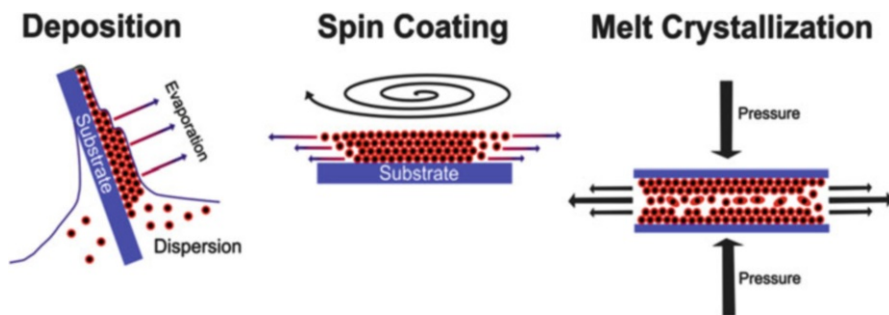


Fig. 3 Common techniques for the self-assembly of monodisperse particle dispersions or ordering in flow fields under pressure

3 Properties and Applications

3.1 Nanohybrid Structural Materials

3.1.1 Coatings

Metal oxides such as SiO_2 , ZrO_2 , Al_2O_3 , and TiO_2 have good chemical stability and are able to protect metal substrates from oxidative and corrosive environment [244–247], but at the same time the oxide coatings are brittle in nature. Thus, it is very challenging to achieve thick coatings to protect metal substrates from corrosion without cracking. At the same time, metal oxide materials are preferred because they exhibit outstanding structural properties [248]. Thus, organic–inorganic hybrid systems have been shown to be highly suitable in order to overcome the limitations related to the brittleness of the ceramic systems [249–252]. The basic application fields for this type of coating are abrasion and scratch resistance, decoration, barrier layers for packaging, corrosion-resistant layers, and antisoiling, antifogging, anti-static, and antireflective applications [253, 254]. Corrosion-protective polymer–ceramic sol–gel coatings on steel substrates using dip-coating techniques have been reported and are summarized in Table 1.

Crack-free polyvinyl butyral- SiO_2 coatings with thickness of ca. 1 μm were deposited on Zn-plated steel substrate and were shown to provide excellent protection against corrosion [255]. Various hybrid coating formulations have been prepared by combining the sol–gel-synthesized ceramic particles (Al_2O_3 , SiO_2) with water-soluble epoxy resin. The coatings showed enhanced mechanical strength such as hardness and abrasion resistance. When cured at elevated temperatures, most of the studied hybrid coatings showed good behavior during wet adhesion testing, although most were water-sensitive when cured at room temperature [244].

The behavior of 316L stainless steel in corrosive conditions was improved upon deposition of nanohybrid coatings based on PMMA- ZrO_2 . The coatings were deposited via dip-coating of sols prepared by mixing zirconium propoxide and

Table 1 Corrosion protective sol–gel coatings on steel substrates using dip coating

Compositions and precursors	Substrate	Thickness (μm)	References
SiO ₂ -PMMA	Steel	1.0	[255]
ZrO ₂ -PMMA	Steel	0.2	[252]
ZrO ₂ -PMMA	Steel	0.2–1.0	[249]
SiO ₂ -PVB	Steel	1.0	[255]
SiO ₂ -PMMA	Aluminum	0.1–0.3	[255]
SiO ₂ -PVB	Aluminum	0.1–0.3	[255]
SiO ₂ -vinylpolymer	Aluminum	3–4	[256]
Ce-SiO ₂ -epoxy	Aluminum	2–3	[257]
ZrO ₂ -TiO ₂ -oil	Aluminum	45–95	[258]

PMMA in a mixture of *iso*-propanol, glacial acetic acid, and water; drying at 50°C for 15 min; and firing at 200°C for 30 min. The use of PMMA-ZrO₂ coatings on the stainless steel was shown to increase its life-time by a factor of up to 30 [249, 252].

Nanohybrid films consisting of titania nanotubes dispersed within a PS matrix were prepared via solution casting. Because titania nanotubes are inherently insulating, they can be used to reinforce insulating polymers without changing their electronic behavior. Thus, PS films reinforced with TiO₂ nanotubes exhibited an 18% increase in Young's modulus and up to 30% increase in tensile strength as compared to PS films. This significant effect was observed at extremely low nanotube loading levels (1 wt%) [259]. Furthermore, the wear resistance of PS-TiO₂ films was improved over that of titania-free PS films [260]. Polydimethylsiloxane (PDMS)-TiO₂ nanohybrid films were prepared via spray coating and exhibited promising photocatalytic activity concerning the decomposition of methylene blue [261].

3.1.2 Bulk Materials

Highly crosslinked polymers have many useful structural properties, such as high Young's modulus and failure strength, low creep, and good stability at elevated temperatures. However, their highly crosslinked structure leads to a brittle behavior, i.e., they exhibit poor resistance to crack initiation and growth. The incorporation of ceramic dispersed phases into the polymer matrix was consequently used to improve the fracture toughness.

Epoxy-based polymeric materials are widely used in the aerospace, automobile, and wind-energy industries due to their outstanding structural stability. Numerous studies were performed in order to understand the effect of silica incorporation within epoxy resins on their mechanical properties [262–264]. It was shown that the incorporation of silica nanoparticles into the epoxy polymer leads to a significant increase in both its fracture toughness K_{Ic} and the cyclic-fatigue behavior [265, 266]. Recently, silica nanoparticles were used to reinforce an epoxy polymer (cured by piperidine). It was shown that the fracture toughness of the nanohybrid material increases steadily as the concentration of silica nanoparticles increases; although

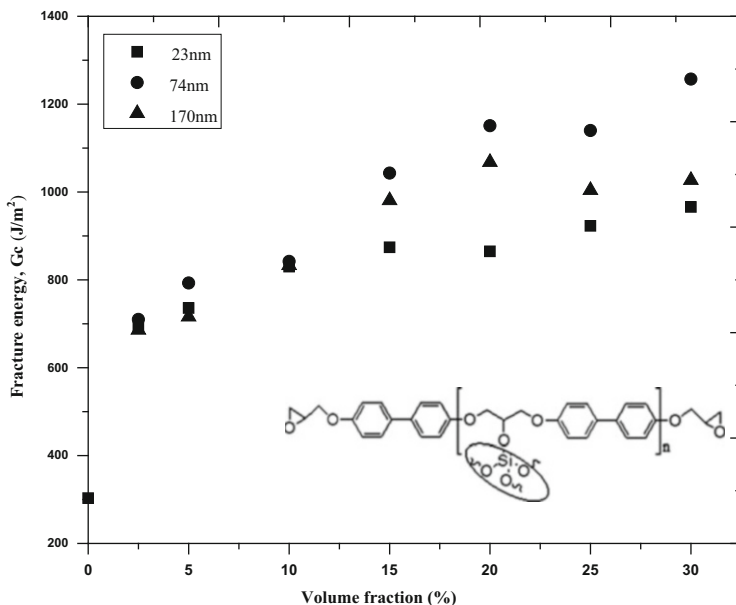


Fig. 4 Fracture energy of epoxy–silica nanohybrid materials as a function of the silica loading, for nanoparticles of three different sizes (adapted from [267], open-access Elsevier)

no significant effect of the size of the silica nanoparticles was observed (Fig. 4) [267].

Even at low silica loadings (e.g., 5 wt% silica), nylon-6–silica nanohybrid materials exhibited a markedly increased tensile strength (by 15%), strain-to-fracture (by 150%), Young’s modulus (by 23%), and impact strength (by 78%) compared with the silica-free polymer [138].

The mechanical properties of PA-based polymers can also be enhanced through the incorporation of inorganic micro- and nanofillers such as silica nanoparticles. Thus, the maximum value of stress at yield point (72 MPa) was observed in hybrid materials containing 10 wt% silica and the maximum stress at break point increased up to 66 MPa in PA-silica hybrids containing 20 wt% silica (compared with 44 MPa for the silica-free PA system). Also, the tensile modulus was found to increase up to 2.59 GPa upon incorporation of 10 wt% silica within the polymeric matrix [268].

SiO₂ nanoparticles grafted with terminally hydroxylated PP (PP-*g*-SiO₂) were melt-mixed with PP to prepare PP-PP-*g*-SiO₂ nanohybrids. PP-PP-*g*-SiO₂ offered advantages as there was more than 30% increment in both the Young’s modulus and the tensile strength as compared to PP [269].

Also, the addition of a 4.5% volume fraction of surface-modified Al₂O₃ nanoparticles to an unsaturated polyester led to a significant increase (by almost 100%) in its fracture toughness [270]. The wear resistance of polytetrafluoroethylene (PTFE) can be similarly increased by a factor of 600 upon addition of 20 wt% alumina nanoparticles [271]. The steady-state wear rates of polyphenylene

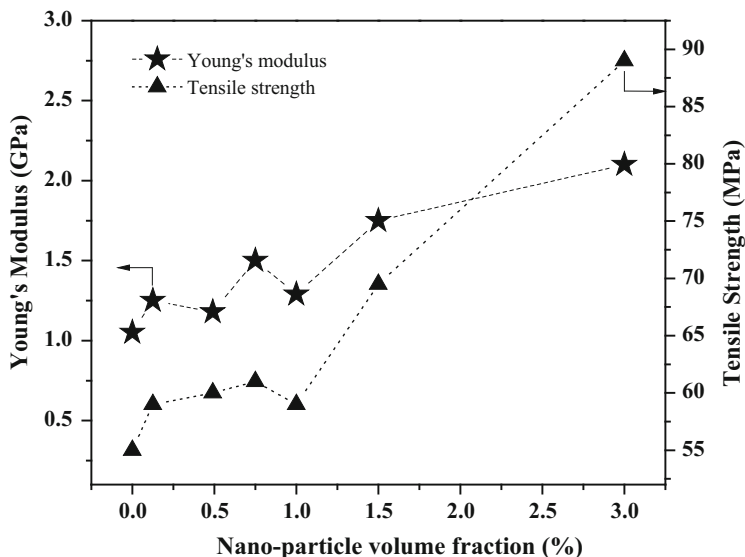


Fig. 5 Tensile strength and Young's modulus of vinyl ester-alumina nanohybrids as a function of the nanoparticle volume fraction (adapted from [274])

sulfide (measured against steel counter faces) were significantly reduced by the addition of 1–2 vol% alumina nanoparticles; whereas large volume fractions of alumina had the opposite effect because the wear rates increased [272].

The addition of Al_2O_3 nanoparticles into a polymer matrix is expected to improve the mechanical properties of polymer without sacrificing the corrosion resistance of the polymer itself. Thus, polymer nanohybrid coatings based on Xylan 1810/D1864 (a commercially available PTFE blend) containing 20 wt% of Al_2O_3 nanoparticles exhibited improved microhardness and scratching resistance (58–62 HV and 59.5 mN, respectively) as compared to the alumina-free polymer coating (55 HV and 28.5 mN, respectively) [273].

The addition of alumina nanoparticles to a vinyl ester resin was shown to improve its Young's modulus and strength (Fig. 5). Thus, the Young's modulus of the polymer–ceramic nanohybrid material containing 3 vol% of alumina nanoparticles increased by 85% as compared to the pure resin; whereas the tensile strength seems to be increased only slightly (55 MPa for the resin; ~56 MPa for the nanohybrid). Surface modification of the alumina nanoparticles with MPS was observed to have little effect on the Young's modulus compared with the nanohybrids containing unmodified alumina nanoparticles; however, the strength of the nanohybrid containing 3 vol% of surface-modified alumina increased by approximately 60% compared with the pure resin (unlike the addition of nonmodified nanoparticles, as mentioned before); this was stated to rely on the strong interaction between the alumina nanoparticles and the resin matrix [274].

The scratch resistance and the toughness of epoxy-based materials were markedly improved by loading it with 10 wt% TiO₂ nanoparticles. The effect was shown to be more significant than that of the incorporation of microparticles within the epoxy matrix [275]. Furthermore, it was demonstrated that the tribological performance of epoxy-TiO₂ nanohybrid materials strongly depends on the dispersion quality of the filler, i.e., the microstructural homogeneity of the composites [276]. A loading as low as 1 vol% of TiO₂ nanoparticles with a size of 21 nm contributed to a significant improvement in the creep resistance of polyamide 6,6 at both room and elevated temperatures [270]. The presence of the TiO₂ particles within the polyester matrix strongly affects its quasi-static fracture toughness, even at volume fractions as low as 1, 2, and 3 vol%, which lead to an increase in toughness of 57, 42, and 41%, respectively, as compared to the neat polyester material [277].

3.2 Nanohybrid Functional Materials

3.2.1 Electrical Materials

The electrical conductivity of poly(2-chloroaniline) (P2ClAn) was improved by almost two orders of magnitude by incorporation of silica nanoparticles (values of 4.6×10^{-7} and 1.3×10^{-5} S cm⁻¹ for P2ClAn and SiO₂-P2ClAn, respectively). This effect was stated to rely on an increased efficiency of the charge transfer between SiO₂ and polymer chains [278].

The synthesis of PANI-TiO₂ nanohybrids was performed by in situ polymerization of aniline in the presence of TiO₂ nanoparticles. The as-synthesized nanocomposite films showed appreciable electrical conductivity (1–10 S/cm), which further increased upon thermal treatment at 80°C [279]. Thus, the electrical conductivity of PANI (6.28×10^{-9} S/m) can be enhanced through the addition of TiO₂, which leads to the formation of a more efficient network for charge transport within the PANI-based matrix [280].

PMMA-grafted titanium dioxide (PMMA-*g*-TiO₂), was synthesized by atom-transfer-radical polymerization (ATRP) and subsequently incorporated into PVDF membranes. The incorporation of PMMA-*g*-TiO₂ was shown to improve the ionic conductivity of the polymeric electrolyte from 2.51×10^{-3} (as for PVdF) to 2.95×10^{-3} S cm⁻¹ (as for the nanohybrid material) [281].

PVDF-HFP films filled with nanoscaled TiO₂ particles exhibited room-temperature ionic conductivities larger than 10^{-3} S cm⁻¹, making them suitable for rechargeable lithium batteries. The nanohybrid materials having 30–40 wt% rutile TiO₂ incorporated within the PVDF-HFP matrix were shown to be the most suitable polymer electrolytes for lithium ion battery applications [282]. Also, gel polymer electrolyte films based on thermoplastic polyurethanes (TPU)/PVDF were investigated with respect to their potential to be used in lithium ion batteries. Thus, neat gel TPU/PVDF films as well as films filled with SiO₂ and TiO₂ nanoparticles were prepared by electrospinning of a polymer solution at room temperature.

A TPU–PVDF membrane containing 3 wt% TiO₂ nanoparticles exhibited the highest ionic conductivity of $4.8 \times 10^{-3} \text{ S cm}^{-1}$ out of all the prepared nanohybrid membranes. Additionally, it presented an electrochemical stability up to 5.4 V versus Li⁺/Li at room temperature, as well as high tensile strength (8.7 MPa) and elongation at break of 110.3% [283].

Nanohybrid polymer electrolytes based on PVDF–HFP and lithium fluoroalkylphosphate were also prepared using ethylene carbonate and diethyl carbonate as plasticizers and Al₂O₃ nanoparticles as filler. The electrolyte containing 2.5 wt% Al₂O₃ exhibited a conductivity of $9.8 \times 10^{-4} \text{ S cm}^{-1}$ at ambient temperature, which was slightly higher than the conductivity of the alumina-free material ($5.1 \times 10^{-4} \text{ S cm}^{-1}$). It was also found that filler contents above 2.5 wt% rendered the membranes less conducting [284]. However, addition of the Al₂O₃ nanopowder significantly improved the mechanical stability of the polymer electrolyte without significantly affecting its electrical conductivity [285].

The concept of nanohybrid materials has been also used for preparing materials with high dielectric constant (high κ materials), which are useful as capacitors and gate materials in integrated electronic circuits. Synthesis of high κ materials has been shown to be of fundamental relevance for the development of new generation dynamic random access memories and micro-electromechanical systems.

Nanohybrid films based on PMMA–TMSPM–SiO₂ exhibited unusually high values for the dielectric constant (between 5 and 14). Such high dielectric constant values were attributed to highly polarizable OH and C=C groups in the hybrid films, the OH groups being part of the residual precursor solvents and the presence of C=C resulting from the incomplete conversion of the precursor monomer (MMA) into PMMA [286, 287]. PANI–TiO₂ nanohybrid materials were also shown to exhibit high dielectric constants; they combine the large band gap and high dielectric constant of TiO₂ with the good thermal stability of PANI [288]. Thus, the dielectric constant of PANI was significantly increased (to 25.5; measured at 1 MHz) upon incorporation of 5 wt% of TiO₂ [280]. Also, epoxy-based nanohybrids containing insulating nanofillers such as TiO₂, ZnO and Al₂O₃ at low filler weight fractions presented interesting dielectric permittivities and dielectric losses [289].

3.2.2 Optical Materials

Ceramic nanoparticles such as TiO₂, Al₂O₃, and ZrO₂ show promising optical properties and thus can be used as “optically effective additives”; while polymers such as PMMA or PS can be used as transparent polymer matrix materials [290, 291]. Hence, new optoelectronic materials based on nanohybrids have been extensively reported and found application in optical coatings (i.e., transparent films with high resistance to cracking and excellent adhesion) [292], color filters for liquid crystal displays [293], high refractive index devices [89, 117], contact lenses [294], optical waveguides [295], and nonlinear optical devices [296]).

UV-absorbing pigments are widely used as additives in order to increase the long-term stability of the polymers or to prepare UV-protective coatings. They obviously have to show high photostability and a high transparency in the visible range, together with a steep absorption in the near UV range ($\lambda < 400$ nm); the most prominent representative within this context is titania, TiO_2 [297].

The UV-vis light transmittance spectra of pure PVA and its nanohybrid films containing different volume fractions of TiO_2 nanoparticles have been studied. The overall light transmittance of PVA-based nanohybrids decreases with increased loading of the TiO_2 nanoparticles. The observed absorption of the nanohybrid materials takes place in the UV region, indicating that they might be suitable as UV-shielding coatings [21]. Optically transparent nanohybrid materials derived from TiO_2 and PMMA were also reported [298] and show promising characteristics as nonlinear optical materials. They show a unique optical behavior with a strong dependence (and consequently tunability) of the two-photon absorption coefficient and the nonlinear refractive index on titania loading [299, 300].

Because epoxy resins have excellent optical transparency, thermal stability, and mechanical properties, they are widely used in coating compounds, adhesive agents, and encapsulation materials. They are particularly suitable for encapsulation of light-emitting diodes (LEDs). In this type of application, a high refractive index is required in order to provide high light extraction efficiencies [301]. Epoxy-based hybrid materials with inorganic nanofillers exhibiting high refractive indices (~ 1.62) have therefore been prepared [90, 124, 301–303].

Acetic-acid-modified TiO_2 nanoparticles can be incorporated into transparent polymers to form transparent nanohybrid thin films with high refractive index (e.g., as high as 2.38) and excellent optical transparency in the visible region [304]. In PS- TiO_2 nanohybrids prepared via melt compounding, the coating of the rutile TiO_2 nanoparticles with SiO_2 or Al_2O_3 led to nanohybrid materials with outstanding photocatalytic stability and excellent retention of tensile and impact properties [305].

PMMA- SiO_2 nanohybrid films were also reported to have excellent optical transparency and tunable refractive index (1.447–1.49 at 633 nm, depending on the silica loading) [286]. Transparent PA- SiO_2 nanohybrid films with high mechanical strength were prepared and their maximum transmittance was found for 5 wt% silica loading [268]. This class of nanohybrid system has been used in optoelectronic and photonic fields, nonlinear optics, as optical guides, in photorefractive materials, and in aerospace and microelectronic devices [306].

PMMA- SiO_2 - ZrO_2 nanohybrid films were prepared successfully using a novel non-hydrolytic sol-gel process and, owing to their excellent optical transparency combined with high thermal stability, were stated to have high potential in applications for optical devices at elevated temperatures [307].

The optical properties of nanohybrid materials can be improved if the dispersed nanoparticles are surface-treated: a better transmittance was reported for PMMA- Al_2O_3 nanohybrids containing silane-treated alumina nanoparticles [308] and for PC- Al_2O_3 materials containing poly(styrene-maleic anhydride)-copolymer-treated

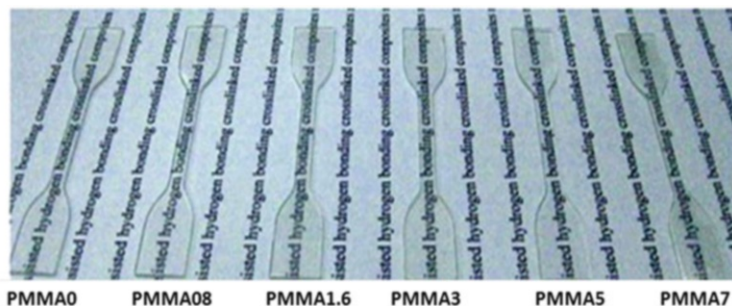


Fig. 6 Highly transparent PMMA- and PMMA/ZrO₂-based samples containing different amounts of ZrO₂ nanoparticles (from [310], with permission from Elsevier)

alumina nanoparticles [309] than for the analogous nanohybrids containing non-surface-treated nanoparticles.

Figure 6 shows dumbbell-shaped neat PMMA and PMMA-ZrO₂ nanohybrid samples containing various amounts ZrO₂ nanoparticles [310]. All samples were highly transparent; the difference in their optical transparency cannot be distinguished with the naked eye, although slight reduction in the transparency was observed with increasing ZrO₂ content and was attributed to the existence of a few ZrO₂ agglomerates [310].

3.2.3 Membranes

Polymer–inorganic nanohybrid membranes represent an interesting approach for improving the separation properties of membranes because they possess the properties of both organic and inorganic membranes such as good permeability, selectivity, mechanical strength, and thermal and chemical stability [311]. Thus, nanohybrid materials can expand the application field of membranes. For instance, the current spectrum of applications for gas-separation membranes include nitrogen enrichment, oxygen enrichment, hydrogen recovery, acid gas (CO₂, H₂S) removal from natural gas, and dehydration of air and natural gas [312, 313].

PI-SiO₂ materials have received special attention for gas permeation applications, which require high chemical and thermal stability of the membranes [96, 314–316]. PI-SiO₂ nanohybrid membranes exhibited higher gas permeabilities, without a large reduction of the permselectivity, as compared to a polyimide membrane [317, 318]. PI-SiO₂-based membranes with relatively large contents of silica nanoparticles (32 wt%) were prepared via sol–gel processing from TMOS and polyamic acid and subsequent thermal imidization (at 60–300°C). They exhibit a higher permeability for CO₂ (PCO₂ = 2.8 Barrer; 1 Barrer = 10⁻¹⁰ cm³(STP) cm/(cm² s) cmHg [319]) and a greater CO₂/N₂ selectivity (α_{CO₂/N₂} = 22) as compared to silica-free PI membranes (PCO₂ = 1.8 Barrer; α_{CO₂/N₂} = 18) [314, 320]. Poly(1-trimethylsilyl-1-propyne) (PTMSP) has the highest gas permeability of all

existing polymers; however, it exhibits a rather poor chemical stability, which can be improved by crosslinking although this affects its permeability. The addition of ceramic nanoparticles (SiO_2 , TiO_2) into the PTMSP matrix was found to be useful for increasing the permeability of the polymer after the crosslinking [321, 322].

Silica nanoparticles were employed to obtain inorganic–organic hybrid coatings via UV curing of an epoxy-based system. The strong decrease in water uptake in the presence of SiO_2 makes these nanocomposite materials particularly interesting for gas-barrier coating applications [171].

Nanohybrid membranes based on TiO_2 and fluorinated PAI were fabricated by the sol–gel method and investigated with respect to their gas separation performance. A specific interaction between gases such as CO_2 and H_2 and the TiO_2 nanoparticles was observed. Selectivities for CO_2/CH_4 and H_2/CH_4 of 33 and 51, respectively, were reported in nanohybrid membranes containing low concentrations of TiO_2 (i.e., 7.3 wt%) [323]. Higher TiO_2 contents resulted in a greater enhancement of the gas separation performance. The H_2 and O_2 permeabilities of the membrane with 25 wt% TiO_2 were 14.1 and 0.72 Barrer, respectively, and were 3.7 times and 4.3 times higher than those of the pure PI. The selectivities of H_2/N_2 and O_2/N_2 ($\alpha_{\text{H}_2/\text{N}_2} = 188$, $\alpha_{\text{O}_2/\text{N}_2} = 9.5$) were also slightly improved compared to those of the pure polymer membrane ($\alpha_{\text{H}_2/\text{N}_2} = 167$, $\alpha_{\text{O}_2/\text{N}_2} = 9.3$) [324].

PVAc- TiO_2 nanohybrid membranes were produced by using the solution casting method. Their permeability for O_2 , CO_2 , and H_2 was increased by 95, 79, and 62%, respectively, with respect to those of the pure PVAc membrane. Also, the selectivity values for the gas pairs O_2/N_2 , H_2/N_2 , CO_2/N_2 were increased by 38, 26.5, and 14%, respectively [325].

Recently, a novel cardo-type PI (cardo polymers contain at least one element in the repeating unit that is included in the cyclic side group [326]) based on 3,3',4,4'-benzophenone-tetracarboxylic dianhydride (BTDA), 9,9'-bis (4-aminophenyl) fluorine (BAPF) and 4,4'-biamino-3,3'-dimethyldiphenyl-methane (DMMDA) was used to prepare gas-separation membranes (Fig. 7). Blending of TiO_2 nanoparticles and the mentioned cardo-type PI resulted in PI- TiO_2 nanohybrids, which were also used for the preparation of mixed matrix membranes. The nanohybrid PI- TiO_2 membranes exhibited gas permeation (PO_2) of 4.5 Barrer and outstanding separation factor ($\alpha_{\text{O}_2/\text{N}_2}$) of 15.8, which were 9.4 and 4.6 times higher, respectively, than those of the titania-free PI-based membrane [327].

Nanohybrid materials have been furthermore used for ultra-/nanofiltration applications. Nanofiltration is a pressure-driven membrane separation process and can be used for the production of drinking water as well as for the treatment of process and waste waters. Some applications are desalination of brackish water, water softening, removal of micropollutants, and retention of dyes. Ultrafiltration membranes based on polysulfones filled with zirconia nanoparticles are usually prepared via a phase-inversion technique and have been used since 1990 [328]. Various studies were done in order to assess the effect of the addition of ZrO_2 to polysulfone-based ultrafiltration membranes [329] and the influence of filler loading on the compaction and filtration properties of membranes. The results indicate that the elastic strain of the nanohybrid membranes decreases and the time-dependent strain

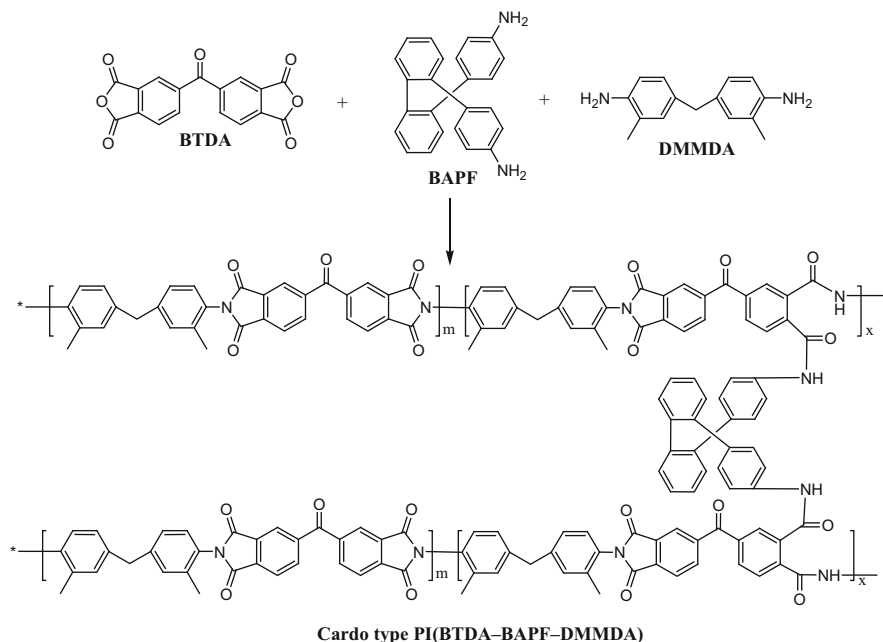


Fig. 7 Preparation path for PI(BTDA–BAPF–DMMDA) (from [327], with permission from Elsevier)

increases as the amount of the nanofiller is increased. In addition, the data reveal that the initial flux increases with increasing nanofiller content; however, the flux declines at higher filler concentrations as well as at higher pressures [330]. Table 2 shows selected published results related to the gas-separation performance data of different polymer–ceramic hybrid membranes.

Furthermore, PVDF-based polymeric membranes as well as PVDF–ZrO₂ and PVDF–Al₂O₃ nanohybrid membranes were prepared and studied with respect to their ultrafiltration performance [345]. For instance, the incorporation of Al₂O₃ nanoparticles to PVDF resulted in nanohybrid ultrafiltration membranes with improved performance as compared to the filler-free PVDF membranes [346].

Polymer electrolyte membranes (proton exchange membranes, PEMs) represent one of the classes of membranes with high relevance for fuel cells, such as proton exchange membrane fuel cells (PEMFC) and direct methanol fuel cells (DMFC). State-of-the-art DMFCs and hydrogen/air fuel cells are based on Nafion as it provides high protonic conductivity and good mechanical and chemical stability. However, due to the reduced performance of Nafion at temperatures above 80°C, together with its high methanol crossover and costs, there is much interest in alternative materials for PEMs. Within this context, the preparation of various nanohybrid PEMs consisting of polymer–SiO₂ (PEO, polypropylene oxide, polytetramethylene oxide) was reported [347–349]. For instance, poly(ethylene glycol) (PEG)–SiO₂ nanohybrid materials [350, 351] were prepared via sol–gel

Table 2 Reported data related to the gas-separation performance of nanohybrid membranes

Hybrid material	P_{CO_2} (Barrer)	P_{CH_4} (Barrer)	P_{N_2} (Barrer)	P_{O_2} (Barrer)	P_{H_2} (Barrer)	α_{CO_2/N_2}	α_{O_2/N_2}	α_{H_2/N_2}	α_{CO_2/CH_4}	α_{CO_2/H_2}	References
PTMSP-SiO ₂	39,280		8,210	11,960	22,960	2.2	1.5	2.8	2.1	2.1	[331]
BPPOdm-SiO ₂	523	34.9	24.9		21				15		[332]
PMP-SiO ₂	11,250		1,780	3,380	6,430	6.3	1.9	3.6			[322]
BPPOdp-SiO ₂	177								15.3		[333]
PU-SiO ₂	120		2.98	7.69	40.26	2.58			13.43		[334]
PI-SiO ₂	2.03		0.1	0.38	20.3	3.8					[320]
PI-SiO ₂	2.8	0.2	0.13		22				14		[314]
PAN-SiO ₂			0.17	2.6			14.9				[335]
PI-SiO ₂	41		7.74		10.3	5.3		1.33		4	[316]
PI-SiO ₂	80	2.16	5		16				37		[336]
PI-SiO ₂	19	0.08	0.46		41				238		[337]
PI-SiO ₂	15		0.3	2.61		50	8.7				[318]
BPPOdp-SiO ₂	436	27.3	15		29				16		[338]
PEBAX-SiO ₂	277		3.52	11.3	79	3.2					[339]
PEG-SiO ₂	67				7.36					9.1	[340]
PEG-SiO ₂	94.2		2.46		38.3						[341]
PPEG-SiO ₂	125		1.4		89						[342]
PS-C60			0.56	2.4			4.3				[343]
PTMSP-SiO ₂		4,234									[321]
PMP-SiO ₂		1,157									[344]
PTMSP-TiO ₂	38,980		7,950	11,540	22,810	4.90	1.5	2.9	2.1		[331]
PMP-TiO ₂	10,970		1,680	3,420	6,270	6.5	1.9	3.7	3.1, 3.2		[322]
PAI-TiO ₂	50		3.4	13.8	100	14.7	4.05	29.41			[323]
PI-TiO ₂			0.07	0.72	14.14		9.5	187.5			[324]
PVAc-TiO ₂	5.26		0.07	0.5	9.2	74.32	7.1	130			[325]

processes and used for the preparation of electrolytic membranes in DMFCs. The synthesis of the nanohybrid materials was performed by means of condensation-polymerization of TEOS in the presence of PEG. Additionally, sulfonated poly(styrene-*co*-maleic anhydride) was attached to the polymeric backbone by hydrogen bonding. The prepared nanohybrid membranes were shown to have performances in DMFC applications comparable with that of Nafion 117, although improved thermal stability [61].

A series of organic–inorganic nanohybrid materials based on PEG-SiO₂ to be used as electrolytic membranes in DMFC have been synthesized. In order to provide the proton conductivity, the network structure of the nanohybrid membranes was modified with 4-dodecylbenzene sulfonic acid [352, 353].

A significant improvement in the performance of DMFC was achieved upon using sPPEK-SiO₂ nanohybrid membranes, which were shown to perform significantly better than the analogous sPPEK membrane and even better than Nafion 117 [354].

PVDF-based ultrafiltration nanohybrid membranes prepared via an immersion-precipitation method using PHEMA-*block*-PMMA-grafted silica nanoparticles as additives were shown to increase the pure water flux, improve the bovine serum albumin (BSA) rejection to a high level (>90%), and reduce membrane fouling at the same time [355].

3.2.4 Biomaterials

It is known that silica-based glass is bioactive because it is able to bond to living bone [356]. As reported in the literature, the essential condition for glasses and glass-ceramics to bond to living bone is the formation of a bone-like apatite layer on their surfaces, which is studied via *in vitro* studies after soaking the bioactive materials in a simulated body fluid [357, 358]. Within this context, glass–polymer hybrid materials were recognized to have high potential because they combine the bioactive properties of glasses or glass-ceramics with the elasticity of polymeric materials and are, consequently, interesting materials for orthopedic applications [359, 360].

The bioactivity of the PCL-SiO₂ hybrid system demonstrated by the formation of a layer of hydroxyapatite on the surface of samples soaked in a fluid simulating the composition of human blood plasma [358, 361]. Studies on the bioactivity of PMMA-SiO₂ nanohybrid materials has indicated that they are suitable materials for use as bioactive bone substitutes or as nanofillers for PMMA bone cement [362].

Furthermore, PMMA-CaO-SiO₂ nanohybrid materials were shown to be suitable for bone cement and dental composite resin applications, due to their good bioactivity and improved mechanical properties [363]. PDMS-zirconia nanohybrids were proposed as suitable materials for tissue-implant integration purposes because they have beneficial effects on the proliferation and viability of human primary osteoblast and fibroblast cells and thus can be used as promising coatings for orthopedic trauma implants [364].

4 Conclusions

This paper summarizes the different preparative techniques for polymer–ceramic-based nanohybrid materials. Various classes and types of polymer–ceramic nanohybrid materials can be prepared using different techniques such as advanced blending techniques, in-situ polymerization, sol–gel-approaches, or self-assembly processes to yield nanohybrid materials with unique microstructures and properties, which are dictated in most cases by the nanoscale dimensions of the phases and by the interfaces between the polymeric matrix and the ceramic nanoparticles. Furthermore, selected structural and functional properties of polymer–ceramic nanohybrids as well as their advanced and prospective applications are addressed.

Due to the unique microstructures and property profiles of polymer–ceramic nanohybrid materials as well as their high versatility and controllable preparation, polymer–ceramic nanohybrids represent a highly emerging class of multifunctional materials that are expected to be relevant for advanced applications such as catalysis, sensing, optoelectronics, biomedicine, and energy harvesting, conversion, and storage.

References

1. Matic P (2003) Overview of multifunctional materials. In: Lagoudas DC (ed) *Smart structures and materials 2003: active materials: behavior and mechanics*. In: SPIE Proceedings 5053. SPIE, Bellingham, WA. doi:[10.1117/12.498546](https://doi.org/10.1117/12.498546)
2. Christodoulou L, Venables J (2003) Multifunctional material systems: the first generation. *JOM* 55(12):39–45
3. Schottner G (2001) Hybrid sol–gel-derived polymers: applications of multifunctional materials. *Chem Mater* 13(10):3422–3435
4. Avnir D, Coradin T, Lev O, Livage J (2006) Recent bio-applications of sol–gel materials. *J Mater Chem* 16(11):1013
5. Alexandra Fidalgo RC, Laura MI, Mario P (2005) Role of the alkyl-alkoxide precursor on the structure and catalytic properties of hybrid sol–gel catalysts. *Chem Mater* 17:6686–6694
6. Minghuo W, Ren'an W, Fangjun W, Lianbing R, Jing D, Zhen L, Hanfa Z (2009) “One-Pot” process for fabrication of organic-silica hybrid monolithic capillary columns using organic monomer and alkoxysilane. *Anal Chem* 81:3529–3536
7. Wu M, Wu R, Zhang Z, Zou H (2011) Preparation and application of organic-silica hybrid monolithic capillary columns. *Electrophoresis* 32(1):105–115
8. Weng X, Bao Z, Xing H, Zhang Z, Yang Q, Su B, Yang Y, Ren Q (2013) Synthesis and characterization of cellulose 3,5-dimethylphenylcarbamate silica hybrid spheres for enantioseparation of chiral beta-blockers. *J Chromatogr A* 1321:38–47
9. Ashby MF, Bréchet YJM (2003) Designing hybrid materials. *Acta Mater* 51(19):5801–5821
10. Sanchez C, Julián B, Belleville P, Popall M (2005) Applications of hybrid organic–inorganic nanocomposites. *J Mater Chem* 15(35–36):3559
11. Mammari F, Bourhis EL, Rozes L, Sanchez C (2005) Mechanical properties of hybrid organic–inorganic materials. *J Mater Chem* 15(35–36):3787
12. KICKELBICK G (2007) Introduction to hybrid materials. In: KICKELBICK G (ed) *Hybrid materials*. Wiley-VCH, Weinheim, pp 1–48

13. Tai CY, Hsiao B-Y, Chiu H-Y (2007) Preparation of silazane grafted yttria-stabilized zirconia nanocrystals via water/CTAB/hexanol reverse microemulsion. *Mater Lett* 61 (3):834–836
14. Tai CY, Lee MH, Wu YC (2001) Control of zirconia particle size by using two-emulsion precipitation technique. *Chem Eng Sci* 56(7):2389–2398
15. Rahman IA, Padavettan V (2012) Synthesis of silica nanoparticles by sol–gel: size-dependent properties, surface modification, and applications in silica-polymer nanocomposites—a review. *J Nanomater* 2012:1–15
16. Chandradass J, Bae D-S (2008) Synthesis and characterization of alumina nanoparticles by Igepal CO-520 stabilized reverse micelle and sol–gel Processing. *Mater Manuf Process* 23 (5):494–498
17. Malik MA, Wani MY, Hashim MA (2012) Microemulsion method: a novel route to synthesize organic and inorganic nanomaterials. *Arabian J Chem* 5(4):397–417
18. Dawson WJ (1988) Hydrothermal synthesis of advanced ceramic powders. *Am Ceram Soc Bull* 67(10):1673–1678
19. Dell’Agli G, Mascolo G (2000) Hydrothermal synthesis of ZrO_2 – Y_2O_3 solid solutions at low temperature. *J Eur Ceram Soc* 20(2):139–145
20. Lee S, Shin H-J, Yoon S-M, Yi DK, Choi J-Y, Paik U (2008) Refractive index engineering of transparent ZrO_2 –polydimethylsiloxane nanocomposites. *J Mater Chem* 18(15):1751
21. Mallakpour S, Barati A (2011) Efficient preparation of hybrid nanocomposite coatings based on poly(vinyl alcohol) and silane coupling agent modified TiO_2 nanoparticles. *Progr Org Coating* 71(4):391–398
22. Mo T-C, Wang H-W, Chen S-Y, Dong R-X, Kuo C-H, Yeh Y-C (2007) Synthesis and characterization of polyimide–silica nanocomposites using novel fluorine-modified silica nanoparticles. *J Appl Polym Sci* 104(2):882–890
23. Takai C, Fuji M, Takahashi M (2007) A novel surface designed technique to disperse silica nano particle into polymer. *Colloids Surf A Physicochem Eng Asp* 292(1):79–82
24. Tang JC, Lin GL, Yang HC, Jiang GJ, Chen-Yang YW (2007) Polyimide-silica nanocomposites exhibiting low thermal expansion coefficient and water absorption from surface-modified silica. *J Appl Polym Sci* 104(6):4096–4105
25. Tang JC, Yang HC, Chen SY, Chen-Yang YW (2007) Preparation and properties of polyimide/silica hybrid nanocomposites. *Polymer Compos* 28(5):575–581
26. Kango S, Kalia S, Celli A, Njuguna J, Habibi Y, Kumar R (2013) Surface modification of inorganic nanoparticles for development of organic–inorganic nanocomposites—a review. *Progr Polym Sci* 38(8):1232–1261
27. Chen C (2011) The manufacture of polymer nanocomposite materials using supercritical carbon dioxide. Virginia Polytechnic Institute and State University, Blacksburg VA
28. Rong MZ, Zhang MQ, Zheng YX, Zeng HM, Walter R, Friedrich K (2001) Structure–property relationships of irradiation grafted nano-inorganic particle filled polypropylene composites. *Polymer* 42(1):167–183
29. Zou H, Wu S, Shen J (2008) Polymer/silica nanocomposites: preparation, characterization, properties, and applications. *Chem Rev* 108(9):3893–3957
30. Rong M, Zhang M, Zheng Y, Zeng H, Walter R, Friedrich K (2000) Irradiation graft polymerization on nano-inorganic particles: An effective means to design polymer-based nanocomposites. *J Mater Sci Lett* 19(13):1159–1161
31. Wu C, Zhang M, Rong M, Friedrich K (2005) Silica nanoparticles filled polypropylene: effects of particle surface treatment, matrix ductility and particle species on mechanical performance of the composites. *Compos Sci Technol* 65(3–4):635–645
32. Rong MZ, Zhang MQ, Zheng YX, Zeng HM, Friedrich K (2001) Improvement of tensile properties of nano- SiO_2 /PP composites in relation to percolation mechanism. *Polymer* 42 (7):3301–3304
33. Ruan W, Zhang M, Rong M, Friedrich K (2004) Polypropylene composites filled with in-situ grafting polymerization modified nano-silica particles. *J Mater Sci* 39(10):3475–3478

34. Rong MZ, Zhang MQ, Pan SL, Friedrich K (2004) Interfacial effects in polypropylene–silica nanocomposites. *J Appl Polym Sci* 92(3):1771–1781
35. Ruan WH, Mai YL, Wang XH, Rong MZ, Zhang MQ (2007) Effects of processing conditions on properties of nano-SiO₂/polypropylene composites fabricated by pre-drawing technique. *Compos Sci Technol* 67(13):2747–2756
36. Wu CL, Zhang MQ, Rong MZ, Friedrich K (2002) Tensile performance improvement of low nanoparticles filled-polypropylene composites. *Compos Sci Technol* 62(10–11):1327–1340
37. Cai LF, Huang XB, Rong MZ, Ruan WH, Zhang MQ (2006) Effect of grafted polymeric foaming agent on the structure and properties of nano-silica/polypropylene composites. *Polymer* 47(20):7043–7050
38. Zhang MQ, Rong MZ, Zhang HB, Friedrich K (2003) Mechanical properties of low nano-silica filled high density polyethylene composites. *Polym Eng Sci* 43(2):490–500
39. Bikiaris DN, Papageorgiou GZ, Pavlidou E, Vouroutzis N, Palatzoglou P, Karayannidis GP (2006) Preparation by melt mixing and characterization of isotactic polypropylene/SiO₂ nanocomposites containing untreated and surface-treated nanoparticles. *J Appl Polym Sci* 100(4):2684–2696
40. Cai LF, Huang XB, Rong MZ, Ruan WH, Zhang MQ (2006) Fabrication of nanoparticle/polymer composites by in situ bubble-stretching and reactive compatibilization. *Macromol Chem Phys* 207(22):2093–2102
41. Bikiaris DN, Vassiliou A, Pavlidou E, Karayannidis GP (2005) Compatibilisation effect of PP-g-MA copolymer on iPP/SiO₂ nanocomposites prepared by melt mixing. *Eur Polym J* 41(9):1965–1978
42. Takahashi S, Paul DR (2006) Gas permeation in poly(ether imide) nanocomposite membranes based on surface-treated silica. Part 1: without chemical coupling to matrix. *Polymer* 47(21):7519–7534
43. Takahashi S, Paul DR (2006) Gas permeation in poly(ether imide) nanocomposite membranes based on surface-treated silica. Part 2: with chemical coupling to matrix. *Polymer* 47(21):7535–7547
44. Merkel TC, Toy LG, Andrady AL, Gracz H, Stejskal EO (2002) Investigation of enhanced free volume in nanosilica-filled poly(1-trimethylsilyl-1-propyne) by ¹²⁹Xe NMR spectroscopy. *Macromolecules* 36(2):353–358
45. Winberg P, DeSitter K, Dotremont C, Mullens S, Vankelecom IFJ, Maurer FHJ (2005) Free volume and interstitial mesopores in silica filled poly(1-trimethylsilyl-1-propyne) nanocomposites. *Macromolecules* 38(9):3776–3782
46. De Sitter K, Winberg P, D’Haen J, Dotremont C, Leysen R, Martens JA, Mullens S, Maurer FHJ, Vankelecom IFJ (2006) Silica filled poly(1-trimethylsilyl-1-propyne) nanocomposite membranes: relation between the transport of gases and structural characteristics. *J Membr Sci* 278(1–2):83–91
47. Kelman SD, Matteucci S, Bielawski CW, Freeman BD (2007) Crosslinking poly(1-trimethylsilyl-1-propyne) and its effect on solvent resistance and transport properties. *Polymer* 48(23):6881–6892
48. Merkel TC, He ZJ, Pinnau I, Freeman BD, Meakin P, Hill AJ (2003) Sorption and transport in poly(2,2-bis(trifluoromethyl)-4,5-difluoro-1,3-dioxole-co-tetrafluoroethylene) containing nanoscale fumed silica. *Macromolecules* 36(22):8406–8414
49. Kim SH, Ahn SH, Hirai T (2003) Crystallization kinetics and nucleation activity of silica nanoparticle-filled poly(ethylene 2,6-naphthalate). *Polymer* 44(19):5625–5634
50. Ahn SH, Kim SH, Lee SG (2004) Surface-modified silica nanoparticle-reinforced poly(ethylene 2,6-naphthalate). *J Appl Polym Sci* 94(2):812–818
51. Bikiaris D, Karavelidis V, Karayannidis G (2006) A new approach to prepare poly(ethylene terephthalate)/silica nanocomposites with increased molecular weight and fully adjustable branching or crosslinking by SSP. *Macromol Rapid Commun* 27(15):1199–1205

52. Cannillo V, Bondioli F, Lusvardi L, Montorsi M, Avella M, Errico ME, Malinconico M (2006) Modeling of ceramic particles filled polymer–matrix nanocomposites. *Compos Sci Technol* 66(7–8):1030–1037
53. Avella M, Bondioli F, Cannillo V, Pace ED, Errico ME, Ferrari AM, Focher B, Malinconico M (2006) Poly(ϵ -caprolactone)-based nanocomposites: influence of compatibilization on properties of poly(ϵ -caprolactone)–silica nanocomposites. *Compos Sci Technol* 66(7–8):886–894
54. Avella M, Bondioli F, Cannillo V, Errico ME, Ferrari AM, Focher B, Malinconico M, Manfredini T, Montorsi M (2004) Preparation, characterisation and computational study of poly(ϵ -caprolactone) based nanocomposites. *Mater Sci Technol* 20(10):1340–1344
55. Lim JS, Noda I, Im SS (2007) Effect of hydrogen bonding on the crystallization behavior of poly(3-hydroxybutyrate-co-3-hydroxyhexanoate)/silica hybrid composites. *Polymer* 48(9):2745–2754
56. Yan S, Yin J, Yang Y, Dai Z, Ma J, Chen X (2007) Surface-grafted silica linked with L-lactic acid oligomer: a novel nanofiller to improve the performance of biodegradable poly(L-lactide). *Polymer* 48(6):1688–1694
57. van Zyl WE, Garcia M, Schrauwen BAG, Kooi BJ, De Hosson JTM, Verweij H (2002) Hybrid polyamide/silica nanocomposites: synthesis and mechanical testing. *Macromol Mater Eng* 287(2):106–110
58. Su Y, Liu Y, Sun Y, Lai J, Wang D, Gao Y, Liu B, Guiver M (2007) Proton exchange membranes modified with sulfonated silica nanoparticles for direct methanol fuel cells. *J Membr Sci* 296(1–2):21–28
59. Lai YH, Kuo MC, Huang JC, Chen M (2007) On the PEEK composites reinforced by surface-modified nano-silica. *Mater Sci Eng A* 458(1–2):158–169
60. Wu Z, Han H, Han W, Kim B, Ahn KH, Lee K (2007) Controlling the hydrophobicity of submicrometer silica spheres via surface modification for nanocomposite applications. *Langmuir* 23(14):7799–7803
61. Oberdisse J, Deme B (2002) Structure of latex-silica nanocomposite films: a small-angle neutron scattering study. *Macromolecules* 35(11):4397–4405
62. Oberdisse J (2002) Structure and rheological properties of latex-silica nanocomposite films: stress-strain isotherms. *Macromolecules* 35(25):9441–9450
63. Oberdisse J, El Harrak A, Carrot G, Jestin J, Boué F (2005) Structure and rheological properties of soft–hard nanocomposites: influence of aggregation and interfacial modification. *Polymer* 46(17):6695–6705
64. Zhang Q, Archer LA (2004) Optical polarimetry and mechanical rheometry of Poly(ethylene oxide) – silica dispersions. *Macromolecules* 37(5):1928–1936
65. Zhang Q, Archer LA (2002) Poly(ethylene oxide)/silica nanocomposites: structure and rheology. *Langmuir* 18(26):10435–10442
66. Boisvert J-P, Persello J, Guyard A (2003) Influence of the surface chemistry on the structural and mechanical properties of silica-polymer composites. *J Polym Sci B Polym Phys* 41(23):3127–3138
67. Bansal A, Yang H, Li C, Benicewicz BC, Kumar SK, Schadler LS (2006) Controlling the thermomechanical properties of polymer nanocomposites by tailoring the polymer–particle interface. *J Polym Sci B Polym Phys* 44(20):2944–2950
68. Inoubli R, Dagreou S, Lapp A, Billon L, Peyrelasse J (2006) Nanostructure and mechanical properties of polybutylacrylate filled with grafted silica particles. *Langmuir* 22(15):6683–6689
69. Hong RY, Fu HP, Zhang YJ, Liu L, Wang J, Li HZ, Zheng Y (2007) Surface-modified silica nanoparticles for reinforcement of PMMA. *J Appl Polym Sci* 105(4):2176–2184
70. Wang Y-J, Kim D (2007) Crystallinity, morphology, mechanical properties and conductivity study of in situ formed PVDf/LiClO₄/TiO₂ nanocomposite polymer electrolytes. *Electrochim Acta* 52(9):3181–3189

71. Yoshida M, Lal M, Kumar ND, Prasad PN (1997) TiO₂ nano-particle-dispersed polyimide composite optical waveguide materials through reverse micelles. *J Mater Sci* 32(15):4047–4051
72. Nussbaumer RJ, Caseri WR, Smith P, Tervoort T (2003) Polymer-TiO₂ nanocomposites: a route towards visually transparent broadband UV filters and high refractive index materials. *Macromol Mater Eng* 288(1):44–49
73. Carter SA, Scott JC, Brock PJ (1997) Enhanced luminance in polymer composite light emitting devices. *Appl Phys Lett* 71(9):1145–1147
74. Li M, Zhou S, You B, Wu L (2005) Study on acrylic resin/alumina hybrid materials prepared by the sol–gel process. *J Macromol Sci B* 44(4):481–494
75. Bhimaraj P, Burris DL, Action J, Sawyer WG, Toney CG, Siegel RW, Schadler LS (2005) Effect of matrix morphology on the wear and friction behavior of alumina nanoparticle/poly (ethylene) terephthalate composites. *Wear* 258(9):1437–1443
76. Naderi N, Sharifi-Sanjani N, Khayyat-Naderi B, Faridi-Majidi R (2006) Preparation of organic–inorganic nanocomposites with core-shell structure by inorganic powders. *J Appl Polym Sci* 99(6):2943–2950
77. Hench LL, West JK (1990) The sol–gel process. *Chem Rev* 90(1):33–72
78. Roy R (1993) Evolution of the solution-sol–gel process – from homogeneity to heterogeneity in 35 years. *Abstr Pap Am Chem S* 205:65
79. Roy R (1981) Sol–gel process – origins, products, problems. *Am Ceram Soc Bull* 60(3):363–363
80. Sakka S (2013) Sol–gel process and applications. In: Somiya S (ed) *Handbook of advanced ceramics*, 2nd edn. Academic, Oxford, pp 883–910
81. Mark JE (1996) Ceramic-reinforced polymers and polymer-modified ceramics. *Polym Eng Sci* 36(24):2905–2920
82. Novak BM (1993) Hybrid nanocomposite materials-between inorganic glasses and organic polymers. *Adv Mater* 5(6):422–433
83. Wu CS (2004) In situ polymerization of titanium isopropoxide in polycaprolactone: properties and characterization of the hybrid nanocomposites. *J Appl Polym Sci* 92(3):1749–1757
84. Durand N, Boutevin B, Silly G, Améduri B (2011) “Grafting From” polymerization of vinylidene fluoride (VDF) from silica to achieve original silica–PVDF core–shells. *Macromolecules* 44(21):8487–8493
85. Przemyslaw P, Robert P, Hieronim M (2013) New approach to preparation of gelatine/SiO₂ hybrid systems by the sol–gel process. *Ceramics Silikáty* 57(1):58–65
86. Joni IM, Purwanto A, Iskandar F, Okuyama K (2009) Dispersion stability enhancement of titania nanoparticles in organic solvent using a bead mill process. *Ind Eng Chem Res* 48(15):6916–6922
87. Sarwar MI, Ahmad Z (2000) Interphase bonding in organic–inorganic hybrid materials using aminophenyltrimethoxysilane. *Eur Polym J* 36(1):89–94
88. Xiong M, Zhou S, Wu L, Wang B, Yang L (2004) Sol–gel derived organic–inorganic hybrid from trialkoxysilane-capped acrylic resin and titania: effects of preparation conditions on the structure and properties. *Polymer* 45(24):8127–8138
89. Wang B, Wilkes GL, Hedrick JC, Liptak SC, Mcgrath JE (1991) New high refractive-index organic inorganic hybrid materials from sol–gel processing. *Macromolecules* 24(11):3449–3450
90. Nakayama N, Hayashi T (2007) Preparation and characterization of TiO₂ and polymer nanocomposite films with high refractive index. *J Appl Polym Sci* 105(6):3662–3672
91. Saegusa T (1991) Organic polymer-silica gel hybrid: a precursor of highly porous silica gel. *J Macromol Sci A Chem* 28(9):817–829
92. Kobayashi S, Kaku M, Saegusa T (1988) Grafting of 2-oxazolines onto cellulose and cellulose diacetate. *Macromolecules* 21(7):1921–1925
93. Silveira KF, Yoshida IVP, Nunes SP (1995) Phase-separation in Pmma silica sol–gel systems. *Polymer* 36(7):1425–1434

94. Nakanishi K, Soga N (1992) Phase separation in silica sol–gel system containing polyacrylic acid II. Effects of molecular weight and temperature. *J Non Crystal Solids* 139:14–24
95. Nakanishi K, Soga N (1992) Phase separation in silica sol–gel system containing polyacrylic acid I. Gel formation behavior and effect of solvent composition. *J Non Crystal Solids* 139:1–13
96. Nunes SP, Peinemann KV, Ohlrogge K, Alpers A, Keller M, Pires ATN (1999) Membranes of poly(ether imide) and nanodispersed silica. *J Membr Sci* 157(2):219–226
97. Sengupta R, Bandyopadhyay A, Sabharwal S, Chaki TK, Bhowmick AK (2005) Polyamide-6,6/in situ silica hybrid nanocomposites by sol–gel technique: synthesis, characterization and properties. *Polymer* 46(10):3343–3354
98. Fitzgerald JJ, Landry CJT, Pochan JM (1992) Dynamic studies of the molecular relaxations and interactions in microcomposites prepared by in-situ polymerization of silicon alkoxides. *Macromolecules* 25(14):3715–3722
99. Landry CJT, Coltrain BK, Landry MR, Fitzgerald JJ, Long VK (1993) Poly(vinyl acetate)/silica-filled materials: material properties of in situ vs fumed silica particles. *Macromolecules* 26(14):3702–3712
100. Landry CJT, Coltrain BK, Wesson JA, Zumbulyadis N, Lippert JL (1992) In situ polymerization of tetraethoxysilane in polymers: chemical nature of the interactions. *Polymer* 33(7):1496–1506
101. Stefanithis ID, Mauritz KA (1990) Microstructural evolution of a silicon oxide phase in a perfluorosulfonic acid ionomer by an in situ sol–gel reaction. 3. Thermal analysis studies. *Macromolecules* 23(8):2397–2402
102. Zoppi RA, Castro CR, Yoshida IVP, Nunes SP (1997) Hybrids of SiO₂ and poly(amide 6-b-ethylene oxide). *Polymer* 38(23):5705–5712
103. Chang C-C, Chen W-C (2002) Synthesis and optical properties of polyimide-silica hybrid thin films. *Chem Mater* 14(10):4242–4248
104. Tsai MH, Whang WT (2001) Low dielectric polyimide/poly(silsesquioxane)-like nanocomposite material. *Polymer* 42(9):4197–4207
105. Wang S, Ahmad Z, Mark JE (1994) Polyimide-silica hybrid materials modified by incorporation of an organically substituted alkoxy silane. *Chem Mater* 6(7):943–946
106. Srinivasan SA, Hedrick JL, Miller RD, Di Pietro R (1997) Crosslinked networks based on trimethoxysilyl functionalized poly(amic ethyl ester) chain extendable oligomers. *Polymer* 38(12):3129–3133
107. Chen Y, Iroh JO (1999) Synthesis and characterization of polyimide silica hybrid composites. *Chem Mater* 11(5):1218–1222
108. Shang XY, Zhu ZK, Yin J, Ma XD (2002) Compatibility of soluble polyimide/silica hybrids induced by a coupling agent. *Chem Mater* 14(1):71–77
109. Mascia L, Kioul A (1995) Influence of siloxane composition and morphology on properties of polyimide-silica hybrids. *Polymer* 36(19):3649–3659
110. Schrotter JC, Smaih M, Guizard C (1996) Polyimide-siloxane hybrid materials: influence of coupling agents addition on microstructure and properties. *J Appl Polym Sci* 61(12):2137–2149
111. Hsiue G-H, Chen J-K, Liu Y-L (2000) Synthesis and characterization of nanocomposite of polyimide–silica hybrid from nonaqueous sol–gel process. *J Appl Polym Sci* 76(11):1609–1618
112. Lee T, Park SS, Jung Y, Han S, Han D, Kim I, Ha C-S (2009) Preparation and characterization of polyimide/mesoporous silica hybrid nanocomposites based on water-soluble poly(amic acid) ammonium salt. *Eur Polym J* 45(1):19–29
113. Hsiue GH, Kuo WJ, Huang YP, Jeng RJ (2000) Microstructural and morphological characteristics of PS-SiO₂ nanocomposites. *Polymer* 41(8):2813–2825
114. Pierre AC, Campet G, Han SD, Duguet E, Portier J (1994) TiO₂-polymer Nano-composites by sol–gel. *J Sol Gel Sci Technol* 2(1–3):121–125

115. Hu Q, Marand E (1999) In situ formation of nanosized TiO₂ domains within poly(amide-imide) by a sol-gel process. *Polymer* 40(17):4833-4843
116. Chiang P-C, Whang W-T (2003) The synthesis and morphology characteristic study of BAO-ODPA polyimide/TiO₂ nano hybrid films. *Polymer* 44(8):2249-2254
117. Lee L-H, Chen W-C (2001) High-refractive-index thin films prepared from trialkoxysilane-capped poly(methyl methacrylate) - titania materials. *Chem Mater* 13(3):1137-1142
118. Zhang J, Wang BJ, Ju X, Liu T, Hu TD (2001) New observations on the optical properties of PPV/TiO₂ nanocomposites. *Polymer* 42(8):3697-3702
119. Zhang J, Ju X, Wang BJ, Li QS, Liu T, Hu TD (2001) Study on the optical properties of PPV/TiO₂ nanocomposites. *Synthetic Met* 118(1-3):181-185
120. Zhang J, Wu ZY, Ju X, Wang BJ, Li QS, Hu TD, Ibrahim K, Xie YN (2003) The interfacial structure of PPV/TiO₂ nanocomposite. *Opt Mater* 21(1-3):573-578
121. Lin Y-T, Zeng T-W, Lai W-Z, Chen C-W, Lin Y-Y, Chang Y-S, Su W-F (2006) Efficient photoinduced charge transfer in TiO₂ nanorod/conjugated polymer hybrid materials. *Nanotechnology* 17(23):5781-5785
122. Fan Q, McQuillin B, Bradley DDC, Whitelegg S, Seddon AB (2001) A solid state solar cell using sol-gel processed material and a polymer. *Chem Phys Lett* 347(4-6):325-330
123. Savitha KU, Prabu HG (2013) Polyaniline-TiO₂ hybrid-coated cotton fabric for durable electrical conductivity. *J Appl Polym Sci* 127(4):3147-3151
124. Guan C, Lü C-L, Liu Y-F, Yang B (2006) Preparation and characterization of high refractive index thin films of TiO₂/epoxy resin nanocomposites. *J Appl Polym Sci* 102(2):1631-1636
125. Lu CL, Cui ZC, Wang YX, Yang B, Shen JC (2003) Studies on syntheses and properties of episulfide-type optical resins with high refractive index. *J Appl Polym Sci* 89(9):2426-2430
126. Seyedjamali H, Pirisedigh A (2011) Synthesis of well-dispersed polyimide/TiO₂ nanohybrid films using a pyridine-containing aromatic diamine. *Polym Bull* 68(2):299-308
127. Liaw W-C, Chen K-P (2007) Preparation and characterization of poly(imide siloxane) (PIS)/titania(TiO₂) hybrid nanocomposites by sol-gel processes. *Eur Polym J* 43(6):2265-2278
128. Tsai M-H, Liu S-J, Chiang P-C (2006) Synthesis and characteristics of polyimide/titania nano hybrid films. *Thin Solid Films* 515(3):1126-1131
129. Tsai M-H, Chang C-J, Chen P-J, Ko C-J (2008) Preparation and characteristics of poly (amide-imide)/titania nanocomposite thin films. *Thin Solid Films* 516(16):5654-5658
130. Li M, Zhou S, You B, Wu L (2006) Preparation and characterization of trialkoxysilane-containing acrylic resin/alumina hybrid materials. *Macromol Mater Eng* 291(8):984-992
131. Kaneko Y, Iyi N, Kurashima K, Matsumoto T, Fujita T, Kitamura K (2004) Hexagonal-structured polysiloxane material prepared by sol-gel reaction of aminoalkyltrialkoxysilane without using surfactants. *Chem Mater* 16(18):3417-3423
132. Kaneko Y, Iyi N, Matsumoto T, Kitamura K (2005) Synthesis of rodlike polysiloxane with hexagonal phase by sol-gel reaction of organotrialkoxysilane monomer containing two amino groups. *Polymer* 46(6):1828-1833
133. Kaneko Y, Iyi N (2007) Sol-gel synthesis of rodlike polysilsesquioxanes forming regular higher-ordered nanostructure. *Z Kristallogr* 222(11/2007)
134. Kaneko Y, Toyodome H, Shoiriki M, Iyi N (2012) Preparation of ionic silsesquioxanes with regular structures and their hybridization. *Int J Polym Sci* 2012:1-14
135. Kaneko Y, Arake T (2012) Sol-gel preparation of highly water-dispersible silsesquioxane/zirconium oxide hybrid nanoparticles. *Int J Polym Sci* 2012:1-6
136. Rehman HU, Sarwar MI, Ahmad Z, Krug H, Schmidt H (1997) Synthesis and characterization of novel aramid-zirconium oxide micro-composites. *J Non Crystal Solids* 211(1-2):105-111
137. Hajji P, David L, Gerard JF, Pascault JP, Vigier G (1999) Synthesis, structure, and morphology of polymer-silica hybrid nanocomposites based on hydroxyethyl methacrylate. *J Polym Sci B Polym Phys* 37(22):3172-3187

138. Ou Y, Yang F, Yu Z-Z (1998) A new conception on the toughness of nylon 6/silica nanocomposite prepared via in situ polymerization. *J Polym Sci B Polym Phys* 36(5):789–795
139. Yang F, Ou YC, Yu ZZ (1998) Polyamide 6 silica nanocomposites prepared by in situ polymerization. *J Appl Polym Sci* 69(2):355–361
140. Reynaud E, Jouen T, Gauthier C, Vigier G, Varlet J (2001) Nanofillers in polymeric matrix: a study on silica reinforced PA6. *Polymer* 42(21):8759–8768
141. Liu WT, Tian XY, Cui P, Li Y, Zheng K, Yang Y (2004) Preparation and characterization of PET/Silica nanocomposites. *J Appl Polym Sci* 91(2):1229–1232
142. Yang Y, Xu H, Gu H (2006) Preparation and crystallization of poly(ethylene terephthalate)/SiO₂ nanocomposites by in-situ polymerization. *J Appl Polym Sci* 102(1):655–662
143. Zheng H, Wu J (2007) Preparation, crystallization, and spinnability of poly(ethylene terephthalate)/silica nanocomposites. *J Appl Polym Sci* 103(4):2564–2568
144. Sugimoto H, Daimatsu K, Nakanishi E, Ogasawara Y, Yasumura T, Inomata K (2006) Preparation and properties of poly(methylmethacrylate)–silica hybrid materials incorporating reactive silica nanoparticles. *Polymer* 47(11):3754–3759
145. Liu Y-L, Hsu C-Y, Hsu K-Y (2005) Poly(methylmethacrylate)-silica nanocomposites films from surface-functionalized silica nanoparticles. *Polymer* 46(6):1851–1856
146. Yang F, Nelson GL (2004) PMMA/silica nanocomposite studies: synthesis and properties. *J Appl Polym Sci* 91(6):3844–3850
147. Kashiwagi T, Morgan AB, Antonucci JM, VanLandingham MR, Harris RH, Awad WH, Shields JR (2003) Thermal and flammability properties of a silica–poly(methylmethacrylate) nanocomposite. *J Appl Polym Sci* 89(8):2072–2078
148. Zhang HJ, Yao X, Zhang LY (2002) The preparation and microwave properties of Ba₃ZnZCo₂-ZFe₂₄O₄₁/SiO₂ microcrystalline glass ceramics by citrate sol–gel process. *Mater Res Innov* 5(3–4):117–122
149. Zhang QJ, Zhang JH, Li M, Zhang QH, Qin Y (2002) Interface structures of Al₂O₃-ZrO₂ coated engineering ceramics by sol–gel process. *J Inorg Mater* 17(1):185–188
150. Liu Y-L, Hsu C-Y, Wei W-L, Jeng R-J (2003) Preparation and thermal properties of epoxy-silica nanocomposites from nanoscale colloidal silica. *Polymer* 44(18):5159–5167
151. Ragosta G, Abbate M, Musto P, Scarinzi G, Mascia L (2005) Epoxy-silica particulate nanocomposites: chemical interactions, reinforcement and fracture toughness. *Polymer* 46(23):10506–10516
152. Preghenella M, Pegoretti A, Migliaresi C (2005) Thermo-mechanical characterization of fumed silica-epoxy nanocomposites. *Polymer* 46(26):12065–12072
153. Preghenella M, Pegoretti A, Migliaresi C (2006) Atomic force acoustic microscopy analysis of epoxy–silica nanocomposites. *Polym Test* 25(4):443–451
154. Sun Y, Zhang Z, Moon K-S, Wong CP (2004) Glass transition and relaxation behavior of epoxy nanocomposites. *J Polym Sci B Polym Phys* 42(21):3849–3858
155. Berriot J, Lequeux F, Monnerie L, Montes H, Long D, Sotta P (2002) Filler–elastomer interaction in model filled rubbers, a ¹H NMR study. *J Non Crystal Solids* 307–310:719–724
156. Berriot J, Montes H, Martin F, Mauger M, Pyckhout-Hintzen W, Meier G, Frielinghaus H (2003) Reinforcement of model filled elastomers: synthesis and characterization of the dispersion state by SANS measurements. *Polymer* 44(17):4909–4919
157. Berriot J, Martin F, Montes H, Monnerie L, Sotta P (2003) Reinforcement of model filled elastomers: characterization of the cross-linking density at the filler–elastomer interface by ¹H NMR measurements. *Polymer* 44(5):1437–1447
158. Saric M, Dietsch H, Schurtenberger P (2006) In situ polymerisation as a route towards transparent nanocomposites: Time-resolved light and neutron scattering experiments. *Colloids Surf A Physicochem Eng Asp* 291(1–3):110–116
159. Kim S, Kim E, Kim S, Kim W (2005) Surface modification of silica nanoparticles by UV-induced graft polymerization of methyl methacrylate. *J Colloid Interface Sci* 292(1):93–98

160. Hsiao Shu C, Chiang H-C, Chien-Chao Tsiang R, Liu T-J, Wu J-J (2007) Synthesis of organic–inorganic hybrid polymeric nanocomposites for the hard coat application. *J Appl Polym Sci* 103(6):3985–3993
161. Bauer F, Flyunt R, Czihal K, Buchmeiser MR, Langguth H, Mehnert R (2006) Nano/micro particle hybrid composites for scratch and abrasion resistant polyacrylate coatings. *Macromol Mater Eng* 291(5):493–498
162. Wang Y-Y, Hsieh T-E (2007) Effect of UV curing on electrical properties of a UV-curable copolyacrylate/silica nanocomposite as a transparent encapsulation resin for device packaging. *Macromol Chem Phys* 208(22):2396–2402
163. Berriot J, Montes H, Lequeux F, Long D, Sotta P (2002) Evidence for the shift of the glass transition near the particles in silica-filled elastomers. *Macromolecules* 35(26):9756–9762
164. Zhang L, Zeng Z, Yang J, Chen Y (2003) Structure–property behavior of UV-curable polyepoxy–acrylate hybrid materials prepared via sol–gel process. *J Appl Polym Sci* 87(10):1654–1659
165. Xu GC, Li AY, Zhang LD, Wu G, Yuan XY, Xie T (2003) Synthesis and characterization of silica nanocomposite in situ photopolymerization. *J Appl Polym Sci* 90(3):837–840
166. Xu GC, Li AY, De Zhang L, Yu XY, Xie T, Wu GS (2004) Nanomechanic properties of polymer-based nanocomposites with nanosilica by nanoindentation. *J Reinf Plast Comp* 23(13):1365–1372
167. Li F, Zhou S, Wu L (2005) Preparation and characterization of UV-curable MPS-modified silica nanocomposite coats. *J Appl Polym Sci* 98(5):2274–2281
168. Li F, Zhou S, Wu L (2005) Effects of preparation method on microstructure and properties of UV-curable nanocomposite coatings containing silica. *J Appl Polym Sci* 98(3):1119–1124
169. Li F, Zhou S, You B, Wu L (2006) Kinetic investigations on the UV-induced photopolymerization of nanocomposites by FTIR spectroscopy. *J Appl Polym Sci* 99(4):1429–1436
170. Cho J-D, Ju H-T, Park Y-S, Hong J-W (2006) Kinetics of cationic photopolymerizations of UV-curable epoxy-based SU8-negative photoresists with and without silica nanoparticles. *Macromol Mater Eng* 291(9):1155–1163
171. Sangermano M, Malucelli G, Amerio E, Priola A, Billi E, Rizza G (2005) Photopolymerization of epoxy coatings containing silica nanoparticles. *Progr Org Coating* 54(2):134–138
172. Wang M, Wang X (2008) PPV/TiO₂ hybrid composites prepared from PPV precursor reaction in aqueous media and their application in solar cells. *Polymer* 49(6):1587–1593
173. Rong Y, Chen H-Z, Wu G, Wang M (2005) Preparation and characterization of titanium dioxide nanoparticle/polystyrene composites via radical polymerization. *Mater Chem Phys* 91(2–3):370–374
174. Erdem B, Sudol ED, Dimonie VL, El-Aasser MS (2000) Encapsulation of inorganic particles via miniemulsion polymerization. I. Dispersion of titanium dioxide particles in organic media using OLOA 370 as stabilizer. *J Polym Sci Pol Chem* 38(24):4419–4430
175. Erdem B, Sudol ED, Dimonie VL, El-Aasser MS (2000) Encapsulation of inorganic particles via miniemulsion polymerization. II. Preparation and characterization of styrene miniemulsion droplets containing TiO₂ particles. *J Polym Sci Pol Chem* 38(24):4431–4440
176. Erdem B, Sudol ED, Dimonie VL, El-Aasser MS (2000) Encapsulation of inorganic particles via miniemulsion polymerization. III. Characterization of encapsulation. *J Polym Sci Pol Chem* 38(24):4441–4450
177. Džunuzović E, Jeremić K, Nedeljković JM (2007) In situ radical polymerization of methyl methacrylate in a solution of surface modified TiO₂ and nanoparticles. *Eur Polym J* 43(9):3719–3726
178. Caris CHM, Kuijpers RPM, van Herk AM, German AL (1990) Kinetics of (CO)polymerizations at the surface of inorganic submicron particles in emulsion-like systems. *Makromol Chem Macromol Symp* 35–36(1):535–548

179. Kim SH, Kwak S-Y, Suzuki T (2006) Photocatalytic degradation of flexible PVC/TiO₂ nanohybrid as an eco-friendly alternative to the current waste landfill and dioxin-emitting incineration of post-use PVC. *Polymer* 47(9):3005–3016
180. Da ZL (2007) Synthesis, characterization and thermal properties of inorganic–organic hybrid. *eXPRESS Polym Lett* 1(10):698–703
181. Matsuyama K, Mishima K (2009) Preparation of poly(methyl methacrylate)–TiO₂ nanoparticle composites by pseudo-dispersion polymerization of methyl methacrylate in supercritical CO₂. *J Supercrit Fluid* 49(2):256–264
182. Agag T, Tsuchiya H, Takeichi T (2004) Novel organic–inorganic hybrids prepared from polybenzoxazine and titania using sol–gel process. *Polymer* 45(23):7903–7910
183. Ochi M, Nii D, Harada M (2011) Preparation of epoxy/zirconia hybrid materials via in situ polymerization using zirconium alkoxide coordinated with acid anhydride. *Mater Chem Phys* 129(1–2):424–432
184. Ochi M, Nii D, Suzuki Y, Harada M (2010) Thermal and optical properties of epoxy/zirconia hybrid materials synthesized via in situ polymerization. *J Mater Sci* 45(10):2655–2661
185. Ochi M, Nii D, Harada M (2010) Effect of acetic acid content on in situ preparation of epoxy/zirconia hybrid materials. *J Mater Sci* 45(22):6159–6165
186. Fan F, Xia Z, Li QS, Li Z, Chen H (2013) ZrO₂/PMMA nanocomposites: preparation and its dispersion in polymer matrix. *Chin J Chem Eng* 21(2):113–120
187. Hu Y, Zhou S, Wu L (2009) Surface mechanical properties of transparent poly(methyl methacrylate)/zirconia nanocomposites prepared by in situ bulk polymerization. *Polymer* 50(15):3609–3616
188. Di Maggio R, Fambri L, Mustarelli P, Campostrini R (2003) Physico-chemical characterization of hybrid polymers obtained by 2-hydroxyethyl(methacrylate) and alkoxides of zirconium. *Polymer* 44(24):7311–7320
189. Wang J, Shi T, Jiang X (2008) Synthesis and characterization of core-shell ZrO₂/PAAEM/PS nanoparticles. *Nanoscale Res Lett* 4(3):240–246
190. Xu K, Zhou S, Wu L (2009) Effect of highly dispersible zirconia nanoparticles on the properties of UV-curable poly(urethane-acrylate) coatings. *J Mater Sci* 44(6):1613–1621
191. Zhou S, Wu L (2008) Phase separation and properties of UV-curable polyurethane/zirconia nanocomposite coatings. *Macromol Chem Phys* 209(11):1170–1181
192. Xu K, Zhou S, Wu L (2010) Dispersion of γ -methacryloxypropyltrimethoxysilane-functionalized zirconia nanoparticles in UV-curable formulations and properties of their cured coatings. *Progr Org Coating* 67(3):302–310
193. Bates FS, Fredrickson GH (1999) Block copolymers—designer soft materials. *Phys Tod* 52(2):32
194. Hamley IW (1998) *The physics of block copolymers*. Oxford University Press, Oxford
195. Khandpur KA, Förster SJ, Bates SF, Hamley WI, Ryan JA, Brass W, Almdal K, Mortensen K (1995) Polyisoprene-polystyrene diblock copolymer phase diagram near the order-disorder transition. *Macromolecules* 28:8796–8806
196. Meins T, Hyun K, Dingenouts N, Fotouhi Ardakani M, Struth B, Wilhelm M (2012) New insight to the mechanism of the shear-induced macroscopic alignment of diblock copolymer melts by a unique and newly developed Rheo–SAXS combination. *Macromolecules* 45(1):455–472
197. Albalak RJ, Thomas EL (1993) Microphase separation of block copolymer solutions in a flow field. *J Polym Sci B Polym Phys* 31:37–46
198. Angelescu DA, Waller JH, Adamson DH, Deshpande P, Chou SY, Register RA, Chaikin PM (2004) Macroscopic orientation of block copolymer cylinders in single-layer films by shearing. *Adv Mater* 16:1736–1740
199. Olszowka V, Tsarkova L, Böker A (2009) 3-Dimensional control over lamella orientation and order in thick block copolymer films. *Soft Matter* 5(4):812
200. Xiang H, Lin Y, Russell PT (2004) Electrically induced patterning in block copolymer films. *Macromolecules* 37:5358

201. Böker A, Knoll A, Elbs H, Abetz V, Müller AHE, Krausch G (2002) Large scale domain alignment of a block copolymer from solution using electric fields. *Macromolecules* 35:1319–1325
202. McCulloch B, Portale G, Bras W, Pople JA, Hexemer A, Segalman RA (2013) Dynamics of magnetic alignment in rod–coil block copolymers. *Macromolecules* 46(11):4462–4471
203. Osuji C, Ferreira JP, Mao G, Ober KC, Van der Sande BJ, Thomas LE (2004) Alignment of self-assembled hierarchical microstructure in liquid crystalline diblock copolymers using high magnetic fields. *Macromolecules* 37:9903–9908
204. Cheng JY, Ross CA, Thomas EL, Smith HI, Vancso GJ (2003) Templated self-assembly of block copolymers: effect of substrate topography. *Adv Mater* 15:1599–1602
205. Aissou K, Shaver J, Fleury G, Pecastaings G, Brochon C, Navarro C, Grauby S, Rampoux JM, Dilhaire S, Hadziioannou G (2013) Nanoscale block copolymer ordering induced by visible interferometric micropatterning: a route towards large scale block copolymer 2D crystals. *Adv Mater* 25(2):213–217
206. Koo K, Ahn H, Kim S-W, Ryu DY, Russell TP (2013) Directed self-assembly of block copolymers in the extreme: guiding microdomains from the small to the large. *Soft Matter* 9(38):9059
207. Koh H-D, Park YJ, Jeong S-J, Kwon Y-N, Han IT, Kim M-J (2013) Location-controlled parallel and vertical orientation by dewetting-induced block copolymer directed self-assembly. *J Mater Chem C* 1(25):4020
208. Roerdink M, Hempenius MA, Gunst U, Arlinghaus HF, Vancso GJ (2007) Substrate wetting and topographically induced ordering of amorphous PI-b-PFS block-copolymer domains. *Small* 3(8):1415–1423
209. Kim M, Han E, Sweat DP, Gopalan P (2013) Interplay of surface chemical composition and film thickness on graphoepitaxial assembly of asymmetric block copolymers. *Soft Matter* 9(26):6135
210. Hsueh HY, Chen HY, Hung YC, Ling YC, Gwo S, Ho RM (2013) Well-defined multibranching gold with surface plasmon resonance in near-infrared region from seeding growth approach using gyroid block copolymer template. *Adv Mater* 25(12):1780–1786
211. Hsueh HY, Chen HY, She MS, Chen CK, Ho RM, Gwo S, Hasegawa H, Thomas EL (2010) Inorganic gyroid with exceptionally low refractive index from block copolymer templating. *Nano Lett* 10(12):4994–5000
212. Park M (1997) Block copolymer lithography: periodic arrays of 1011 holes in 1 square centimeter. *Science* 276(5317):1401–1404
213. Vukovic I, Brinke G, Loos K (2013) Block copolymer template-directed synthesis of well-ordered metallic nanostructures. *Polymer* 54(11):2591–2605
214. Bosc F, Ayrat A, Albouy P-A, Guizard C (2003) A simple route for low-temperature synthesis of mesoporous and nanocrystalline anatase thin films. *Chem Mater* 15:2463–2468
215. Deshpande AS, Pinna N, Smarsly B, Antonietti M, Niederberger M (2005) Controlled assembly of preformed ceria nanocrystals into highly ordered 3D nanostructures. *Small* 1(3):313–316
216. Ba J, Polleux J, Antonietti M, Niederberger M (2005) Non-aqueous synthesis of tin oxide nanocrystals and their assembly into ordered porous mesostructures. *Adv Mater* 17(20):2509–2512
217. Guldin S, Kolle M, Stefik M, Langford R, Eder D, Wiesner U, Steiner U (2011) Tunable mesoporous bragg reflectors based on block-copolymer self-assembly. *Adv Mater* 23(32):3664–3668
218. Rauda EI, Buonsanti R, Saldarriaga-Lopez CL, Benjauthrit K, Schelhas TL, Stefik M, Augustyn V, Ko J, Dunn B, Wiesner U, Milliron JD, Tolbert HS (2012) General method for the synthesis of hierarchical nanocrystal-based mesoporous materials. *ACS Nano* 6(7):6386–6399
219. Kamperman M, Garcia WBC, Du P, Ow H, Wiesner U (2004) Ordered mesoporous ceramics stable up to 1500°C from diblock copolymer mesophases. *J Am Chem Soc* 126:14708

220. Riedel R, Mera G, Hauser R, Klenczynski A (2006) Silicon-based polymer-derived ceramics: synthesis properties and applications a review. *J Ceram Soc Jpn* 114:425–444
221. Nghiem DQ, Kim P-D (2008) Direct preparation of high surface area mesoporous SiC-based ceramic by pyrolysis of a self-assembled polycarbosilane-block-polystyrene diblock copolymer. *Chem Mater* 20:3735–3739
222. Matsumoto K, Matsuoka H (2005) Synthesis of core-crosslinked carbosilane block copolymer micelles and their thermal transformation to silicon-based ceramics nanoparticles. *J Polym Sci A Polym Chem* 43(17):3778–3787
223. Nguyen CT, Hoang PH, Perumal J, Kim DP (2011) An inorganic–organic diblock copolymer photoresist for direct mesoporous SiCN ceramic patterns via photolithography. *Chem Commun (Camb)* 47(12):3484–3486
224. Malenfant PR, Wan J, Taylor ST, Manoharan M (2007) Self-assembly of an organic–inorganic block copolymer for nano-ordered ceramics. *Nat Nanotechnol* 2(1):43–46
225. Thomas KR, Ionescu A, Gwyther J, Manners I, Barnes CHW, Steiner U, Sivaniah E (2011) Magnetic properties of ceramics from the pyrolysis of metallocene-based polymers doped with palladium. *J Appl Phys* 109:073904
226. Cao L, Massey JA, Winnik MA, Manners I, Riethmüller S, Banhart F, Spatz JP, Möller M (2003) Reactive ion etching of cylindrical polyferrocenylsilane block copolymer micelles: fabrication of ceramic nanolines on semiconducting substrates. *Adv Funct Mater* 13:271–276
227. Clendenning SB, Han S, Coombs N, Paquet C, Rayat SM, Grozea D, Brodersen MP, Sodhi SNR, Yip CM, Lu Z-H, Manners I (2004) Magnetic ceramic films from a metallopolymer resist using reactive ion etching in a secondary magnetic field. *Adv Mater* 16:291–296
228. Temple K, Kulbaba K, Power-Billard NK, Manners I, Leach AK, Xu T, Russell PT, Hawker JC (2003) Spontaneous vertical ordering and pyrolytic formation of nanoscopic ceramic patterns from poly(styrene-*b*-ferrocenylsilane). *Adv Mater* 15:297–300
229. Cheng JY, Ross CA, Chan VZ-H, Thomas EL, Lammertink RGH, Vancso GJ (2001) Formation of a cobalt magnetic dot array via block copolymer lithography. *Adv Mater* 13:1174–1178
230. Francis A, Ionescu E, Fasel C, Riedel R (2009) Crystallization behavior and controlling mechanism of iron-containing Si-C-N ceramics. *Inorg Chem* 48(21):10078–10083
231. Hojamberdiev M, Prasad RM, Fasel C, Riedel R, Ionescu E (2013) Single-source-precursor synthesis of soft magnetic Fe₃Si- and Fe₅Si₃-containing SiOC ceramic nanocomposites. *J Eur Ceram Soc* 33(13–14):2465–2472
232. Hardy CG, Ren L, Ma S, Tang C (2013) Self-assembly of well-defined ferrocene triblock copolymers and their template synthesis of ordered iron oxide nanoparticles. *Chem Commun* 49:4373–4375
233. Scheid D, Cherkashinin G, Ionescu E, Gallei M (2014) Single-source magnetic nanorattles by using convenient emulsion polymerization protocols. *Langmuir* 30(5):1204–1209
234. Xia Y, Gates B, Yin Y, Lu Y (2000) Monodispersed colloidal spheres: old materials with new applications. *Adv Mater* 12:693–713
235. Hynninen AP, Thijssen JH, Vermolen EC, Dijkstra M, van Blaaderen A (2007) Self-assembly route for photonic crystals with a bandgap in the visible region. *Nat Mater* 6:202–205
236. Maldovan M, Thomas EL (2006) Simultaneous localization of photons and phonons in two-dimensional periodic structures. *Appl Phys Lett* 88:251907-3
237. De La Rue R (2003) Photonic crystals: microassembly in 3D. *Nat Mater* 2:74–76
238. Gonzalez-Urbina L, Baert K, Kolaric B, Perez-Moreno J, Clays K (2012) Linear and nonlinear optical properties of colloidal photonic crystals. *Chem Rev* 112:2268–2285
239. Galisteo-López JF, Ibisate M, Sapienza R, Froufe-Pérez LS, Blanco Á, López C (2011) Self-assembled photonic structures. *Adv Mater* 23:30–69
240. von Freymann G, Kitaev V, Lotsch BV, Ozin GA (2013) Bottom-up assembly of photonic crystals. *Chem Soc Rev* 42:2528–2554
241. Pursiainen OJ, Baumberg JJ, Winkler H, Viel B, Spahn P, Ruhl T (2008) Shear-induced organization in flexible polymer opals. *Adv Mater* 20:1484–1487

242. Ruhl T, Spahn P, Hellmann GP (2003) Artificial opals prepared by melt compression. *Polymer* 44:7625–7634
243. Schäfer CG, Viel B, Hellmann GP, Rehahn M, Gallei M (2013) Thermo-cross-linked elastomeric opal films. *ACS Appl Mater Interfaces* 5:10623–10632
244. Galliano P, De Damborenea JJ, Pascual MJ, Duran A (1998) Sol–gel coatings on 316L steel for clinical applications. *J Sol Gel Sci Technol* 13(1–3):723–727
245. Vasconcelos DCL, Carvalho JAN, Mantel M, Vasconcelos WL (2000) Corrosion resistance of stainless steel coated with sol–gel silica. *J Non Crystal Solids* 273(1–3):135–139
246. Fedrizzi L, Rodriguez FJ, Rossi S, Deflorian F, Di Maggio R (2001) The use of electrochemical techniques to study the corrosion behaviour of organic coatings on steel pretreated with sol–gel zirconia films. *Electrochim Acta* 46(24–25):3715–3724
247. Masalski J, Gluszek J, Zabrzewski J, Nitsch K, Gluszek P (1999) Improvement in corrosion resistance of the 316L stainless steel by means of Al_2O_3 coatings deposited by the sol–gel method. *Thin Solid Films* 349(1–2):186–190
248. Wang D, Bierwagen GP (2009) Sol–gel coatings on metals for corrosion protection. *Progr Org Coating* 64(4):327–338
249. Messaddeq SH, Pulcinelli SH, Santilli CV, Guastaldi AC, Messaddeq Y (1999) Microstructure and corrosion resistance of inorganic–organic (ZrO_2 –PMMA) hybrid coating on stainless steel. *J Non Crystal Solids* 247(1–3):164–170
250. Sayilkhan H, Sener S, Sener E, Sulu M (2003) The sol–gel synthesis and application of some anticorrosive coating materials. *Mater Sci* 39(5):733–739
251. Jianguo L, Gaoping G, Chuanwei Y (2006) Enhancement of the erosion–corrosion resistance of Dacromet with hybrid SiO_2 sol–gel. *Surf Coating Technol* 200(16–17):4967–4975
252. Atik M, Luna F, Messaddeq S, Aegerter M (1997) ORMocer (ZrO_2 –PMMA) films for stainless steel corrosion protection. *J Sol Gel Sci Technol* 8(1–3):517–522
253. Du YJ, Damron M, Tang G, Zheng HX, Chu CJ, Osborne JH (2001) Inorganic/organic hybrid coatings for aircraft aluminum alloy substrates. *Progr Org Coating* 41(4):226–232
254. Haas KH, Amberg-Schwab S, Rose K, Schottner G (1999) Functionalized coatings based on inorganic–organic polymers (ORMOCER®s) and their combination with vapor deposited inorganic thin films. *Surf Coating Technol* 111(1):72–79
255. Ono S, Tsuge H, Nishi Y, Hirano S-I (2004) Improvement of corrosion resistance of metals by an environmentally friendly silica coating method. *J Sol Gel Sci Technol* 29(3):147–153
256. Voevodin N, Jeffcoate C, Simon L, Khobaib M, Donley M (2001) Characterization of pitting corrosion in bare and sol–gel coated aluminum 2024-T3 alloy. *Surf Coating Technol* 140(1):29–34
257. Kasten LS, Grant JT, Grebasch N, Voevodin N, Arnold FE, Donley MS (2001) An XPS study of cerium dopants in sol–gel coatings for aluminum 2024-T3. *Surf Coating Technol* 140(1):11–15
258. Ballard RL, Williams JP, Njus JM, Kiland BR, Soucek MD (2001) Inorganic–organic hybrid coatings with mixed metal oxides. *Eur Polym J* 37(2):381–398
259. Byrne MT, McCarthy JE, Bent M, Blake R, Gun'ko YK, Horvath E, Konya Z, Kukovec A, Kiricsi I, Coleman JN (2007) Chemical functionalisation of titania nanotubes and their utilisation for the fabrication of reinforced polystyrene composites. *J Mater Chem* 17(22):2351
260. Matsuno R, Otsuka H, Takahara A (2006) Polystyrene-grafted titanium oxide nanoparticles prepared through surface-initiated nitroxide-mediated radical polymerization and their application to polymer hybrid thin films. *Soft Matter* 2(5):415
261. Tavares MTS, Santos ASF, Santos IMG, Silva MRS, Bomio MRD, Longo E, Paskocimas CA, Motta FV (2014) TiO_2 /PDMS nanocomposites for use on self-cleaning surfaces. *Surf Coating Technol* 239:16–19
262. Kinloch AJ, Mohammed RD, Taylor AC, Sprenger S, Egan D (2006) The interlaminar toughness of carbon-fibre reinforced plastic composites using 'hybrid-toughened' matrices. *J Mater Sci* 41(15):5043–5046

263. Kinloch AJ, Mohammed RD, Taylor AC, Eger C, Sprenger S, Egan D (2005) The effect of silica nano particles and rubber particles on the toughness of multiphase thermosetting epoxy polymers. *J Mater Sci* 40(18):5083–5086
264. Kinloch AJ, Masania K, Taylor AC, Sprenger S, Egan D (2007) The fracture of glass-fibre-reinforced epoxy composites using nanoparticle-modified matrices. *J Mater Sci* 43(3):1151–1154
265. Blackman BRK, Kinloch AJ, Sohn Lee J, Taylor AC, Agarwal R, Schueneman G, Sprenger S (2007) The fracture and fatigue behaviour of nano-modified epoxy polymers. *J Mater Sci* 42(16):7049–7051
266. Liu H-Y, Wang G, Mai Y-W (2012) Cyclic fatigue crack propagation of nanoparticle modified epoxy. *Compos Sci Technol* 72(13):1530–1538
267. Bray DJ, Dittanet P, Guild FJ, Kinloch AJ, Masania K, Pearson RA, Taylor AC (2013) The modelling of the toughening of epoxy polymers via silica nanoparticles: the effects of volume fraction and particle size. *Polymer* 54(26):7022–7032
268. Sarwar MI, Zulfiqar S, Ahmad Z (2008) Polyamide–silica nanocomposites: mechanical, morphological and thermomechanical investigations. *Polym Int* 57(2):292–296
269. Taniike T, Toyonaga M, Terano M (2014) Polypropylene-grafted nanoparticles as a promising strategy for boosting physical properties of polypropylene-based nanocomposites. *Polymer* 55(4):1012–1019
270. Zhang M, Singh RP (2004) Mechanical reinforcement of unsaturated polyester by Al_2O_3 nanoparticles. *Mater Lett* 58(3–4):408–412
271. Sawyer WG, Freudenberg KD, Bhimaraj P, Schadler LS (2003) A study on the friction and wear behavior of PTFE filled with alumina nanoparticles. *Wear* 254(5–6):573–580
272. Schwartz CJ, Bahadur S (2000) Studies on the tribological behavior and transfer film–counterface bond strength for polyphenylene sulfide filled with nanoscale alumina particles. *Wear* 237(2):261–273
273. Wang Y, Lim S, Luo JL, Xu ZH (2006) Tribological and corrosion behaviors of Al_2O_3 /polymer nanocomposite coatings. *Wear* 260(9–10):976–983
274. Guo Z, Pereira T, Choi O, Wang Y, Hahn HT (2006) Surface functionalized alumina nanoparticle filled polymeric nanocomposites with enhanced mechanical properties. *J Mater Chem* 16(27):2800
275. Ng CB, Schadler LS, Siegel RW (1999) Synthesis and mechanical properties of TiO_2 -epoxy nanocomposites. *Nanostruct Mater* 12(1–4):507–510
276. Rong MZ, Zhang MQ, Liu H, Zeng HM (2001) Microstructure and tribological behavior of polymeric nanocomposites. *Ind Lubr Tribol* 53(2):72–77
277. Evora V, Shukla A (2003) Fabrication, characterization, and dynamic behavior of polyester/ TiO_2 nanocomposites. *Mater Sci Eng A* 361(1–2):358–366
278. Al G, Şen S (2006) Preparation and characterization of poly(2-chloroaniline)/ SiO_2 nanocomposite via oxidative polymerization: comparative UV–vis studies into different solvents of poly(2-chloroaniline) and poly(2-chloroaniline)/ SiO_2 . *J Appl Polym Sci* 102(1):935–943
279. Su S-J, Kuramoto N (2000) Processable polyaniline–titanium dioxide nanocomposites: effect of titanium dioxide on the conductivity. *Synthetic Met* 114(2):147–153
280. Mo T-C, Wang H-W, Chen S-Y, Yeh Y-C (2008) Synthesis and dielectric properties of polyaniline/titanium dioxide nanocomposites. *Ceram Int* 34(7):1767–1771
281. Cui W-W, Tang D-Y, Gong Z-L (2013) Electrospun poly(vinylidene fluoride)/poly(methyl methacrylate) grafted TiO_2 composite nanofibrous membrane as polymer electrolyte for lithium-ion batteries. *J Power Sourc* 223:206–213
282. Kim K (2003) Characterization of poly(vinylidene fluoride-co-hexafluoropropylene)-based polymer electrolyte filled with rutile TiO_2 nanoparticles. *Solid State Ionics* 161(1–2):121–131

283. Wu N, Cao Q, Wang X, Li S, Li X, Deng H (2011) In situ ceramic fillers of electrospun thermoplastic polyurethane/poly(vinylidene fluoride) based gel polymer electrolytes for Li-ion batteries. *J Power Sourc* 196(22):9751–9756
284. Aravindan V, Vickraman P, Kumar TP (2008) Polyvinylidene fluoride–hexafluoropropylene (PVDF–HFP)-based composite polymer electrolyte containing $\text{LiPF}_3(\text{CF}_3\text{CF}_2)_3$. *J Non Crystal Solids* 354(29):3451–3457
285. Croce F, Bonino F, Panero S, Scrosati B (1989) Properties of mixed polymer and crystalline ionic conductors. *Philos Mag B* 59(1):161–168
286. Morales-Acosta MD, Alvarado-Beltrán CG, Quevedo-López MA, Gnade BE, Mendoza-Galván A, Ramírez-Bon R (2013) Adjustable structural, optical and dielectric characteristics in sol–gel PMMA– SiO_2 hybrid films. *J Non Crystal Solids* 362:124–135
287. Morales-Acosta MD, Quevedo-López MA, Gnade BE, Ramírez-Bon R (2011) PMMA– SiO_2 organic–inorganic hybrid films: determination of dielectric characteristics. *J Sol Gel Sci Technol* 58(1):218–224
288. Dey A, De S, De A, De SK (2004) Characterization and dielectric properties of polyaniline– TiO_2 nanocomposites. *Nanotechnology* 15(9):1277–1283
289. Singha S, Thomas MJ (2008) Dielectric properties of epoxy nanocomposites. *IEEE Trans Dielectr and Electr Insul* 15(1):12–23
290. Houbertz R, Domann G, Cronauer C, Schmitt A, Martin H, Park JU, Fröhlich L, Buestrich R, Popall M, Streppel U, Dannberg P, Wächter C, Bräuer A (2003) Inorganic–organic hybrid materials for application in optical devices. *Thin Solid Films* 442(1–2):194–200
291. Caseri WR (2008) Inorganic nanoparticles as optically effective additives for polymers. *Chem Eng Commun* 196(5):549–572
292. Ershad-Langroudi A, Mai C, Vigier G, Vassoille R (1997) Hydrophobic hybrid inorganic–organic thin film prepared by sol–gel process for glass protection and strengthening applications. *J Appl Polym Sci* 65(12):2387–2393
293. Carotenuto G, Her YS, Matijevic E (1996) Preparation and characterization of nanocomposite thin films for optical devices. *Ind Eng Chem Res* 35(9):2929–2932
294. Philipp G, Schmidt H (1984) New materials for contact lenses prepared from Si- and Ti-alkoxides by the sol–gel process. *J Non Crystal Solids* 63(1–2):283–292
295. Yoshida M, Prasad PN (1996) Sol–gel-processed $\text{SiO}_2/\text{TiO}_2$ /Poly(vinylpyrrolidone) composite materials for optical waveguides. *Chem Mater* 8(1):235–241
296. Yuwono AH, Bi L, Xue J, Wang J, Elim HI, Ji W, Li Y, White TJ (2004) Controlling the crystallinity and nonlinear optical properties of transparent TiO_2 ? PMMA nanohybrids. *J Mater Chem* 14(20):2978
297. Li S, Meng Lin M, Toprak MS, Kim Do K, Muhammed M (2010) Nanocomposites of polymer and inorganic nanoparticles for optical and magnetic applications. *Nano Rev* 1:5214. doi:10.3402/nano.v1i0.5214
298. Zhang JUN, Luo S, Gui L (1997) Poly(methyl methacrylate)–titania hybrid materials by sol–gel processing. *J Mater Sci* 32(6):1469–1472
299. Yuwono AH, Xue J, Wang J, Elim HI, Ji W, Li Y, White TJ (2003) Transparent nanohybrids of nanocrystalline TiO_2 in PMMA with unique nonlinear optical behavior. *J Mater Chem* 13(6):1475
300. Elim HI, Ji W, Yuwono AH, Xue JM, Wang J (2003) Ultrafast optical nonlinearity in poly(methylmethacrylate)- TiO_2 nanocomposites. *Appl Phys Lett* 82(16):2691–2693
301. Kobayashi M, Saito H, Boury B, Matsukawa K, Sugahara Y (2013) Epoxy-based hybrids using TiO_2 nanoparticles prepared via a non-hydrolytic sol–gel route. *Appl Organometal Chem* 27(11):673–677
302. Tao P, Viswanath A, Li Y, Siegel RW, Benicewicz BC, Schadler LS (2013) Bulk transparent epoxy nanocomposites filled with poly(glycidyl methacrylate) brush-grafted TiO_2 nanoparticles. *Polymer* 54(6):1639–1646
303. Chau JLH, Tung C-T, Lin Y-M, Li A-K (2008) Preparation and optical properties of titania/epoxy nanocomposite coatings. *Mater Lett* 62(19):3416–3418

304. Chau JL, Lin Y-M, Li A-K, Su W-F, Chang K-S, Hsu SL-C, Li T-L (2007) Transparent high refractive index nanocomposite thin films. *Mater Lett* 61(14–15):2908–2910
305. Chandra A, Turng L-S, Gong S, Hall DC, Caulfield DF, Yang H (2007) Study of polystyrene/titanium dioxide nanocomposites via melt compounding for optical applications. *Polym Compos* 28(2):241–250
306. Tommalieh MJ, Zihlif AM (2010) Optical properties of polyimide/silica nanocomposite. *Physica B Condensed Matter* 405(23):4750–4754
307. Wang H, Xu P, Zhong W, Shen L, Du Q (2005) Transparent poly(methyl methacrylate)/silica/zirconia nanocomposites with excellent thermal stabilities. *Polymer Degrad Stabil* 87(2):319–327
308. Ritzhaupt-Kleissl E, Boehm J, Hausselt J, Hanemann T (2006) Thermoplastic polymer nanocomposites for applications in optical devices. *Mater Sci Eng C* 26(5–7):1067–1071
309. Chandra A, Turng L-S, Gopalan P, Rowell RM, Gong S (2008) Study of utilizing thin polymer surface coating on the nanoparticles for melt compounding of polycarbonate/alumina nanocomposites and their optical properties. *Compos Sci Technol* 68(3–4):768–776
310. Hu Y, Gu G, Zhou S, Wu L (2011) Preparation and properties of transparent PMMA/ZrO₂ nanocomposites using 2-hydroxyethyl methacrylate as a coupling agent. *Polymer* 52(1):122–129
311. Cong H, Radosz M, Towler B, Shen Y (2007) Polymer–inorganic nanocomposite membranes for gas separation. *Separ Purif Technol* 55(3):281–291
312. Pandey P, Chauhan RS (2001) Membranes for gas separation. *Progr Polym Sci* 26(6):853–893
313. Koros WJ, Mahajan R (2000) Pushing the limits on possibilities for large scale gas separation: which strategies? *J Membr Sci* 175(2):181–196
314. Joly C, Goizet S, Schrotter JC, Sanchez J, Escoubes M (1997) Sol–gel polyimide-silica composite membrane: gas transport properties. *J Membr Sci* 130(1–2):63–74
315. Kusakabe K, Ichiki K, Hayashi J-I, Maeda H, Morooka S (1996) Preparation and characterization of silica–polyimide composite membranes coated on porous tubes for CO₂ separation. *J Membr Sci* 115(1):65–75
316. Smaih M, Schrotter J-C, Lesimple C, Prevost I, Guizard C (1999) Gas separation properties of hybrid imide–siloxane copolymers with various silica contents. *J Membr Sci* 161(1–2):157–170
317. Suzuki T, Yamada Y (2006) Characterization of 6FDA-based hyperbranched and linear polyimide–silica hybrid membranes by gas permeation and 129Xe NMR measurements. *J Polym Sci B Polym Phys* 44(2):291–298
318. Park HB, Kim JK, Nam SY, Lee YM (2003) Imide-siloxane block copolymer/silica hybrid membranes: preparation, characterization and gas separation properties. *J Membr Sci* 220(1–2):59–73
319. Alter H (1962) A critical investigation of polyethylene gas permeability. *J Polym Sci* 57(165):925–935
320. Joly C, Smaih M, Porcar L, Noble RD (1999) Polyimide–Silica composite materials: how does silica influence their microstructure and gas permeation properties? *Chem Mater* 11(9):2331–2338
321. Gomes D, Nunes SP, Peinemann K-V (2005) Membranes for gas separation based on poly(1-trimethylsilyl-1-propyne)–silica nanocomposites. *J Membr Sci* 246(1):13–25
322. Shao L, Samseth J, Hägg M-B (2009) Crosslinking and stabilization of nanoparticle filled PMP nanocomposite membranes for gas separations. *J Membr Sci* 326(2):285–292
323. Hu Q, Marand E, Dhingra S, Fritsch D, Wen J, Wilkes G (1997) Poly(amide-imide)/TiO₂ nano-composite gas separation membranes: fabrication and characterization. *J Membr Sci* 135(1):65–79
324. Kong Y, Du H, Yang J, Shi D, Wang Y, Zhang Y, Xin W (2002) Study on polyimide/TiO₂ nanocomposite membranes for gas separation. *Desalination* 146(1–3):49–55

325. Ahmad J, Hågg MB (2013) Polyvinyl acetate/titanium dioxide nanocomposite membranes for gas separation. *J Membr Sci* 445:200–210
326. Korshak VV, Vinogradova SV, Vygodskii YS (1974) Cardo polymers. *J Macromol Sci C* 11(1):45–142
327. Sun H, Ma C, Yuan B, Wang T, Xu Y, Xue Q, Li P, Kong Y (2014) Cardo polyimides/TiO₂ mixed matrix membranes: synthesis, characterization, and gas separation property improvement. *Separ Purif Technol* 122:367–375
328. Schaep J, Vandecasteele C, Leysen R, Doyen W (1998) Salt retention of Zirfon® membranes. *Separ Purif Technol* 14(1–3):127–131
329. Genné I, Kuypers S, Leysen R (1996) Effect of the addition of ZrO₂ to polysulfone based UF membranes. *J Membr Sci* 113(2):343–350
330. Aerts P, Greenberg AR, Leysen R, Krantz WB, Reinsch VE, Jacobs PA (2001) The influence of filler concentration on the compaction and filtration properties of Zirfon®-composite ultrafiltration membranes. *Separ Purif Technol* 22–23:663–669
331. Shao L, Samseth J, Hågg M-B (2009) Crosslinking and stabilization of nanoparticle filled poly(1-trimethylsilyl-1-propyne) nanocomposite membranes for gas separations. *J Appl Polym Sci* 113(5):3078–3088
332. Hu X, Cong H, Shen Y, Radosz M (2007) Nanocomposite membranes for CO₂ separations: silica/brominated poly(phenylene oxide). *Ind Eng Chem Res* 46(5):1547–1551
333. Cong H, Hu X, Radosz M, Shen Y (2007) Brominated poly(2,6-diphenyl-1,4-phenylene oxide) and its silica nanocomposite membranes for gas separation. *Ind Eng Chem Res* 46(8):2567–2575
334. Sadeghi M, Semsarzadeh MA, Barikani M, Pourafshari Chenar M (2011) Gas separation properties of polyether-based polyurethane–silica nanocomposite membranes. *J Membr Sci* 376(1–2):188–195
335. Iwata M, Adachi T, Tomidokoro M, Ohta M, Kobayashi T (2003) Hybrid sol–gel membranes of polyacrylonitrile–tetraethoxysilane composites for gas permselectivity. *J Appl Polym Sci* 88(7):1752–1759
336. Hibshman C, Cornelius CJ, Marand E (2003) The gas separation effects of annealing polyimide–organosilicate hybrid membranes. *J Membr Sci* 211(1):25–40
337. Suzuki T, Yamada Y (2005) Physical and gas transport properties of novel hyperbranched polyimide – silica hybrid membranes. *Polym Bull* 53(2):139–146
338. Radosz M, Shen Y (2007) Brominated poly(2,6-diphenyl-1,4-phenylene oxide) and its nanocomposites as membranes for CO₂ separations. Patent WO 2007133708 A1 (WO patent application PCT/US2007/011,458). <http://www.google.com/patents/WO2007133708A1?cl=en>
339. Kim JH, Lee YM (2001) Gas permeation properties of poly(amide-6-b-ethylene oxide)-silica hybrid membranes. *J Membr Sci* 193(2):209–225
340. Patel NP, Miller AC, Spontak RJ (2003) Highly CO₂-permeable and selective polymer nanocomposite membranes. *Adv Mater* 15(9):729–733
341. Kim H, Lim C, Hong S-I (2005) Gas permeation properties of organic–inorganic hybrid membranes prepared from hydroxyl-terminated polyether and 3-isocyanatopropyltriethoxysilane. *J Sol Gel Sci Technol* 36(2):213–221
342. Sforça ML, Yoshida IVP, Nunes SP (1999) Organic–inorganic membranes prepared from polyether diamine and epoxy silane. *J Membr Sci* 159(1–2):197–207
343. Higuchi A, Agatsuma T, Uemiya S, Kojima T, Mizoguchi K, Pinnau I, Nagai K, Freeman BD (2000) Preparation and gas permeation of immobilized fullerene membranes. *J Appl Polym Sci* 77(3):529–537
344. Merkel TC, Freeman BD, Spontak RJ, He Z, Pinnau I, Meakin P, Hill AJ (2002) Sorption, transport, and structural evidence for enhanced free volume in poly(4-methyl-2-pentyne)/fumed silica nanocomposite membranes. *Chem Mater* 15(1):109–123
345. Bottino A, Capannelli G, Comite A (2002) Preparation and characterization of novel porous PVDF-ZrO₂ composite membranes. *Desalination* 146(1–3):35–40

346. Yan L, Li YS, Xiang CB, Xianda S (2006) Effect of nano-sized Al_2O_3 -particle addition on PVDF ultrafiltration membrane performance. *J Membr Sci* 276(1–2):162–167
347. Honma I, Takeda Y, Bae JM (1999) Protonic conducting properties of sol–gel derived organic/inorganic nanocomposite membranes doped with acidic functional molecules. *Solid State Ionics* 120(1–4):255–264
348. Honma I, Hirakawa S, Yamada K, Bae JM (1999) Synthesis of organic/inorganic nanocomposites protonic conducting membrane through sol–gel processes. *Solid State Ionics* 118(1–2):29–36
349. Honma I, Nomura S, Nakajima H (2001) Protonic conducting organic/inorganic nanocomposites for polymer electrolyte membrane. *J Membr Sci* 185(1):83–94
350. Lin C, Thangamuthu R, Chang P (2005) PWA-doped PEG/SiO proton-conducting hybrid membranes for fuel cell applications. *J Membr Sci* 254(1–2):197–205
351. Thangamuthu R, Lin C (2005) DBSA-doped PEG/SiO proton-conducting hybrid membranes for low-temperature fuel cell applications. *Solid State Ionics* 176(5–6):531–538
352. Chang HY, Lin CW (2003) Proton conducting membranes based on PEG/SiO₂ nanocomposites for direct methanol fuel cells. *J Membr Sci* 218(1–2):295–306
353. Chang HY, Thangamuthu R, Lin CW (2004) Structure–property relationships in PEG/SiO₂ based proton conducting hybrid membranes—A 29Si CP/MAS solid-state NMR study. *J Membr Sci* 228(2):217–226
354. Su Y-H, Liu Y-L, Sun Y-M, Lai J-Y, Guiver MD, Gao Y (2006) Using silica nanoparticles for modifying sulfonated poly(phthalazinone ether ketone) membrane for direct methanol fuel cell: a significant improvement on cell performance. *J Power Sourc* 155(2):111–117
355. Zhi S-H, Xu J, Deng R, Wan L-S, Xu Z-K (2014) Poly(vinylidene fluoride) ultrafiltration membranes containing hybrid silica nanoparticles: preparation, characterization and performance. *Polymer* 55:1333–1340
356. Hench LL (2013) Chronology of bioactive glass development and clinical applications. *New J Glass Ceram* 3(2):67–73
357. Ohtsuki C, Kokubo T, Yamamuro T (1992) Mechanism of apatite formation on $\text{CaOSiO}_2\text{P}_2\text{O}_5$ glasses in a simulated body fluid. *J Non Crystal Solids* 143:84–92
358. Catauro M, Raucci MG, De Gaetano F, Marotta A (2003) Sol–gel synthesis, characterization and bioactivity of polycaprolactone/SiO₂ hybrid material. *J Mater Sci* 38(14):3097–3102
359. Mills KL, Zhu X, Takayama S, Thouless MD (2008) The mechanical properties of a surface-modified layer on poly(dimethylsiloxane). *J Mater Res* 23(1):37–48
360. Martin RA, Yue S, Hanna JV, Lee PD, Newport RJ, Smith ME, Jones JR (2012) Characterizing the hierarchical structures of bioactive sol–gel silicate glass and hybrid scaffolds for bone regeneration. *Philos Trans Ser A Mathemat Phys Eng Sci* 370(1963):1422–1443
361. Camargo PHC, Satyanarayana KG, Wypych F (2009) Nanocomposites: synthesis, structure, properties and new application opportunities. *Mater Res* 12:1–39
362. Rhee S-H, Choi J-Y (2002) Preparation of a bioactive poly(methyl methacrylate)/silica nanocomposite. *J Am Ceram Soc* 85(5):1318–1320
363. Lee KH, Rhee SH (2009) The mechanical properties and bioactivity of poly(methyl methacrylate)/SiO(2)-CaO nanocomposite. *Biomaterials* 30(20):3444–3449
364. Thomas NP, Tran N, Tran PA, Walters JL, Jarrell JD, Hayda RA, Born CT (2013) Characterization and bioactive properties of zirconia based polymeric hybrid for orthopedic applications. *J Mater Sci Mater Med* 25(2):347–354

Soft Nanohybrid Materials Consisting of Polymer–Clay Networks

Kazutoshi Haraguchi

Abstract New types of soft nanohybrid materials with novel organic–inorganic network structures, such as nanocomposite gels (NC gels: hydrogel), soft nanocomposites (M-NCs: solid), and their derivatives (MD-NC gels, Zw-NC gels, Pt-NC gels, and P/C-NC microspheres) are described. All soft nanohybrid materials including NC gels and M-NCs were synthesized by in-situ free-radical polymerization in the presence of exfoliated clay nanoplatelets in aqueous systems and were obtained in various forms and sizes with a wide range of clay contents. Here, disk-like inorganic clay nanoplatelets function as multifunctional crosslinking agents to form new types of network structures. The NC gels exhibited extraordinary optical, mechanical, and swelling–deswelling properties, in addition to a number of new characteristics relating to optical anisotropy, polymer/clay morphology, biocompatibility, stimuli-sensitive surfaces, micropatterning, self-healing, etc. The M-NCs also exhibited dramatic improvements in optical and mechanical properties; the latter include ultrahigh reversible extensibility and well-defined yielding behavior, despite their high clay contents. Thus, the serious disadvantages (intractability, mechanical fragility, optical turbidity, poor processing ability, low stimulus sensitivity, etc.) associated with conventional, chemically crosslinked polymeric materials were overcome in the soft nanohybrid materials because of their unique organic–inorganic network structures. Furthermore, several soft nanohybrids with advanced characteristics were developed based on the technologies of NC gel and M-NC syntheses, e.g., new stimuli-responsive NC gels (MD-NC gels), zwitterionic NC gels (Zw-NC gels), platinum nanoparticle-incorporated NC gels (Pt-NC gels), and aqueous dispersions of polymer–clay NC (P/C-NC) microspheres.

K. Haraguchi (✉)

Department of Applied Molecular Chemistry, College of Industrial Technology, Nihon University, Izumi-cho, Narashino, Chiba 275-8575, Japan
e-mail: haraguchi.kazutoshi@nihon-u.ac.jp

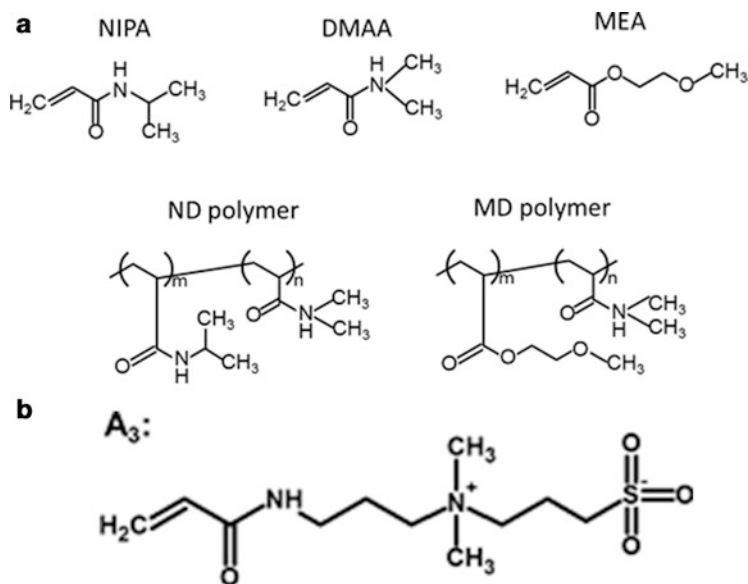
Keywords Clay • Hydrogel • Nanocomposite • Organic–inorganic network • Stimuli sensitivity

Contents

1	Introduction	188
2	Breakthrough in Polymer Hydrogels	193
3	Nanocomposite Gels	193
3.1	Synthesis of NC Gels	193
3.2	Organic–Inorganic Network Structure of NC Gels	195
3.3	Basic Properties of NC Gels	206
4	New Characteristics of NC Gels	220
4.1	Optical Anisotropy	220
4.2	Sliding Friction Behavior	221
4.3	High Water Contact Angles	222
4.4	Cell Cultivation	224
4.5	Porous NCs with a Layered Morphology	225
4.6	Reversible Force Generation	226
4.7	Self-Healing in NC Gels	226
4.8	Complicated Shapes and Surface Patterns	229
5	Further Developments in Advanced Soft Nanohybrid Materials	230
5.1	New Stimuli-Responsive NC Gels and Soft Nanocomposites	230
5.2	Zwitterionic NC Gels	232
5.3	Aqueous Dispersion of Polymer–Clay Nanocomposite Microspheres	234
5.4	Clay-Mediated Platinum-Nanocomposite Gels (Pt-NC Gels)	234
5.5	Soft Polymer Nanocomposites (M-NCs)	238
5.6	Further Extensions	244
6	Conclusion	244
	References	245

1 Introduction

Polymer hydrogels are defined as materials consisting of three-dimensional polymer networks with large amounts of water filling the interstitial spaces of the networks. The polymer hydrogels are soft, wet materials with the characteristics of both solids (well-defined shape) and liquids (free water in most cases), and their properties are determined by the types of polymer and crosslink, in addition to the water content ($R_{\text{H}_2\text{O}}$) and crosslink density (ν). Depending on the type of crosslink, polymer hydrogels are classified into two broad categories: “chemical gels” and “physical gels”. In chemical gels, the network of polymer chains is formed via covalent bonds using an organic crosslinker with two or more functional groups, or by γ -ray irradiation of a polymer in solution or during polymerization. In physical gels, the network of polymer chains is formed via various types of noncovalent bond interactions such as hydrogen bonding, ionic bonding, coordinate bonding, hydrophobic bonding, entanglement, microcrystallization, and helix formation. In practical applications such as soft contact lens and superabsorbent polymers,



Scheme 1 Chemical structures and abbreviations of monomers and copolymer systems: *NIPA* *N*-isopropylacrylamide, *DMAA* *N,N*-dimethylacrylamide, *MEA* 2-methoxyethyl acrylate, *ND polymer* polymer based on *NIPA* and *DMAA*, *MD polymer* polymer based on *MEA* and *DMMA*, *A₃* *N,N*-dimethyl(acrylamidopropyl) ammonium propane sulfonate

chemical gels have been widely used because their network composition and degree of crosslinking can be easily controlled.

Of the various kinds of polymer hydrogels, stimuli-responsive hydrogels have attracted considerable attention as promising smart, soft materials because their properties (such as transparency, gel volume, mechanical properties, adsorption/desorption properties, and surface properties) exhibit dramatic and dynamic changes with changes in environmental conditions or external stimuli [1–5]. The stimulus sensitivity generally arises from the changes in conformation or solubility of the constituent polymer. Thus far, one of the most typical stimulus-sensitive polymers used to synthesize responsive hydrogels is poly(*N*-isopropylacrylamide) (PNIPA) (Scheme 1) [6–12]. Because PNIPA contains both hydrophilic (–CONH–) and hydrophobic [–CH(CH₃)₂] groups in one monomer unit, it shows a well-defined coil-to-globule transition in aqueous media at a temperature slightly below that of the human body [13]. Here, the transition temperature, at which the conformation of the PNIPA chain changes from an expanded random coil to a compactly contracted globule, is termed the lower critical solution temperature (LCST). At temperatures below the LCST (ca. 32°C), *N*-isopropyl groups are hydrophobically hydrated in water via the formation of a clathrate structure (i.e., hydrophobic hydration cluster) [14]. Above the LCST, the clathrate structure is destroyed and PNIPA chains are aggregated as a result of the hydrophobic interaction between *N*-isopropyl groups.

The polymer networks of PNIPA hydrogel are generally formed by chemical crosslinking that is achieved by copolymerization with an organic crosslinker, e.g., *N,N*-methylenebisacrylamide (BIS), at a concentration (C_{BIS}) of 0.5–3 mol% relative to the monomer. Hereinafter, the chemically crosslinked polymer hydrogel is referred to as an OR gel, because it is prepared using an organic crosslinker. In the resulting PNIPA hydrogels with chemically crosslinked networks (referred to as N-OR gels), the gel volumes and properties change depending on various types of external stimuli such as temperature [15], salt [16], solvent [17], and pressure [18]. To date, extensive studies have been conducted into the feasibility of using PNIPA hydrogels in various systems such as artificial insulin-control systems [9], efficient bioseparation devices [8], drug delivery systems [6], and biotechnological and tissue engineering devices [7, 10].

However, in most studies, only small pieces of hydrogel (e.g., in the form of rods or spheres with diameters of a few millimeters or less) have been used in practice as N-OR gels. This is partly because the kinetics of changes in gel volume strongly depend on the typical size of the hydrogel, that is, the rate of gel volume contraction at a temperature above the LCST is inversely proportional to the square of the typical length of the gel particle [15]. Therefore, large-sized N-OR gels require a long time to contract to their equilibrium state. A more relevant reason for the difficulties in the use of large-sized N-OR gels is the fact that OR gels are always mechanically weak and brittle. Figure 1a-1, a-2 illustrates the brittle fractures in tensile tests for OR gels prepared with different concentrations of organic crosslinker (BIS) [19, 20]. These weak, brittle properties of OR gels are attributed to their network structure, with a broad distribution of chain lengths between crosslinking points (Fig. 1c-2) [19]. Then, on unidirectional extension, polymer chains are successively broken as a result of stress localization in the shorter chains present at any instant, regardless of the crosslink density (ν) (Fig. 1c-3). Also, structural inhomogeneity (opaqueness) due to the heterogeneous aggregation of crosslinking points often occurs when the crosslinker concentration is high (Fig. 1a-2, c-1) [20].

Figure 2a shows tensile stress–strain curves for OR gels prepared with different C_{BIS} over a wide range ($C_{\text{BIS}} = 0.001\text{--}3$ mol%) [21]. Also included are data for an aqueous solution of PNIPA (LR), prepared under the same conditions as OR gel except for the absence of a crosslinker and which formed a very viscous, sticky, gel-like material. The LR could be irreversibly elongated extensively (near to or more than 3,000%) at very low stress (<4 kPa). This is because the PNIPA has a high molecular weight and forms a slightly self-crosslinked network, including topological entanglements [22]. Figure 2a also shows that the initial modulus (E) gradually increases with increasing C_{BIS} , with a simultaneous rapid decrease in elongation at break (ϵ_b). Consequently, the ultimate tensile strength (σ) remained low (ca. 10 kPa) throughout the whole range of C_{BIS} ($\propto \nu$). These weak, brittle properties of OR gels are attributed to their network structure (Fig. 1c-2, c-3). Thus, OR gels, including stimuli-responsive N-OR gels, have several serious disadvantages associated with chemically crosslinked networks: (1) poor mechanical strength ($\sigma \leq 10$ kPa) and brittleness ($\epsilon_b < 50\%$); (2) optical opacity at a high ν ;

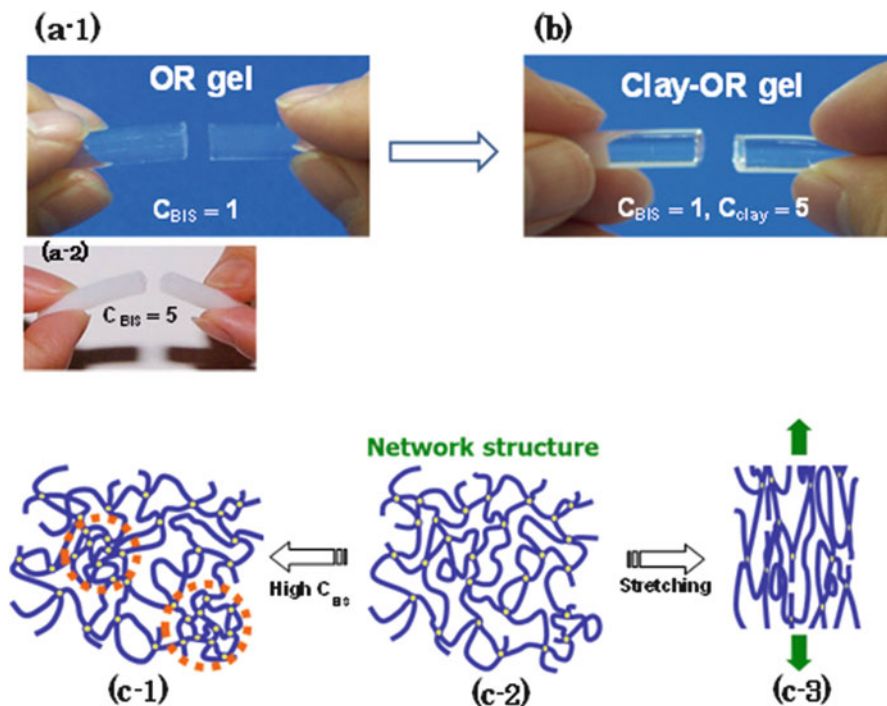


Fig. 1 *Top*: Chemically crosslinked OR gels with different BIS contents: **(a-1)** $C_{\text{BIS}} = 1$ mol% and **(a-2)** $C_{\text{BIS}} = 5$ mol%. **(b)** Clay-dispersed OR gel with $C_{\text{BIS}} = 1$ mol% and $C_{\text{clay}} = 5$ mol%. *Bottom*: Representations of networks of chemically crosslinked OR gels: **(c-1)** heterogeneous network structure of an OR gel ($C_{\text{BIS}} = 5$ mol%), **(c-2)** uniform network structure of an OR gel ($C_{\text{BIS}} = 1$ mol%), and **(c-3)** rupture of crosslinked chains in a unidirectional extension of an OR gel

and (3) low degree of swelling and slow deswelling rate as a result of restrictions in the movement of polymer chains by chemical crosslinks, even at the moderate crosslinker concentrations commonly used [19, 20].

In order to overcome these limitations, we extend the concept of “organic–inorganic nanocomposites” to the field of “polymer hydrogels” under the strategy of fabricating novel organic–inorganic structures [19]. To date, polymer-based organic–inorganic nanocomposites (P-NCs) have been widely investigated in order to develop new, value-added polymeric materials based on existing polymers and inorganic nanoparticles (e.g., silica, silsesquioxane, titania, clay, carbon nanotubes) by utilizing sol–gel reactions of metal alkoxides or organic pre-modification of nanoparticles [23–27]. The resulting P-NCs show significant improvements in some properties such as modulus, heat-distortion temperature, hardness, gas impermeability, etc. However, the P-NCs developed so far have encountered inherent difficulties in preparation and processing as the inorganic content increases. In the case of polymer/clay nanocomposites, in general, only a few weight per cent of clay can actually be incorporated into NCs (<10 wt%, at the

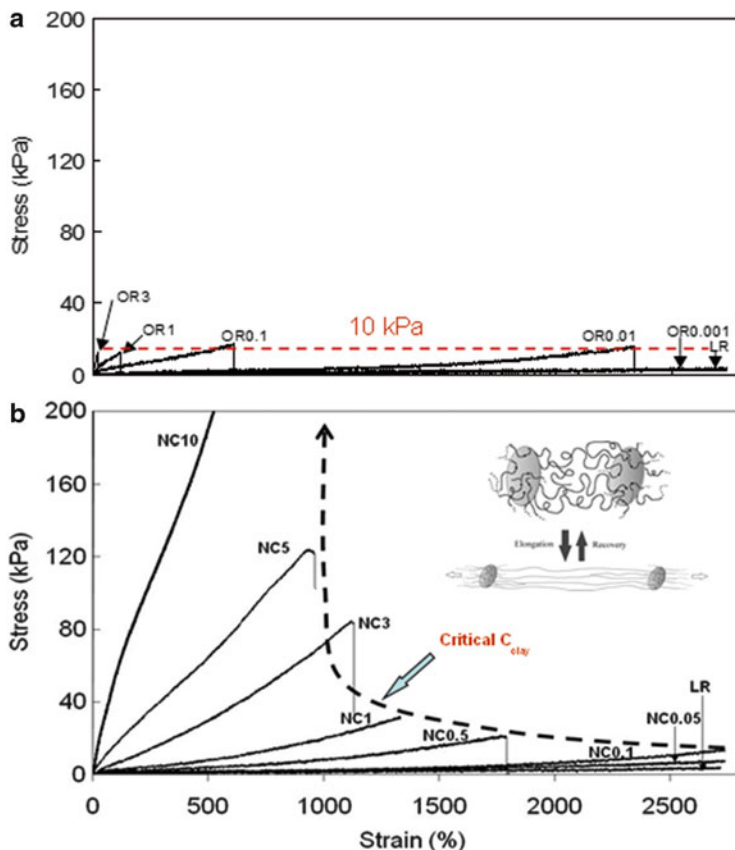


Fig. 2 (a) Tensile stress–strain curves for N-OR gels with different C_{BIS} (0.001–3 mol%) and for an aqueous solution of PNIPA (LR) ($C_{BIS} = 0$). (b) Tensile stress–strain curves for N-NC gels with different C_{clay} (0.05–10 mol%) and for LR. *Inset*: Representation of the unit structure of an organic–inorganic network. Reprinted from Haraguchi [21], Copyright 2007, with permission of Wiley

most) in the form of organic modified clay [23, 25, 26]. Further increases in clay content often cause structural inhomogeneities because of inadequate dispersion or irregular aggregation of the clay, and always result in disadvantageous optical and mechanical properties and processability.

In this chapter, we present an overview of the development of novel soft, nanohybrid materials (e.g., nanocomposite gels [19, 21, 28–30] and soft polymer nanocomposites [31–33]) with unique organic–inorganic network structures that overcome the previous limitations and exhibit excellent optical and mechanical properties in addition to outstanding new characteristics.

2 Breakthrough in Polymer Hydrogels

Because the chemically crosslinked network structure is a principal factor responsible for the fragility of OR gels, to dramatically enhance the mechanical properties of these gels, it is necessary to fabricate new network structures, preferably by reducing or nearly eliminated stress localization. In recent work, the mechanical properties of polymeric hydrogels have been improved remarkably by creating new types of network structures using different strategies [34, 35], such as networks with sliding crosslinks (slide-ring gels) [36], organic–inorganic networks (nanocomposite gels) [19], interpenetrating networks (double-network gels) [37], and tetra-polyethylene glycol (PEG) networks [38]. Among these polymeric hydrogels, nanocomposite gels (abbreviated as NC gels) consisting of organic polymer and inorganic clay not only overcame all the problems associated with OR gels but also exhibited a number of new characteristics.

In order to create a super hydrogel (NC gel), the concept of the “fabrication of a novel three-dimensional network structure” is important. For example, the simple dispersion of inorganic nanomaterials such as silica, titania, clay, and CNT into the network of an OR gel hardly improved the mechanical properties, regardless of the kind and size (aspect ratio) of the nanoparticles and the dispersion uniformity, as shown in Fig. 1b for clay (4 wt%)-dispersed OR1 gel. Also, almost no reinforcement was observed for the systems with other kinds of nanoparticles.

3 Nanocomposite Gels

3.1 Synthesis of NC Gels

NC gels were prepared by in-situ free-radical polymerization of water-soluble monomers containing amide groups, such as NIPA, *N,N*-dimethylacrylamide (DMAA) (Scheme 1), and acrylamide (AAm), in the presence of inorganic clay that had been exfoliated and uniformly dispersed in aqueous media [19, 20, 39–41]. A variety of clay minerals with layered crystal structures and good water swellability can be used as the inorganic component; examples are the smectite-group clays (hectorite, saponite, montmorillonite, etc.) and mica-group clays (synthetic fluorine mica). Among these, the synthetic hectorite “Laponite XLG” (Rockwood Ltd., UK; $[\text{Mg}_{5.34}\text{Li}_{0.66}\text{Si}_8\text{O}_{20}(\text{OH})_4]\text{Na}_{0.66}$; layer size 30 nm (diameter) \times 1 nm (thickness); cation-exchange capacity 104 mequiv/100 g) [40, 42], which has a 2:1 layered structure (Fig. 3a), was most effective because of its high degree of swellability and exfoliation, high purity, sufficiently small platelet size, and good interaction with PNIPA.

In some cases, commercially modified “Laponite XLS”, which is mixed with pyrophosphate-Na as an additive to reduce the viscosity of clay aqueous solutions (i.e., increase the dispersion), is used [30, 43, 44]. In particular, Laponite XLS has

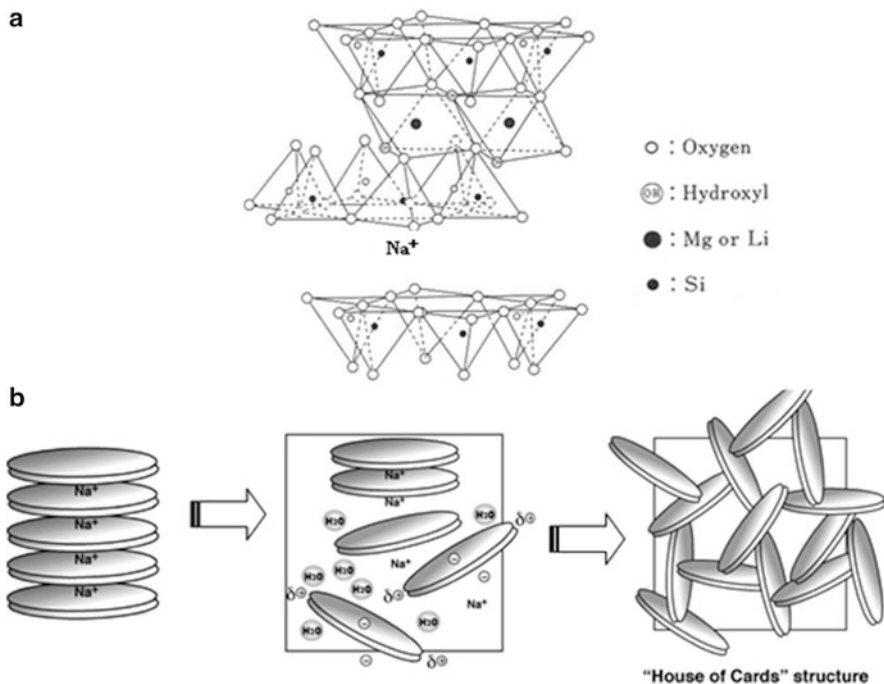


Fig. 3 (a) Structure of hectorite (Laponite XLG; $[\text{Mg}_{5.34}\text{Li}_{0.66}\text{Si}_8\text{O}_{20}(\text{OH})_4]\text{Na}_{0.66}$). (b) Exfoliation in aqueous media and formation of house-of-cards structure [39]

often been used to prepare poly(*N*-alkyl acrylamides) based NC gels [44–46] because AAm monomer interacts strongly with clay. However, as shown later in Sect. 3.3.2, the NC gels prepared using Laponite XLS always show lower initial modulus and tensile strength in fixed monomers (e.g., NIPA and DMAA) than those prepared using Laponite XLG [43]. This indicates that XLG forms crosslinks with poly(*N*-alkyl acrylamides) more effectively than XLS does. Here, it should be noted that a simple increase in the elongation at break in tensile tests does not indicate improved mechanical properties, since the largest elongations are observed in viscous (slightly crosslinked) polymer solutions (Fig. 2a). In this review, inorganic clay refers to Laponite XLG, unless otherwise stated. For example, to synthesize an N-NC3 gel (see the nomenclature below), a transparent aqueous solution consisting of water (20 mL), clay (XLG, 0.457 g), monomer (NIPA, 2.26 g), initiator [potassium persulfate (KPS), 0.02 g] and accelerator [*N,N,N',N'*-tetramethylenediamine (TEMED), 16 μL] was prepared at ice bath temperature and then the temperature was increased to 20°C to initiate in-situ free-radical polymerization.

Consequently, structurally uniform, transparent hydrogels (NC gels) are obtained without syneresis or phase separation. Polymerization yields are almost 100%, regardless of the NC gel composition. By strictly controlling the polymerization conditions, it is possible to decrease the residual monomer content to less

than 10 ppm. The compositions of NC gels can, therefore, be precisely controlled over a wide range by altering those of the initial reaction solutions. It should be noted that for the synthesis of NC gels, organic crosslinkers, which afford chemically crosslinked networks, are not required. More specifically, such crosslinkers should not be used in conjunction with clay. When two crosslinkers, clay and BIS, are used together, the resulting hydrogel (NC-OR gel) becomes weak and brittle on elongation, similar to an OR gel (Fig. 1b) [47].

The nomenclature codes used to identify NC and OR gels are based on the monomer used (N- and D- for NIPA and DMAA, respectively) and the concentrations of clay and monomer relative to water. Thus, N-NC n -M m indicates an NC gel prepared using $n \times 10^{-2}$ mol (equivalent to $n \times 0.762$ wt%) of clay and m mol of NIPA in 1 L H₂O, and D-OR n' indicates an OR gel prepared using n' mol% of BIS relative to monomer and 1 M of DMAA. When m is 1, the last symbol (-M1) is often omitted for simplicity. Also, the initial symbol (N- or D-) is sometimes omitted in NC and OR gels where there is no possibility of confusion. The clay, polymer, and BIS contents of NC and OR gels (C_{clay} , C_{p} , and C_{BIS}) are expressed using simplified numerical values of n , m , and n' , respectively.

The methods used to prepare NC gels are simple and versatile, i.e., injection of reaction solutions into closed vessels followed by polymerization at ambient temperature. Hence, NC gels can be readily formed in various shapes and sizes, such as films, sheets, rods, spheres, hollow tubes, etc. (Fig. 4a) [21, 29]. NC gels can also be prepared by photoinitiated free-radical polymerization using very low concentrations (e.g., 0.1 wt% relative to the monomer) of a hydrophobic photoinitiator in aqueous systems (Fig. 4b) [48]. Furthermore, the other type of NC gel, i.e., tetra-PEG-based NC gels, with good biocompatibility can be prepared by incorporating clay nanoparticles into the tetra-PEG network [30].

3.2 Organic–Inorganic Network Structure of NC Gels

3.2.1 Formation of Networks with Clay

Gel formation, i.e., formation of polymer networks with inorganic clay (in the absence of an organic crosslinker), was confirmed by their swelling and dynamic mechanical properties. In dynamic mechanical measurements at 22°C [21], it was observed for D-NC5 gel that the storage modulus (G') is always greater than the loss modulus (G'') in the frequency range 10^{-1} – 10^2 rad s⁻¹, and that G' and G'' change little with frequency (Fig. 5a). The constantly high G' ($>G''$) indicates that viscoelastic relaxation does not occur on this time scale. These observations are consistent with the dynamic viscoelastic properties that characterize hydrogels with three-dimensional networks. In addition, network formation in NC gels was confirmed by their rubbery nature, such as reversible large deformation and recovery in stretching and compression tests, as shown in a later section (3.3.2).

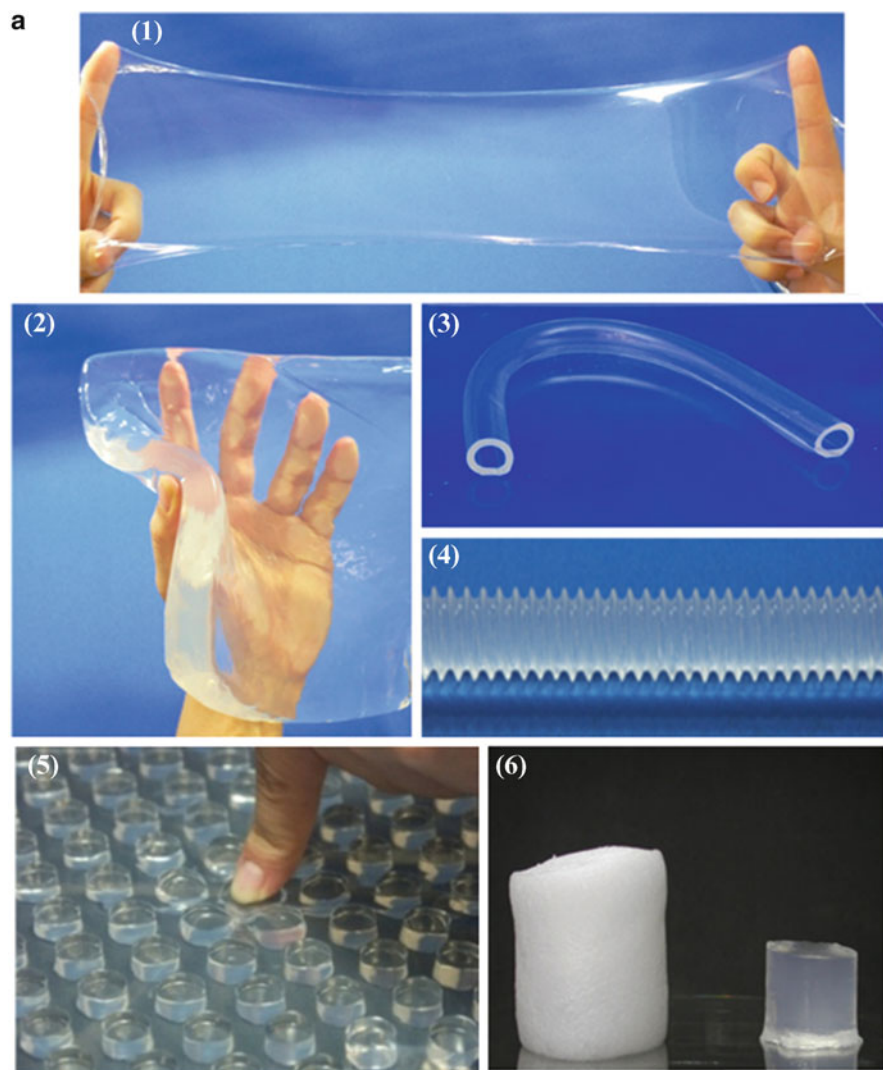


Fig. 4 (continued)

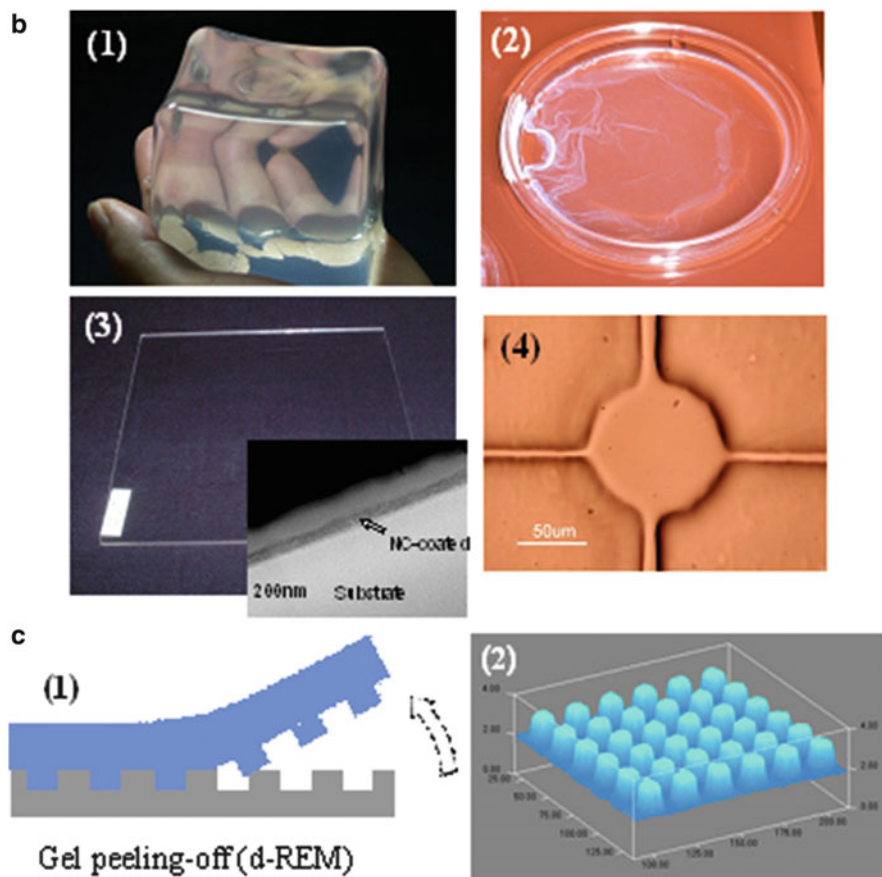
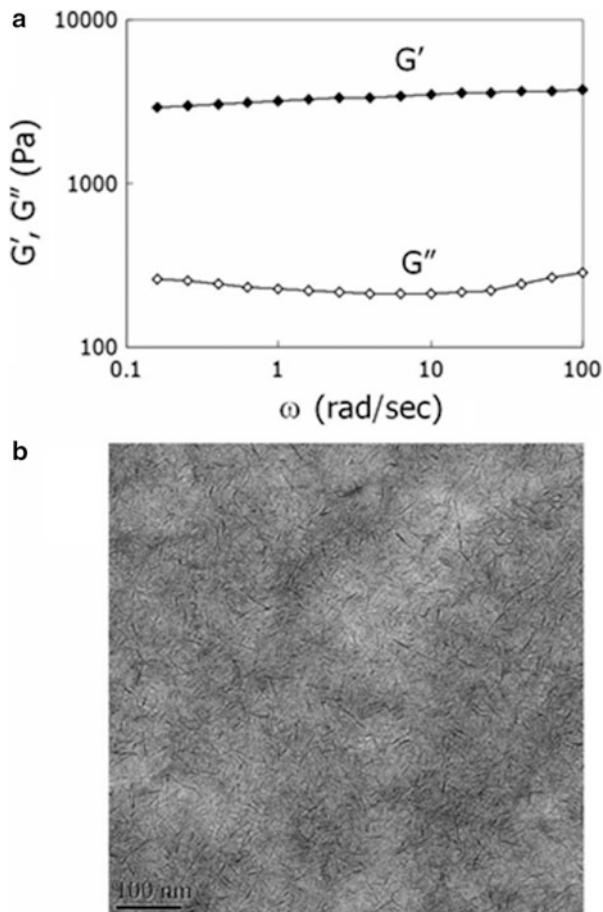


Fig. 4 (a) NC gels with various shapes and forms: (1) thin film, (2) sheet, (3) hollow tube, (4) bellows, (5) sheet with uneven surface, and (6) porous NC gel.[21, 29]. (b) Various NC gels prepared by photopolymerization: (1) bulk, (2) thin film, (3) coating, and (4) pattern. (c) (1) The process of surface-patterning by direct replica molding (REM); (2) confocal optical microscopy 3D image of the surface pattern of NC gel film prepared by direct REM using a quartz template with an array of 10 μm square dot holes with 10 μm intervals. (b) Reprinted from Haraguchi and Takada [48], Copyright 2010, with permission of ACS. (c) Reprinted from Song et al. [49], Copyright 2008, with permission of SPSJ

Network formation in NC gels was further ascertained by swelling measurements. NC gels do not dissolve in water but swell until they reach an equilibrium state, with no free linear polymer chains or free clay particles separating from the network [20, 40]. These results indicate that NC gels form three-dimensional networks in which all the polymer chains and clay particles are incorporated. In general, the degree of equilibrium swelling (DES) of a hydrogel is inversely proportional to ν . In the case of NC gels, the degree of swelling changes with the gel composition, i.e., DES tends to decrease with increasing C_{clay} and C_p [40].

Fig. 5 (a) Dynamic viscoelastic properties (G' and G'') of D-NC5 gel measured at 22°C in the range of 0.2–100 rad/s [21]. (b) TEM images of dried N-NC5 gel. The scale bar indicates 100 nm. (a) Reprinted from Haraguchi [21], Copyright 2007, with permission of Wiley



This indicates that the networks in NC gels are formed by crosslinking polymer chains with clay in a specific manner.

3.2.2 Polymer–Clay Network Structure

Various analytical studies [transmission electron microscopy (TEM), thermogravimetry, X-ray diffraction (XRD), differential-scanning calorimetry (DSC), and Fourier-transform infrared spectroscopy (FTIR) for dried NC gels; dynamic light scattering (DLS) and small-angle neutron scattering (SANS) for NC gels] revealed the following structural aspects of NC gels [19, 20, 39, 40, 50–54]: (1) Disk-like inorganic clay nanoparticles (30 nm diameter \times 1 nm thick), resulting from exfoliation of the layered clay mineral (hectorite), are uniformly dispersed in a polymer matrix (as shown by XRD and TEM; see Fig. 5b for TEM

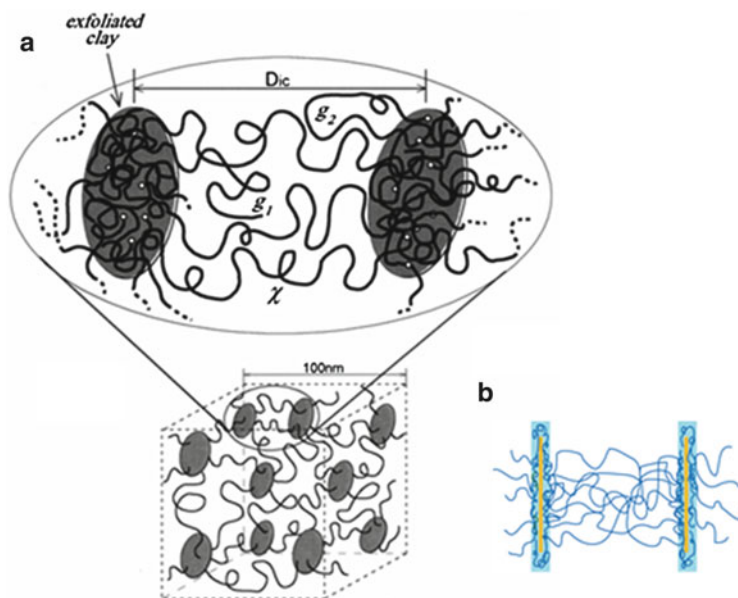


Fig. 6 (a) Structural model showing organic (polymer)–inorganic (clay) networks in the NC gel. D_{ic} is the interparticle distance of exfoliated clay sheets. χ , g_1 , and g_2 represent crosslinked chain, grafted chain, and looped chain, respectively. In the model, only a small number of polymer chains are depicted for simplicity [19, 20, 54]. (b) Decorated clay platelet sandwiched by polymer layer [52]. (a) Reprinted from Haraguchi and Li [54], Copyright 2009, with permission of Wiley

image of dried N-NC5 gel). (2) Flexible polymer chains with the same glass transition temperature (T_g) as that of the linear polymer exist in NC gels (as shown by DSC). (3) There is no distinct difference between the absorptions of PNIPA and clay in the dried NC gels and those of pure PNIPA or clay (as shown by FTIR). This is probably because in the dried state, PNIPA shows strong hydrogen bonding, which prevents hydrogen bonding with clay from being clearly identified in dried NC gels.

On the basis of the analytical data obtained and the excellent optical, mechanical, and swelling–deswelling properties of NC gels, it was concluded that NC gels possess a unique organic (polymer)–inorganic (clay) network structure (Fig. 6a) [19, 20, 39, 40, 52, 54], in which exfoliated clay nanoparticles (uniformly dispersed in an aqueous medium) are interlinked by a number of flexible polymer chains. Here, D_{ic} is the interparticle distance between exfoliated clay sheets. In the network, various types of polymer chains, such as grafts with free chain-ends, looped chains, and topologically crosslinked chains, might be present in addition to the crosslinking chains. Interaction between polymers and clay nanoparticles is ascribed to noncovalent bonds, probably hydrogen bonds between the amide side groups on the polymer and the surface of the clay (SiOH, Si–O–Si units).

In the polymer–clay network structures, it was considered that a number of polymer chains interact with a single clay platelet and that each polymer chain can interact with the clay surface at multiple points [19, 20, 39, 40]. In other words, the exfoliated clay platelets act as multifunctional crosslinkers and, hence, the polymer chains in NC gels are crosslinked by a planar series of crosslinks. These results were confirmed by the molecular characteristics of PNIPA separated from NC gels and contrast-variation SANS measurements. By successful separation of PNIPA from the N-NC gel, without damage, by decomposing the clay in the network using hydrofluoric acid (Fig. 7a) [55], it became clear that clay platelets play an important role in preventing the formation of self-crosslinked PNIPA networks [22]. These studies also showed that PNIPA in N-NC gels has a high molecular weight ($M_w = 5.6 \times 10^6$ g/mol) [55], almost regardless of C_{clay} (1–25 wt%), indicating that a single polymer chain repeatedly links neighboring clay sheets. In contrast-variation (CV) SANS measurements, it was shown that the polymer chains aggregate to form 1 nm-thick layers on the clay surface (Fig. 6b) [52]. For the deformation mechanism of NC gel under uniaxial stretching, it was concluded from CV-SANS that clay platelets orient parallel to the stretching direction and that the orientation is saturated by $\epsilon = 300\%$. Furthermore, structural change occurs preferentially in the polymer phase, i.e., stretching of polymer chains along the stretching direction as well as peeling off of polymer chains from the adsorbed layer [57]. When the strain of the specimen was removed, the polymer chain tended to be adsorbed again to the surface of the clay platelets [58].

The number of crosslinked polymer chains per unit volume of NC gel, N^* , can be estimated by Eq. (1), based on the kinetic theory of rubber elasticity [59]:

$$F = \Phi N^* k_B T \left\{ \alpha - (1/\alpha)^2 \right\} \quad (1)$$

Here, F is the force per unit original (undeformed) cross-sectional area of the swollen network, Φ is a front factor ($=1$), α is the elongation ratio, and k_B and T are Boltzmann's constant and the absolute temperature, respectively. From the tensile stress–strain curves and Eq. (1), N^* and the number of crosslinked chains per clay sheet were calculated for NC gels with different C_{clay} [40]. The results revealed that neighboring clay sheets in NC gels are linked by at least tens of flexible polymer chains (a few tens to more than 100).

The effective crosslink densities (ν_e) of NC gels were calculated using the DES, according to the Flory–Rehner theory [60]. Here, although an NC gel is a kind of ionic polymer gel containing ionic clay platelets, the effect of clay on the swelling was totally different from that of the usual organic ionic groups. In NC gels, the swelling decreased with increasing C_{clay} [20, 40], although normal ionic polymer gels exhibit increased swelling with increasing concentrations of ionic groups. This is because the clay platelets act as effective crosslinkers. Therefore, to calculate ν_e for an NC gel, Eq. (2), which corresponds to an affine network model for nonionic gel systems, was used to simplify the condition:

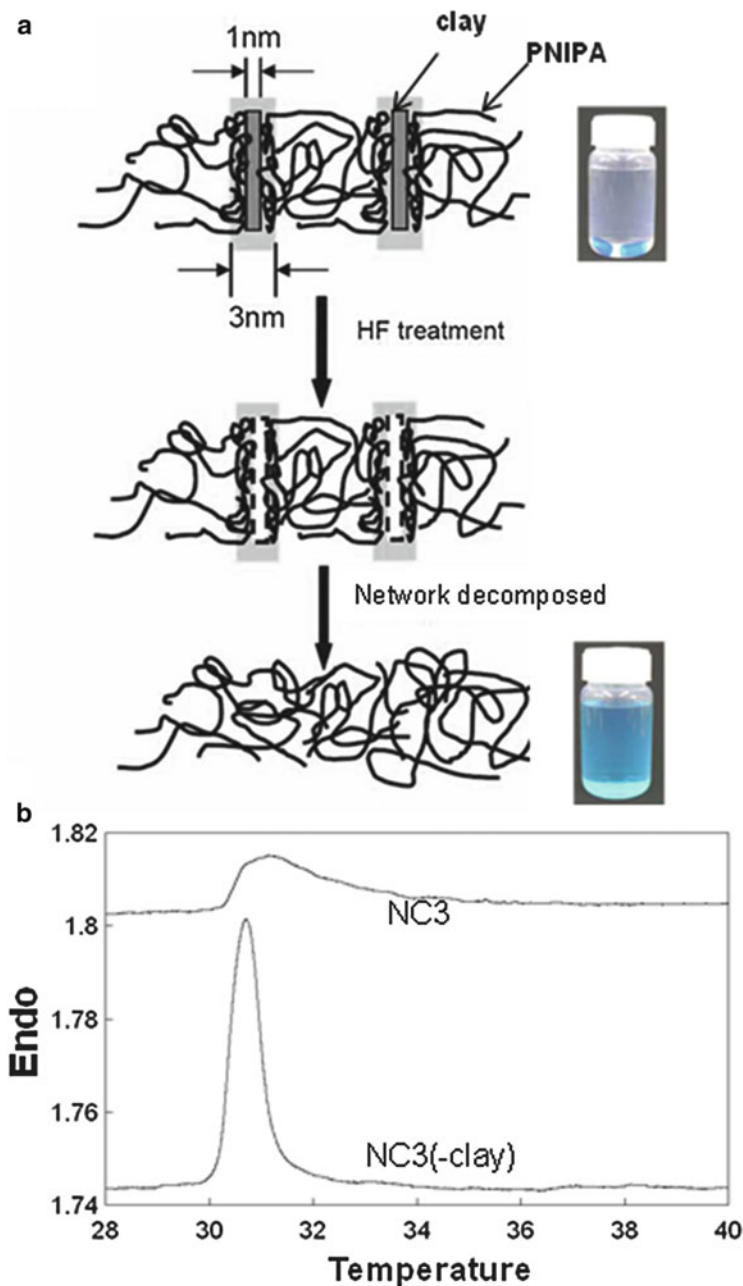


Fig. 7 (a) Process of separation of PNIPA from NC gels through the decomposition of the clay. (b) DSC thermograms of PNIPA in NC3 gel and PNIPA separated from NC3 gel (*NC3(-clay)*). Heating rate was $0.5^{\circ}\text{C}/\text{min}$ and $C_{\text{PNIPA}} = 10 \text{ wt}\%$. (a) Reprinted from Haraguchi et al. [55], Copyright 2010, with permission of Wiley. (b) Reprinted from Haraguchi and Xu [56], Copyright 2012, with permission of Springer

Table 1 Degree of equilibrium swelling (DES) and effective network density (ν_e) for NC and OR gels

Hydrogel	NC1	NC5	NC10	NC15	NC20	OR1	OR5
DES ($W_{\text{H}_2\text{O}}/W_{\text{dry}}$)	50.94	28.94	22.57	17.61	12.94	16.93	8.55
ν_e (mol/L)	0.0048	0.0099	0.0127	0.0170	0.0256	0.0431	0.1582

Calculations were made according to the Flory–Rehner theory, Eq. (2)

Reprinted from Haraguchi et al. [62], Copyright 2007, with permission of ACS

$$\phi + \ln(1 - \phi) + \chi\phi^2 = -V_s\nu_e \left[\left(\frac{\phi}{\phi_0} \right)^{1/3} - \frac{2}{f} \left(\frac{\phi}{\phi_0} \right) \right] \quad (2)$$

Here, ϕ and ϕ_0 are network volume fractions at equilibrium swelling and in a reference state, respectively. The value of $(2/f)$ (where f is the functionality) is 0.5 for BIS, and almost 0 for clay in NC gels because of its high functionality. V_s is the molar volume of water. $\chi = \chi_1 + \phi\chi_2$, where $\chi_1 = (\Delta H - T\Delta S)/k_{\text{B}}T$, $\chi_2 = 0.518$, $\Delta H = -12.462 \times 10^{-21}$ J, and $\Delta S = -4.717 \times 10^{-23}$ J/K [61]. The calculated values of ν_e for NC and OR gels are listed in Table 1 [62]. The effect of C_{clay} on ν_e in NC gels is analogous to that of C_{BIS} on ν_e in OR gels, i.e., the ν_e of NC gels increases with C_{clay} . In Table 1, the ν_e of soft NC1 gel is about one-ninth of that of the commonly used OR1 gel. Even in the case of NC10 gel, which has excellent mechanical properties (initial modulus and tensile strength), ν_e is only one-third of that of OR1 gel. The fact that values of ν_e for NC gels are generally smaller than those of OR gels is consistent with the results obtained for the mechanical properties. Thus, it was concluded that, in NC gels, relatively small numbers of crosslinks are effectively formed on the surfaces of the clay platelets.

The thermal behavior, i.e., coil-to-globule transition and glass transition, of PNIPA chains were investigated by DSC measurements [56]. It was revealed that the LCST of PNIPA in an aqueous solution and the glass transition temperature (T_g) in the dried state both remained constant (30.6 and 138°C, respectively) regardless of the molecular weight (M_w , 0.19×10^6 – 4.29×10^6 g/mol). On the other hand, the enthalpy of the coil-to-globule transition of PNIPA in NC gels decreased with increasing C_{clay} , while the onset temperature (\equiv LCST) was almost constant, regardless of C_{clay} . Furthermore, from the comparison of PNIPA before and after removal of the clay from the NC gels, the transition of PNIPA to the hydrophobic globular state was restricted by interactions with the clay (Fig. 7b).

3.2.3 Mechanism of Polymer–Clay Network Formation

The formation of three-dimensional polymer networks during the synthesis process has long been an important subject in polymer chemistry and physics [63–66]. The mechanism of formation of the organic (polymer)–inorganic (clay) network structure of NC gels was elucidated on the basis of changes in viscosity, optical transparency, XRD, and mechanical properties [39].

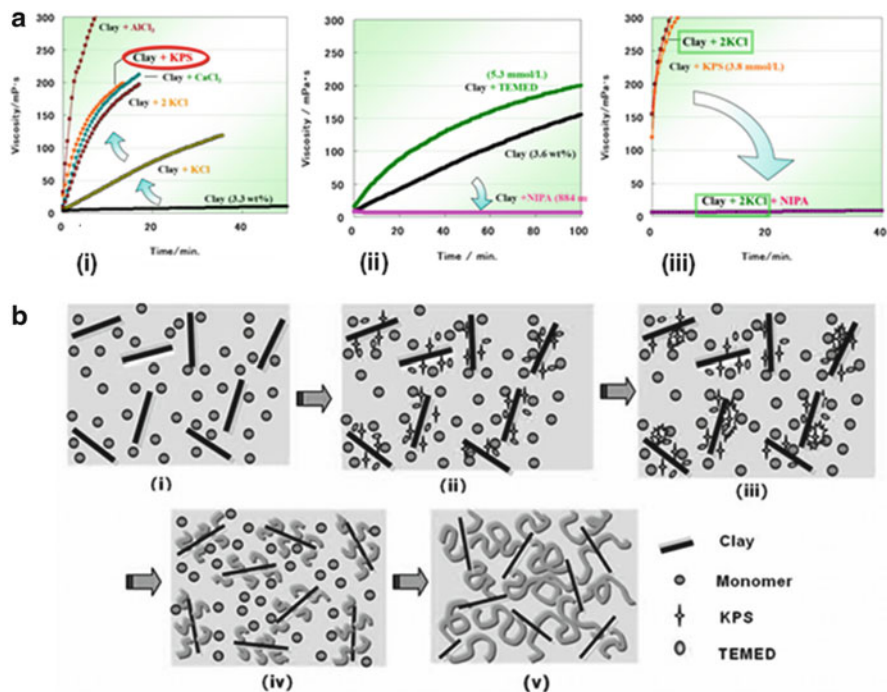


Fig. 8 (a) Changes in the viscosity of aqueous clay suspensions: *i*) Effects of addition of various salts ($C_{\text{clay}} = 3.0$ wt%); the concentration of salt was 3.7 mmol/L, unless otherwise noted. *ii*) Effects of adding NIPA and TEMED ($C_{\text{clay}} = 3.8$ wt%); the same concentrations of NIPA and TEMED as those in a typical reaction solution were used ($C_{\text{NIPA}} = 1$ mol/L, $C_{\text{TEMED}} = 800$ $\mu\text{L/L}$). *iii*) Changes in the viscosity of aqueous solutions containing clay, KCl (KPS), and NIPA. (b) Model structures for the reaction solutions and the mechanisms for forming organic-inorganic network structures in NC gels: *i*) Aqueous solution consisting of clay and NIPA. *ii*) Reaction solution consisting of clay, NIPA, KPS, and TEMED. *iii*) Radical formation near the clay surface in the reaction solution. *iv*) Formation of clay-brush particles. *v*) Formation of organic-inorganic networks. In the models, only a small number of monomer (polymer), KPS, and TEMED molecules are depicted for simplicity. Reprinted from Haraguchi et al. [39], Copyright 2005, with permission of ACS

Figure 8a(i) shows the effect of adding salts on the viscosity of an aqueous clay suspension ($C_{\text{clay}} = 3.0$ wt%). The viscosity increases with increasing ionic strength of salt, and the transition from sol to gel was accelerated. By including the results of XRD measurements, it was concluded that KPS strongly interacts with clay platelets through ionic interactions and that KPS molecules are closely associated with the clay surface in aqueous suspensions. The effect of NIPA monomer is the reverse of that for addition of KPS. As shown in Fig. 8a(ii), the increase in viscosity of a aqueous clay suspension with retention time was markedly depressed by the addition of NIPA. The solution containing C_{clay} at 3.8 wt% and NIPA of 1 mol/L, which were the same concentrations as used in the synthesis of an N-NC5-M1 gel, was very stable, and the sol-gel transition did not occur for at least 1 month,

whereas the same clay suspension without NIPA became a gel within a few hours. This indicates that nonionic NIPA monomers effectively surround each clay platelet, with a mild interaction between ionic clay and dipolar NIPA molecules. When both NIPA and KPS or all three components (NIPA, KPS, and TEMED) were added to the aqueous clay suspension, the viscosity of the resulting solution was very stable or increased slightly with retention time. This indicates that the effect of NIPA in depressing the viscosity change predominates over the accelerating effects of KPS and TEMED.

Model structures relating to the process of formation of NC gels are shown in Fig. 8b [39]. During the preparation of the initial reaction solutions, a specific solution structure was formed, where monomer (NIPA) largely prevents gel formation of clay itself [Fig. 8b(i)], and initiator and accelerator are located near the clay surface through ionic interactions [Fig. 8b(ii)]. Then, by increasing the solution temperature, free-radical polymerization was initiated by the redox system close to the surface of clay [Fig. 8b(iii)]. By this mechanism, we propose that “clay-brush particles,” composed of exfoliated clay platelets with numbers of polymer chains grafted to their surfaces, are formed in the early stages of NC gel synthesis, as depicted in Fig. 8b(iv).

The formation of clay-brush particles was confirmed by the time dependence of optical transmittance during in-situ polymerization. A distinct drop in transparency was observed in the very early stage of in-situ polymerization (Fig. 9a; N-NC2 gel) [39] which could correspond to the formation of assemblies of clay-brush particles. Monomer conversion at the point of minimum transparency was approximately 7%, where the polymer-to-clay weight ratio was about 0.2:1. Transparency was re-established on further polymerization. In contrast, no transparency changes were observed during the polymerization of OR gels or LR (Fig. 9a), or even in the case of PNIPA containing silica or titania particles. Therefore, it was concluded that the newly observed transparency changes were a characteristic of NC gel synthesis, i.e., the changes are related to the formation of clay-brush particles and the subsequent formation of an organic–inorganic network structure. This was also confirmed by XRD measurements [39]. The decrease in transparency was not observed in the case of the PAAm-XLS system [44], probably because of the weak interactions between PAAm and XLS clay and the high dispersion of the resulting complex.

The proposed mechanism of formation of the organic–inorganic network structure was supported by the fact that the stress–strain curves obtained for NC gels with different polymer contents exhibit characteristic two-step changes for D-NC2.5-*Mm* gels (Fig. 9b) [39], which correspond to the formation of a primary network (first step, $m \leq 0.5$) and a subsequent increase in the number of crosslinked polymer chains (second step, $m \geq 1$). Furthermore, DLS and SANS measurements showed that the gelation in NC gels is classified as an ergodic–nonergodic transition, similar to that in OR gels; the only difference being that huge clusters of NC microgels (corresponding to clay-brush particles) are formed before the gelation threshold in the case of the former [52].

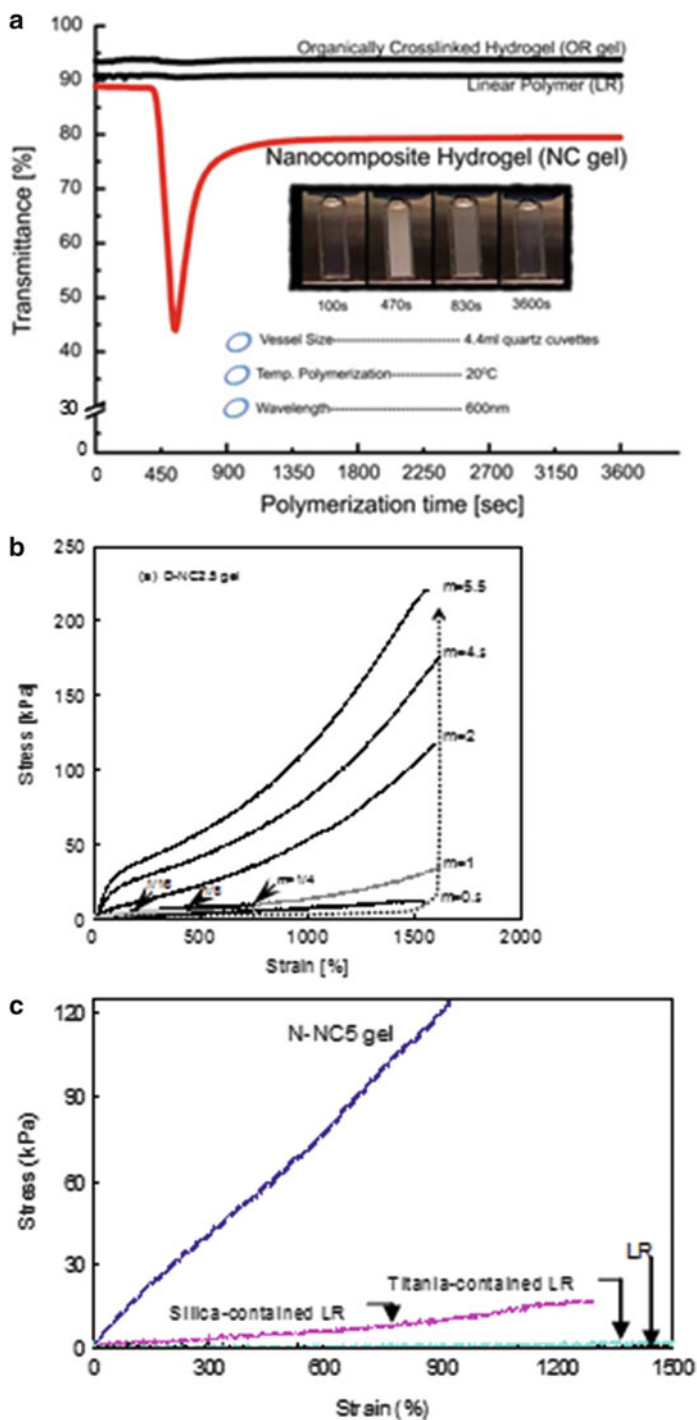


Fig. 9 (a) Changes in optical transparency during the polymerization of NC gel (N-NC2-M1 gel), OR gel (N-OR1-M1 gel) and linear polymer (LR). The *photos* were obtained during the

NC gels with excellent mechanical properties and structural homogeneity could not be prepared by other methods, such as those involving mixing of clay and polymer solutions, or by in-situ polymerization in the presence of the other inorganic nanoparticles such as silica or titania, as shown in Fig. 9c [39]. These results indicate that the formation of organic–inorganic network structures in NC gels is highly specific and is achieved only by in-situ free-radical polymerization in the presence of clay. The specific role of clay, as distinct from silica, in the preparation of NC gels is also confirmed from investigations of the nature of PNIPA after eliminating clay and silica from the gels [55].

3.3 Basic Properties of NC Gels

The optical, mechanical, and swelling–deswelling properties of NC gels are superior to those of conventional OR gels. Furthermore, these basic properties can be controlled as desired by altering the network composition or by modifying the network structures.

3.3.1 Optical Transparency

The optical transparency of hydrogels generally reflects the spatial inhomogeneity in the networks. The main factors affecting the transparency of NC gels are the degree of dispersion of the clay nanoparticles in aqueous media and clay–monomer or clay–polymer interactions. Translucent or opaque NC gels are obtained when the clay is insufficiently exfoliated in the reaction solution or when microscopic aggregations of the clay and monomers or polymers are formed. The effect of the clay content ($C_{\text{clay}} = 1\text{--}9\text{ wt\%}$) in N-NC gels, and that of the BIS content ($C_{\text{BIS}} = 1\text{--}9\text{ mol\%}$) in N-OR gels, on transparency measured at 1°C are shown in Fig. 10 [20]. Transparent OR gels generally become opaque with increasing C_{BIS} , because of the inhomogeneous distribution of crosslinking points (Fig. 1c-1); the critical value above which the transmittance decreases changes with the type of polymer used, e.g., 5 mol% (N-OR) and 8 mol% (D-OR). In contrast, NC gels are generally transparent, regardless of the C_{clay} and C_{p} or the type of polymer used.

With regard to the temperature dependence of gel transparency, D-NC gels are always transparent regardless of the temperature, whereas N-NC gels exhibit reversible changes in transparency at the LCST as a result of the coil–globule

Fig. 9 (continued) polymerization of NC gel. (b) Effects of polymer content (m) on the stress–strain curves of D-NC2.5 gel ($m = 1/16\text{--}5.5$). (c) Stress–strain curves for N-NC5-M1 gel, LR (N-LR-M1), and silica- or titania-containing LRs. Silica and titania were contained in the same weight as clay in N-NC5-M1 gels. Reprinted from Haraguchi et al. [39], Copyright 2005, with permission of ACS

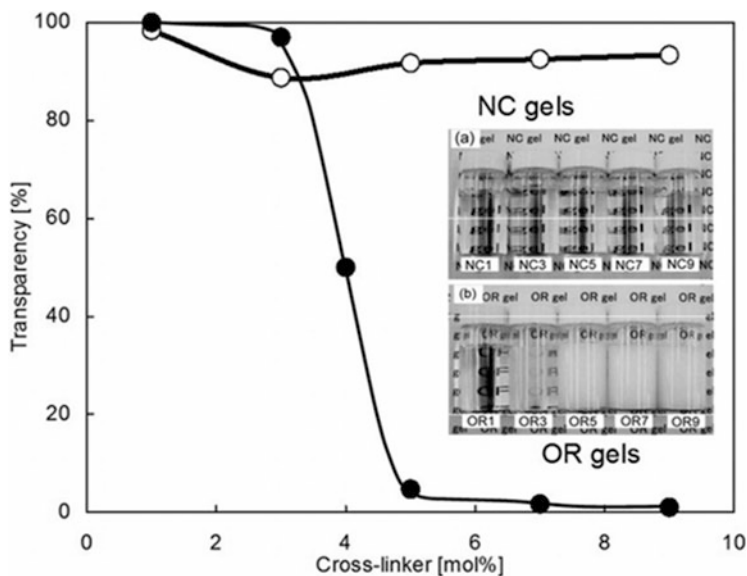


Fig. 10 Changes in optical transparency of N-NC and N-OR gels produced by altering the crosslinker contents. Optical transmittance was measured at 1°C for hydrogels. Reprinted from Haraguchi et al. [20], Copyright 2002, with permission of ACS

transition of PNIPA. Thus, for example, N-NC3 and N-NC5 gels became opaque (white) above the LCST. However, the extent of the change in transparency at the LCST varies dramatically with C_{clay} , as shown in Fig. 11 [28]. The decrease in transparency gradually reduced as C_{clay} increased. Eventually, for C_{clay} greater than $C_{\text{clay}}^{\text{crit(opt}(1))}$ ($=10$), there was no loss in transparency and gels remained transparent regardless of the temperature (see inset to Fig. 11) [28]. This indicates that, in NC gels with C_{clay} greater than $C_{\text{clay}}^{\text{crit(opt}(1))}$, thermoresponsive dehydration of PNIPA chains (i.e., the conformational change to a globular, hydrophobic form) is hindered in PNIPA chains attached to, or lying close to, hydrophilic clay surfaces. This is the first observation of nonthermosensitive PNIPA hydrogels where the coil-to-globule transition of PNIPA chains is completely restricted by the presence of inorganic nanoparticles. The transition temperatures of NC gels, identified as a decrease in optical transmittance by 50%, increases with increasing C_{clay} , although the transmittance starts to decrease at a slightly lower temperature [62]. Furthermore, the transition temperature decreased or increased markedly on adding an inorganic salt (e.g., NaCl, CaCl₂, AlCl₃) or a cationic surfactant (e.g., hexadecyltrimethylammonium chloride) to the gel [67].

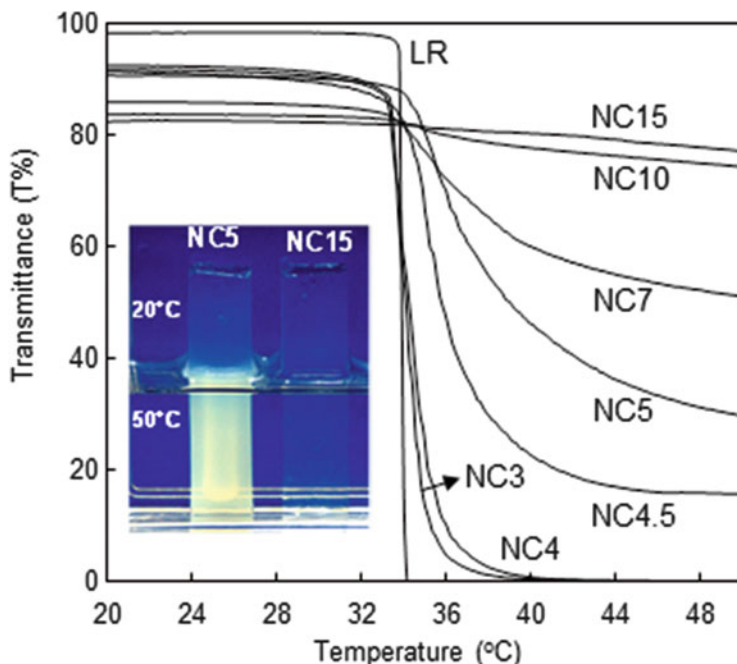


Fig. 11 Temperature dependence of the optical transmittance for PNIP solution (*LR*) and NC gels with different C_{clay} (NC3–NC15). *Inset*: Transparency of NC5 and NC15 gels below (*upper part*: in air at 20°C) and above LCST (*lower part*: in water at 50°C). The transparency change observed for NC5 gel was not observed for NC15 gel. Reprinted from Haraguchi and Li [28], Copyright 2005, with permission of Wiley

3.3.2 Mechanical Properties

For a long time, the tensile mechanical properties of hydrogels such as PNIP hydrogels were not investigated, because hydrogels with chemically crosslinked networks (OR gels) cannot withstand mechanical stretching, bending, or even being tightly grasped between the chucks. However, the creation of NC gels has made it possible to conduct all kinds of mechanical test. The most striking characteristics of NC gels are their excellent mechanical properties such as high elongation ($\epsilon_b > 1,000\%$), high tenacity (bending by more than 360°), and high tensile strength ($\sigma > 100$ kPa); these properties were entirely unexpected and distinct from those of OR gels having the same composition, except for the type of crosslinker.

Figure 2b shows the changes in the tensile stress–strain curves for NC gels with different C_{clay} ($C_{\text{clay}} = 0.05\text{--}10$ wt%) [21]. At low C_{clay} (< 1 wt%), the initial modulus (E) increased slightly with C_{clay} , but ϵ_b decreased sharply to about 1,000%. However, when C_{clay} was higher than that for NC1, E and σ increased greatly, as indicated by the dotted line in Fig. 2b, while values of ϵ_b were approximately constant ($\epsilon_b \approx 1,000\%$). Thus, the effects of crosslinker, BIS, and clay on the tensile mechanical properties are totally different from each other. In NC gels,

clay platelets play a specific role, acting as effective multifunctional crosslinkers to form polymer–clay networks. The critical concentration $C_{\text{clay}}^{\text{crit}(1)}$, above which a well-defined organic–inorganic network is formed, is approximately 1, for the present system ($C_{\text{NIPA}} = 1 \text{ M}$).

Because the number of crosslinkers per unit volume is different in NC and OR gels (e.g., 10 and 5,400 units/ 10^6 nm^3 for NC3 and OR1, respectively), the D_{ic} in NC gels should be very large with a narrower distribution than for OR gels. The reason for the high ε_{b} in NC gels, regardless of the high C_{clay} , is attributed to the high deformability of the long, flexible polymer chains in the unit structure of the polymer–clay networks (inset of Fig. 2b). E and σ for NC gels also increases with increasing C_{p} [39] because the number of polymer chains linking neighboring clay platelets increases with C_{p} .

Figure 12a shows tensile stress–strain curves for N-NC gels with different C_{clay} (NC5–NC25) [28, 41], where both E and σ increase markedly with C_{clay} , as shown

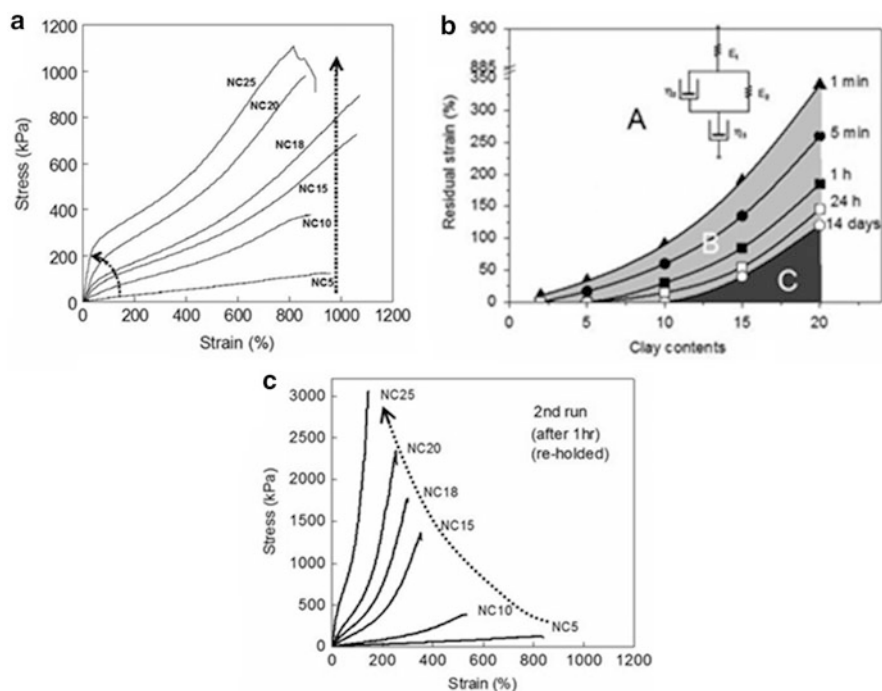


Fig. 12 (a) Tensile stress–strain curves for N-NC gels with different C_{clay} (NC5–NC25). All samples tested had the same ratio of water to polymer (10:1.13 w/w). (b) Time dependence of residual strain for NC gels with different C_{clay} after release from stress from an initial elongation of 900% (or 800% for NC20 and NC25); *A* quick recovery, *B* time-dependent recovery, and *C* pseudo-permanent strain. *Inset*: Four-element mechanical model adopted for NC gels. (c) Tensile stress–strain curves for once-elongated NC gels with different C_{clay} , which were prepared by elongation to 900% (or 800% for NC20 and NC25) and subsequently relaxed for 1 h. Reprinted from Haraguchi and Li [41], Copyright 2006, with permission of ACS

by the arrow. The value of σ exceeds 1,000 kPa in the N-NC25 gel. The steep increase in E at high C_{clay} is probably due to the formation of rigid structures involving clay–clay interactions, similar to a house-of-cards structure [68] (Fig. 3b) or a nematic-like clay structure [62]. In fact, the optical anisotropy of as-prepared NC gels is pronounced in NC gels with $C_{\text{clay}} \geq 10$ wt% [41]. Thus, the tensile mechanical properties can be controlled over a wide range by altering C_{clay} and C_p . It should be noted that the changes in mechanical properties of NC gels are unique, i.e., totally different from those observed in normal polymeric materials. In the case of the latter, an increase in E is generally accompanied by a decrease in ε_b because the increase is normally caused by the orientation of polymer chains or modification of the polymer structure to a rigid form. In contrast, in NC gels, E and σ can increase without a large sacrifice of ε_b because of the polymer–clay network structure. From the area under the tensile stress–strain curve, the fracture energies (ξ_f) for NC and OR gels and the dependence of ξ_f on the crosslinker content are determined [28, 41]. The ξ_f of NC gels increases in proportion to C_{clay} , whereas that of OR gels remains almost constant, regardless of C_{BIS} ($\xi_f = 0.0014$ J). The value of ξ_f for NC25 is nearly 3,300 times that of OR gels [41]. This is a very striking result because NC and OR gels differ only in the crosslinker used. NC gels prepared using Laponite XLS also showed similar results for both the tensile mechanical properties, with the exception of large ε_b (\equiv low crosslink density), and the swelling–deswelling properties [69].

NC gels showed characteristic recovery from high elongation. The time dependence of the residual strain after an elongation of 900% followed by immediate stress release is shown in Fig. 12b for various clay contents [41]: region A, instant recovery (within 1 min); region B, time-dependent residual strain; and region C, pseudo-permanent strain (remains for more than 2 weeks). For N-NC gels with a low C_{clay} (<NC10), 90–99% instantaneous recovery was observed. However, for NC gels with high C_{clay} (NC10–20), the permanent strain gradually increased with C_{clay} , which is attributed to the irreversible orientation of the clay platelets. These elongation and recovery patterns of NC gels can be explained using a typical four-element mechanical model (inset of Fig. 12b).

The stress–strain curves of N-NC gels in the second cycle were different from those observed in the first cycle (Fig. 12c) [41]. For NC gels with higher C_{clay} , remarkable increases in E and σ and a significant decrease in ε_b were observed in the second cycle. The effect of C_{clay} on the σ and E of N-NC gels in the first and second cycles are summarized in Fig. 13 [41]. The critical value of $C_{\text{clay}}^{\text{crit}(2)}$, above which the mechanical properties in the second cycle become very different from those in the first cycle, was found to be approximately 10. The change in the relative magnitudes of E_{10-50} and $E_{100-200}$ were attributed to the rigidity of the as-prepared gels and the permanent orientation of the clay platelets (and PNIPAA chains attached thereto) after the first elongation.

The tensile mechanical properties of NC gels could also be varied by changing the type of clay used (Table 2) [43]. The modification of clay, e.g., by fluorine substitution (SWF and B in Table 2) and/or by the addition of a dispersant such as

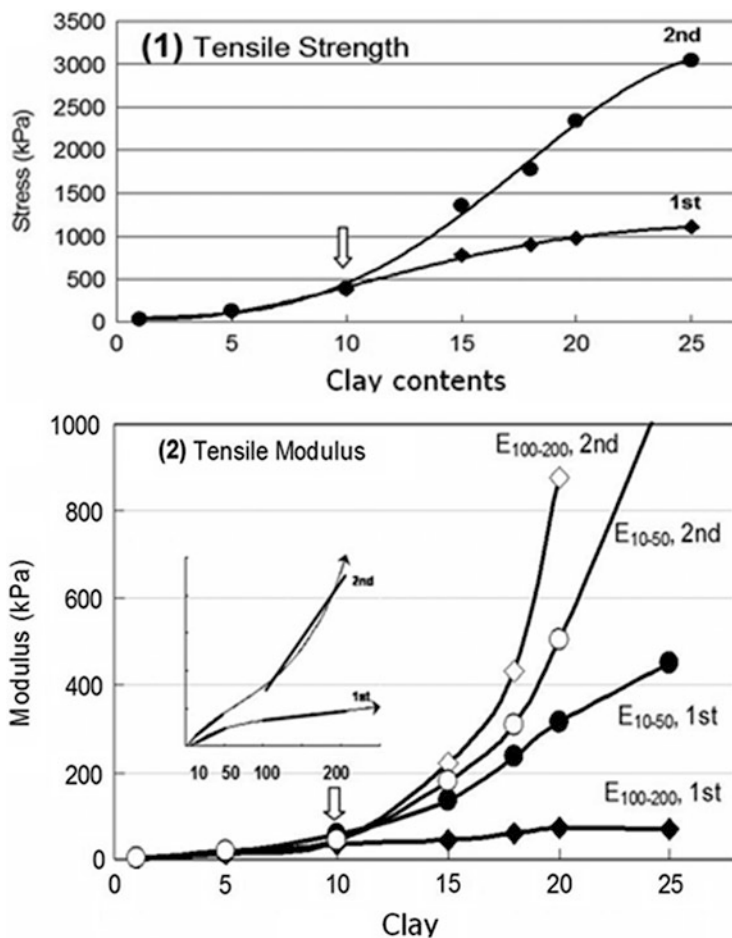


Fig. 13 Changes in tensile strength (*top*) and tensile modulus (*bottom*) for two series of NC gels. As-prepared NC gels (*diamonds* first cycle) and once-elongated NC gels (*circles* second cycle). Two tensile moduli, E_{10-50} and $E_{100-200}$, were calculated from the slopes in the ranges 10–50 and 100–200% elongation, respectively. The *arrow* indicates the critical clay concentration ($C_{\text{clay}}^{\text{crit}(2)}$), above which the mechanical properties of the second cycle are largely changed. Reprinted from Haraguchi and Li [41], Copyright 2006, with permission of ACS

pyrophosphate-Na (XLS and S), had a marked effect on the mechanical properties, where E and σ decreased but ε_b increased (Fig. 14). Similar tendencies were also observed in the NC gels prepared using clay with a large particle size (montmorillonite, size >300 nm; F in Table 2 and Fig. 14).

The use of clay as a multifunctional crosslinking agent is the most crucial point in the fabrication of NC gel with excellent properties. After NC gel was prepared successfully for the first time using exfoliated clay platelets [19], different kinds of inorganic or organic materials were adopted as multifunctional crosslinkers for NC

Table 2 Compositions of various inorganic clays

Clay	Type	Composition (wt%)					
		SiO ₂	MgO	Li ₂ O	Na ₂ O	F	P ₂ O ₅
<i>Water swelling</i>							
XLG ^a	Synthetic hectorite	59.5	27.5	0.8	2.8	–	–
SWN ^b	Synthetic hectorite	54.3	27.9	1.6	2.7	–	–
XLS ^a	XLG + dispersing agent	54.5	26.0	0.8	5.6	–	4.1
SWF ^b	Fluorinated hectorite	54.5	27.2	1.6	5.8	2.9	–
B ^a	Fluorinated hectorite	55.0	27.0	1.4	3.8	5.6	–
S ^a	B + dispersing agent	51.0	25.0	1.3	6.0	5.0	3.3
<i>Partially swelling in water</i>							
F ^c	Natural montmorillonite	61.3	3.43	–	4.1	Al ₂ O ₃ = 22, Fe ₂ O ₃ = 1.9	
<i>Nonswelling in water</i>							
IGS ^d	Sepiolite	Magnesium silicate					

^aRockwood Additive Ltd.^bCoop Chemical Ltd.^cKunimine Ind.Co.^dTomoe Ind.Co.

Reprinted from Haraguchi and Li [43], Copyright 2004, with permission of Japan Thermosetting Plastics Industry Association

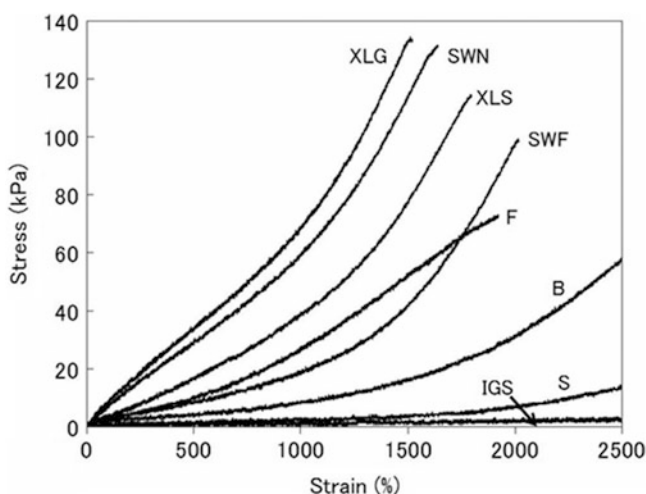


Fig. 14 Stress–strain curves of D-NC gels prepared by using various kinds of clay: hectorite (XLG, SWN), fluorinated hectorite (SWF, B), hectorite modified with a dispersing agent (XLS), montmorillonite (F), B + dispersing agent (S), and sepiolite (IGS). Reprinted from Haraguchi and Li [43], Copyright 2004, with permission of Japan Thermosetting Plastics Industry Association

gels in the following systems: attapulgite (fibrillar clay mineral) and copolymer [70], octa(propylglycidyl ether) polyhedral oligomeric silsesquioxane and PNIPA [71], layered double hydroxides and agarose [72], Fe₃O₄ (surface-treated by silanization) and PNIPA [73], organic hydrophobic association and PAAm [74], chitosan nanofibers and PAAm [75], and cellulose rods and PAAm [76].

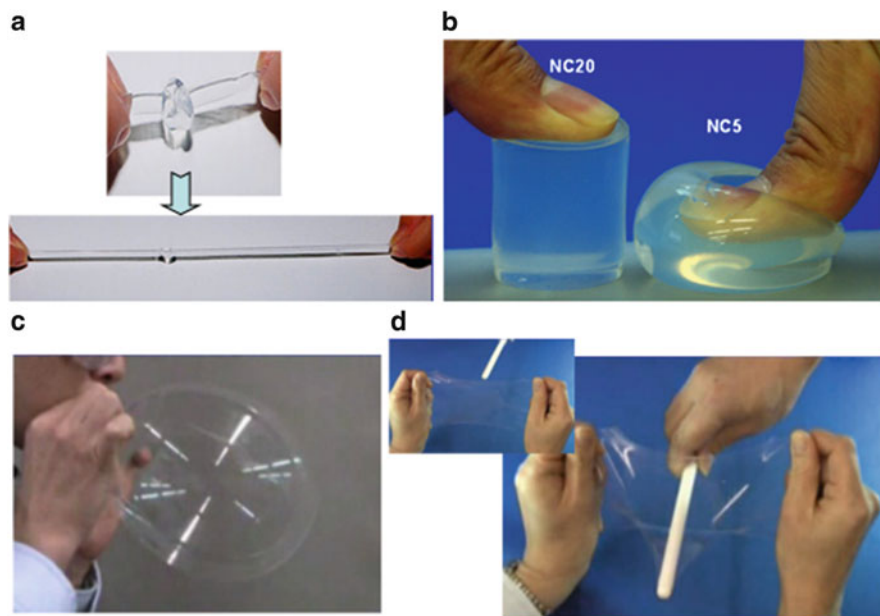


Fig. 15 (a) Knotted and stretched NC5 gel. (b) Compression of NC5 and NC20 gel. (c) Balloon formation from an NC5 gel thin tube sample. (d) Strong resistance against bar-pushing by a thin film of NC10 gel. (a) Reprinted from Haraguchi et al. [20], Copyright 2002, with permission of ACS. (b) Reprinted from Haraguchi and Li [28], Copyright 2005, with permission of Wiley

NC gels can withstand high levels of deformation in all modes, including compression, torsion, tearing and bending, in addition to elongation. For example, NC gels can be tied into a knot without being damaged, and the knotted NC gel can be stretched without breaking at the knot (Fig. 15a) [20]. In compression tests, NC gels generally withstand a compression of up to 90% (Fig. 15b) [28, 41]. The compression modulus and strength of N-NC gels increase almost proportionally with C_{clay} . The strength reaches 5 MPa at 80% strain for N-NC20 gels [41]. Furthermore, NC gels exhibited striking features in more complicated deformation modes, such as balloon formation from thin tubes of NC gel (Fig. 15c) and strong resistance against bar-pushing by NC gel thin films (Fig. 15d).

On the other hand, the ultimate tensile properties of rubbery NC gels changed considerably when the water content ($R_{\text{H}_2\text{O}} = W_{\text{H}_2\text{O}}/W_{\text{dry}}$) was varied over a wide range (Fig. 16) [54]. At a high $R_{\text{H}_2\text{O}}$, where PNIPA chains are fully hydrated, N-NC4 gels retain their rubbery tensile properties. However, when $R_{\text{H}_2\text{O}}$ is decreased, these gels undergo plastic-like deformation. Consequently, for a series of N-NC4 gels with different $R_{\text{H}_2\text{O}}$, a peculiar line (or “failure envelope”) was obtained by connecting the rupture points in the stress–strain curves (Fig. 16). Here, a counter-clockwise movement of the rupture point was observed on increasing the strain rate or decreasing $R_{\text{H}_2\text{O}}$. Thus, a decrease in $R_{\text{H}_2\text{O}}$ in NC gels produces an effect similar to that produced by a decrease in temperature in an amorphous elastomer (e.g., styrene-butadiene rubber, SBR) [77], although the mechanisms

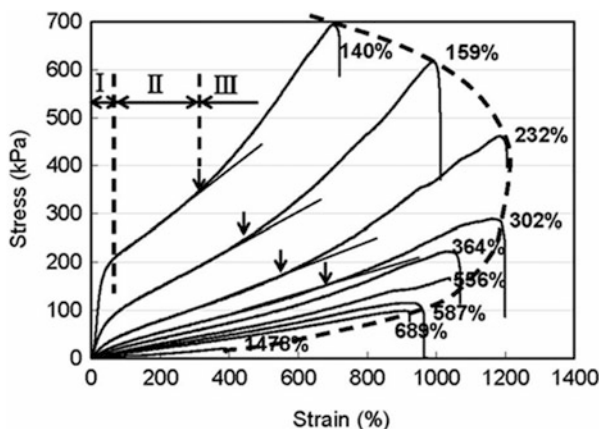


Fig. 16 Stress–strain curves for N-NC4 gels with different $R_{\text{H}_2\text{O}}$ (wt%). The numerical values indicate $R_{\text{H}_2\text{O}}$. The $R_{\text{H}_2\text{O}}$ value for the as-prepared NC4 gel is 689 wt%. A dashed line illustrates the failure envelope obtained by connecting the rupture points. The arrows represent the threshold strain points (ϵ_t) above which the strain-hardening occurs. I, II, and III indicate the distinct stages of tensile deformation. Reprinted from Haraguchi and Li [54], Copyright 2009, with permission of Wiley

are different in the two cases, i.e., entropic elasticity in the elastomer and plasticization in the NC gel.

The stability of the polymer–clay network was investigated through precise control of the swelling and drying processes [78]. The tensile and swelling properties of NC gels were not changed by swelling treatments, but were modified by drying treatments; i.e., once-dried (dried and re-swollen) NC gels exhibited higher E and σ , and lower ϵ_b values as well as lower degrees of swelling, compared with as-prepared NC gels. These changes were attributed to the irreversible rearrangement of the polymer–clay network structures, in which additional crosslinks were formed because of additional contacts between polymer chains and clay in the concentrated state. The rearranged network structures remained almost unchanged after repeated drying and heating.

While modifying the network structure by simultaneously using two crosslinkers, i.e., inorganic clay and very small amounts of organic BIS (e.g., $C_{\text{BIS}} = 0.001\text{--}0.02$ mol%), it was found that in co-crosslinked PNIPA hydrogels (NC-OR gels) the controllable region in the correlation between the compression strength and the modulus was expanded, as shown in Fig. 17 [47]. This change was attributed to the formation of a microcomplex structure with relatively high chemical crosslink densities in proximity to the clay surface (lower inset in Fig. 17). Here, the combination of high strength and low modulus, which is often required for biomaterials but usually difficult to achieve in materials design, could be obtained. Also, by using this modification, it became possible to sterilize NC gels by autoclave treatment (121°C , 2 atm) without any macroscopic damage (i.e. no change of form by creep), as shown in the upper inset of Fig. 17.

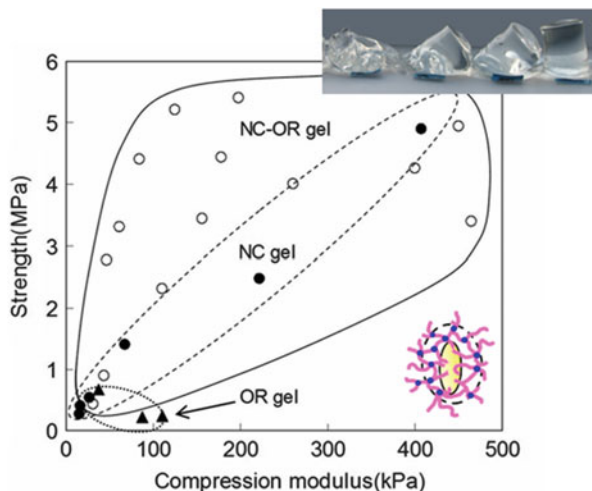


Fig. 17 Correlation of compression strength and modulus, which is controllable in NCn , ORm , and $NCn-ORm$ gels by altering $n = 0-10$ and $m = 0-5$. The modulus–strength relationship can be controlled within each rounded region. Here, the strength for NC and NC-OR gels are at 80% compression (without fracture), whereas the strength for OR gels are the maximum at break. *Lower inset*: preferential distribution of chemical crosslinks (BIS) close to the clay platelets. *Upper inset*: increasing resistance against autoclave treatment at 121°C and 2 atm as a result of slight increases in m . Reprinted from Haraguchi and Song [47], Copyright 2007, with permission of ACS

3.3.3 Swelling–Deswelling Properties

With regard to swelling in water at 20°C, NC gels normally exhibit greater swelling than OR gels, as shown in Fig. 18a [20] and Table 1 (the dependence of DES on the crosslinker content). These effects are attributed to the lower crosslink density of NC gels compared with that of OR gels. In the case of PNIPA hydrogels, both N-NC and N-OR gels exhibited volume changes at the LCST in response to the coil-to-globule transition of PNIPA chains. Thermosensitivity and its control in PNIPA hydrogels have attracted much attention because of their many potential applications

However, N-OR gels, consisting of chemically crosslinked networks, generally have several important limitations, such as low volume change and slow deswelling rate, as well as poor mechanical properties [6–10]. Among these disadvantages, the slow rate of deswelling has been studied most extensively. As a result, fast deswelling has been achieved by introducing porosities [79], structural inhomogeneities [80], or tailored graft structures [81] into OR gels. However, in most cases, other properties such as the mechanical properties, swelling ratio, and optical transparency were not improved and were often made worse.

All these limitations are overcome by N-NC gels, which show large volume changes and high deswelling rates coupled with excellent mechanical properties

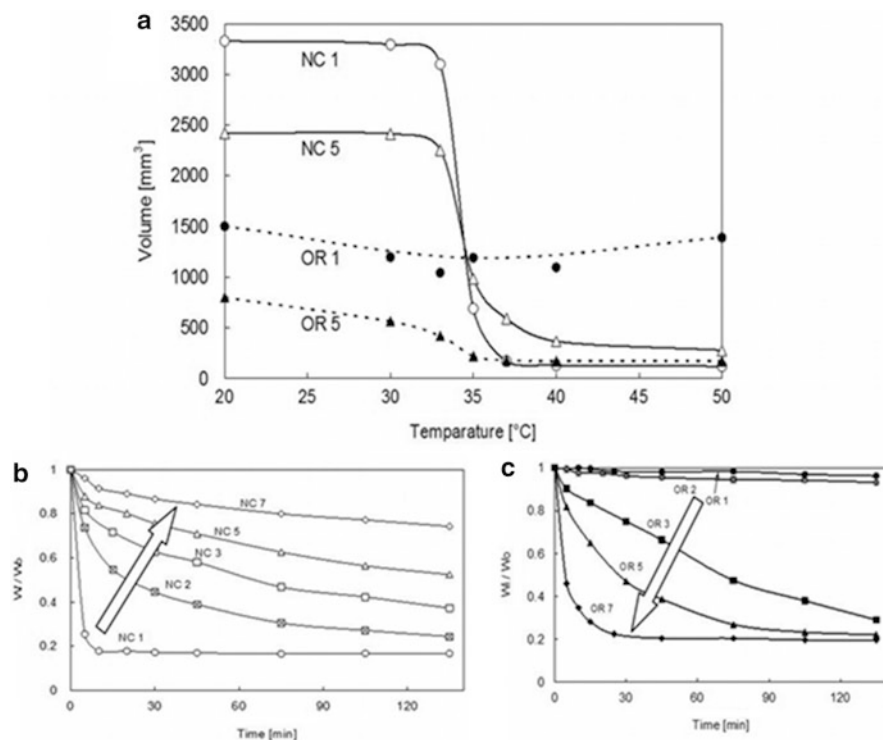


Fig. 18 (a) Temperature dependence of the gel volume for NC and OR gels with different crosslinker contents. All original gels had the same water to polymer ratio (10:1 w/w) and the same size (5.5 mm diameter \times 30 mm length). Each gel was first swollen at 20°C for 48 h and subsequently maintained in a water bath at a specific temperature for 8 h before measurement. (b, c) Deswelling kinetics (time dependence of weight) at 40°C for (b) NC gels and (c) OR gels with different crosslinker (clay and BIS) contents. All original gels had the same water to polymer ratio (10:1 w/w) and sample size (5.5 mm diameter \times 30 mm length). Arrows indicate the direction of increasing crosslink density. Reprinted from Haraguchi et al. [20], Copyright 2002, with permission of ACS

[19, 20]. N-NC gels, particularly those with low C_{clay} , show outstanding stimulus sensitivity because the PNIPAA chains in the network adopt flexible, random conformations, as described in the preceding sections. The temperature dependence of gel volume for NC and OR gels with different crosslinker contents is shown in Fig. 18a. NC gels exhibit larger volume changes than OR gels. For example, NC1-5 gels exhibit about 30- to 50-fold changes in volume, whereas volume changes for OR5 gel are less than 15-fold. Also, OR gels with low BIS contents (e.g., OR1 gel) did not show the apparent swelling–deswelling behavior under these experimental conditions. This may be due to the very low rate of shrinking of OR1 gel; OR gels with low BIS contents required far longer to shrink than the gel used in these experiments.

The deswelling kinetics for N-NC gels in water at 40°C ($>$ LCST) and the effect of crosslinker content are shown in Fig. 18b, and those for N-OR gels are shown for

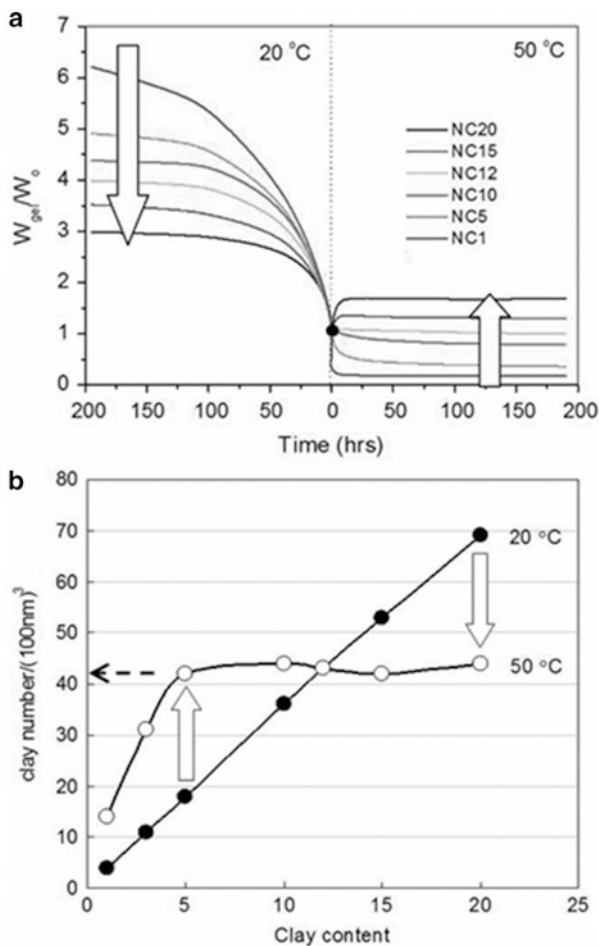
comparison in Fig. 18c [20]. Because deswelling rates are inversely proportional to the square of typical gel dimensions, and the initial samples used have large volumes (712 mm^3), transparent N-OR gels with low C_{BIS} , such as N-OR1 and N-OR2 (which are most commonly used as PNIPA hydrogels), undergo low degrees of deswelling, i.e., the time taken to shrink is more than a month. In contrast, the N-NC1 gel exhibited the rapid response, and shrinking was almost complete within 10 min. This is because, in the structurally homogeneous N-OR1 gel, the gel first forms a hydrophobic, collapsed polymer skin on the macroscopic gel surface by eliminating near-surface water, through which the subsequent water permeation from the gel interior is very limited. In contrast, in NC gels with low C_{clay} , shrinking proceeds rapidly as water is squeezed from the gel interiors through large numbers of water channels formed by microphase separation of the flexible PNIPA chains, including grafts. This concept is consistent with the fact that shrinking occurs rapidly when additional grafts are intentionally introduced into the chemically crosslinked networks [81].

Another interesting point of note is that N-NC and N-OR gels exhibit entirely opposite tendencies with respect to the effects of crosslinker content (C_{clay} and C_{BIS}) on the deswelling rate (Fig. 18b, c). This is because, in NC gels, the mobility of PNIPA chains is gradually restricted as C_{clay} increases, while the homogeneous network structure is retained. The deswelling rate, therefore, gradually decreases as C_{clay} increases; this relationship differs from that stated in the Tanaka–Fillmore theory [82]. In contrast, in N-OR gels, deswelling rates increase with C_{BIS} . This is due to the water changes formed in optically turbid (structurally inhomogeneous) N-OR gels with high C_{BIS} as a result of heterogeneous distribution of crosslinking points. The different characteristics of N-NC and N-OR gels during swelling–deswelling are clearly shown by experiments performed using alternating temperature changes [20]. Here, increases in C_{clay} in N-NC gels resulted in decreased volume changes, whereas increases in C_{BIS} in N-OR gels caused the volume change to increase.

With further increases in C_{clay} , the degree of thermosensitive deswelling decreased markedly [28, 62]. As shown in Fig. 19a, no volume contraction was observed for N-NC gels with C_{clay} greater than 12 wt%. Instead, NC gels underwent swelling, even at 50°C ($>\text{LCST}$), where PNIPA behaved as a hydrophilic polymer with no thermosensitive transition [62]. Thus, volume changes on swelling or deswelling of N-NC gels are controllable through large variations in C_{clay} . Analysis of the number of clay platelets per unit gel volume (n_{clay}) in as-prepared NC gels and in gels stored at 50°C , showed that n_{clay} at 50°C was almost the same ($n_{\text{clay}} \approx 42$ per 10^6 nm^3 of gel) for all NC gels with $C_{\text{clay}} \geq 5 \text{ wt}\%$ (Fig. 19b); this observation indicates that during volume contraction, n_{clay} increases to an upper limit of 42 per 10^6 nm^3 . Also, NC gels with high clay loadings in the as-prepared state, such as NC15 and NC20, tend to expand even at 50°C , until they reach the same value of n_{clay} (≈ 42) [62].

In order to enhance the swelling capability or introduce pH-sensitivity in addition to thermosensitivity, ionic monomers such as acrylic acid (AAc), sodium acrylate (NaAA), methacrylic acid (MAAc), sodium methacrylate (NaMAA), and

Fig. 19 (a) Swelling–deswelling behavior of NC gels with different C_{clay} , measured in water at 20 and 50°C. Changes in weight ratio (W_{gel}/W_0) with elapsed time are plotted, W_0 being the initial weight of the as-prepared gel (initial size was 5.5 mm diameter \times 30 mm length). Arrows indicate the direction of weight change by increasing C_{clay} . (b) C_{clay} dependence on the number of clay platelets per unit of gel volume (10^6 nm^3) calculated for as-prepared NC gels at 20°C (filled circles) and for corresponding shrunken NC gels at 50°C (open circles). Arrows indicate the direction of change of n_{clay} by increasing temperature. Reprinted from Haraguchi et al. [62], Copyright 2007, with permission of ACS



dimethylaminoethyl methacrylate (DMAEMA) can be introduced into the NC gel network through copolymerization. Several reports have been published on different systems such as NIPA-AAc/Laponite XLG [83], NaAA/montmorillonite [84], NIPA-MAAc/Laponite XLG+pyrophosphate [85], NIPA-AAm-AAc/montmorillonite [86], AAm-NaAA/Laponite XLG [87], and NIPA-NaMAA/Laponite XLS [88]. Moreover, some studies have been conducted on cationic polymer–clay network systems such as NIPA-DMAEMA/Laponite XLG [85], cationic AAm/bentonite [89], and AAm-DMAEMA/Laponite XLS [90].

To ensure that NC gels showed outstanding swelling–deswelling behavior in response to both temperature and pH, while retaining their remarkable tensile mechanical properties, NC gels were prepared with a semi-interpenetrating organic–inorganic network structure by using linear poly(acrylic acid) (PAAc) [83]. The PAAc content (C_{PAAc}) that is required to achieve good mechanical properties, as well as good temperature- and pH-sensitivities, changed with C_{clay} , and the upper critical value of $C_{\text{PAAc}}/C_{\text{clay}}$ was approximately 2.5–3. NC gels with

semi-interpenetrating organic–inorganic networks were also prepared using linear sodium carboxymethylcellulose and the PNIPA–clay network [91], and equally dual sensitivities and good mechanical properties were achieved.

In NC gels, unique swelling–deswelling behavior was observed in long-term swelling for both nonthermosensitive NC gels (e.g., D-NC gel) and thermosensitive N-NC gels at temperatures lower than the LCST [92, 93]. Ren et al. revealed that the spontaneous deswelling of the gel after attaining a maximum degree of swelling (Fig. 20a) is attributed to the combined effects of the high swelling capacity of an NC gel as a polyelectrolyte gel and continuous releases of sodium ions from the

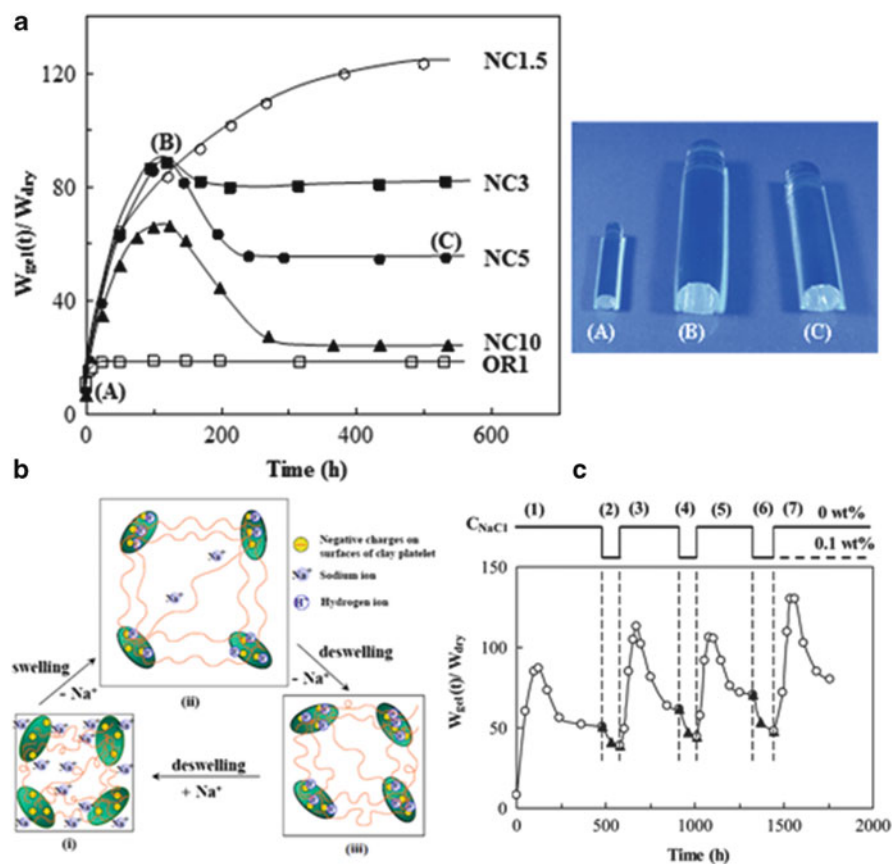


Fig. 20 Swelling behavior of D-NC gels: (a) Changes in the swelling ratios, $W_{\text{gel}}(t)/W_{\text{dry}}$, of D-NC n gels ($n = 1.5\text{--}15$) in water as a function of swelling time. Photos A–C indicate the swelling of gels labeled A–C in the graph. (b) Estimated changes in PDMAA–clay network structures during long-term swelling: (i) as-prepared state, (ii) maximum swelling (DS_{max}) state, and (iii) equilibrium swelling state. (c) Cyclic swelling tests for a D-NC5 gel alternating between pure water and aqueous NaCl solution ($C_{\text{NaCl}} = 0.1 \text{ wt\%}$). Other swelling conditions: initial gel size = 5.5 mm diameter and 30 mm length; amount of water = 200 mL; frequent water changes; 20°C. Reprinted from Ren et al. [93], Copyright 2011, with permission of ACS

network during swelling (Fig. 20b) [93]. Thus the swelling–deswelling behavior of NC gels can be reversed by reintroducing sodium ions into the network (Fig. 20c). Furthermore, both swelling and subsequent deswelling of NC gels was strongly depressed by the introduction of multivalent cations into them.

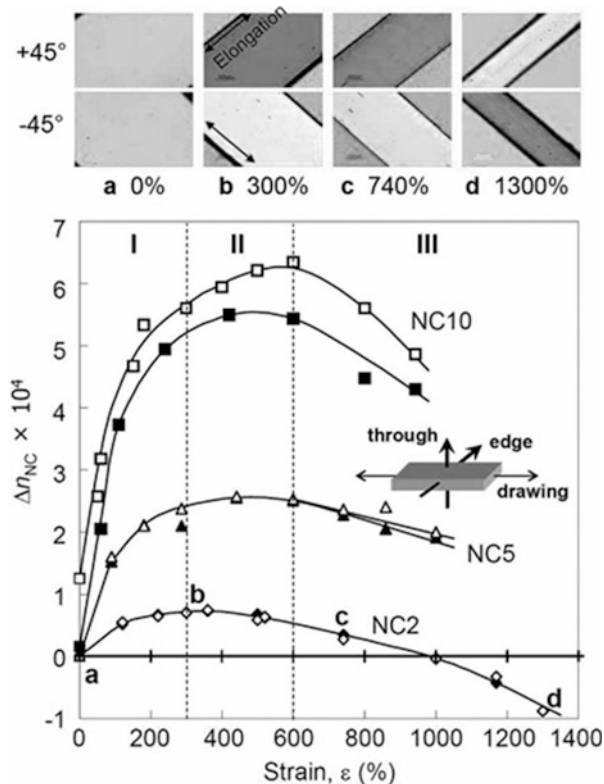
4 New Characteristics of NC Gels

4.1 Optical Anisotropy

Because polymeric hydrogels consist of amorphous polymer networks swollen with large amounts of water, the hydrogels are normally amorphous (optically isotropic). To date, optical anisotropy has only been studied in polymeric hydrogels containing mesogenic groups [94] or in gels orientated by a flow-gelation process [95] or an electric field [96]. In contrast, NC gels exhibit optical anisotropy with increasing C_{clay} and uniaxial deformation because they contain clay nanoparticles with an anisotropic, disk-like shape and are also capable of large deformations. For example, when C_{clay} exceeds a critical value ($C_{\text{clay}}^{\text{crit(opt2)}} = 10$), N-NC gels show optical anisotropy in the as-prepared (unstretched) state [41], whereas N-OR gels show no optical anisotropy at any value of C_{BIS} . This $C_{\text{clay}}^{\text{crit(opt2)}}$ is consistent with the critical value calculated for spontaneous clay aggregation (layer stacking) in NC gels [62]. It should also be noted that $C_{\text{clay}}^{\text{crit(opt2)}}$ is consistent with the other critical values of C_{clay} , $C_{\text{clay}}^{\text{crit(opt1)}}$ [28, 62], and $C_{\text{clay}}^{\text{crit(2)}}$ [41], described in the previous sections (3.3.1 and 3.3.2).

The optical anisotropy of an NC gel changes in a unique manner on uniaxial deformation, regardless of its optical characteristics in the original (as-prepared) state; that is, when stretched uniaxially, all N-NC gels show remarkable optical anisotropy, as can be seen in Fig. 21 [97]. Their birefringence (Δn_{NC}) strongly depends on C_{clay} . An interesting point is that Δn_{NC} shows a distinct maximum at a strain of around 300–600% and a sign inversion on further elongation. Here, an NC2 gel stretched to its intersection point with the strain axis is optically isotropic (990%; $\Delta n_{\text{NC}} = 0$), although it definitely has a highly orientated network structure. By evaluating the separate contributions of clay and PNIPA, assuming that $\Delta n_{\text{NC}} = \Delta n_{\text{PNIPA}} + \Delta n_{\text{clay}}$, we concluded that Δn_{clay} increases rapidly in the early stages of elongation and saturates at 300–600% strain. On the other hand, Δn_{PNIPA} changes monotonically increase in negative value when the NC gels are stretched. As a result, elongation of the chains brought about a decrease in the net birefringence and could nullify the contribution from the clay (positive Δn_{clay}), and eventually reverse the sign of Δn_{NC} . Also, values of Δn_{NC} for NC gels with high C_{clay} ($\geq C_{\text{clay}}^{\text{crit(opt2)}}$) were different in different directions (Fig. 21); this was attributed to the partial plane-orientation of clay platelets [97]. The orientations of clay and

Fig. 21 Birefringence, Δn_{NC} , of NC gels with different C_{clay} (NC2–NC10) as a function of strain. Closed and open symbols were measured in through and edge directions (see inset), respectively. Photos *a–d* show the polarized-light micrographs for stretched NC2 gels (through direction) under crossed polarizers in conjunction with a 530 nm retardation plate, where $+45^\circ$ (-45°) orientation is parallel to the slow (fast) axis of the retardation plate. Each photo corresponds to same point (*a–d*) on the Δn_{NC} –strain curve for the NC2 gel. *I*, *II*, and *III* indicate the distinct stages of molecular orientation. Reprinted from Murata and Haraguchi [97], Copyright 2007, with permission of RSC

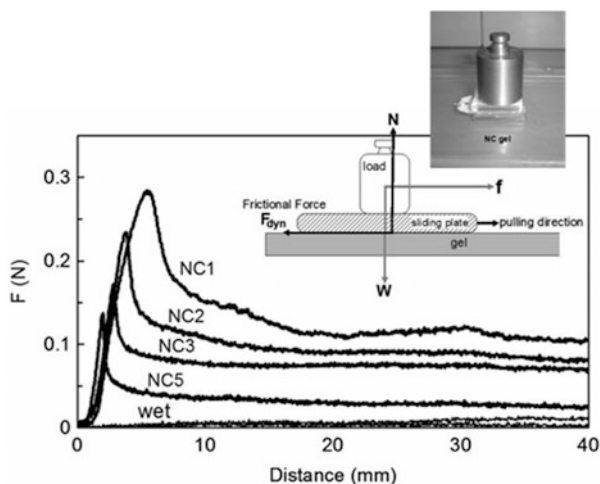


PNIPA during the stretching were confirmed by contrast-variation SANS measurements [57].

4.2 Sliding Friction Behavior

In general, because OR gels are readily damaged by sliding, sliding friction measurements have rarely been conducted at the surfaces of OR gel films, except when the films were wet. In contrast, NC gels are mechanically tough and, hence, sliding friction tests have been performed at their surfaces under different environmental conditions and even under high loading. Sliding frictional forces at NC gel surfaces are sensitive to the gel composition, loading, and surrounding environment (wet, in-air, and temperature) (Fig. 22) [98]. In air, NC gels show a force profile with a maximum static frictional force (max-SFF) and a subsequent constant dynamic frictional force. In contrast, NC gels show very low frictional forces when wet. The change in sliding friction behavior with the surroundings is most prominent for NC gels with low C_{clay} . For example, max-SFF for N-NC1 gel decreases by a factor greater than 10^2 when its environment is changed from air

Fig. 22 Effect of clay content of NC gels on the sliding frictional behavior. The force profiles were measured in air and wet for N-NC gels with different clay contents (NC1–NC5). *Inset:* The principle of sliding frictional force measurement on the gel surface and a picture of sliding friction measurement on NC gel. Reprinted from Haraguchi and Takada [98], Copyright 2005, with permission of Wiley



to wet. Also, under wet conditions, the dynamic frictional coefficient, μ_d , decreases with increasing load and becomes very small at high loads ($\mu_d < 0.01$). Thus, the frictional characteristics of N-NC1 gels can alternate between sticky and slippery depending on their surroundings. The sliding frictional forces for N-NC gels in air also decrease when they are heated to 50°C ($>\text{LCST}$), because of the coil-to-globule transition of PNIPA chains [48]. The results are used to identify the important role played by dangling chains at the gel–air and gel–water interfaces.

4.3 High Water Contact Angles

Surface wettability is one of the most important properties of all materials, since it reflects the real structure and chemical composition at the outermost surface. As expected from their compositions, polymeric hydrogels, which consist largely of water and a hydrophilic polymer network, are naturally hydrophilic and their surfaces generally show very low contact angles for water (θ_w). The relation between the surface wettability of PNIPA hydrogels (N-OR gels) or surface-grafted PNIPA and the hydrophilic (coil)-to-hydrophobic (globule) transition occurring at the LCST has been studied extensively [99–101]. It has been reported that θ_w at the N-OR gel surface is low (e.g., $\sim 60^\circ$) below the LCST, but relatively high (e.g., $\sim 80^\circ$) above the LCST. In contrast, N-NC gel surfaces showed extraordinarily high hydrophobicity (high θ_w) below the LCST (Fig. 23a) [102, 104], although all individual components of the N-NC gels were hydrophilic under the test conditions. Values of θ_w for N-NC gels were generally greater than 100° for a broad range of C_{clay} and $R_{\text{H}_2\text{O}}$ and reached a maximum of 151° at a specific composition (Fig. 23b) [102]. These results were astonishing because values of θ_w for N-NC gels were higher than those of polypropylene and poly(tetrafluoroethylene). The high

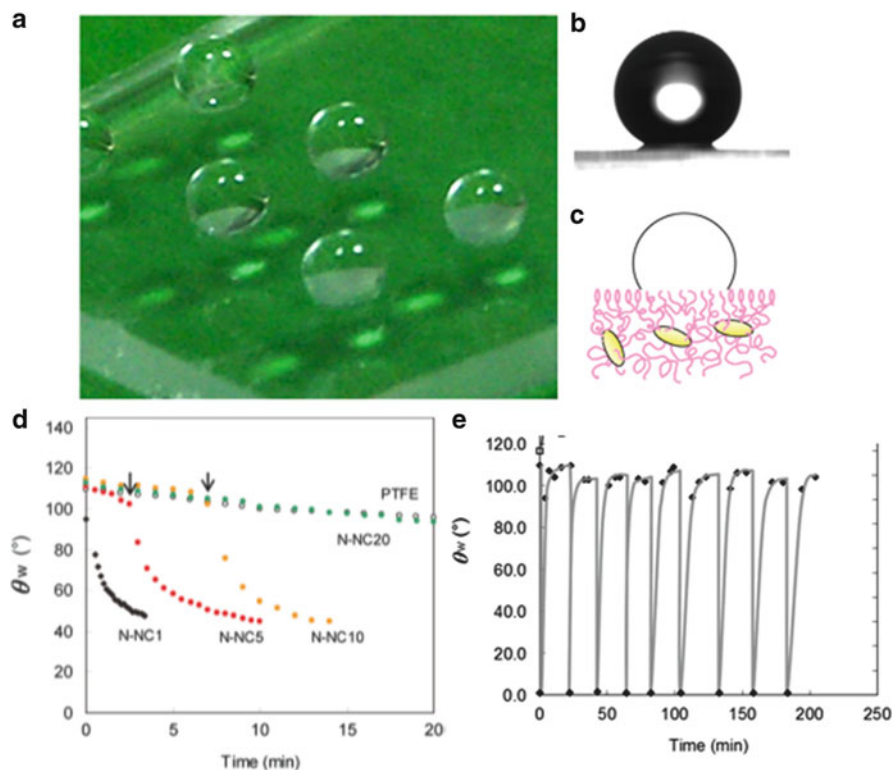


Fig. 23 (a) Water droplets on an N-NC6 gel film. (b) Water contact angle (151.6°) for a sessile drop on the surface of an N-NC6 gel with a water content of 210 wt%. (c) Model of a sessile drop on the surface of an N-NC gel. (d) Time dependence of θ_w for various N-NC n gels with different C_{clay} (NC1–NC20) and for hydrophobic PTFE substrate. (e) Changes in θ_w by alternating between wet and dry conditions on the surfaces of N-NC5 gel. (a, b) Reprinted from Haraguchi et al. [102], Copyright 2007, with permission of ACS. (d, e) Reprinted from Haraguchi et al. [103], Copyright 2008, with permission of Elsevier

hydrophobicity of N-NC gels was primarily attributed to the amphiphilicity of PNIPA and, more specifically, to the spontaneous alignment of *N*-isopropyl groups at the gel–air interface (Fig. 23c) [102, 103]. The hydrophobicity was also enhanced by other factors such as the network structure and water content, whereas the effects of surface roughness, copolymerization, interpenetration of a hydrophilic polymer, and adsorption of a hydrophilic (cationic) dye were negligible [103, 105]. Because the alignment of the *N*-isopropyl group at the gel–air interface is very sensitive to the ambient circumstances, the θ_w of N-NC gels changed considerably with elapsed time and the environment. During long-term measurements, the high values of θ_w gradually decreased and showed an abrupt decrease after a certain elapsed time (Fig. 23d) [103]. The latter change, which was attributed to the interaction between the hydrogel surface and the water droplet, varied depending on C_{clay} and was only observed for NC gels with lower C_{clay} levels (≤ 10 wt%). It was also found that the

surfaces of N-NC gels underwent reversible hydrophobic-to-hydrophilic changes when the environment was changed from air to wet, and vice versa (Fig. 23e) [103].

4.4 Cell Cultivation

Culturing cells on a substrate is one of the most important and indispensable experimental procedures in medical, biological, pharmaceutical, and tissue engineering research. It is known that N-OR gels [106] or PNIPA coatings of thickness greater than 30 nm [107] cannot be used as substrates. However, it was found that cells can be cultured on the surfaces of normal or dried N-NC gels, regardless of the gel thickness (Fig. 24a) [108]. To the best of our knowledge, this is the first report on the successful culturing of cells on a PNIPA hydrogel. Various types of cells, such as human hepatoma (HepG2) cells, normal human dermal fibroblasts (NHDFs), and normal human umbilical vein endothelial (HUVEC) cells, were

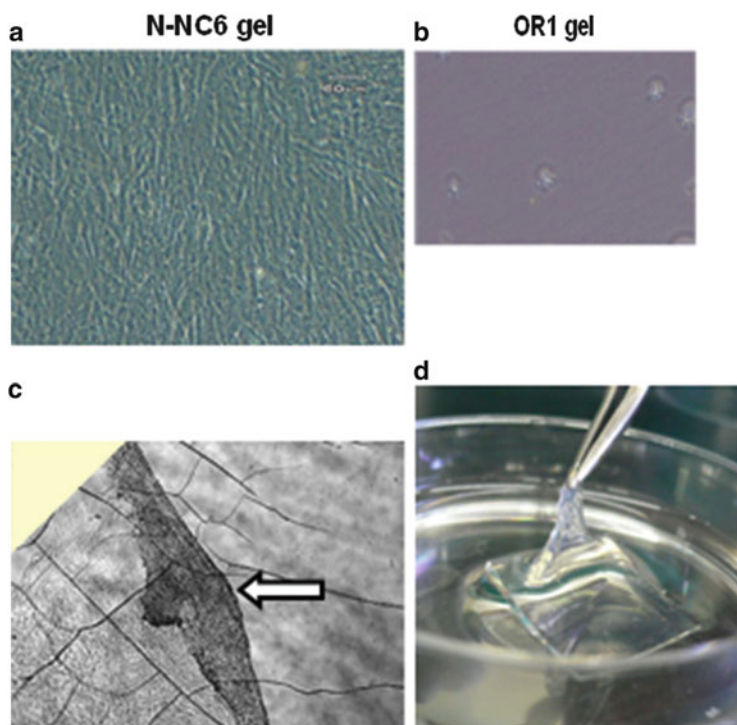


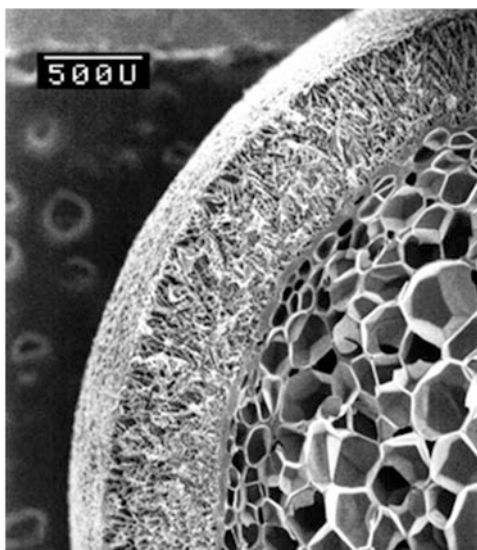
Fig. 24 (a, b) Phase-contrast photomicrographs of normal human dermal fibroblast (NHDF) cultures on the surfaces of (a) N-NC6 gel and (b) N-OR1 gel after 5 days. (c) Cell sheet detachment (*arrow*) of NHDF caused by a decrease in the temperature to 10–20°C. (d) NHDF cell sheet detached from an N-NC6 gel [108]

cultured to be confluent on the surface of an N-NC6 gel. The development of the cell cultures showed little dependence on the water content or thicknesses of the N-NC gel sheets. In contrast, cell cultures did not develop on the surfaces of N-OR gels, regardless of the crosslinker content (Fig. 24b). Cell culture on the surfaces of D-NC and D-OR gels also failed, probably because of the hydrophilic nature of the gel surfaces. Hence, it was thought that cells adhered to and proliferated only on the surfaces of N-NC gels because of the combined effects of the hydrophobicity of the dehydrated PNIPA chains and the surface charges on the incorporated exfoliated clay. Furthermore, it was found that when the temperature was decreased to below the LCST (10–20°C), the cell cultures detached from the surfaces of the N-NC gels without trypsin treatment (Fig. 24c) [108]. Confluent layers of NHDF cells could be spontaneously separated as sheets from the gel surface (Fig. 24d). Recently, the acceleration of cell sheet detachment has been reported for semi-interpenetrating NC gels prepared by incorporating alginate (water-soluble natural polysaccharide) into PNIPA–clay networks [109]; this acceleration is possibly due to the rough surface texture and faster water penetration of these gels.

4.5 Porous NCs with a Layered Morphology

Novel, porous nanocomposites (porous-NCs) with characteristic layered morphologies were prepared by freeze-drying NC gels without the use of a porogen [110]. The most typical morphology was a concentric three-layer morphology consisting of, successively, a fine-porous layer, a dense layer, and a coarse-porous layer from the exterior to the interior (Fig. 25). In the coarse layer, a regular

Fig. 25 Three-layer morphology observed by SEM for a cross-section of porous-NC (freeze-dried NC gel in liquid nitrogen). Fine-porous, dense, and coarse-porous layers were observed from the outer surface to the interior. *Scale bar* indicates 500 μm . Reprinted from Haraguchi and Matsuda [110], Copyright 2005, with permission of ACS



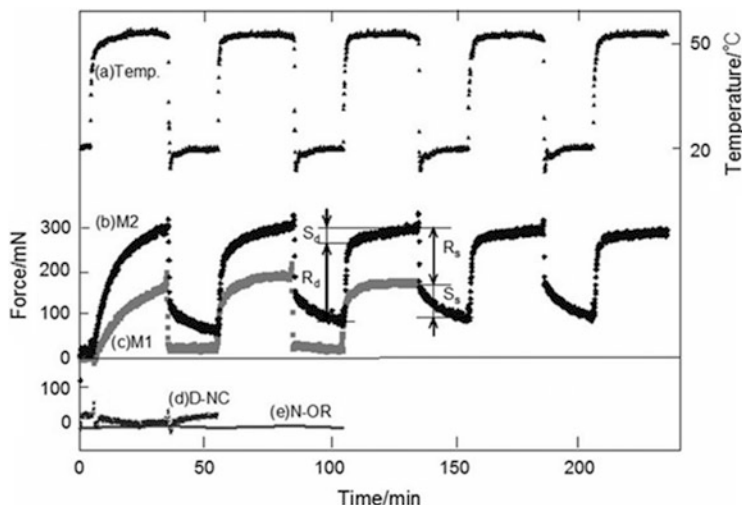


Fig. 26 Force profiles obtained on alternating the temperature: (a) temperature change, (b) force profile for the N-NC4-M2 gel, (c) force profile for the N-NC4-M1 gel, (d) force profile for the D-NC4-M2 gel, and (e) force profile for the N-OR2-M2 gel. Reprinted from Haraguchi et al. [111], Copyright 2005, with permission of Wiley

assembly of polyhedral pores was formed spontaneously. A possible mechanism underlying the spontaneous formation of the unique three-layer morphology, and other morphologies, during the freeze-drying process, was proposed.

4.6 Reversible Force Generation

Using temperature-sensitive N-NC gels, we discovered the generation of reversible retractive tensile forces in samples constrained to constant length in an aqueous environment in response to alternating temperature changes (Fig. 26) [111]. This is the first observation of a retractive mechanical force generated as a result of conformational changes (coil-to-globule transition) in the PNIPA chains across the LCST. In contrast, no such force was generated in the case of D-NC and N-OR gels under the same experimental conditions.

4.7 Self-Healing in NC Gels

Self-healing, which is the ability of a system or material to autonomously and spontaneously heal or repair itself, or more specifically repair surface or internal damage, has received considerable attention as a function of smart materials

[112]. Self-healing is an important characteristic that is generally observed in living organisms, and is a requirement for sustaining life. The development of smart materials, pre-designed to undergo self-repair, is significant from both academic and industrial points of view [113–115]. Thus far, polymers or polymer composites with self-repair capabilities based on several different strategies have been reported. One system utilizes the nature of reversible bonds such as Diels–Alder cycloaddition and the retro-Diels–Alder reaction [116, 117], reversible photo-induced or radical exchange reactions [118, 119], and the reversible reaction of thiol-disulfide bridges in a polyrotaxane network [120]. Another self-repairing system utilized healing agents such as monomers, resins, and crack-adhering adhesives, which were embedded in the matrix in a dormant form [121–123]. For rubbery materials, three different systems were recently reported: a thermoreversible rubber formed by supramolecular assembly [124]; a polyurethane network consisting of an oxetane-substituted chitosan precursor that underwent self-repair by exposing the network to ultraviolet light [125]; and a polymer hydrogel composed of three different ionic components, a dendritic molecular binder (PEG-G3-dendron: positive), clay (negative), and a polymer (sodium polyacrylate: negative) [126], which showed self-healing of freshly cut surfaces after pushing them into contact.

It was found that NC gels can exhibit the striking feature of complete self-healing through autonomic reconstruction of crosslinks across a damaged interface [127]. Mechanical damage in NC gels was repaired without the use of a healing agent, and even sections of NC gels separated by cutting (from the same or different kinds of NC gel) perfectly (re-)combined simply by putting the cut surfaces together at mildly elevated temperatures (Fig. 27a). The stress–strain curves for the self-healed samples differed depending on conditions such as contact time, temperature, and pressure, which are factors that affect the rate of healing. For example, under conditions of close contact at 50°C, self-healing of once-separated D-NC3 gels increased with increasing contact time (Fig. 27b). Here, when D-NC3 gel was self-healed for 1 and 4 h, the tensile strength recovered to about 27 and 57%, respectively, of the original values and the sample subsequently broke along the same plane as the original cut. Complete self-healing (i.e., 100% recovery of tensile strength) was achieved by maintaining contact for 10 h, and the gel broke at a different place on subsequent elongation. Similar self-healing behavior was also observed for D-NC5 gels at 80°C within 30 min (Fig. 27b). The effects of temperature and time on the recovery of ultimate tensile stress for self-healing in D-NC3 gels are summarized in Fig. 27c. The same complete self-healing was accomplished under different time and temperature conditions, such as 100 h at 37°C and 20 min at 80°C. Here, it should be noted that the rubber-like materials [124] and hydrogels [126] described above cannot be repaired completely unless the sectioned surfaces are adjoined immediately after cutting. However, in NC gels [127], the autonomic fusion of cut surfaces as well as self-healing could be achieved not only immediately after being cut but also after a long waiting time; that is, NC gels have long-lasting healing ability.

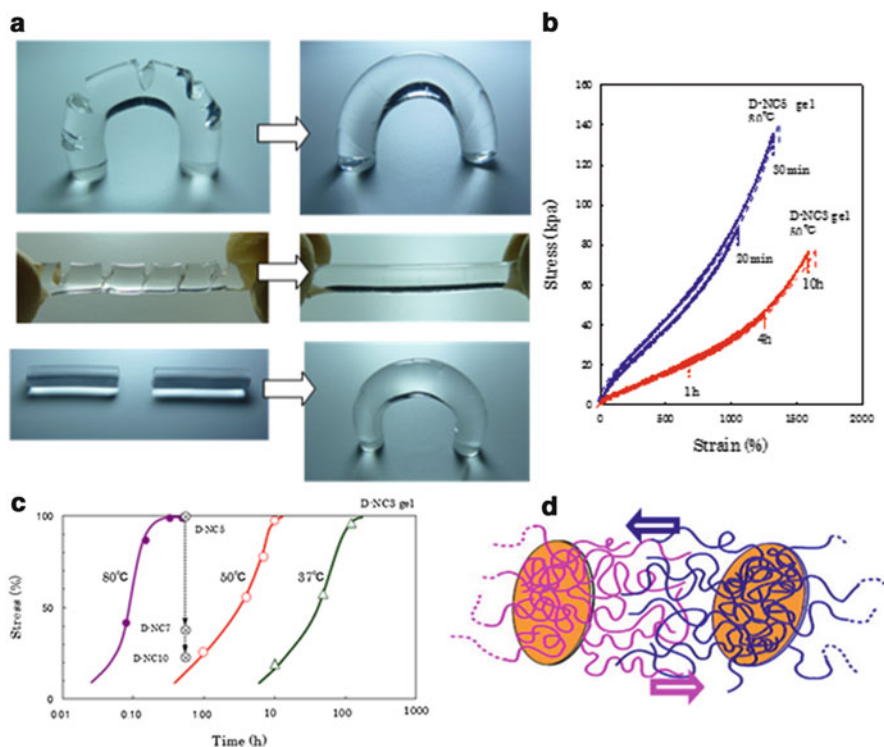


Fig. 27 (a) Self-healing of D-NC gels with mechanical damage: *Top and center*: D-NC3 gel with damage (several knife cuts) were self-healed by keeping the cut surfaces in contact for 48 h at 37°C. *Bottom*: Separated D-NC3 gels were self-rejoined by keeping cross-sectional surfaces in contact at 37°C for 100 h in closed vessel. In both cases, no healing agent was used. (b) Tensile stress–strain curves of original and self-healed D-NC gels from once-separated NC gels by cutting. Original is shown as a dotted line. D-NC3 gels were self-healed at 50°C for 1, 4, and 10 h. D-NC5 gels were self-healed at 80°C for 20 and 30 min. (c) Effects of self-healing conditions (time and temperature) on the recovery of tensile strength of self-healed D-NC3 gels, in addition to those of D-NC5, D-NC7, and D-NC10 gels self-healed at 80°C for 30 min. (d) Representation of outermost surface of separated NC gel with organic(polymer)–inorganic(clay) network structure. Reprinted from Haraguchi et al. [127], Copyright 2011, with permission of Wiley

The self-healing capability of D-NC gels described above can be attributed to the unique polymer–clay network structure [127]. As depicted schematically in Fig. 27d, the macroscopic self-healing of NC gels arises from reconstruction of the network at the interface due to mutual diffusion of long, grafted chains and their subsequent interactions with clay. In contrast, OR gels do not show any self-healing due to the inability of the short dangling polymer chains created at the cut surfaces to autonomously form new crosslinks. Figure 28 shows that different kinds of NC gel (e.g., D-NC and N-NC gels), combined by joining each cut surface at ambient temperature for a while (e.g., 25°C, 48 h), exhibit unique swelling–deswelling behavior [127]. The self-combining process of simply adjoining the cross-sectional

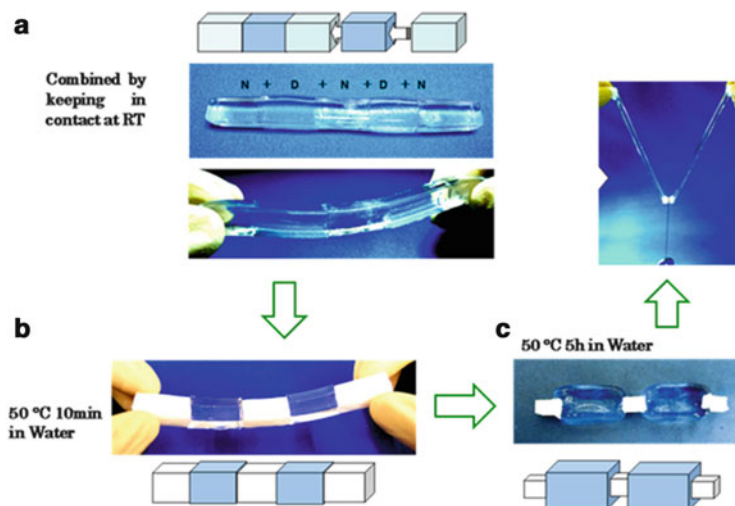


Fig. 28 Combined cut surfaces of different kinds of NC gels: (a) Combined N-NC3 and D-NC3 gels with a cuboid shape, where cut surfaces were brought into contact at 25°C for 48 h and were united. (b, c) Changes in N-NC3/D-NC3 gels by immersion in hot water (50°C) for (b) 10 min and (c) 5 h. N-NC3 sections became opaque and shrank, whereas D-NC3 sections became swollen. Elongation of combined and subsequently shrunk/swollen N-NC3/D-NC3 gels is also shown. Reprinted from Haraguchi et al. [127], Copyright 2011, with permission of Wiley

surfaces makes it possible to design and fabricate complex NC gels in terms of stimuli-sensitivity and shape.

4.8 Complicated Shapes and Surface Patterns

In addition to various shapes, NC gel films with a wide range of thicknesses (10^{-3} – 10^3 mm) and sizes can be prepared. Also, NC gels with uneven surfaces, for example, surfaces with a regular array of pillars or bellows-like rods, can be obtained (Fig. 4a) [21]. Bellows-like rods can be prepared by simply extracting the as-prepared NC gel from the mold without breaking or opening the template; this is because the protuberances on the surface are flexible and can be reversibly deformed during extraction. In addition, lightweight NC gels, i.e., porous NC gels, which are very soft (very low modulus) and have a density of 0.05–1.0 g/cm³, can be prepared using a porogen or air (Fig. 4a) [21]. NC gels synthesized by photopolymerization can be used to produce various forms (Fig. 4b) such as thin films, coatings on substrates, pattern formation using photolithography, and microchannel flow systems containing thermosensitive valves composed of photo-NC gels [48].

Furthermore, micrometer-scale surface-patterned NC gel films were successfully prepared by direct replica molding without any chemical surface treatment of

the template [49]. Small ($\sim 1 \mu\text{m}$) microstructures were precisely transferred onto the surfaces of NC gel films without defects (Fig. 4c). Also, the sizes of the patterns could be modified (enlarged or miniaturized) by subsequent swelling, deswelling, and drying without disturbing the patterns. OR gels with the aforementioned shapes and forms are difficult to prepare and handle because of their brittleness.

5 Further Developments in Advanced Soft Nanohybrid Materials

By extending the synthetic technology of NC gels, novel nanohybrid materials such as new stimuli-responsive NC gels (non-PNIPA systems), zwitterionic NC gels, aqueous dispersions of polymer–clay nanocomposite microspheres, Pt-NC gels with clay-mediated platinum nanoparticles, and soft hydrophobic polymer nanocomposites have been developed, as described below.

5.1 *New Stimuli-Responsive NC Gels and Soft Nanocomposites*

A novel series of nanocomposite copolymer hydrogels (MD-NC gels) were prepared that consisted of inorganic clay (hectorite) and specific copolymers with different chemical affinities for water, e.g., MD copolymers composed of hydrophobic (2-methoxyethyl acrylate; MEA) and hydrophilic (DMAA) units [128]. The clay morphology in MD-NC gels gradually changed on increasing the molar ratio of DMAA from a clay shell network of 20 nm thickness to a uniform dispersion of exfoliated clay platelets in a polymer matrix. MD-NC gels showed outstanding stimuli-sensitivities in response to changes in temperature, pH, salt concentration, and solvents in the surrounding aqueous solution due to the balance of hydrophilic and hydrophobic units as well as ionic clay platelets (Fig. 29a). Figure 29b shows the thermoresponsive reversible changes in gel size. Moreover, MD-NC gels could be utilized as drug- or chemical-releasing substrates, with the rate of release being controlled by altering the gel composition as well as the absorbing and releasing conditions (Fig. 29c) [129]. Further, MD-NC gels exhibited excellent, composition-dependent mechanical properties (Fig. 29d). After drying, the gels were changed into transparent, soft nanocomposites (MD-NCs) with high mechanical toughness and safety in *in vitro* cytotoxicity tests [128].

For tissue engineering and regenerative medicine, stem cells should be effectively cultured *in vitro* [130, 131]. Novel thermoresponsive MD-NC gels could be applied in cell culture and cell harvesting without trypsinization, specifically using mesenchymal stem cells (MSCs) [132]. The composition of the MD-NC gel (the ratio of the two monomer types and the clay content) was found to determine its

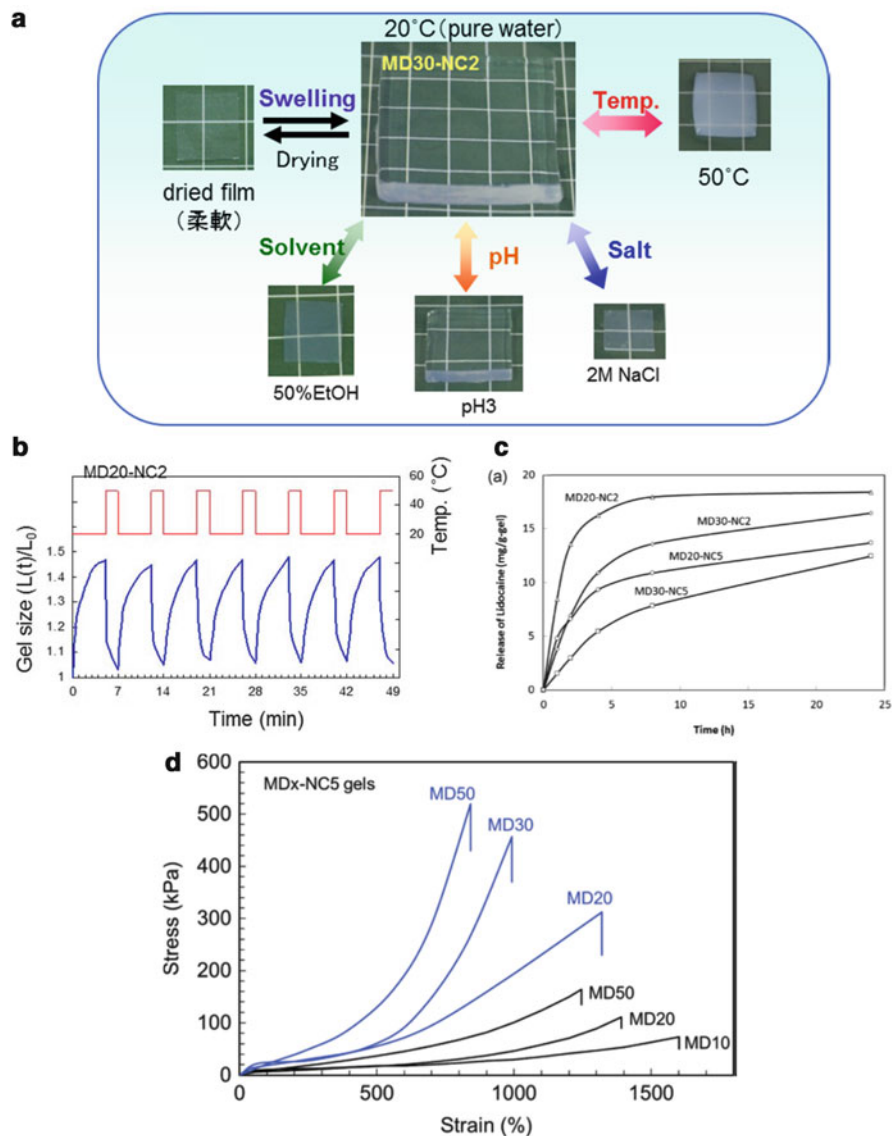
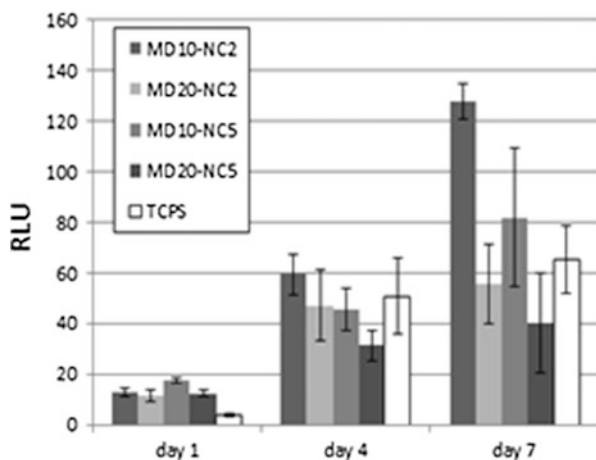


Fig. 29 (a) Transparent and mechanically tough MD30-NC2 gel and the soft nanocomposite obtained by drying. The MD30-NC2 gel exhibits stimuli-sensitivity in response to temperature ($20 \leftrightarrow 50^\circ\text{C}$), pH ($7 \leftrightarrow 3$), salt concentration (NaCl, $0 \leftrightarrow 0.6$ M), and solvent (ethanol, $0 \leftrightarrow 50$ wt %) in the surrounding aqueous solution. Different views of the same sample under different conditions are shown. (b) Thermoreversible change in the gel size (length) of an MD20-NC2 gel by alternating the temperature between 20 and 50°C . The initial dried gel size was 0.6 mm (width) \times 0.09 mm (thickness) \times 30 mm length. (c) Time-dependent release of Lidocaine from the surface of MD x -NC n gel films at 37°C . (d) Tensile stress–strain curves for as-prepared NC x -NC5 gels ($x = 10$ –50) (black lines). The blue lines represent the once-dried and re-swollen NC x -NC5 gels ($W_{\text{H}_2\text{O}}/W_{\text{dry}} = 400\%$). (a, b, d) Reprinted from Haraguchi et al. [128], Copyright 2012, with permission of ACS. (c) Reprinted from Haraguchi et al. [129], Copyright 2013, with permission of Wiley

Fig. 30 Mesenchymal stem cell (MSC) proliferation on the surface of MD x -NC n gels and tissue culture polystyrene (TCPS) on days 1, 4, and 7, as demonstrated by ATP assay ($n = 3$). The data represent mean \pm standard deviation. Reprinted from Kotobuki et al. [132], Copyright 2013, with permission of Wiley



swelling properties in the culture medium, thermosensitivity, protein adsorption, and cell attachment and proliferation. Various kinds of human cells, including MSCs (Fig. 30), osteoblast (HOS) cells, NHDF cells, and epithelial cells could be effectively cultured on MD-NC gels. In particular, on an MD10-NC2 gel with relatively low DMAA and clay content, the cells could be harvested by decreasing the temperature (Fig. 31), either as a cell sheet (MSCs or NHDF cells) or as a population of suspension cells (HOS cells). Further, it was found that the MD10-NC2 gel is suitable for stem cell differentiation. Because of their thermosensitivity, controllable modulus, and surface properties, MD-NC gels are promising cell culture substrates for tissue engineering and regenerative medicine.

5.2 Zwitterionic NC Gels

Zwitterionic polymers and their hydrogels are expected to be promising functional materials, useful in scientific research and in various industrial and biomedical applications [133–136]. Among various types of zwitterionic polymers, sulfobetaine polymers are generally thermosensitive in aqueous solutions and exhibit upper critical solution temperature (UCST) phase transitions due to changes in the intra- and/or interchain interactions between zwitterionic groups [137, 138]. Two specific sulfobetaine polymers, A₃ (shown in Scheme 1) and A₄, were selected on the basis of their interactions with monomers and clay. The A₃ and A₄ polymers formed physically crosslinked gels when C_m was 1 M and formed chemically crosslinked gels when an organic crosslinker was used [139]. However, both the physically and chemically crosslinked gels had serious disadvantages in terms of mechanical properties, stability, and thermosensitivity [139]. For example, physically crosslinked gels dissolved in hot water or in NaCl aqueous solution at room temperature. Moreover, both types of gel were mechanically weak and, in the

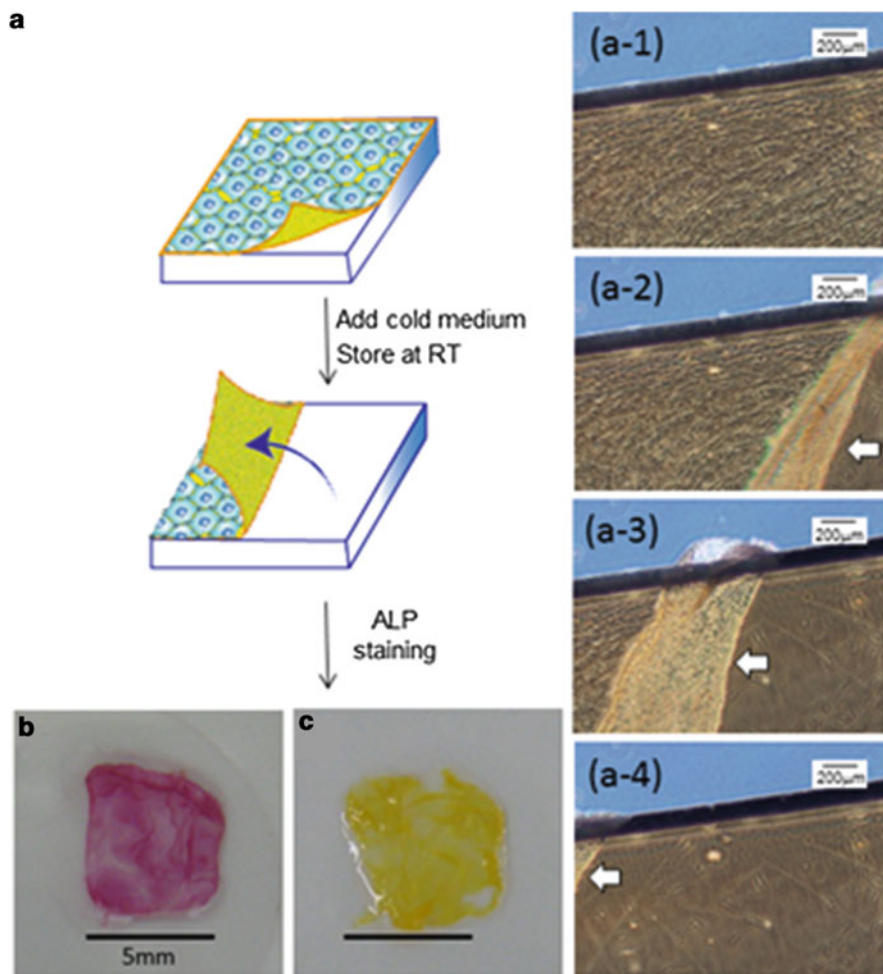


Fig. 31 Mesenchymal stem cell (MSC) behavior on MD10-NC2 gel. After the medium was replaced by cold medium (4°C) and MD10-NC2 gel was stored at room temperature for 10 min (**a**), MSCs were peeled from MD10-NC2 gel continuously (**a-1** to **a-4**). With ALP staining, the cell sheet cultured with osteogenic medium took on the red stain (**b**), but the cell sheet cultured without osteogenic medium was not stained (**c**). Reprinted from Kotobuki et al. [132], Copyright 2013, with permission of Wiley

case of the A_4 polymer gel, the UCST was too high (ca. 95°C). It was therefore important to develop zwitterionic polymer hydrogels with high uniformity and stability, controlled thermosensitivity, and superior mechanical properties. We showed that all of these requirements were met by developing zwitterionic NC gels (Zw-NC gels) consisting of zwitterionic (co)polymers and inorganic clay platelets [140]. In particular, Zw-NC gels consisting of sulfobetaine A_3 -DMAA or A_4 -DMAA copolymers and inorganic clay, e.g., A_3Dx -NC3 and A_4Dx -NC3 gels,

were uniform and stable in hot water and NaCl aqueous solutions and exhibited excellent tensile mechanical properties and appropriate UCSTs when x was small (≤ 20) (Fig. 32a). The mechanical properties and UCSTs were further controlled by altering the clay concentration and polymer composition in the Zw-NC gel (Fig. 32b, c) [140, 141]. Thus, Zw-NC gels exhibit outstanding mechanical and thermosensitive characteristics and could extend the range of scientific study and applications of zwitterionic hydrogels.

5.3 Aqueous Dispersion of Polymer–Clay Nanocomposite Microspheres

Polymer–clay nanocomposite (P/C-NC) microspheres consisting of organic (co) polymers with different hydrophilic/hydrophobic nature and inorganic clay were synthesized through photo- and thermally initiated free-radical polymerization in the presence of exfoliated clay platelets in a diluted aqueous system [142]. Because the clay platelets can function as crosslinkers and stabilizers, uniform aqueous dispersions of P/C-NC microspheres with diameters of ~ 70 nm (photopolymerization) and 100–300 nm (thermal polymerization) can be obtained for all of the polymer–clay systems without using a surfactant (Fig. 33a; PNIPA–clay system). The sol–gel boundary, transparency, thermosensitivity (LCST), viscosity, and average particle size varied depending on the type of polymer, composition, and polymerization conditions. In particular, the well-defined LCST was controlled over a wide range, depending on the DMAA content, in (NIPA-DMAA)-clay (Fig. 33b) and (MEA-DMAA)-clay systems. The aqueous dispersions of P/C-NC microspheres thus obtained showed promising potential as functional microspheres, with a number of interesting properties associated with those of NC gels and M-NCs. For example, reversible and efficient thermosensitive optical shutters were prepared by using thermosensitive P/C-NC aqueous dispersions and D-NC gels applied within double-layer glass plates (Fig. 33c).

5.4 Clay-Mediated Platinum-Nanocomposite Gels (Pt-NC Gels)

Platinum nanoparticles (Pt NPs) are currently used in many areas of nanoscience and technology, and play a critical role as high performance catalysts in various reactions and applications, including fuel cells [143], sensors [144], automobile exhaust systems [145], and petroleum cracking [146]. Although numerous studies have been reported on the design of Pt and Pt-based nanomaterials, there have only been limited studies on Pt NP–hydrogel composites [147, 148] because it is difficult to prepare a material with fine and well-dispersed Pt NPs immobilized within a

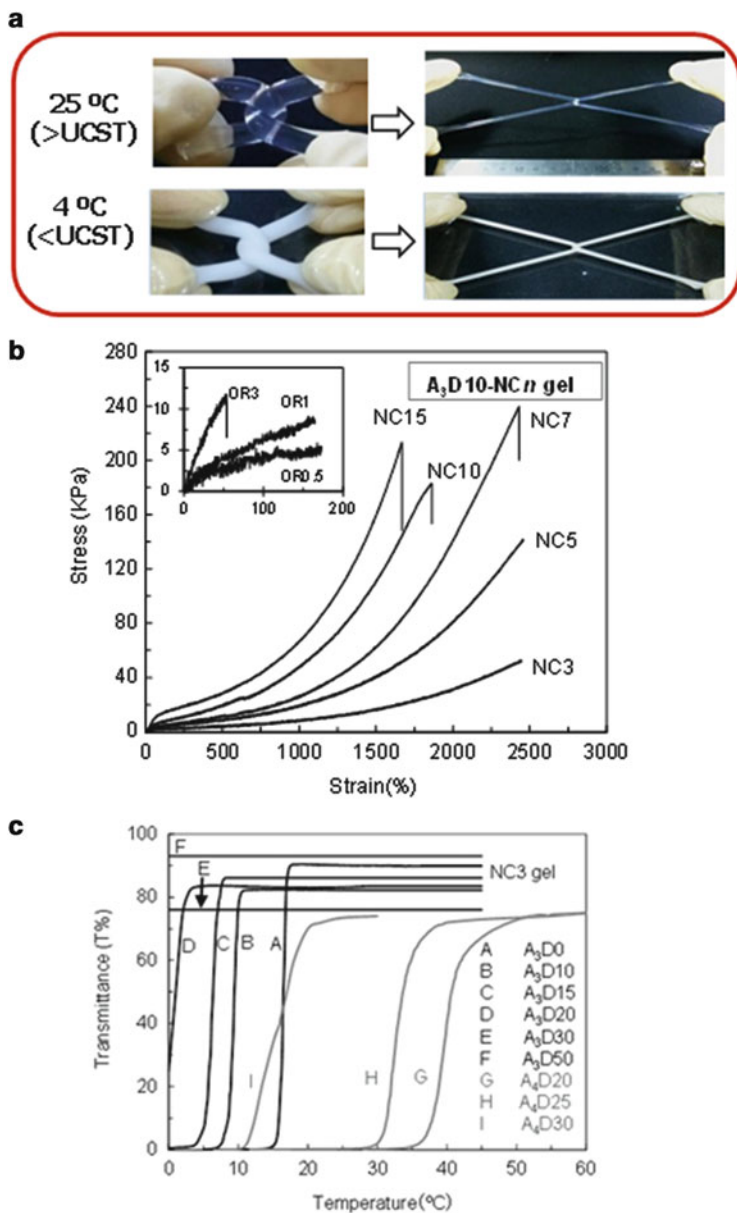


Fig. 32 Tensile mechanical properties of zwitterionic copolymer NC gels: (a) Elongation of crossed ($A_3D10-NC3$) gel samples at two temperatures, namely 25°C (>UCST) and 4°C (<UCST). (b) Tensile stress–strain curves for $A_3D10-NCn$ gels with different n ($n = 3–15$) and $A_3D10-ORx$ gels with different x ($x = 0.5–3$). Here, the NC3 and NC5 gels were not broken, even when stretched to more than 2,300%. (c) UCSTs of zwitterionic copolymer NC gels. Transmittance changes for $A_3Dm-NC3$ gels ($m = 0–50$) are shown as a function of temperature, measured during cooling at a rate of 10°C/h. Reprinted from Ning et al. [140], Copyright 2013, with permission of ACS

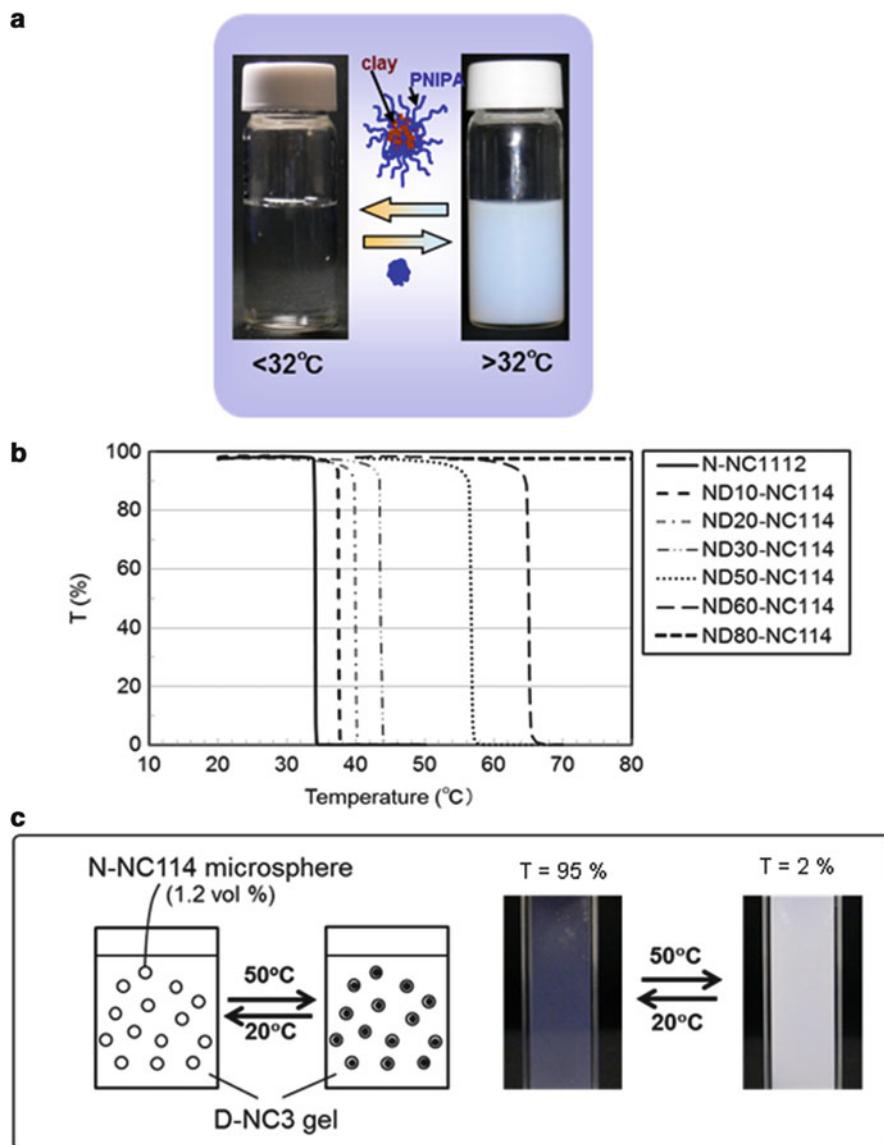


Fig. 33 (a) Change in transparency of an aqueous dispersion of PNIPAA/clay-NC microspheres by alternating temperature changes across the LCST (32°C). (b) Changes in optical transmittance with temperature for ND γ -NC114 ($\gamma = 0\text{--}80$). (c) Structure of a complex hydrogel consisting of thermosensitive N-NC114 microspheres dispersed in thermostable D-NC3 gel (left) and its reversible change in transparency between 20 and 50°C (right). Reprinted from Haraguchi and Takada [142], Copyright 2014, with permission of Wiley

hydrogel. We synthesized a novel hydrogel-based nanostructured Pt material, Pt-NC gel (Fig. 34a) [149], consisting of ultrafine Pt NPs with average diameters of 1.25–1.75 nm, strongly immobilized within a unique polymer–clay network, in particular, on the surfaces of clay nanoplatelets (Fig. 34b). The Pt-NC gels were synthesized on the basis of exfoliated clay-mediated in-situ reduction of Pt ions at ambient temperatures [150]. The proposed mechanism underlying the formation of Pt NPs in the NC gel is shown in Fig. 34c. Ultrafine Pt NPs were also obtained as a stable suspension from the NC gel, without any stabilizing agents [149]. The Pt-NC gels exhibited many interesting characteristics such as thermoresponsive swelling–deswelling behavior, high mechanical toughness, and exceptional stability; further, they could be produced in various forms and sizes, and with different surface morphologies. The gels and Pt NPs showed excellent catalytic properties

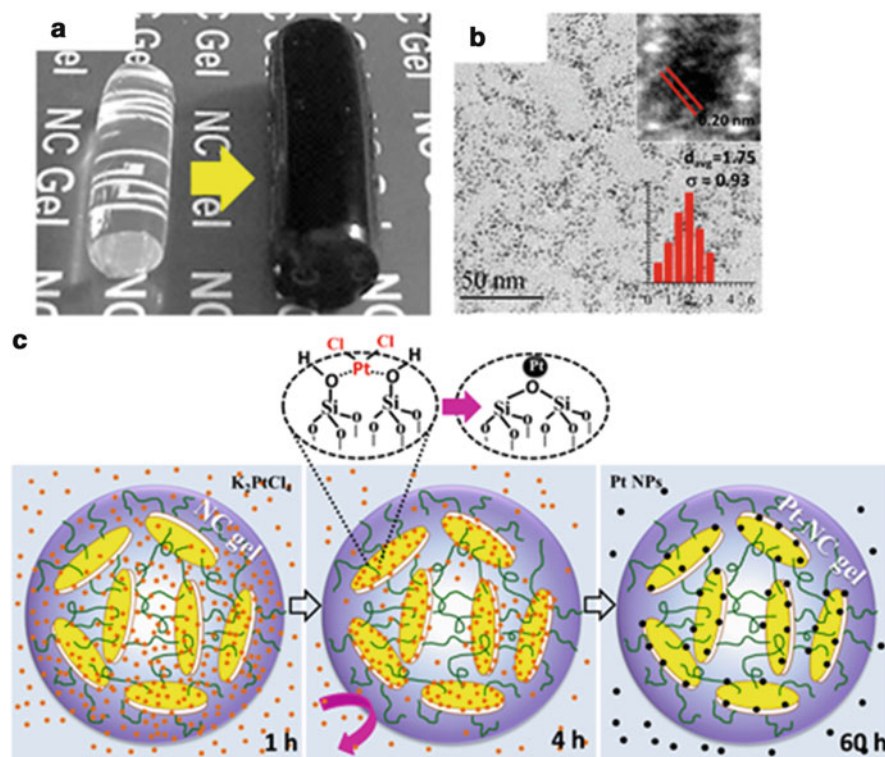
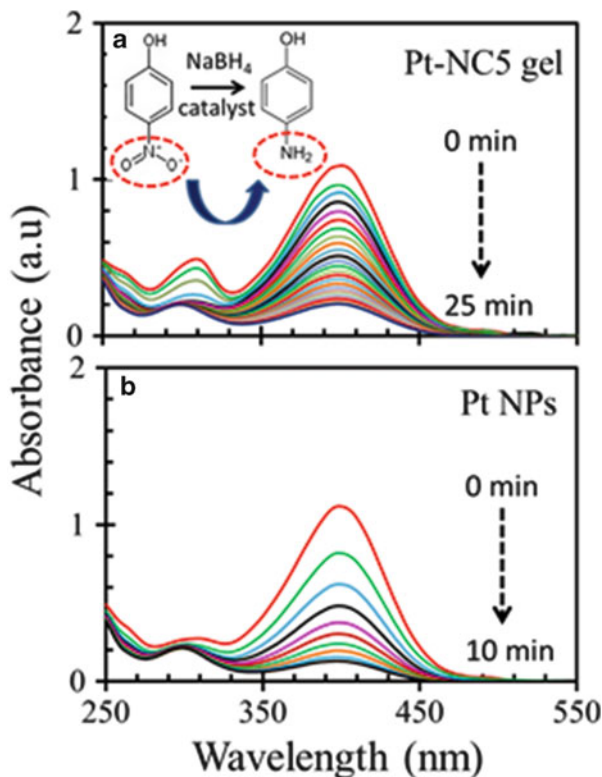


Fig. 34 (a) Color changes of N-NC5 gel kept in an aqueous solution of K_2PtCl_4 in the dark at $25^\circ C$ for 60 h. (b) TEM image of the dried Pt-NC5 gel. The *histogram* shows the Pt NP size distribution in the Pt-NC5 gel. *Inset*: HR-TEM image revealing the lattice fringes of crystalline Pt NPs. (c) Scheme of the formation of the Pt-NC gel: after 1 h, Pt ions penetrate the N-NC gel; after 4 h, Pt ions ($PtCl_4^{2-}$) interact with the silanol groups on the clay surface and are reduced to Pt^0 ; after 60 h, Pt NPs are formed by the migration of Pt, and are subsequently trapped on the clay surface. Reprinted from Haraguchi and Varade [149], Copyright 2014, with permission of Elsevier

Fig. 35 Catalytic reduction of 4-nitrophenol by NaBH_4 in the presence of (a) dried Pt-NC5 gel powder (3.5 mg), and (b) dried Pt NPs (1 mg) in the surrounding solution. The strong UV absorption peak at 400 nm corresponds to the nitrophenolate ion. Reprinted from Haraguchi and Varade [149], Copyright 2014, with permission of Elsevier



(Fig. 35) [149], which further expands the scope of their application in many advanced research fields.

5.5 Soft Polymer Nanocomposites (M-NCs)

As described in the Introduction (Sect. 1), the P-NCs developed as advanced composites are mainly obtained by the dispersion of small amounts of inorganic nanoparticles in a polymer matrix [24, 26, 27]. There are a few reports of P-NCs with high inorganic content, such as nylon66/silica (or clay) P-NCs [151] and epoxy resin/silica P-NCs [152]. However, these P-NCs have still certain limitations, particularly in terms of optical transparency, tractability, and processability.

Novel transparent, soft P-NCs with high contents of inorganic clay were developed by extending the concept of NC gels and their synthesis to the field of solid P-NCs [31, 32]. These novel P-NCs (abbreviated as M-NCs), which consist of hydrophobic poly(2-methoxyethyl acrylate) (PMEA) (Scheme 1) and hydrophilic inorganic clay (hectorite), have superior optical and mechanical properties, despite

their high C_{clay} , because of the unique organic–inorganic network structure composed of aggregated clay and PMEAs. Here, PMEAs are basically hydrophobic polymers with a low T_g (-34°C) [31, 153] and are considered to have promising applications in medical devices such as cardiopulmonary bypass [154–156], although in practical applications, PMEAs have only been used as an ingredient of copolymers or as a thin coating because of their mechanical weakness and intractability.

5.5.1 Synthesis of M-NCs

A new type of soft P-NC (M-NC) was synthesized using a modified version of the preparative method for NC gels, i.e., by in-situ free-radical polymerization of water-soluble MEAs in the presence of exfoliated clay, and subsequent drying [31]. Here, the essential point of the synthesis is that hydrophilic (monomer)-to-hydrophobic (polymer) transitions occur during in-situ polymerization along with micro- and macrophase separations. The initial transparent solution turned opaque (white) in the early stages of polymerization (within a few minutes) as a result of microscopic phase separation, which was caused by exclusion of the unaltered hydrophilic clay from the hydrophobic PMEAs chains. Subsequently, the system underwent macroscopic phase separation (after a few tens of minutes), which was accompanied by syneresis and volume contraction. Consequently, a uniform white gel consisting of nanostructured PMAA–clay with 400 wt% water (relative to the solid component) was obtained. In the subsequent drying process, the white gel first shrank, releasing a large amount of water, and finally turned into a transparent soft solid (M-NC). The resulting M-NCs were always uniform, colorless, and transparent ($>90\%$ transmittance), regardless of C_{clay} , as shown in Fig. 36a (M-NC23) [31]. The inset of Fig. 36a shows the high optical transmittance for both M-NC11 and M-NC46. The water uptake on immersion in water was only 0.5–15 wt%. This is totally different from NC gels [19, 28, 40], in which dried NC gels can revert to highly swollen hydrogels. Also, M-NCs did not dissolve even in good solvents for PMEAs, but could swell uniformly and extensively ($W_{\text{solvent}}/W_{\text{dry}} = 2\text{--}25$). These results strongly indicate that some kind of stable, three-dimensional network is formed in M-NCs, although no organic crosslinking agent was used in their synthesis. The sample code for M-NCs is based on the clay content (C_{clay} is given in n wt%) as M-NC n . C_{clay} can be varied over a wide range (1–50 wt% or higher) by altering the composition of the reaction solution.

5.5.2 Mechanical Properties of M-NCs

M-NCs have extraordinary mechanical properties, with two striking aspects: (1) an extremely large ϵ_b , as high as 1,000–3,000%, with good recovery on release; and (2) a well-defined yielding behavior in the early stages of elongation, as shown in Fig. 37 [31]. The high extensibility of M-NCs is accompanied by a distinctive

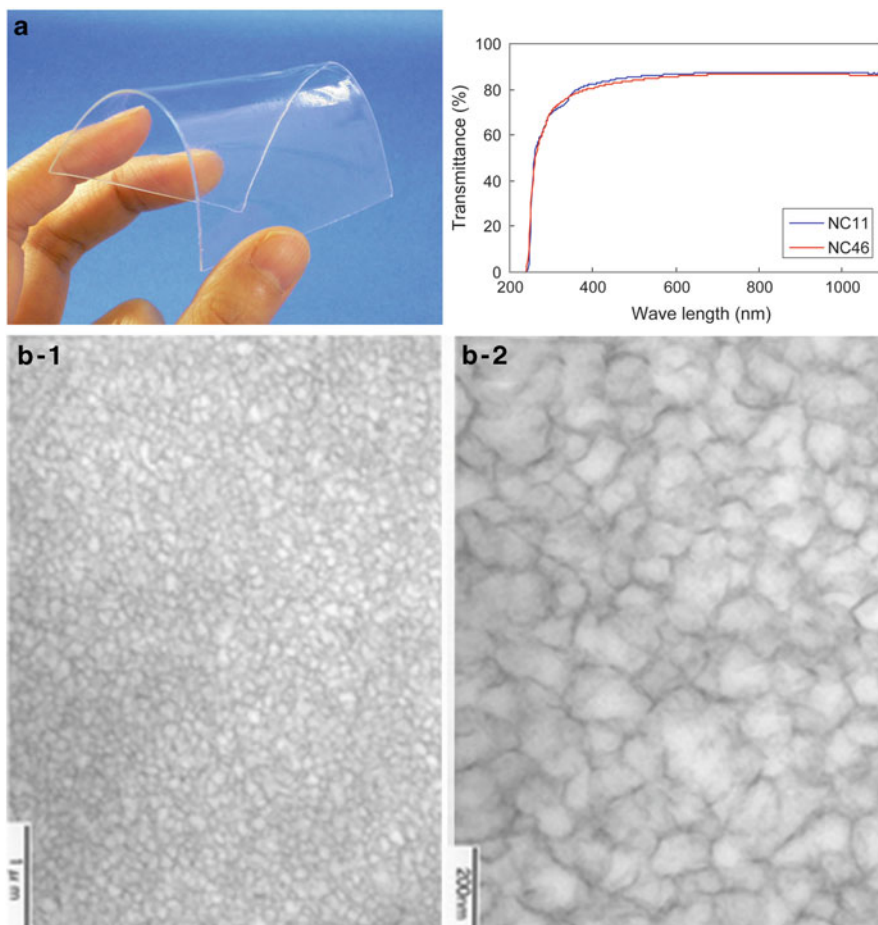


Fig. 36 (a) Transparent and soft M-NC23 film, containing 23 wt% inorganic clay. (b-1, b-2) TEM images for M-NC11 are at different magnifications (1 μm and 200 nm) as indicated by the scale bars. Reprinted from Haraguchi et al. [31], Copyright 2006, with permission of Wiley

yielding behavior: a yield point (I_b) at maximum stress, a necking region (II) at constant stress, and a strain-hardening region (III) from the end of the necking region (II_b). This is evident from the stress-strain curve (Fig. 37) and direct observations (the inset to Fig. 37). This characteristic yielding behavior is observed for all M-NCs with different C_{clay} , although it is more pronounced in M-NCs with C_{clay} greater than 10 wt%. On the other hand, M-ORs with the same composition as M-NCs, except for the crosslinker used, were brittle and ruptured at very low

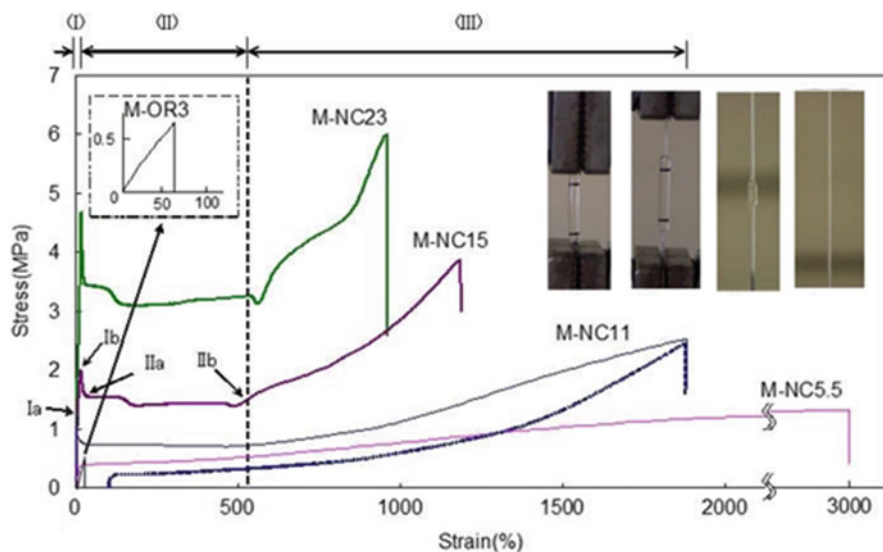


Fig. 37 Stress–strain curves for M-NCs with different clay contents (M-NC5.5–M-NC23) and for chemically crosslinked M-OR3. I, II, and III indicate the distinct stages of tensile deformation. A stress–strain curve for the second cycle of M-NC11 after the first elongation up to 1,800% is also shown as a *dotted line*. *Inset*: Example of yielding behavior observed for M-NC11 with two necking points, which start at both ends where a high stress concentration initially occurred at the grips. Reprinted from Haraguchi et al. [31], Copyright 2006, with permission of Wiley

elongation (M-OR3 in Fig. 37). The fracture energy of M-NC23 could be 200 times greater than that of M-OR3.

In M-NCs, more than 90% of the total elongation is recovered. Once elongated beyond point II_b, an M-NC exhibits simple stress–strain behavior, i.e., it undergoes large deformation similar to the original (as-prepared) M-NC, although no well-defined necking phenomenon is observed for M-NC11 (Fig. 37). Thus, the large deformation associated with necking becomes reversible on repeated cycling, but the necking phenomenon (i.e., the formation of a neck) itself is irreversible. This is the first report on the necking behavior in P-NCs. In extensive studies in polymeric materials such as crystalline polymers and high-impact polymer blends, the yielding (necking) behavior and associated large deformation were generally observed as a type of cold drawing, which was irreversible.

5.5.3 Network Structures in M-NCs

In order to explain the origins of the dramatic changes in the mechanical properties of M-NCs, while retaining high transparency and low water absorption, we proposed the formation of nanostructured M-NCs on the basis of the analytical data, such as DSC (T_g is the same as for free, uncrosslinked PMEA), XRD [evidence for

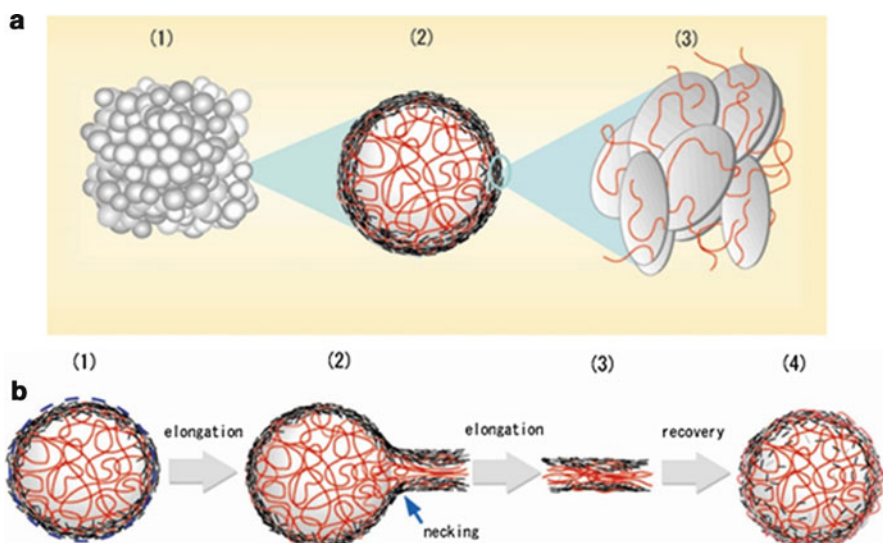


Fig. 38 (a) Clay network morphology: (1) clay network structure, (2) a clay–PMEA sphere, and (3) clay outer shell. (b) The deformation process for M-NC11: (1) elastic deformation of clay–PMEA sphere, (2) deformation with necking point, (3) further elongation over necking point, and (4) structure after recovery from large elongation. Reprinted from Haraguchi et al. [31], Copyright 2006, with permission of Wiley

stacking of clay–polymer–clay (2.7 nm) and clay–clay (1.1 nm) aggregates], FTIR (PMEA–clay interactions) and TEM [31]. Because the TEM images of M-NC11 (Fig. 36b-1, b-2) were the same regardless of the cutting direction, it was concluded that M-NC11 consists of clay networks that form a large number of connected clay spheres (100–300 nm in diameter), with a 20-nm-thick outer clay shell and the bulk of the flexible PMEA packed inside.

The clay network structure proposed is depicted graphically in Fig. 38a. The following mechanism for its formation is suggested: As the hydrophobic PMEA chains tend to aggregate during the course of in-situ polymerization, the primary clay platelets are squeezed out of these regions and form clay aggregates in which PMEA chains are attached to their surfaces. These clay aggregates and the bulk of the PMEA form nanometer-sized spherical structures consisting of an outer shell of aggregated clay (Fig. 38a, part 3) and an inner PMEA core (Fig. 38a, part 2). Thus, a nanostructured morphology is latently formed in the pre-formed gel state, becoming apparent when water is removed. Because each sphere is connected to neighboring spheres, a three-dimensional clay network is formed (Fig. 38a, part 1). Experimentally, the sphere diameter varied with C_{clay} and naturally decreased with an increase in C_{clay} . When C_{clay} was very low, a ribbon-like structure was formed instead of a spherical structure, as expected. Despite the formation of such structures, M-NCs are transparent because the thickness of the clay shell is very small and the refractive indices of PMEA (1.47) and clay (1.50) are similar.

The characteristic tensile deformation of M-NCs (Fig. 36, stages I–III) is also explicable in terms of the proposed model for the clay network, as shown in Fig. 38b. The extraordinarily high elongations (1,000–3,000%) observed in M-NCs are attributable to two main factors. One factor is the highly contracted form of the randomly coiled PMEA chains, which is the result of syneresis during polymerization and shrinkage during the drying process. In the case of deswollen polymer networks, it has been reported that extensibility can increase considerably, reaching $\lambda_{\max} = 18\text{--}30$ [157] because of its supercoiled structure. The results for M-NCs are consistent with those obtained for supercoiled polymer chains. The other factor is the formation of a crosslinked structure between PMEA and the clay. If there are no crosslinks to bear the applied stress, the contracted polymer chains can simply be drawn (at very low stress) by slipping. This has been observed in the case of M-LR. In the case of M-NCs, the supercoiled PMEA chains, whose ends may interact with the exfoliated clay, undergo extensive elongation and may retract.

5.5.4 Cell Culture Substrates

Substrata expected to be useful in future cytology and regenerative medicine will be transparent, flexible, and stretchable (i.e., elastomeric) biocompatible materials that are also capable of forming various shapes (such as thin films, rods, spheres, and hollow tubes) so that they can be utilized *in vivo* or *in vitro* under various static and dynamic conditions. Mechanically tough M-NC films can be used as novel soft, transparent, and elastomeric hydrophobic substrates that satisfy all the requirements described above, as well as having capabilities for cell cultivation and subsequent cell detachment (and therefore for harvesting living cells), without the use of an enzyme treatment [33].

Various types of cells (such as 3T3, HepG2, NHDF, HUVEC, and BAEC) can be cultivated to confluence on the surface of M-NC $_n$ films with clay contents of $n = 10\text{--}23$ wt%, although the cells hardly cultivated on the surface of chemically crosslinked PMEA and linear PMEA films. Further, the cells cultured on the surfaces of M-NC films can be detached, without any enzymatic digestion, by decreasing the medium temperature and/or simultaneously using gentle pipetting. The detached film was obtained as a single cell or a contiguous cell sheet, both of which were viable and could be re-cultured. It was estimated that the cell cultivation and subsequent temperature-regulated cell detachment are attributed to the combined effects of organic PMEA (hydrophobic, low protein-adsorptive, non-cell-adhesive) and inorganic clay nanoparticles (hydrophilic and cell-adhesive), in the form of a peculiar PMEA–clay network structure [33]. Thus, the M-NC film is potentially a very promising soft, transparent substrate for tissue engineering.

5.6 Further Extensions

Based on the results for NC gels, MD-NC gels, and M-NCs, new organic or inorganic advanced materials are being developed. For example, the advanced organic copolymer amphiphilic triblock (MDM) and four-arm block (MD)₄, which consist of hydrophobic PMEA (M) and hydrophilic PDMAA (D) segments, have been synthesized by RAFT polymerization [158]. The block copolymers were prepared using a versatile one-pot synthesis in high yields (~100%) and had high molecular weights (~200,000 g/mol), and exhibited high protein repellency, suspension cell culture thereon, and superior thrombogenicity, as well as good adhesion on various substrates. As advanced inorganic materials, nanostructured Pt-clay materials have been prepared in aqueous dispersions by using clay as a mild and effective reducing agent for Pt ions and also as an outstanding stabilizer for the resulting Pt nanoparticles [150]. The Pt-clay nanocomposites feature very high surface areas (312 m² g⁻¹), thermal stability (500°C), CO oxidation, and excellent catalytic activity, as kinetically evaluated via the reduction of 4-nitrophenol with NaBH₄ [159]. Other thermally stable Pt-clay NCs were prepared by using fluorinated clay and the same synthetic procedure [160]. In addition, ordered self-assembling nanostructures of Ag or Pd NPs [161], Au-LDH (layered double hydroxide) nanocomposites [162], and bimetallic core-shell nanocrystal/clay composites [163] have been developed. In the latter, clay plays a crucial role in the formation and stabilization of core-shell Pd-Pt or Au-Pt nanocrystals and affords high stability and large BET surface areas, and stimulates the exceptional catalytic activity of the core-shell NCs.

6 Conclusion

Using exfoliated clay nanoplatelets as network structure-determining agents and/or stabilizing agents, we created new types of soft nanohybrid materials, e.g., super-hydrogels (NC gels) and soft NCs with high C_{clay} (M-NCs), by in-situ free-radical polymerization in the presence of clay nanoparticles in aqueous systems. NC gels and M-NCs had extraordinary optical, mechanical, and stimuli-sensitive properties, in addition to a number of new characteristics including “super-functions” (the internal consistency of pairs of mutually conflicting properties) such as softness and toughness, extensibility and rigidity, swelling and deswelling, elongation and recovery, optical isotropy and anisotropy, hydrophilicity and hydrophobicity, cell cultivation and detachment, inorganic inclusion and transparency, and toughness and self-healing. All of the properties and new characteristics can be attributed to the unique organic (polymer)–inorganic (clay) network structures. NC gels, M-NCs, and their derivatives can be prepared in various forms and sizes, and their properties can be controlled over a wide range by changing the compositions and their circumstances. Thus, NC gels expand the possibilities of polymer

hydrogels as environmentally friendly (water-based) materials, and M-NCs similarly have potential as advanced nanocomposites with high inorganic content. NC gels and M-NCs, which overcome most of the serious disadvantages of conventional hydrogels and polymer nanocomposites, are promising soft nanohybrid materials that may open new doors in advanced materials chemistry and physics and will be utilized in various fields, including medical, biomedical, analytical, and civil engineering, and in electronic devices.

Acknowledgements I thank collaborators, Dr. HJ Li, Mr. T Takehisa, Dr. T Takada, Dr. K Murata, Dr. D Varade and other colleagues in my laboratory. I also thank Prof. M Shibayama (University of Tokyo), Prof. M Zhu and Prof G Li, (Donghua University), and Prof. GC Eastmond (Liverpool University) for collaboration and fruitful discussions. The works introduced in this review paper were carried out in Kawamura Institute of Chemical Research (Chiba, Japan) and supported by DIC Co. (Tokyo, Japan). I acknowledge the financial support provided by the Ministry of Education, Science, Sports and Culture, Japan (Grant-in-Aid for Scientific Research: 26600050, 23350117, 20350109, 16550181), and by the New Energy and Industrial Technology Development Organization (NEDO), Japan (Project 2006–2008).

References

1. Kopecek J (2009) *J Polym Sci A Polym Chem* 47:5929
2. Bin IA, Seki T, Takeoka Y (2010) *Polym J* 42:839
3. Messing R, Schmidt AM (2011) *Polym Chem* 2:18
4. Xia LW, Xie R, Ju XJ, Wang W, Chen Q, Chu LY (2013) *Nat Commun* 4:3226
5. Richtering W, Saunders BR (2014) *Soft Mater* 10:3695
6. Okano T, Bae YH, Jacobs H, Kim SW (1990) *J Control Release* 11:255
7. Stayton PS, Shimoboji T, Long C, Chilkoti A, Chen G, Harris JM, Hoffman AS (1995) *Nature* 378:472
8. Cai W, Anderson EC, Gupta RB (2001) *Ind Eng Chem Res* 40:2283
9. Matsumoto A, Yoshida R, Kataoka K (2004) *Biomacromolecules* 5:1038
10. Yamato M, Okano T (2004) *Mater Today* 7:42
11. Matsukuma D, Yamamoto K, Aoyagi T (2006) *Langmuir* 22:5911
12. Kretlow JD, Hacker MC, Klouda L, Ma BB, Mikos AG (2010) *Biomacromolecules* 11:797–805
13. Heskens M, Guillet JE (1968) *J Macromol Sci A2*:1441
14. Cho EC, Lee J, Cho K (2003) *Macromolecules* 36:9929
15. Matsuo ES, Tanaka T (1988) *J Chem Phys* 89:1695
16. Annaka M, Motokawa K, Sasaki S, Nakahira T, Kawasaki H, Maeda H, Amo Y, Tominaga Y (2000) *J Chem Phys* 113:5980
17. Otake K, Inomata H, Konno M, Saito S (1990) *Macromolecules* 23:283
18. Takigawa T, Araki H, Takahashi K, Masuda T (2000) *J Chem Phys* 113:7640
19. Haraguchi K, Takehisa T (2002) *Adv Mater* 14:1120
20. Haraguchi K, Takehisa T, Fan S (2002) *Macromolecules* 35:10162
21. Haraguchi K (2007) *Macromol Symp* 256:120
22. Xu Y, Li G, Haraguchi K (2010) *Macromol Chem Phys* 211:977
23. Giannelis EP (1996) *Adv Mater* 8:29
24. Mark JE (2003) *Macromol Symp* 201:77
25. Okada K, Usuki A (2006) *Macromol Mater Eng* 291:1449

26. Usuki A, Kojima Y, Kawasumi M, Okada A, Fukushima Y, Kurauchi T, Kamigaito O (1993) *J Mater Res* 8:1179
27. Convertino A, Tamborra M, Striccoli M, Leo G, Agostiano A, Curri ML (2011) *Thin Solid Films* 519:3931.
28. Haraguchi K, Li HJ (2005) *Angew Chem Int Ed* 44:6500
29. Haraguchi K (2007) *Curr Opin Solid State Mater Sci* 11:47–54
30. Fukasawa M, Sakai T, Chung UI, Haraguchi K (2010) *Macromolecules* 43:4370
31. Haraguchi K, Ebato M, Takehisa T (2006) *Adv Mater* 18:2250
32. Editor's Choice (2006) *Science* 314:19
33. Haraguchi K, Masatoshi S, Kotobuki N, Murata K (2011) *J Biomater Sci Polym Ed* 22:2389
34. Tanaka Y, Gong JP, Osada Y (2005) *Prog Polym Sci* 30:1
35. Johnson JA, Turro NJ, Koberstein JT, Mark JE (2010) *Prog Polym Sci* 35:332–337
36. Okumura Y, Ito K (2001) *Adv Mater* 13:485
37. Gong JP, Katsuyama Y, Kurokawa T, Osada Y (2003) *Adv Mater* 15:1155
38. Sakai T, Matsunaga T, Yamamoto Y, Ito C, Yoshida R, Suzuki S, Sasaki N, Shibayama M, Chung UI (2008) *Macromolecules* 41:5379
39. Haraguchi K, Li HJ, Matsuda K, Takehisa T, Elliot E (2005) *Macromolecules* 38:3482
40. Haraguchi K, Farnworth R, Ohbayashi A, Takehisa T (2003) *Macromolecules* 36:5732
41. Haraguchi K, Li HJ (2006) *Macromolecules* 39:1898
42. Rosta L, von Gunten HR (1990) *J Colloid Interface Sci* 134:397
43. Haraguchi K, Li H-J (2004) *J Network Polym Jpn* 25:2
44. Zhu M, Liu Y, Sun B, Zhang W, Liu X, Yu H, Zhang Y, Kuckling D, Adler HJP (2006) *Macromol Rapid Commun* 27:1023
45. Xiong L, Hu X, Liu X, Tong Z (2008) *Polymer* 49:5064
46. Li P, Kim NH, Siddaramaiah, Lee JH (2009) *Compos B Eng* 40:275
47. Haraguchi K, Song L (2007) *Macromolecules* 40:5526
48. Haraguchi K, Takada T (2010) *Macromolecules* 43:4294
49. Song L, Zhu M, Chen Y, Haraguchi K (2008) *Polym J* 40:800
50. Shibayama M, Suda J, Karino T, Okabe S, Takehisa T, Haraguchi K (2004) *Macromolecules* 37:9606
51. Miyazaki S, Karino T, Endo H, Haraguchi K, Shibayama M (2006) *Macromolecules* 39:8112
52. Miyazaki S, Endo H, Karino T, Haraguchi K, Shibayama M (2007) *Macromolecules* 40:4287
53. Nie J, Du B, Oppermann W (2006) *J Phys Chem B* 110:11167
54. Haraguchi K, Li HJ (2009) *J Polym Sci B Polym Phys* 47:2328
55. Haraguchi K, Xu Y, Li G (2010) *Macromol Rapid Commun* 31:718
56. Haraguchi K, Xu Y (2012) *Colloid Polym Sci* 290:1627
57. Nishida T, Endo H, Osaka N, Li HJ, Haraguchi K, Shibayama M (2009) *Phys Rev E* 80:030801R
58. Nishida T, Obayashi A, Haraguchi K, Shibayama M (2012) *Polymer* 53:4533
59. Tobolsky AV, Carlson DW, Indictor N (1961) *J Polym Sci* 54:175
60. Flory PJ, Rehner JJR (1943) *J Chem Phys* 11:521
61. Baker JP, Hong LH, Blanch HW, Prausnitz JM (1994) *Macromolecules* 27:1446
62. Haraguchi K, Li H-J, Song L, Murata K (2007) *Macromolecules* 40:6973
63. Flory PJ (1953) *Principles of polymer chemistry*. Cornell University Press, Ithaca, Chapter 9
64. Gordon M, Ross-Murphy SB (1975) *Pure Appl Chem* 43:1
65. Stauffer DJ (1976) *Chem Soc Faraday Trans II* 72:1354
66. de Gennes PG (1979) *Scaling concept in polymer physics*. Cornell University Press, Ithaca, Chapter 5
67. Haraguchi K (2011) *Colloid Polym Sci* 289:455
68. Dijkstra M, Hansen JP, Madden PA (1995) *Phys Rev Lett* 75:2236
69. Liu Y, Zhu M, Liu X, Zhang W, Sun B, Chen Y, Adler HJP (2006) *Polymer* 47:1
70. Xiang Y, Peng Z, Chen D (2006) *Eur Polym J* 42:2125
71. Mu J, Zheng S (2007) *J Colloid Interface Sci* 307:377

72. Hibino T (2010) *Appl Clay Sci* 50:282
73. Chen T, Cao Z, Guo X, Nie J, Xu J, Fan Z, Du B (2011) *Polymer* 52:172
74. Jiang G, Liu C, Liu X, Chen Q, Zhang G, Yang M, Liu F (2010) *Polymer* 51:1507
75. Zhou C, Wu Q (2011) *Colloids Surf B* 84:155
76. Zhou C, Wu Q, Yue Y, Zhang Q (2011) *J Colloid Interface Sci* 353:116
77. Smith TL, Stedry PJ (1960) *J Appl Phys* 31:1892
78. Haraguchi K, Li H-J, Ren H, Zhu M (2010) *Macromolecules* 43:9848
79. Zhang X, Zhuo R (2001) *Langmuir* 17:12
80. Okajima T, Harada I, Nishio K, Hirotsu S (2000) *Jpn J Appl Phys* 39:L875
81. Yoshida R, Uchida K, Kaneko Y, Sakai K, Kikuchi A, Sakurai Y, Okano T (1995) *Nature* 374:240
82. Tanaka T, Fillmore DJ (1979) *J Chem Phys* 70:1214
83. Song L, Zhu M, Chen Y, Haraguchi K (2008) *Macromol Chem Phys* 209:1564
84. Xu K, Wang J, Xiang S, Chen Q, Zhang W, Wang P (2007) *Appl Clay Sci* 38:139
85. Mujumdar SK, Siegel RA (2008) *J Polym Sci A Polym Chem* 46:6630
86. Janovak L, Varga J, Kemeny L, Dekany I (2009) *Appl Clay Sci* 43:260
87. Xiong L, Zhu M, Hu X, Liu X, Tong Z (2009) *Macromolecules* 42:3811
88. Hu X, Xiong L, Wang T, Lin Z, Liu X, Tong Z (2009) *Polymer* 50:1933
89. Xu S, Zhang S, Yang J (2008) *Mater Lett* 62:3999
90. Zhu M, Xiong L, Wang T, Liu X, Wang C, Tong Z (2010) *React Funct Polym* 70:267
91. Ma J, Xu Y, Fan B, Liang B (2007) *Eur Polym J* 43:2221
92. Can V, Abdurrahmanoglu S, Okay O (2007) *Polymer* 48:5016
93. Ren HY, Zhu M, Haraguchi K (2011) *Macromolecules* 44:8516
94. Urayama K (2007) *Macromolecules* 40:2277
95. Yokoyama F, Achife EC, Matsuoka M, Shimamura K, Yamashita Y, Monobe K (1991) *Polymer* 32:2911
96. Stellwagen J, Stellwagen NC (1989) *Nucleic Acids Res* 17:1537
97. Murata K, Haraguchi K (2007) *J Mater Chem* 17:3385
98. Haraguchi K, Takada T (2005) *Macromol Chem Phys* 206:1530
99. Zhang J, Pelton R, Deng Y (1995) *Langmuir* 11:2301
100. Teare DOH, Barwick DC, Schofield WCE, Garrod RP, Beeby A, Badyal JPS (2005) *J Phys Chem B* 109:22407
101. Sun T, Wang G, Feng L, Liu B, Ma Y, Jiang L, Zhu D (2004) *Angew Chem Int Ed* 43:357
102. Haraguchi K, Li HJ, Okumura N (2007) *Macromolecules* 40:2299
103. Haraguchi K, Li HJ, Song L (2008) *J Colloid Interface Sci* 326:41
104. Haraguchi K (2007) *Research highlights. Nature* 446:350
105. Haraguchi K, Li HJ (2010) *Macromol Symp* 291:159
106. Takizawa T, Mori Y, Yoshizato K (1990) *Biotechnology* 8:854
107. Akiyama Y, Kikuchi A, Yamato M, Okano T (2004) *Langmuir* 20:5506
108. Haraguchi K, Takehisa T, Ebato M (2006) *Biomacromolecules* 7:3267
109. Wang T, Liu D, Lian C, Zheng S, Liu X, Wang C, Tong Z (2011) *React Funct Polym* 71:447
110. Haraguchi K, Matsuda M (2005) *Chem Mater* 17:931
111. Haraguchi K, Taniguchi S, Takehisa T (2005) *Chem Phys Chem* 6:238
112. Ghosh SK (2009) *Self-healing materials: fundamentals, design strategies, and applications*. Wiley, Weinheim
113. Bergman SD, Wudl F (2008) *J Mater Chem* 18:41
114. Hager MD, Greil P, Leyens C, Van der Zwaag S, Schuber US (2010) *Adv Mater* 22:5424
115. Brochu ABW, Craig SL, Reichert WM (2010) *J Biomedical Mater Res A* 96A:492
116. Chen X, Dam MA, Ono K, Mal A, Shen H, Nutt SR, Sheran K, Wudl F (2002) *Science* 295:1698
117. Liu YL, Chen YW (2007) *Macromol Chem Phys* 208:224
118. Scott TF, Schneider AD, Cook WD, Bowman CN (2005) *Science* 308:1615
119. Higaki Y, Otsuka H, Takahara A (2006) *Macromolecules* 39:2121

120. Oku T, Furusho Y, Takata T (2004) *Angew Chem Int Ed* 43:966
121. Bleay SM, Loader CB, Hawyes VJ, Humberstone L, Curtis PT (2001) *Composites A* 32:1767
122. Coillot D, Mear FO, Podor R, Montagne L (2010) *Adv Funct Mater* 20:4371
123. White SR, Sottos NR, Geubelle PH, Moore JS, Kessler MR, Sriram SR, Brown EN, Viswanathan S (2001) *Nature* 409:794
124. Cordier P, Tourmilhac F, Soulie-Ziakovic C, Leibler L (2008) *Nature* 451:977
125. Ghosh B, Urban MW (2009) *Science* 323:1458
126. Wang Q, Mynar JL, Yoshida M, Lee E, Lee M, Okuro K, Kinbara K, Aida T (2010) *Nature* 463:339
127. Haraguchi K, Uyama K, Tanimoto H (2011) *Macromol Rapid Commun* 32:1253
128. Haraguchi K, Murata K, Takehisa T (2012) *Macromolecules* 45:385
129. Haraguchi K, Murata K, Takehisa T (2013) *Macromol Symp* 329:150
130. Miyahara Y, Nagaya N, Kataoka M, Yanagawa B, Tanaka K, Hao H, Ishino K, Ishida H, Shimizu T, Kangawa K (2006) *Nat Med* 12:459
131. Kuroda R, Ishida K, Matsumoto T, Akisue T, Fujioka H, Mizuno K, Ohgushi H, Wakitani S, Kurosaka M (2007) *Osteoarthritis Cartil* 15:226
132. Kotobuki N, Murata K, Haraguchi K (2013) *J Biomed Mater Res A* 101:537
133. Lowe AB, McCormick CL (2002) *Chem Rev* 102:4177
134. Kudaibergenov S, Jaeger W, Laschewsky A (2006) *Adv Polym Sci* 201:175
135. Kimura M, Takai M, Ishihara K (2007) *J Biomed Mater Res A* 80:45
136. Carr LR, Zhou Y, Krause JE, Xue H, Jiang S (2011) *Biomaterials* 32:6893
137. Seuring J, Agarwal S (2012) *Macromol Rapid Commun* 33:1898
138. Shih YJ, Chang Y (2010) *Langmuir* 26:17286
139. Ning J, Kutoba K, Li G, Haraguchi K (2013) *React Funct Polym* 73:969
140. Ning J, Li G, Haraguchi K (2013) *Macromolecules* 46:5317
141. Ning J, Li G, Haraguchi K (2014) *Macromol Chem Phys* 215:235
142. Haraguchi K, Takada T (2014) *Macromol Chem Phys* 215:295
143. Stamenkovic VR, Fowler B, Mun BS, Wang G, Ross PN, Lucas CA, Markovic NM (2007) *Science* 315:493
144. Zhai D, Liu B, Shi Y, Pan L, Wang Y, Li W, Zhang R, Yu G (2013) *ACS Nano* 7:3540
145. Bedenbaugh JE, Kim S, Sasmaz E, Lauterbach J (2013) *ACS Comb Sci* 15:491
146. Tian M, Wu G, Chen A (2012) *ACS Catal* 2:425
147. Adhikari B, Biswas A, Banerjee A (2012) *ACS Appl Mater Interfaces* 4:5472
148. Zhang L, Zheng S, Kang DE, Shin JY, Suh H, Kim I (2013) *RSC Adv* 3:4692
149. Haraguchi K, Varade D (2014) *Polymer* 55:2496
150. Varade D, Haraguchi K (2013) *Langmuir* 29:1977
151. Idemura S, Haraguchi K (2000) US Patent P6,063,862
152. Goda H, Higashino T (2003) US Patent P6,525,160
153. Tanaka M, Motomura T, Ishii N, Shimura K, Onishi M, Mochizuki A, Hatakeyama T (2000) *Polym Int* 49:1709
154. Saito N, Motoyama S, Sawamoto J (2000) *Artif Organs* 24:547
155. Baykut D, Bernet F, Wehrle J, Weichelt K, Schwartz P, Zerkowski HR (2001) *Eur J Med Res* 6:29
156. Tanaka M, Mochizuki A, Ishii N, Motomura T, Hatakeyama T (2002) *Biomacromolecules* 3:36
157. Urayama K, Kohjiya S (1998) *Eur Phys J B* 2:75
158. Haraguchi K, Kubota K, Takada T, Mahara S (2014) *Biomacromolecules* 15(6):1992–2003
doi:10.1021/bm401914c
159. Varade D, Abe H, Yamauchi Y, Haraguchi K (2013) *ACS Appl Mater Interfaces* 5:11613
160. Varade D, Haraguchi K (2013) *Phys Chem Chem Phys* 15:16477
161. Varade D, Haraguchi K (2012) *Soft Matter* 8:3743
162. Varade D, Haraguchi K (2012) *J Mater Chem* 22:17649
163. Varade D, Haraguchi K (2014) *Chem Commun* 50:3014

Fabrication of Metal Oxide–Polymer Hybrid Nanocomposites

Yuvaraj Haldorai and Jae-Jin Shim

Abstract The synthesis of polymer/metal oxide hybrid nanocomposites has attracted increasing attention because of their potential applications. The advances in polymer science have provided the ability to prepare a wide range of materials with controllable mechanical, thermal, and electroactive properties. As part of this renewed interest in nanocomposites, many researchers have begun seeking new strategies for engineering nanocomposite materials that combine the desirable properties of nanoparticles (NPs) with those of polymers. Previous research has revealed a number of key challenges in producing nanocomposites with the desired behavior. The greatest hindrance to the large-scale production and commercialization of nanocomposites is the lack of cost-effective methods for controlling the dispersion of NPs in their polymeric hosts. Nanoscale particles typically aggregate, which negates any benefit associated with their small dimensions. The particles must be integrated in such a way that isolated, well-dispersed primary NPs are found inside the matrix. Processing techniques are needed that are effective on the nanoscale yet applicable to macroscopic processing. Synthetic strategies for nanocomposites with high homogeneity are a challenge. Several attempts have been made to synthesize nanocomposites and they can be classified under two major categories: ex-situ and in-situ processes. This review discusses both ex-situ and in-situ methods with appropriate examples.

Keywords Applications · Metal oxide · Nanocomposites · Polymers · Properties

Y. Haldorai (✉)

School of Chemical Engineering, Yeungnam University, Gyeongsan, Gyeongbuk 712-749, Republic of Korea

Department of Energy and Materials Engineering, Dongguk University-Seoul, Seoul, Republic of Korea

e-mail: yuvraj_pd@yahoo.co.in

J.-J. Shim

School of Chemical Engineering, Yeungnam University, Gyeongsan, Gyeongbuk 712-749, Republic of Korea

Contents

1	Introduction	250
2	Synthesis of Metal Oxide Nanoparticles	251
3	Synthesis of Polymer/Metal Oxide Hybrid Nanocomposites	252
3.1	Blending or Direct Mixing	253
3.2	Sol-gel Process	258
3.3	In-Situ Synthesis	260
4	Properties of Nanocomposites	269
4.1	Optical Properties	269
4.2	Magnetic Properties	273
5	Applications of Nanocomposites	275
6	Conclusions	275
	References	276

1 Introduction

Nanostructured hybrid materials are a special class of composite system composed of organic and inorganic components distributed on the nanoscale. Over the last two decades, the synthesis of organic-inorganic nanocomposites has been studied extensively because of their unique properties and widespread potential applications [1–4]. The effective properties of composites are dependent on the properties of the constituents, the volume fraction of the components, the shape and arrangement of inclusions, and the interfacial interactions between the matrix and inclusion. With the recent development in the nanoscience and nanotechnology fields, the correlation of the material properties with the filler size has become a focal point of significant interest. The synergistic combination of two components of a single material on the nanoscale provides novel properties for the development of multifunctional materials [5–8]. Two key approaches have been used to produce composite structures on the nanometer scale: self-aggregation and dispersion. Using the self-aggregation approach, ordered hybrid materials are normally obtained, whereas disordered composites are often prepared by dispersing nanoparticles in a matrix. Nanostructured self-aggregated hybrid composites are materials with spatially well-defined domains for both the organic and inorganic components and a controlled mutual arrangement on the nanoscale. On the other hand, combination by the dispersion of low dimensional dispersed fillers with soft matter, particularly polymers, allows the easy preparation of hybrid materials with improved properties. The interesting properties of these unique structural nanocomposites enable a wide range of applications in the fields of energy, biomedicine, optoelectronics, etc. [5–8].

Fillers are small particles (<1,000 μm in length) added to matrices as admixtures, normally at high loadings, for the formulation of composites. Fillers are basically divided into inactive and functional fillers. The term “inactive” is related to the primary use of fillers focused on reducing the final material cost, whereas the term “functional” is used to emphasize the modern use of fillers that are employed to modify the specific properties of the final composite product, such as density,

shrinkage, expansion coefficient, conductivity, permeability, mechanical properties, or thermal behavior [8, 9]. The addition of fillers to matrices to form composite materials can have many very different purposes, ranging from fire retardant effects to the hardening of soft matter (polymers, plastics) [10, 11]. The use of nanoparticles (NPs) as fillers has attracted considerable interest. Nanotechnology has developed to a stage that allows the large-scale production of different tailored single-component nanosized entities, ranging from metal NPs to carbon nanotubes. Therefore, at this stage, a major challenge is to demonstrate the feasibility of the fabrication of complex nanostructured products or devices, such as nanostructured composites. On one hand, current bottom-up mass-production methods (vapor-related physical routes or liquid-related chemical bulk processes) to further develop heterostructures of various nanoentities have severe limitations related to their high cost and reduced purity. On the other hand, the surface-functionalization of NPs is an essential step in effectively exploring the remarkable properties of nanocomposites and in manipulating the NPs to form nanostructured hybrid composites. The reason is that the as-prepared inorganic fillers are often incompatible with organic soft matrices, owing to the low interfacial interactions between the two phases [12]. This is particularly relevant to nanofillers, which have a large surface area-to-volume ratio [13]. The lack of filler–matrix coupling or bonding often leads to the preparation of hybrid materials with nonisotropic properties and relatively poor mechanical behavior, which limits their application [14, 15]. Therefore, enhanced dispersion of nanofillers in the bulk of diverse organic matrices through surface modification is technically required [16]. Moreover, the effects of weathering (e.g., wetting, permeability, fouling, and corrosion) in the formed composite can be suppressed, or at least mitigated, by treating the surface of the inorganic filler, which increases the durability of the final material. The high surface reactivity of most inorganic fillers facilitates their surface modification and functionalization.

This review examines the synthesis of polymer/metal oxide nanocomposites using ex-situ and in-situ methods. Selected metal oxide NPs, such as zinc oxide (ZnO), titanium oxide (TiO₂), copper oxide (CuO), magnetite (Fe₃O₄), and maghemite (γ -Fe₂O₃), as well as their composites, are discussed with the appropriate examples. Note that it is impossible to completely describe this field because of the vast number of papers published on the synthesis of polymer/metal oxide nanocomposites. Therefore, this article will provide a general overview of the techniques and strategies used to prepare nanocomposites. Selected examples that represent different routes and systems will be described. More detailed descriptions of the specific themes will be referred to from the related references.

2 Synthesis of Metal Oxide Nanoparticles

Over the last few decades, considerable research has been focused the synthesis of metal oxide NPs, and many reports have described efficient approaches to the production of shape-controlled, stable, and monodispersed NPs. NPs can be

synthesized from many materials using a range of physical and chemical methods, with the particles differing in elemental composition, shape, size, and chemical or physical properties [17]. The methods for preparing metal oxide NPs can be divided into physical and chemical methods, based on whether chemical reactions are involved. On the other hand, these methods can also be classified into gas phase, liquid phase, and solid phase methods based on the state of the reaction system. The gas phase methods include gas-phase evaporation methods (resistance heating, high frequency induction heating, plasma heating, electron beam heating, laser heating, electric heating evaporation method, vacuum deposition on the surface of flowing oil, and exploding wire method), chemical vapor reactions (heating heat pipe gas reaction, laser induced chemical vapor reaction, plasma enhanced chemical vapor reaction), chemical vapor condensation, and sputtering methods. The liquid phase methods for synthesizing nanoparticles include mainly precipitation, hydrolysis, spray, solvent thermal methods (high temperature and high pressure), solvent evaporation pyrolysis, oxidation reduction (room pressure), emulsion, radiation chemical synthesis, and sol-gel processing. Solid phase methods include thermal decomposition, solid state reactions, and spark discharge, stripping, and milling methods.

Physical methods generally involve vapor deposition and depend on the principle of subdividing bulk precursor materials into smaller NPs. The synthesis of metal oxide NPs by chemical methods has proven to be more effective than physical methods. The properties of nanoscale materials can differ considerably from their bulk counterparts. As the size of the material decreases, the proportion of surface atoms increases, which increases the reactivity, making them highly reactive catalysts with the surface atoms being the active centers for elementary catalytic processes. Therefore, NPs possess unique electronic, optical, magnetic, and mechanical properties that arise explicitly because of their nanometer-scale size. Because of these unique properties, metal oxide NPs can be employed in applications in a range of fields, such as catalysis, wastewater treatment, textiles, paints, drug delivery, magnetic resonance imaging (MRI), tissue engineering, and cancer treatment. Table 1 summarizes the synthesis, properties, and applications of selected metal oxides such as ZnO, TiO₂, CuO, Fe₃O₄, and γ -Fe₂O₃ [18–106].

3 Synthesis of Polymer/Metal Oxide Hybrid Nanocomposites

Generally, there are three preparative methods for synthesizing polymer/metal oxide nanocomposites (Fig. 1). The first is direct mixing or blending of a polymer and metal oxide NPs, either as discrete phases (known as melt mixing) or in solution (solution mixing). The second is a sol-gel process, which starts with a molecular precursor at ambient temperature and then forms a metal oxide framework by hydrolysis and condensation. The third is in-situ polymerization of monomers in the presence of metal oxide NPs.

Table 1 Synthesis, properties, and applications of selected metal oxides

Nanoparticle	Synthesis	Properties	Applications	References
ZnO	Sol–gel, mechanical milling, homogeneous precipitation, microwave method, organometallic synthesis, spray pyrolysis, thermal evaporation, mechanochemical synthesis, hydrothermal, solvothermal and thermal decomposition	Optical, electrical, sensing, transport, magnetic electronic, and catalytic properties, thermal conductivity	Optoelectronic and electronic device applications, gas sensor, photocatalytic degradation of organic pollutants, cosmetics, medical filling materials, and antimicrobial applications	[18–49]
TiO ₂	Sol–gel, hydrothermal, sonochemical, reverse micelles, solvothermal, flame spray pyrolysis, nonhydrolytic approach, chemical vapor deposition, and microwave method	Optical, electronic, spectral, structural, mechanical, sensing, catalytic, and anticorrosion properties	Dye-sensitized solar cells, gas sensor, nanomedicine, skin care products, photocatalytic degradation of organic pollutants, and antimicrobial applications	[50–75]
Magnetic	Co-precipitation, microemulsions, sol–gel, solvothermal, pulsed laser ablation, electrochemical, sonochemical, microwave, and thermal decomposition method	Magnetic, caloric, physical, sensing, and hydrodynamic properties	Biomedicine, cancer treatment, MRI, drug delivery, removal of toxic metal ions, and antimicrobial properties	[76–94]
CuO	Sonochemical, solvothermal, direct thermal decomposition, electrochemical methods, colloid-thermal synthesis process, microwave radiation, precipitation, and solution plasma method.	Electrical, optical, magnetic, dielectric, sensing, thermal, and photoconducting properties	Antioxidant, antibacterial, thermal conductivity, antimicrobial, catalytic, battery solar cells, and gas sensor	[95–106]

3.1 Blending or Direct Mixing

Blending is the simplest method of preparing polymer/metal oxide nanocomposites. The ex-situ method is popular because it does not set a limitation on the nature of the NPs and host polymers used. According to the conditions, blending can

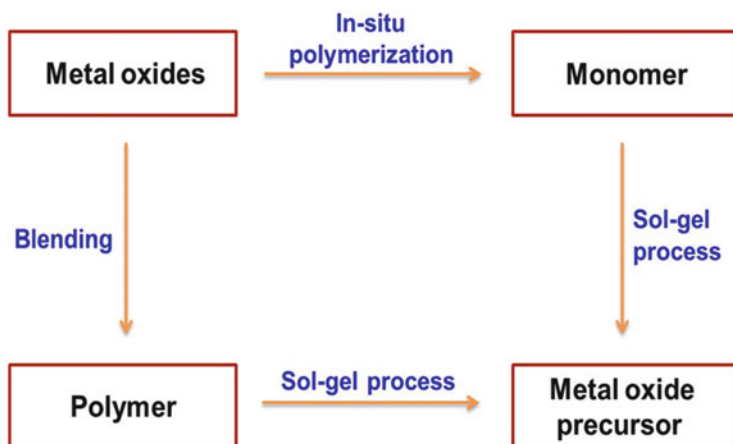


Fig. 1 Three general methods for the preparation of polymer/metal oxide hybrid nanocomposites

normally be divided into melt blending and solution blending. The main difficulty in the mixing process is always the effective dispersion of NPs in the polymer matrix because the NPs tend to agglomerate. Direct mixing of NPs with a polymer melt in technical polymer processes, such as extrusion, is a classical method for preparing composite materials from thermoplastic polymers. This process is mainly used for the compounding of clay materials in polyolefins. Currently, this process is used for a wide range of materials, such as metal oxides and carbon nanotubes. The strength of melt blending is the large quantity of material that can be produced by extrusion, and most polymer blends are produced commercially in this way. Melt blending offers a number of appealing advantages, such as no requirement for a solvent, ease of processing with conventional blending devices such as extruders, relatively low cost, and being environmentally sound.

3.1.1 Melt Blending

Only a few studies on the synthesis of polymer/metal oxide nanocomposites by melt blending have been reported. Hong et al. [107] prepared ZnO/low density polyethylene (LDPE) nanocomposites by melt blending. They attempted to understand how ZnO NPs and their surfaces affected the electrical properties of composites compared with those filled with conventional submicron-sized ZnO. The same group examined the dielectric constants of composites with ZnO concentrations up to 40% [108]. Dang et al. [109] also calculated the dielectric properties of LDPE/ZnO composites. Low dielectric constants were reported for composites with ZnO volume fractions of up to 60 vol%. They considered that there is no percolation threshold in LDPE/ZnO composites because of their low dielectric constant. Tjong and Liang [110] prepared LDPE/ZnO nanocomposites via a melt-blending route and determined the dielectric and resistivity characteristics. The structural

properties of the LDPE/ZnO composite were discussed in terms of the interparticle distance and percolation threshold theory. They also examined the electrical properties of thermally treated nanocomposites [111]. The results showed that the thermal treatments had a pronounced effect on the electrical properties of composites. Recently, Wong et al. [112] reported the changes in the glass transition temperature of melt-blended poly(methyl methacrylate) (PMMA) nanocomposites containing finely dispersed ZnO quantum dots (QDs) that had been surface-modified using a silane coupling agent, 3-(trimethoxysilyl) propyl methacrylate (MPTMS). Zhao and Li [113] investigated the photodegradation characteristics of polypropylene (PP) nanocomposites filled with silane coupling agent-modified ZnO NPs. UV irradiation induced significant photodegradation of the unfilled PP.

Miyauchi et al. [114] fabricated poly(butylene succinate)/TiO₂ nanocomposites using a high-shear extruder, and evaluated their photoinduced decomposition and biodegradability in relation to the dispersion state of TiO₂ particles. Ou et al. [115] prepared melt compounded PP/polyamide 6 (PA6) (70/30) blends, as well as their nanocomposites, with toluene-2,4-diisocyanate-functionalized TiO₂ using a rotating twin-screw extruder. Maleated PP was used as a compatibilizer. The mechanical properties of the composites were improved significantly due to the synergistic effect of functionalized TiO₂ and the compatibilizer. Li et al. [116] examined the impact of isopropyl tri(dioctyl phosphate)-modified TiO₂ on the crystallization behavior of polybutylene terephthalate. Recently, Chiu et al. [117] investigated the elongation flow properties of TiO₂/PP nanocomposite fibers prepared by melt spinning. Knor et al. [118] reported the mechanical and thermal properties of nano-TiO₂-reinforced polyetheretherketone (PEEK) composites produced by optimized twin screw extrusion. More recently, Zohrevand et al. [119] reported the effects of adding TiO₂ NPs at various volume concentrations (up to 15 vol%, 45.5 wt%) on the PP structure as well as on the thermal and mechanical properties of the resulting PP/TiO₂ nanocomposites. The correlation of these properties on the nanocomposite microstructure was also considered. To achieve a better interaction between the PP and TiO₂ phases, an anhydride-modified PP was used as a compatibilizer.

Kong et al. [120] prepared a magnetic nanocomposite composed of magnetic NPs and natural rubber by melt blending and examined the temperature-dependent magnetic behavior of the composite. Chung et al. [121] prepared flexibly crosslinked shape memory polyurethane (PU)/Fe₃O₄ composites by melt mixing. The composites displayed excellent mechanical and shape memory properties. Vunain et al. [122] prepared polymer nanocomposites composed of ethylene-vinyl acetate, poly(ϵ -caprolactone) (PCL) and Fe₃O₄ with different weight percentages by melt blending. The nanocomposites were used as effective adsorbent materials for the removal of As(III) ions and some metal ions from aqueous solutions. Although polymer processing conditions were optimized to achieve a good uniform dispersion of the metal oxide NPs in the polymer matrix, surface characterization indicated the clustering of NPs. Agglomeration was attributed to the particle interactions mediated by steric forces in the polymer matrix. Overall, the reasonable dispersion and control over the magnetic properties achieved in the above reports is promising for a range of applications. On the other hand, the

blending of polymers and metal oxide NPs to produce homogeneous and well-dispersed NPs in the polymer poses significant challenges.

Despite the previously mentioned advantages of melt blending, polymer degradation might be a considerable issue that should not be overlooked. Because a certain high temperature is normally required during melt blending, the polymer matrix and compatibilizer might degrade the organic surfactant, which can lead to a significant decrease in the mechanical properties of the final products.

3.1.2 Solution Blending

Solution blending is a liquid-state powder processing method that produces a good molecular level of mixing and is used widely in material preparation and processing. The benefits of solution blending include the rigorous mixing of the inorganic filler with the polymer in a solvent, which facilitates filler NP de-aggregation and dispersion. This method consists of three steps: dispersion of the filler NPs in a suitable solvent, mixing with the polymer (at room temperature or elevated temperature), and recovery of the nanocomposite by precipitating or casting a film. Both organic and aqueous media have been used to produce nanocomposites. In this method, the dispersion of filler NPs can be achieved by magnetic stirring, shear mixing, reflux or, most commonly, by ultrasonication.

Polystyrene (PS)/ZnO nanocomposites were prepared by solution mixing in *N,N*-dimethylacetamide, followed by film casting [123]. Solution mixing allowed the homogeneous dispersion of hydrophilic ZnO NPs in a hydrophobic PS matrix. This is because the co-solvent can break the NP agglomerates apart and prevent re-agglomeration during solution mixing and film casting. The nanocomposite film showed UV-absorbance without losing transparency. In addition, the nanocomposites exhibited enhanced thermal and mechanical properties. Li et al. [124] prepared PU-based coatings reinforced by ZnO NPs via solution blending. Significant improvement in the Young's modulus and tensile strength of the PU films was achieved by incorporating up to 2.0 wt%, ZnO NPs and that the abrasion resistance of the PU coats was enhanced considerably due to the addition of ZnO NPs. Seo et al. prepared a series of polypropylene carbonate/ZnO nanocomposite films with different ZnO contents [125], and evaluated the morphological structures, thermal properties, oxygen permeability, water sorption, and antibacterial properties of the films as a function of the ZnO concentration. Hejazi et al. [126] prepared superhydrophobic PP surfaces by the incorporation of ZnO NPs using the phase separation method via simple solution casting. A high content of ZnO NPs could be detrimental for superhydrophobicity because of their migration into the coating surface and the presence of hydrophilic –OH groups residing on ZnO surfaces.

Recently, considerable attention has been focused on the blends of biocompatible and biodegradable polymers in view of their potential environmental and biomedical applications. Song et al. [127] fabricated polylactide (PLA) nanofibers and the formation of nanocomposites with TiO₂ via solution blending. The results

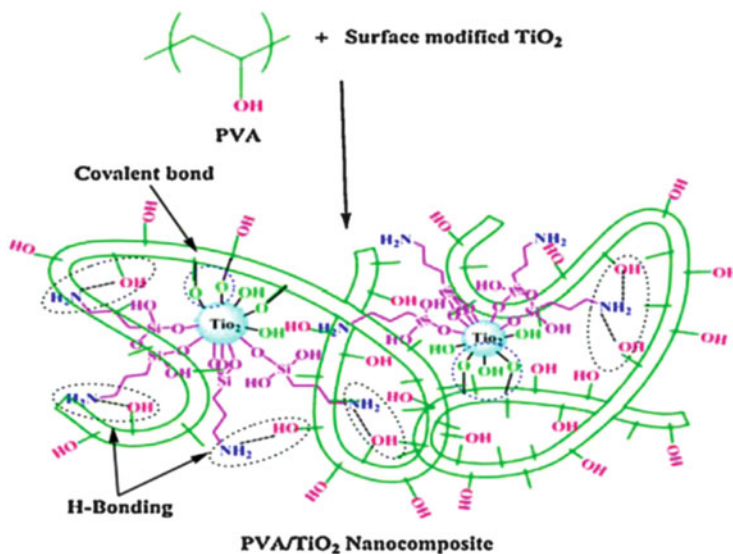


Fig. 2 Preparation of PVA/TiO₂ nanocomposites. Reprinted with permission from [131]. Copyright 2011 Elsevier

showed that the drug molecules and/or DNA self-assembled readily on the surface of the blends of nano-TiO₂-PLA nanofibers so that the new nanocomposites efficiently facilitated the relative biorecognition of daunorubicin [128]. Nakayama and Hayashi [129] prepared PLA/TiO₂ nanocomposite films by incorporating surface-modified TiO₂ NPs into polymer matrices. The nanocomposite films were photodegraded more efficiently by UV irradiation than the pure PLA films. Buzarovska [130] also prepared surface-modified TiO₂ and PLA composites by solution blending to achieve photodegradability, thermal stability, and puncture characteristics. Recently, poly(vinyl alcohol) (PVA)/TiO₂ nanocomposite coatings were synthesized with different loadings of modified TiO₂ using an ultrasonic irradiation process. These nanocomposite coatings were used to synthesize PVA/TiO₂ films via a solution-casting method, as shown in Fig. 2 [131].

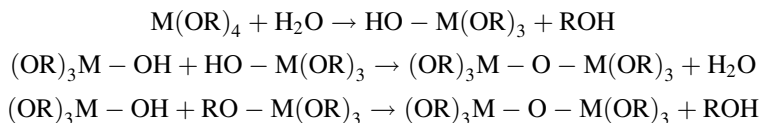
Magnetic NPs are excellent candidates as building blocks in nanocomposite materials with engineered physicochemical properties. In particular, nanocomposites of polymers and magnetic NPs can pave the way to novel sensing, actuation, molecular separation, electromagnetic wave absorption, and biomedical applications. Yang et al. [132] examined the particle size effect on the magneto-dielectric properties of surface-modified Fe₃O₄ and styrene-*b*-ethylene/butylene-*b*-styrene block copolymer composites at radio frequencies. The dielectric permittivity of the polymer was increased by the addition of surfactant-modified Fe₃O₄ NPs, but the particle size had little effect. On the other hand, higher magnetic permeability was obtained using larger Fe₃O₄ NPs. Kaushik et al. [133] dispersed Fe₃O₄ nanoparticles in a chitosan solution to fabricate nanocomposite films on indium–tin

oxide glass plate for glucose detection. This nanocomposite bioelectrode showed a response time of 5 s, linearity of 10–400 mg dL⁻¹ glucose, sensitivity of 9.3 μ A/(mg dL cm²), and a shelf life of approximately 8 weeks under refrigerated conditions. Pisanello et al. [134] prepared polydimethylsiloxane/iron-oxide NPs to obtain a flexible, biocompatible elastomeric nanocomposite with tunable dielectric and magnetic properties in the radio frequency range. The experimental results showed that colloidal iron oxide used as simple electromagnetic filler in the radio frequency range increased the dielectric permittivity without perturbing the magnetic permeability of the polymers for particle sizes ranging from 15 to 29 nm.

Solution blending can overcome some of the limitations of melt mixing if both the polymer and nanoparticles are dissolved or dispersed in a solution. On the other hand, for industrial applications, melt processing is the preferred choice because of its low cost and simplicity for large scale production for commercial applications.

3.2 Sol-gel Process

Several approaches have been developed to improve the compatibility between the organic and inorganic components. Among the numerous methods under development, the sol-gel route has been applied broadly because of its capability to control the miscibility between organic and inorganic components at the molecular level. The term sol-gel is associated with two reaction steps: sol and gel. A sol is a colloidal suspension of solid particles in a liquid phase and a gel is the interconnected network formed between the phases. The sol-gel process consists of two main reactions: hydrolysis and condensation, which are multistep processes that occur sequentially. Hydrolysis involves cleavage of the organic chain bonding to metal and the subsequent replacement with -OH groups through nucleophilic addition. The protonated species leave the hydrolyzed metal as an alcohol. Condensation is based on oxygen, metal, and oxygen bond formation (-O-M-O-). By definition, the condensation reaction releases small molecules, such as water or alcohol [135].



The metal reactivity, amount of water, solvent, temperature, and the use of complexing agents or catalysts are the main reaction parameters. Whether to use a catalyst or not depends on the chemical nature of the metal atom and steric hindrance of the alkoxide group. The electrophilic character of the metal atom and its ability to increase the coordination number appears to be the main parameter. This route requires a lower temperature and less energy than physical mixing [135].

Organic–inorganic nanocomposites are normally prepared by the sol–gel process in the solvent containing precursors and organic polymers. The most direct way is to hydrolyze and condense the precursors in the presence of a polymer in a solvent system. Materials prepared by sol–gel processing have uniformity, high purity, and low sintering temperatures compared to those prepared by conventional solid state reactions [136]. Sol–gel materials are classified by the mode of formation and types of bonds between the organic, organometallic, and inorganic components. One method involves the polymerization of organic functional groups from a preformed sol–gel network; vinyl or epoxy groups and free radical or cationic polymerization processes are common [137, 138]. On the other hand, this classification has not received sufficient recognition. Alternatively, sol–gel hydrolysis and condensation of a precursor such as tetraethoxysilane or tetrabutyl titanate can be carried out starting from preformed functional organic polymers. Figure 3 shows the typical preparation route for TiO_2 /polymer nanocomposites with covalent linkages by the in-situ sol–gel process [139]. Wu [140] reported the synthesis of novel PCL/ TiO_2 and PCL-*g*-acrylic acid/ TiO_2 nanocomposites using tetraisopropyl orthotitanate and PCL as the ceramic precursor and continuous phase, respectively, using an in situ sol–gel process. Du et al. [141] carried out the sol–gel synthesis of a ZnO/polyvinylpyrrolidone (PVP) nanocomposite thin film for superoxide radical sensor applications. Gao et al. [142] prepared novel hybrid films of fluorinated hyperbranched polyimide (HBPI) and ZnO via an in-situ sol–gel polymerization technique, where mono-ethanolamine was used as the coupling agent between the termini of HBPI and the precursor of ZnO. The nanocomposite exhibited good optical transparency. Hu and Marand [143] reported the in-situ synthesis of nanosized TiO_2 domains within poly(amide–imide) via a sol–gel process. The composite films exhibited excellent optical transparency. Wang et al. [144] synthesized polystyrene maleic anhydride (PSMA)/ TiO_2 nanocomposites via the hydrolysis and condensation reactions of multicomponent sol because PSMA has functional groups that can anchor TiO_2 and prevent aggregation. Liu and Lee [145] reported the synthesis of polyethylene oxide (PEO)/ TiO_2 nanocomposite electrolytes using a sol–gel approach. Other researchers also used this method to produce TiO_2 poly(*p*-phenylenevinylene) [146], polyimide (PI) [147, 148], PMMA [149, 150], polyarylene ether ketone/sulfone [151], polythiourethane [152], and copolymer of PS and MPTMS [153] nanocomposites.

Yoshida et al. [154] combined sol–gel and solution mixing approaches to prepare transparent PI/ TiO_2 nanocomposites. In the first step, the TiO_2 NPs were produced through reverse micelles using the sol–gel method. The reverse micellar solution was prepared by dissolving sodium bis(2-ethyl hexyl) sulfosuccinate in isooctane. The resulting solution was then filtered, and the required amount of distilled water was added. Titanium isopropoxide diluted with isopropanol was then injected into the reverse micellar solution with mild stirring. After the hydrolysis reaction, the TiO_2 NPs were then extracted. In the second step, a fluorinated PI solution was added to this *N*-methyl pyrrolidone solution containing TiO_2 under stirring. The mixture was coated on a glass substrate, and a PI/ TiO_2 nanocomposite was produced after heat treatment.

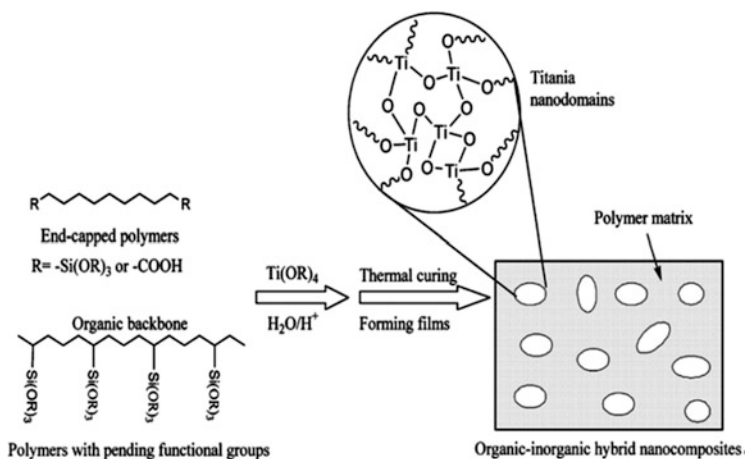


Fig. 3 Preparation of TiO₂-polymer nanocomposites via the in-situ sol-gel route. Reprinted with permission from [139]. Copyright 2009 Royal Society of Chemistry

The largest problem associated with the sol-gel process is that the gel process leads to a considerable decrease in internal stress, which could result in the contraction of brittle materials due to the evaporation of solvents, small molecules, and water. Moreover, this method requires the polymers in the sol-gel system to be dissolved in the condensate. In addition, the precursors are expensive and sometimes toxic, preventing further improvement and application.

3.3 In-Situ Synthesis

Ex-situ processes generally suffer from the high agglomeration tendency of NPs because the NP agglomerates are difficult to destroy, even using high external shear forces. In-situ polymerization methods have been developed to overcome this problem. In-situ polymerization involves the dispersion of inorganic fillers directly in a monomer or monomer solution and the subsequent polymerization of the monomer dispersion using standard polymerization techniques.

3.3.1 Solution Polymerization

A promising method for the in-situ growth of metal oxide NPs in the presence of a polymer is the thermal decomposition of precursors forming metal oxide NPs within the polymeric matrix. In the early 1990s, Ziolo et al. [155] used a one-step chemical method to synthesize finely dispersed γ -Fe₂O₃ NPs in a crosslinked PS

resin. They used a synthetic ion-exchange resin and aqueous solutions of Fe(II) or Fe(III)-chlorideto exchange the ions. Cao et al. [156] synthesized Fe₃O₄/PMMA composite particles using a one-pot hydrothermal method. Zhang et al. [157] reported a new and simple approach for the in-situ preparation of transparent ZnO/PMMA nanocomposite films. Poly(methyl methacrylate-*co*-zinc methacrylate acetate), poly(MMA-*co*-ZnMAAc), copolymer was synthesized by free-radical polymerization between MMA and ZnMAAc, where asymmetric ZnMAAc with only one terminal double bond (C=C) was used as the precursor for ZnO NPs and to avoid crosslinking. Subsequently, transparent ZnO/PMMA nanocomposite films were obtained by in-situ thermal decomposition.

Polymer/metal oxide nanocomposites were also prepared using other in-situ methods. Park et al. [158] synthesized iron oxide/epoxy vinyl ester nanocomposites using an in-situ polymerization method. Evora and Shukla [159] produced polyester/TiO₂ nanocomposites by in-situ polymerization. Althues et al. [160] prepared ZnO NP-embedded poly(butanediolmonoacrylate) via in-situ photopolymerization. PMMA/ZnO composites were obtained by the thermally induced polymerization of a mixture of MMA/initiator with dispersed ZnO NPs [161]. Luminescent PMMA/ZnO composites were synthesized using a two-stage method by the hydrolysis of zinc acetate in the presence of monoethanolamine in an alcohol medium, followed by the addition of MMA and an initiator and polymerization of the system at 70°C [162]. Wang et al. [163] reported a new method for preparation of PMMA/TiO₂ composites by electron irradiation-induced polymerization. On the other hand, dispersion and adhesion at the polymer–metal oxide interfaces are the most important factors affecting the properties of composites. Metal oxide NPs can be dispersed homogeneously in the polymer matrices when they are surface-modified.

Amphiphilic molecules (such as oleic acid, oleic amine, or long chain alcohols) can adsorb on the particle surface via ionic attractions, hydrogen bonding, or coordinative bonding. The surfactant molecules arrange on the mineral surfaces and construct a hydrophobic interface protecting the NPs from agglomeration. The surfactant molecules do not participate directly in polymerization but monomers can dissolve into the hydrophobic surfactant layer, and the inorganic fillers are embedded in the growing polymer during the polymerization process [164]. Liu and Su [165] prepared PMMA/ZnO nanocomposites by radical polymerization of the MMA in the presence of oleic acid (OA)-modified ZnO NPs. Dzunuzovic et al. [166] synthesized PMMA/TiO₂ nanocomposites via the in situ radical polymerization of MMA in a toluene solution of 6-palmitate ascorbic acid-modified TiO₂ NPs. Demir et al. [167, 168] prepared composites of PMMA with metal oxides, such as ZnO and TiO₂, by in-situ bulk polymerization. The NPs were surface-modified by alkylphosphonic acids to render them dispersible in the monomer. OA-capped γ -Fe₂O₃ NPs were synthesized and used to fabricate PMMA/ γ -Fe₂O₃ composites by in-situ polymerization. The presence of OA on the metal oxide surface increased the compatibility of the metal oxide NPs with the polymeric matrix and yielded bulk homogeneous and highly transparent PMMA/ γ -Fe₂O₃ composites [169]. Magnetic vinyl ester resin nanocomposites

containing Fe₂O₃ NPs functionalized with a bifunctional coupling agent, MPTMS, were also reported. Particle functionalization favored nanocomposite fabrication with a lower curing temperature than the as-received NP-filled vinyl ester resin nanocomposites [170]. Inkyo et al. [171] dispersed TiO₂ NPs in MMA, which had been surface-modified using (3-acryloxypropyl) trimethoxysilane, and TiO₂-PMMA nanocomposites were synthesized by subsequent polymerization.

3.3.2 Emulsion Polymerization

Recently, the in-situ synthesis of nanocomposites, particularly core-shell type particles, has attracted considerable attention because of their potential applications [172]. In particular, emulsion polymerization is a traditional method for producing monodispersed metal oxide/polymer core-shell composites. Ai et al. [173] reported the preparation of polyacrylate core/TiO₂ shell nanocomposite particles through in-situ emulsion polymerization. In this method, no surface-modification of the TiO₂ NPs or the addition of functional comonomer was necessary. Cetyltrimethylammonium bromide (CTAB) was used as a stabilizer to provide the latex particles with a positive charge to ensure the formation of TiO₂ coatings without free TiO₂ NPs. Inexpensive titanium tetrachloride was used as a precursor for TiO₂ NPs. Daniel et al. [174] prepared magnetic polymer particles by first mixing organic-based magnetic NPs with hydrophobic vinyl monomer and emulsifier. The polymerization resulted in a magnetic NP core and polymer shell. Charmot and Vidil [175] used a similar technique to prepare core-shell composites with the addition of a vinyl crosslinker. Dresco et al. [176] reported the one-step synthesis of magnetic composites using an inverse emulsion technique. Inverse microemulsion droplets were first prepared by mixing water-soluble monomer (methacrylic acid, hydroxyethyl methacrylate), crosslinker, surfactant, and aqueous based magnetic NPs in toluene. Copolymerization of these emulsion droplets provided stable composites. Wormuth [177] also used this approach to encapsulate magnetic NPs in the diblock copolymer poly(ethylene oxide-*co*-methacrylic acid) matrix. Recently, Mazrouaal et al. [178] prepared PS-*co*-PVP/CuO and PS-*co*-PVP/ZnO nanocomposites by Pickering emulsion polymerization. Petchthanasombat et al. [179] synthesized hybrid materials comprising ZnO NPs encapsulated in core-shell polymer particles with a PMMA core and chitosan shell by emulsifier-free emulsion polymerization.

Miniemulsion polymerization, a type of heterogeneous polymerization, is being used increasingly for the synthesis of various novel organic-inorganic hybrid materials. Miniemulsion is a thermodynamically stable homogeneous liquid, in which stable oil drops with sizes ranging from 50 to 500 nm are dispersed in an aqueous continuous phase. The oil drops are confined by surfactant micelles and a highly water-insoluble compound (i.e., hydrophobe). El-Asser et al. [180–182] modified TiO₂ NPs first with polybutylene succinimide diethyl triamine and dispersed 5 wt% of the hydrophobized particles in styrene prior to the miniemulsion process; approximately 89 wt% of TiO₂ could be encapsulated in PS. In addition to

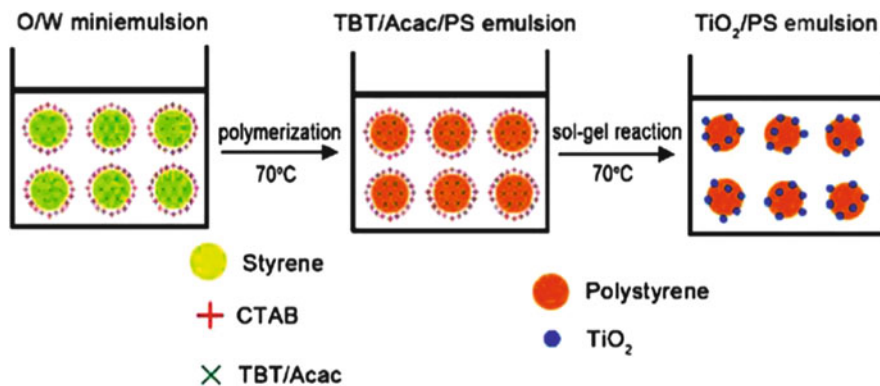


Fig. 4 Formation of PS/TiO₂ nanocomposites in a single step (see text for details). Reprinted with permission from [184]. Copyright 2010 Elsevier

the encapsulation of TiO₂ inside polymer particles, TiO₂ NPs can also be coated onto the surfaces of polymer particles by miniemulsion polymerization. The incorporation of acrylic acid as a comonomer can increase the interactions between TiO₂ and polymer cores, and the addition of a hydrophobic agent effectively prevents the monomer diffusing into the aqueous phase [183]. Wu et al. [184] synthesized PS/TiO₂ nanocomposite spheres successfully using a miniemulsion technique with both an organic monomer and inorganic precursor trapped in the miniemulsion droplets. Figure 4 shows a schematic diagram of the formation of nanocomposites. First, the oil/water (O/W) miniemulsion with oil composed of acetylacetonate chelated tetra-*n*-butyl titanate (TBT) and styrene was prepared. The oil droplets were stabilized by cationic surfactant CTAB and co-stabilizer hexadecane. Hence, the oil droplets were positively charged because CTAB was adsorbed on the surfaces. The polymerization of styrene and the sol-gel reaction of TBT occurred inside the miniemulsion droplets, causing formation of PS/TiO₂ nanocomposite spheres. The hydrophilic TBT diffused to the O/W interface during the polymerization of styrene, and TiO₂ NPs formed by the hydrolysis and condensation of TBT were adsorbed successfully onto the surfaces of the polymer through electrostatic interactions. Ramírez and Landfester [185] prepared a core-shell Fe₃O₄/PS composite by miniemulsion polymerization using hexadecane and sodium dodecyl sulfate (SDS) as hydrophobe and emulsifier, respectively. The composite particles had a narrow size distribution. Luo et al. [186] also prepared PS/Fe₃O₄ composite particles via miniemulsion polymerization in the presence of potassium persulfate as an initiator, SDS as a surfactant, and hexadecane or sorbitanmonolaurate as a costabilizer. Tang and Dong [187] fabricated PS/ZnO nanocomposite latex by miniemulsion polymerization in the presence of the coupling agent 3-aminopropyltriethoxysilane and hexadecane as hydrophobe.

Another novel and interesting technology, ultrasonic-induced miniemulsion polymerization, can predigest the conventional three-step process, and a rapid rate and relatively high percentage of monomer to polymer conversions can be

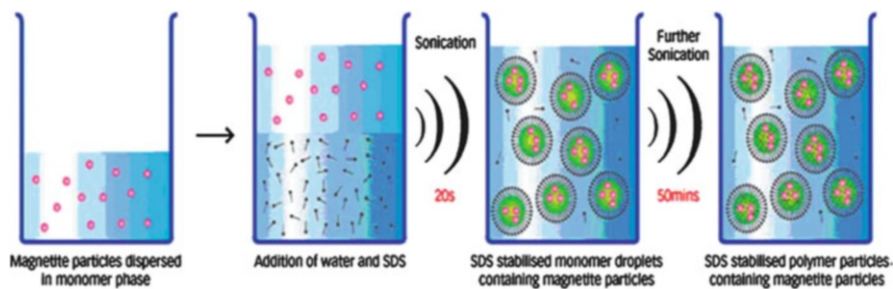


Fig. 5 Process for preparation of magnetite nanocomposite spheres by sonochemically driven miniemulsion polymerization. Reprinted with permission from [188]. Copyright 2009 American Chemical Society

achieved. For example, Teo et al. [188] developed a one-pot method for preparing poly(butylmethacrylate) latex beads with a large Fe_3O_4 NP loading using the process shown schematically in Fig. 5. The hydrophobic Fe_3O_4 NPs were dispersed in *n*-butyl methacrylate by stirring in a reaction vessel. A water-continuous miniemulsion was prepared by adding water with SDS as the dispersant to the NP/monomer dispersion. After deaerating the mixture by bubbling with argon, the liquid mixture was then sonicated to generate a uniform miniemulsion. The polymerization reaction was commenced by subjecting the emulsion mixture to continuous sonication without an initiator.

Inverse miniemulsion polymerization can also be used to synthesize organic–inorganic hybrid composites. Xu et al. [189] synthesized magnetic core–shell composites via the inverse miniemulsion polymerization of acrylamide and a crosslinker in the presence of poly(methacrylic acid) (PMA)-coated magnetic NPs. The hydrophilic magnetic nanocomposite spheres can also be synthesized by inverse miniemulsion polymerization with a water-based magnetic ferrofluid as the dispersed phase, and an organic solvent and monomers as the continuous phase [177, 190, 191]. For example, to synthesize thermoresponsive and superparamagnetic hydrogel microspheres based on poly(*N*-isopropylacrylamide) (PNIPAAm), poly(acrylic acid) oligomers were used as stabilizers to produce a stable water-based Fe_3O_4 ferro-fluid, which could mix well with the water-soluble monomers. The poly(NIPAAm-*co*-MA)/ Fe_3O_4 composite latex particles were then synthesized with ammonium persulfate/sodium metabisulfite as the redox initiator via W/O miniemulsion polymerization [191]. Moreover, W/O miniemulsion polymerization could be used to synthesize hollow superparamagnetic nanocomposite spheres at room temperature and under ambient pressure without hard templates. According to the process shown schematically in Fig. 6, magnetic NPs tended to assemble at the water–oil interface because of their amphipathicity. When the inverse miniemulsion was irradiated with γ -rays, many active intermediates were generated due to the radiolysis of water. As these radicals attempted to enter the oil phase, they first met the active hydroxyl groups at the surfaces of the magnetic NPs

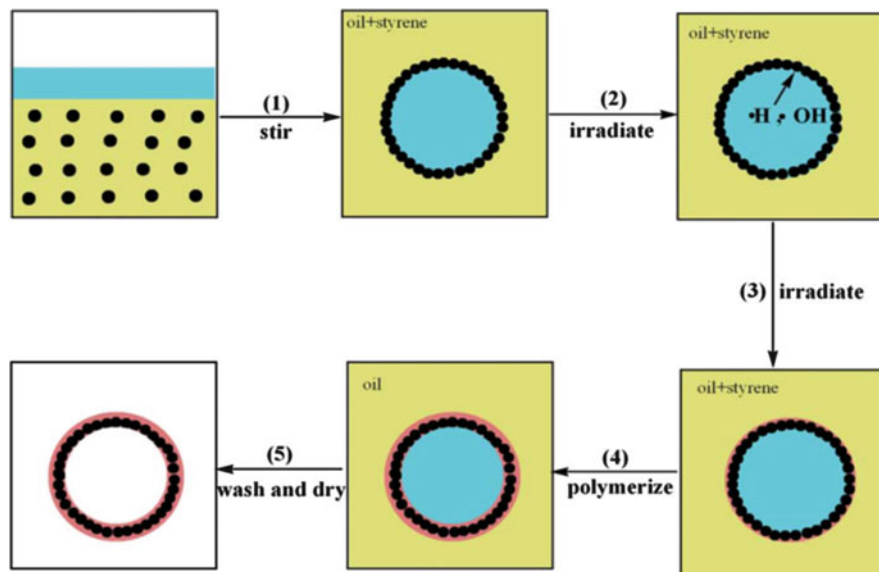


Fig. 6 Preparation of hollow superparamagnetic nanocomposite microspheres. Reprinted with permission from [192]. Copyright 2008 Wiley-VCH

located at the water–oil interface and abstracted hydrogen from them, leading to the formation of free radicals at the surfaces of magnetic NPs. Therefore, polymerization was carried out on the surfaces of the NPs to form the hollow magnetic nanocomposite microspheres [192]. On the other hand, the composite particles produced by emulsion, inverse emulsion, or miniemulsion methods had a very broad size distribution. In addition, it was difficult to remove the residual surfactants adsorbed on the resulting particle surface.

3.3.3 Graft Polymerization

Graft polymerization is another method for avoiding phase separation, whereby NPs are dispersed in the monomer or monomer solution and the resulting mixture is polymerized using standard polymerization methods. This process provides flexibility in engineering the powder surface in the composites. In addition, by tailoring the specific properties in composites through relatively strong interactions, the layer of polymer bonded to the NPs can control the aggregation of NPs.

An improved approach would be to modify the surface of inorganic fillers by the covalent attachment of stabilizing polymer ligands using either the “grafting from” or “grafting to” methods. The “grafting from” technique involves growing the polymer chains from the inorganic backbone, whereas the “grafting to” technique involves the attachment of preformed polymer chains to the backbone, minimizing agglomeration while strengthening the interactions between the inorganic filler and

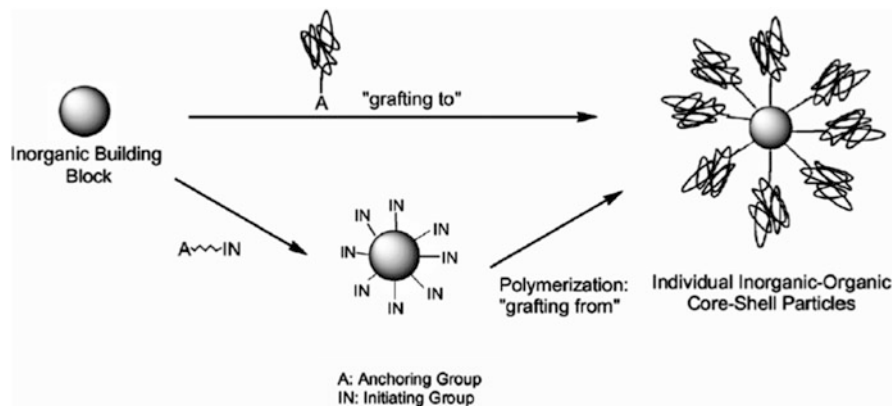


Fig. 7 Two approaches for graft polymerization. Reprinted with permission from [136]. Copyright 2003 Elsevier

polymer matrix, as illustrated schematically in Fig. 7. Using the “grafting from” approach, the surface density can be controlled by varying the amount of initiator immobilized on the surface of the inorganic fillers. For these reasons, the “grafting from” approach has become the most promising route for the synthesis of polymer-grafted inorganic filler nanostructures in a controlled manner. Flesch et al. [193] reported the coating of γ - Fe_2O_3 NPs with PCL using a covalent “grafting to” technique. ω -Hydroxy-PCL was first synthesized by the ring-opening polymerization of ϵ -caprolactone, with aluminum isopropoxide and benzyl alcohol as the catalytic system. The hydroxy end groups of PCL were then derivatized with 3-isocyanatopropyltriethoxysilane in the presence of tetraoctyltin. The triethoxysilane-functionalized PCL macromolecules were finally allowed to react on the surface of the γ - Fe_2O_3 NPs. Takafuji et al. [194] grafted poly(1-vinyl imidazole) with a trimethoxysilyl group onto the surface of γ - Fe_2O_3 through a siloxane bond. Figure 8 shows a schematic representation of this “grafting to” approach. Tang et al. [195] modified the surface of ZnO NPs by grafting or anchoring PMA chains on the particles surfaces to create a better dispersion in an aqueous system. The $-\text{OH}$ groups on the ZnO surface interact with carboxyl groups (COO^-) in PMMA to form a poly(zinc methacrylate) complex on the surface. Wang et al. [196] reported the synthesis of PMMA-grafted TiO_2 NPs by a photocatalytic polymerization process. The PMMA chains were grafted directly to the surfaces of the TiO_2 NPs in water under sunlight illumination.

A higher percentage of successful grafts can be obtained in polymer-grafted inorganic fillers by initiating graft polymerization from the initiating groups placed on the particle surface. The polymerization process, which might include radical, anionic, and cationic polymerization methods, involves the propagation of the grafted polymers from the surface of the particle. Sidorenko et al. [197] examined the radical polymerization of styrene and MMA on the surface of the TiO_2 NPs by the adsorbed hydroperoxide macroinitiators. Shirai et al. [198] carried out the

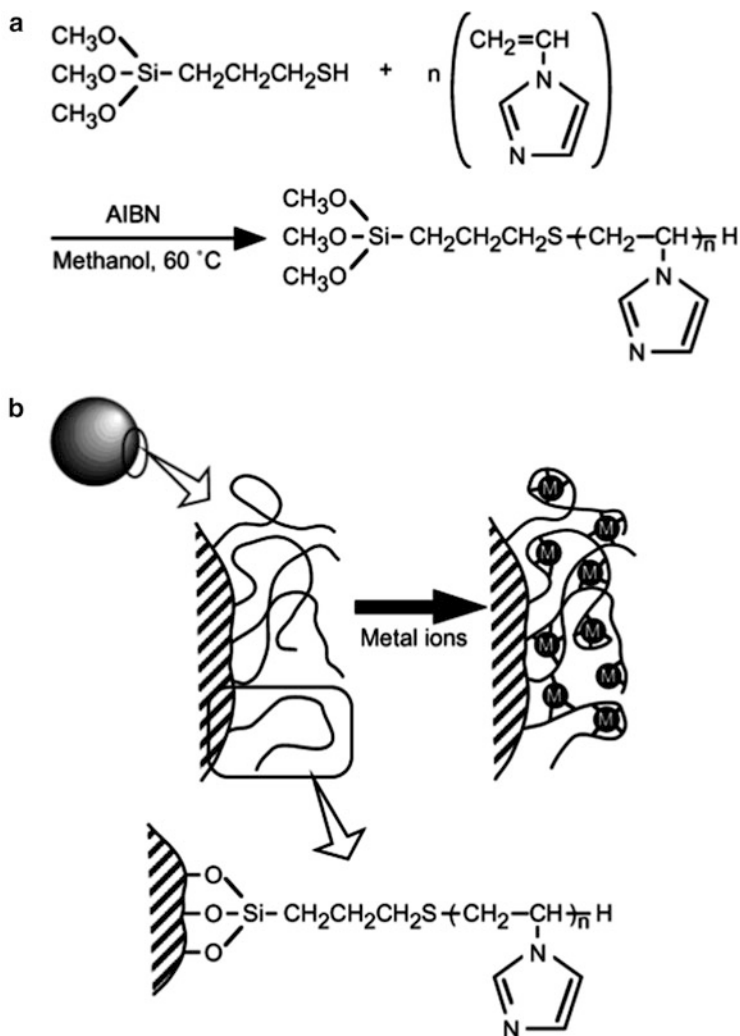


Fig. 8 Synthesis of poly(1-vinylimidazole) (a) and polymer-grafted magnetic particles (b). Reprinted with permission from [194]. Copyright 2004 American Chemical Society

radical graft polymerization of vinyl monomers on the surface of polymethylsiloxane-coated TiO_2 NPs that had been modified further with alcoholic $-\text{OH}$ groups initiated by azo groups. Tang et al. [199] prepared nano-ZnO/poly(MMA-MA) composite particles by radical copolymerization. The carboxyl groups of MA can react with $-\text{OH}$ groups on the surface ZnO to form a poly(zinc methacrylate) complex. The copolymer chain were grafted and encapsulated on the ZnO surface. Fan et al. [200] reported the surface-initiated graft polymerization of MMA from TiO_2 NPs through a biomimetic initiator. Hong et al. [201] modified

the surface of ZnO NPs using the silane coupling agent, MPTMS, which introduced functional double bonds onto the surface of ZnO NPs, followed by the radical grafting of PMMA in a nonaqueous medium. Similarly, Guo et al. [202] used a coupling agent (MPTMS) to functionalize CuO NPs, which were then polymerized with vinyl-ester resin to fabricate nanocomposites. Bach et al. [203] grafted PMMA onto Fe₃O₄ NPs using a “grafting from” approach based on thiol-lactam-initiated radical polymerization.

3.3.4 Atom Transfer Radical Polymerization

Polymerization needs to be controlled precisely to achieve the most appropriate polymer grafting density, polydispersity, composition, and microstructure. Over the last few decades, this field has developed rapidly and many controlled polymerization strategies have been used. Surface-initiated atom transfer radical polymerization (ATRP) is one of the most robust and versatile approaches for synthesizing polymer films. ATRP is a transition metal-catalyzed, controlled (“living”) radical polymerization mechanism, offering the advantages of good control of the molecular weight and polydispersity. Liu and Wang [204] reported the grafting of poly(hydroxyethyl acrylate) from the surface of ZnO NPs using a copper-mediated surface-initiated ATRP (SI-ATRP) technique using bromo-acetamide-modified ZnO NPs as macroinitiators with the 1,10-phenanthroline and Cu(I)Br catalysts in water. Wang et al. [205] prepared core-shell PS grafted γ -Fe₂O₃ NPs using a combination of ligand exchange and SI-ATRP. Using a similar strategy, Duan et al. [206] conducted the SI-ATRP of 2-dimethylamino ethyl methacrylate from γ -Fe₂O₃ NPs. Fukuda et al. [207, 208] used silane coupling agents to covalently anchor ATRP initiating sites onto iron oxide NPs to prepare PMMA-coated core-shell colloids. Abbasian et al. [209] also used a silane coupling agent to modify ZnO NPs, which were then reacted with α -chloro phenyl acetyl chloride to prepare the ATRP macroinitiator. The metal-catalyzed radical polymerization of MMA with ZnO macroinitiator was performed using a copper catalyst system to provide the ZnO/PMMA nanocomposite. Fan et al. [200] synthesized core-shell nanocomposites by grafting PMMA from TiO₂ NPs via SI-ATRP. A bifunctional polymerization initiator, L-3,4-dihydroxyphenylalanine, was used to modify the TiO₂ NPs. Gelbrich et al. [210] prepared thermoresponsive magnetic core-shell NPs by SI-ATRP of 2-methoxyethyl methacrylate from a colloidal Fe₃O₄ initiator. Using SI-ATRP, iron oxide NPs were also coated with a copolymer shell of oligo(ethylene glycol) methylether methacrylate and showed adjustable thermoresponsive behavior in water [211]. Sato et al. [212] prepared PMMA/ZnO or carbazole polymer/ZnO nanocomposites by ATRP initiated by 2-bromo-2-methylpropionyl groups introduced onto the ZnO surface. The introduction of the initiator group onto the ZnO surface was achieved by the esterification of -OH groups of the ZnO (Fig. 9). Recently, Nam et al. [213] prepared novel poly(hydroxyethyl methacrylate)/TiO₂ nanocomposites with a nanophase separated hierarchical structure by ATRP.

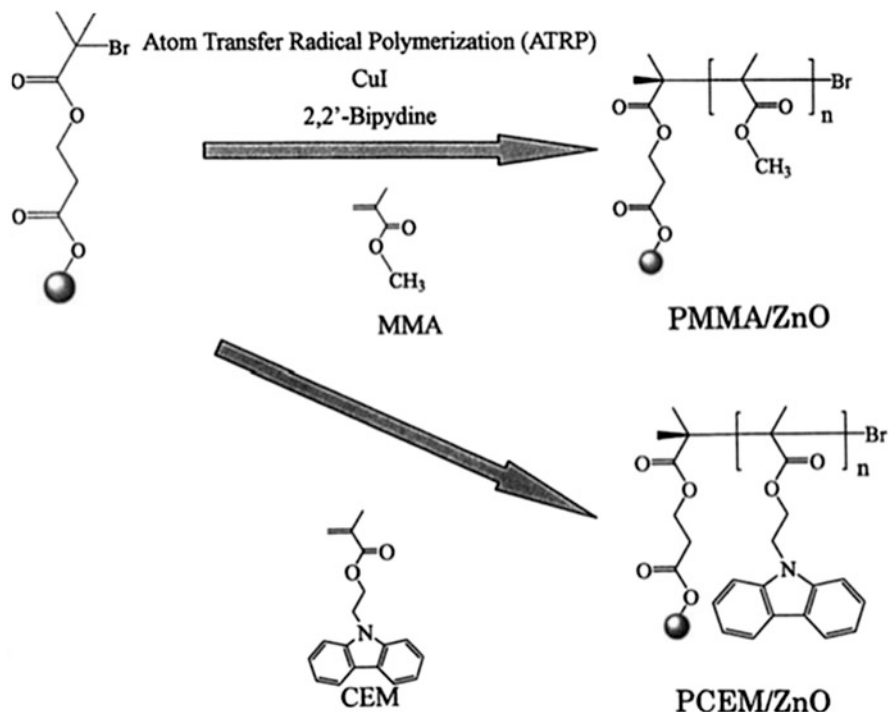


Fig. 9 Synthesis of the prepared poly(methyl methacrylate) (PMMA)/ZnO or poly[2-(carbazol-9-yl)ethyl methacrylate] (PCEM)/ZnO nanocomposites by ATRP. Reprinted with permission from [212]. Copyright 2008 Elsevier

4 Properties of Nanocomposites

4.1 Optical Properties

The optical properties of composite films consisting of metal oxide NPs embedded in a polymer matrix have long been of interest. Polymer/metal oxide nanocomposites show great promise as they could provide the necessary stability and easy processability together with interesting optical properties. The useful optical properties of composites, such as light absorption (UV and visible), photoluminescence, and refractive index, have made composites an important class of functional materials for centuries. The optical properties of these composites depend upon the size and spatial distribution of metal oxide NPs in the polymer matrix [214].

UV-absorbing pigments are widely used as additives to increase the long-term stability of polymers or to prepare UV-protective coatings. Even though a huge range of organic UV-absorbers are available, they suffer from long-term instability. Alternately, inorganic materials are of great interest due to their high photostability.

For most applications, a high transparency in the visible range and a steep absorption in the near UV range are required. The most promising materials are TiO_2 and ZnO , with bulk bandgap energies of about 3 eV. Li et al. [215] prepared transparent ZnO /epoxy nanocomposites via in-situ polymerization. The optical properties of ZnO /epoxy nanocomposites, such as visible light transparency and UV light shielding efficiency, were studied. The optical properties depended on the particle size and amount of ZnO . The nanocomposites containing a very low amount (0.07 wt%) of ZnO NPs, with an average particle size of 26.7 nm after calcination at 350°C , possessed the most optimal optical properties, namely high visible-light transparency and high UV-light shielding efficiency, which are desirable for many important applications. Althues et al. [160] prepared a ZnO /poly(butanediol monoacrylate) nanocomposite via photopolymerization that showed high transparency in the visible range and a steep UV-absorption band at a wavelength below 360 nm. Even low concentrations (0.1%) of ZnO NPs caused a significant UV-shielding effect. However, for the protection of substrates using UV-absorbing coatings, higher concentrations are needed. To increase the UV resistance of the polymer matrix itself, 1–5 wt% of ZnO or TiO_2 NPs were typically used. Studies on the stability of such nanocomposites against UV irradiation revealed an enormous effect of the additives. A significant reduction in the carbonyl index, a measure of the photo-oxidation of polymers, was found for ZnO /PP and ZnO /PE nanocomposites compared with pure polymers in two different studies [113, 216]. Degradation tests with TiO_2 /polymer nanocomposites showed the opposite effect [217]. In PE, the NPs showed photocatalytic activity, leading to a faster and stronger increase in yellow color and carbonyl index compared with pure PE. The surface activity of TiO_2 also depends on its crystal structure, as a lower activity was observed for the rutile modification than for anatase [218]. Lu and coworkers [219] prepared ZnO /polymer composite films by dispersing different concentration of ZnO into monomer mixtures of urethane methacrylate oligomer and 2-hydroxyethyl methacrylate followed by UV-initiated polymerization. The ZnO NPs with a diameter of 3–5 nm were uniformly dispersed in the polymer matrix and no aggregation was observed, which contributed to the high transparency of the nanocomposites. They found that these composite films have the potential to be used as a UV absorber and luminescent material in the design of optical coatings.

The optical properties of monodisperse colloidal ZnO QDs having various degrees of dispersion in epoxy have been systematically studied by Sun et al. [220]. Exfoliated R-zirconium phosphate (ZrP) nanoplatelets, instead of organic capping agents, were utilized to control the state of dispersion of ZnO QDs. The epoxy hybrid nanocomposites containing well-dispersed ZnO QDs and exfoliated ZrP nanoplatelets showed transparency similar to that of the neat epoxy and exhibit high UV-absorption efficiency. The nanocomposites also give off sharp UV emission upon excitation. The optical absorption and photoluminescence of well-dispersed ZnO QDs in the epoxy exhibited a red-shift as the QD concentration was increased, as a result of the QD coupling effect. Guo et al. [221] studied the optical properties of ZnO NPs capped by PVP. The absorption and

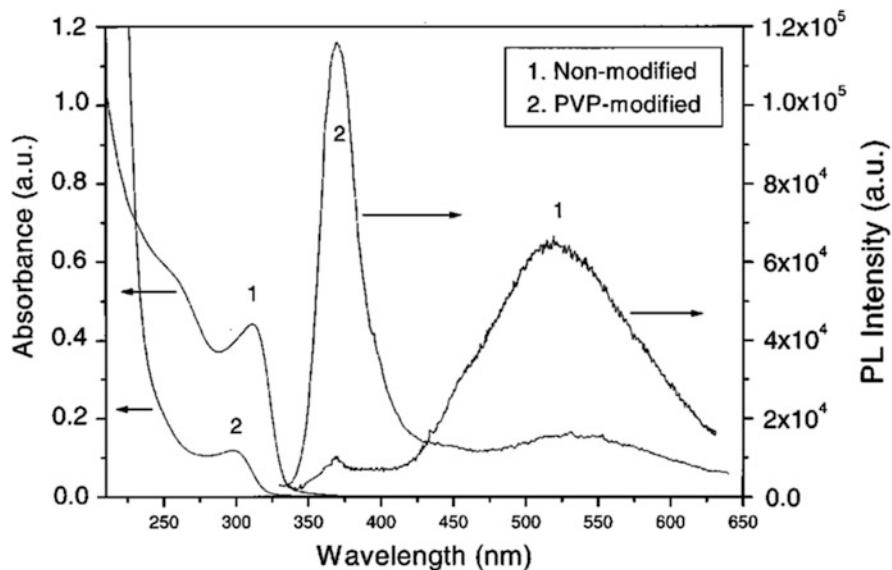


Fig. 10 Optical absorption and photoluminescence (PL) spectra of the uncapped and PVP-capped ZnO nanoparticles. Reprinted with permission from [221]. Copyright 2000 American Physical Society

photoluminescence spectra of unmodified and modified ZnO are shown in Fig. 10. ZnO exhibited exciton absorption peaks at 300 nm for both capped and uncapped NPs and the peaks were substantially blue-shifted relative to those of the bulk ZnO (373 nm) due to the strong restriction effect. For example, the excitonic absorption peak (~303 nm) of the PVP-capped ZnO NPs was slightly blue-shifted compared with the uncapped NPs (~312 nm). This might be attributed to the smaller size of the PVP-capped ZnO NPs. Another difference between the two absorption spectra was the appearance of a bump at 260 nm for the uncapped ZnO NPs, which was absent in the case of PVP-capped ZnO NPs. Later research showed that PVP could control the ZnO crystallization and morphology [222] and could improved the ZnO UV emission significantly because of physical adsorption [223]. On the one hand, PVP-capped ZnO was appropriate for growing into one-dimensional nanomaterials because PVP preferred to physically adsorb on a specific crystallographic plane of ZnO, which passivated this plane and facilitated the crystal growth along the *c*-axis. On the other hand, the PVP passivation effect reduced the surface defects of ZnO so as to increase the UV emission. It should be mentioned that PVP itself has a strong blue-emission. When PVP was mixed with ZnO NPs, the emission spectra overlapped with each other and depended on the excitation wavelength [224]. If the PVP content was high enough in the PVP/ZnO nanocomposite, visible emission was also enhanced [223].

To study the complex interactions between polymer and ZnO NPs, Xiong et al. [225] prepared PEO/ZnO composite films. The photoluminescence emission

spectra were dependent on the weight ratio of ZnO/PEO in the composite films. As the ZnO content increased, the ZnO emission wavelength red-shifted and its intensity decreased gradually, indicating that the NPs were heavily aggregated. When the ZnO/PEO weight ratio was increased to 0.5, the emission intensity of the composite film was close to that of ZnO. In a different work, Abdullah et al. synthesized poly(ethylene glycol) (PEG)-protected ZnO NPs via in-situ method [226, 227]. They dissolved LiOH and PEG in hot ethanol and then mixed the solution with zinc acetate. The resulting mixture was dried at 40°C for about 3 days to produce composite films. They found that incorporation of PEG could improve ZnO luminescence efficiency and, more importantly, adding excess LiOH resulted in highly blue-emitting products. Recently, Sun and Sue [228] mixed ZnO QDs, α -zirconium phosphate nanoplatelets, and PMMA in acetone, and then evaporated the solvents to cast films with a uniform thickness of 100 μm . The films dried in ambient conditions exhibited both UV emission and visible luminescence, but the films dried at 120°C overnight showed only one strong UV emission. The authors proposed that heating removed the solvents adsorbed on ZnO, and then the surface defects were passivated by PMMA. However, they did not consider the effects of oxidation by air. In fact, heating ZnO NPs in air always quenches the visible luminescence because oxygen fills the vacancies on the ZnO surface. After heating treatments, the ZnO photoluminescence emission red-shifted from 365 to 387 nm as the ZnO concentration in PMMA increased from 0.5 to 3.0 wt%. This phenomenon was explained by the coupling effect between QDs, i.e., when the QDs are in close contact with each other, significant dipole–dipole interactions between adjacent QDs lead to quantum tunneling. Obviously, such coupling effects proved that ZnO QDs were not passivated completely by PMMA, because the PMMA molecules would obstruct electron/hole tunneling between QDs if they had exchanged completely with solvent on the ZnO surface.

Wang et al. [229] also observed photoluminescence in a TiO_2 /PMMA nanocomposite with an emission maximum at 420 nm [229]. Similarly, a strong luminescence was found in core–shell composite particles made of ZnO and PMMA [230, 231]. The luminescence of nonconducting oxide/polymer composite was mainly attributed to the presence of carboxylate groups at the interface between ceramic and PMMA, whereas ZnO as a semiconductor exhibited an inherent luminescence. These authors also found a strong influence of the polymer coating on luminescence. The variation in coating organic compounds leads to significant changes in the emission spectrum. Furthermore, an influence of the particle size on emission maxima was observed for ZnO. A further development was multifunctional nanocomposite particles where magnetic properties and luminescent properties were combined in one particle [232]. The particles consisted of a superparamagnetic Fe_2O_3 core, coated with an organic dye, and finally with a protective polymer layer. Depending on the organic dye used, the photoluminescence could be adjusted.

According to the above reports, mixing ZnO and polymers physically is not a good method for improving ZnO visible luminescence. Although this method is easy, it has several drawbacks: first, many polymers are able to quench ZnO visible

emission through passivating the ZnO NP surface; second, polymers such as PEO, PVA, and PMMA cannot suppress ZnO NP aggregation effectively; third, some polymers such as PVP themselves have fluorescence and so interfere with ZnO emission. On the other hand, neither is incorporation into polymers a good method for enhancing ZnO UV emission. The excitons arising from ZnO NPs are separated into electrons and holes on the interface between ZnO and polymer, which is not favorable for ZnO UV emission.

4.2 Magnetic Properties

Magnetic NPs have attracted great attention due to their potential applications in MRI, drug delivery, magnetic recording media, high-frequency applications, cancer treatment, magneto-optical storage, interference suppression, biomedical sensing, etc. [76–79]. However, for some highly specialized applications, there is a practical need to disperse the magnetic NPs in nonmagnetic matrices that can be easily processed. The as-synthesized magnetic NPs usually have poor stability and dispersibility because of self-aggregation, making it difficult to use them in practical applications. Therefore, the incorporation of magnetic NPs into polymers offers the possibility to tailor several properties of the nanocomposite material, such as magnetic response and microwave absorption. Magnetic properties are investigated by magnetic hysteresis to show the influence of the incorporated soft magnetic oxide NPs on the magnetic behavior of the nanocomposites. Because it is impossible to completely describe the magnetic properties of all nanocomposites, we restrict our discussion to some representative examples.

The magnetic material, γ -Fe₂O₃/polymer nanocomposite, with an appreciable optical transmission in the visible region and free of hysteresis at room temperature, has been reported by Ziolo et al. [155]. They showed a saturation magnetization (M_s) of 15 Am²/kg for the nanocomposite containing 21.8 wt% of γ -Fe₂O₃. Sohn and Cohen [233] developed optically transparent thin films of block copolymers containing superparamagnetic γ -Fe₂O₃ NPs. They observed an M_s of 0.5 Am²/kg for the composite containing 2.6 wt% of γ -Fe₂O₃. Vollath and Szabó [232] prepared a superparamagnetic Fe₂O₃/polymer composite containing 15.3 wt% of γ -Fe₂O₃ that showed an M_s of around 30 Am²/kg. Zhan et al. [234] developed superparamagnetic nanocomposite films composed of PI and γ -Fe₂O₃. They reported an increase in the M_s value from 1.354×10^{-2} to 4.220×10^{-2} A for nanocomposite films with increasing Fe₃O₄ content (2–8 wt%). Thus, the magnetic properties of nanocomposites can be controlled by varying the Fe₃O₄ content. Nan and coworkers [235] synthesized surface-modified Fe₃O₄/PCL composite by microwave irradiation. Figure 11 shows the magnetization curves of 3-hydroxy-2-oxopropanoic acid-modified Fe₃O₄ and Fe₃O₄/PCL composite. Both surface-modified NPs and nanocomposite showed superparamagnetic behavior, as expected for magnetite NPs. The M_s values of the surface-modified NPs and nanocomposite were found to be 69 and 54.9 emu/g, respectively. The magnetic properties such as

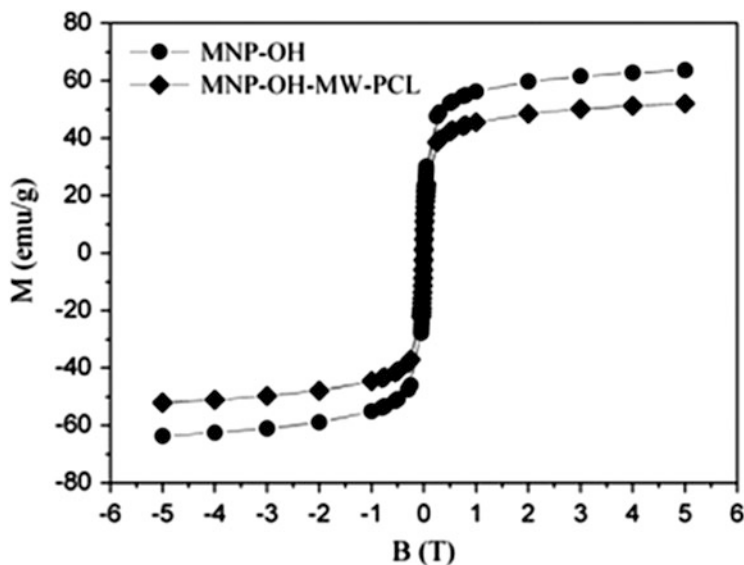


Fig. 11 Magnetization versus applied magnetic field at room temperature for surface-modified magnetite NPs (*MNP-OH*) and magnetite/PCL nanocomposite (*MNP-OH-MW-PCL*). Reprinted with permission from [235]. Copyright 2009 Wiley-VCH

superparamagnetic behavior and the relatively high magnetization values indicate that the composite is suitable for biomedical applications. Zhong et al. [236] synthesized PS/Fe₃O₄ nanocomposite via bulk polymerization. The hysteresis curves of the OA-Fe₃O₄ NPs and PS/Fe₃O₄ nanocomposite showed superparamagnetic properties with M_s values of 32 and 40 emu/g, respectively. This indicated that the polymerization did not affect the magnetic properties of the NPs. The M_s value of the nanocomposite was higher than that of the OA-Fe₃O₄ NPs because of excellent dispersion of the magnetic NPs. Xu et al. [237] prepared poly(vinylidene fluoride) (PVDF)/Fe₃O₄ magnetic nanocomposite by a simple co-precipitation method. The M_s and remnant magnetization (M_R) of the nanocomposite increased with increasing Fe₃O₄ content. The M_s and M_R values along the parallel direction were higher than those along the perpendicular direction at the same Fe₃O₄ content. Bhatt and coworkers [238] also reported the magnetic properties of the PVDF/Fe₃O₄ nanocomposites prepared by the spin-coating method. The M_S , M_R , and coercive force (H_c) values of Fe₃O₄ NPs were determined as 74.50 emu/g, 6.4 emu/g, and 82 Oe, respectively. This reveals the ferromagnetic nature of the NPs. As expected, the M_S of PVDF/Fe₃O₄ composites were comparatively lower. This is a result of the incorporation of Fe₃O₄ NPs into the polymer matrix (nonmagnetic). The M_S value of the composite increased with increasing Fe₃O₄ content. The above results suggest that the ferromagnetic behavior of composites arises from the magnetic Fe₃O₄ NPs.

Table 2 Potential applications of polymer/metal oxide hybrid nanocomposites [239–257]

Nanocomposites	Applications	References
High-density PE/TiO ₂	Bone repair	[239]
Chitosan/TiO ₂	Photocatalyst and antibacterial agent	[240]
Poly(amide–imide)/TiO ₂	Composite membranes for gas separation	[241]
PLA/TiO ₂	Biorecognition of anticancer drugs	[128]
Poly(butylene succinate)/TiO ₂	Photocatalyst	[114]
Epoxy/ZnO	Light-emitting diodes	[242]
Poly(ethylene glycol) monomethacrylate/ ZnO	In-vitro cell imaging	[243]
Chitosan/ZnO	Photocatalyst and antibacterial agent	[244]
PMMA/ZnO	Memory cells	[245]
PEG/ZnO	Biosensor	[246]
Chitosan/CuO	Photocatalyst and antibacterial agent	[247]
Polymer/CuO	Humidity sensor	[248]
PVA/CuO	Nanofluids	[249]
PMMA/iron oxide	Drug delivery and cell separation	[250, 251]
Starch/iron oxide	MRI and drug delivery	[252, 253]
Chitosan/Fe ₃ O ₄	Potentiometric urea biosensor	[254]
Chitosan/iron oxide	Heavy metal ion adsorption	[255]
PEG/iron oxide	MRI of cancer cells	[256]
Poly(methyl acrylate)/Fe ₃ O ₄	Waste-water purification	[257]

5 Applications of Nanocomposites

The applications of polymer/metal oxide nanocomposites have been growing at a rapid rate. The advantages of incorporating metal oxide NPs into polymer matrices can lead to potential applications. These areas include photocatalysts, membranes for gas separation, sensors, and environmental and biomedical applications. Hence, nanocomposites are emerging as new materials that can provide opportunities and rewards, creating a new world of interest. The potential applications of polymer/metal oxide hybrid nanocomposites are given in Table 2.

6 Conclusions

Polymer/metal oxide nanocomposites have attracted considerable interest over the last few decades, providing scope for improving the mechanical, thermal, optical, rheological, magnetic, and electrical properties. Improvements in the functional properties of polymers can be achieved at very low metal oxide NP loadings. Although significant work has been carried out on the preparation and properties of polymer/metal oxide nanocomposites, effort is still needed to determine the interrelationships between the processing, morphology, and functional properties

of the resulting nanocomposites. The properties of nanocomposites are affected by a large number of factors, including microstructural distributions generated during nanocomposite processing as well as the state of the NP distribution in polymer systems. Understanding the relationship between the processing, morphology, and functional properties of nanocomposites will be very helpful for optimizing the ultimate properties of nanocomposites as well as for improving the models to predict the properties of nanocomposite systems. This review article is expected to help readers with a wide range of backgrounds to understand the impact of various processing methods and NPs on the properties and applications of nanocomposites.

Acknowledgement This study was supported by DG Economic Circle Leading Industry R&D Program of the Ministry of Knowledge and Economy (MOKE) (R0001657)

References

1. Mukheerjee M, Datta A, Chakravorty D (1994) *Appl Phys Lett* 64:1159
2. Chen TK, Tien YI, Wei KH (2000) *Polymer* 41:1345
3. Zhu ZK, Yin J, Cao F, Shang XY, Lu QH (2000) *Adv Mater* 12:1055
4. Ramos J, Millan A, Palacio F (2000) *Polymer* 41:8461
5. Sanchez C, De GJ, Soler-Illia AA, Ribot F, Lalot T, Mayer CR, Cabuil V (2001) *Chem Mater* 13:3061
6. Ajayan PM, Schadler LS, Braun PV (2003) *Nanocomposite science and technology*. Wiley, Weinheim
7. Gómez-Romero P, Sanchez C (2004) *Functional hybrid materials*, 6th edn. Wiley, Weinheim
8. KICKELBICK G (2007) *Hybrid materials: synthesis, characterization, and applications*, 1st edn. Wiley, Weinheim
9. Nielsen LE, Landel RF (1993) *Mechanical properties of polymers and composites*, 1st edn. CRC, New York
10. ROTHON RN (2007) *Fillers and their surface modifiers for polymer applications*. *Plastics Informations Direct*, Bristol
11. Hornsby PR (2001) *Int Mater Rev* 46:199
12. Liu Y, Yang R, Yu J, Wang K (2002) *Polym Compos* 23:28
13. Domingo C, Loste E, Fraile J (2006) *J Supercrit Fluids* 37:72
14. Zhou Y, Cooper K, Li Y, Li Z (2009) Use of coupling agents to improve the interface in absorbable polymer composites. US Patent 20,090,149,873
15. WERNETT PC (2009) Surface treated inorganic particle additive for increasing the toughness of polymers. WO Patent 2,009,077,860
16. Rong MZ, Zhang MQ, Ruan WH (2006) *Mater Sci Tech* 22:787
17. Masala O, Seshadri R (2004) *Annu Rev Mater Res* 34:41
18. Chu SY, Yan TM, Chen SL (2000) *Ceram Int* 26:733
19. Westin G, Ekstrand A, Nygren M, Sterlund RO, Merkelbach P (1994) *J Mater Chem* 4:615
20. Tokumoto MS, Briois V, Santilli CV (2003) *J Sol-Gel Sci Technol* 26:547
21. Kim JH, Choi WC, Kim HY, Kang Y, Park YK (2005) *Powder Technol* 153:166
22. Damonte LC, Zelis LAM, Soucase BM, Fenollosa MAH (2004) *Powder Technol* 148:15
23. Kahn ML, Monge M (2005) *Adv Funct Mater* 15:458
24. Komarneni S, Bruno M, Mariani E (2000) *Mater Res Bull* 35:1843
25. Zhao XY, Zheng BC, Li CZ, Gu HC (1998) *Powder Technol* 100:20

26. Dai ZR, Pan ZW, Wang ZL (2003) *Adv Funct Mater* 13:9
27. Padmavathy N, Vijayaraghavan R (2008) *Sci Technol Adv Mater* 9:035004/1
28. Pillai SC, Kelly JM, McCormack DE, Ramesh R (2004) *J Mater Chem* 14:1572
29. Ao WQ, Li JQ, Yang HM, Zeng XR, Ma XC (2006) *Powder Technol* 168:148
30. Ismail AA, El-Midany A, Abdel-Aal EA, El-Shall H (2005) *Mater Lett* 59:1924
31. Pinna N, Garnweitner G, Antonietti M, Niederberger M (2005) *J Am Chem Soc* 127:5608
32. Baskoutas S, Giabouranis P, Yannopoulos SN, Dracopoulos V, Toth L, Chrissanthopoulos A, Bouropoulos N (2007) *Thin Solid Films* 515:8461
33. Kundu TK, Kark N, Barik P, Saha S (2011) *Int J Soft Comput Eng* 1:19
34. Dakhlaoui A, Jendoubi M, Smiri LS, Kanaev A, Jouini N (2009) *J Cryst Growth* 311:3989
35. Drath BE, Martin S, Mogens C, Brummerstedt IB (2012) Particle size effects on the thermal conductivity of ZnO. *AIP Conf Proc* 1449:335–338
36. Singh AK (2010) *Adv Powder Technol* 21:609
37. Carrey J, Kahn ML, Sanchez S, Chaudret B, Respaud M (2007) *Eur Phys J Appl Phys* 40:71
38. Garcia MA, Merino JM, Pinel EF, Quesada A, de la Venta J, Gonzalez MLR et al (2007) *Nano Lett* 7:1489
39. Ton-That C, Philips MR, Foley M, Moody SJ, Stampfl APJ (2008) *Appl Phys Lett* 92:261916/1
40. Chopra L, Major S, Pandya DK, Rastogi RS, Vankar VD (1983) *Thin Solid Films* 1021:1
41. Jiang P, Zhou JJ, Fang HF, Wang CY, Wang ZL, Xie SS (2007) *Adv Funct Mater* 17:1303
42. Chakrabarti S, Dutta BK (2004) *J Hazard Mater* 112:269
43. Chen C, Liu J, Liu P, Yu B (2011) *Adv Chem Eng Sci* 1:9
44. Tan TK, Khiew PS, Chiu WS, Radiman S, Abd-Shukor R, Huang NM et al (2011) *World Acad Sci Eng Tech* 79:791–796
45. Zhou J, Xu N, Wang ZL (2006) *Adv Mater* 18:2432
46. Jones N, Ray B, Ranjit KT, Manna AC (2008) *FEMS Microbiol Lett* 279:71
47. Jin T, Sun D, Su Y, Zhang H, Sue HJ (2009) *J Food Sci* 74:46
48. Ugur SS, Sariisik M, Aktas AH, Ucar MC, Erden E (2010) *Nanoscale Res Lett* 5:1204
49. Li J, Guo D, Wang X, Wang H, Jiang H, Chen B (2010) *Nanoscale Res Lett* 5:1063
50. Jitputti J, Rattanavoravipa T, Chuangchote S, Pavasupree S, Suzuki Y, Yoshikawa S (2009) *Catal Commun* 10:378
51. Mizukoshi Y, Makise Y, Shuto THJ, Tominaga A, Shironita S, Tanabe S (2007) *Ultrason Sonochem* 14:387
52. Zhang Y, Zheng H, Liu G, Battaglia V (2009) *Electrochim Acta* 54:4079
53. Li XL, Peng Q, Yi JX, Wang X, Li Y (2006) *Chem Eur J* 12:2383
54. Zhang DB, Qi LM, Cheng HM, Ming JMA (2003) *Chin Chem Lett* 14:100
55. Anwar NS, Kassim A, Lim HN, Zakarya SA, Huang NM (2010) *Sains Malays* 39:261
56. Rahim S, Radiman S, Hamzah A (2012) *Sains Malays* 41:219
57. Yang H, Zhang K, Shi R, Li X, Dong X, Yu Y (2006) *J Alloys Compd* 413:302
58. Jagadale TC, Takale SP, Sonawane RS, Joshi HM, Patil SI, Kale BB, Ogale SB (2008) *J Phys Chem C* 112:14595
59. Teleki A, Pratsinis SE, Kalyanasundaram K, Gouma PI (2006) *Sensor Actuator B* 119:683
60. Parala H, Devi A, Bhakta R, Fischer RA (2002) *J Mater Chem* 12:1625
61. Chen X, Mao SS (2007) *Chem Rev* 107:2891
62. Zhao Y, Li C, Liu X, Gu F, Jiang H, Shao W, Zhang L, He Y (2007) *Mater Lett* 61:79
63. Barnard AS, Erdin S, Lin Y, Zapol P, Halley JW (2006) *Phys Rev B* 73:205405/1
64. Auvinen S, Alatalo M, Haario H, Jalava JP, Lamminmaki RJ (2011) *J Phys Chem C* 115:8484
65. Hoang VV, Zung H, Trong NHB (2007) *Eur Phys J D* 44:515
66. Shao W, Nabb D, Renevier N, Sherrington I, Fu Y, Luo J (2012) *J Electrochem Soc* 159:671–676
67. Carp O, Huisman CL, Reller A (2004) *Prog Solid State Chem* 32:33
68. Lee KM, Hu CW, Chen HW, Ho KC (2008) *Sol Energ Mater Sol Cells* 92:1628
69. Mohammadi MR, Fray DJ, Cordero-Cabrera MC (2007) *Sensor Actuator B* 124:74

70. Wang YQ, Zhang HM, Wang RH (2007) *Colloids Surf B* 65:190
71. Adesina AA (2004) *Catal Surv Asia* 8:265
72. Chitose N, Ueta S, Yamamoto TA (2003) *Chemosphere* 50:1007
73. Kabra K, Chaudhary R, Sawhney RL (2004) *Ind Eng Chem Res* 43:7683
74. Kuhn KP, Cahberry IF, Massholder K, Stickler M, Benz VW, Sonntag HG, Erdinger L (2003) *Chemosphere* 53:71
75. Choi JY, Kim KH, Choy KC, Oh KT, Kim KN (2007) *J Biomed Mater Res B: Appl Biomater* 80:353
76. Jolivet JP, Chaneac C, Tronc E (2004) *Chem Commun* 2004(5):481
77. Wan SR, Huang JS, Yan HS, Liu KL (2006) *J Mater Chem* 16:298
78. Zhou ZH, Wang J, Liu X, Chan HSO (2001) *J Mater Chem* 11:1704
79. Albornoz C, Jacobo SE (2006) *J Magn Magn Mater* 305:12
80. Hou YL, Yu JF, Gao S (2003) *J Mater Chem* 13:1983
81. Pascal C, Pascal JL, Favier F, Payen C (1999) *Chem Mater* 11:141
82. Franzel L, Bertino MF, Huba ZJ, Carpenter EE (2012) *Appl Surf Sci* 261:332
83. Vijayakumar R, Koltypin Y, Felner I, Gedanken A (2000) *Mater Sci Eng A* 286:101
84. Sun S, Zeng H (2002) *J Am Chem Soc* 124:8204
85. Wu W, He Q, Jiang C (2008) *Nanoscale Res Lett* 3:397
86. Bandyopadhyay M, Bhattacharya J (2006) *J Phys Condens Matter* 18:11309
87. Akbarzadeh A, Samiei M, Davaran S (2012) *Nanoscale Res Lett* 7:144
88. Martchenko I, Dietsch H, Moitzi C, Schurtenberger P (2011) *J Phys Chem B* 115:14838
89. Roca AG, Costo R, Rebolledo AF, Veintemillas-Verdaguer S, Tartaj P, Gonzalez- Carreno T, Morales MP, Serna CJ (2009) *J Phys D* 42:224002/1
90. Chan DCF, Kirpotin DB, Bunn PA (1993) *J Magn Magn Mater* 122:374
91. Babes L, Denizot B, Tanguy G, Le Jeune JJ, Jallet P (1999) *J Colloid Interface Sci* 212:474
92. Chertok B, Moffat BA, David AE, Yu F, Berqemann C, Ross BD et al (2008) *Biomaterials* 29:487
93. Khodabakhshi A, Amin MM, Mozaffari M (2011) *Iran J Environ Health Sci Eng* 8:189
94. Tran N, Mir A, Mallik D, Sinha A, Nayar S, Webster TJ (2010) *Int J Nanomedicine* 5:277
95. Sambandam A, Lee GJ, Wu J (2012) *Ultrason Sonochem* 19:682
96. Darezereshki E, Bakhtiari F (2011) *J Min Metal Sect B* 47:73
97. Borgohain K, Singh J, Rao M, Shripathi T (2000) *Phys Rev B* 61:11093
98. El-Trass A, ElShamy H, El-Mehasseb I, El-Kemary M (2012) *Appl Surf Sci* 258:2997
99. Kumar RV, Mastai Y, Diamant Y, Gedanken A (2000) *Chem Mater* 12:2301
100. Lim Y, Choi J, Hanrath T (2012) *J Nanomater* 2012:4
101. Yuan G, Jiang H, Lin C, Liao S (2007) *J Cryst Growth* 303:400
102. Poizat P, Hung C, Nikiforov M, Bohannan E, Switzer J (2003) *Electrochem Solid State Lett* 6:C21
103. Son D, You C, Ki T (2009) *Appl Surf Sci* 255:8794
104. Wang H, Xu J, Zhu J, Chen H (2002) *J Cryst Growth* 244:88
105. Kida T, Oka T, Nagano M, Ishiwata Y, Zheng X (2007) *J Am Ceram Soc* 90:107
106. Saito G, Hosokai S, Tsubota M, Akiyama T (2011) *J Appl Phys* 110:023302
107. Hong JI, Schadler LS, Siegel RW (2003) *Appl Phys Lett* 82:1956
108. Hong JI, Winberg P, Schadler LS, Siegel RW (2005) *Mater Lett* 59:473
109. Dang ZM, Fan LZ, Zhao SJ, Nan CW (2003) *Mater Res Bull* 38:499
110. Tjong SC, Liang GD (2006) *Mater Chem Phys* 100:1
111. Tjong SC, Liang GD, Bao SP (2006) *J Appl Polym Sci* 102:1436
112. Wong M, Tsuji R, Nutt S, Su S-J (2010) *Soft Matter* 6:4482
113. Zhao H, Li RKY (2006) *Polymer* 47:3207
114. Miyauchi M, Li Y, Shimizu H (2008) *Environ Sci Technol* 42:4551
115. Ou B, Li D, Liu Y (2009) *Compos Sci Technol* 69:421
116. Li G-J, Fan S-R, Wang K, Ren X-L, Mu X-W (2010) *Iran Polym J* 19:115
117. Chiu C-W, Lin C-A, Hong PD (2011) *J Polym Res* 18:367

118. Knör N, Walter R, Hauptert F (2011) *J Thermoplast Compos Mater* 24:185
119. Zohrevand A, Ajji A, Mighri F (2014) *Polym Eng Sci* 54:874
120. Kong I, Ahmad SH, Abdullah MH, Yusoff AN (2009) The effect of temperature on magnetic behavior of magnetite nanoparticles and its nanocomposites. *AIP Conf Proc* 1136:830–834
121. Chung Y-C, Choi JW, Choi MW, Chun BC (2012) *J Thermoplast Compos Mater* 25:283
122. Vunain E, Mishra AK, Krause RW (2013) *J Inorg Organomet Polym* 23:293
123. Chae DW, Kim BC (2005) *Polym Adv Technol* 16:846
124. Li JH, Hong RY, Li MY, Li HZ, Zheng Y, Ding J (2009) *Prog Org Coat* 64:504
125. Seo J, Jeon G, Jang ES, Khan SB, Han H (2011) *J Appl Polym Sci* 122:1101
126. Hejazi I, Hajalizadeh B, Seyfi J, Sadeghi GMM, Jafari S-H, Khonakdar HA (2014) *Appl Surf Sci* 293:116
127. Song M, Pan C, Li J, Wang X, Gu Z (2006) *Electroanalysis* 18:1995
128. Song M, Pan C, Chen C, Li J, Wang X, Gu Z (2008) *Appl Surf Sci* 255:610
129. Nakayama N, Hayashi T (2007) *Polym Degrad Stab* 92:1255
130. Buzarovska A (2013) *Polym Plast Technol* 52:280
131. Mallakpour S, Barati A (2011) *Prog Org Coat* 71:391
132. Yang TI, Brown RNC, Kempel LC, Kofinas P (2008) *J Magn Magn Mater* 320:2714
133. Kaushik A, Khan R, Solanki PR, Pandey P, Alam J, Ahmad S, Malhotra BD (2008) *Biosens Bioelectron* 24:676
134. Pisanello F, Paolis RD, Lorenzo D, Nitti S, Monti G, Fragouli D, Athanassiou A, Manna L, Tarricone L, Vittorio MD, Martiradonna L (2013) *Microelectron Eng* 111:46
135. Hench LL, West JK (1990) *Chem Rev* 90:33
136. Kikelbick G (2003) *Prog Polym Sci* 28:83
137. Hsiue GH, Kuo WJ, Jeng RJ (2000) *Polymer* 41:2813
138. Song KY, Crivello JV, Ghoshal R (2001) *Chem Mater* 13:1932
139. Lu C, Yang B (2009) *J Mater Chem* 19:2884
140. Wu CS (2004) *J Appl Polym Sci* 92:1749
141. Du T, Song H, Ilegbusi OJ (2007) *Mater Sci Eng C* 27:414
142. Gao H, Yorifuji D, Wakita J, Jiang Z-H, Ando S (2010) *Polymer* 51:3173
143. Hu Q, Marand E (1999) *Polymer* 40:4833
144. Wang SX, Wang M, Zhang LD (1999) *J Mater Sci Lett* 18:2009
145. Liu Y, Lee JY (2003) *J Appl Polym Sci* 89:2815
146. Yang BD, Yoon KH (2004) *Synth Met* 142:21
147. Chiang PC, Whang WT (2003) *Polymer* 44:2249
148. Chiang PC, Whang WT, Tsai MH, Wu SC (2004) *Thin Solid Films* 359:447
149. Chen WC, Lee SJ, Liu JL (1999) *J Mater Chem* 9:2999
150. Lee LH, Chen WC (2001) *Chem Mater* 13:1137
151. Wang B, Wilkes GL, McGrath JE (1991) *Macromolecules* 24:3449
152. Lu C, Cui Z, Guan C, Guan J, Yang B, Shen J (2003) *Macromol Mater Eng* 288:717
153. Rao Y, Chen S (2008) *Macromolecules* 41:4838
154. Yoshida M, Lal M, Deepark-Kumar N, Prasad PN (1997) *J Mater Sci* 32:4047
155. Ziolo RF, Giannelis EP, Weinstein BA, Ohoro MP, Ganguly BN, Mehrotra V, Russell MW, Huffman DR (1992) *Science* 257:219
156. Cao Z, Jiang WQ, Ye XZ, Gong XL (2008) *J Magn Magn Mater* 320:1499
157. Zhang L, Li F, Chen Y, Wang X (2011) *J Lumin* 131:1701
158. Park SS, Bernet N, Roche DLS, Hahn HT (2003) *J Compos Mater* 37:465
159. Evora VMF, Shukla A (2003) *Mater Sci Eng A* 361:358
160. Althues H, Simon P, Philipp F, Kaskel S (2006) *J Nanosci Nanotechnol* 6:409
161. Anzlovar A, Orel ZC, Zigon M (2010) *Eur Polym J* 46:1216
162. Li S, Toprak MS, Jo YS, Dobson J, Kim DK, Muhammed M (2007) *Adv Mater* 19:4347
163. Wang ZG, Zu XT, Xiang X (2006) *J Mater Sci* 41:1973
164. Bourgeat-Lami E (2002) *J Nanosci Nanotechnol* 2:1
165. Liu P, Su Z (2006) *J Macromol Sci B Phys* 45:131

166. Dzunuzovic E, Jeremic K, Nedeljkovic JM (2007) *Eur Polym J* 43:3719
167. Demir MM, Castignolles P, Akbey U, Wegner G (2007) *Macromolecules* 40:4190
168. Demir MM, Koynov K, Akbey U, Bubeck C, Park I, Lieberwirth I, Wegner G (2007) *Macromolecules* 40:1089
169. Li S, Qin J, Fornara A, Toprak M, Muhammed M, Kim DK (2009) *Nanotechnology* 20:6
170. Guo Z, Lei K, Li Y, Ng HW, Prikhodko S, Hahn HT (2008) *Compos Sci Tech* 68:1513
171. Inkyo M, Tokunaga Y, Tahara T, Iwaki T, Iskandar F, Hogan CJ, Okuyama K (2008) *Ind Eng Chem Res* 47:2597
172. Zou H, Wu S, Shen J (2008) *Chem Rev* 108:3893
173. Ai Z, Sun G, Zhou Q, Xie C (2006) *J Appl Polym Sci* 102:1466
174. Daniel JC, Schuppiser JL, Tricot M (1982) Magnetic polymer latex and preparation process. US Patent 4,358,388
175. Charmot D, Vidil C (1994) Magnetizable composite microspheres of hydrophobic crosslinked polymer, process for preparing them and their application in biology. US Patent 5,356,713
176. Dresco PA, Zaitsev VS, Gambino RJ, Chu B (1999) *Langmuir* 15:1945
177. Wormuth K (2001) *J Colloid Interface Sci* 241:366
178. Mazrouaal A, Badawi A, Mansour N, Fathy M, Elsabee M (2013) *J Nano Electron Phys* 5:04063
179. Petchthanasombat C, Tiensing T, Sunintaboon P (2012) *J Colloid Interface Sci* 369:52–57
180. Erdem B, Sudol ED, Dimonie VL, El-Asser MS (2000) *J Polym Sci A Polym Chem* 38:4419
181. Erdem B, Sudol ED, Dimonie VL, El-Asser MS (2000) *J Polym Sci A Polym Chem* 38:4431
182. Erdem B, Sudol ED, Dimonie VL, El-Asser MS (2000) *J Polym Sci A Polym Chem* 38:4441
183. Zhang M, Gao G, Li CQ, Liu F (2004) *Langmuir* 20:1420
184. Wu Y, Zhang Y, Xu J, Chen M, Wu L (2010) *J Colloid Interface Sci* 343:18
185. Ramirez LP, Landfester K (2003) *Macromol Chem Phys* 204:22
186. Luo Y-D, Dai C-A, Chiu W-Y (2008) *J Polym Sci A Polym Chem* 46:1014
187. Tang E, Dong S (2009) *Colloid Polym Sci* 287:1025
188. Teo BM, Chen F, Hatton TA, Grieser F, Ashokkumar M (2009) *Langmuir* 25:2593
189. Xu ZZ, Wang CC, Yang WL, Deng YH, Fu SK (2004) *J Magn Magn Mater* 277:136
190. Chen Y, Qian Z, Zhang Z (2008) *Colloids Surf A* 312:209
191. Lin C, Chiu W, Don T (2006) *J Appl Polym Sci* 100:3987
192. Yang S, Liu H, Zhang Z (2008) *J Polym Sci A Polym Chem* 46:3900
193. Flesch C, Delaite C, Dumas P, Bourgeat-Lami E, Duguet E (2004) *J Polym Sci A Polym Chem* 42:6011
194. Takafuji M, Ide S, Ihara H, Xu Z (2004) *Chem Mater* 16:1977
195. Tang E, Cheng G, Ma X, Pang X, Zhao Q (2006) *Appl Surf Sci* 252:5227
196. Wang X, Song X, Lin M, Wang H, Zhao Y, Zhong W, Du Q (2007) *Polymer* 48:5834
197. Sidorenko A, Minko S, Gafijchuk G, Voronov S (1999) *Macromolecules* 32:4539
198. Shirai Y, Kawatsura K, Tsubokawa N (1999) *Prog Org Coat* 36:217
199. Tang E, Cheng G, Ma X (2006) *Powder Technol* 161:209
200. Fan X, Lin L, Messersmith PB (2006) *Compos Sci Technol* 66:1195
201. Hong RY, Qian JZ, Cao JX (2006) *Powder Technol* 163:160
202. Guo Z, Liang X, Pereira T, Scaffaro R, Thomas Hahn H (2007) *Compos Sci Technol* 67:2036
203. Bach LG, Islam Md R, Kim JT, Seo SY, Lim KT (2012) *Appl Surf Sci* 258:2959
204. Liu P, Wang T (2008) *Curr Appl Phys* 8:66
205. Wang Y, Teng X, Wang J-S, Yang H (2003) *Nano Lett* 3:789
206. Duan H, Kuang M, Wang D, Kurth DG, Moehwald H (2005) *Angew Chem Int Ed* 44:1717
207. Ninjbadgar T, Yamamoto S, Fukuda T (2004) *Solid State Sci* 6:879
208. Marutani E, Yamamoto S, Ninjbadgar T, Tsujii Y, Fukuda T, Takano M (2004) *Polymer* 45:2231
209. Abbasian M, Aali NL, Shoja SE (2013) *J Macromol Sci A Pure Appl Chem* 50:966
210. Gelbrich T, Feyen M, Schmidt A (2006) *Macromolecules* 39:3469

211. Gelbrich T, Marten G, Schmidt A (2010) *Polymer* 51:2818
212. Sato M, Kawata A, Morito S, Sato Y, Yamaguchi I (2008) *Eur Polym J* 44:3430
213. Nam K, Tsutsumi Y, Yoshikawa C, Tanaka Y, Fukaya R, Kimura T, Kobayashi H, Hanawa T, Kishida A (2011) *Bull Mater Sci* 34:1289
214. Caseri W (2009) *Chem Eng Commun* 196:549
215. Li Y-Q, Fu S-Y, Mai Y-W (2006) *Polymer* 47:2127
216. Ammala A, Hill AJ, Meakin P, Pas SJ, Turney TW (2002) *J Nanopart Res* 4:167
217. Allen NS, Edge M, Ortega A, Sandoval G, Liauw CM, Verran J, Stratton J, McIntyre RB (2004) *Polym Degrad Stab* 85:927
218. Christensen PA, Dilks A, Egerton TA (1999) *J Mater Sci* 34:5689
219. Lu N, Lu X, Jin X, Lu C (2007) *Polym Int* 56:138
220. Sun D, Sue H-J, Miyatake N (2008) *J Phys Chem C* 112:16002
221. Guo L, Yang S, Yang C, Yu P, Wang J, Ge W, Wong GKL (2000) *Appl Phys Lett* 76:2901
222. Zhang J, Liu H, Wang Z, Ming N, Li Z, Biris AS (2007) *Adv Funct Mater* 17:3897
223. Wei SF, Lian JS, Jiang Q (2009) *Appl Surf Sci* 255:6978
224. Singla ML, Shafeeq MM, Kumar M (2009) *J Lumin* 129:434
225. Xiong HM, Zhao X, Chen JS (2001) *J Phys Chem B* 105:10169
226. Abdullah M, Lenggono IW, Okuyama K, Shi FG (2003) *J Phys Chem B* 107:1957
227. Abdullah M, Morimoto T, Okuyama K (2003) *Adv Funct Mater* 13:800
228. Sun DZ, Sue HJ (2009) *Appl Phys Lett* 94:253106
229. Wang ZG, Zu XT, Zhu S, Xiang X, Fang LM, Wang LM (2006) *Phys Lett B* 350:252
230. Vollath D, Szabó DV, Schlabach S (2004) *J Nanopart Res* 6:181
231. Wang ZG, Zu XT, Xiang X, Yu HJ (2006) *J Nanopart Res* 8:137
232. Vollath D, Szabó DV (2004) *Adv Eng Mater* 6:117
233. Sohn BH, Cohen RE (1997) *Chem Mater* 9:264
234. Zhan J, Tian G, Jiang L, Wu Z, Wu D, Yang X, Jin R (2008) *Thin Solid Films* 516:6315
235. Nan A, Turcu R, Craciunescu I, Pana O, Schaft H, Liebscher J (2009) *J Polym Sci A Polym Chem* 47:5379
236. Zhong W, Liu P, Shi HG, Xue DS (2010) *Express Polym Lett* 4:183
237. Xu C, Ouyang C, Jia R, Li Y, Wang X (2009) *J Appl Polym Sci* 111:1763
238. Bhatt AS, Bhat DK, Santosh MS (2011) *J Appl Polym Sci* 119:968
239. Hashimoto M, Takadama H, Mizuno M, Kokubo T (2006) *Mater Res Bull* 41:515
240. Haldorai Y, Shim JJ (2014) *Polym Compos* 35:327
241. Camargo P, Satyanarayana K, Wypych F (2009) *Mater Res* 12:1
242. Yang Y, Li YQ, Fu SY, Xiao HM (2008) *J Phys Chem C* 112:10553
243. Xiong HM, Xu Y, Ren QG, Xia YY (2008) *J Am Chem Soc* 130:7522
244. Haldorai Y, Shim JJ (2013) *Compos Interfac* 20:365
245. Son DA, Park DH, Choi WK, Cho SH, Kim WT, Kim TW (2009) *Nanotechnology* 20:195203
246. Sinha R, Ganesana M, Andreescu S (2010) *Anal Chim Acta* 661:195
247. Haldorai Y, Shim JJ (2013) *Int J Photoenergy* 2013:245646
248. Yuan C, Xu Y, Deng Y, Jiang N, He N, Dai L (2010) *Nanotechnology* 21:415501
249. Pandey V, Mishra G, Verma SK, Wan M, Yadav RR (2012) *Mater Sci Appl* 3:664
250. Zhu DM, Wang F, Han M, Li HB, Xu Z (2007) *Chin J Inorg Chem* 23:2128
251. Singh H, Laibinis PE, Hatton TA (2005) *Langmuir* 21:11500
252. Kim DK, Maria M, Wang FH, Jan K, Borje B, Zhang Y, Tsakalacos T, Muhammed M (2003) *Chem Mater* 15:4343
253. Wang W, Zhang ZK (2007) *J Dispers Sci Technol* 28:557
254. Ali A, AlSalhi MS, Atif Anees M, Ansari A, Israr MQ, Sadaf JR, Ahmed E, Nur O, Willander M (2003) *J Phys Conf Ser* 414:012024
255. Wan Ngaha WS, Teonga LC, Hanafiah MAKM (2011) *Carbohydr Polym* 83:1446
256. Vannier EA, Cohen-Jonathan S, Gautier J, Herve-Aubert K, Munnier E, Souce M, Legras P, Passirani C, Chourpa I (2012) *Eur J Pharm Biopharm* 81:498
257. Liu Z, Yang H, Zhang H, Huang C, Li L (2012) *Cryogenics* 52:699

Semiconductor–Polymer Hybrid Materials

**Sarita Kango, Susheel Kalia, Pankaj Thakur, Bandna Kumari,
and Deepak Pathania**

Abstract Semiconductor nanoparticles have attracted much attention due to their unique size and properties. Semiconductor–polymer hybrid materials are of great importance in the field of nanoscience as they combine the advantageous properties of polymers with the unique size-tunable optical, electronic, catalytic and other properties of semiconductor nanoparticles. Due to combination of the unique properties of organic and inorganic components in one material, these semiconductor–polymer hybrids find application in environmental, optoelectronic, biomedical and various other fields. A number of methods are available for the synthesis of semiconductor–polymer hybrid materials. Two methods, i.e. melt blending and in-situ polymerization, are widely used for the synthesis of semiconductor–polymer nanocomposites. The first part of this review article deals with the synthesis, properties and applications of semiconductor nanoparticles. The second part deals with the synthesis of semiconductor–polymer nanocomposites by melt blending and in-situ polymerization. The properties and some applications of semiconductor–polymer nanocomposites are also discussed.

S. Kango

Department of Physics and Materials Science, Jaypee University of Information Technology,
Waknaghat, Solan, Himachal Pradesh 173234, India

S. Kalia (✉) and B. Kumari

Department of Chemistry, Bahra University, Waknaghat (Shimla Hills), Solan, Himachal
Pradesh 173234, India

e-mail: susheel.kalia@gmail.com; susheel_kalia@yahoo.com

P. Thakur

Center for Advanced Biomaterials for Health Care(Istituto Italiano Di Tecnologia), Largo
Barsanti e Matteucci 53, 80125 Naples, Italy

Department of Chemistry, Shoolini University, Solan, Himachal Pradesh 173212, India

D. Pathania

Department of Chemistry, Shoolini University, Solan, Himachal Pradesh 173212, India

Keywords Biomedical applications · Electronic applications · Environmental applications · Polymer nanocomposites · Quantum dots · Semiconductor nanoparticles

Contents

1	Introduction	284
2	Semiconductor Nanoparticles	285
2.1	Synthesis of Semiconductor Nanoparticles	285
2.2	Quantum Dots	290
2.3	Properties of Semiconductor Nanoparticles	292
2.4	Applications of Semiconductor Nanoparticles	294
3	Polymer Composites with Semiconductor Nanoparticles	299
3.1	Synthesis of Semiconductor–polymer Nanocomposites	299
3.2	Applications of Semiconductor–Polymer Nanocomposites	304
	Conclusions	304
	References	304

1 Introduction

Semiconductor nanoparticles have attracted much interest during the past decade due to their unique size and properties. Numerous reports are available in the literature on synthetic techniques as well as potential applications of nanosized semiconductor particles [1–7]. Nanoparticles of ZnO, Fe₂O₃, SiO₂, MoS₂, CdS, HgS, GaP, Cd₃P₂, BiI₃, PbI₂ and a number of other semiconductors have been synthesized [8–14]. Many synthesis methods have been developed for the synthesis of semiconductor nanoparticles [15–22]. Semiconductor nanostructures have drawn considerable attention due to their various potential applications in light-emitting devices, nanolasers, photodetectors, solar cells, biomedical imaging etc. The combination of fluorescent semiconductor nanoparticles with optical polymers yields a new class of materials that show both transparency and fluorescence characteristics [23, 24]. Composite structures formed by semiconductor nanocrystals (NCs) embedded into a polymer matrix are now promising systems for light-emitting and photovoltaic devices. Nanocomposites of organic and inorganic semiconductors dispersed in polymer matrices are multifunctional materials often suggested as elements of nonlinear optical devices and for development of plastic solar cells [1, 2]. These unique physical properties give rise to many potential applications in areas such as nonlinear optics, luminescence, electronics, catalysis, telecommunication amplifiers, solar energy conversion and optoelectronics [25–27]. Semiconductor nanocrystals are also used for biolabelling. Luminescent semiconductor nanocrystal have been successfully integrated into thin film polymer-based light-emitting diodes (LEDs) as emitting materials [28, 29].

This article is divided in two main parts. In first part, the synthesis of semiconductor nanoparticles by different methods, some properties and applications are

discussed. The second part deals with the synthesis of semiconductor–polymer nanocomposites based on different types of polymers. The properties and applications of semiconductor–polymer nanocomposites are also discussed.

2 Semiconductor Nanoparticles

Semiconductor nanoparticles exhibit size- and shape-dependent electronic and optical properties that make them much attractive materials. There are two types of semiconductors, i.e. elemental and compound semiconductors. Group IV silicon (Si) and germanium (Ge) are elemental semiconductors with four valence electrons in their outermost shell. Si and Ge both are indirect bandgap materials. Compound semiconductors include group III–V and group II–VI semiconductors. GaN, GaP, GaAs, InP and InAs are III–V semiconductors, while ZnO, ZnS, CdS, CdSe and CdTe are II–VI semiconductors. Several other oxides such as TiO₂, WO₃ etc. also exhibit semiconductive behaviour [30]. Doping of these semiconductor nanoparticles with magnetic metals gives rise to another class of materials called diluted magnetic semiconductors (DMS), which possess the characteristics of semiconductors as well as magnetic properties. In DMS a fraction of the cations in the lattice are replaced substitutionally by magnetic ions and the atomic spin on these magnetic dopants is expected to interact with the carriers in the lattice to bring about global ferromagnetic order in the material. Thus, these materials have unusual magnetic characteristics due to the presence of isolated magnetic ions in semiconducting lattice. DMS include simple oxides like SnO₂ [31–33], ZnO [34–36] and TiO₂ [37, 38] or mixed oxides [39, 40] doped with several transition metals (Fe, Co, Ni, Mn) [31, 32] or rare earths metals (Dy, Eu, Er) [33].

2.1 Synthesis of Semiconductor Nanoparticles

2.1.1 Sol–Gel Method

Synthesis of a variety of nanoparticles, including semiconductor nanoparticles, by the sol–gel method has been reported in the literature. This method generally involves the transition of a system from a liquid “sol” (mostly colloidal) into a solid “gel” phase [41]. The homogeneity of the gels mainly depends on the solubility of the reagents in the solvent, sequence of addition of reactants, temperature and the pH of the solution. For sol–gel synthesis and doping of nanoparticles, generally, organic alkoxides, acetates or acetylacetonates as well as inorganic salts such as chlorides are used as precursors and alcohols are largely used as solvents. This method can be performed at low temperatures and is suitable for large-scale production of nanoparticles with relatively narrow size distribution [42]. Spherically shaped ZnO nanoparticles were synthesized by the sol–gel method using TEA

(triethanolamine) as a surfactant [43]. TiO₂ semiconductor nanoparticles were synthesized in anatase phase by a sol–gel low temperature method from titanium tetra-isopropoxide (TTIP) as the titanium precursor in the presence of acetic acid (AcOH). The effect of synthesis parameters such as AcOH-to-water ratios, sol formation time, synthesis and calcination temperature on the photocatalytic activity of TiO₂ nanoparticles was also studied [44].

Sugimoto and coworkers developed a novel two-step sol–gel process to synthesize TiO₂ nanoparticles at a large scale. In this method, oxide particles were synthesized via two steps: (1) formation of a hydroxide gel and (2) nucleation and growth to oxide particles. Therefore, it is different from the conventional sol–gel method [45–52]. Lee et al. [53] also carried out synthesis of shape-controlled anatase TiO₂ nanoparticles with uniform morphology and size using the two-step sol–gel method. Sambasivam et al. [54] and Mălăeru et al. [55] carried out sol–gel synthesis of Er-doped SnO₂ and of Ni-doped ZnO DMS nanoparticles, respectively. Tetragonal phase SnO₂ nanoparticles were synthesized by the sol–gel method using SnCl₂·2H₂O and polyethylene glycol (PEG) at different calcination temperatures. Particle size was found to decrease with a decrease in temperature and molecular weight of PEG. These results suggest that the calcination temperatures and molecular weight of PEG play a significant role in determining the size of SnO₂ nanoparticles synthesized via this method [56].

InAs nanocrystals embedded in SiO₂ gel–glasses were synthesized by a sol–gel method. Heqing et al. synthesized gels through hydrolysis of a complex solution of Si(OC₂H₅)₄, As₂O₃ and InCl₃·4H₂O, which were heated at 450°C in O₂ atmosphere and then heated from 200 to 500°C in H₂ atmosphere to form fine cubic InAs crystals. It was observed that size of the nanoparticles increases from 6 to 29 nm with an increase in the heat treatment temperature and molar ratio of InAs to SiO₂ [57]. A number of other studies on sol–gel synthesis of semiconductor nanoparticles have also been reported in the literature [58–64].

2.1.2 Hydrothermal Method

In the hydrothermal method, reactions are carried out in an aqueous medium in reactors or autoclaves at high vapour pressure (generally in the range 0.3–4 MPa) and high temperature (generally in the range 130–250°C) [65]. This process has also been utilized to grow dislocation-free single crystal particles, and grains formed in this process could have a better crystallinity than those from other methods. One-pot hydrothermal synthesis of citrate-stabilized CdSe nanoparticles in high temperature water was reported for the first time by Williams and co-authors. The base-case experimental conditions of 200°C, Cd to Se molar ratio of 8:1 and a reaction time of 1.5 min produced nanoparticles that exhibited quantum confinement behaviour. The quantum yield was 1.5%, but it was easily increased to approximately 7% by adding a CdS shell. The authors reported that the particle size increased with increasing reaction time, temperature, stabilizer concentration and Cd to Se ratio and decreased with increasing pH [66]. A number of researchers have

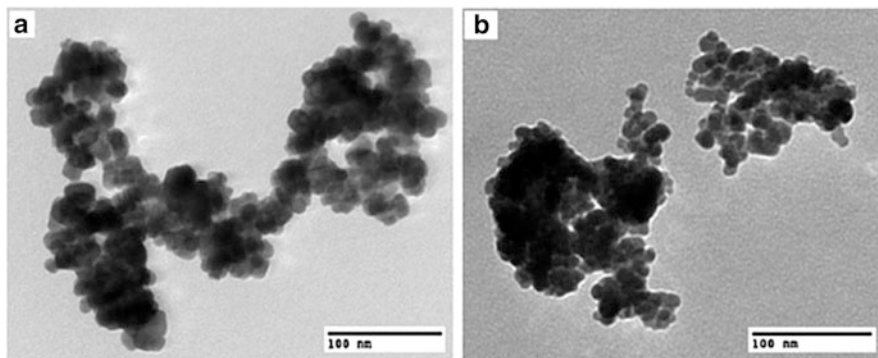


Fig. 1 TEM micrograph of (a) pure and (b) 6% Fe-doped CdSe nanoparticles. Reprinted from [72], Copyright 2012, with permission from Springer

synthesized semiconductor nanoparticles by this method, including copper sulfide [67], CdTe [68], ZnO [69], SnO₂ [70], CdS and CdS/ZnO [71]. Cd_{1-x}Fe_xSe (where $x = 0.00, 0.02, 0.04, 0.06, 0.08, 0.10$) diluted magnetic semiconductor nanoparticles were synthesized using sodium dodecyl sulfate (SDS) as a capping agent via a hydrothermal technique at 160°C. Figure 1 shows transmission electron microscopy (TEM) images of pure and 6% Fe-doped CdSe nanoparticles, which reveals that both the pure and doped nanoparticles were spherical in shape with an average particle size of around 14 nm for pure CdSe nanoparticles and 10 nm for 6% Fe-doped CdSe nanoparticles [72]. Lu et al. [73] carried out hydrothermal synthesis of spherical InAs nanocrystals of 30–50 nm at 120°C. The nanocrystals showed a 100 meV blue shift of bandgap absorption and phonon confinement of optical vibration mode. Study of the hydrothermal formation mechanism indicated that crystalline InAs could be obtained in an extended pH range (~ -0.15 to 14). Many other studies were also reported on the synthesis of doped and undoped semiconductor nanoparticles by hydrothermal methods [74–83].

2.1.3 Microemulsion Method

A microemulsion is a thermodynamically stable three-component system: two immiscible components (generally water and oil) and a surfactant molecule that lowers the interfacial tension between water and oil resulting in the formation of a transparent solution. Water-in-oil microemulsions involve dispersion of the aqueous phase as nanosized droplets (5–25 nm in diameter) surrounded by a monolayer of surfactant molecules in the continuous hydrocarbon phase. These micellar droplets exhibit a dynamic exchange of their contents, which further facilitates the reactions between reactants dissolved in different droplets. One can synthesize size-controlled crystallites by carrying out a wide variety of chemical reactions in nanodroplets using this micellar exchange. Different types of microemulsions are

known, such as water-in-oil (W/O), oil-in-water (O/W) and water-in-supercritical CO_2 (w/sc- CO_2) [84].

Petit et al. synthesized CdS nanoparticles in anionic bis(2-ethylhexyl) sulfosuccinate (AOT) and Triton X-100 reverse micelles using a functional surfactant such as cadmium lauryl sulfate and cadmium AOT. The authors found that the average diameter of the particles depended on the relative amount of Cd^{2+} and S^{2-} and that the particles obtained from AOT were smaller and more monodisperse than those obtained from the Triton reverse micelles. Colloidal CdS was prepared in the mixed sodium AOT/cadmium AOT/isooctane reverse micelle [85]. A number of semiconductor nanoparticles such as CdS, PbS, CuS, Cu_2S and CdSe were also synthesized using this method [86–89]. Wang et al. synthesized ZnO nanoparticles by mixing a Zn^{2+} -containing water-in-oil microemulsion with a NaOH-containing microemulsion in a microchannel reactor system (Fig. 2). In the microchannel reaction system, three phases were involved in the reaction: droplets of $\text{M}(\text{Zn}^{2+})$ and droplets of $\text{M}(\text{NaOH})$ dispersed in the organic phase, as shown in Fig. 3. The microemulsions provide confined space for the reactants, which is favourable for controllable reaction and nucleation, thus avoiding the formation of large particles. The authors tested three Zn^{2+} sources, $\text{Zn}(\text{NO}_3)_2$, ZnSO_4 , and ZnCl_2 , in the synthesis of ZnO nanoparticles. Of these, $\text{Zn}(\text{NO}_3)_2$ showed best performance, yielding ZnO particles with the smallest average grain size. The authors also investigated

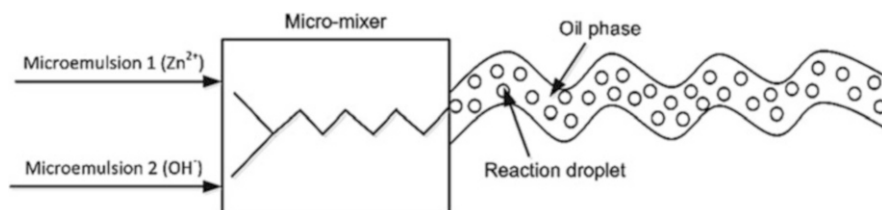


Fig. 2 Synthesis of nanoparticles by microemulsion in a microreactor. Reprinted from [90], Copyright 2014, with permission from Elsevier

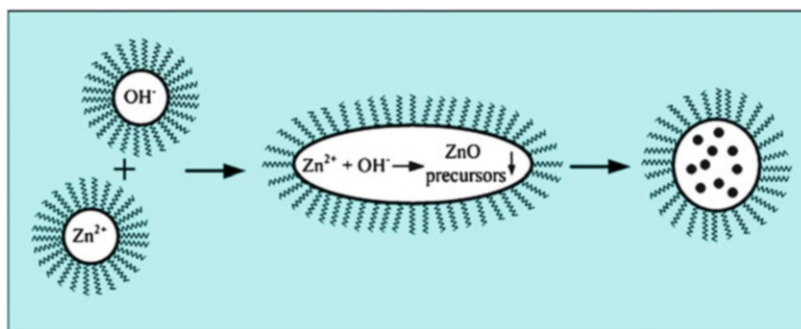


Fig. 3 Synthesis of ZnO precursor by microemulsions dispersed in an oil phase. Reprinted from [90], Copyright 2014, with permission from Elsevier

effects of Zn^{2+} concentration, reaction temperature, and feed flow rate on the average particle size of ZnO nanoparticles and at optimal conditions, ZnO nanoparticles with average size of 16 nm were obtained [90].

2.1.4 Chemical Precipitation

Chemical precipitation is also one of the important chemical methods used by researchers to synthesize various nanoparticles, including semiconductor nanoparticles. Kripal et al. [91] synthesized ZnO nanoparticles by a simple co-precipitation method using thioglycerol as a capping agent and methanol as solvent. The powder sample was divided into two parts; one was kept at room temperature and the other was annealed at 300°C for 3 h. Pure ZnO nanoparticles and ZnO nanoparticles doped with 5 mol% of Ag, 5 mol% of Co individually doped and co-doped (Ag, Co) were synthesized by a simple chemical co-precipitation method and their structural, morphological and optical properties and antibacterial activity studied. The crystal structure and grain size were characterized by X-ray diffractometry and revealed that all synthesized ZnO samples had hexagonal structures and that the sizes of the ZnO nanoparticles were 23, 20, 17 and 25 nm for undoped ZnO, ZnO doped with 5 mol% Co, doped with 5 mol% Ag and co-doped with Ag and Co, respectively [92]. Naje et al. [93] carried out synthesis of SnO_2 tetragonal rutile nanoparticles of 8–10 nm size by a chemical precipitation method at 550°C. Rutile titanium dioxide nanopowders doped with different amounts of Fe ions were prepared by co-precipitation. Doping with Fe ions greatly influenced the optical properties of the host material. Reflection measurements showed that doping of TiO_2 with Fe^{3+} causes a shift of the absorption threshold towards the visible spectral region [94]. A number of other studies on the synthesis of semiconductor nanoparticles by chemical precipitation have also been reported [95–105].

2.1.5 Other Methods

There are certain other methods available for the synthesis of semiconductor nanoparticles such as sol–gel autocombustion, spray pyrolysis, electrochemical, solid state metathesis and chemical aerosol synthesis. Sol–gel autocombustion synthesis of samarium-doped TiO_2 nanoparticles and their photocatalytic activity under visible light irradiation was investigated by Xiao et al. [106] and the results showed a high photocatalytic activity of Sm^{3+} -doped TiO_2 nanoparticles. Didenko et al. [107] reported chemical aerosol flow synthesis of high quality fluorescent CdS, CdSe and CdTe nanoparticles. Treece et al. [108] carried out synthesis of III–V semiconductors by solid state metathesis. The general reaction scheme is given by:



where $M = \text{Al, Ga, In}$; $X = \text{F, Cl, I}$; and $\text{Pn} = \text{Pnictogen} = \text{P, As, Sb}$. The reaction has been used to synthesize crystalline powders of III–V semiconductors. Hwang et al. [109] investigated the Li reaction behaviour of GaP nanoparticles prepared by a sodium naphthalenide reduction method. During the first discharge reactions, lithium intercalated Li_2GaP and irreversible Li_nP_7 phases were formed. Li_2GaP was only stable above 0.36 V, after which it decomposed to Li_xGa and electrochemically inactive Li_nP phases. Overall, the reversible capacity contribution (~ 800 mAh/g) was from the reversible phase transformation between the Li_xGa and Ga phases. A number of other methods such as combustion of silane, ultrasonic reduction, thermolysis, gas-aerosol, phase solution reaction and arrested precipitation have also been reported in the literature for synthesis of group IV [Si (silica coated), Ge], group III–V (GaN, GaP, GaAs, InP, etc.) and group II–VI (CdS, CdSe, ZnO, CdTe, etc.) semiconductor nanoparticles [110–122].

2.2 Quantum Dots

Quantum dots (QDs) are nanosized semiconductor particles of group II–VI or III–V main group elements with diameters of less than 10 nm [123]. These were first characterized in 1983 by Brus [124] as small semiconductor spheres in a colloidal suspension. QDs due to their nanoscale dimensions are subject to strong quantum confinement, which results in unique optical properties. Thus, in the last two decades, synthesis of QDs has attracted a lot of attention and generated a large number of publications [125]. A variety of methods have been proposed and implemented for synthesis of QDs. Of these methods, colloidal synthesis is the most accessible method for producing QDs suspended in solution. Colloidal synthesis of CdSe QDs is shown in Fig. 4. A cadmium compound is heated to 320°C

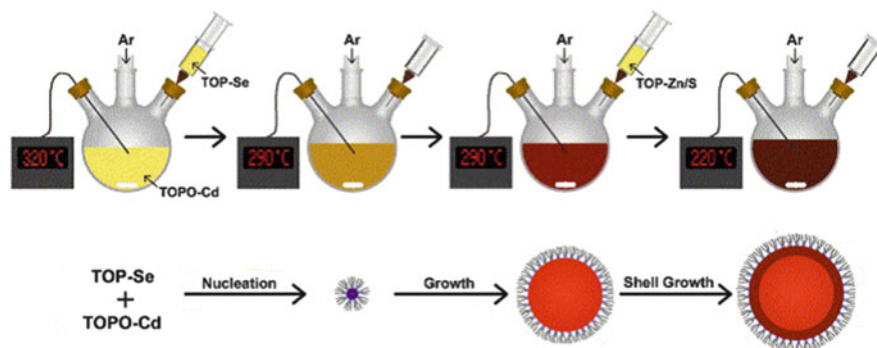


Fig. 4 Colloidal synthesis of CdSe quantum dots. *TOP* trioctylphosphine, *TOPO* trioctylphosphine oxide. Reprinted from [126], Copyright 2004, with permission from Elsevier

and dissolved in an organic solvent. A room temperature selenium compound dissolved in a different organic solvent is injected into the reaction vessel, causing supersaturation of the resultant CdSe solution. As the temperature drops to around 290°C, nucleation of new crystals stops and existing crystals grow. After a period of growth, the length of which determines the size of the QDs, the solution is cooled to 220°C, stopping growth. A small amount of zinc sulfide is injected into the reaction vessel to coat the QDs and prevent them from reacting with the environment [126].

Madler et al. [127] carried out synthesis of stable ZnO nanocrystallites down to 1.5 nm in diameter by spray combustion of Zn/Si precursors. These crystallites exhibited a quantum size effect: a blue shift of light absorption with decreasing crystallite size and the wet-phase-made ZnO QDs nicely followed a correlation between particle size and optical energy gap from the literature.

High aspect ratio cadmium sulfide (CdS) quantum rods were synthesized at room temperature in the environment of water-in-oil microemulsions by using mixture of two surfactants, i.e. AOT and the zwitterionic phospholipid L- α -phosphatidylcholine (lecithin). These highly acicular particles, obtained from a water-in-oil microemulsion containing an equimolar mixture of AOT and lecithin, possess an average width of 4.1 ± 0.6 nm, with lengths ranging from 50 to 150 nm. In contrast, conventional spherical CdS quantum dots are obtained from the AOT water-in-oil microemulsion system, with an average particle diameter of 5.0 ± 0.6 nm [128]. Cirillo et al. [129] reported the “flash” synthesis of CdSe/CdS core-shell QDs. This new method, based on a seeded growth approach and using an excess of a carboxylic acid, led to an isotropic and epitaxial growth of a CdS shell on a wurtzite CdSe core. The method is particularly fast and efficient, allowing the controllable growth of very thick CdS shells (up to 6.7 nm in that study) in no more than 3 min, which is considerably less than in previously reported methods (Fig. 5). Several other studies have been reported on semiconductor QDs. [130–137].

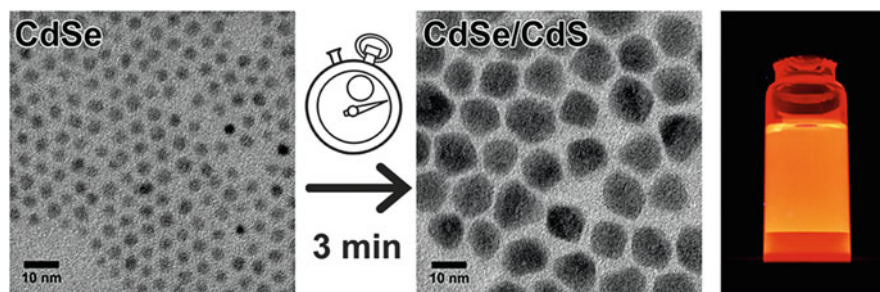


Fig. 5 Flash synthesis of CdSe/CdS core-shell quantum dots. Reprinted from [129], Copyright 2013, with permission from American Chemical Society

2.3 Properties of Semiconductor Nanoparticles

Semiconductor nanoparticles exhibit size-dependent unique optical and electronic properties that are different from their bulk counterpart due to quantum confinement. Bulk semiconductor crystal is considered as one large molecule, and electronic excitation of semiconductor crystals generates an electron-hole pair. The size of the delocalization area of this electron-hole pair is generally many times larger than the lattice constant. Decrease in the size of a semiconductor crystal down to a size comparable with the delocalization area of the electron-hole pair or to that of the Bohr excitonic radius of those materials modifies the electronic structure of the nanocrystals. When the particle radius decreases below the Bohr excitonic radius, there is widening in the energy band gap, which results in a blue shift in the excitonic absorption band of a semiconductor crystal. For example, in CdS semiconductor material, the blue shift of the excitonic absorption band is observed to begin at a crystal size of 5–6 nm [138–141].

Moreover, the surface state also plays a very important role in the nanoparticles, due to their large surface area-to-volume ratio, with a decrease in particle size (surface effects). In the case of semiconductor nanoparticles, radiative or nonradiative recombination of an exciton at the surface states becomes dominant in its optical properties with a decrease in particle size. Therefore, the decay of an exciton at the surface states will influence the qualities of the material for an optoelectronic device. Ultrasmall semiconductor crystals are known in the literature as nanocrystals, particles with quantum size effect or nanoparticles [141].

Attributed to the energy band structure of the semiconductor and the nanosize, semiconductor nanoparticles or QDs also exhibit photoluminescence (PL) properties, as illustrated in Fig. 6. QDs have discrete energy levels in both the valence band (VB) and the conduction band (CB). When the excitation energy (E_{ex}) is higher than the bandgap energy (E_g), electrons (represented by the solid circle in Fig. 6) in the valence band absorb the energy and ‘jump’ to the conduction band, forming short-lived electron-hole pairs or excitons. Electrons and holes (represented by the open circles in Fig. 6) may then recombine quickly, emitting photons with a specific energy that corresponds to the band gap, which is the band-edge emission. Because part of the energy may be released in a nonradiative way due to the Stokes shift (ΔE), the emission energy (E_{em0}) is usually lower than the excitation energy. When there are some trap states existing in the band gap, more possible emissions can happen with various energies (i.e. E_{em1} , E_{em2} , E_{em3} , E_{em4}), which are usually lower than the bandgap emission energy (E_{em0}). Luminescence may result from band-edge or near band-edge transitions [142].

The spectral position of the emission band of CdSe nanocrystals does not shift considerably during the growth of the ZnS shell, showing that in the excited state both electron and hole remain confined to the CdSe core. Using CdSe nanocrystals of different sizes for growing the core-shell particles, a series of colloidal solutions emitting from blue to red. with the emission band as narrow as 25–35 nm (FWHM) and room temperature photoluminescence quantum yield as high as 50–70%, have been synthesized (Fig. 7). In fact, the ZnS epitaxial shell can also be grown at the

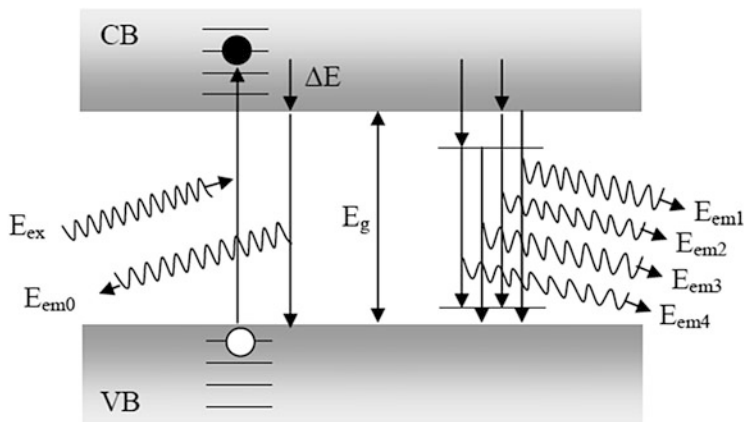


Fig. 6 Excitation and emission of quantum dots with the typical energy band structure of semiconductor. Reprinted from [142], Open access 2008



Fig. 7 Size-dependent change of the emission colour of colloidal solutions of CdSe/ZnS core-shell nanocrystals. The particles with the smallest (~ 1.7 nm) CdSe core emit blue; the particles with the largest (~ 5 nm) core emit red. Reprinted from [143], Copyright 2004, with permission from John Wiley and Sons

surface of CdSe nanorods, providing highly luminescent nanocrystals with polarized emission [143]. Diluted magnetic semiconductor nanoparticles also exhibit magnetic properties with electronic and optical properties. A number of studies on size-dependent optical, electronic and magnetic properties of various semiconductor nanoparticles have been reported in the literature [144–149].

2.4 Applications of Semiconductor Nanoparticles

Semiconductor nanoparticles and QDs are widely used in various fields such as luminescent biolabels [150–152] and have been demonstrated as components in regenerative solar cells [153–155], optical gain devices [24] and electroluminescent devices [23, 156, 157]. DMS have applications in spin-based electronics technologies, or spintronics [158–161]. Spintronic devices such as magnetic-optic switches, magnetic sensors, spin valve transistors and spin LEDs can be activated by implanting ferromagnetic Mn, Ni, Co and Cr in semiconductors [162–165]. Some of the applications of semiconductor nanoparticles or QDs have been explained in this section.

2.4.1 Environmental Applications

Group II–VI semiconductor nanoparticles such as TiO_2 and ZnO have emerged as promising photocatalysts for water purification [166, 167]. They can serve both as oxidative and reductive catalysts for organic and inorganic pollutants. The removal of total organic carbon from waters contaminated with organic wastes was greatly enhanced by the addition of TiO_2 nanoparticles in the presence of UV light, as shown by Chitose et al. [168]. Yang et al. [169] investigated the effect of the pH of the solution, H_2O_2 addition, TiO_2 phase composition and recycled TiO_2 on the photocatalytic degradation of methyl orange in TiO_2 suspensions under UV illumination. The results indicate that a low pH value, proper amount of H_2O_2 and pure anatase TiO_2 facilitate the photocatalytic oxidation of the methyl orange solution. The degree of photodegradation decreases with increasing pH of the solution and varies with different amounts of H_2O_2 . Pure anatase TiO_2 shows better photocatalytic activity for methyl orange decolorization than biphasic TiO_2 .

Adsorption and photocatalytic reduction of toxic mercury(II) from aqueous solutions at different pH values were investigated with the synthesized TiO_2 nanoparticles [170]. The experimental results showed that the removal of mercury(II) in aqueous solutions was increased with an increase of pH in the range of 3.0–7.0. Mercury(II) removal was more than 65% by TiO_2 nanoparticles after 30 min under UV illumination. Daneshvar et al. [171] and Rahman et al. [172] used ZnO nanoparticles as photocatalysts for effective photocatalytic degradation of azo dye acid red 14 and rhodamine B dye. Devipriya and Yesodharan [173] carried out photocatalytic degradation of chemical pollutants in water using semiconductor oxide catalysts, (ZnO and TiO_2) and phenol as the substrate. The authors studied the influence of various parameters such as the characteristics of the catalyst, irradiation time, substrate and catalyst concentrations and pH on the degradation of phenol in water. In terms of activity and durability, TiO_2 is far superior to ZnO. Mixing ZnO with TiO_2 does not affect its activity significantly. The process is especially relevant in view of its potential for the treatment of wastewater containing pollutants, using solar radiation as the energy source.

Mahdavi et al. [174] investigated the removal of Cd^{2+} , Cu^{2+} , Ni^{2+} and Pb^{2+} from aqueous solutions with novel nanoparticle sorbents (Fe_3O_4 , ZnO and CuO) using a range of experimental approaches, including pH, competing ions, sorbent masses and contact time. The maximum uptake values (sum of four metals) in multiple component solutions were 360.6, 114.5 and 73.0 mg g^{-1} for ZnO , CuO and Fe_3O_4 , respectively. Based on the average metal removal by the three nanoparticles, the following order was determined for single-component solutions: $\text{Cd}^{2+} > \text{Pb}^{2+} > \text{Cu}^{2+} > \text{Ni}^{2+}$, whereas the following order was determined in multiple-component solutions: $\text{Pb}^{2+} > \text{Cu}^{2+} > \text{Cd}^{2+} > \text{Ni}^{2+}$. A number of other studies have been reported on the photocatalytic degradation of dyes, phenols, benzoic acid and removal of other pollutants such as heavy metal ions using group III–V semiconductor nanoparticles [175–183].

2.4.2 Electronic and Optoelectronic Applications

Semiconductor nanoparticles, as a result of their size-dependent electronic and optical properties, are promising materials for electronic and optoelectronic applications such as light-emitting devices, photovoltaic or solar cells, gas sensors, liquid crystal displays, heat mirrors and surface acoustic wave devices [184, 185]. Gallium nitride (GaN)-based semiconductor devices find application in LEDs, which operate in the blue and green wavelength regions. GaN-based LEDs have attracted interest for use in full-colour display panels and solid-state lighting [186] because they have advantages such as low energy consumption, long lifetime and relatively small size compared with conventional planar LEDs where the light extraction efficiency is limited by several factors including the high refractive index of p-type GaN (p-GaN) (approximately 2.52), leading to a low total internal reflection angle [187]. Thus, to enhance the output light power, various strategies such as surface texturing [188, 189], photonic crystals [190–192] and use of metal oxide nanoparticles [193–196] have been studied.

Jin et al. [197] fabricated gold (Au) nanoparticles on the surface of p-GaN to enhance the output power of the light from GaN-based LEDs. Quasi-aligned Au nanoparticle arrays were synthesized by depositing Au thin film on an aligned suspended carbon nanotube (CNT) thin film surface and then putting the Au-CNT system on the surface of p-GaN and thermally annealing the sample. The size and position of the Au nanoparticles were confined by the carbon nanotube framework, and no other additional residual Au was distributed on the surface of the p-GaN substrate. The output power of the light from the LEDs with Au nanoparticles was enhanced by 55.3% for an injected current of 100 mA, with the electrical properties unchanged compared with conventional planar LEDs.

A light-emitting device with commercially available ZnO nanoparticles as an active layer was realized without the help of organic support layers. A tight ZnO nanoparticle layer with thickness of 500 nm was spin-coated on top of an indium tin oxide fused silica substrate. After evaporation of a top aluminium electrode, diode-like I – V characteristics and a pronounced electroluminescence in the visible

spectral range were obtained [198]. Many studies have been reported on fabrication of luminescent semiconductor nanocrystals into thin film polymer-based LEDs as emitting materials [13, 14, 199–201]. The use of CdSe/CdS core–shell nanocrystals in combination with optimized layer thickness allowed the achievement of external quantum efficiencies of up to 0.22% at a brightness of 600 cd/m² [199], which is close to a realistic specification for LED applications. Recently, a device emitting in the near-IR spectral region with an external efficiency of ~0.5% based on InAs/ZnSe core–shell nanocrystals has been reported [4]. Another strategy for the fabrication of LEDs is based on the use of aqueous thiol-capped CdTe nanocrystals assembled via the layer-by-layer technique [13] or integrated into a polyaniline or polypyrrole semiconducting matrix [14, 202].

A solar cell is a detector that has to convert a broad incoming spectrum into an electric current, with a minimum amount of loss. Solar cells based on low-cost poly- and nanocrystalline semiconductor materials have gained great interest for both scientific and industrial purposes. Earlier solar cells consisted of a large silicon *p-n* junction, for which solar cell efficiency was a theoretical maximum of 33.7% [203, 204]. GaAs semiconductors have also been used in solar cell applications. This is illustrated in Fig. 8 for a solar cell that is built up from Ga_{0.49}In_{0.51}P (1.9 eV), Ga_{0.99}In_{0.01}As (1.4 eV) and Ge (0.7 eV) [205]. Recently, a modern version of solar cells called Grätzel-type cells have emerged. These types of cells are formed by sensitization of wide-bandgap semiconductors, mainly highly porous nanocrystalline TiO₂, with organic dyes that absorb visible light and inject electrons into the conduction band of TiO₂ (so-called Grätzel cells) [206]. Semiconductor nanoparticles have a number of potential advantages as light-absorbing materials in Grätzel-type cells and efficient charge transfer from the nanocrystals to the conduction band of wide-bandgap semiconductors (TiO₂, ZnO, Ta₂O₅) [207–209] in combination with high extinction coefficients in the visible spectral range [210] makes them attractive for applications in Grätzel-type cells.

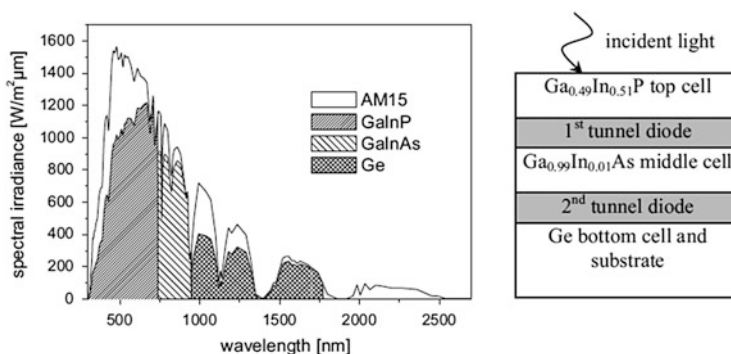


Fig. 8 *Left*: Spectral irradiance of the solar AM1.5 spectrum together with the parts of the spectrum that can be utilized by a GaInP/GaInAs/Ge 3-junction solar cell. *Right*: General structure of the solar cell. Reprinted from [205], Copyright 2006, with permission from John Wiley and Sons

Omar et al. [211] studied the influence of the organic dyes Orange IV and Eosin Y as photosensitizers on the photovoltaic parameters of ZnO photoelectrode dye-sensitized solar cells (DSSCs) and reported that the Orange IV-sensitized cell showed better performance than the cell sensitized with the Eosin Y. This happened because of the higher molar extinction coefficient of Orange IV dye. Lee et al. [212] investigated the performance of DSSCs consisting of anatase TiO₂ using electron transport and optical characterization. They studied the effect of particle size distribution on the performance of DSSC by comparing synthesized TiO₂ nanoparticles and commercial TiO₂ nanoparticles (P25) and found that the synthesized nanoparticles significantly enhanced the photovoltaic conversion efficiency by 32.5% because of a larger specific surface area, higher electrolyte penetration ability and lower optical reflectance than P25. Therefore, the photoelectrode of the synthesized TiO₂ nanoparticles enhanced the adsorption of dye sensitizers (N719), promoted the transfer of photo-generated carriers and decreased the ratio of reflected solar spectrum that is not harnessed. As a result, the energy conversion efficiency of DSSCs increased to 6.72% without the use of a scattering layer and co-adsorbants. The authors also reported that an increase in the aspect ratio of the synthesized nanomaterials resulted in an increase in carrier lifetime. Furthermore, a decrease in the density of grain boundaries suppressed the trapping of carriers and the subsequent recombination of electron-hole pairs. Thus, these nanomaterials provide a way to achieve an appreciable efficiency of photoconversion devices.

Sensors based on nanoparticle-decorated ZnO microdisks exhibited high response values, fast response recovery, good selectivity and long-term stability against 1–4,000 ppm acetylene at 420°C. In addition, even 1 ppm acetylene could be detected with high response ($S = 7.9$). The hierarchical structure can facilitate fixation of the ZnO nanoparticles, leading to a less aggregated configuration, which is expected to contribute to the excellent acetylene-sensing properties at high temperatures. The structure and photograph of an as-fabricated sensor are shown in Fig. 9a and inset of Fig. 9b, respectively [213].

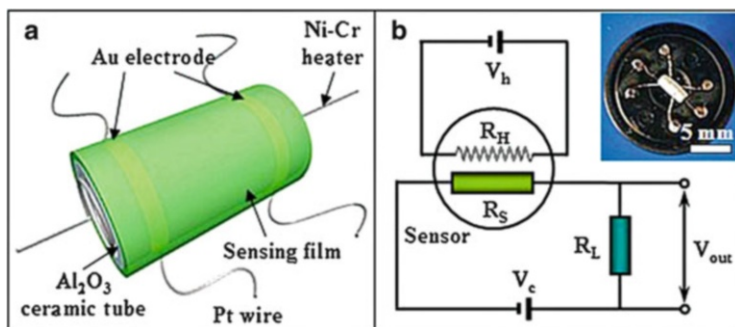


Fig. 9 (a) Gas sensor structure. (b) The measuring electric circuit of the gas sensor. *Inset*: Photograph of an as-prepared sensor. Reprinted from [213], Copyright 2011, with permission from Elsevier

2.4.3 Biomedical Applications

Semiconductor nanoparticles and QDs have been widely used in biomedical applications such as diagnosis, imaging, drug delivery and tumour treatment. Semiconductor nanoparticles that are less than 10 nm in size (known as QDs) have proved to be especially biocompatible and are widely used as carriers with integrated functionalities for in-vivo imaging, as tags for other drug carriers, tumour cell markers, bimodal molecular imaging, immunoassay, detection of viral infections and so on [214–219].

Hanley et al. [220] carried out preferential killing of cancer cells and activated human T cells using ZnO nanoparticles. They found that ZnO nanoparticles exhibit a strong preferential ability to kill cancerous T cells (approximately 28–35 \times) as compared to normal cells. The activation state of the cell contributes toward nanoparticle toxicity, as resting T cells displayed a relative resistance whereas cells stimulated through the T cell receptor and CD28 co-stimulatory pathway showed greater toxicity in direct relation to the level of activation. Toxicity occurs due to generation of reactive oxygen species, with cancerous T cells producing higher inducible levels than normal T cells. In addition, nanoparticles were found to induce apoptosis, and the inhibition of reactive oxygen species was found to be protective against nanoparticle-induced cell death. These results indicate a potential utility of ZnO nanoparticles in the treatment of cancer and/or autoimmunity.

Zhang and Sun [221] investigated the photocatalytic killing effect of TiO₂ nanoparticles on Ls-174-t human colon carcinoma cells. The authors reported that cultured human colon carcinoma cells were effectively killed by photo-excited TiO₂ nanoparticles in vitro. Further, they found that high concentrations of TiO₂ affected the photocatalytic killing effect. When the concentration of TiO₂ was below 200 $\mu\text{g}/\text{mL}$, there was only a slight decrease in survival ratio after UVA irradiation for more than 30 min. It was almost the same as that of UVA irradiation alone. But, with an increase in TiO₂ concentration to above 200 $\mu\text{g}/\text{mL}$, the survival ratio decreased rapidly. This indicated that major rupture of cell membranes and decomposition of essential intracellular components was taking place, thus accelerating cell death. The photocatalytic killing effect of TiO₂ nanoparticles on human colon carcinoma cells suggests that TiO₂ nanoparticles and light irradiation could be used for cancer treatment.

Cervera et al. [222] studied the controlled release of phenytoin, which is an anticonvulsant drug for the treatment of epilepsy, from nanostructured TiO₂ reservoirs. They loaded the TiO₂ reservoirs with 5 wt% phenytoin, and studied the release kinetics in a pH 7.2 buffer by measuring the ultraviolet–visible (UV–vis) absorbance spectrum as a function of time. The authors also explored the relationship between the phenytoin release rate and the properties of the TiO₂ nanomaterials used in the preparation of the reservoir. The results showed that the reservoirs are capable of releasing phenytoin for more than 45 days, and that the release kinetics are characterized by two regimes: an initial fast release and a subsequent slow release. The slow release rate is independent of time and showed

a weak dependence on the morphology of the nanomaterial. The phenytoin constant release rate was found to be between 0.017 and 0.030 mg/day, depending on the properties of the nanomaterial. Zhang and Wang [223] described the use of QDs for molecular sensing and diagnostics applications. Baba and Nishida [224] reviewed different techniques for employing QDs for single-molecule tracking in living cells. Clift and Stone [225] focused on the biological interaction of QDs and their relevance to clinical use. Yong et al. [226] reported the recent development of QD–drug nanoparticle formulations for traceable targeted delivery and therapy applications. They also discussed different “packaging” methods for preparing QD–drug formulations.

3 Polymer Composites with Semiconductor Nanoparticles

3.1 *Synthesis of Semiconductor–polymer Nanocomposites*

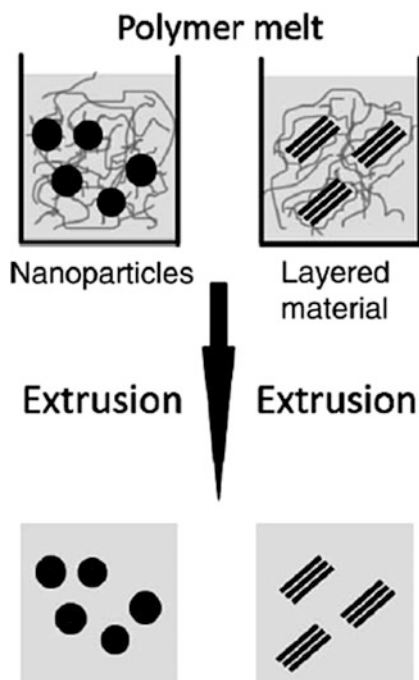
In recent years, the development of semiconductor–polymer nanocomposite materials has become an important research area of nanoscience and nanotechnology as these nanocomposites combine the advantageous properties of polymers with the unique size-tunable optical, electronic, catalytic, and other properties of semiconductor nanoparticles [227–229]. A number of methods are available for producing hybrids of polymers with semiconductor nanoparticles. Two widely used methods, i.e. melt blending and in-situ polymerization, for synthesis of semiconductor–polymer nanocomposites are discussed here.

3.1.1 Melt Blending

Melt blending is the most simple and conventional method for the synthesis of various polymer hybrids with inorganic nanoparticles, including semiconductor nanoparticles. In melt processing, inorganic nanoparticles are dispersed into the polymer matrix and then polymer nanocomposites are obtained by extrusion. Figure 10 shows a representation of melt blending for the synthesis of polymer nanocomposites [230].

Hong et al. [231] have used this simple technique for the synthesis of ZnO–low-density polyethylene composites. ZnO nanoparticles and branched low-density polyethylene was melt-compounded in a high-shear mixer to prepare polymer nanocomposites with an improved resistance to thermal degradation. They also mixed submicron-sized ZnO particles with low-density polyethylene for a comparison and reported that the surface properties of nanoparticles (<100 nm) resulted in an increased thermal stability of nanocomposites. Ma et al. [232] also used melt blending for the synthesis of silane-modified ZnO–polystyrene resin nanocomposites. Incorporation of ZnO nanoparticles results in an increased flexural

Fig. 10 Melt blending for preparation of nanocomposites. Reprinted from [230], Open access 2010



modulus, glass transition temperature and thermal degradation temperature and a low flexural strength of the synthesized nanocomposites. Melt-blended polymer nanocomposites were synthesized by dispersing ZnO quantum dots in a poly (methyl methacrylate) and the resulting nanocomposites were characterized by differential scanning calorimetry and dynamic mechanical analysis. A linear increase in glass transition temperature (T_g) suggested that the T_g of the system is described by a power law of the interparticle distance, hp , where the percolation exponent, ν , was 0.55–0.64 [233].

Isotactic polypropylene and TiO_2 were melt-blended to prepare nanocomposites containing 1–15 vol% (4.6–45.5 wt%) of the nanoparticles. The effect of an anhydride-modified polypropylene as a compatibilizer on the dispersion, mechanical properties, thermal stability and crystallinity of TiO_2 nanoparticles was studied. Scanning electron microscopy (SEM) results revealed an improved particle dispersion, which further significantly affected the thermal stability and crystalline structure of the nanocomposites. The elastic modulus and yield strength of nanocomposites were reduced. Micromechanical analysis showed an improved interaction between organic and inorganic phases of the compatibilized nanocomposites [234]. In another study, TiO_2 nanoparticles were pretreated with toluene-2,4-di-isocyanate and melt-blended with polypropylene/polyamide-6 blends (PP/PA6). Surface functionalization of TiO_2 nanoparticles results in an improved interfacial interaction and compatibility between TiO_2 and the polymer matrix. Nanocomposites with functionalized TiO_2 nanoparticles showed higher

tensile and impact strength in comparison to those filled with bare TiO_2 or pure PP/PA6 blends. They also exhibit strong antimicrobial activities against *Bacillus subtilis*, *Staphylococcus aureus* and *Escherichia coli* [235].

CdSe–CdS–ZnS core–multishell polymer nanocomposites were prepared by direct dispersion of CdSe–CdS–ZnS core–multishell QDs in an epoxy polymer matrix via a melt mixing technique. Nanocomposites filled with yellow-emitting QDs were more transparent than pure epoxy polymer. A shift in the luminescence of pure epoxy from the blue region to the yellow region was observed in the nanocomposite. Synthesized nanocomposites also showed enhanced tensile properties in comparison to pure epoxy polymer [236]. Several other studies reported the use of a melt blending process for the synthesis of semiconductor–polymer nanocomposites [237–241].

Melt processing of semiconductor nanoparticles in polymer melt may result in turbidity/translucency of the resulting composite materials due to strong tendency of nanoparticles to form aggregates [230]. The method of in-situ polymerization has been developed and widely used to overcome this problem.

3.1.2 In-Situ Polymerization

In this method, semiconductor nanoparticles are dispersed directly in monomeric solution prior to a polymerization process. Guan et al. [242] used this method for synthesis of transparent polymer nanocomposites with high ZnS nanophase contents using a one-pot route via in-situ bulk polymerization. Uniform distribution of ZnS nanoparticles in the polymer matrix was observed due to covalent bonding between ZnS nanoparticles and the polymer matrix. This uniform distribution improved the thermal stability and mechanical properties of the nanocomposite. The nanocomposites also exhibited good transparency and adjustable refractive index due to controlled structure and ZnS content.

2,2'-Azobisisobutyronitrile-initiated in-situ bulk polymerization of *N,N*-dimethylacrylamide, styrene and divinylbenzene in the presence of 2-mercaptoethanol (ME)-capped ZnS nanoparticles was carried out for the synthesis of transparent ZnS–polymer nanocomposites. Synthesized nanocomposites showed good mechanical properties and excellent thermal stability below 245°C. The refractive index of nanocomposites increased from 1.536 for the matrix to 1.584 with an increase in ME-capped ZnS nanoparticle content to 30 wt%, whereas the T_g of the nanocomposites decreased, probably due to the plasticizing effect of the nanoparticles [243]. PMMA– TiO_2 nanocomposites were synthesized by an in-situ free radical polymerization of methyl methacrylate with surface-modified TiO_2 nanoparticles. The thermal stability of nanocomposite was significantly improved by incorporation of nanoparticles into the polymer matrix [244]. Evora and Shukla [245] used in-situ polymerization for the synthesis of polyester– TiO_2 nanocomposites and investigated the quasi-static fracture toughness, tension, compression testing and dynamic fracture toughness properties. The fracture toughness and dynamic fracture toughness relative to the quasi-static fracture toughness of the

nanocomposites was increased [245]. In-situ polymerization was used to synthesize poly(ethylene terephthalate)-TiO₂ nanocomposites and a homogeneous dispersion of nanoparticles was observed with TiO₂ content of <2 wt%. Nanoparticles provided an improvement in modulus, strength and elongation break of nanocomposites at rather low filler content [246]. Zapata et al. [247] carried out in-situ polymerization for the synthesis of TiO₂-polyethylene composites with 2 and 8 wt% filler content. The crystallinity of the composites was increased slightly when the different nanofillers were added and the elastic modulus increased up to 15% in comparison with neat polyethylene.

Polyaniline-ZnO nanocomposites were synthesized by in-situ oxidative polymerization of aniline monomer in the presence of different amounts of ZnO nanostructures. ZnO nanostructures were prepared in the absence and presence of surfactant. The effect of ZnO nanostructure concentration on the conducting behaviour of nanocomposites was evaluated by a two-probe method. The results showed that the conductivity of nanocomposites was increased with an increased concentration of ZnO nanostructures as compared with neat polyaniline. Optimum conductivity was observed with incorporation of 60% ZnO nanostructures into the polyaniline matrix [248]. Polymethylmethacrylate-ZnO nanocomposites were fabricated by solution radical copolymerization of methyl methacrylate and oleic acid-modified ZnO nanoparticles using 2,2'-azobisisobutyronitrile as initiator in toluene. The UV-vis analysis showed that resulting nanocomposites exhibited high absorption in the ultraviolet region and low absorption in the visible region [249].

Hybrid materials of SnO₂ hollow spheres and polythiophene were synthesized by an in-situ chemical oxidative polymerization method. A strong synergetic interaction between SnO₂ and polythiophene was observed and the synthesized nanocomposite had higher thermal stability than pure polythiophene [250]. Two types of polyurethane-indium tin oxide (ITO) nanocomposites, i.e. optically active polyurethane@indium tin oxide and racemic polyurethane@indium tin oxide nanocomposites, were synthesized by graft polymerization of organics onto the surfaces of silane-modified ITO nanoparticles. Polyurethane was successfully grafted onto the surfaces of ITO without destroying the crystalline structure. Both the composites were observed with lower infrared emissivity values than the bare ITO nanoparticles due to the interfacial interactions. Furthermore, optically active polyurethane@indium tin oxide nanocomposites exhibited lower infrared emissivity value as a result of the regular secondary structure and more interfacial synergistic interactions between organics and inorganics, as compared with racemic polyurethane-ITO nanocomposites. Figure 11 shows the method of synthesis for optically active polyurethane-ITO nanocomposites and the racemic polyurethane-ITO nanocomposite was synthesized in a similar way [251]. WO₃-polythiophene nanocomposites were prepared by in-situ polymerization of adsorbed thiophene monomers on the surface of a WO₃ framework [252].

In-situ polymerization technique was used by several researchers for the synthesis of QD-polymer nanocomposites [253-255]. Lee et al. [256] carried out synthesis of highly luminescent CdSe-poly(lauryl methacrylate) nanocomposites by in-situ bulk radical polymerization. Currently, researchers are also using

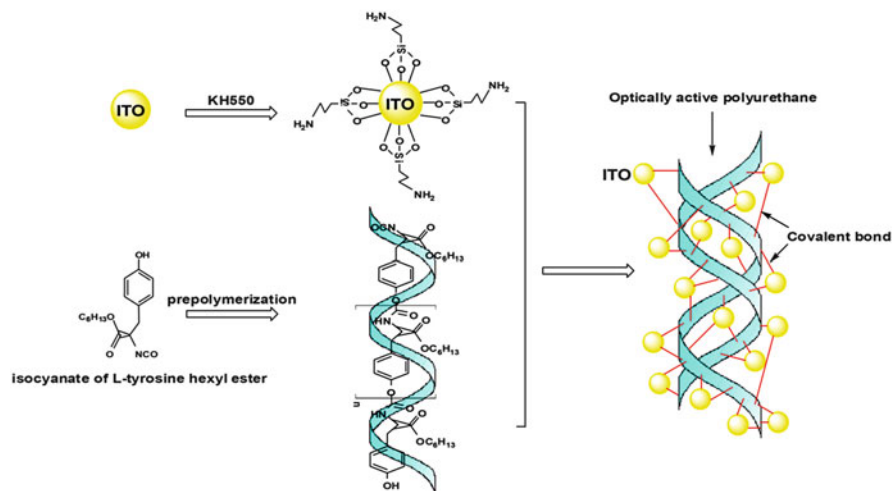


Fig. 11 Preparation of optically active polyurethane–indium tin oxide (ITO) nanocomposite. Reprinted from [251], Copyright 2012, with permission from Elsevier

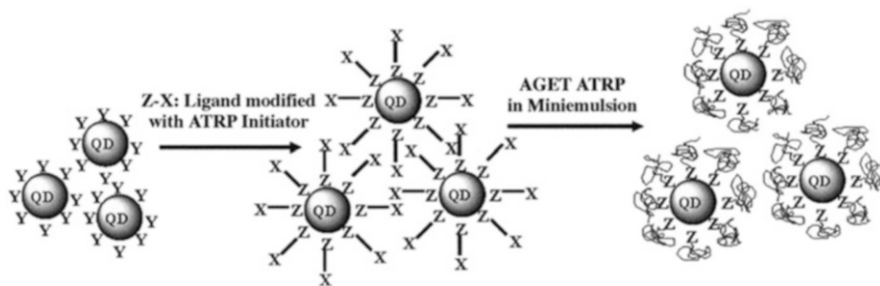


Fig. 12 Synthetic strategy for the preparation of QD–polymer nanocomposites by AGET ATRP in miniemulsion. Reprinted from [258], Copyright 2007, with permission from John Wiley and Sons

mini-emulsion polymerization for the polymer encapsulation of inorganic materials because of its ability to yield well-dispersed nanocomposite materials [257]. Esteves et al. [258] synthesized QD–polymer nanocomposites by grafting polymer chains directly from the surface of functionalized QDs [with trialkylphosphine oxide (Y) modified with a chlorine-based atom transfer radical polymerization (ATRP) initiator (Z–X)] (Fig. 12). The authors used a recently developed catalytic system termed activators generated by electron transfer (AGET) for the synthesis of these nanocomposites [259, 260]. AGET ATRP in a miniemulsion avoids the use of conventional radical initiators that can degrade the QDs and also initiate free polymer chains. Joumaa et al. [261] successfully encapsulated individual CdSe–ZnS–trioctylphosphine oxide (TOPO) nanocrystals in polystyrene beads by using a similar miniemulsion approach. A number of researchers have used the in-situ

Table 1 Some potential applications of semiconductor–polymer nanocomposites

Nanocomposites	Applications	References
High-density polyethylene/TiO ₂	Bone repair	[269]
Poly(amide-imide)/TiO ₂	Composite membranes for gas separation	[270]
Low density polyethylene/ZnO/Ag	Orange juice packaging	[271]
Polyaniline/ZnO	Chemical vapour sensing	[272]
Polyethylene/TiO ₂	Antimicrobial	[235]
Polymer/CdSe nanocrystal	Selective vapour sensing	[273]
Polymethylmethacrylate/CdSe	Gas nanosensors	[274]
Polythiophene/SnO ₂	Gas sensing	[275]
CdSe quantum dot/PMMA	Hydrocarbon sensor	[276]
Polymer/ZnO	Anticancer drug delivery	[277]
Hybrid polymer/TiO ₂	Solar cells	[278]

polymerization method for the synthesis of a variety of semiconductor–polymer nanocomposites [262–268].

3.2 Applications of Semiconductor–Polymer Nanocomposites

Semiconductor–polymer nanocomposites have wide range of applications in various fields, including environmental, sensors, solar cells and biomedical applications. Some potential applications of semiconductor–polymer nanocomposites are listed in Table 1.

Conclusions

Semiconductor–polymer hybrids are an important class of materials because of their combined properties of polymers and semiconductor nanoparticles. A number of methods are available for the synthesis of semiconductor–polymer hybrids from semiconductor nanoparticles, such as melt blending and in-situ polymerization. Semiconductor–polymer hybrids find applications in environmental, optoelectronic, biomedical and various other fields.

References

1. Henglein A (1982) *J Phys Chem* 86:2291
2. Rossetii R, Nakahara S, Brus LE (1983) *J Chem Phys* 79:1086
3. Tamborra M, Striccoli M, Comparelli R, Curri ML, Petrella A, Agostiano A (2004) *Nanotechnology* 15:5240
4. Tessler N, Medvedev V, Kazes M, Kan S, Banin U (2002) *Science* 295:1506

5. Klimov VL, Mikhailowsky AA, Xu S, Malko A, Hallingsworth JA, Leatherdole CA (2000) *Science* 290:340
6. Battaglia D, Peng X (2002) *Nano Lett* 2:1027
7. Abdulkhadar M, Thomas B (1995) *Nanostruct Mater* 5:289
8. Lee GJ, Nam HJ, Hwangbo CK, Lim H, Cheong H, Kim HS, Yoon CS, Min SK, Han SH, Lee YP (2010) *Jpn J Appl Phys* 49:105001
9. Lee GJ, Lee YP, Lim HH, Cha M, Kim SS, Cheong H, Min SK, Han SH (2010) *J Korean Phys Soc* 57:1624
10. Kamat PV, Meisel D (eds) (1996) *Semiconductor nanoclusters. Studies in surface science and catalysis*. Elsevier, Amsterdam, p 103
11. Weller H (1993) *Angew Chem Int Ed Engl* 32:41
12. Weller H (1993) *Adv Mater* 5:88
13. Gao MY, Lesser C, Kirstein S, Mohwald H, Rogach AL, Weller H (2000) *Appl Phys* 87:2297
14. Gaponik NP, Talapin DV, Ro-Gach AL, Eychmuller A (2000) *J Mater Chem* 10:2163
15. Pileni MP (1993) *J Phys Chem* 97:6961
16. Pileni MP (1997) *Langmuir* 13:3266
17. Korgel A, Monbouquette HG (1996) *J Phys Chem* 100:346
18. Spanhel L, Hasse M, Weller H, Henglein A (1987) *J Am Chem Soc* 109:5649
19. Vossmeier T, Katsikas L, Giersig M, Popovic IG, Diesner K, Chemseddine A, Eychmuller A, Weller H (1994) *J Phys Chem* 98:7665
20. Rockenberger J, Troger L, Kornowski A, Vossmeier T, Eychmuller A, Feldhaus J, Weller W (1997) *J Phys Chem B* 101:2691
21. Murray AB, Norris DJ, Bawendi MG (1993) *J Am Chem Soc* 115:8706
22. Diaz B, Rivera M, Ni T, Rodriguez JC, Castillo-Blum SE, Nagesha D, Robles J, Alvarez-Fregoso OJ, Kotov NA (1999) *J Phys Chem B* 103:9854
23. Colvin VL, Schlamp MC, Alivisato AP (1994) *Nature* 370:354
24. Klimov VI, Mikhailovsky AA, Xu S, Malko A, Hollingsworth JA, Leatherdale CA, Eisler HJ, Bawendi MG (2000) *Science* 290:314
25. Ozgur U, Alivov YI, Liu C, Teke A, Reshchikov MA, Dogan S, Avrutin V, Cho SJ, Morkoc H (2005) *J Appl Phys* 98:041301
26. Djuricic AB, Leung YH (2006) *Small* 2:944
27. Chan SW, Barille R, Nunzi JM, Tam KH, Leung YH, Chan WK, Djuricic AB (2006) *Appl Phys B* 84:351
28. Voss T, Kudyk I, Wischmeier L, Gutowski J (2009) *Phys Status Solidi B* 246:311
29. Cho S, Ma J, Kim Y, Sun Y, Wong GKL, Ketterson JB (1999) *Appl Phys Lett* 75:2761
30. Williams JV (2008) *Hydrothermal synthesis and characterization of cadmium selenidenano-crystals*. Doctoral thesis, University of Michigan
31. Gopinadhan K, Kashyap SC, Pandya DK, Chaudhary S (2007) *J Appl Phys* 102:113513
32. Vadivel K, Arivazhagan V, Rajesh S (2011) *Int J Sci Eng Res* 2(4):43–47 http://www.ijser.org/Journal_April_2011_Edition.pdf
33. Kant KM, Sethupathi K, Rao MSR (2004) *Magnetic properties of 4f element doped SnO₂*. Paper presented at the international symposium of research students on materials science and engineering, Chennai, India, 20–22 Dec 2004
34. Santi M, Jakkapon S, Chunpen T, Jutharatana K (2006) *J Magn Magn Mater* 301:422
35. Lakshmi YK, Srinivas K, Sreedhar B, Raja MM, Vithal M, Reddy PV (2009) *Mater Chem Phys* 113:749
36. Jiang Y, Wang W, Jing C, Cao C, Chu J (2011) *Mater Sci Eng B* 176:1301
37. Li X, Wu S, Hu P, Xing X, Liu Y, Yu Y, Yang M, Lu J, Li S, Liu W (2009) *J Appl Phys* 106:043913(1)
38. Gan'shina EA, Granovsky AB, Orlov AF, Perov NS, Vashuk MV (2009) *J Magn Magn Mater* 321:723
39. Ianculescu A, Gheorghiu FP, Postolache P, Oprea O, Mitoseriu L (2010) *J Alloys Compd* 504:420

40. Gingasu D, Oprea O, Mindru I, Culita DC, Patron L (2011) *Digest J Nanomater Biostruct* 6:1215
41. Zhang K, Zhang X, Chen H, Chen X, Zheng L, Zhang J, Yang B (2004) *Langmuir* 20:11312
42. Qin J (2007) Nanoparticles for multifunctional drug delivery systems. Licentiate thesis, The Royal Institute of Technology, Stockholm
43. Vafae M, SasaniGhamsari M (2007) *Mater Lett* 61:3265
44. Behnajady MA, Eskandarloo H, Modirshahla N, Shokri M (2011) *Photochem Photobiol* 87:1002
45. Sugimoto T, Okada K, Itoh HJ (1997) *Colloid Interface Sci* 193:140
46. Sugimoto T, Okada K, Itoh HJ (1998) *Dispers Sci Technol* 19:143
47. Sugimoto T, Zhou X, Muramatsu AJ (2002) *Colloid Interface Sci* 252:339
48. Sugimoto T, Zhou XJ (2002) *Colloid Interface Sci* 252:347
49. Sugimoto T, Zhou X, Muramatsu AJ (2003) *Colloid Interface Sci* 259:43
50. Sugimoto T, Zhou X, Muramatsu AJ (2003) *Colloid Interface Sci* 259:53
51. Kanie K, Sugimoto TJ (2003) *Am Chem Soc* 125:10518
52. Kanie K, Sugimoto T (2004) *Chem Commun* 2004:1584
53. Lee S, Cho I-S, Lee JH, Kim DH, Kim DW, Kim JY, Shin H, Lee J-K, Jung HS, Park N-G, Kim K, Ko MJ, Hong KS (2010) *Chem Mater* 22:1958
54. Sambasivam S, Joseph DP, Jeong JH, Choi BC, Lim KT, Kim SS, Song TK (2011) *J Nanoparticle Res* 13:4623
55. Mălăeșu T, Neamțu J, Morari C, Sbarcea G (2012) *Rev Roum Chim* 57:857
56. Aziz M, Abbas SS, Wan Baharom WR (2013) *Mater Lett* 91:31
57. Heqing Y, Banglao Z, Shouxin L, Yu F, Liangying Z, Xi Y (2001) *Acta Chim Sinica* 59:224
58. Zhang L, Wang X (2011) Preparation of GaN powder by sol-gel and theoretical calculation. In: *Proceedings photonics and optoelectronics (SOPO) symposium, Wuhan, 16–18 May 2011*, pp 1–4. doi: 10.1109/SOPO.2011.5780494
59. Liu YA, Xue CS, Zhuang HZ, Zhang XK, Tian DH, Wu YX, Sun LL, Ai YJ, Wang FX (2006) *Acta Phys Chim Sin* 22:657
60. Samat NA, Nor RM (2013) *Ceram Int* 39:S545
61. Kolekar TV, Bandgar SS, Shirguppikar SS, Ganachari VS (2013) *Archiv Appl Sci Res* 5:20
62. Bhattacharjee B, Ganguli D, Iakoubovskii K, Stesmans A, Chaudhuri S (2002) *Bull Mater Sci* 25:175
63. Rao AY, Enkateswara KV, Srinivasa SP (2012) *Int Proc Chem Biol Environ* 48:156
64. Kondawar S, Mahore R, Dahegaonkar A, Agrawal S (2011) *Adv Appl Sci Res* 2:401
65. Wu W, He Q, Jiang C (2008) *Nanoscale Res Lett* 3:397
66. Williams JV, Adams CN, Kotov NA, Savage PE (2007) *Ind Eng Chem Res* 46:4358
67. Lu Q, Gao F, Zhao D (2002) *Nano Lett* 2:725
68. Yang R, Yan Y, Mu Y, Ji W, Li X, Zou MQ, Fei Q, Jin Q (2006) *J Nanosci Nanotechnol* 6:220
69. Aneesh PM, Jayaraj MK (2010) *Bull Mater Sci* 33:227
70. Gnanam S, Rajendran V (2010) *Digest J Nanomater Biostruct* 5(2):623-628 http://www.chalcogen.ro/623_Gnanam-urgent.pdf
71. Yan C, Sun L, Fu X, Liao C (2002) *Mat Res Soc Symp Proc* 692:549
72. Singh J, Verma NK (2012) *J Supercond Nov Magn* 25:2425
73. Lu J, Wei S, Yu W, Zhang H, Qian Y (2004) *Inorg Chem* 43:4543
74. Zhang X, Dai J, Ong H (2011) *Open J Phys Chem* 1:6
75. Rashad MM, Rayan DA, El-Barawy K (2010) *J Phys Conf Ser* 200:072077. doi:10.1088/1742-6596/200/7/072077
76. Tokeer A, Sarvari K, Kelsey C, Samuel LE (2013) *J Mater Res* 28:1245
77. Ghosh K, Kahol PK, Bhamidipati S, Das N, Khanra S, Wanekaya A, DeLong R (2012) *AIP Conf Proc* 1461:87
78. Yong SM, Muralidharan P, Jo SH, Kim DK (2010) *Mater Lett* 64:1551
79. Zhang L, Zhao J, Zheng J, Li L, Zhu Z (2011) *Sensors Actuators B* 158:144

80. Ni YH, Wei XW, Hong JM, Ye Y (2005) *Mater Sci Eng B Solid State Mater Adv Technol* 121:42
81. Chiu H-C, Yeh CS (2007) *J Phys Chem C* 111:7256
82. Firooz AA, Mahjoub AR, Khodadadi AA (2011) *World Acad Sci Eng Technol* 5:04
83. Jain K, Srivastava V, Chouksey A (2009) *Indian J Eng Mater Sci* 16:188
84. Malik MA, Wani MY, Hashim MA (2012) *Arabian J Chem* 5:397
85. Petit C, Ixon L, Pileni MP (1990) *J Phys Chem* 94:1598
86. Eastoe J, Cox AR (1995) *Colloid Surf A Physicochem Eng Asp* 101:63
87. Eastoe J, Warne M (1996) *Curr Opin Colloid Interface Sci* 1:800
88. Robinson BH, Towey TF, Zourab S, Visser AJWG, Van Hoek A (1991) *Colloid Surf* 61:175
89. Haram SK, Mahadeshwar AR, Dixit SG (1996) *J Phys Chem* 100:5868
90. Wang Y, Zhang X, Wang A, Li X, Wang G, Zhao L (2014) *Chem Eng J* 235:191
91. Kripal R, Gupta AK, Srivastava RK, Mishra SK (2011) *Spectrochimica Acta Part A* 79:1605
92. Reddy BS, Reddy SV, Reddy NK, Kumari JP (2013) *Res J Mater Sci* 1:11
93. Naje AN, Norry AS, Suhail AM (2013) *Int J Innovative Res Sci Eng Technol* 2:7068
94. Abazovic ND, Mirengi L, Jankovic IA, Bibic N, Sojic DV, Abramovic BF, Comor MI (2009) *Nanoscale Res Lett* 4:518
95. Shwe LT, Win PP (2013) Preparation of CuO nanoparticles by precipitation method. Paper presented at international workshop on nanotechnology, Serpong, Indonesia, 2-5 Oct 2103. http://www.academia.edu/4929894/PREPARATION_OF_CuO_NANOPARTICLES_BY_PRECIPITATION_METHOD
96. Rao BS, Kumar BR, Reddy VR, Rao TS (2011) *Chalcogenide Lett* 8:177
97. Bandaranayake RJ, Smith M, Lin JY, Jiang HX, Sorensen CM (2002) *IEEE Trans Magn* 30:4930
98. Chauhan R, Kumar A, Chaudhary RP (2010) *J Chem Pharm Res* 2:178
99. Kumar SS, Venkateswarlu P, Rao VR, Rao GN (2013) *Int Nano Lett* 3:30(1)
100. Shanthi S, Muthuselvi U (2012) *Int J Chem Appl* 4:39
101. Dehbashi M, Aliahmad M (2012) *Int J Phys Sci* 7:5415
102. Lanje AS, Sharma SJ, Pode RB, Ningthoujam RS (2010) *Arch Appl Sci Res* 2:127
103. Mishra R, Bajpai PK (2010) *J Int Acad Phys Sci* 14:245
104. Rahnam A, Gharagozlou M (2012) *Opt Quant Electron* 44:313
105. Devi BSR, Raveendran R, Vaidyan AV (2007) *Pharm J Phys* 68:679
106. Xiao Q, Si Z, Yu Z, Qiu G (2007) *Mater Sci Eng B* 137:189
107. Didenko YT, Suslick KS (2005) *J Am Chem Soc* 127:12196
108. Treece RE, Macala GS, Rao L, Franke D, Eckert H, Kaner RB (1993) *Inorg Chem* 32:2745
109. Hwang H, Kim MG, Cho J (2007) *J Phys Chem C* 111:1186
110. Fojtik A, Henglein A (1994) *Chem Phys Lett* 221:363
111. Carpenter JP, Lukehart CM, Henderson DO, Mu R, Jones BD, Glosser R, Stock SR, Wittig JE, Zhu JG (1996) *Chem Mater* 8:1268
112. Kornowski A, Giersig M, Vogel M, Chemseddine A, Weller H (1993) *Adv Mater* 5:634
113. Heath JR, Shiang JJ, Alivisatos APJ (1994) *Chem Phys* 101:1607
114. Jegier JA, McKernan S, Gladfelter WL (1998) *Chem Mater* 10:2041
115. Micic OI, Sprague JR, Curtis CJ, Jones KM, Machol JL, Nozic A, Giessen JH, Fluegel B, Mohs G, Peyghambarian N (1995) *J Phys Chem* 99:7754
116. Salata OV, Dobson PJ, Hull PJ, Hutchison JL (1994) *Appl Phys Lett* 65:189
117. Sercel PC, Saunders WA, Atwater HA, Vahala KJ, Flagan RC (1992) *Appl Phys Lett* 61:696
118. Kher SS, Wells RL (1994) *Chem Mater* 6:2056
119. Olshavsky MA, Goldstein AN, Alivisatos APJ (1990) *Am Chem Soc* 112:9438
120. Trindade T, O'Brien P (1996) *Adv Mater* 8:161
121. Trindade T, O'Brien P, Zhang X (1997) *Chem Mater* 9:523
122. Yu S, Wu Y, Yang J, Han Z, Xie Y, Qian Y, Liu X (1998) *Chem Mater* 10:2309
123. Mansur HS (2010) *Wiley Interdiscip Rev Nanomed Nanobiotechnol* 2:113
124. Brus L (1983) *J Chem Phys* 79:5566

125. Gaponik N, Rogach AL (2010) *Phys Chem Chem Phys* 12:8685
126. Bailey RE, Smith AM, Nie S (2004) *Physica E* 25:1
127. Madler L, Stark WJ, Pratsinisa SE (2002) *J Appl Phys* 92:6537
128. Simmons BA, Li S, John VT, McPherson GL, Bose A, Zhou W, He J (2002) *Nano Lett* 2:263
129. Cirillo M, Aubert T, Gomes R, Van Deun R, Emplit P, Biermann A, Lange H, Thomsen C, Brainis E, Hens Z (2014) *Chem Mater* 26:1154
130. Greenberg MR, Smolyakov GA, Jiang Y-B, Boyle TJ, Osinski M (2006) Synthesis and characterization of in-containing colloidal quantum dots. In: *Proceedings of SPIE* 6096, Colloidal quantum dots for biomedical applications, 60960D. doi: 10.1117/12.663315
131. Du Y, Zhou X, Liu Y, Wang X (2012) *J Nanosci Nanotechnol* 12:8487
132. Forleo A, Francioso L, Capone S, Siciliano P, Lommens P, Hens Z (2010) *Sensors Actuators B Chem* 146:111
133. Vrik HS, Sharma P (2010) *J Nano Res* 10:69
134. Yu WW (2008) *Expert Opin Biol Ther* 8:1571
135. Ribeiro RT, Dias JMM, Pereira GA, Freitas DV, Monteiro M, Cabral Filho PE, Raelle RA, Fontes A, Navarro M, Santos BS (2013) *Green Chem* 15:1061
136. Nordell KJ, Boatman EM, Lisensky GC (2005) *J Chem Educ* 82:1697
137. Sai LM, Kong XY (2011) *Nanoscale Res Lett* 6(1):399
138. Efros AL, Fiz ALF (1982) *Tekh Poluprovodn* 16:1209
139. Brus LE (1984) *J Chem Phys* 80:4403
140. Henglein A (1989) *Chem Rev* 89:1861
141. Khairutdinov RF (1998) *Russ Chem Rev* 67:109
142. Li H (2008) Synthesis and characterization of aqueous quantum dots for biomedical applications. Doctoral thesis, Drexel University
143. Rogach AL, Talapin DV, Weller H (2004) Semiconductor nanoparticles. In: Caruso F (ed) *Colloids and colloids assemblies: synthesis, modification, organization and utilization of colloid particles*. Wiley, New York, pp 52–95
144. Ramos LE, Degoli E, Cantele G, Ossicini S, Ninno D, Furthmuller J, Bechstedt F (2007) *J Phys Condens Matter* 19:466211(1)
145. Furdyna JK, Samarth N (1987) *J Appl Phys* 61:3526
146. Garcia MA, Merino JM, Pinel EF, Quesada A, de la Venta J, Ruiz González ML, Castro GR, Crespo P, Llopis J, González-Calbet JM, Hernando A (2007) *Nano Lett* 7:1489
147. Sivasubramanian V, Arora AK, Premila M, Sundar CS, Sastry VS (2006) *Phys E* 31:93
148. Son DI, No YS, Kim SY, Oh DH, Kim WT, Kim TW (2009) *J Korean Phys Soc* 55:1973
149. Hamizi NA, Johan MR (2012) *Int J Electrochem Sci* 7:8458
150. Chan WCW, Nie S (1998) *Science* 281:2016
151. Gao X, Nie S (2003) *Trends Biotechnol* 21:371
152. Bruchez M, Moronne JM, Gin P, Weiss S, Alivisatos AP (2013) *Science* 281:2013
153. Zaban A, Micic OI, Gregg BA, Nozik AJ (1998) *Langmuir* 14:3153
154. Plass R, Pelet S, Krueger J, Graetzel M, Bach U (2002) *J Phys Chem B* 106:7578
155. Huynh WU, Dittmer JJ, Alivisatos AP (2002) *Science* 295:2425
156. Dabbousi BO, Bawendi MG, Onitsuka O, Rubner MF (1995) *Appl Phys Lett* 66:1316
157. Coe S, Woo WK, Bawendi MG, Bulovic V (2002) *Nature* 420:800
158. Wolf SA, Awschalom DD, Buhrman RA, Daughton JM, von Molnár S, Roukes ML, Chthelkanova AY, Treger DM (2001) *Science* 294:1488
159. Awschalom DD, Flatte ME, Samarth N (2002) *Sci Am* 286:66
160. Engel HA, Recher P, Loss D (2001) *Solid State Commun* 119:229
161. Ferrand D, Wasiela A, Tatarenko S, Cibert J, Richter G, Grabs P, Schmidt G, Molenkamp LW, Diet T (2001) *Solid State Commun* 119:237
162. Ip K, Frazier RM, Heo YW, Norton DP, Abernathy CR, Pearton SJ (2003) *J Vac Sci Technol B* 21:1476
163. Liu C, Yun F, Morkoc H (2005) *J Mat Sci Mater Electron* 16:555

164. Polyakov AY, Govorkov AV, Smirnov NB, Pashkova NV, Pearnton SJ, Overberg ME, Abernathy CR, Norton DP, Zavada JM, Wilson RG (2003) *Solid-State Electron* 47:1523
165. Roberts BK, Pakhomov AB, Shutthanandas VS, Krishnan KM (2005) *J Appl Phys* 97 (1):10D310
166. Adesina AA (2004) *Catal Surv Asia* 8:265
167. Chakrabarti S, Dutta BK (2004) *J Hazard Mater B* 112:269
168. Chitose N, Ueta S, Yamamoto TA (2003) *Chemosphere* 50:1007
169. Yang H, Zhang K, Shi R, Li X, Dong X, Yu Y (2006) *J Alloys Compd* 413:302
170. Dou B, Chen H (2011) *Desalination* 269:260
171. Daneshvar N, Salari D, Khataee AR (2004) *J Photochem Photobiol A Chem* 162:317
172. Rahman QI, Ahmad M, Misra SK, Lohani M (2013) *Mater Lett* 91:170
173. Devipriya SP, Yesodharan S (2010) *J Environ Biol* 31:247
174. Mahdavi S, Jalali M, Afkhami A (2012) *J Nanoparticle Res* 14:846(1)
175. Kansal SK, Ali AH, Kapoor S (2010) *Desalination* 259:147
176. Santana-Aranda MA, Morán-Pineda M, Hernández J, Castillo S (2005) *Superficies y Vacío* 18(1):46-49
177. Pardeshi SK, Patil AB (2008) *Sol Energy* 82:700
178. Benhebal H, Chaib M, Salmon T, Greens J, Leonard A, Lambert SD, Crine M, Heinrichs B (2013) *Alexandria Eng J* 52:517
179. Sharma S, Ameta R, Malkani RK, Ameta SC (2011) *Maced J Chem Chem Eng* 30:229
180. Pathania D, Sarita S, Rathore BS (2011) *Chalcogenide Lett* 8:396
181. Pathania D, Sarita, Singh P, Pathania S (2014) *Desalin Water Treat* 52:3497-3503
182. Loryuengyong V, Jarunsak N, Chuangchai T, Buasri A (2014) *Adv Mater Sci Eng* 2014:348427(1)
183. Singh N, Singh SP, Gupta V, Yadav HK, Ahuja T, Tripathy SS, Rashmi (2013) *Environ Progr Sustain Energy* 32:1023–1029
184. Chopra L, Major S, Pandya DK, Rastogi RS, Vankar VD (1983) *Thin Solid Films* 1021:1
185. Nirmal M et al (1996) *Nature* 383:802
186. Wierer J, David A, Megens M (2009) *Nat Photonics* 3:163
187. Jin Y, Li Q, Zhu Z (2012) *Opt Express* 20:15818
188. Zhang H, Zhu J, Jin G (2013) *Opt Express* 21:13492
189. Fu X, Zhang B, Zhang GY (2011) *Opt Express* 19:1104
190. Chan C-H, Lee CC, Chen C-C (2007) *Appl Phys Lett* 90:242106
191. Cho C-Y, Kang S-E, Kim KS (2010) *Appl Phys Lett* 96:18110
192. Zhou W, Min G, Song Z (2010) *Nanotechnology* 21:205304
193. Chiu CH, Yu P, Chang CH (2009) *Opt Express* 23(17):21250
194. Yoon K-M, Yang K-Y, Byeon K-J (2010) *Solid-State Electron* 54:484
195. Tsai C-F, Su Y-K, Lin C-L (2009) *IEEE Photon Technol Lett* 21:996
196. Kim KS, Kim S-M, Jeong H (2010) *Adv Funct Mater* 20:1076
197. Jin Y, Li Q, Li G, Chen M, Liu J, Zou Y, Jiang K, Fan S (2014) *Nanoscale Res Lett* 9:7(1)
198. Neshataeva E, Kummell T, Ebbers A, Bacher G (2008) *Elect Lett* 44:1485
199. Schlamp MC, Peng X, Alivisatos AP (1997) *J Appl Phys* 82:5837
200. Matioussi H, Radzilowski LH, Dabbousi BO, Thomas EL, Bawendi MG, Rubner MF (1998) *J Appl Phys* 83:7965
201. Colvin VL, Schlamp MC, Allvi-Satos AP (1994) *Nature* 370:354
202. Gaponik NP, Talapin DV, Ro-Gach A (1999) *Phys Chem Chem Phys* 1:1787
203. Shockley W, Queisser HJ (1961) *J Appl Phys* 32:510
204. Barnham KW, Duggan G (1990) *J Appl Phys* 67:3490
205. Dimroth F (2006) *Phys Stat Sol (C)* 3:373
206. Ó'regan B, Grätzel M (1991) *Nature* 353:737
207. Hotchandani S, Kamat PV (1992) *J Phys Chem* 96:6834
208. Vogel R, Hoyer P, Weller H (1994) *Phys Chem* 98:3183
209. Vogel R, Poh K, Weller H (1990) *Chem Phys Lett* 174:241

210. Bruchez MP, Moronne M, Gin P, Weiss S, Alivisatos AP (1998) *Science* 281:2013
211. Omair NAA, Reda SM, Hajri FML (2014) *Adv Nanopart* 3:31
212. Lee S, Cho I-S, Lee JH, Kim DH, Kim DW, Kim JY, Shin H, Lee JK, Jung OHS, Park N-G, Kim K, Ko MJ, Hong KS (2010) *Chem Mater* 22:1958
213. Zhang L, Zhao J, Zheng J, Li L, Zhua Z (2011) *Sensors Actuators B* 158:144
214. Qi L, Gao X (2008) *Expert Opin Drug Deliv* 5:263
215. Pandurangan DK, Mounika KS (2012) *Int J Pharm Pharm Sci* 4:24–31
216. Zrazhevskiy P, Gao X (2009) *Nano Today* 4:414
217. Vengala P, Dasari A, Yeruva N (2012) *Int J Pharm Technol* 4:2055
218. Mukherjee S, Das U (2011) *Int J Pharm Sci Rev Res* 7:59
219. Mishra P, Vyas G, Harsoliya MS, Pathan JK, Raghuvanshi D, Sharma P et al (2011) *Int J Pharm Pharm Sci Res* 1:42
220. Hanley C, Layne J, Punnoose A, Reddy KM, Coombs I, Coombs A, Feris K, Wingett D (2008) *Nanotechnology* 19:295103(1)
221. Zhang A-I, Sun YP (2004) *World J Gastroenterol* 10:3191
222. Cervera BEH, Azcorra SAG, Gattorno GR, López T, Islas EQ, Oskam G (2009) *Sci Adv Mater* 1:63
223. Zhang Y, Wang T-H (2012) *Theranostics* 2:631
224. Baba K, Nishida K (2012) *Theranostics* 2:655
225. Clift MJD, Stone V (2012) *Theranostics* 2:668
226. Yong K-T, Wang Y, Roy I et al (2012) *Theranostics* 2:681
227. Balazs AC, Emrick T, Russell TP (2006) *Science* 314:1107
228. Huynh WU, Dittmer JJ, Alivisatos AP (2002) *Science* 295:2425
229. Godovsky DY (2000) *Biopolymers/Pva Hydrogels/Anionic Polymerisation Nanocomposites* 153:163–205
230. Li S, Lin MM, Toprak MS, Kim DK, Muhammed M (2010) *Nano Rev* 1:5214(1)
231. Hong JI, Cho KS, Chung CI, Schadler LS, Siegel RW (2002) *J Mater Res* 17:940
232. Ma CCM, Chen YJ, Kuan HC (2006) *J Appl Polym Sci* 100:508
233. Wong M, Tsuji R, Nutt S, Sue H-J (2010) *Soft Matter* 6:4482
234. Zohrevand A, Ajji A, Mighri F (2013) *Polym Eng Sci* 54:874
235. Ou B, Li D, Liu Q, Zhou Z, Xiao Q (2012) *Polym Plast Technol* 51:849
236. Mohan S, Oluwafemi OS, Songca SP, Osibote OA, George SC, Kalarikkal N, Thomas S (2014) *New J Chem* 38:155
237. Wacharawichanant S, Thongbunyoung N, Churdchoo P, Sookjai T (2010) *Sci J UBU* 1:21
238. Miyauchi M, Li Y, Shimizu H (2008) *Environ Sci Technol* 42:4551
239. Tuan VM, Jeong DW, Yoon HJ, Kang SY, Giang NV, Hoang T, Thinh TI, Kim MY (2014) *Int J Polym Sci* 2014:758351(1)
240. Redhwi HH, Siddiqui MN, Andraday AL, Hussain S (2013) *J Nanomater* 2013:654716(1)
241. Murariu M, Doumbia A, Bonnaud L, Dechief AL, Paint Y, Ferreira M, Campagne C, Devaux E, Dubois P (2011) *Biomacromolecules* 12:1762
242. Guan C, Lu CL, Cheng YR, Song SY, Yang BA (2009) *J Mater Chem* 19:617
243. Cheng Y, Lu C, Lin Z, Liu Y, Guan C, Lu H, Yang B (2008) *J Mater Chem* 18:4062
244. Dzunuzovic E, Jeremic K, Nedeljkovic JM (2007) *Eur Polym J* 43:3719
245. Evora VMF, Shukla A (2003) *Mater Sci Eng A* 361:358
246. Kaleel SHA, Bahuleyan BK, Masihullah J, Al-Harhi M (2011) *J Nanomater* 2011:964353(1)
247. Zapata PA, Palza H, Delgado K, Rabagliati FM (2012) *J Polym Sci Part A: Polym Chem* 50:4055
248. Sharma D, Kaith BS, Rajput J (2014) *Sci World J* 2014:904513(1)
249. Liu P, Su Z (2006) *J Macromol Sci Part B: Phys* 45:131
250. Xu M, Zhang J, Wang S, Guo X, Xia H, Wang Y, Zhang S, Huang W, Wu S (2010) *Sensors Actuators B Chem* 146:8
251. Yang Y, Zhou Y, Ge J, Yang X (2012) *Mater Res Bull* 47:2264

252. Bai S, Zhang K, Sun J, Zhang D, Luo R, Li D, Liu C (2014) *Sensors Actuators B Chem* 197:142
253. O'Brien P, Cummins SS, Darcy D, Dearden A, Masala O, Pickett NL, Ryleya S, Sutherland AJ (2003) *Chem Commun* 2003:2532
254. Skaff H, Ilker MF, Coughlin EB, Emrick T (2002) *J Am Chem Soc* 124:5729
255. Guo W, Li JJ, Wang A, Peng X (2003) *J Am Chem Soc* 125:3901
256. Lee J, Sundar VC, Heine JR, Bawendi MG, Jensen KF (2000) *Adv Mater* 12:1102
257. Landfester K (2001) *Macromol Rapid Commun* 22:896
258. Esteves ACC, Bombalski L, Trindade T, Matyjaszewski K, Barros-Timmons A (2007) *Small* 3:1230
259. Jakubowski W, Matyjaszewski K (2005) *Macromolecules* 38:4139
260. Min K, Gao H, Matyjaszewski K (2005) *J Am Chem Soc* 127:3825
261. Joumaa N, Lansalot M, ThJretz A, Elaissari A, Sukhanova A, Artemyev M, Nabiev I, Cohen JHM (2006) *Langmuir* 22:1810
262. Vassiltsova OV, Jayez DA, Zhao Z, Carpenter MA, Petrukhhina MA (2010) *J Nanosci Nanotechnol* 10:1635
263. Liu SH, Qian XF, Yuan JY, Yin J, He R, Zhu ZK (2003) *Mater Res Bull* 38:1359
264. Zhu J, Wei S, Zhang L, Mao Y, Ryu J, Mavinakuli P, Karki AM, Young DP, Guo Z (2010) *J Phys Chem C* 114:16335
265. Althues H, Palkoits R, Rumpelcker A, Simon P, Sigle W, Bredol M, Kynast U, Kaskel S (2006) *Chem Mater* 18:1068
266. Kondawar S, Mahore R, Dahegaonkar A, Sikha A (2011) *Adv Appl Sci Res* 2:401
267. Anzlovar A, Kogej K, Orel ZC, Zigon M (2011) *eXpress Polym Lett* 5:604
268. Uygun A, Turkoglu O, Sen S, Ersoy E, Yavuz AG, Batir GG (2009) *Curr Appl Phys* 9:866
269. Hashimoto M, Takadama H, Mizuno M, Kokubo T (2006) *Mater Res Bull* 41:515
270. Camargo P, Satyanarayana K, Wypych F (2009) *Mater Res* 12:1
271. Emamifar A, Kadivar M, Shahedi M, Solaimanianzad S (2011) *Food Control* 22:408
272. Kondawar SB, Patil PT, Agrawal SP (2014) *Adv Mater Lett* 5:389
273. Potyrailo RA, Leach AM, Cheryl MS (2012) *Comb Sci* 14:170
274. Potyrailo RA, Leach AM (2006) *Appl Phys Lett* 88:134110(1)
275. Xu M, Zhang J, Wang S, Guo X, Xia H, Wang Y, Zhang S, Huang W, Wu S (2010) *Sensors Actuators B Chem* 146:8
276. Zhao Z, Arrandale M, Vassiltsova OV, Petrukhhina MA, Carpenter MA (2009) *Sensors Actuators B Chem* 141:26
277. Zhang ZY, Xu YD, Ma YY, Qiu LL, Wang Y, Kong JL, Xiong HM (2013) *Angew Chem Int Ed* 52:4127
278. Shankar K, Mor GK, Prakasam HE, Varghese OK, Grimes CA (2007) *Langmuir* 23:12445

Shape Memory Polymer–Inorganic Hybrid Nanocomposites

Radu Reit, Benjamin Lund, and Walter Voit

Abstract Shape memory polymers (SMPs) have been the focus of much research over the last few decades. From the novelty of temporarily fixing a three-dimensional shape from a planar polymer sheet, to the uses that SMPs are seeing today as softening biomedical implants and self-deploying hinges, this class of smart materials has successfully been used to tackle a variety of biological, electrical, and mechanical problems. However, the properties of these networks are limited by the organic nature of the SMPs. To enhance their properties, researchers across the globe have looked into imparting the desirable properties of inorganic composite materials to these polymer networks. As the field of shape memory polymer composites began to grow, researchers quantified the unique enhancements that came at varying filler loading levels as a result of controlled

R. Reit

Department of Bioengineering, The University of Texas at Dallas, 800 West Campbell RD, Mailstop RL 10, Richardson, TX 75080, USA

B. Lund

Department of Chemistry, The University of Texas at Dallas, 800 West Campbell RD, Mailstop RL 10, Richardson, TX 75080, USA

Department of Materials Science and Engineering, The University of Texas at Dallas, 800 West Campbell RD, Mailstop RL 10, Richardson, TX 75080, USA

W. Voit (✉)

Department of Bioengineering, The University of Texas at Dallas, 800 West Campbell RD, Mailstop RL 10, Richardson, TX 75080, USA

Department of Chemistry, The University of Texas at Dallas, 800 West Campbell RD, Mailstop RL 10, Richardson, TX 75080, USA

Department of Materials Science and Engineering, The University of Texas at Dallas, 800 West Campbell RD, Mailstop RL 10, Richardson, TX 75080, USA

Department of Mechanical Engineering, The University of Texas at Dallas, 800 West Campbell RD, Mailstop RL 10, Richardson, TX 75080, USA

e-mail: wev012000@utdallas.edu

material interface interactions. Specifically, the incorporation of nanofillers of various shapes and sizes leads to increased internal interfacial area relative to micro- and macrocomposites at identical loading fractions and imparts interesting mechanical, optical, electrical, thermal, and magnetic properties to these emerging nanocomposites. This new class of material, referred to in this review as shape memory polymer–inorganic nanocomposites (SMPINCs), allows a host of new interactions between the smart polymer and its surrounding environment as a result of the ability to control the internal environment of the polymer network and nanofiller. In this work, the reader is introduced to both the methods of preparing these composites and the effects the fillers have on the biological, electromagnetic, and mechanical properties of the resulting composite.

Keywords Inorganic nanocomposite · Shape memory polymer · Smart composite · Stimuli-responsive material

Contents

1	Introduction	315
2	SMP–Organic Composites	319
3	SMPINCs for Increased Mechanical Strength	322
3.1	Motivation and the Merging of Fields	322
3.2	Emergence of SMPINCs	325
3.3	Years 2010–2014: Interface Chemistry of SMPINCs Leads to Enhanced Thermomechanics	329
4	SMPINCs for Biocompatibility	335
4.1	Enhancing Biocompatibility	335
4.2	Stronger Biopolymers	337
5	SMPINCs with Electromagnetic Properties	339
5.1	Magnetite Filled SMPINCs	339
5.2	Thermoregulated Networks	341
5.3	Particle Coating Effects	341
5.4	Light Activation of SMPINCs	342
5.5	Electro-active Systems	343
6	Conclusion: The Future of SMPINCs	343
	References	344

Abbreviations

AuCd	Gold-cadmium alloy
BMP	Bone morphogenetic protein
BNNT	Boron nitride nanotube
CNT	Carbon nanotube
DMA	Dynamic mechanical analysis
DSC	Differential scanning calorimetry
Fe ₂ O ₃	Iron(III) oxide
Fe ₃ O ₄	Iron(II,III) oxide
HA	Hydroxyapatite

LSPR	Localized surface plasmon resonance
MMT	Montmorillonite
MWCNT	Multiwalled carbon nanotube
Na-MMT	Sodium montmorillonite
PCL	Poly(ϵ -caprolactone)
PDLLA	Poly(D,L-lactide)
PEG	Poly(ethylene glycol)
PEMA	Poly(ethyl methacrylate)
PEO	Poly(ethylene oxide)
PLA	Poly(lactic acid)
PMMA	Poly(methyl methacrylate)
POSS	Polyhedral oligomeric silsesquioxane
SiC	Silicon carbide
SMP	Shape memory polymer
SMPC	Shape memory polymer composite
SMPINC	Shape memory polymer–inorganic nanocomposite
T_d	Degradation temperature
T_g	Glass transition temperature
TiO ₂	Titanium dioxide
T_m	Melting temperature

1 Introduction

The study of shape memory polymers (SMPs) has increased dramatically in the past decade as more uses for these stimuli-responsive materials have become apparent. With the application of an external input, usually in the form of thermal energy, smart materials can recover from a temporarily fixed, often complex, shape to the globally stable shape in which they were originally fixed. Recent reviews on SMPs show the various ways in which these systems can be transitioned between these or more intermediate states using, not only thermal stimulation, but also an array of other stimuli such as changes in pH, electromagnetic radiation, pressure gradients, and many more methods limited only by the imagination of current researchers, the laws of nature, and the congressional research budget [1–9]. Meng and Li detailed a comprehensive review of these stimuli-responsive materials in 2013 in which many of the mechanisms for network formation (Fig. 1) are described in an easy-to-follow visual manner [6]. However, relying only on the organic network structure severely limits the properties that researchers can tease out of these smart materials at any given time; to truly push the bounds of what these materials are capable of, a new wave of SMPs has to make its way into mainstream research.

This wave has come in the form of SMP composites (SMPCs). With SMPCs, researchers have been able to reliably tune the mechanical, optical, electrical, and biological properties of the smart networks meant to tackle many of the materials problems faced by industry today. By incorporating many different types of fillers

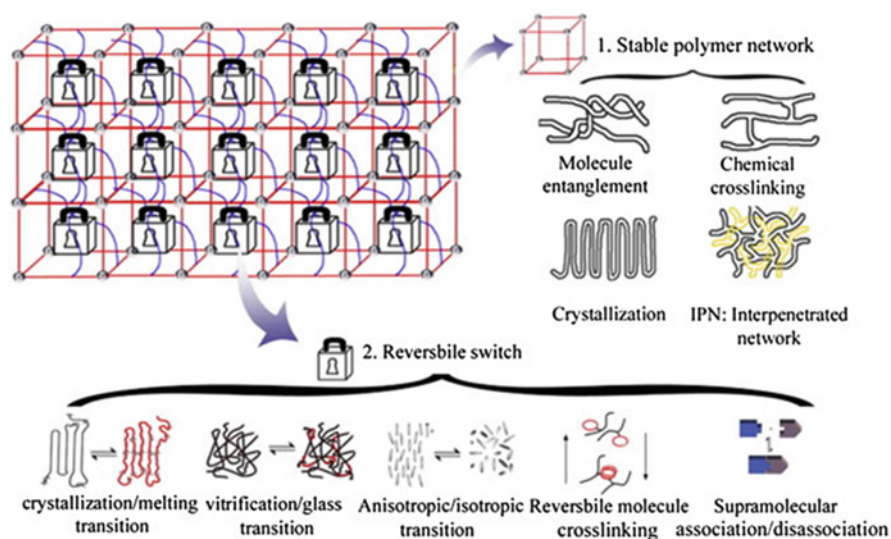


Fig. 1 Summary of the mechanisms for the shape memory effect in polymer networks. Reprinted from Meng and Li [6], Copyright 2013, Open Access

(such as graphene, carbon nanotubes, and metal nanoparticles), researchers have been able to show SMPCs with highly exotic properties and methods of activation. Many previous reviews in this area have described the properties of SMPCs [10–15] with various types of organic and inorganic fillers. Some reviews have also focused on single subtypes of smart composites such as ionomers [16], porous SMPs [17], or polyhedral oligomeric silsesquioxane (POSS) composites [18]. These comprehensive titles excellently describe some of the current research in the general area of composites that exhibit shape memory properties. Because the fields of SMPs and SMPCs have begun to fragment and move in many directions simultaneously, more focused reviews are now required that specialize in narrower areas and can devote additional time and attention to the specific phenomena that are relevant for specific subclasses of smart materials. Over the past two decades, researchers have been pushing the bounds of the size of the fillers that are incorporated into polymer networks. At identical weight loading fractions, nanocomposites can exhibit vastly enhanced properties over micro- and macrocomposites as a result of the exponential increase in internal interfacial area between polymers and composite materials. Much work has been carried out to find ways to properly disperse nanocomposites in liquid monomer solutions before polymerization into thermoplastics or thermosets and ways to properly disperse nanomaterials into melted thermoplastic resins via extrusion, blending, and mixing. Other hierarchical schemes involve clever intercalation methods, wherein other polymer systems are inserted into inorganic lattices of nanoparticles to change the reactivity or functional surface of the intercalated particle, rod, or thin film to modify reactions with the surrounding polymer network.

Although much of the work that has helped in explaining and highlighting polymer nanocomposites has been completed outside of the shape memory polymer arena, many of the polymer systems described as compatible with nanofillers can be engineered to exhibit shape memory properties. The purpose of this review is to fill in the gaps in current understanding of the development and application of SMP–inorganic nanocomposites (SMPINCs).

Over the past decade, an increasing array of researchers has begun to specifically characterize the shape memory properties of nanocomposites. They have observed increases in recoverable stresses and recoverable strains at optimized loading fractions. They have derived nonlinear relationships between loading and various thermomechanical properties, but the work has been largely experimental. This is an area ripe for new partnerships in computational materials, as national endeavors like the Materials Genome Initiative seek to find better and faster ways to predict the properties of emerging materials by computational methods. What is so fascinating specifically about SMPINCs is the array of different properties that make these materials so difficult to model. On a macroscale, strains above 200% are common. At the nanoscale, interfacial physics at the molecular chain level dictate emergent properties. Atomistically, multi-atom simulations do not possess the size to observe macroscale behavior. Continuum models have difficulty accounting for the subtle, yet powerful, effects at small interfaces. Molecular dynamics and quantum models are at such short time and length scales that viscoelastic behavior becomes difficult to model accurately. For instance, to the authors' knowledge, there is no group today that can accurately predict *a priori* how a change in surface chemistry, loading fraction, nanomaterial geometry, and processing methods would specifically change the recovery stress or the shape fixity of an SMPINC. Thus, the emergence of this field has been driven by experimentalists who have, largely by trial-and-error, observed what effects different nanomaterials (specifically surface-modified nanoclays) have on shape memory polymer systems at different loading densities, particle sizes, and intercalation schemes. We challenge the modeling community and top experimentalists in this area to find ways of utilizing the growing tome of experimental evidence to help develop and train models in this crucial area, which will be the engine of creation for new functional materials in healthcare, defense, and aerospace.

In this review, we have collected some of the recent (2012–2014) experimental work that has not yet been well collated and refer back to milestone achievements and other excellent reviews to cover experimental work in SMPINCs before 2012. The intended audience is researchers who seek to build interdisciplinary teams to tackle some of the crucial material challenges of the next decade and who can utilize this collection of anecdotes (i.e., spotted experimental evidence in a vastly complex parameter space) to find new ways to predict, create, characterize, redevelop, and deploy smart material-based inorganic nanocomposites.

More specifically, the authors aim to quantify how, via the addition of small amounts of inorganic fillers, the shape memory effect can be fully maintained or even strengthened in SMPs, all the while adding novel new properties to the network. Research groups around the world have explored the influence of

inorganic nanoparticles on general polymer networks [19] and how the surface modification of these particles affects composite behavior [20]. However, a focused summary of the narrow but important state-of-the-art in SMPINCs has remained unwritten. With this attempt, the authors hope that the reader will gain a familiarity with the current state of SMPINCs and the types of research undertaken, as well as with the commercial uses these hybrid smart materials may see in the near future. More importantly, the authors hope that directed narratives such as this one can serve as a call to action for researchers from disparate fields to join forces to find better models than the current trial-and-error approach and thus facilitate progress in this important field.

To ground the readers and provide benchmarks for comparisons of the SMPINCs, Section 2 presents a brief outline of recent advances in shape memory polymer–organic composites, with a focus on carbon nanomaterials such as graphene, carbon nanotubes, and carbon black.

Section 3 provides an overview of the relevant mechanical properties of SMPINCs and highlights data points from key works that have helped advance the field over the past two decades. The section provides a more rigorous look at advances from the past 2 years that have not been adequately covered in other reviews. Teams that want to address emerging structural materials problems in construction, aerospace, orthopedics, and other mechanically driven applications should focus on this area.

Section 4 presents SMPINCs that have been analyzed and tested for biocompatibility. Researchers that are less concerned with pure strength and the ultimate mechanical properties of composites, but instead want to focus on ways in which shape change can provide interesting functionality inside the body, should focus on this area. Of utmost concern is the chemical surface that materials present and how composites interact with biological tissue in various parts of the body. Researchers are exploring ways to maximize the functionality of shape changing, modulus changing materials and often use nanocomposites not as structural reinforcers but rather as chemical modifiers to control how cells interact with materials, how proteins adsorb onto the surface of the materials, and how the body's immune and inflammatory responses can be mediated through the incorporation of specific nanoparticles. This area of research is being approached from two directions. There is a mixed bag of researchers from the materials end of the spectrum that are trying to push their nanocomposites into the medical arena, both to solve problems and to find new sources of funding to continue their research agendas. These scientists are in some sense problem-agnostic, but have expertise in nanomaterial–polymer interactions and want to apply these broadly. These researchers tend to understand in detail the limitations of materials, but are often less versed in the physiological ramifications of use of these composites. At the other end of the spectrum, clinicians are seeking to pull SMPINC technologies to target very specific problems, disease states, or pathways inside the body and are often largely materials-agnostic, as long as the developed material can solve the specific problem at hand. This balance of technology push and pull presents a compelling environment for tackling crucial problems in healthcare. The authors encourage

computational modelers to form the third pillar of this partnership and help link the best materials, correct composites, optimal loading, and the most suitable chemically modified surfaces with the right biomedical problems, whose solutions could save and better countless lives.

In a similar vein, Section 5 aims to catalyze the efforts of materials scientists and computational modelers with those of materials, electrical, mechanical and bioengineers looking to take advantage of the unique electrical, optical, and magnetic properties that SMPINCs can provide. This section outlines the relevant wave-based phenomena, in which these composites can often outperform other materials. Early work in this area focused on nanomagnetite and on using an inductive field to remotely trigger shape recovery for applications such as morphing aircraft wings. More recent inquiries seek to balance electro-active and thermal properties or light-induced phenomena with the mechanical demands of complex systems.

Section 6 and the conclusion provide the author's brief and feeble attempt to encircle an exploding field with guidelines and structure to help researchers from many different disciplines to contribute to this exciting research area.

2 SMP–Organic Composites

Although the main focus of this review is the use of inorganic fillers as materials to substantially increase the mechanical, electromagnetic, and biological properties of SMPs, it is important to remember that many of these same properties have been explored through the use of organic fillers. Much relevant information about interface physics and composite mechanics can be gleaned from leading researchers in these areas. In addition, the funding climate around carbon nanomaterials over the past two decades has been favorable for a variety of reasons, so many top research groups have used these kinds of composites and composite analyses to push forward their larger research agendas. This section of the review serves as a brief introduction to these organic composites (with a focus on organic nanocomposites) and their unique properties so that the reader can experience and adequately compare the advancing direction of SMPCs using either organic or inorganic fillers.

The most enticing carbon-based fillers for SMPCs have been found in parallel with the recent surge in research on carbon nanotubes (CNTs) and graphene particles. Carbonaceous materials allow a slew of mechanical, electrical, and optical properties to be imparted to the SMPC using the same basic filler backbone. In 2007, Miaudet et al. demonstrated broad glass transition temperatures as a result of incorporation of CNT fillers [21]. Further, in 2010, Lu et al. modified a styrene-based shape memory polymer resin from the Ohio-based Cornerstone Research Group with carbon black fillers and carbon fiber fillers [22]. Nji and Li developed both a three-dimensional (3D) woven fabric reinforced SMP composite based on organic materials for impact resistance [23, 24] and an SMP composite

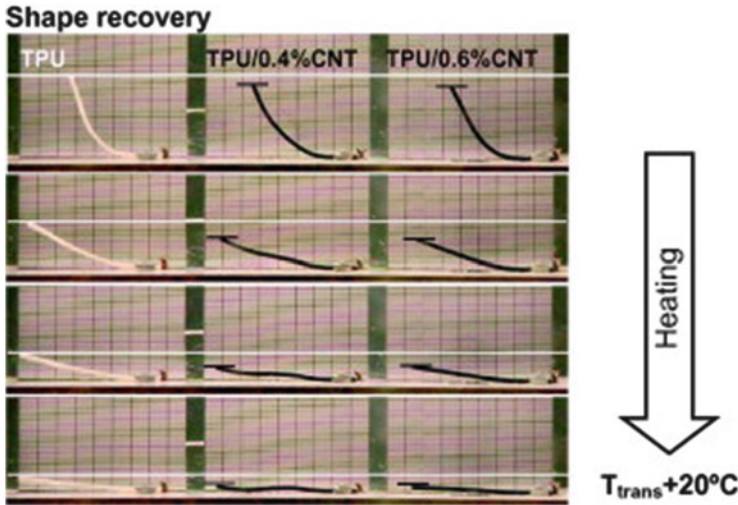


Fig. 2 CNT-loaded thermoplastic polyurethane (TPU) SMPs show a faster recovery with increasing CNT fill percentage. Reprinted from Fonseca et al. [27], Copyright 2013, with permission from Elsevier

based on biomimicry. In 2012, Kohlmeyer et al. described composites of SMPs and single-wall carbon nanotubes (SWCNTs) [25]. In 2013, Tridech et al. developed systems to explore active stiffness control in polymer/carbon fiber nanocomposites [26].

In 2013, Fonseca et al. showed that thermoplastic polyurethane SMPs could be loaded with CNTs to modulate the thermomechanical properties of the network. In that study, the authors demonstrated significant increases in the glass transition temperature (T_g) and degradation temperature (T_d), which moved from -25°C to -16°C and from 307.5°C to 360°C , respectively, with only a 0.5 wt% loading of CNTs [27]. This improvement in mechanical properties was also demonstrated by a significantly more rapid recovery when heated past T_g (Fig. 2), postulated to be due to the nucleation of soft segments that can improve the overall crystallinity of the network. In a similar study, researchers at the Harbin Institute of Technology showed the loading of an epoxy thermoset with up to 0.81 wt% multiwalled carbon nanotubes (MWCNTs), followed by analysis of the mechanical properties of the network. In this study, the authors noted a significant difference in the composite's compressive modulus during the glass transition ($T_g = 100^\circ\text{C}$) [28]. With this study, the researchers noted the dependence of the deformation temperature on the efficiency with which CNTs reinforced the network; in the glassy and rubbery regimes ($T = 25^\circ\text{C}$ and $T = 150^\circ\text{C}$, respectively) the CNT loading showed no significant effect on mechanical properties. Many other studies on SMP-CNT composites have looked at the reinforcement effects of CNTs on poly(ethylene oxide) (PEO) [29], poly(ethersulfone) [30], and poly(azo-pyridylurethane) [31], as well as on already formed SMP composites of polyurethane and halloysite [32].

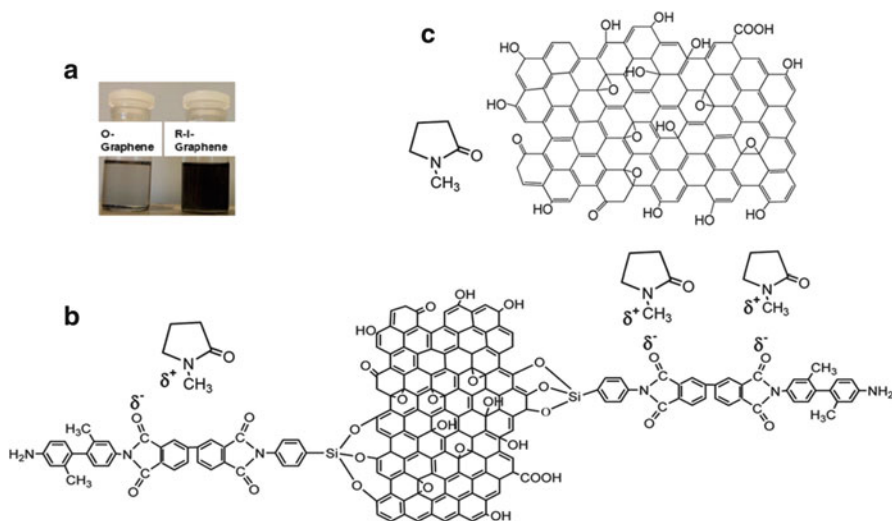


Fig. 3 (a) Dispersion of unmodified graphene in *N*-methyl-2-pyrrolidone (NMP) (*left*) compared with the dispersion of rigid imidized graphene in NMP (*right*) after 60 days. (b) Structure of the rigid imide surface modifier covalently bonded to graphene. (c) Oxygenated graphene with NMP. Reprinted from Yoonessi et al. [33], Copyright 2012, with permission from the American Chemical Society

For graphene oxide composites, researchers were able to show various electrical and thermal property increases in polymers containing both the reduced and surface-functionalized versions of the material. In 2012, Yoonessi et al. showed that polyimide–graphene nanocomposites can increase the modulus (up to a 2.5-fold change with 4 wt% graphene loading) as well as the onset temperature for thermal degradation (up to $T_d \sim 545^\circ\text{C}$ with 8 wt% loading versus $T_d = 504^\circ\text{C}$ for the unloaded version) [33]. In this same study, the authors also modified the graphene with imide functionalities to study the properties of composites with graphene incorporated into the main chain (Fig. 3). With this modification, no significant change was observed in the thermal behavior of the final network apart from the previously described dependence of thermal degradation onset on the loading percentage. Another group studied the incorporation of graphene into a polyurethane SMP and showed a significant increase in electrical conductivity, from a conductivity of 1.96×10^{-12} S/cm for the native polymer to as much as 2.84×10^{-3} S/cm for the composite with 2 wt% graphene loading [34]. These, along with other innovative uses of graphene fillers such as those at UCLA where researchers soldered Ag nanowires using dried reduced graphene oxide for use in polymer light-emitting diodes (PLEDs) [35], have led to robust SMP networks that are able to incorporate some of the properties of the chosen organic filler while maintaining the same smart material characteristics that are expected of SMPs.

In addition to graphene and CNT fillers, and the exciting properties found by incorporating them into polymers, other types of fibers have found their way into

SMP networks. In an epoxy-amine system described by Iyengar et al., the loading of up to 0.2 wt% poly(methyl methacrylate) (PMMA) fibers increased the tensile strength and Young's modulus of the material, while minimally decreasing the percentage strain recovered by the network [36]. Similarly, another major area of research into fiber-based SMPCs has been the use of carbon nanofibers in conjunction with boron nitride as a carbon nanopaper for Joule heating of SMP networks. In both cases, the researchers observed a faster shape recovery for an epoxy-amine system over an 80 sec heating period, reaching a maximal internal temperature of 87°C for carbon nanofiber-loaded epoxies and 185°C for carbon nanofiber/boron nitride composites [37, 38]. Other fiber composites have seen uses in deployable satellites as the articulations for a solar panel skeleton in solar-powered satellites [39].

As shown in this section, organic SMP composites have been extensively used for their enhanced mechanical, electrical, and thermal properties. With speculative uses in self-healing applications [24], moisture-activated networks [40, 41], and other thermally and electrically actuated networks [42, 43], organic SMPCs demonstrate the capability to adapt neatly to the challenges presented by niche problems. However, the prime focus of this review is the loading of various inorganic fillers into SMP networks to tackle issues that are currently unattainable because of both the physical and cost limitations of organic fillers.

3 SMPINCs for Increased Mechanical Strength

3.1 *Motivation and the Merging of Fields*

The shape memory effect was first elucidated as early as 1932 by Chang and Read, who were exploring the elastic properties of AuCd among other interesting materials [44]. The effect was spotted in inquiries over the next 80 years with increasing frequency and excellent, detailed reviews on these early histories should be consulted [2, 3, 10, 14, 15, 45]. The re-emergence of shape memory polymers and shape memory polymer systems began in the late 1990s and the push towards shape memory polymer nanocomposites took flight after the publication of several seminal works published at the turn of the twenty-first century.

In 2000, Alexandre and Dubois described the preparation, processing, and properties of a new class of materials called polymer-layered silicate nanocomposites [46]. A schematic of naming conventions is described in Fig. 4, adapted from that work. Although this work did not explicitly describe shape memory effects in inorganic nanocomposites, the general nature of the work presented approaches for synthesizing, producing, and testing complex polymer nanocomposites that have served to catalyze efforts in the field ever since. The team outlined a host of polymer nanocomposites, including polymer systems with fillers consisting of graphite, metal chalcogenides, carbon oxides, metal phosphates,

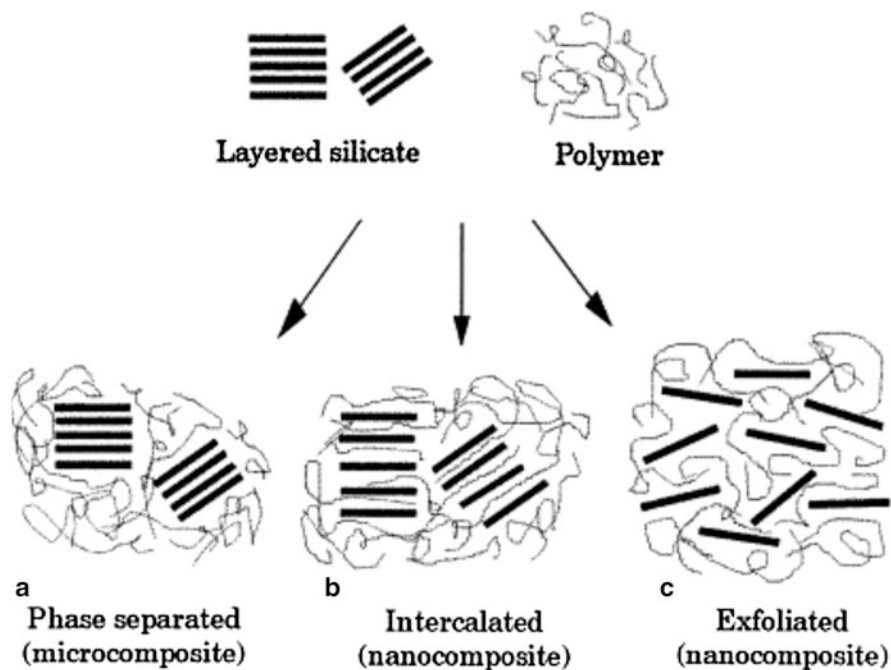


Fig. 4 Early work in inorganic nanoclay–polymer composites helped define terminology that has persisted in the field. This scheme demonstrates the differences between phase separated, intercalated, and exfoliated nanocomposites, noticeably when the filler exists in thin platelet or rod geometries. Reprinted from Alexandre and Dubois [46], Copyright 2000, with permission from Elsevier

layered double hydroxides, clays, and layered silicates such as montmorillonite (MMT), hectorite, saponite, fluoromica, fluorohectorite, vermiculite, kaolinite, and magadiite. In this work, nanocomposites were defined as materials in which at least one dimension of the dispersed particles in the polymer matrix is in the nanometer range.

Nanocomposites can be divided into three key domains on the basis of the dimensionality of the nanoparticles, nanofillers, or nanomaterials:

3D nanomaterial composites – Three dimensions of the nanoparticle fillers are on the nanometer scale. These fillers are also called isodimensional nanoparticle composites. Examples include silica obtained by in-situ sol–gel methods, semiconductor nanoclusters that are dispersed in polymers, and systems in which polymers are subsequently polymerized around nanostructures.

2D nanomaterial composites – Two dimensions of the nanomaterials are on the nanometer scale. Fillers include materials such as carbon nanotubes, cellulose whiskers, metal whiskers, and rod-like clay fillers.

Table 1 Polymer matrix materials described and quantified for use in polymer nanocomposites

Short name	Polymer matrix materials described in [46]
ALA	Aminolauric acid
APP	Ammonium polyphosphate
BDMA	Benzyl dimethylamine
BTFA	Boron trifluoride monomethylamine
DGEBA	Diglycidyl ether of bisphenol A
EVA	Ethylene vinyl acetate copolymer
HDPE	High density poly(ethylene)
HPMC	Hydroxypropylmethylcellulose
MAO	Methylaluminoxane
NBR	Nitrile rubber
NMA	Nadic methyl anhydride
PAA	Poly(acrylic acid)
PAN	Poly(acrylonitrile)
PANI	Poly(aniline)
PBD	Poly(butadiene)
PCL	Poly(ϵ -caprolactone)
PDDA	Poly(dimethyldiallylammonium)
PDMS	Poly(dimethylsiloxane)
PEO	Poly(ethylene oxide)
PI	Poly(imide)
PLA	Poly(lactide)
PMMA	Poly(methyl methacrylate)
PP	Poly(propylene)
PP-MA	Maleic anhydride modified poly(propylene)
PP-OH	Hydroxyl modified poly(propylene)
PPV	Poly(<i>p</i> -phenylenevinylene)
PS	Poly(styrene)
PS3Br	Poly(3-bromostyrene)
PVA	Poly(vinyl acetate)
PVCH	Poly(vinylcyclohexane)
PVOH	Poly(vinyl alcohol)
PVP	Poly(2-vinyl pyridine)
PVPyr	Poly(vinylpyrrolidone)
PXDMS	Poly(<i>p</i> -xylenylene dimethylsulfonium bromide)
SBS	Symmetric(styrene \pm butadiene \pm styrene) block copolymer

1D nanomaterial composites – One dimension of the nanomaterial is on the nanometer scale. Examples include thin films, sheets, and platelets. Polymer-layered crustal nanocomposites fall into this category.

For polymer matrices, Alexandre and Dubois discussed a host of polymer systems compatible with nanocomposites, including those listed in Table 1 (adapted from Alexandre and Dubois [46]).

Although the shape memory properties of the polymer nanocomposites were not explicitly described for all of these nanocomposites, many of the materials have independently been shown to have shape memory properties and the descriptions of the polymer nanocomposites from the year 2000 remain relevant today for the field and ongoing research.

Separately, the field of SMPs was reinvigorated by detailed studies in polymer thermomechanics applied to solve novel problems in the sectors of healthcare and aerospace. In 2002, Lendlein and colleagues described SMPs for biomedical devices across a number of systems and applications [47–49]. This re-emergence spurred a new generation of researchers to build upon the ideas and methods of previous researchers and seek ways to incorporate new techniques, new materials, and new composites into shape memory materials, with a growing focus on shape memory polymers. Over the next decade, researchers pushed the recovery mechanics of SMPs in a host of biomedical applications that ranged from self-locking stents, such as ureteral stents [50], to self-tying sutures [48], unfolding stents [51–53], slow-inserting intracortical electrodes [54], coiling nerve cuff electrodes [55], self-opening foams for the treatment of aneurysms [56, 57], and autoreleasing drug carriers. Mechanical phenomena have been used in a variety of ways for biomedical applications, which are explored in more detail in the next subsection. More recently, smart composites have sought to replace neat SMPs due to their enhanced ability to recover shape at high stresses and the enhanced structural integrity of the underlying materials.

3.2 Emergence of SMPINCs

In 2002, Gall et al. developed what might be the first SMPINCs in which the explicit shape memory properties of the nanocomposites were described. These materials were epoxy resins based on silicon carbide (SiC) filler that could recover large strains upon the application of heat. They used SiC nanoparticles with average diameters of 300 nm and loading fractions of up to 40%. This system utilized a proprietary resin from Composite Technology Development Inc. (CTD), called DP-7, which is a thermoset epoxy resin. A drop in T_g from about 80°C to about 70°C was observed upon incorporation of 20% SiC filler. The team noticed an increase in constrained recovery, or the strength with which an SMPINC can recover, that was 40% greater upon inclusion of the SiC filler [58]. In 2004, Gall et al. expanded upon this work to identify internal stress storage mechanisms in these composites [59] while a similar team, this time led by Liu et al., dove deeper into the thermomechanics of the SMP composites [60].

As the field of SMP inorganic composites began to pick up steam, Cho and Lee (also in 2004) observed the influence of silica on the shape memory effect in polyurethanes [61]. They incorporated varying amounts of tetraethoxysilane into SMPs and observed changes in mechanical properties. What was interesting in their results was that varying the amount of hard segments in the polyurethane from 30 to

50% had a much larger mechanical influence than the concentration of silica. At high loadings of the silica, the breaking stress began to drop, ranging from above 2.0 kgf/mm^2 ($\sim 19.6 \text{ MPa}$) at 10% silica loading to less than 1.0 kgf/mm^2 ($\sim 9.8 \text{ MPa}$) at 30% loading. Over that range, the modulus remained fairly constant but varied greatly from the 30% hard segment polyurethane, at near 1.5 kgf/mm^2 (15 MPa), to the 50% hard segment polyurethane with a modulus of $5\text{--}6 \text{ kgf/mm}^2$ ($\sim 49\text{--}58 \text{ MPa}$). This indicated that control of the polymer network plays a much greater role in dictating properties at these low to mid-range loadings.

At the same time, a pioneering research group at the Air Force Research Labs led by Rich Vaia added to the discussion of SMP properties through work on carbon nanotube composites [62]. This was probably built upon Vaia's PhD thesis work in which he developed a lattice model for intercalation by molten polymers [63, 64]. Vaia's work was specifically important in the SMP composites field at this time for elucidating new mechanisms for using anisotropic nanocomposites to generate large recovery stresses, not possible with neat resins. Furthermore, it indicated willingness on the part of the Air Force to invest in this emerging area, which had largely been bolstered by needs in the automotive industry during the previous decade. These results continued to spur on research for new mechanisms for deployment of bulky structures for aerospace applications by demonstrating a previously unreachable parameter space for recovery stress, mechanical strength, and shape memory properties.

In 2005, a group led by Gall at UC Boulder and Steven Arzberger, a researcher at CTD Inc., described the use of elastic memory composites based on CTD's proprietary TEMBO shape memory polymers, which are epoxy or cyanoacrylate resins with low outgassing and high strain-to-failure and reinforced with carbon, glass, Kevlar, conventional filler, and nano-reinforcements. These materials were developed for deployable space applications (such as morphing aircraft wings) with very tight application needs and demands. The materials were used as hinges, deployable satellite panels, solar arrays, and flexible satellite booms with proposed uses as deployable antennas, deployable optics, and other deployable systems [65]. The TEMBO nanocomposite systems were compared with traditional microcomposite systems: use of nanofillers led to increased interfacial surface area (1,000-fold increase) and fewer material defects.

Other groups sought various ways to increase the mechanical strength of SMPINCs [66]. Ohki et al. explored glass fiber SMP composites and reached tensile stresses near 90 MPa at temperatures below T_g and strains of 225% at stresses of $\sim 9 \text{ MPa}$ at 20°C above the T_g of 45°C . Interestingly, the DiAPLEX materials studied (MM4510), which are thermoplastic polyurethanes, exhibited the evolution of large permanent cyclic strains at 10 wt% glass fiber loading, but appeared to stabilize at 20 and 30% strain such that successive cycles did not induce further permanent strain, as shown in Fig. 5 [66].

In 2006, C.P. Wong's research group at Georgia Tech developed a tantalum-filled SMP composite for both its mechanical and radiographic properties [67]. The 3% tantalum filler (325 mesh or $40\text{--}50 \mu\text{m}$ particles) had very little effect on the mechanical properties of the material. The authors demonstrated a 3°C increase in

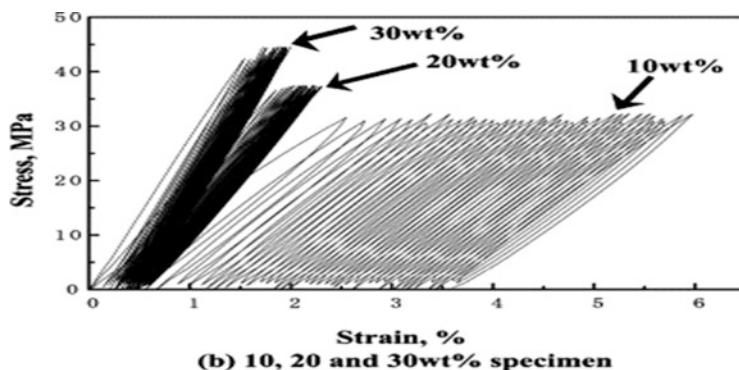


Fig. 5 The stress–strain response is shown for a glass fiber–SMP composite with a thermoplastic polyurethane matrix. At 10 wt% glass fiber loading, permanent strain evolves in the material, whereas 20 and 30 wt% loadings help stabilize the network structure and lead to less permanent deformation over successive cyclic loading. Reprinted from Ohki et al. [66], Copyright 2004, with permission from Elsevier

T_g (as shown by both dynamic mechanical analysis, DMA, and differential scanning calorimetry, DSC) with the filler and an increase in glassy modulus from 1,400 to 1,710 MPa with a standard deviation of 120 MPa. Thus, there was a slight increase in glassy stiffness, but no corresponding change in the rubbery modulus after tantalum loading. Interestingly, the recovery stress was slightly elevated at the onset of T_g , but lower at and above T_g with the inorganic (but not nano-) filler.

A popular filler in the SMPC world is Cloisite 30B. In the MMT clay manufactured by Southern Clay Products, the particle size distribution is such that 90% of the particles (dry weight) are of less than 13 μm diameter, while 50% of the particles are less than 6 μm and 10% are less than 2 μm [68]. This breakdown makes Cloisite in some sense a nanoclay, but in reality still a microclay. TEM images presented by Schulz et al. [68] did indicate 500 nm particles in Cloisite 30B. Cloisite 30B is, however, comprised of platelets that are approximately 120 nm in diameter and as small as 3 nm thick [69]. Under the correct pre-processing conditions, these platelets can be incorporated into polymer networks to varying degrees of uniformity and success at very different size scales.

In 2007, Cao and Jana at Akron tethered Cloisite 30B clay particles onto SMP polyurethanes [70]. The polyurethanes were synthesized from aromatic diisocyanates, a crystalline polyester polyol, and poly(ϵ -caprolactone) (PCL) diol. The monomer ratios were cleverly balanced between an excess ratio of isocyanate in the polymer system and the pendant alcohol groups ($-\text{CH}_2\text{CH}_2\text{OH}$) on the quaternary ammonium ions from the Cloisite 30B. The team observed an increase in the rubbery modulus at 100°C ($T_m + \sim 50^\circ\text{C}$) of nearly one order of magnitude, from 4–5 MPa without loading to more than 20 MPa with loading. In the carefully crafted study, the authors determined that at high (5%) clay content, a more rapid relaxation of induced tensile stress reduces the recovery force of SMPs. In addition,

they proved that the clay fillers deter soft segment crystallization and adversely impact room temperature properties between the T_g and T_m .

In 2007, Razzaq and Frommann in Clausthal, Germany filled polyurethane SMPs with aluminum nitride (AlN) and exhaustively studied the resulting mechanical properties [71]. The AlN came in three particle sizes with distributions (1) between 200 and 350 nm, (2) between 800 nm and 1.8 μm , and (3) between 2.3 and 4.5 μm . SEM micrographs showed nice dispersion at 30 and 40 wt% loadings in the polyurethane nanocomposites. The team observed a drop in T_g from 55 to 45°C and an increase in thermal conductivity from 0.2 W to 0.4 W/mK at loadings of 0 and 40% AlN, respectively. Most importantly, the team showed a drop in shape recovery from above 95% for the neat polymer to about 85% for the 30 wt% AlN filling and below 75% shape recovery at 40 wt% AlN loading. At pre-strains of 50%, the neat polymers were able to fix approximately 42% of the strain, whereas the 40 wt% AlN SMPINCs could fix closer to 45%. This increase in fixity, although perhaps not intuitive, can be explained by interconnectivity of the AlN network at high loadings, which impedes soft segment motion during shape fixing or cooling the SMP in a strained state to below T_g or T_m and measurement of deformation (cold) after the applied stress is removed.

In 2007, Rezanejad and Kokabi developed a low density polyethylene (LDPE)/nanoclay composite with shape memory properties [72]. Although all SMPs do not necessarily rely on a two-phase structure such as that of melt processed LDPE, extrapolation from this work can be made for a wide range of SMP systems. The team used organically modified Cloisite 15A nanoclay as filler and demonstrated a 300% increase in both E' and E'' upon addition of up to 8% nanoclay. Although the neat polymer system had nearly 100% shape recovery, the 8% loaded sample recovered nearly 80% at pre-strains of both 50 and 100%. Recovery stress, however, was dramatically increased from 1 MPa for the neat LDPE to about 3 MPa at 50% pre-strain and above 3 MPa at 100% pre-strain.

In 2007, Kim, Jun, and Jeong designed a complex composite [73]. The team from Ulsan, Korea used a macro-azoinitiator containing a poly(ethylene glycol) (PEG) segment that was intercalated in the gallery of sodium montmorillonite (Na-MMT). This was further used to prepare a composite with poly(ethyl methacrylate) (PEMA). The macro-azoinitiator was the condensation polymer of 4,4'-azobis(4-cyano-pentanoic acid) and carefully used to intercalate the clay. The team paid special attention to segment mobility of PEMA relative to the clay and showed decreasing mobility with increasing loading. The materials were loaded with up to 9% Na-MMT. By dynamic mechanical thermal analysis (DMTA), the glassy (elastic) modulus in bending at 25°C was shown to have increased from 7 GPa (neat PEMA) to above 10 GPa (9% loaded composite) and the rubbery modulus was reported to have increased from about 4 MPa to above 20 MPa with the loading. The authors observed the cyclic tensile behavior of the samples and showed that the emergence of permanent strain was minimized in the neighborhood of 1–5% loading. Complex viscosity versus frequency at high temperatures (160°C) become closer to linear, with higher loading at low frequencies, as did the shear modulus (G') at 160°C. The team ultimately showed that a small amount of clay

filler can help stabilize thermoplastic SMPs such as PEMA, giving them better cyclic life and enhanced recovery stress.

In 2009, Hu et al. explored polyurethane SMPs with attapulgite clay $(\text{Mg, Al})_2\text{Si}_4\text{O}_{10}(\text{OH})\cdot 4(\text{H}_2\text{O})$ as filler. Compared with the Na-MMT and Cloisite fillers described in previous works, these fillers were dispersed in rod-like formations that had rod diameters of 20–50 μm and were several microns in length, with 40–100 length/diameter aspect ratios. The fillers were blended with Mitsubishi's MM5520 thermoplastic polyurethane resins. The team demonstrated an increase in hardness from 100 to 160 MPa for treated clay fillers and a detrimental reduction to below 20 MPa for untreated particles. Interestingly, the authors described a three-stage heat-treating process. At 100°C, moisture is lost from the attapulgite powder from its free water content. At 200°C, the zeolite tube is destroyed, which coincides with the loss of hygroscopic water and zeolitic water. Beyond 450°C, the hydroxyl groups are gradually reduced. This work presents a compelling case for careful analysis of filler before blending so that the resulting thermomechanical properties of the composite can be properly optimized.

Toward the end of the first decade in the twenty-first century, the field had begun to mature such that excellent reviews began to emerge that highlighted important advances in the biomedical, mechanical, thermal, optical, electronic, and magnetic properties of both organic and inorganic shape memory polymer composites. This review has selected several important works from the late 1990s and early 2000s and extracted mechanical details as a frame of reference for more recent works, but leaves it to other reviews (such as the comprehensive tome by Ratna and Karger-Kocsis [14]) to provide a more detailed assessment of SMP composites described between the 1950s and 2006–2007. In 2010, Meng and Hu provided another such review with a focus on both organic and inorganic SMP blends [10], while Huang et al. described recent advanced in SMP composites [1].

3.3 *Years 2010–2014: Interface Chemistry of SMPINCs Leads to Enhanced Thermomechanics*

The last 4 years have seen an explosion in targeted research on SMPINCs, with researchers largely seeking to precisely control interfacial forces and linking chemistries in scalable ways. The decade began with an excellent work in emerging chemistries. In 2010, Xu and Song compared SMP composites made with polyhedral oligomeric silsesquioxane (POSS) cores with a composite made with acetal-protected organic cores. The POSS cages were functionalized at all eight vertices of the POSS cubes with poly(lactic acid) (PLA) arms, which could then be functionalized into the SMP network. Using longer PLA arms on the POSS cage cores led to higher recoverable strains but less stability in the rubbery plateau above the T_g . The T_g , as determined by DSC, in the POSS composites ranged from 42.8°C with short PLA arms to 48.4°C for POSS functionalized with longer PLA arms.

These measurements were approximately 10°C lower than the peak of $\tan \delta$, as measured by a DMA in tension at 1 Hz. The glassy modulus of the polymer–POSS composites ranged from 2.0270 ± 0.0383 GPa with short PLA arms (M_n by ^1H NMR $\sim 7,328$) to 2.2868 ± 0.0627 GPa with intermediate length arms (M_n by ^1H NMR $\sim 13,576$) and 2.2347 ± 0.0171 GPa with long PLA arms (M_n by ^1H NMR $\sim 25,788$). Interestingly, the biodegradable shape memory polymer [142] composites based on POSS were more effective in minimizing excessive global entanglement of tethered network chains and improved their ability to participate in the shape memory effect. These materials open the possibility for locally delivering therapeutics within composites that are mechanically robust at body temperature but that vanish as the polyester scaffold breaks apart.

In 2011, Ratna explored poly(ethylene oxide) (PEO)/clay nanocomposites [74] and in 2013 continued to innovate by combining PEO clay nanocomposites with MWCNTs to build hybrid organic–inorganic composites [29]. In 2012, Ali et al. reinforced polyurethane nanocomposites with palm oil polyol precursors as an environmentally friendly way to build high strength composites using the nanoclay Cloisite 30B. The team showed that the presence of reactive nanoclay particles limited crystallization and that above 5% loading it began to affect both shape fixity and shape recovery in the hyperbranched polyurethanes [75]. Cuevas et al. explored the thermomechanical properties of glass fiber-reinforced SMPS [76]. In 2012, efforts led by George determined thermomechanical properties of self-healing polymer nanocomposites [77]. Some of the interesting work emerging in the recovery of micro- and nanodamage in ceramic cracks should be of interest to the SMP inorganic nanocomposite community [78].

In 2012, Han et al. developed a creative method using zinc ions to help trigger triple shape memory effects in hydrogels [79]. The team synthesized poly(acrylonitrile-*co*-2-methacryloyloxyethyl phosphorylcholine) [P(AN-*co*-MPC)] hydrogels. The SMP nanocomposite community can draw design strategies from an approach such as this one. The authors utilized Zn particles from a ZnCl solution to trigger changes in the mechanical properties of the triple shape memory polymers. Zinc ions were able to selectively complex with the nitrile's lone pair of electrons, causing the dissociation of nitrile–nitrile intramolecular interactions. This interaction is shown schematically in Fig. 6 [79]. The zinc ions had a tremendous effect on the mechanical properties and shape memory properties of the material. For one of the tested P(AN-*co*-MPC) materials, the Young's modulus was enhanced from 7.36 MPa in water to 37.57 MPa in 30% ZnCl₂ solution, and dropped to 0.053 MPa in 50% ZnCl₂ solution. One could envision a next generation of SMP nanocomposites that employ clever ways to take advantage of similar phenomena.

In 2004, a comprehensive volume was edited by Utracki that provides a thorough description of the thermodynamics, polymer mechanics, and composite mechanics of clay-containing polymer nanocomposites [69]. In 2012, Woodhead Publishing led by editor Gao published an extensive review of recent advances in polymer nanocomposites [80]. Chapter 11 of that book describes in detail the progress made in the manufacture and characterization of thermoplastic

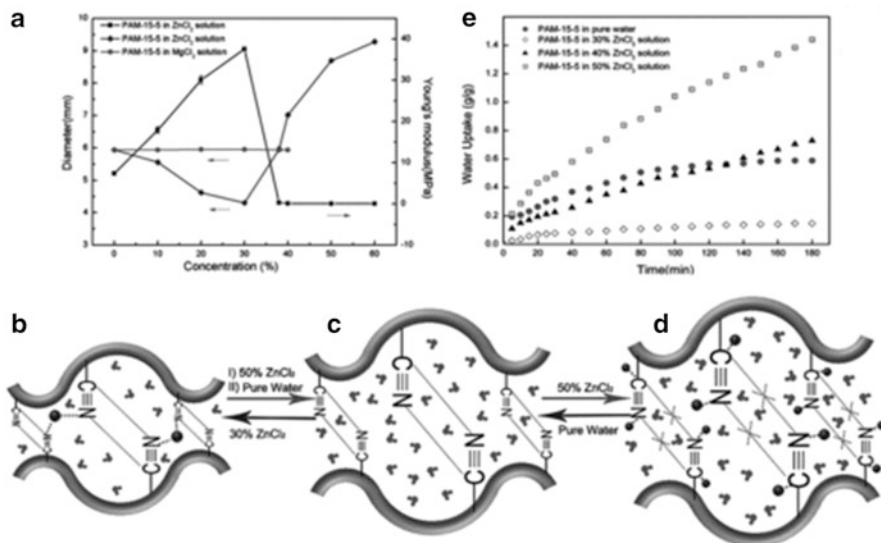


Fig. 6 The response of a well-engineered polymer to a ZnCl solution triggers incorporation of Zn particles into the network to complex with side chains and create the emergence of CN–CN dipole pairing (b–d). The effects of this phenomenon on mechanical properties such as swelling (a) and water uptake (e) are dramatic, providing a potential method for creative engineering with polymer nanocomposites. Reprinted from Han et al. [79], Copyright 2012, with permission from John Wiley and Sons

polyurethane nanocomposites, including thermoplastic elastomers, styrene block copolymers, thermoplastic olefins, thermoplastic vulcanizates, and copolyester elastomers [81]. The work describes nanocomposites with fumed silica, POSS cages, nanomagnetite, SWCNTs, and MWCNTs. The review does a comprehensive job of compiling several leading sources in the arena of thermoplastic polyurethane nanocomposites and will be of excellent utility to the reader.

The application of nanoclays to polymers with tunable T_g s has generated significant research interest. LeBaron et al. showed that nanoclay Laponite RD has a greater tendency to aggregate in the polyether-based thermoplastic polyurethane (TPU) than Cloisite 20A, which was modified with dimethyl dehydrogenated tallow quaternary ammonium ions [82]. Padmanabhan showed that MMT modified with quaternary ammonium bromide with a hydroxyl group exhibits better affinity for polyester–TPUs than Cloisite 30B due to the ester–polyol hydrophilicity [83]. Furthermore, the hydroxyl group on the outer surface of the clay in the MMT/OH system was proposed to make available hydrogen bonding sites as compared to clays with shorter hydroxyalkyl chain modifiers such as Cloisite 30B. Korley et al. and Edwards observed good dispersion of Cloisite 30B with intercalated/exfoliated silicate layers throughout the TPU matrix [84]. In fact a 5 wt % incorporation of this modified Cloisite 30B led to a 152.48% increase in tensile strength. Edwards made interesting discoveries concerning nanoclay modifiers in

his 2007 PhD thesis at the University of Queensland [85]. TPU nanocomposites of Laponite RDS (containing a pyrophosphate-based peptizer) were modified with both cetyl trimethyl ammonium bromide (cLS) and with 1, 3, 5, and 7 wt% dodecyl amine hydrochloride (dLS). The nanocomposites exhibited quite different properties. The cLS-based TPU nanocomposites showed partly exfoliated intercalated and aggregated structures at 1 wt% loading but aggregated at 5% loading. This led to a 200% increase in storage modulus in both the glassy and rubbery states at 1 wt% loading but a subsequent decrease with further increase in clay content. However, the dLS-based TPU nanocomposites showed a spherical cluster-type structure for all studied clay contents up to 7%, which led to an increase in storage modulus across that range.

Quadrini et al. developed a solid-state process to yield epoxy foams with different contents of nanoclay (up to 10%wt) [86]. They demonstrated excellent shape memory properties for the nanocomposite foams with low filler loadings and were able to control porosity by varying the solid precursors during the foaming process.

Tan et al. studied the shape memory polymer properties of a series of MMT polyurethane–epoxy composites [87]. The team concluded that tensile strength reached a maximum value at 3 wt% loading while the maximum value of elongation at break was at 2 wt% MMT loading.

Tarablsi et al. utilized maghemite intercalated MMT at 1 and 2 wt% loadings in photopolymerized difunctional acrylates [88]. The team noted that polymer nanocomposites are usually prepared by in situ polymerization, sol–gel processing, or melt-compounding. They noted several works combining both clays and iron oxide nanoparticles, but claimed to be the first group to use UV-curable resins with both clay and iron oxide fillers. Maghemite intercalated montmorillonite ($\gamma\text{Fe}_2\text{O}_3$ -MMT) was prepared using (1) ion exchange of interlayer sodium ions with iron(III) ions, (2) formation of goethite, and (3) thermal solid-state transformation of goethite into maghemite intercalated MMT. Then, this new nanofiller was incorporated into photopolymerizable formulations containing 1,6-hexanediol diacrylate (HDDA) and polyethylene glycol (PEG 400) diacrylate before UV curing. The authors demonstrated an increase in rubbery modulus (at 25°C) on 100- μm thick films by DMA at 1 Hz, with a 20 μm displacement amplitude from 32 to 53 MPa with 2% of the compound filler. The T_g of their loaded system at -7°C remained unchanged while the glassy modulus increased with 2 wt% loading from approximately 3 GPa to about 4 GPa. The authors did not propose methods for curing thicker specimens using this processes, but emerging 3D printing technologies in stereolithography or polyjet processing have high throughput and could potentially successively cure thin layers of such a composite by UV light.

In 2013, Chiu et al. described multiple intercalation strategies in clay/polymer hybrids [89] and described self-organization of organics in clay interlayer galleries. The review did not explicitly focus on shape memory polymers, but much relevant and sophisticated interface physics and chemical surface modifications and many clever processing approaches can be found in this excellent and comprehensive

work. The authors developed a compelling timeline for 2000 to 2011 that details many of the interesting advances in the field of polymer composites during that span.

Zhang, Petersen, and Grunlan from Texas A&M University have described new materials based on inorganic–organic shape memory polymer foams [90]. They describe potential uses for these foams in applications requiring diffusivity and permeability, such as embolic sponges to treat aneurysms and tissue engineering scaffolds. The team built copolymers of PCL and PDMS, which were synthesized utilizing a salt fusion process to create SMP foams with highly interconnected pores of 400–500 μm pore size. This approach led to unique compressive strength with low densities. The approach could serve as an interesting template for the fabrication of porous SMP nanoparticles composites.

Zhang et al. described a method for using microcapsules and small molecule catalysts to trigger self-healing in polymer systems [91]. The capsules were filled with unreacted monomer that, upon exposure to the catalyst, could self-heal as a result of cracking or deformation. Zhang's team went on to combine these systems with woven materials as composites. We feel that this area represents a fertile intersection for new SMPINCs with self-healing properties. In 2013, Basit et al. manufactured laminated shape memory polymer composites with two-way and multimemory effects [92]. Although their laminates were not nanolaminates, the array of force measurements, recovery stresses, and recovery strain in quasi-static, dynamic, and cyclic environments present a compelling roadmap for researchers documenting the properties of SMPINCs. Jumahat et al. observed that the inclusion of more than 3% nanoclay content had a detrimental effect on the fracture toughness of epoxy resins [93]. In 2013, Li et al. presented work on a water (plasticization)-triggered shape memory effect in polyurethanes modified with ZnO composites. Also in 2013, Wu et al. developed polyurethanes grafted with poly (methacrylic acid) chains to allow for the formation of long percolation networks in the inorganic clay composites. Senses and Akcora described a different interesting stiffening mechanism in polymer nanocomposites through a responsive polymer than can control chemical regulators affecting interface physics in the composite or alter crosslinking in the system [94]. The pair used PMMA processed by atom transfer radical polymerization (ATRP) to achieve a polydispersity index of 1.03 and to measure the effects of incorporation of 13-nm silica nanoparticles. They carefully observed the effects of particle–polymer interactions under deformation to explore adaptive mechanical behavior.

Xu et al. developed a titania-based hydrogel nanocomposite with excellent mechanical properties, good water stability, and a water-activated shape memory effect by relying on the titania nanoparticles as crosslinkers [95]. The hydrogels were formed by in situ free radical copolymerization of acrylic acid (AA) and *N,N*-dimethylacrylamide (DMAA) in TiO_2 colloidal solutions. Hydrogels with 10 wt% TiO_2 crosslinker were reported to swell and accommodate strains of more than 1,100% before failure. A content of 20 wt% brought the strain to failure down to 855%, 30 wt% TiO_2 further decreased this to 172% strain, and 40 wt% TiO_2 dropped the strain capacity to less than 90%. In those four samples, the

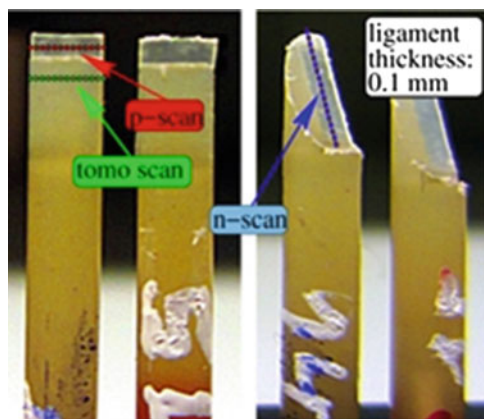


Fig. 7 Polypropylene nanocomposites with montmorillonite filler were characterized in unique ways using small-angle X-ray scattering techniques. Different types of scan are shown: *p-scan* parallel scan across a horizontal web; *n-scan* normal scan across a slanted web; *tomo scan* scan across the full rod. These approaches hold tremendous promise for understanding morphological phenomena in SMPINCs. Reprinted from Stribeck et al. [97], Copyright 2014, Open Access

modulus correspondingly increased from 19.96 kPa to 52.69 kPa, 64.70 kPa, and 85.87 kPa. The tensile strength peaked at 20% loading and fell off precipitously by 40% loading.

Kang et al. investigated the adhesion between titanium alloys and shape memory polymer nanocomposites [96]. The team showed that surface modification of titanium alloys with silane coupling agents improved adhesion strength. The SMP was toughened with both 5 wt% poly(*n*-butylene oxide)-*block*-poly(ethylene oxide) and 2 wt% carbon nanotubes and tested against surface-modified titanium alloy, showing up to 113.5% increase in adhesion strength compared with the non-toughened control. The adhesion mechanisms were elucidated by observing the adhesive fracture surface by tracking the locus of failure using high-resolution electron microscopy and energy dispersive X-ray spectroscopy.

In 2014, Stribeck et al. observed the properties of injection-molded polypropylene (PP)/MMT composites by microbeam small-angle X-ray scattering [97]. They were interested in studying gradient effects along the radius of injection-molded nanocomposite rods. This analysis is crucial in translating emerging polymer nanocomposite research into practical use. To prepare samples, the team melt-mixed exfoliated MMT with the PP. The team observed semicrystalline regions in the neat PP and determined an average distance of 12 nm between adjacent crystalline layers. The manuscript provides detailed references for reading and interpreting SAXS patterns for those not familiar with the measurements. Figure 7, taken from that article, pictures the different SAXS patterns used for studying neat PP and PP/MMT composites, looking both at the nanocomposite surface and at its core across the radius of a composite rod. The neat PP was shown to be consistent everywhere on the rod for all types of scans (the *n-scan* is shown in

Fig. 7). For the composites, however, the PP scattering and MMT scattering were discrete on the surface of the rod, but inside the nanocomposite rods only discrete scattering of the MMT was observed. This led to a fascinating discussion about the evolution of primary and secondary crystalline domains and concluded that the PP matrix of the composite must exhibit deteriorated mechanical properties. In effect, the work presents an interesting approach using SAXS to make predictions about the mechanical properties of semicrystalline composites.

4 SMPINCs for Biocompatibility

One of the main challenges in designing complex SMPINCs with many available inorganic fillers is predicting the bioresponse to the introduction of these materials into a biological system. Traditionally, materials that do not present the expected surface functionality *in vivo* perform poorly in terms of the immune response and scar formation around an implant site. For acutely used materials, this may not pose a risk because the organism is only exposed briefly to the potentially toxic by-products. However, when SMPINCs have to perform the role of chronic or permanent prosthetics or implants, the biocompatibility of the material becomes of great significance. By introducing various inorganic nanofillers such as phosphate salts and metal nanoparticles, researchers have been able to drastically change the interaction between SMPINCs and their biotic counterparts. Meng and Li, as well as Madbouly and Mather, have provided excellent reviews on some of the initial results from the incorporation of inorganic fillers into biocompatible SMPs [6, 13] and on the properties of the subsequent composites. For an in-depth analysis of the theory behind the relationship between filler ratios and subsequent mechanical properties, Kazakeviciute-Makovska and Steeb described a model for the prediction of elastic modulus changes resulting from the addition of nanofillers [98]. Together, these resources serve as an excellent introduction to biocompatible SMPINCs and their novel properties based on the inorganic fillers chosen. In this section we explore the most recent uses of these fillers to enhance the biomechanical properties, to tune the degradable nature of SMPINCs, and most importantly, to inhibit the potentially cytotoxic nature of the polymer networks.

4.1 *Enhancing Biocompatibility*

For most SMPINCs, the use of various inorganic fillers for their unique composite properties is prohibitive in a biological setting because of the cytotoxicity of the nanofillers. However, researchers have recently been adding biocompatible inorganics to polymer networks in order to obtain more biofriendly properties. For example, when researchers added the bone mineral-mimicking hydroxyapatite (HA) to a poly(D,L-lactide) (PDLLA) network, they not only validated a SMPINC

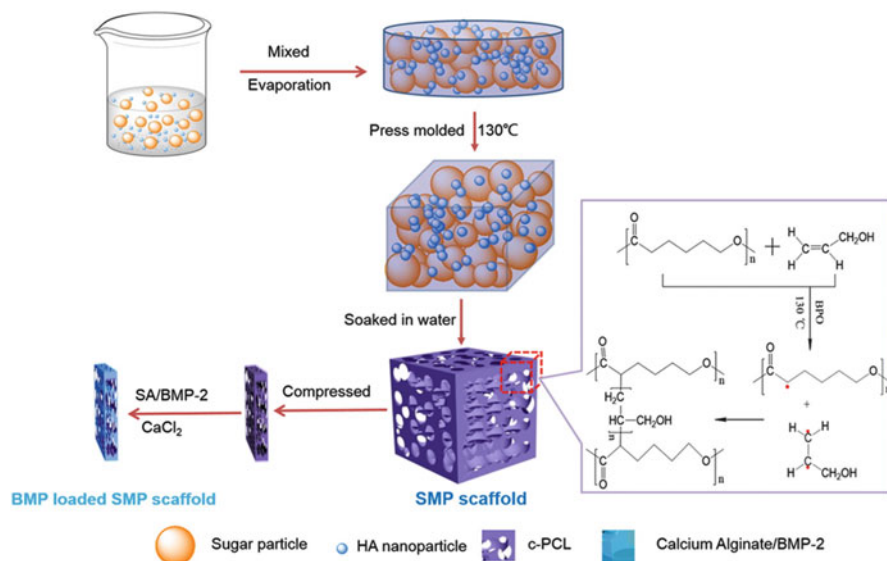


Fig. 8 Fabrication, loading, and shape fixation of a porous crosslinked poly(ϵ -caprolactone) (*c*-PCL) network with bone morphogenetic protein 2 (BMP-2) prior to implantation in a rabbit mandibular bone defect; HA hydroxyapatite. Reprinted from Liu et al. [101], Copyright 2014, with permission from the American Chemical Society

with fully explored biocompatibility but also showed a network with significantly increased shape recovery ratios of up to 99.5%, depending on the ratio of HA to PDLLA [99, 100]. HA has also been used in a growth factor delivery system, where the HA loading of the chemically crosslinked poly(ϵ -caprolactone) (*c*-PCL) was used to create uniform pore sizes in the smart network [101]. The process described in Fig. 8 shows the use of this smart network as a compressible implant for minimizing the wound area required for insertion. The resulting scaffolds loaded with bone morphogenetic protein (BMP) showed a significant increase in bone mineral density, as well as trabecular thickness and number, compared with the porous scaffold alone and an untreated control. For further reading as a comprehensive introduction to the biocompatibility of HA and its uses in polymer composites as a bone regenerative accelerant, an excellent book chapter is provided by Pielichowska and Blazewicz [102] on this topic.

A shift from HA and the traditionally low mechanical properties of HA-based SMPINCs to another commonly found mineral (boehmite) led Guo and colleagues to incorporate nanoplatelets of the octahedrally coordinated aluminum oxide, AlO₆. This study showed a marked increase in the tensile strength and final rubbery modulus [103], without any sacrifice in the viability of L929 mouse fibroblasts in vitro. Of note, the degradation of these polymers also showed acceleration with increases in boehmite nanoplatelet loading, losing up to 300% more mass than the native poly(propylene sebacate) over the course of 60 days. A similar study was conducted with β -tricalcium particulates embedded in a PDLLA network, which

was investigated for the *in vitro* cytotoxic effects of the constituent degradation products. In this study, Zheng and colleagues demonstrated a SMPINC capable of not only maintaining a stable environmental pH after 56 days of degradation (pH = 7.1–7.3 from a 3:1 to 1:1 PDLLA/ β -tricalcium composite versus a pH of 6.6 from native PDLLA degradation), but also increasing shape recovery as the network degraded [104]. In contrast to these PDLLA networks, PCL SMPINCs seem to demonstrate opposing effects on mechanical properties when filled with Fe₂O₃ nanoparticles. To demonstrate this, Yu et al. showed the decreased recovery ratios of a magnetite-filled, crosslinked PCL network. After up to 14 weeks in phosphate-buffered saline, the total recovery time and gel fraction of the networks significantly decreased, showing a notable relationship between increasing magnetite filler ratio and decreased mechanical properties [105].

4.2 Stronger Biopolymers

Enhancement of the mechanical properties of biocompatible SMPINCs is important for researchers that are looking for mechanically robust devices. Recently, researchers have demonstrated biocompatible networks with a wide array of improved mechanical properties, ranging from increased tensile strength to higher thermal stability. In 2013, Saralegi et al. demonstrated the tuning of hard-segment nucleation in semicrystalline shape memory polymer networks via the introduction of chitin nanocrystals into polyurethane networks [106]. Through this method, biocompatibility of the network was preserved while increasing the stiffness of the overall system. In a similar study, researchers were able to demonstrate shape memory characteristics in clay tactoid-reinforced starch blends. By increasing the total composition of MMTs in the system, up to 10% of total mass, an almost threefold increase in Young's modulus was noted [107]. In one study, researchers added boron nitride nanotubes (BNNTs) to a copolymer of polylactide and PCL to investigate the effects on mechanical strength and biocompatibility in tandem. Besides an astounding 1,370% increase in Young's modulus from the addition of 5 wt% BNNTs, these composites also increased the viability of osteoblast precursors, eventually also showing an increased differentiation rate into osteoblasts on the stiffer 5 wt% BNNT/PCL nanocomposite [108].

The addition of nontoxic metal nanoparticles has also seen increasing use for strengthening SMPINCs while introducing interesting properties to a shape memory network. By adding Fe₃O₄ nanoparticles to a hyperbranched polyurethane network, Kalita and Das et al. were able to demonstrate a homogeneous network of magnetic particles within a biocompatible shape memory polymer, with increasing recovery forces based on the loading of nanoparticles (Fig. 9) that led to faster shape recovery [109–111]. Intriguingly, these polymers also demonstrated antimicrobial properties when degradation products of the network were flowed over cultures of *Staphylococcus aureus* MTCC96 and *Klebsiella pneumoniae*. Such magnetoresponsive polymers show great promise as remotely deployable biomedical implants with advantages as both smart materials and bacterial wardens.

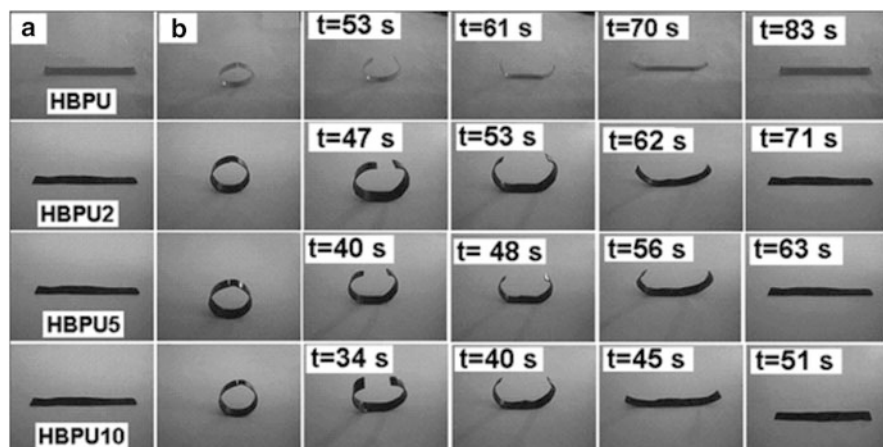


Fig. 9 Increased recovery stresses in a biocompatible hyperbranched polyurethane (HBPU) SMP as a function of Fe_3O_4 loading (0, 2, 5 and 10 wt%). Photographs show the initial shape (a), the deformed shape (b), and the shape after various recovery times. Reprinted from Kalita and Karak [109], Copyright 2013, with permission from Springer

Other classes of metal nanoparticle composites using TiO_2 have been demonstrated to have uses in mechanical improvement of SMPINCs. Lu and colleagues demonstrated that a TiO_2 /poly(L-lactide-co- ϵ -caprolactone) nanocomposite can have up to 113% increase in tensile strength and up to 11% elongation at break with only 5 wt% TiO_2 [112]. In addition to these mechanical properties, titania nanoparticles also show a degree of thermal stabilization in certain shape memory polymer systems. In 2014, Seyedjamali and Pirisedigh showed that incorporation of L-cysteine-functionalized titania nanoparticles also increased the degradation onset temperature T_d by more than 100°C in a poly(ether-imide) matrix, stabilizing the network from a previous degradation temperature of about 400°C to over 525°C with as little as 3 wt% TiO_2 [113]. For a polystyrene/ TiO_2 SMPINC, Wang et al. induced the shape memory effect using UV irradiation of the sample, taking advantage of the photoelectric properties of the incorporated nanoparticles to remotely and precisely release the constrained shape [114]. In a study by Rodriguez et al., the addition of fine tungsten powder (4 wt%) into a polyurethane foaming SMP resulted in a mechanically robust network. Besides the almost twofold increase in breaking tensile strength and strain, this SMPINC also demonstrated the radio-opacity necessary for polymeric biomedical implants [115].

Another important area of research in biocompatible SMPINCs is the use of polyhedral oligomeric silsesquioxanes (POSS). In recent studies, these POSS cages primarily served as anchor sites for PCL chains to make organosilica SMPINCs with a wide variety of properties, ranging from triple-shape POSS/PCL networks [116], dynamic microscale surface features [117], ultrasoft networks post-transition [118], and bimodally oriented POSS/PCL lamellae with shape memory properties [119]. Many other studies on POSS-based composites can be found in a previously

mentioned review by Madbouly and Lendlein [13], where the effects of filler type and concentration are more thoroughly explored.

5 SMPINCs with Electromagnetic Properties

SMPINCs have also been investigated as a means of modulating the electromagnetic properties of these novel actuating materials. Research has largely focused on non-contact activation of the SMP through inductive heating. Normally, SMP systems are locally heated (either by convection or conduction) to drive the polymer through its transition and activate its stored shape. Although suitable for most systems, some exceptions, including remotely deployable biomedical devices and implants, necessitate the use of remote activation with control of local heating. Some advantages of remote actuation enumerated by Buckley are paraphrased below and include [120]:

- Elimination of power transition lines (giving simplified design and eliminating points of failure; can be non-invasive as an implant)
- More complex device shapes are possible while retaining uniform heating (compared with laser heating)
- Selective heating of parts of the sample are possible (allowing new design variables and new types of devices)
- Remote activation means the possibility of delayed actuation (e.g., for tissue scaffolds)

This remote activation can be achieved by doping the SMP with magnetic micro- or nanoparticles and inductively heating the SMP through energy transfer from the particles to the matrix. This heating is achieved through the application of a strong alternating magnetic field, which causes magnetic hyperthermia through thermal loss mechanisms (including hysteresis losses, eddy current losses, and anomalous losses) [121]. The thermal energy generated by the relaxation of the magnetic particles is sufficient, in engineered systems, to drive the SMPINC through its transition and enable shape recovery.

5.1 *Magnetite Filled SMPINCs*

Although work on ferrofluids and ferrogels had begun to probe the area of SMPs actuated via magnetic stimulation, it was Mohr et al. in 2006 who published the seminal work on the topic [122]. Using magnetic hyperthermia (the application of an alternating magnetic field to generate thermal losses) they demonstrated that this mechanism could be used to activate shape memory polymers, driving them through their switching temperature to release a stored shape (Fig. 10). Lendlein utilized magnetic nanoparticles of iron(III) oxide coated in silica to achieve

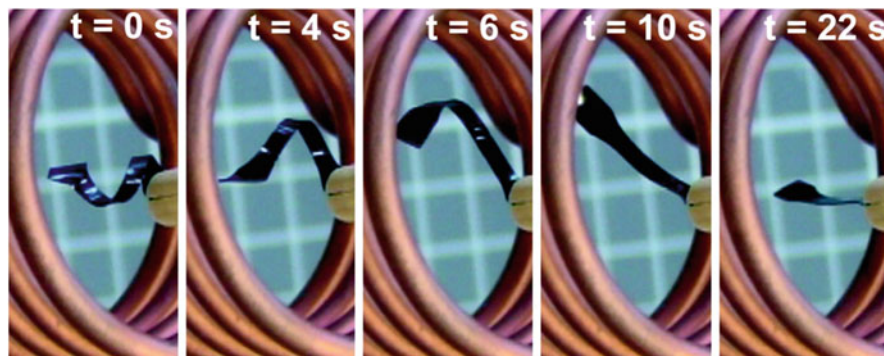


Fig. 10 Utilization of magnetic hyperthermia to drive shape actuation. The stored, corkscrew shape is released to the global minimum, flat shape by the application of an alternating magnetic field. Reprinted from Mohr et al. [122], Copyright 2006, with permission from the National Academy of Sciences, USA

actuation in a polyurethane blend with a multiblock copolymer of poly (*p*-dioxanone) and PCL. This work was expanded upon in 2007 when Weidenfeller and colleagues studied the effect of injection-molding polyurethanes with 10–40 vol% magnetite particles (9 μm diameter) and explored the effect of particle loading on the properties of the material. Significant changes in the storage modulus were observed, especially at 20°C above T_g [71]. These magnetic microparticles were found to have a percolation limit of 30 vol% in the polymer matrix. The T_g of the composite system was found to decrease slightly with increasing loading, whereas thermal stability was virtually unaffected. Further studies by Weidenfeller explored the effect of loading on the electrical properties of the system and the ability of these micron-sized magnetite particles to effectively achieve thermal heating and shape activation [123]. Weidenfeller found that the resistivity of the composite material decreased four orders of magnitude and that the thermal conductivity increased 0.40 W/mK at high loading levels. In 2009, Lendlein and colleagues expanded on their previous work to explore the ability of magnetic hyperthermia to achieve the specific temperatures required for shape activation [121]. They probed the effect of specific absorption rate, particle distribution and content, polymer matrix, sample geometry, and nature of the environment. In 2009, Gall et al. undertook an extensive systematic study of the effect of crosslinking and particle loading on the thermomechanical and shape memory properties of a polymer matrix [124]. They found that increasing particle concentration had little effect on the T_g but caused a significant decrease in the rubbery modulus through a decrease in crosslink density. Further, for low crosslinked systems, high particle loading caused a large degree of plastic deformation during shape recovery. In 2008, acrylate systems were explored by Liou et al., who found that nanomagnetic particles dispersed in a poly(MMA-*co*-MAA-*co*-BA) matrix had a significant effect on the stress–strain relationship of the polymer [125]. Additionally, in 2014 Mosleh et al. researched the effect of doping levels on the mechanical properties of magnetic nanoparticle composites of polyurethane/PCL blends [126].

5.2 *Thermoregulated Networks*

Although magnetic hyperthermia is an excellent means by which SMPINCs can be remotely activated, it presents potentially disastrous extreme local heating to sensitive environments. For magnetic hyperthermia to be useful, mechanisms to constrain and regulate the potential thermal energy build-up and transfer need to be integrated into any system. In 2006, Buckley et al. investigated the concept of Curie-thermoregulated inductive heating in SPMINC systems [120]. Buckley et al. demonstrated that by positioning the Curie temperature (the temperature at which the ferromagnetic material becomes paramagnetic and thus loses its ability to inductively heat through a hysteresis loss mechanism) below the temperature at which tissue may become effected (42°C), tissue damage can be avoided and the need for feedback controls mitigated. This was demonstrated with 50 μm zinc ferrite ferromagnetic particles at 10 wt% loading; heating up to 42°C was demonstrated in a 12.2 MHz field. Concern, however, still exists around the biocompatibility of these systems, which must be carefully investigated before use in vivo.

5.3 *Particle Coating Effects*

Particle loading and surface chemistry significantly affect the ability of any filler material to reinforce or enhance the matrix into which they are deposited. For instance, if a particle's surface chemistry is incompatible with the matrix the particles will tend to aggregate and precipitate out of the system. Further, if loading levels are too low or too high the particles will perform inefficiently through insufficient quantity or percolation. Therefore, careful study of particle loading and surface chemistry is warranted. In 2006, Schmidt explored the effect of compatibilizing the magnetic nanoparticles dispersed in the matrix by coating them with a PCL shell [67]. This was done to ensure homogeneity in the composite by improving the interaction of the particles and the matrix, thus preventing aggregation. Schmidt found that copolymers of oligo(ϵ -caprolactone) dimethacrylate and butyl acrylate effectively dispersed 2–12 wt% of the nanoparticles (11 nm diameter) and achieved activation of the SMP composite (43°C). This concept was further explored by Yang et al. in 2011 who researched the effect of nanoparticle coating on magnetite particles coated with acetylacetonate in a polynorbormene matrix [127]. They achieved a transition temp of 51°C with a shape recovery time of 186 sec. In 2012, Williams et al. showed that magnetic nanoparticles in epoxy matrices tended to aggregate as a result of incompatibilities between the matrix and the filler [128]. Modification of the epoxy matrix with oleic acid (up to 20 wt%) was shown to enhance dispersion of magnetite particles that had been surface-modified with oleic acid (up to 8 wt% dispersion), achieving a temperature increase of 25°C when activated by a magnetic field.

5.4 Light Activation of SMPINCs

Although magnetic activation of SMPINCs holds promise, other sources of heating, including photothermal, have been explored for SMPINCs. In 2013, Xiao et al. used lasers and gold nanorods and nanospheres to actuate SMP [129] (as shown in Fig. 11).

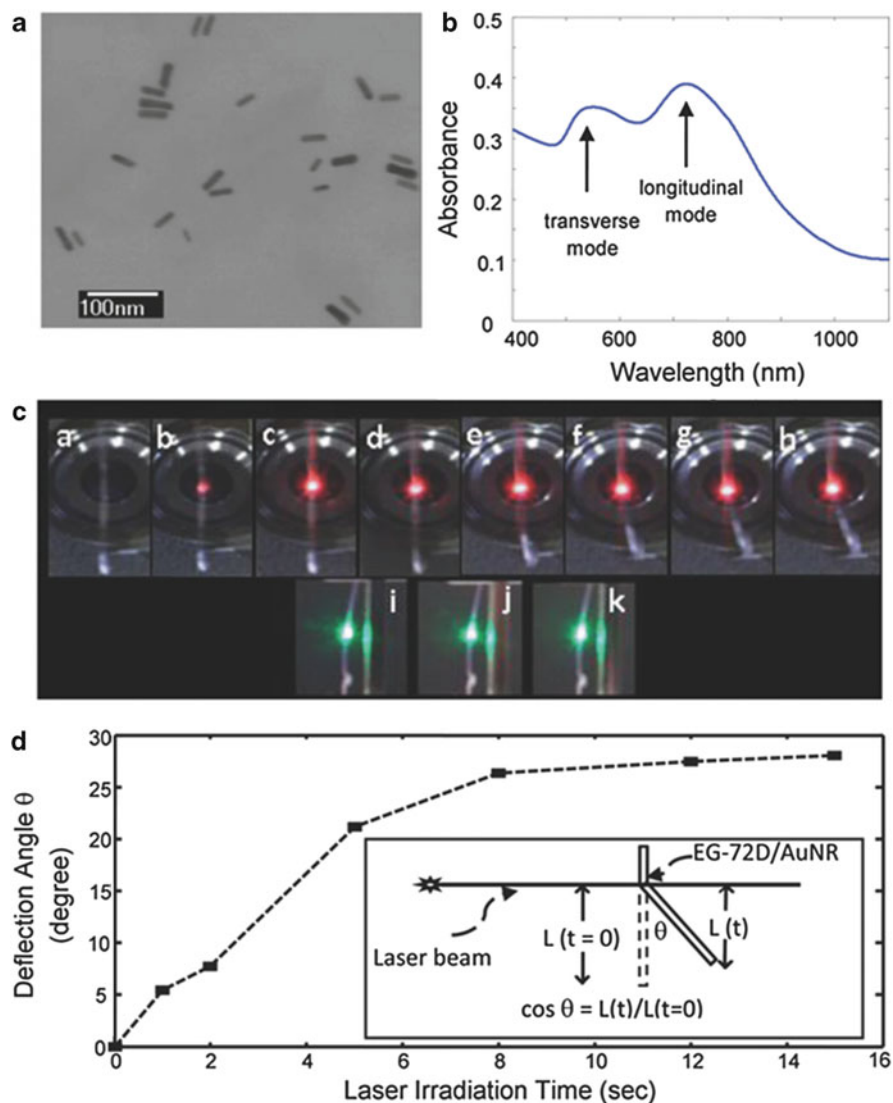


Fig. 11 Photothermal activation of the shape memory effect employing gold nanorods: particle morphology (a), spectra (b), and time-dependent response of programmed material to laser irradiation (c, d). Reprinted from Xiao et al. [129], Copyright 2013, with permission from John Wiley and Sons

The nanoparticle doping achieved thermal activation at extremely low loadings (0.1 wt%) and was remotely triggered by a low power laser. Gold nanorods (at 0.1 wt%) were shown to be significantly more sensitive than nanospheres (at 1.0 wt%), producing significantly more thermal energy than spheres under the same activation conditions. Heating was achieved by the localized surface plasmon resonance (LSPR) enhanced photothermal effect of magnetic nanoparticles. In 2014, Mezzenga showed that light could be used to control the magnetic properties of a shape memory composite material, affecting magnetic memory as well as shape activation [130].

5.5 *Electro-active Systems*

Although the electronic properties of magnetic SMP systems have been explored, this has usually been seen as a secondary focus. However, in 2012 Fu et al. showed that Joule heating of a CNT nanocomposite in a polystyrene matrix was able to achieve a shape change while imparting electro-active properties to the SMP [131]. The electrical properties were shown to be strongly dependent on CNT concentration, testing frequency, and temperature.

SMPINCs doped with electromagnetic active particles possess many useful properties, including remote activation, controllable heating, and variable electronic properties. Although significant challenges remain in this field, especially in terms of biocompatibility for more exotic systems, electromagnetic SMPINCs will remain strong contenders for specific applications and present a fruitful domain for research.

6 Conclusion: The Future of SMPINCs

Although there has been much research regarding the effects of various inorganic nanofillers on the intrinsic properties of shape memory networks, there is still significant room at both the fundamental and the applied research levels for investigating novel methods that explore and elucidate the structure–property relationships, synthesis, and mass fabrication of SMPINCs. After observing the current applications for these composites in the oil and gas industry [132], as intelligent fabrics [133], and many more [134, 135], there is an obvious untapped potential for SMPINCs.

However, the future success of these materials lies not in the creative experimentation carried out by top materials researchers around the world. Instead, this field must look at a more rational design of materials and a thorough understanding of the interfacial phenomena observed when loading SMPs with inorganic fillers. Although the rational design of SMPINCs has been brute-forced by understanding the effects of loading ratios, resin choice, and other tunable

variables on the polymer properties, there is still much to understand regarding prediction of material properties from the constituent components.

One way to overcome this guess-and-check approach is through the use of computational models that can partially predict materials properties before experiments make it to the lab bench. This type of focused brainstorming is not unheard of in the material science world: since the launch of the Materials Genome Initiative in June 2011, hundreds of millions of dollars have been funneled from industry, academia, and federal agencies towards the creation of new institutes and interdisciplinary efforts for rapid material discovery and development [136]. Much like the cooperative effort of Harvard and IBM in releasing millions of computationally derived organic molecule models for open access analysis [137], SMPINCs and composite materials in general could similarly benefit from an open-access, computationally derived framework from which experimental endeavors could be launched.

With the advent of SMPINCs, a number of the challenges that researchers have seen with native shape memory networks have been overcome. From remote actuation [124, 138], to electrically conductive networks [42, 139–141] and all the way to enhanced compatibility within the biological space [99, 100], SMPINCs have demonstrated the value of the addition of inorganic particles to a variety of shape memory polymer networks. In this new space of imparting added functionality to shape memory polymers, researchers are continuing to demonstrate innovation in the creation of smart materials that respond to external stimuli. Using these systems, many of the obstacles that industry faces can be overcome in the near future using these new materials that are sensitive and quickly responsive to their environment. However, a more rapid pace of advancement would be possible in this field if researchers embraced the age of atomistic and mesoscale computation and modeling for understanding the composite–property space at a more fundamental level. With this type of approach, the next decade could see a cascade of significant advances in the shape memory field, particularly in areas such as aerospace, personalized healthcare, and energy harvesting.

References

1. Huang W et al (2010) Thermo-moisture responsive polyurethane shape-memory polymer and composites: a review. *J Mater Chem* 20(17):3367–3381
2. Liu C, Qin H, Mather P (2007) Review of progress in shape-memory polymers. *J Mater Chem* 17(16):1543–1558
3. Lu H, Huang W, Yao Y (2013) Review of chemo-responsive shape change/memory polymers. *Pigment Resin Technol* 42(4):237–246
4. Mather PT, Luo X, Rousseau IA (2009) Shape memory polymer research. *Annu Rev Mater Res* 39:445–471
5. Behl M, Zotzmann J, Lendlein A (2010) Shape-memory polymers and shape-changing polymers. In: Lendlein A (ed) *Shape-memory polymers*. *Advances in Polymer Science*, vol 226. Springer, Berlin, pp 1–40

6. Meng H, Li G (2013) A review of stimuli-responsive shape memory polymer composites. *Polymer* 54(9):2199–2221
7. Xie T (2011) Recent advances in polymer shape memory. *Polymer* 52(22):4985–5000
8. Santhosh Kumar K, Biju R, Reghunadhan Nair C (2013) Progress in shape memory epoxy resins. *React Funct Polym* 73(2):421–430
9. Anis A et al (2013) Developments in shape memory polymeric materials. *Polym Plast Technol Eng* 52(15):1574–1589
10. Meng Q, Hu J (2009) A review of shape memory polymer composites and blends. *Compos A Appl Sci Manuf* 40(11):1661–1672
11. Leng J, Lan X, Du S (2010) Shape-memory polymer composites. In: Leng J, Du S (eds) *Shape-memory polymers and multifunctional composites*. CRC, Boca Raton, p 203
12. Leng J et al (2011) Shape-memory polymers and their composites: stimulus methods and applications. *Prog Mater Sci* 56(7):1077–1135
13. Madbouly SA, Lendlein A (2010) Shape-memory polymer composites. In: Lendlein A (ed) *Shape-memory polymers*. *Advances in Polymer Science*, vol 226. Springer, Berlin, pp 41–95
14. Ratna D, Karger-Kocsis J (2008) Recent advances in shape memory polymers and composites: a review. *J Mater Sci* 43(1):254–269
15. Wei Z, Sandström R, Miyazaki S (1998) Shape-memory materials and hybrid composites for smart systems: part I shape-memory materials. *J Mater Sci* 33(15):3743–3762
16. Zhang L, Brostowitz NR, Cavicchi KA, Weiss RA (2014) Perspective: ionomer research and applications. *Macromol React Eng* 8:81–99
17. Silverstein MS (2014) PolyHIPEs: recent advances in emulsion-templated porous polymers. *Prog Polym Sci* 39(1):199–234
18. Zhang W, Müller AH (2013) Architecture, self-assembly and properties of well-defined hybrid polymers based on polyhedral oligomeric silsesquioxane (POSS). *Prog Polym Sci* 38(8):1121–1162
19. Park D-H et al (2013) Polymer–inorganic supramolecular nanohybrids for red, white, green, and blue applications. *Prog Polym Sci* 38(10):1442–1486
20. Kango S et al (2013) Surface modification of inorganic nanoparticles for development of organic–inorganic nanocomposites—a review. *Prog Polym Sci* 38(8):1232–1261
21. Miaudet P et al (2007) Shape and temperature memory of nanocomposites with broadened glass transition. *Science* 318(5854):1294–1296
22. Lu H et al (2010) Mechanical and shape-memory behavior of shape-memory polymer composites with hybrid fillers. *Polymer Int* 59(6):766–771
23. Nji J, Li G (2010) A self-healing 3D woven fabric reinforced shape memory polymer composite for impact mitigation. *Smart Mater Struct* 19(3):035007
24. Nji J, Li G (2010) A biomimic shape memory polymer based self-healing particulate composite. *Polymer* 51(25):6021–6029
25. Kohlmeier RR, Lor M, Chen J (2012) Remote, local, and chemical programming of healable multishape memory polymer nanocomposites. *Nano Lett* 12(6):2757–2762
26. Tridech C et al (2013) High performance composites with active stiffness control. *ACS Appl Mater Interfaces* 5(18):9111–9119
27. Fonseca M et al (2013) Shape memory polyurethanes reinforced with carbon nanotubes. *Compos Struct* 99:105–111
28. Li H et al (2013) The reinforcement efficiency of carbon nanotubes/shape memory polymer nanocomposites. *Compos B Eng* 44(1):508–516
29. Ratna D, Jagtap SB, Abraham T (2013) Nanocomposites of poly(ethylene oxide) and multiwall carbon nanotube prepared using an organic salt-assisted dispersion technique. *Polymer Eng Sci* 53(3):555–563
30. Yang J-P et al (2012) Cryogenic mechanical behaviors of carbon nanotube reinforced composites based on modified epoxy by poly(ethersulfone). *Compos B Eng* 43(1):22–26
31. Kausar A, Hussain ST (2013) Effect of modified filler surfaces and filler tethered polymer chains on morphology and physical properties of poly(azo-pyridylurethane)/multi-walled

- carbon nanotube nanocomposites. *J Plast Film Sheeting* 30: 181–204. doi:[10.1177/8756087913493633](https://doi.org/10.1177/8756087913493633)
32. Jiang L et al (2014) Simultaneous reinforcement and toughening of polyurethane composites with carbon nanotube/halloysite nanotube hybrids. *Compos Sci Technol* 91:98–103
 33. Yoonessi M et al (2012) Graphene polyimide nanocomposites; thermal, mechanical, and high-temperature shape memory effects. *ACS Nano* 6(9):7644–7655
 34. Choi JT et al (2012) Shape memory polyurethane nanocomposites with functionalized graphene. *Smart Mater Struct* 21(7):075017
 35. Liang J et al (2014) Silver nanowire percolation network soldered with graphene oxide at room temperature and its application for fully stretchable polymer light-emitting diodes. *ACS Nano* 8:1590
 36. Iyengar PK et al (2013) Polymethyl methacrylate nanofiber-reinforced epoxy composite for shape-memory applications. *High Perform Polymer* 25(8):1000–1006
 37. Lu H, Huang WM, Leng J (2014) Functionally graded and self-assembled carbon nanofiber and boron nitride in nanopaper for electrical actuation of shape memory nanocomposites. *Compos B Eng* 62:1–4
 38. Lu H, Lei M, Leng J (2014) Significantly improving electro-activated shape recovery performance of shape memory nanocomposite by self-assembled carbon nanofiber and hexagonal boron nitride. *J Appl Polym Sci* 131:40506
 39. Hollaway L (2011) Thermoplastic–carbon fiber composites could aid solar-based power generation: possible support system for solar power satellites. *J Compos Construct* 15(2):239–247
 40. Wu T, O’Kelly K, Chen B (2014) Poly (vinyl alcohol) particle-reinforced elastomer composites with water-active shape-memory effects. *Eur Polym J* 53:230–237
 41. Yang B et al (2005) Qualitative separation of the effects of carbon nano-powder and moisture on the glass transition temperature of polyurethane shape memory polymer. *Scr Mater* 53(1):105–107
 42. Dorigato A et al (2013) Electrically conductive epoxy nanocomposites containing carbonaceous fillers and in-situ generated silver nanoparticles. *Express Polym Lett* 7(8):673
 43. Garle A et al (2012) Thermoresponsive semicrystalline poly(ϵ -caprolactone) networks: exploiting cross-linking with cinnamoyl moieties to design polymers with tunable shape memory. *ACS Appl Mater Interfaces* 4(2):645–657
 44. Chang L, Read T (1951) Behavior of the elastic properties of AuCd. *Trans Met Soc AIME* 189:47
 45. Sillion B (2002) Shape memory polymers. *Actual Chim* 3:182–188
 46. Alexandre M, Dubois P (2000) Polymer-layered silicate nanocomposites: preparation, properties and uses of a new class of materials. *Mater Sci Eng R Rep* 28(1–2):1–63
 47. Lendlein A, Schmidt AM, Langer R (2001) AB-polymer networks based on oligo(varepsilon-caprolactone) segments showing shape-memory properties. *Proc Natl Acad Sci USA* 98(3):842–847
 48. Lendlein A, Langer R (2002) Biodegradable, elastic shape-memory polymers for potential biomedical applications. *Science* 296(5573):1673–1676
 49. Lendlein A, Kelch S (2002) Shape-memory polymers. *Angew Chem Int Ed* 41:2034
 50. Voit W, Ware T, Gall K (2011) Shape memory polymers and process for preparing. WO Patent 2,011,049,879
 51. Wischke C, Lendlein A (2010) Shape-memory polymers as drug carriers—a multifunctional system. *Pharm Res* 27(4):527–529
 52. Yakacki CM et al (2007) Unconstrained recovery characterization of shape-memory polymer networks for cardiovascular applications. *Biomaterials* 28(14):2255–2263
 53. Gall K et al (2005) Thermomechanics of the shape memory effect in polymers for biomedical applications. *J Biomed Mater Res A* 73A(3):339–348
 54. Sharp AA et al (2006) Toward a self-deploying shape memory polymer neuronal electrode. *J Neural Eng* 3(4):L23

55. Ware T et al (2012) Three-dimensional flexible electronics enabled by shape memory polymer substrates for responsive neural interfaces. *Macromol Mater Eng* 297
56. Baer G et al (2007) Shape-memory behavior of thermally stimulated polyurethane for medical applications. *J Appl Polym Sci* 103(6):3882–3892
57. Small IVW et al (2010) Biomedical applications of thermally activated shape memory polymers. *J Mater Chem* 20(17):3356–3366
58. Gall K et al (2002) Shape memory polymer nanocomposites. *Acta Mater* 50(20):5115–5126
59. Gall K et al (2004) Internal stress storage in shape memory polymer nanocomposites. *Appl Phys Lett* 85(2):290–292
60. Liu Y et al (2004) Thermomechanics of shape memory polymer nanocomposites. *Mech Mater* 36(10):929–940
61. Cho JW, Lee SH (2004) Influence of silica on shape memory effect and mechanical properties of polyurethane–silica hybrids. *Eur Polym J* 40:1343–1348
62. Koerner H et al (2004) Remotely actuated polymer nanocomposites—stress-recovery of carbon-nanotube-filled thermoplastic elastomers. *Nat Mater* 3(2):115–120
63. Krishnamoorti R, Vaia RA, Giannelis EP (1996) Structure and dynamics of polymer-layered silicate nanocomposites. *Chem Mater* 8(8):1728–1734
64. Vaia RA et al (1997) Relaxations of confined chains in polymer nanocomposites: glass transition properties of poly(ethylene oxide) intercalated in montmorillonite. *J Polym Sci B* 35(1):59–67
65. Arzberger SC et al (2005) Elastic memory composites (EMC) for deployable industrial and commercial applications. In: White EV (ed) *Proceedings of the SPIE 5762: Smart structures and materials 2005:Industrial and commercial applications of smart structures technologies*. International Society for Optics and Photonics, Bellingham. doi:[10.1117/12.600583](https://doi.org/10.1117/12.600583)
66. Ohki T et al (2004) Mechanical and shape memory behavior of composites with shape memory polymer. *Compos A Appl Sci Manuf* 35(9):1065–1073
67. Schmidt AM (2006) Electromagnetic activation of shape memory polymer networks containing magnetic nanoparticles. *Macromol Rapid Commun* 27(14):1168–1172
68. Schulz MJ, Kelkar AD, Sundaresan MJ (eds) (2004) *Nanoengineering of structural, functional and smart materials*, CRC, Boca Raton
69. Utracki LA (2004) *Clay-containing polymeric nanocomposites*, vol 1. Smithers Rapra Technology, Shawbury, UK
70. Cao F, Jana SC (2007) Nanoclay-tethered shape memory polyurethane nanocomposites. *Polymer* 48(13):3790–3800
71. Razzaq MY, Frommann L (2007) Thermomechanical studies of aluminum nitride filled shape memory polymer composites. *Polym Compos* 28(3):287–293
72. Rezanejad S, Kokabi M (2007) Shape memory and mechanical properties of cross-linked polyethylene/clay nanocomposites. *Eur Polym J* 43(7):2856–2865
73. Kim MS, Jun JK, Jeong HM (2008) Shape memory and physical properties of poly(ethyl methacrylate)/Na-MMT nanocomposites prepared by macroazoinitiator intercalated in Na-MMT. *Compos Sci Technol* 68(7):1919–1926
74. Ratna D (2011) Processing and characterization of poly(ethylene oxide)/clay nanocomposites. *J Polymer Eng* 31(4):323–327
75. Ali ES, Zubir SA, Ahmad S (2012) Clay reinforced hyperbranched polyurethane nanocomposites based on palm oil polyol as shape memory materials. *Adv Mater Res* 548:115–118
76. Cuevas J et al (2012) Shape memory composites based on glass-fibre-reinforced poly(ethylene)-like polymers. *Smart Mater Struct* 21(3):035004
77. George G (2012) *Self-healing supramolecular polymer nanocomposites*. PhD thesis, Deakin University, Melbourne
78. Greil P (2012) Generic principles of crack-healing ceramics. *J Adv Ceram* 1(4):249–267
79. Han Y et al (2012) Zinc ion uniquely induced triple shape memory effect of dipole–dipole reinforced ultra-high strength hydrogels. *Macromol Rapid Commun* 33(3):225–231

80. Gao F (ed) (2012) *Advances in polymer nanocomposites: types and applications*. Woodhead, Cambridge
81. Martin DJ, Osman AF, Andriani Y, Edwards GA (2012) Thermoplastic polyurethane (TPU)-based polymer nanocomposites. In: Gao F (ed) *Advances in polymer nanocomposites: types and applications*. Woodhead, Cambridge, pp 321–350
82. LeBaron PC, Wang Z, Pinnavaia TJ (1999) Polymer-layered silicate nanocomposites: an overview. *Appl Clay Sci* 15(1):11–29
83. Padmanabhan K (2001) Mechanical properties of nanostructured materials. *Mater Sci Eng A* 304:200–205
84. James Korley LT et al (2006) Preferential association of segment blocks in polyurethane nanocomposites. *Macromolecules* 39(20):7030–7036
85. Edwards GA (2007) *Optimisation of organically modified layered silicate based nanofillers for thermoplastic polyurethanes*. PhD thesis. University of Queensland, Brisbane
86. Quadri F, Santo L, Squeo EA (2012) Solid-state foaming of nano-clay-filled thermoset foams with shape memory properties. *Polym Plast Technol Eng* 51(6):560–567
87. Tan H et al (2012) Effect of clay modification on the morphological, mechanical, and thermal properties of epoxy/polypropylene/montmorillonite shape memory materials. In: *Proceedings of the SPIE 8409: Third international conference on smart materials and nanotechnology in engineering*. International Society for Optics and Photonics, Bellingham. doi:[10.1117/12.923306](https://doi.org/10.1117/12.923306)
88. Tarablsi B et al (2012) Maghemite intercalated montmorillonite as new nanofillers for photopolymers. *Nanomaterials* 2(4):413–427
89. Chiu C-W, Huang T-K, Wang Y-C, Alamani BG, Lin J-J (2013) Intercalation strategies in clay/polymer hybrids. *Prog Polym Sci* 39:443–485
90. Zhang D, Petersen KM, Grunlan MA (2012) Inorganic–organic shape memory polymer (SMP) foams with highly tunable properties. *ACS Appl Mater Interfaces* 5(1):186–191
91. Zhang M, Rong M (2012) Design and synthesis of self-healing polymers. *Sci China Chem* 55(5):648–676
92. Basit A et al (2013) Thermally activated composite with two-way and multi-shape memory effects. *Materials* 6(9):4031–4045
93. Jumahat A et al (2013) Fracture toughness of nanomodified-epoxy systems. *Appl Mech Mater* 393:206–211
94. Senses E, Akcora P (2013) An interface-driven stiffening mechanism in polymer nanocomposites. *Macromolecules* 46(5):1868–1874
95. Xu B et al (2013) Nanocomposite hydrogels with high strength cross-linked by titania. *RSC Adv* 3(20):7233–7236
96. Kang JH et al (2014) Enhanced adhesive strength between shape memory polymer nanocomposite and titanium alloy. *Compos Sci Technol* 96:23
97. Stribeck N et al (2014) Studying nanostructure gradients in injection-molded polypropylene/montmorillonite composites by microbeam small-angle X-ray scattering. *Sci Tech Adv Mater* 15(1):015004
98. Kazakevičiūtė-Makovska R, Steeb H (2013) Hierarchical architecture and modeling of bio-inspired mechanically adaptive polymer nanocomposites. In: Altenbach H, Forest S, Krivtsov A (eds) *Generalized continua as models for materials. Advanced structured materials*, vol 22. Springer, Berlin, pp 199–215
99. Zheng X et al (2006) Shape memory properties of poly(D, L-lactide)/hydroxyapatite composites. *Biomaterials* 27(24):4288–4295
100. Du K, Gan Z (2014) Shape memory behavior of HA-g-PDLLA nanocomposites prepared via in-situ polymerization. *J Mater Chem B* 2:3340
101. Liu X et al (2014) Delivery of growth factors using a smart porous nanocomposite scaffold to repair a mandibular bone defect. *Biomacromolecules* 15:1019

102. Pielichowska K, Blazewicz S (2010) Bioactive polymer/hydroxyapatite (nano) composites for bone tissue regeneration. In: Abe A, Dusek K, Kobayashi S (eds) *Biopolymers*. Springer, Berlin, pp 97–207
103. Guo W et al (2012) Stronger and faster degradable biobased poly(propylene sebacate) as shape memory polymer by incorporating boehmite nanoplatelets. *ACS Appl Mater Interfaces* 4(8):4006–4014
104. Zheng X et al (2008) Effect of In vitro degradation of poly(D, L-lactide)/ β -tricalcium composite on its shape-memory properties. *J Biomed Mater Res B Appl Biomater* 86B(1):170–180
105. Yu X et al (2009) Influence of in vitro degradation of a biodegradable nanocomposite on its shape memory effect. *J Phys Chem C* 113(41):17630–17635
106. Saralegi A et al (2013) Shape-memory bionanocomposites based on chitin nanocrystals and thermoplastic polyurethane with a highly crystalline soft segment. *Biomacromolecules* 14(12):4475–4482
107. Coativy G et al (2013) Shape memory starch–clay bionanocomposites. *Carbohydr Polym*. doi:[10.1016/j.carbpol.2013.12.024](https://doi.org/10.1016/j.carbpol.2013.12.024)
108. Lahiri D et al (2010) Boron nitride nanotube reinforced polylactide–polycaprolactone copolymer composite: Mechanical properties and cytocompatibility with osteoblasts and macrophages in vitro. *Acta Biomater* 6(9):3524–3533
109. Kalita H, Karak N (2013) Hyperbranched polyurethane/ Fe_3O_4 thermosetting nanocomposites as shape memory materials. *Polym Bull* 70(11):2953–2965
110. Das B et al (2013) Bio-based hyperbranched polyurethane/ Fe_3O_4 nanocomposites: smart antibacterial biomaterials for biomedical devices and implants. *Biomed Mater* 8(3):035003
111. Kalita H, Karak N (2013) Bio-based hyperbranched polyurethane/ Fe_3O_4 nanocomposites as shape memory materials. *Polymer Adv Technol* 24(9):819–823
112. Lu X-L et al (2013) Preparation and shape memory properties of TiO_2 /PLCL biodegradable polymer nanocomposites. *Trans Nonferr Metal Soc China* 23(1):120–127
113. Seyedjamali H, Pirisedigh A (2014) L-cysteine-induced fabrication of spherical titania nanoparticles within poly(ether-imide) matrix. *Amino Acids* 46:1321–1331
114. Wang W, Liu Y, Leng J (2013) Influence of the ultraviolet irradiation on the properties of TiO_2 -polystyrene shape memory nanocomposites. In: *Proceedings of the SPIE 8793: Fourth international conference on smart materials and nanotechnology in engineering*. International Society for Optics and Photonics, Bellingham. doi:[10.1117/12.2027860](https://doi.org/10.1117/12.2027860)
115. Rodriguez JN et al (2012) Opacification of shape memory polymer foam designed for treatment of intracranial aneurysms. *Ann Biomed Eng* 40(4):883–897
116. Bothe M et al (2012) Triple-shape properties of star-shaped POSS-polycaprolactone polyurethane networks. *Soft Matter* 8(4):965–972
117. Ishida K et al (2012) Soft bacterial polyester-based shape memory nanocomposites featuring reconfigurable nanostructure. *J Polym Sci B* 50(6):387–393
118. Xu J, Shi W, Pang W (2006) Synthesis and shape memory effects of Si–O–Si cross-linked hybrid polyurethanes. *Polymer* 47(1):457–465
119. Alvarado-Tenorio B, Romo-Urbe A, Mather PT (2012) Stress-induced bimodal ordering in POSS/PCL biodegradable shape memory nanocomposites. *MRS Proc* 1450:3–23. doi:[10.1557/opl.2012.1327](https://doi.org/10.1557/opl.2012.1327)
120. Buckley PR et al (2006) Inductively heated shape memory polymer for the magnetic actuation of medical devices. *IEEE Trans Biomed Eng* 53(10):2075–2083
121. Weigel T, Mohr R, Lendlein A (2009) Investigation of parameters to achieve temperatures required to initiate the shape-memory effect of magnetic nanocomposites by inductive heating. *Smart Mater Struct* 18(2):025011
122. Mohr R et al (2006) Initiation of shape-memory effect by inductive heating of magnetic nanoparticles in thermoplastic polymers. *Proc Natl Acad Sci USA* 103(10):3540–3545
123. Razaq MY et al (2007) Thermal, electrical and magnetic studies of magnetite filled polyurethane shape memory polymers. *Mater Sci Eng A* 444(1):227–235

124. Yakacki CM et al (2009) Shape-memory polymer networks with Fe₃O₄ nanoparticles for remote activation. *J Appl Polym Sci* 112(5):3166–3176
125. Nguyen T et al (2011) Characterisation of mechanical properties of magnetite-polymer composite films. *Strain* 47(s1):e467–e473
126. Mosleh Y et al (2014) TPU/PCL/nanomagnetite ternary shape memory composites: studies on their thermal, dynamic-mechanical, rheological and electrical properties. *Iranian Polym J* 23(2):137–145
127. Yang D et al (2012) Electromagnetic activation of a shape memory copolymer matrix incorporating ferromagnetic nanoparticles. *Polym Int* 61(1):38–42
128. Puig J et al (2012) Superparamagnetic nanocomposites based on the dispersion of oleic acid-stabilized magnetite nanoparticles in a diglycidylether of bisphenol a-based epoxy matrix: magnetic hyperthermia and shape memory. *J Phys Chem C* 116(24):13421–13428
129. Xiao Z et al (2013) Shape matters: a gold nanoparticle enabled shape memory polymer triggered by laser irradiation. *Part Part Syst Char* 30(4):338–345
130. Haberl JM et al (2014) Light-controlled actuation, transduction, and modulation of magnetic strength in polymer nanocomposites. *Adv Funct Mater* 24:3179
131. Xu B et al (2012) Electro-responsive polystyrene shape memory polymer nanocomposites. *Nanosci Nanotechnol Lett* 4(8):814–820
132. Matteo C et al (2012) Current and future nanotech applications in the oil industry. *Am J Appl Sci* 9(6):784
133. Mofarah SS, Moghaddam S (2013) Application of smart polymers in fabrics. *J Am Sci* 9(4s):282
134. Akhras G (2012) Smart and nano systems – applications for NDE and perspectives. In: Proceedings of the 4th international CANDU in-service inspection workshop and NDT in Canada 2012 conference. *e-J Nondestruct Test* 17(09):13118
135. Carrell J et al (2013) Shape memory polymer nanocomposites for application of multiple-field active disassembly: experiment and simulation. *Environ Sci Technol* 47(22):13053–13059
136. Holdren JP (2011) Materials genome initiative for global competitiveness. Executive Office of the President, National Science and Technology Council, Washington, p 18
137. Hachmann J et al (2011) The Harvard clean energy project: large-scale computational screening and design of organic photovoltaics on the world community grid. *J Phys Chem Lett* 2(17):2241–2251
138. Hawkins AM, Puleo DA, Hilt JZ (2012) Magnetic nanocomposites for remote controlled responsive therapy and in vivo tracking. In: Bhattacharyya D, Schäfer T, Wickramasinghe SR, Daunert S (eds) *Responsive membranes and materials*. Wiley, Chichester, p 211
139. Jung YC, Goo NS, Cho JW (2004) Electrically conducting shape memory polymer composites for electroactive actuator. In: Bar-Chen Y (ed) *Proceedings of the SPIE 5385: Smart structures and materials 2004: Electroactive polymer actuators and devices*. International Society for Optics and Photonics, Bellingham. doi: [10.1117/12.540228](https://doi.org/10.1117/12.540228)
140. Kim SH et al (2013) Conductive functional bisrolled polymer and carbon nanotube yarns. *RSC Adv* 3(46):24028–24033
141. Perets YS et al (2014) The effect of boron nitride on electrical conductivity of nanocarbon-polymer composites. *J Mater Sci* 49(5):2098–2105
142. Xu J, Song J (2010) High performance shape memory polymer networks based on rigid nanoparticle cores. *Proc Natl Acad Sci* 107(17):7652–7657

Frontiers in Nanofabrication via Self-Assembly of Hybrid Materials into Low Dimensional Nanostructures

Amir Fahmi

Abstract Nanofabrication via self-assembled hybrid building blocks into well-defined structures is a powerful tool for engineering functional materials with designed properties. This review demonstrates different concepts for fabrication of one-dimensional (1D) nanostructures based on hybrid materials via directed self-assembly. The concepts describe how different types of self-assembled organic phases drive the unidirectional assembly of the inorganic moieties. The organic matrices are used to control the size and size distribution of the generated inorganic nanoparticles. Formation of the 1D structures is dependent on many parameters, such as nature of chemical composition of the hybrid organic–inorganic materials, the pH of the wet chemistry medium and the types of interactions at the interface that drive the structure formation. The collective properties of the designed 1D structures are induced by means of the degree of anisotropy and the alignment of different types of inorganic nanoparticles within the organic matrices. This cost-effective approach could potentially be extended to fabricate varieties of hybrid low dimensional nanostructures possessing unique collective electronic and optical properties, leading to a wide range of applications such as catalysis, bionanotechnology, nanoelectronics, photonics and optoelectronics.

Keywords Hybrid nanofibres · In-situ fabrication · Nanofabrication · Nanoparticles · Self-assembly

A. Fahmi (✉)

Rhein-Waal University of Applied Sciences, Faculty Technology and Bionics, Marie-Curie-Strasse 1, 47533 Kleve, Germany
e-mail: Amir.Fahmi@hochschule-rhein-waal.de

Contents

1	Introduction	352
1.1	Organic–Inorganic Building Blocks	353
1.2	Self-Assembly and Nanostructures	353
2	Functional One-Dimensional Hybrid Materials Based on Block Copolymers and Inorganic Nanoparticles	355
3	Hybrid Nanofibres via Self-Assembly of Elastin-Like Polymers Templating Cadmium Selenide Nanoparticles	357
3.1	Preparation and Characterization of ELP-CdSe Nanofibres	358
3.2	Effect of pH/Acidity	362
3.3	Investigation of Electronic and Optical Properties	362
3.4	Cytotoxicity and Cell Proliferation	364
4	Hybrid Nanofibres via Self-Assembly of Short Thiol Surfactant Templating Gold Nanoparticles	366
4.1	Spontaneous Self-Assembly of In-Situ Synthesized Gold Nanoparticles	368
4.2	Preparation of Nanofibres Based on Gold Nanoparticles	368
4.3	Investigation of Parameters Affecting the Formation of Fibres	372
5	Conclusion and Future Prospects	377
	References	378

1 Introduction

Design of collective properties via precise control over the assembly of inorganic nanoparticles into well-defined nanostructures is a major challenge for the manufacture of the next generation of miniaturized devices. Self-assembly is used as a cost-effective tool in the field of nanofabrication for accessing highly ordered nanostructures at different dimensions and length scales [1]. Recently, self-assembly processes have been used to fabricate functional one-dimensional (1D) nanomaterials because of their unique intrinsic properties. For instance, from the family of 1D nanostructures, the organic, organometallic and organic–inorganic hybrid nanostructures are particularly attractive not only because of their chemically tuneable properties but also because they can serve as building blocks in nanodevices to provide functional properties such as unique electron transport and optical activity, which are essential in electronics, optics, sensing and biomedical devices.

Highly anisotropic 1D nanostructures composed of closely packed nanoparticles have been prepared using linear macromolecular or supramolecular templates such as polyelectrolytes [2, 3], carbon nanotubes [2–5], DNA [6–9], peptide nanofibrils [10, 11], tubulin [12, 13] and bacteriophage and tobacco mosaic virus rods [14, 15]. Moreover, 1D arrays are produced by spontaneous alignment of nanoparticles with intrinsic electric dipoles to form anisotropic chains of metallic nanoparticles, driven by heterogeneities in the surface chemistry and polarity of the nanoparticles [16]. These methods have been recently used to obtain defined nanostructures, predominantly in many steps and not defect free, with inhomogeneous metallic nanoparticle distribution.

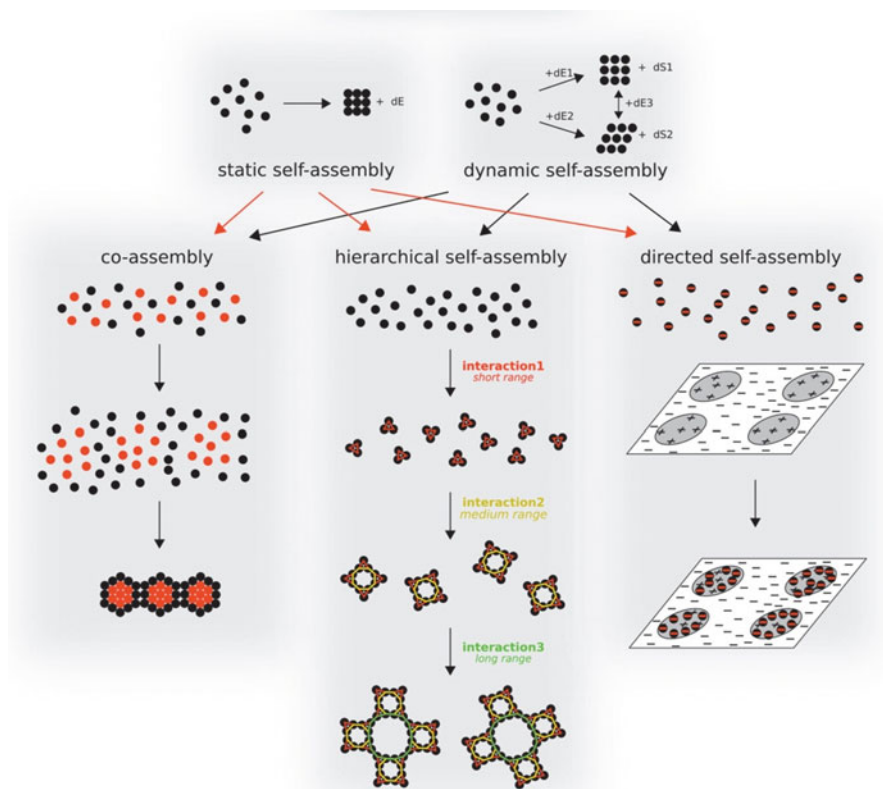
This review outlines different concepts to fabricate well-defined low dimensional nanostructures based on densely ordered inorganic nanoparticles templated within self-assembled organic matrices. These simple wet chemistry methods are used to generate functional unidirectional nanostructures of supramolecular hybrid building blocks formed in solution at a moderate pH and at room temperature. The review starts with a general introduction to the nanofabrication of unidirectional structures via self-assembly of different types of hybrid materials based on preprogrammed organic–inorganic building blocks. The subsequent discussion outlines the driving forces that allow varieties of organic matrices to direct the structural formation, with control over the size and size distribution of the inorganic moieties within the unidirectional structure. We demonstrate the concepts mainly with nanostructured hybrid materials from our own recent work; namely, three different types of self-assembled organic matrices, block copolymers, elastin-like polymers (ELP) and short commercial surfactant templated varieties of inorganic moieties. Finally, we discuss the crucial parameters and finer synthesis methods that allow more control over the fabrication and processing techniques to enable formation of more complex structures possessing unique collective properties.

1.1 Organic–Inorganic Building Blocks

Combining the two worlds of organic and inorganic materials, linked in hybrid building blocks, to fabricate functional nanostructured materials is a unique concept that holds potential for the creation of new advanced materials. While the organic molecules introduce flexibility and facilitate the self-assembly process, the inorganic moieties contribute unique physical properties, including magnetization, fluorescence and plasmon resonance. For instance, polymer-coated inorganic nanoparticles, in which the inorganic nanoparticles are surrounded by functionalized polymer chains, provide a major impetus for controlling the alignment of the inorganic nanoparticles into higher dimensions [17]. A more robust approach is to prepare the inorganic nanoparticle template within the polymeric matrix via the in-situ approach. This enables more control over the size and size distribution of the generated inorganic nanoparticles to enhance the ultimate collective properties of the designed functional material [18–20].

1.2 Self-Assembly and Nanostructures

Self-assembly is the process of spontaneous and reversible organization of a disordered system of pre-existing building blocks into a higher ordered state via minimization of the free energy balance of the system [21]. Assembling hybrid building blocks into well-defined nanostructures via self-assembly processes depends on the ability to control the shape and surface properties of the building



Scheme 1 Static and dynamic self-assembly and how they relate to co-assembly, hierarchical assembly and directed assembly. Reprinted with permission from Ozin et al. [24]. Copyright 2009, Elsevier; open access

blocks. This is achieved through design of their surface chemistry such that it facilitates spontaneous alignment at a higher level of structural complexity, driven by a map of forces operating over multiple length scales [22].

There are two main categories of self-assembly: static and dynamic. The processes of static and dynamic self-assembly are then subdivided into co-assembly, hierarchical self-assembly and directed self-assembly, as shown in Scheme 1. Co-assembly represents simultaneous self-assembly of different building blocks inside one system to form a synergic architecture. In comparison, hierarchical self-assembly is characterized by the organization of building blocks over multiple length scales so that the first building block becomes a building block for higher assembly. This process can lead to several orders of complexity, to create functional structures. Directed assembly is applied by controlling the alignment of building blocks by selective external forces that are placed during the design step [23].

The following section demonstrates the use of self-assembly as a nanofabrication tool in diverse examples of hybrid building blocks, mainly from our recent research. These involve different types of self-assembly aimed at the design of functional nanostructures at different length scales. The driving forces and functionality of these hybrid architectures are linked to the degree of anisotropic morphology, which reflects different levels of interaction and complex self-assembly.

2 Functional One-Dimensional Hybrid Materials Based on Block Copolymers and Inorganic Nanoparticles

Block copolymers in solution can be self-assembled into a variety of architectures. Micelles are common self-assembled structures formed by block copolymers when dissolved in a “selective solvent”, which is a good solvent for one of the polymer blocks but a poor solvent for the blocks of the other polymer. Binding one of the copolymer blocks with inorganic moieties leads to the formation of micelles. The inorganic moieties are localized within the core of the micelles and coated with a thin shell of the other copolymer blocks. For example, Taton’s group prepared a unidirectional structure of hybrid micelles based on amphiphilic polystyrene-*block*-poly(acrylic acid) (PS-*b*-PAA) and gold nanoparticles (AuNPs) (Fig. 1) [25].

The 1D structure was formed by adding extra additives such as salt, acid or cationic carbodiimide to the suspension of encapsulated AuNPs [25]. In contrast, Wiesner et al. pioneered another concept by using a defined volume fraction of ligand-stabilized metal nanoparticles linked within self-assembled poly(isoprene-*block*-dimethyl aminoethyl methacrylate) (PI-*b*-PDMAEMA) block copolymers to generate hybrid unidirectional nanostructures [26].

Complementary strategy is based on self-assembly of block copolymers template inorganic nanoparticles in binary solvents medium to form compact unidirectional structure. For instance, Fahmi et al. developed a simple concept whereby water acts as a trigger for morphological changes in water-in-toluene emulsions of

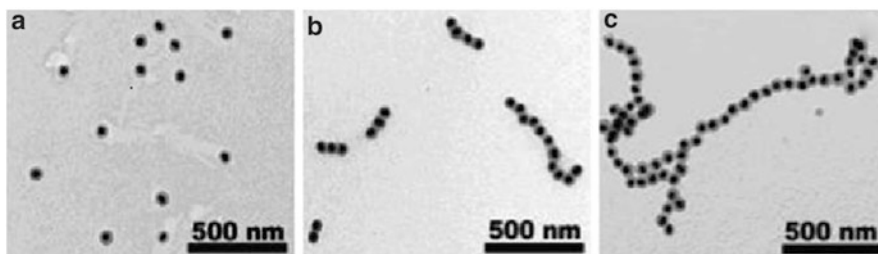


Fig. 1 (a–c) TEM images of transition of Au nanoparticles encapsulated with polystyrene-*block*-poly(acrylic acid) from a spherical to unidirectional structure. Reprinted with permission from Kang et al. [25]. Copyright, 2005 American Chemical Society

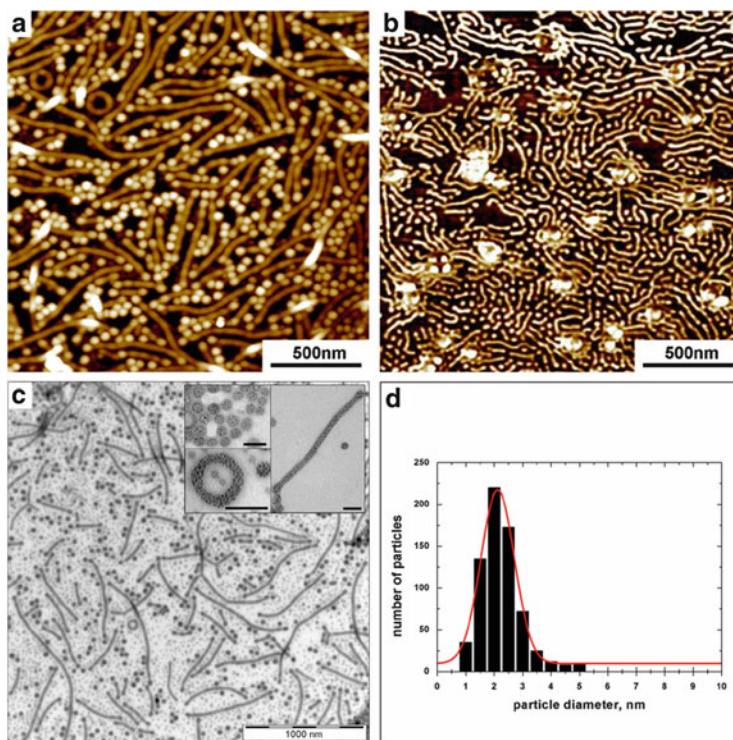


Fig. 2 (a) Topographic AFM image of self-assembled spherical, rod- and ring-like nano-objects of PS206-*b*-P4VP(HAuCl₄)₁₉₇. (b) AFM phase image of PS206-*b*-P4VP(Au)₁₉₇. The morphology is preserved when the reduction agent is added to the solution to form metallic nano-objects (c) TEM micrograph of metallic nano-objects (gold nanoparticles appear as *black spots*). The *inset* shows individual morphologies including spheres, rods and rings; *scale bars* 150 nm. (d) Plot of the particle size distribution as determined directly from TEM measurements. A Gaussian fit yields a mean particle diameter of 2.3 nm and a standard deviation of 0.6 nm. Reprinted with permission from Pietsch et al. [27]. Copyright, 2008, Elsevier

poly(styrene-*block*-4-vinylpyridine) (PS-*b*-P4VP) to template synthesis of gold nanoparticles (Fig. 2). Starting within the nonpolar solvent, core-shell structures are constructed in which the polar P4VP block templates the AuNPs; these are then grown to form the 1D nanostructure by adding a significant fraction of the polar solvent [27].

Another approach, by the Winnik group, demonstrates directed construction of hybrid cylinder micelles with high degree of anisotropy via electrostatic interaction. The concept uses selective patterning of poly(ferrocenyldimethylsilane)-*block*-poly(2-vinylpyridine) (PFS-*b*-P2VP) to prepare discrete cylindrical co-micelles that consist of a positively charged PFS core with a quaternized P2VP corona. Afterwards, PFS-*b*-P2VP assembled into the two ends of the positively charged micelles, driven by epitaxial crystallization of the PFS blocks. This led to the generation of

discrete block co-micelles with a positively charged central block and uncharged end blocks. Subsequently, negatively charged AuNPs or PbS quantum dots (QDs) were added to the co-micelle solution, allowing the negatively charged nanoparticles to selectively bind to the positively charged central blocks of the co-micelles by electrostatic interaction [28].

3 Hybrid Nanofibres via Self-Assembly of Elastin-Like Polymers Templating Cadmium Selenide Nanoparticles

Utilizing self-assembly of biomolecules to direct the assembly of inorganic nanoparticles into well-defined nanostructures offers an interesting approach for merging the fields of materials science and biology [29]. The advantages of templating inorganic nanoparticles within self-assembled biomolecular structures lie in their chemical diversities which facilitate defined hybrid nanoarchitectures while retaining the intact function of the biomolecules [30]. Biomolecules are currently used to control the nucleation and growth of semiconductor nanoparticles [31]. Moreover, they also have the potential to direct (through self-assembly) the spatial arrangement of the nanoparticles used in biosensing, bio-imaging and recognition of artificial receptors [32, 33]. However, one of the great challenges in using bioconjugated nanocrystals in biological applications is to fabricate well-defined hybrid 1D nanostructures with high aspect ratios that are suitable for biological environments. Explicitly, it is necessary to develop new synthesis strategies and technologies for highly water-soluble, biocompatible materials that are resistant to photobleaching and have high optical efficiencies at a wide range of temperatures and at moderate pH [30–33].

In this context, Fahmi et al. reported a unique approach to the generation of semiconductor cadmium selenide (CdSe) nanofibres prepared via self-assembled elastin-like polymers (ELPs) $[(VPGVG)_2(VPGEG)(VPGVG)_2]_{15}$ in aqueous solution at room temperature. The biomolecule controls the size and size distribution of the CdSe nanoparticles and directs the structure formation into hybrid nanofibres [34].

ELPs are based on repetition of short peptide sequences, where the number of the repeated units varies between two and a few hundred individual segments. This architecture provides a high diversity and excellent control over the molecular structure, which makes ELPs unique among the known polymers. The most common ELP is based on the repeating unit (GVGVP) where G stands for glycine, V for L-valine and P for L-proline. The corresponding polymer $(GVGVP)_n$ is widely regarded as a standard model for the ELPs [35]. However, the repetition and length of sequences have to be adjusted in order to control the stereochemistry, which affects both the structure and the physical properties of the ELPs. Recently, specific sequences of polypeptides have been used as scaffolds for metals and semiconductor nanoparticles to produce highly crystalline nanofibres [36]. Furthermore, the formation of self-assembled structures depends on a large number of driving forces,

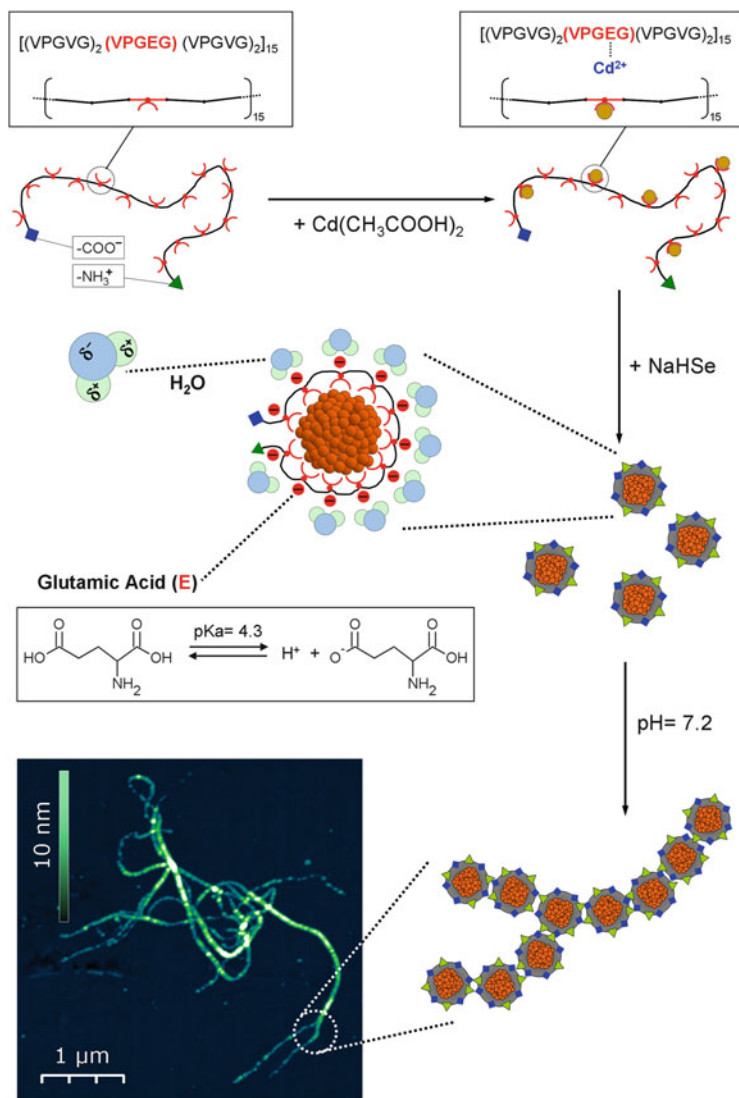
such as electrostatic and dipole interactions between the polar species as well as between hydrophobic segments, van der Waals interactions between apolar segments and the competition between the hydration processes of the hydrophobic and hydrophilic segments.

3.1 Preparation and Characterization of ELP-CdSe Nanofibres

The ELP [(VPGVG)₂(VPGEV)(VPGVG)₂]₁₅ used as a stabilizing and structure-directing agent for CdSe QDs was synthesized as described elsewhere [37]. A simple, wet chemical method (Scheme 2) was used to prepare colloidal solutions of ELP-stabilized CdSe QDs in aqueous solution at room temperature. In principle, complexing the Cd(II) precursor to the glutamic acid groups of the ELPs, followed by selenization with freshly prepared NaHSe in aqueous medium, generates hybrid nanofibres under the influence of electrostatic (Coulomb) interactions. These hybrid nanofibres consist of aggregates of ELP/CdSe core-shell building blocks, where the CdSe core is surrounded by a heterogeneous shell of charged (polar) and hydrophobic (nonpolar) segments of ELP chains. In the surrounding polar medium, aggregation of the hydrophobic segments of the hybrid building blocks forms the nanofibres. In contrast, hydration of the hydrophilic (polar/ionized) sequences of the ELP chain counteracts these conformational changes (Scheme 2). The charge distribution along the ELP chains is strongly affected by the pH conditions; so that nanofibres are formed only under appropriate conditions at a natural pH value (pH = 7.2). This concept demonstrates a simple self-assembly approach for generating readily water-soluble CdSe nanoparticles in biological environments. At neutral pH, nanofibres are based on the 1D assembly of core-shell building blocks consisting of CdSe QDs in the core, stabilized by a heterogeneously charged polypeptide shell (as shown in Scheme 2).

Another self-assembly concept that provides a nanoscale linear template for protein and inorganic nanoparticles was developed by the Zuckermann group. For instance, they demonstrate a reversible molecular tool for assembly of modified peptides in the presence of divalent metal ions. The generated nanofibres could be disassembled by adding a strong metal-chelating reagent such as EDTA [38].

The ELP-CdSe nanofibres were deposited onto a solid substrate to characterize their morphology by atomic force microscopy (AFM). Figure 3b shows an AFM height image of ELP-CdSe nanofibres deposited on a Si/SiO₂ substrate. The nanofibres have lengths of several micrometres; different morphologies can be observed including branched Y-shaped, stretched, and coiled fibres. The inset in Fig. 3b shows a magnified image of a single, stretched ELP-CdSe nanofiber, revealing a narrow diameter distribution of 6–8 nm and lengths between 500 nm and several micrometres. In fact a diverse range of self-assembled biomolecule architectures have been used as supramolecular templates for the construction of



Scheme 2 Generation of self-assembled nanofibres composed of ELP-CdSe nanoparticles prepared via an in-situ approach. Reprinted with permission from Fahmi et al. [34]. Copyright 2010, Wiley-VCH

hybrid nanofibres. For example, Stupp's group have demonstrated different principles for self-assembly of hybrid supramolecular biomaterials with inorganic moieties to precisely control their shape and size for nonlinear optics and

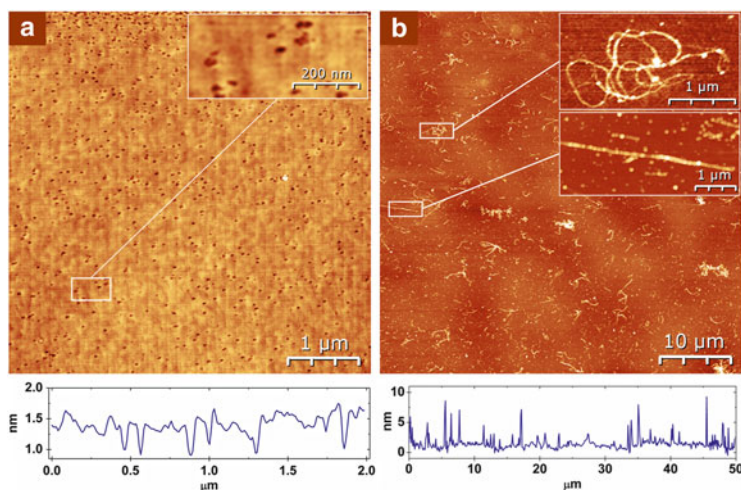


Fig. 3 AFM height image of (a) neat ELP thin film deposited on Si/SiO₂ and (b) ELP-CdSe nanofibres deposited on Si/SiO₂; the *insets* show magnified areas of the images. Reprinted with permission from Reguera et al. [42]. Copyright, 2004, American Chemical Society

stereoselective catalysis [39–41]. In order to investigate the role of the CdSe nanoparticles in fibre formation, thin films of neat ELPs were cast onto native oxidized Si substrates [42]. The AFM image in Fig. 3a shows a nanoporous thin film but no fibres can be seen, which demonstrates that the ELP does not form 1D aggregates without the CdSe nanoparticles.

The transmission electron microscopy (TEM) image in Fig. 4 shows a core–shell structure based on a CdSe nanoparticle core (dark spots) stabilized by an ELP shell (Fig. 4a). The high resolution (HR)-TEM micrograph in Fig. 4b reveals fringe structures that confirm the crystallinity of the semiconductor core. Moreover, the polydispersity of the CdSe nanoparticles was evaluated and showed a narrow distribution. Figure 4d shows a histogram with Gaussian fit, which yielded estimates of a mean particle diameter of 2.4 nm and a standard deviation of 0.53 nm. On the other hand, fine-tuning structural parameters such as pH is an effective tool for assembling the core–shell building blocks into unidirectional structures, as illustrated in Fig. 4c. The ELP-CdSe nanofibres had uniform diameter and lengths of up to several micrometres, as revealed in Fig. 4e. In fact, ELPs are small molecules with a “programmable” sequence of amino acids designed to stabilize the CdSe inorganic nanoparticles by various functional groups. These are sensitive to external parameters and can be used to tune the structure formation [43]. The next section discusses key parameters such as pH and looks at the effect of the charged building block on the formation of CdSe nanofibres.

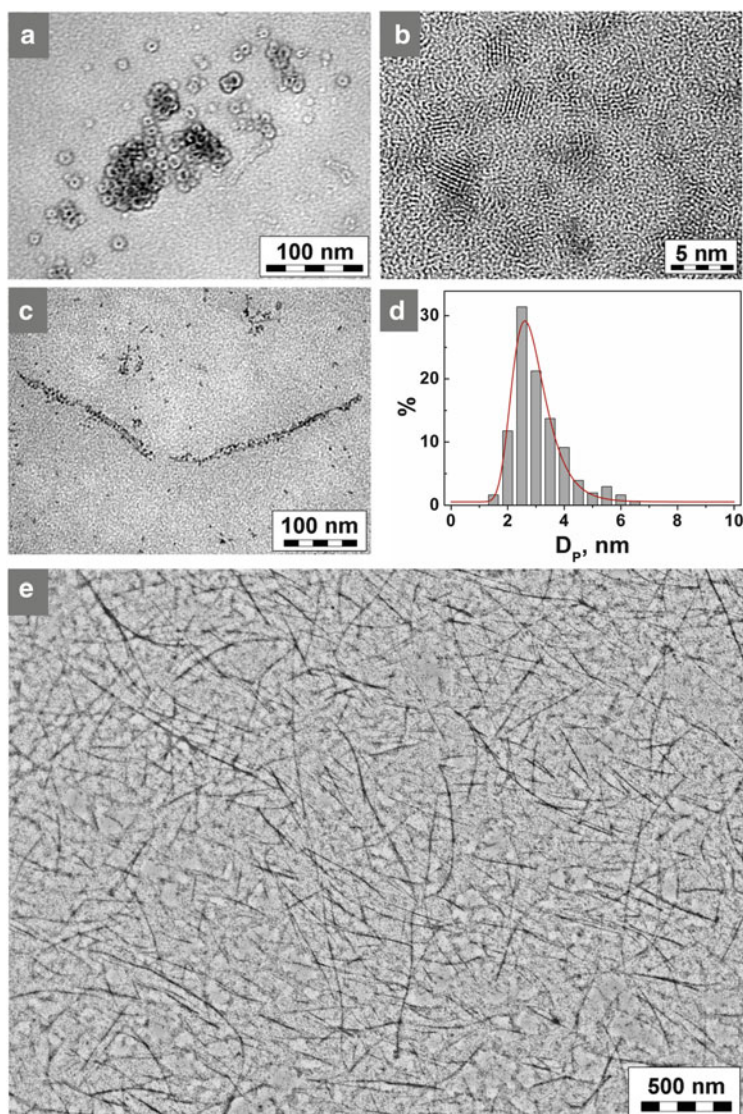


Fig. 4 (a) TEM micrograph of core-shell structures of CdSe nanoparticles stabilized with ELP. (b) HR-TEM micrograph of CdSe nanoparticles synthesized inside the ELP matrix. (c) TEM micrograph of individual ELP-CdSe fibres; the CdSe nanoparticles appear as *dark spots* inside the ELP matrix. (d) Histogram of the CdSe particle diameter. A Gaussian fit yields a mean particle diameter of 4.2 nm and a standard deviation of 0.53 nm. (e) TEM micrograph of ELP-CdSe nanofibres. Reprinted with permission from Fahmi et al. [34]. Copyright, 2010, Wiley-VCH

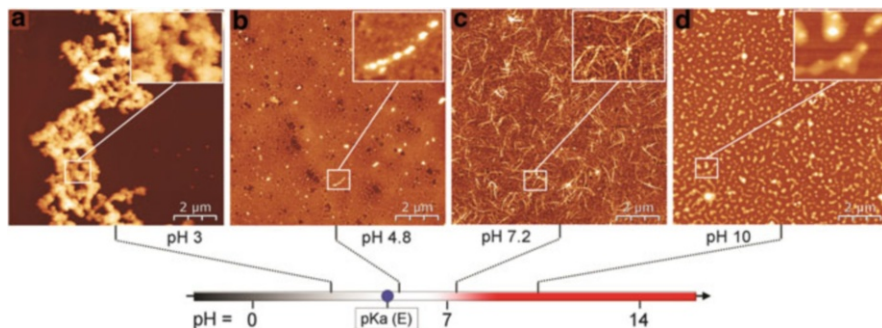


Fig. 5 AFM height images demonstrating the effect of pH on the morphology of self-assembled ELP-CdSe nanostructures: (a) random aggregates, (b) lace-like structures, (c) nucleation of unidirectional structures and (d) disruption of nanofibres. Reprinted with permission from Fahmi et al. [34]. Copyright, 2010, Wiley-VCH

3.2 Effect of pH/Acidity

It is well known that tuning the charge distribution along the ELP chains is an effective tool for controlling the formation of nanofibres. In acidic medium at pH 3, protonation of the glutamic acid takes place to obtain an apolar shell of the ELP-CdSe, resulting in random aggregates (Fig. 5a) [44]. A slight increase in the pH to 4.8 results in partial deprotonation of the glutamic acid, which induces polarity of the ELP shell and leads to reduced agglomeration of ELP-CdSe nanoparticles to form lace-like-structures (Fig. 5b). At a moderate pH of 7, nucleation of unidirectional structures takes place, as shown in Fig. 5c. This is caused by elevation in the total charge of the carboxyl groups in the ELP shell to form heterogeneous surface properties, which in aqueous medium facilitate aggregation of apolar sequences to stabilize the nanofibres [45]. In contrast, at a higher pH of 10, the charge density is increased, resulting in strong hydration of the ELP shell to disrupt the nanofibre formation, as shown in Fig. 5d. This mechanism demonstrates the strong correlation between the pH and the amino acid conformation during fibre formation [46].

3.3 Investigation of Electronic and Optical Properties

Measuring the physical properties of the hybrid nanofibres is essential to reveal the efficiency of the nanofibre functions. The generated building blocks are designed to use the unique fluorescence properties of the CdSe nanoparticles in biological applications. Coating these toxic semiconductor nanoparticles with ELP shells has made them accessible for biological applications. Figure 6 displays UV–vis absorption and photoluminescence (PL) emission spectra of CdSe nanoparticles stabilized within the nanofibres. An absorption band at around 548 nm was

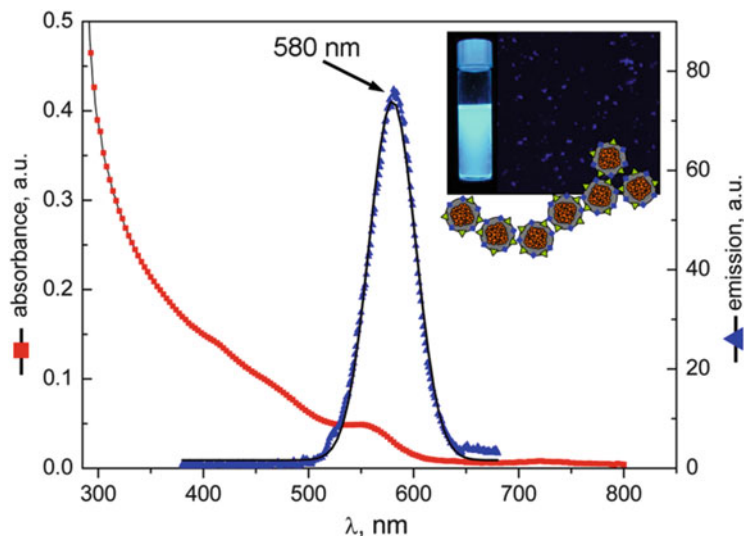


Fig. 6 UV-vis absorbance (red symbols) and PL emission (blue symbols) of ELP-stabilized CdSe nanoparticles. A Gaussian fit (dashed line) to the emission curve yields a maximum at 580 nm and a FWHM (full width at half maximum) of 44 nm, indicating a relatively narrow emission band, which is typical for the quantum dots. The inset shows a photograph of an aqueous solution of EL-CdSe nanofibres taken under UV illumination (365 nm) together with a fluorescence microscopy image. Reprinted with permission from Fahmi et al. [34]. Copyright, 2010, Wiley-VCH

observed and the PL spectrum (excitation at 350 nm) revealed a symmetric narrow emission band (FWHM = 44) that reflects the narrow size distribution of the generated CdSe QDs within ELP matrices [47]. These results confirmed that the wave functions of CdSe QDs in the nanofibres do not overlap sufficiently to alter the fluorescence properties of the ELP-CdSe nanoparticles not in a 1D structure. Moreover, the UV-vis absorption band of the bright yellow solutions at 548 nm is distinctive for CdSe nanoparticles in the size range below 10 nm, also confirmed with HR-TEM as shown in Fig. 4b. The broader emission band at 580 nm indicates a low quantum yield of the CdSe QDs compared with the near-monodisperse QD nanoparticles stabilized with trioctylphosphine oxide /trioctylphosphine (TOPO/ TOP) [48].

The electrical property of CdSe nanofibres is an important aspect of the optoelectronic properties, which are dependent on quantum confinement effects. Electric force microscopy (EFM) was used to measure the dielectric behaviour of CdSe QDs to explore the use of the generated nanofibres in different applications [49]. The Coulomb interactions between the EFM probe and the CdSe nanoparticles were different to the ELP matrix. These reflected in form of a phase-shift of the cantilever oscillation [34]. This phase-shift resolves differences in the electrostatic interaction forces, as shown in Fig. 7. The EFM image shown in Fig. 7b, in comparison with the AFM image in Fig. 7a, reveals the alignment of discrete CdSe nanoparticles separated by the ELP shell within the nanofibres.

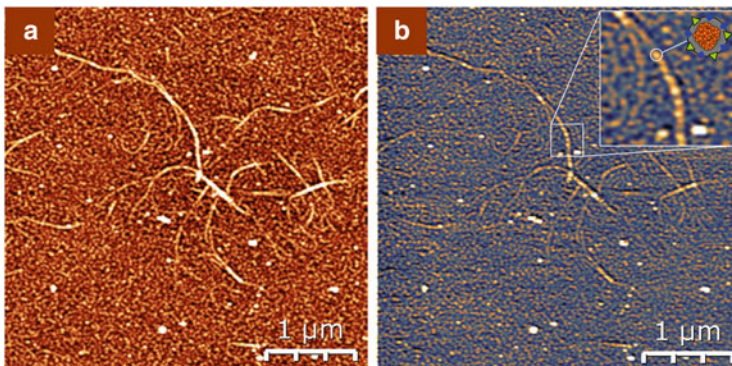


Fig. 7 AFM height images (a) and electric force microscopy (EFM) phase image (b) of ELP-CdSe nanofibres deposited on Si/SiO₂ substrates. The *inset* in (b) shows a magnified section of an individual nanofibre; the CdSe nanoparticles within the fibres are visible. Reprinted with permission from Fahmi et al. [34]. Copyright, 2010, Wiley-VCH

To confirm the EFM results, oxygen-plasma etching was applied to remove the biomolecule matrix and to reveal the length scale between the discrete CdSe nanoparticles within the nanofibres. This is a vital step that decides the key characteristics of the generated nanofibres in electronic and optoelectronic applications. The AFM images in Fig. 8 show that the discrete alignment of the CdSe nanoparticles mimics the contour of the original nanofibres, with average spacing of ~ 85 nm. Overall, it seems that ELPs can be used not only to template the QD nanoparticles with controlled size and size distribution but also to direct the assembly of the CdSe nanoparticles in a unidirectional nanostructure. In order to apply the hybrid nanofibres in biomedical applications such as bio-imaging and biosensing, it is necessary to conduct cytotoxicity tests on the hybrid nanofibres and the CdSe nanoparticles to reveal the functional results of coating CdSe nanoparticles with ELPs.

3.4 Cytotoxicity and Cell Proliferation

We used B14 fibroblast cells as a platform to assess the cytotoxicity of the hybrid nanofibres and their effect on cell proliferation. The reasons for using this type of cell are the relatively short cell cycle and their sensitivity to proapoptotic stimuli [32]. As shown in Fig. 9a, the hybrid nanofibres based on ELP-CdSe building blocks did not exhibit any cytotoxicity toward B14 cells at concentrations up to 2 mg/mL, whereas adding uncoated CdSe nanoparticles caused a significant drop in cell viability. The results from the preliminary study shown in Fig. 9b demonstrate the effect of particle dose on the proliferation rate of B14 cells for both unmodified and ELP-CdSe nanoparticles. On the other hand, trials on the morphology of B14

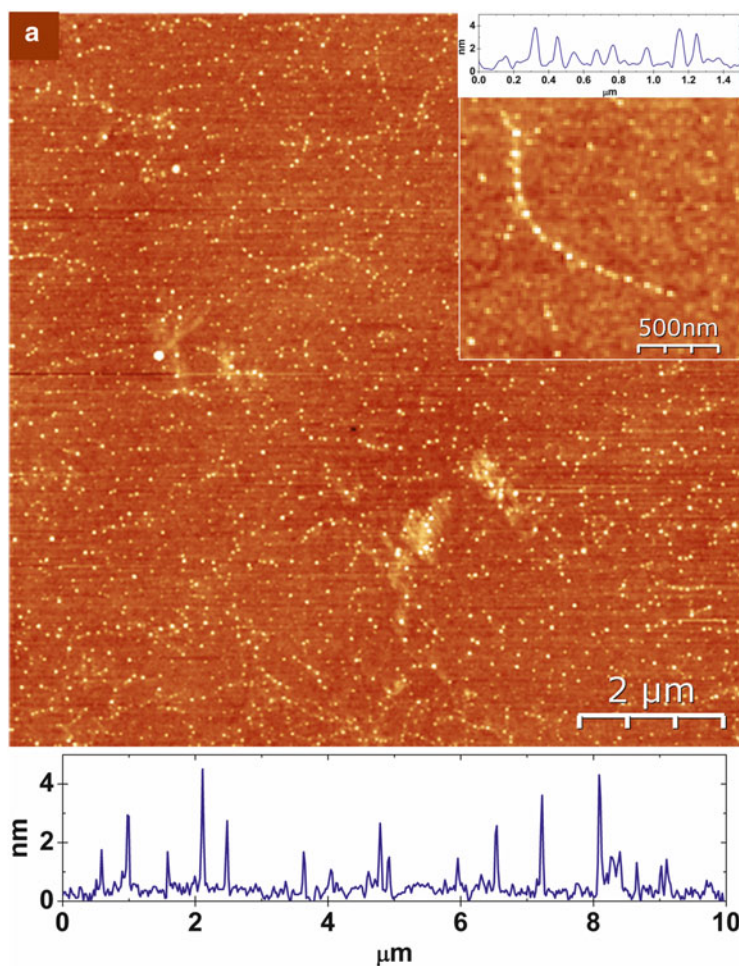


Fig. 8 AFM height image and corresponding cross-section of CdSe quantum dots obtained after oxygen-plasma etching of the ELP-CdSe nanofibres. The *inset* shows a magnified image of CdSe quantum dots that mimic the contour of the original ELP-CdSe nanofibre. Reprinted with permission from Fahmi et al. [34]. Copyright, 2010, Wiley-VCH

cells confirmed that incubating the cells with hybrid nanofibres of ELP-CdSe did not cause any visible impact on cell number, shape or size (Fig. 9c). Nevertheless, it was observed that a small number of cells underwent apoptosis during prolonged culture (72 h) of both control cells and cells treated with ELP-CdSe without medium change. This small percentage of apoptotic cells did not vary significantly from that found for control cells after ELP-CdSe treatment (Fig. 9d). Therefore, we can assume that the small percentage of apoptotic cells treated with ELP-CdSe did not induce apoptotic cell death.

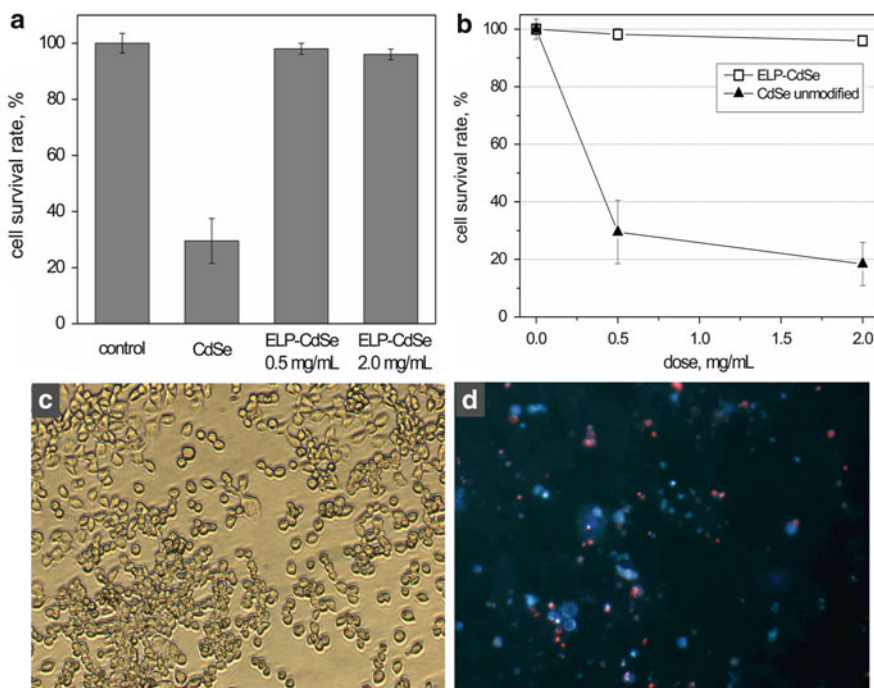


Fig. 9 Cytotoxicity of ELP-CdSe nanoparticles in B14 cells. (a) Cell viability after treatment with unmodified CdSe and different concentrations of ELP-CdSe nanoparticles. (b) Effect of particle concentration on B14 cell proliferation. (c) Optical and (d) fluorescence microscopy of B14 cells after 72 h treatment with 2 mg/mL ELP-CdSe. Reprinted with permission from Fahmi et al. [34]. Copyright, 2010, Wiley-VCH

This section has discussed a diverse range of self-assembled synthetic macromolecules such as block copolymers and elastin-like polymers for template-directed assembly of different types of inorganic nanoparticles into anisotropic 1D nanostructures. In the next section, we introduce a simple and cost-effective approach for directing the assembly of gold nanoparticles into 1D structures via self-assembly of a short commercially available surfactant.

4 Hybrid Nanofibres via Self-Assembly of Short Thiol Surfactant Templating Gold Nanoparticles

Gold nanoparticles (AuNPs) are unique building blocks for building higher dimensional functional structures because of their size-dependent optical properties. In particular, closely spaced AuNPs in a 1D structure exhibit surface plasmon coupling and can be used as subwavelength plasmonic waveguides in a wide range of applications such as bionanotechnology, photonics and optoelectronics [50–53].

Early work introduced by Turkevich in 1951 described the synthesis of AuNPs using citrate to reduce the gold precursor hydrogen tetrachloroaurate (HAuCl_4) in water [54]. Another interesting approach was introduced by Brust and Schiffrin, who used thiol ligands to stabilize the generated gold nanoparticles [55]. The size of AuNPs can be controlled by varying the thiol-to-gold ratio, where functionalization of the AuNPs is accessible through conventional organic methods in nonaqueous solvents [56, 57]. Recently, citrate-decorated AuNP building blocks have been found to assemble into nanofibres via partial ligand exchange of the adsorbed citrate ions by mercaptoethanol (MEA) or thioglycolic acid [58, 20]. This spontaneous assembly of the citrate-decorated AuNP building blocks is a result of the electric dipole formed by the anisotropic organization of the ligands on the surface of the NPs [46].

Small molecules such as surfactants are often inexpensive molecules frequently used for capping-directed assembly of inorganic nanoparticles into well-defined 1D nanostructures. This has been achieved by utilizing well-defined noncovalent interactions such as H-bonding, van der Waals, hydrophobic/solvophobic, charge transfer coordinating bonding and electrostatic/ionic interactions as driving forces in supramolecular chemistry [59–61]. In the case of spherical nanoparticle building blocks, self-assembly of in-situ synthesized nanoparticles in both aqueous and nonaqueous media allows a high degree of ligand anisotropy on the nanoparticle surface [20]. This facilitates the unidirectional alignment needed to fabricate a 1D nanostructure. For instance, Stellaci et al. exploited ligand anisotropy on stabilized AuNPs. The ligands situated at the poles of a particle are stabilized by intermolecular interactions to drive the building blocks to generate the 1D nanostructure [62].

In general, the template-directed self-assembly of NPs into a well-defined 1D nanostructure shows certain key characteristics that are influenced by interparticle interactions via one or more driving forces such as hydrogen bonding, van der Waals interactions or electrostatic forces. For example, Wang and colleagues demonstrated that negatively charged thioglycolic acid-capped nanoparticles experienced weaker electrostatic repulsion to drive 1D alignment than nanoparticles with a side-chain attachment [63]. It is also worth mentioning the constraints of self-assembly to control the alignment of nanoparticles in solution because particles at the nanoscale possess a high tendency to undergo self-aggregation. Therefore, self-assembly of uncharged nanoparticles with size below 5 nm in solution is difficult in the case of unidirectional nanostructures [61].

In the next section, we investigate the use of hybrid thiol building blocks to direct the assembly of in-situ synthesized AuNPs into 1D nanostructures via a cost-effective, one-step self-assembly process. Moreover, the effect of crucial parameters such as molar ratio, pH, temperature and solvent on the 1D structure formation is examined [47].

4.1 *Spontaneous Self-Assembly of In-Situ Synthesized Gold Nanoparticles*

A solution of thiol ligands was prepared at 1 mg/mL in dimethylformamide (DMF). The gold precursor HAuCl_4 (0.2 equivalents to thiol ligand) was added to the solution and stirred overnight. The polar DMF was chosen because of its ability to efficiently solubilize both the gold precursor and the ligands. The inorganic precursor dissociates in solution, resulting in $[\text{AuCl}_4]^-$ complexes that thereafter react with the thiol molecules. The formation of gold nanoparticles is obtained through the addition of a reducing agent (NaBH_4 dissolved in water) to reduce Au^{3+} to Au^0 , resulting in a colour change of the solution from slightly yellow to dark red [47].

4.2 *Preparation of Nanofibres Based on Gold Nanoparticles*

The formation of nanofibres via the self-assembly of AuNPs is usually performed in two steps: synthesis of AuNPs followed by ligand exchange to induce the self-assembly. In this section, a novel concept is proposed for the synthesis of nanofibres via an in-situ approach. A one-pot chemical process is utilized for the self-assembly of building blocks based on AuNPs stabilized with a short surfactant to form well-defined 1D nanostructures.

The method relies on the synthesis of AuNPs in a one-phase system in the presence of thiols. The selection of the thiol monomer is vital for the formation of fibres due to the nature of the functional groups, the length of the alkyl backbones and the introduction of branching. Herein linear short hydroxyl terminated thiol 2-mercaptoethanol (MEA) is used to fabricate nanofibres. The presence of the hydroxyl group was expected to favour self-assembly via the formation of hydrogen bonds. Using MEA as a ligand, nanofibres with high aspect ratios were formed. The AFM image in Fig. 10a reveals the formation of 1D nanofibres with a diameter of ≈ 70 nm and a height of 2–4 nm. However, after reducing the gold precursor with NaBH_4 in solution, large aggregates were generated, as seen in Fig. 10b. These aggregates probably resulted from the folding of the 1D arrays from a linear to a globular shape because of disruption of specific interactions between the gold particles and the surrounding solvent. To determine whether the 1D nanostructures resulted from the self-assembly of AuNPs with a well-defined distance between the AuNPs, oxygen plasma was used for 20 min to extract the organic thiol ligand and leave only the metallic AuNPs on the solid substrate. The AFM height image of the sample after plasma etching reveals the alignment of particles within the unidirectional nanostructure (Fig. 10c, white arrows), thus supporting the theory that the self-assembly used AuNPs as building blocks to form nanofibres.

Transmission electron microscopy (TEM) was used to determine the size and size distribution of the AuNPs. The nanoparticles are observed as dark spots because of their higher density as compared with the organic ligand. The TEM micrographs show the formation of long nanofibres consisting of AuNPs (Fig. 11a).

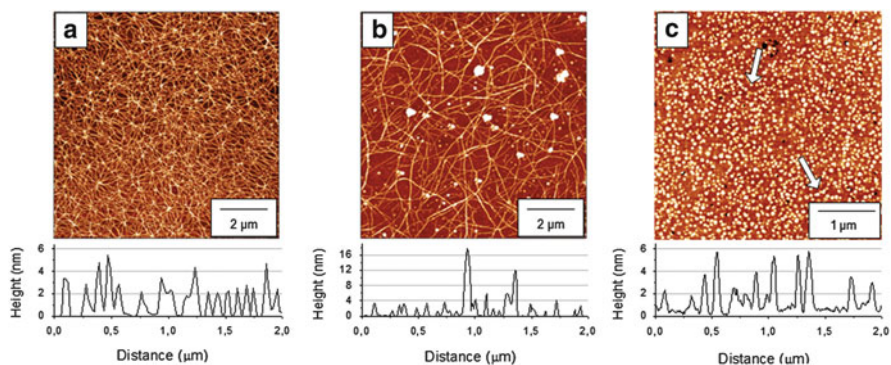


Fig. 10 AFM height image and surface profile of (a) MEA/HAuCl₄ (molar ratio of 5:1), (b) MEA/HAuCl₄ (5:1) after reduction by NaBH₄ and (c) MEA/HAuCl₄ (5:1) after oxygen-plasma etching; *white arrows* indicate the alignment of particles within the unidirectional nanostructure. Reprinted with permission from Walter et al. [47]. Copyright, 2012, Langmuir, American Chemical Society; open access

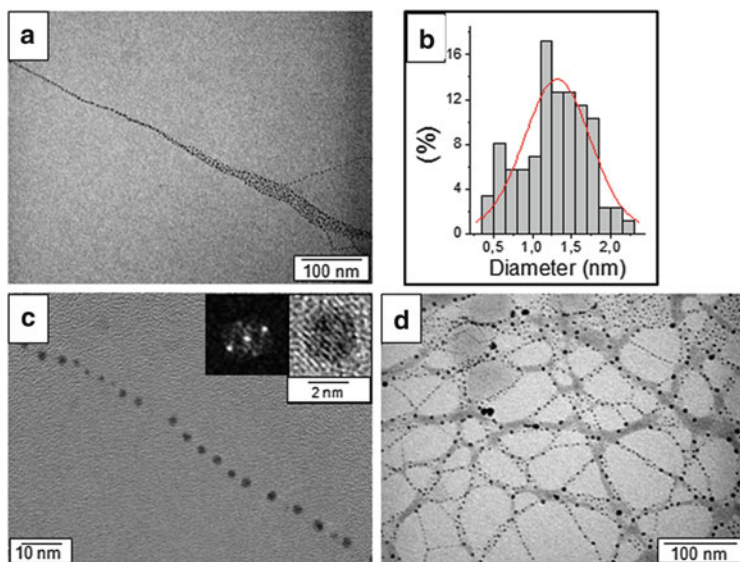


Fig. 11 (a) TEM micrograph of gold nanoparticles obtained from MEA/HAuCl₄ (molar ratio of 5:1). (b) Size distribution of the gold nanoparticles, from TEM studies conducted on a solution of MEA/HAuCl₄ (5:1). (c) High resolution TEM micrograph of gold nanoparticles obtained from MEA/HAuCl₄ solution (5:1). The *insets* show the crystalline structure. (d) TEM micrograph of gold nanoparticles obtained from MEA/HAuCl₄ (5:1) after reduction by NaBH₄. Reprinted with permission from Walter et al. [47]. Copyright, 2012, Langmuir, American Chemical Society; open access

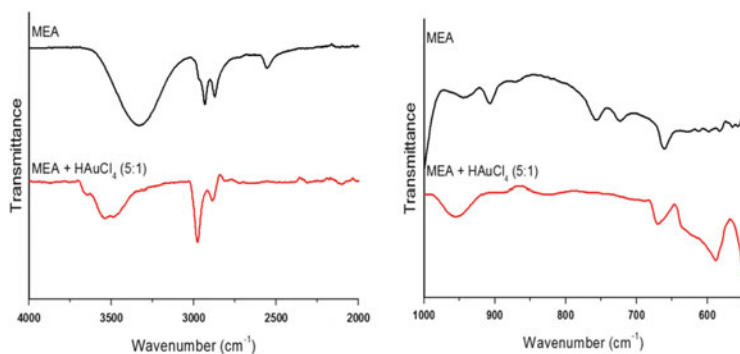
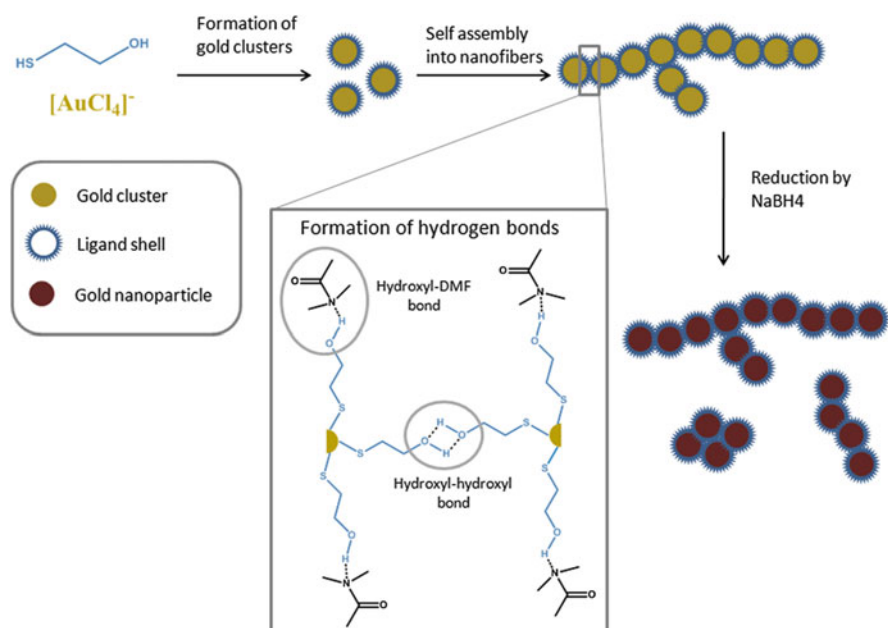


Fig. 12 Infrared spectra of pure MEA and MEA/HAuCl₄ (molar ratio of 5:1) hybrid materials. Reprinted with permission from Walter et al. [47]. Copyright, 2012, Langmuir, American Chemical Society; open access

The nanoparticles are well defined with an average diameter of 1.5 nm (Fig. 11b). HR-TEM measurements were conducted to evaluate the crystalline structure of the particles, as presented in Fig. 11c. The characteristic fringes observed on the HR-TEM confirm the monocrystallinity of the particles. The interparticle distance was estimated to be 2–4 nm in the linear fibres. However, after reduction of the gold precursor by NaBH₄ in solution, the capped AuNPs tended to aggregate and form large particles, as observed in Fig. 11d. The results from the TEM analyses are in agreement with the AFM measurements.

In order to understand better the nature of the interactions involved in nanofibre formation, attenuated total reflection Fourier-transform infrared (FTIR) spectroscopy analyses were conducted on pure MEA and a MEA/HAuCl₄ system, before reduction of the gold precursor. The disappearance of the signal at 2,554.3 cm (corresponding to the vibration of the thiol) after addition of gold precursor confirms the formation of an Au–S bond in the system, as shown in Fig. 12. Moreover, the appearance of a new signal at 3,648 cm and the shift observed for the OH vibration frequency reveal the presence of hydrogen bonds in the fibres [62, 63].

The results suggest that the AuNPs are assembled into nanofibres as a result of formation of hydrogen bonds between MEA molecules on one side and between MEA and DMF molecules on the other side. The model presented in Scheme 3 demonstrates the formation of nanofibres in solution. A suggested mechanism explains that S–H groups interact with gold precursor in solution. Upon addition of MEA, gold complexes aggregate to form a gold cluster composed of a gold core capped by a thiol ligand shell. Adding a fivefold excess of thiol to the gold precursor saturates the surface of the gold cluster with the ligands. The clusters can therefore self-assemble via the formation of hydrogen bonds between the hydroxyl groups of the MEA monomers. It is believed that the Au-cluster assembly is directed into nanofibres as a result of the competitive formation of hydrogen bonds between the hydroxyl group of the MEA and the nitrogen atom of the DMF molecules.



Scheme 3 Proposed model for the linear alignment of gold nanoparticles in DMF to form nanofibres. Reprinted with permission from Walter et al. [47]. Copyright 2012, Langmuir, American Chemical Society; open access

Therefore, controlling these two types of interactions is crucial for the formation of a unidirectional 1D structure. TEM and AFM observations of nanofibres after plasma etching reveal discrete gold nanoparticles with a constant interparticle distance. Certainly, some irregularities in the spacing are observed when disulfide bonds are formed by oxidation of the MEA, resulting in intercalation between the particles. This disulfide forms hydrogen bonds with the hydroxyl groups of two MEA-capped AuNPs and increases the spacing between the AuNPs. Branching occurs when one AuNP participates in more than two interparticle interactions.

Disassembly of the nanofibres is simply conducted by adding water into the system, resulting in disruption of specific hydrogen bonds between the capped AuNPs. Therefore, changing the complementary functional group or the structure of the thiol ligand disrupts the formation of nanofibres. These indicate a narrow window of parameters that can be tuned to direct the self-assembly of the AuNP building blocks into a unidirectional structure. In the next section, we study the parameters and conditions that influence the morphology of the generated nanofibres.

4.3 Investigation of Parameters Affecting the Formation of Fibres

It is well known that self-assembly of nanoparticles can be controlled by several types of driving forces and interactions, such as hydrogen bonding, electrostatic interactions, van der Waals interactions, chemical bonding and/or a combination of these forces [60]. These forces are affected by a wide range of parameters, such as the surface charge of the particle, the chemical structure of the ligands and the temperature of the system, to name a few. In the model described above (Scheme 3), the formation of a unidirectional structure was attributed to the formation of hydrogen bonds between the hydroxyl groups of the ligands on the one hand and between the hydroxyl groups of the ligands and the solvent on the other hand. To confirm this model, the effects of the molar ratio of thiol to gold precursor, temperature, pH and solvent on the formation of nanofibres were studied.

4.3.1 Effect of the Molar Ratio of Thiol to Gold Precursor

The molar ratio between thiol and gold precursor is a vital parameter and was investigated by preparing samples using an equimolar ratio (1:1) and up to a 50-fold excess of thiol (50:1). AFM images of thiol/HAuCl₄ solutions spin-coated onto silicon substrates are presented in Fig. 13. No fibres were observed when an equimolar ratio of thiol to gold precursor was used (Fig. 13a), whereas increasing the amount of thiol up to a 20-fold excess resulted in the formation of nanofibres of different thicknesses and densities at the air–solid interface (Fig. 13b–d).

Increasing the concentration of thiol even more, up to a 50-fold excess with respect to the amount of the gold precursor, disrupted the formation of nanofibres. Markedly, the thickness of the nanofibres was found to be independent of the molar ratio between thiol and gold precursor. For instance, fibres of 50–100 nm in thickness were observed for molar ratios of 3:1, 5:1, 10:1 or 20:1 thiol to gold precursor. The number of MEA molecules at low concentration adsorbed on the gold surface is low and the molecules can adopt a gauche conformation, lying on the surface [64]. In contrast, at higher concentration of MEA, large numbers of the MEA molecules are adsorbed on the surface and adopt a linear *trans* conformation, as illustrated in Scheme 4. This makes the hydroxyl groups more accessible for formation of hydrogen bonds [64].

4.3.2 Effect of Temperature

Temperature is an important parameter that influences nanofibre generation as a result of hydrogen bond formation between the hybrid building blocks. AFM measurements were conducted on spun-coated nanofibre films (Fig. 14) directly after heating solutions of the nanofibres at 50°C and after cooling for 24 h. After

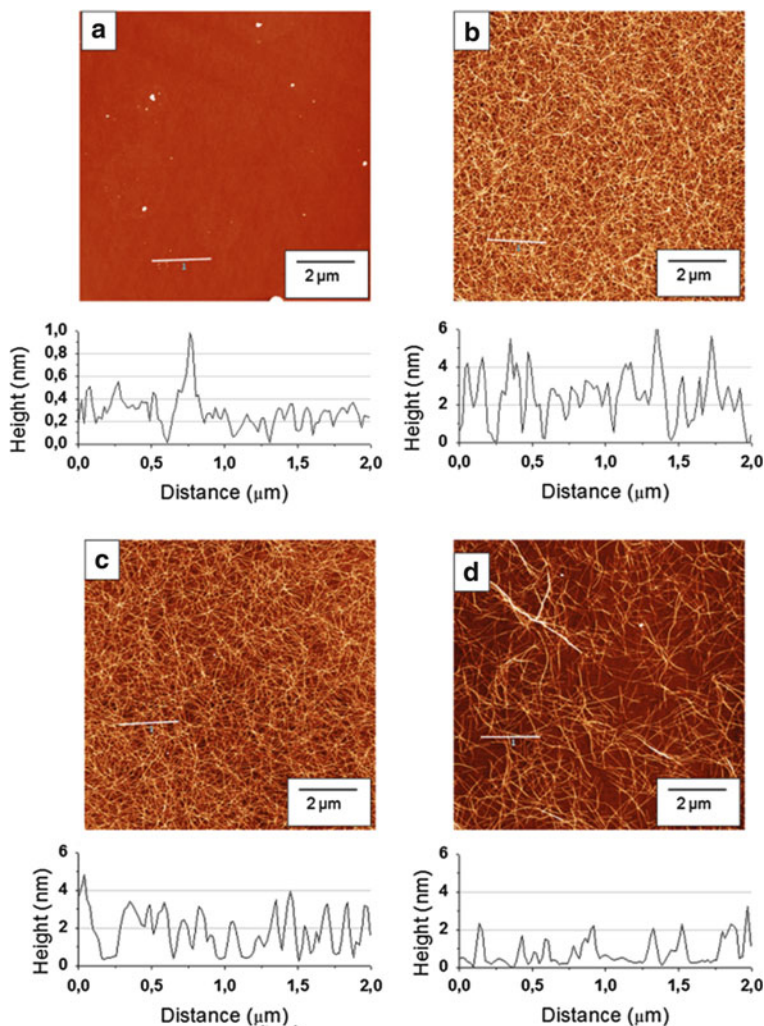
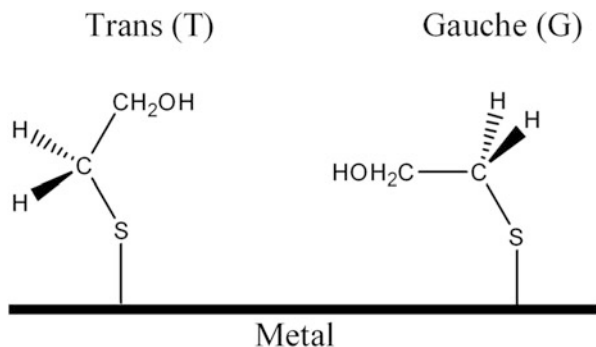


Fig. 13 AFM height images and surface profiles of thiol/ HAuCl_4 at different thiol-to-gold precursor ratios: (a) 1:1, (b) 3:1, (c) 10:1 and (d) 20:1. Reprinted with permission from Walter et al. [47]. Copyright, 2012) Langmuir, American Chemical Society; open access

heating the nanofibres at 50°C for 1 h, large numbers of nanodots were observed between the particle chains (Fig. 14a). In contrast, after cooling, the dots disappeared and thick nanofibres were observed of up to 200 nm thick (Fig. 14b). Increasing the temperature of the nanofibre solution to 100°C for 1 h resulted in a smooth surface both before and after cooling. No nanofibres or dots were observed on the solid substrate at this temperature.



Scheme 4 Representation of the *trans* and *gauche* conformations of MEA, as described by Kudelski. Reprinted with permission from Kudelski [64]. Copyright 2003, Langmuir, American Chemical Society

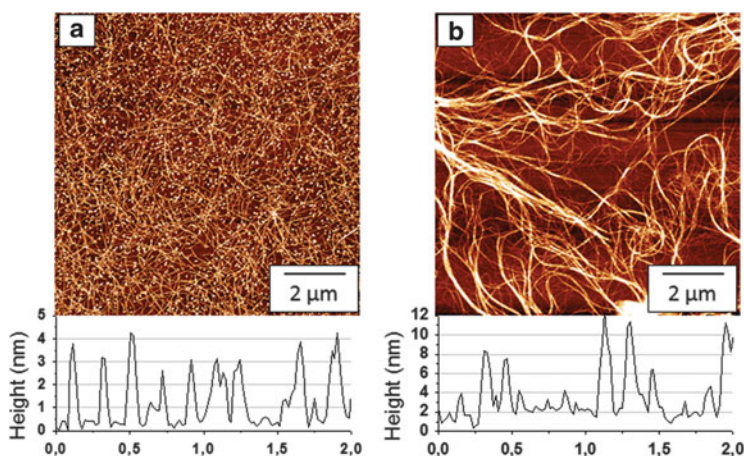
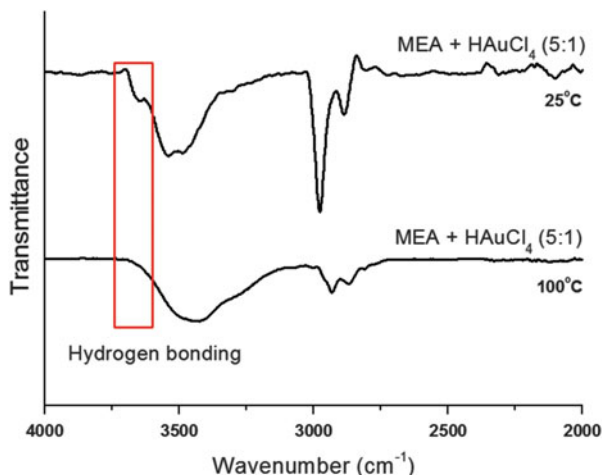


Fig. 14 AFM height images and surface profiles of thiol/HAuCl₄ (molar ratio of 5:1) after heating for 1 h at 50°C (a) before and (b) after cooling. Reprinted with permission from Walter et al. [47]. Copyright, 2012, Langmuir, American Chemical Society; open access

To summarize the effect of temperature on the nanofibers, heating the solution at 50°C brings enough energy to partially break the nanofibers into nanodots/small fragments due to the disruption of the hydrogen bonds that hold the hybrid building blocks (nanoparticles) together. After cooling, agglomeration occurs between the nanodots/small fragments via new sets of hydrogen bonds to form thicker nanofibers. In contrast, heating the solution to 100°C delivers enough energy into the system to break the assembly of hybrid building blocks. These results demonstrate that higher temperatures not only disturb the formation of nanofibers by breaking the hydrogen bonds, but also change the structure of the hybrid building blocks to inhibit the unidirectional morphology. Raman spectroscopy studies have

Fig. 15 FTIR spectra of the MEA/HAuCl₄ system before (*top*) and after (*bottom*) heating at 100°C for 1 h. Reprinted with permission from Walter et al. [47]. Copyright, 2012, Langmuir, American Chemical Society; open access



confirmed that at higher temperatures the adsorbed MEA on a gold surface could promote the oxidative cleavage of the C–S bond, resulting in thiolated nanoparticles [63]. To validate this hypothesis, infrared spectroscopy was performed on the MEA/HAuCl₄ system before and after heating at 100°C for 1 h (Fig. 15).

After heating the solution, the signal at 3,648 cm (corresponding to the formation of hydrogen bonds) disappears, confirming the disruption of the hydrogen bonds. This study further confirms the presence of hydrogen bonds between the hybrid building blocks AuNPs and suggests that the nanofibre thickness could be tailored by varying the temperature of the nanofibre solution.

4.3.3 Effect of pH

The pH of the nanofibre solution was studied. Even though the pH of the DMF solution cannot be accurately determined with a pH meter, we found the pH of thiol and gold precursor in DMF solution (molar ratio of 5:1) to be 2.2. The relative acidity of the initial solution is due to the dissociation of the gold precursor into H⁺ and [AuCl₄]⁻. AFM measurements were conducted on solutions of pH 7, 10 and 14, prepared by addition of an aqueous NaOH solution. The images in Fig. 16 demonstrate that the hybrid nanofibres were stable only in acidic medium at pH 2.2. The nanofibres were destroyed on increasing the pH of the solution by the addition of aqueous NaOH. It seems that the hydroxyl group of the MEA was partly deprotonated, resulting in a heterogeneous charge distribution. This induced electrostatic repulsion between the negatively charged building blocks and caused the disassembly of the nanofibres. These results confirm that switching the surface charge of the hybrid building blocks via tuning the pH values significantly influences nanofibre formation. Interestingly, this process is irreversible, as

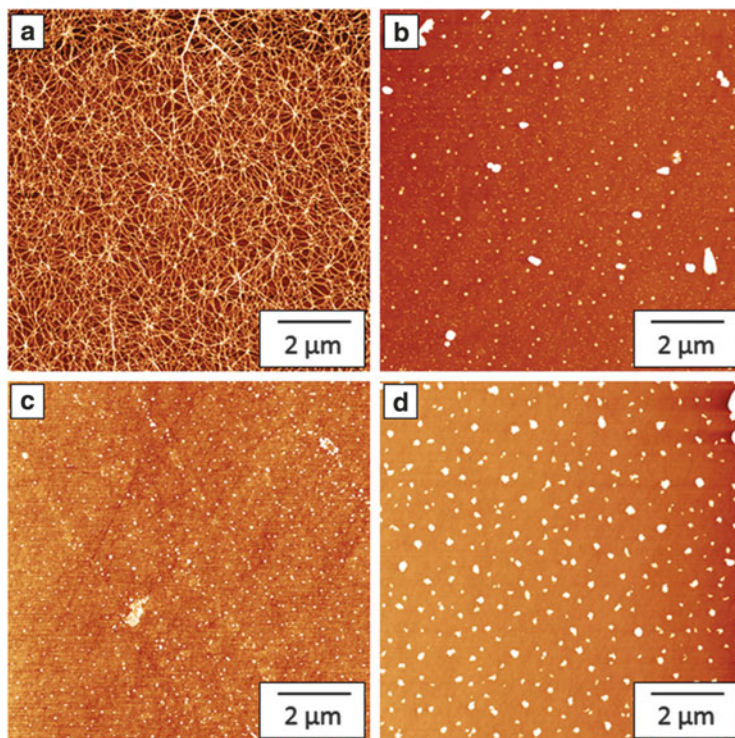


Fig. 16 AFM height images of the thiol/ HAuCl_4 system (molar ratio of 5:1) at different pH values: (a) 2.2, (b) 7, (c) 10 and (d) 14. Reprinted with permission from Walter et al. [47]. Copyright, 2012, Langmuir, American Chemical Society; open access

decreasing the pH of the solution back to its initial value does not permit the reformation of nanofibers. One explanation is that the introduction of water to the system competes with the formation of hydrogen bonds and prevents the alignment of the building blocks to form the nanofibers.

4.3.4 Effect of Solvent

The effect of different solvents on the stability of the fibres was also examined. MEA was dissolved in different solvents such as ethanol, water and dimethyl sulfoxide (DMSO) as an alternative to DMF. In water and ethanol, precipitates were formed upon addition of gold precursor, revealing that the AuNPs were not stabilized efficiently by the short surfactant. In DMSO, the formation of aggregates was observed (Fig. 17). A significant difference between DMF and DMSO is the presence of a lone pair of electrons on the nitrogen atom within the DMF. This can contribute to hydrogen bond formation between the polar solvent and the hybrid building blocks to direct the self-assembly of the hybrid building blocks into

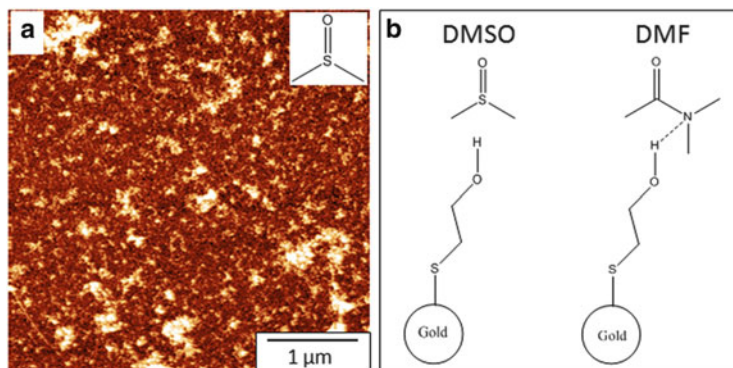


Fig. 17 (a) AFM height images of MEA/HAuCl₄ (molar ratio of 5:1) in DMSO. (b) Scheme showing the absence of an H-bond between the MEA and DMSO and the formation of an H-bond between MEA and DMF. Reprinted with permission from Walter et al. [47]. Copyright, 2012, Langmuir, American Chemical Society; open access

nanofibres. The formation of hydrogen bonds between the DMF and the hydroxyl group of the ligand also prevents the agglomeration of nanoparticles. In contrast, in the case of DMSO as solvent, the hydroxyl groups of the MEA interact with each other and, consequently, aggregates are formed (Fig. 17).

5 Conclusion and Future Prospects

Simple and cost-efficient concepts are presented in this review for the fabrication of low dimensional 1D nanostructures of hybrid building blocks based on linear organic matrices template in-situ conductive and semiconductive inorganic nanoparticles by linear organic matrices. The nanoparticles were prepared by simple wet chemistry approaches. For example, hybrid gold 1D nanostructures can be generated by reducing the gold precursor HAuCl₄ in the presence of block copolymers and mercaptoethanol. Another example is the synthesis of CdSe hybrid nanofibres, which starts with complexation of Cd(II) precursor to the functional groups of amino acids within elastin-like polymers, followed by selenization with freshly prepared NaHSe in aqueous media. These processes have been described in this review and demonstrate spontaneous self-assembly of hybrid building blocks into unidirectional nanostructures with well-defined interparticle distances. Furthermore, the driving forces that dominate 1D structure formation are also discussed and found to be single or combinations of noncovalent interactions such as hydrogen bonding, van der Waals and electrostatic forces. Certainly, these interactions are mainly dependent on the nature of the hybrid building blocks and the length scale of the constructed 1D structures.

These approaches can be applied to fabricate a wide range of functional 1D nanostructures based on hybrid building blocks of different types of templated

metallic, magnetic and semiconductor nanoparticles. Undoubtedly, these types of self-assembled functional 1D structures will be integrated into the next generation of miniaturized devices. However, before the industrialization of these nanofabrication techniques, many challenges must be overcome. For instance, governing the growth of the material via control of the size and distance between the inorganic nanoparticles in the 1D nanostructure is a vital step in obtaining collective physical properties. On the other hand, control of the alignment and length of the generated 1D nanostructures at different dimensions and length scales is the key to integrating multiscale compartments. Moreover, accurate prediction and tailoring of the physical properties via theoretical and semi-empirical models are still major challenges. These are essential for adjusting the mass fabrication parameters for highly efficient functions of the generated hybrid nanostructured compartments for a broad spectrum of applications, including nanoelectronics, optoelectronic, catalysis, nanomedicine and filtration.

References

1. Fahmi A, Pietsch T, Mandoza C (2009) *Mater Today* 12:44
2. Schatz G (2010) *J Phys Chem Lett* 1:2980–2981. doi:[10.1021/jz101284n](https://doi.org/10.1021/jz101284n)
3. Kalekar AM, Sharma KKK, Lehoux A, Audonnet F, Remita H, Saha A, Sharma GK (2013) *Langmuir* 29(36):11431–11439
4. Taton TA, Mirkin CA, Letsinger RL (2000) *Science* 289:1757–1760
5. Willner I, Willner B (2010) *Nano Lett* 10(10):3805–3815
6. Wang H, Wang D, Peng Z, Tang W, Li N, Liu F (2013) *Chem Commun* 49:5568–5570
7. Ma Z, Chen W, Schuster GB (2012) *Chem Mater* 24(20):3916–3922
8. Wang Y, Mirkin CA, Park S (2009) *ACS Nano* 3(5):1049–1056
9. Wirth GF, Hähnel G, Csáki A, Jahr N, Stranik O, Paa W, Fritzsche W (2011) *Nano Lett* 11(4):1505–1511
10. Kaur P, Maeda Y, Mutter AC, Matsunaga T, Xu Y, Matsui H (2010) *Angew Chem Int Ed* 49(45):8375–8378
11. Ling S, Lin C, Adamcik J, Wang S, Shao Z, Chen X, Mezzenga R (2014) *ACS Macro Lett* 3(2):146–152
12. Mironava T, Hadjiargyrou M, Simon M, Jurukovski V, Rafailovich MH (2010) *Nanotoxicology* 4(1):120–137
13. Xu J, Teslaa T, Wu T-H, Chiou P, Teitell MA, Weiss S (2012) *Nano Lett* 12(11):5669–5672
14. Khan AA, Fox EK, Górzny ML, Nikulina E, Brougham DF, Wege C (2013) *Langmuir* 29(7):2094–2098
15. Lee JH, Domaille DW, Cha JN (2012) *ACS Nano* 6(6):5621–5626
16. Xu F, Fahmi A, Zhao Y, Xia Y, ZY (2012) *Nanoscale* 4:7031
17. Mann S (2009) *Nat Mater* 8:781–792
18. Cozzoli PD, Fanizza E, Curri ML, Laube D, Agostiano A (2005) *Chem Commun* 2005:942–944
19. Sudeep PK, Emrick T (2009) *ACS Nano* 3(10):2870–2875
20. Lin S, Li M, Dujardin E, Girard C, Mann S (2005) *Adv Mater* 17:2553–2559
21. Gröschel AH, Walther A, Löbbling TI, Schacher FH, Schmalz H, Müller AHE (2013) *Nature* 503:247–251
22. Cademartiri L, Ozin GA (2009) *Concepts of nanochemistry*. Wiley-VCH, Weinheim
23. Whitesides GM, Grzybowski B (2002) *Science* 295:2418

24. Ozin GA, Hou K, Lotsch BV, Cademartiri L, Puzzo DP, Scotognella F, Ghadimi A, Thomson J (2009) *Mater Today* 12(5):12–23
25. Kang Y, Erickson KJ, Taton TA (2005) *J Am Chem Soc* 127:13800–13801
26. Li Z, Sai H, Warren SC, Kamperman M, Arora H, Gruner SM, Wiesner U (2009) *Chem Mater* 21(23):5578–5584
27. Pietsch T, Gindy N, Fahmi A (2008) *Polymer* 49(4):914–921
28. Wang H, Patil AJ, Liu K, Petrov S, Mann S, Winnik MA et al (2009) *Adv Mater* 21:1805–1808
29. Rosi NL, Mirkin CA (2005) *Chem Rev* 105:1547–1562
30. Gottlieb D, Morin SA, Jin S, Raines RT (2008) *J Mater Chem* 18:3865–3870
31. Niemeyer CM (2003) *Angew Chem Int Ed* 42(47):5796–5800
32. Selvan ST, Thatt T, Tan Y, Yi DK, Jana NR (2010) *Langmuir* 26(14):11631–11641
33. Hoffmann C, Mazari E, Gosse C, Bonnemay L, Hostachy S, Gautier J, Gueroui Z (2013) *ACS Nano* 7(11):9647–9654
34. Fahmi A, Pietsch T, Bryszewska M, Rodríguez-Cabello JC, Chyla AK, Arias FJ, Rodrigo MA, Gindy N (2010) *Adv Funct Mater* 20:1011
35. Vanrella RH, Rinco'na AC, Alonsob M, Rebotob V, Molina-Martinez IT, Rodr RC, Cabellco G (2005) *J Control Release* 102:113–122
36. Nath N, Hyun J, Ma H, Chilkoti A (2004) *Surf Sci* 570:98–110
37. Aili D, Enander K, Baltzer L, Liedberg B (2007) *Biochem Soc Trans* 35:532–534
38. Lee BC, Zuckermann RN (2010) *Chem Commun* 46:1634–1636
39. Palmer LC, Stupp SI (2008) *Acc Chem Res* 41(12):1674–1684
40. Khan S, Sur S, Dankers PYW, da Silva RMP, Boekhoven J, Poor TA, Stupp SI (2014) *Bioconjug Chem* 25(4):707–717
41. Aida T, Meijer EW, Stupp SI (2012) *Science* 335(6070):813–817
42. Reguera J, Fahmi A, Moriarty P, Girotti A, Rodríguez-Cabello JC (2004) *J Am Chem Soc* 126:13212–13213
43. Kumar S, Aswal VK, Callow P (2014) *Langmuir* 30(6):1588–1598
44. Hartgerink JD, Beniash E, Stupp SI (2005) *Science* 294(5547):1684–1688
45. Spanier JE et al (2006) *Nano Lett* 6:735–739
46. Li M, Johnson S, Guo H, Dujardin E, Mann S (2011) *Adv Funct Mater* 21(5):851–859
47. Walter MV, Cheval N, Liszka O, Malkoch M, Fahmi A (2012) *Langmuir* 28(14):5947–5955
48. Talapin DV, Rogach AL, Kornowski A, Haase M, Weller H (2001) *Nano Lett* 1(4):207–211
49. Zhou X, Dayeh SA, Wang D, Yu ET (2007) *Appl Phys Lett* 90:233118
50. Lau CY, Duan H, Wang F, He CB, Low HY, Yang JKW (2011) *Langmuir* 27(7):3355–3360
51. Pissuwan D, Niidome T, Cortie MB (2011) *J Control Release* 149(1):65–71
52. Cohen-Karni T, Jeong KJ, Tsui JH, Reznor G, Mustata M, Wanunu M, Graham A, Marks C, Bell DC, Langer R, Kohane DS (2012) *Nano Lett* 12(10):5403–5406
53. Dhandayuthapani B, Mallampati R, Sriramulu D, Dsouza RF, Valiyaveetil S (2014) *ACS Sustain Chem Eng* 2(4):1014–1021
54. Turkevich J, Stevenson PC, Hillier J (1951) *Discuss Faraday Soc* 11:55–75
55. Brust M, Walker M, Bethell D, Schiffrin DJ, Whyman R (1994) *J Chem Soc Chem Commun* 1994(7):801–802
56. Stoeva S, Zaikovski V, Prasad BLV, Stoimenov P, Sorensen C, Klabunde K (2005) *Langmuir* 21:10280–10283
57. Chen S, Murray RW (1998) *Langmuir* 15(3):682–689
58. Fung ZH, K-H HJ, Chan CT, Wang D (2008) *J Phys Chem C* 112(43):16830–16839
59. Llusar M, Sanchez C (2008) *Chem Mater* 20:782–820
60. Grzelczak M, Vermant J, Furst EM, Liz-Marzan LM (2010) *ACS Nano* 4(7):3591–3605
61. Lee J, Zhou H, Lee J (2011) *J Mater Chem* 21(42):16935–16942
62. DeVries GA, Brunnbauer M, Hu Y, Jackson AM, Long B, Neltner BT, Uzun O, Wunsch BH, Stellacci F (2007) *Science* 315:358–361
63. Zhang H, Wang D (2008) *Angew Chem Int Ed* 47(21):3984–3987
64. Kudelski A (2003) *Langmuir* 19(9):3805–3813

Index

A

ABS/EPDM, 32
2-Acrylamido-2-methylpropane-sulfonic acid, 50
Acrylonitrile-butadiene-styrene (ABS), 32
Ag nanowires, 321
Ag NP-chitosan, 105
Alcohol dehydrogenase, 63
Alginate-*g*-poly(acrylic acid-*co*-acrylamide)/humic acid, 59
Alginate-palygorskite, 57
Aluminum nitride (AlN), 328
Aluminum oxide (Al₂O₃), 97, 150
Aminopropyl triethoxysilane (APTES), 50, 146, 151
Arabinoxylan, 54
ATO/PMMA, 25
Atomic layer deposition (ALD), 107
Attapulgate, 42
AuCd, 322
AuNPs, 355, 366
Azo dyes, 97
Azobis(4-cyano-pentanoic acid), 328

B

Barium strontium titanyl oxalate (BSTO), 7
BaTiO₃/bisphenol-A dicyanate [2,2-bis(4-cyanatophenyl)isopropylidene] (BADCy), 13
Ba_xSrTi_{1-x}O₃ (BST), 5, 19
Benzophenone-tetracarboxylic dianhydride (BTDA), 164
Biamino-3,3-dimethyldiphenyl-methane (DMMDA), 164

Bimodal molecular imaging, 298
Biocompatibility, SMPINCs, 335
Biomedical applications, 283
Bionanocomposites, 39, 51
Bioplastics, 39, 53, 60
Biopolymers, 39
Bis(4-aminophenyl) fluorine (BAPF), 164
Bis(triethoxysilylpropyl)tetrasulfane (TESPT), 12
Boehmite, 336
Boron nitride nanotubes (BNNTs), 337
1-Butyl-3-methylimidazolium chloride (BMIMCl), 54
tert-Butylhydroquinone (TBHQ), 64

C

Cadmium sulfide (CdS), 98, 103
 quantum rods, 291
Cancer cells, 298
Carbon black nanoparticles, 30
Carbon nanotubes (CNTs), 8, 27, 72, 295, 319
 MWCNTs, 28, 47, 64, 72, 320, 330
 SWCNTs, 13, 320
Carboxyethyl-chitosan/PEO/glutaraldehyde/
 Ag NPs, 103
Carboxymethylcellulose (CMC), 57
Carcinogenicity, 42
CdSe, 357
CdSe-CdS-ZnS, 301
CdSe-ZnS-triethoxyphosphine oxide (TOPO), 303
Cell proliferation, 364
Cellulose acetate (CA), 110
Chemical vapor deposition, 8

Chitosan, 53
 PEO/glutaraldehyde/Ag NPs, 103
 Chlorpyrifos, 57
 Clays, 39, 99, 187
 Coatings, 113, 156, 341
 Co-precipitation, 7
 Collagen, 62
 Concanavalin A, 128
 Conducting carbon–fibrous clay
 nanocomposites, 70
 Conducting polymer–fibrous clay
 nanocomposites, 68
 Copper, 57, 104
 Copper oxide, 251
 Copper sulfide, 287
 Corrosion protective sol–gel coatings, 157
 Cr(III), 56
 Cytotoxicity, 230, 335, 364

D
 Diclofenac sodium (DS), 59
 Diluted magnetic semiconductors (DMS), 285
 Direct dispersion electrospinning, 93
 DNA, 39, 65, 67, 257, 352
 Drug carriers, tumour cell markers, 298
 Dye-sensitized solar cells (DSSCs), 297

E
 Elastin-like polymers (ELPs), 357
 Electronic applications, 283
 Electrospinning, 87, 124
 inorganic dispersions in polymer solutions,
 92
 sol–gel, 113
 Electrospinning, 121
 Environmental remediation, 56
 Enzymes, 63
 Ethylene-propylene-diene rubber (EPDM), 33
 EPDM-*g*-MAH, 33

F
 Fluorohectorite, 323
 Fluoromica, 323
 Functional properties, 143

G
 Gallium nitride, 295
 Gas-separation performance, 166
 Gas–solid reaction, 111

Gelatin, 41, 51, 60, 62, 105, 119, 123, 127
 Germanium, 285
 Glucose oxidase, 64
 Glycidyl methacrylate (GMA), 11
 Gold nanoparticles (AuNPs), 355, 366
 Grafting-from, 10
 Grafting-to, 11
 Graphene oxide, 321

H

HA/chitosan/collagen, 105
 Hafnium oxide, 98
 Halloysite, 320
 Heavy metals, 58
 Hectorite, 193, 230, 323
 Hemicelluloses, 54
 Hexafluoro-2-propanol (HFIP), 105
 4,4-(Hexafluoro-isopropylidene)*bis*
 (4-phenoxyaniline), 147
 4,4-(Hexafluoro-isopropylidene)diphenol, 147
 Hg(II), 59
 Horseradish peroxidase (HRP), 72
 Hybrid fibers, 87
 nanofibres, 351
 organic–inorganic, 127
 Hydrogels, 49, 187
 Hydrogen tetraaurochlorate, 367
 Hydrothermal method/synthesis, 7, 108
 3-Hydroxy-2-oxopropanoic acid-modified
 $\text{Fe}_3\text{O}_4/\text{PCL}$, 273
 Hydroxypropylmethylcellulose (HPMC), 57
 12-Hydroxystearic acid (HSA), 93

I
 Immunoassays, 298
 In-situ fabrication, 351
 Indigo, 44
 Inorganic nanocomposites, 313
 Iron oxide, 101, 273, 339

K

Kaolinite, 323
 KH550, 9

L

Lanthanides, 57
 Laponite XLS, 193
 Light-emitting diodes (LEDs), 284, 295
 Lipases, 63

- Lipids, 65
Liquid phase deposition (LPD), 106
Low density polyethylene (LDPE)/nanoclay, 328
Luminescence, 284
- M**
Magadiite, 323
Maghemite, 251, 332
Magnetic suspensions, 17
Magnetite, 103, 251, 273, 339
Magnetorheological fluid (MRF), 17
Maleic anhydride (MAH), 33
 grafted polypropylene (PP)/expanded
 graphite nanocomposites, 12
Maya Blue, 44
Melt blending, 13
Membranes, 163
Mercury(II), 59, 121
 removal, 294
Metal ions reduction, 109
Metal oxides, 249
Methacryloxypropyltrimethoxysilane
 (APTMS), 50
 KH570, 9
Methyl methacrylate (MMA), 11
Methylenebisacrylamide, 190
Molecular dyes, 44
Molten salt synthesis, 5
Montmorillonite (MMT), 12, 40, 55, 99, 105,
 193, 211, 323, 332
Mucoadhesivity, 59
Multifunctional materials, 143
Multiwalled carbon nanotubes (MWCNTs),
 27, 47, 72, 320
 cyanate ester (CE), 14
 polycarbonate (PC), 13
 polypropylene (PP), 28
- N**
Nafion, 150
Nanocomposites, 187, 249, 283
 fibrous clay-based, 39
 gels (NC gels), 193
 inorganic, 313
 organic–inorganic, 87
 semiconductor–polymer, 283
Nanofabrication, 351
Nanofibers, 87
Nanofillers, 45
 fluorescent/photoluminescent, 98
- Nanofiltration, 164
Nanohybrids, functional materials, 160
 polymer–ceramic, 143
Nanoparticles, 1, 351
 inorganic, 9
 modification, 9
 synthesis, 17
NC gels, self-healing, 226
Nucleic acids, 67
Nylon-6, 10, 14, 40, 45, 103–108
 graphene, 14
 montmorillonite, 105
- O**
Oleic acid, 147
Oligo(ϵ -caprolactone) dimethacrylate, 341
Org-attapulgitite, 10
Organic–inorganic nanocomposites, 1, 87
 networks, 187
Organoclays, 39, 65
Oxydianiline, 151
- P**
Palygorskite, 39, 42
Pectin, 57
Phenytoin, 298
Phospholipids, 39, 64
Photocatalysts, 294
Phyllosilicates, 40, 42
PI(BTDA–BAPF–DMMDA), 165
Plasma methods, 8
Plasma surface modification, 11
Platinum nanoparticle-incorporated NC gels
 (Pt-NC gels), 187, 234
Platinum-nanocomposite gels (Pt-NC gels),
 187, 234
Polyacrylamide (PAM), 58
Polyacrylic acid (PAA), 50, 58, 109, 111, 129,
 150, 218
Polyacrylonitrile (PAN), 70, 95, 149
Polyamide (PA)-SiO₂, 147
Polyamide-6 (PA-6), 46
Polyaniline (PANI), 68, 150
Polyaniline–ZnO, 302
Polyarylene ether ketone/sulfone, 259
Polybutylacrylate, 148
Polycarbonates (PC), 148
Polyesters, biodegradable, 51
Polyethylene terephthalate (PET), 45
Polyhedral oligomeric silsesquioxane (POSS),
 316, 329, 338

- Polyimide (PI), 108, 259
 Polyimide-graphene, 321
 Polylactic acid (PLA), 51, 93
 Polymer-ceramic nanohybrids/interface, 143
 Polymer-clay NC (P/C-NC) microspheres, 187, 234
 Polymer-clay network structure, 198
 Polymer-metal oxide hybrid nanocomposites, 252
 Polymer light-emitting diodes (PLEDs), 321
 Polyphenylene sulfide (PPS)/BST, 14
 Polyphosphazenes, 127
 Polypropylene (iPP), 13
 Polypyrrole (PPy), 68
 Polysaccharides, 39, 53
 Polystyrene (PS), 11, 148
 Polystyrene-*block*-poly(acrylic acid) (PS-*b*-PAA), 355
 Polysulfone (PSU), 96
 Polythiourethane, 259
 Polyurethane (PU), 27, 48, 227, 255, 302, 325
 indium tin oxide (ITO), 302
 Polyvinyl alcohol (PVA), 49
 Polyvinyl butyral-SiO₂ coatings, 156
 Polyvinylpyrrolidone (PVP), 148
 modified CB nanoparticles, 32
 Poly(acrylonitrile-*co*-2-methacryloyloxyethyl phosphorylcholine) [P(AN-*co*-MPC)] hydrogels, 330
 Poly(amide-6-*b*-ethylene oxide), 150
 Poly(amide-imide) (PAI), 150
 Poly[(amino acid ester)phosphazene], 127
 Poly(azo-pyridylurethane), 320
 Poly[bis(*p*-methylphenoxy)phosphazene], 127
 Poly(butyl acrylate), 10
 Poly(*n*-butylene oxide)-*block*-poly(ethylene oxide), 334
 Poly(butylene succinate) (PBS), 53
 Poly(ϵ -caprolactone) (PCL), 52, 96, 255, 336
 MWCT, 13
 SiO₂, 147
 Poly[2-(carbazol-9-yl)ethyl methacrylate] (PCEM)/ZnO, 269
 Poly(2-chloroaniline) (P2ClAn), 160
 Poly(*p*-dioxanone), 340
 Poly-[di(propargylamine)phosphazene], 128
 Poly(ether ether ketone) (PEEK), 147, 255
 Poly(ether imide), 150
 Poly(ether sulfone), 70, 320
 Poly(ethyl methacrylate) (PEMA), 328
 Poly(3,4-ethylenedioxythiophene) (PEDOT), 68
 Poly(ethylene 2,6-naphthalate)-SiO₂, 147
 Poly(ethylene glycol) (PEG), 95, 272, 328
 Poly(ethylene 2,6-naphthalate)-SiO₂, 147
 Poly(ethylene oxide) (PEO), 44, 97, 148, 320
 clay, 330
 Poly(ethylene oxide-*co*-methacrylic acid), 262
 Poly(ethylene terephthalate) (PET)-SiO₂, 147
 TiO₂, 302
 Poly(ferrocenyldimethylsilane)-*block*-poly(2-vinylpyridine) (PFS-*b*-P2VP), 356
 Poly(3-hydroxybutyrate-*co*-3-hydroxyhexanoate)-SiO₂, 147
 Poly(3-hydroxybutyrate-*co*-3-hydroxyvalerate) (PHBV), 52
 Poly(3-hydroxybutyric acid) (PHB), 122
 Poly(2-hydroxyethyl methacrylate) (PHEMA), 97
 Poly(isoprene-*block*-dimethyl aminoethyl methacrylate) (PI-*b*-PDMAEMA), 355
 Poly(*N*-isopropylacrylamide) (PNIPA), 189
 Poly(L-lactic acid) (PLLA), 97
 Poly(L-lactide)-SiO₂, 147
 Poly(LA-*co*-CL)/gelatin, electrospun, 123
 Poly(lactide-*co*-glycolide) (PLGA), 95
 Poly(2-methoxy-5(2-ethyl)hexoxy-phenylenevinylene (MEH-PPV), 148
 Poly(2-methoxyethyl acrylate) (PMEA), 238
 Poly(methyl methacrylate) (PMMA), 14, 95, 148, 255, 322
 Poly(MMA-*co*-MAA-*co*-BA), 340
 Poly(phenylenevinylene), 150, 259
 Poly(phthalazinone ether ketone), sulfonated (sPPEK), 147
 Poly(propylene sebacate), 336
 Poly(propylene-*graft*-maleic anhydride) copolymer (PP-*g*-MA), 13
 Poly(styrene-*b*-isoprene), 124
 Poly(styrene-*co*-3-(trimethoxysilyl) propyl-methacrylate], 129
 Poly(styrene-*b*-4-vinylpyridine) (PS-*b*-P4VP), 356
 Poly(vinyl acetate) (PVAc), 103, 148
 Poly(vinyl alcohol) (PVA), 94, 148, 257
 Poly(vinylidene difluoride) (PVDF), 95
 Poly(vinylidene fluoride-*co*-hexafluoropropylene) (PVDF-HFP), 11
 Poly(4-vinylpyridine) (PVP), 109, 148
 Printing ink, 32
 Proteins, 39, 60
 Psyllium gum, 50
 Pyromellitic dianhydride, 151
- Q**
 Quantum dots, 98, 283, 290, 358

R

Reactive magnetron sputtering, 8
Reversible force generation, 226

S

Sacran, 57
Saponite, 323
Self-assembly, 154, 351, 353
Semiconductor nanoparticles, 283
 environmental applications, 283, 294
Semiconductor–polymer nanocomposites,
 283, 299
Sepiolite, 39, 212
Shape memory polymers, 313
 inorganic nanocomposites (SMPINCs), 314
Silica nanoparticles, 26
Silicon carbide (SiC), 325
Silk fibroin, 63
Single-wall carbon nanotubes (SWCNTs), 13,
 320
SiO₂/polymer hybrid fibers, 115
Sliding friction behavior, 221
Smart composites, 313
Sodium bis(2-ethyl hexyl) sulfosuccinate, 259
Sodium montmorillonite (Na-MMT), 328
Soft polymer nanocomposites (M-NCs), 238
Sol–gel process, 6, 148, 258, 285
Solar cells, 296
Solid-state reaction, 5
Solution blending, 12
Stimuli sensitivity, 187
Stimuli-responsive materials, 313
 NC gels (MD-NC gels), 187, 230
Surface modification, 1

T

TEMBO, 326
TEOS sol + PVA, 115
Tetra-isopropyl titanate, 10

Thermal evaporation, 7

Thermoplastic polyurethane (TPU), 331
Thermoregulated networks, 341
Tin oxide, antimony-doped (ATO), 25
Titanium (IV) tetra-butoxide, 150
Titanium oxide (TiO₂), 96, 251
 polymer hybrid fibers, 116
Titanium tetra-isopropoxide (TTIP), 286
Toxicity, 65, 298
β-Tricalcium phosphate (β-TCP) fillers, 100
Tubulin, 352
Tyrosinase, 64

V

Vanadium dioxide, 98
Vermiculite, 323
Viral infections, detection, 298

W

Water, contact angle, 223
Water purification, semiconductor
 nanoparticles, 294
Water-borne polyurethanes (WPU), 49
WO₃–polythiophene, 302

X

Xanthan, 60

Z

Zeolitic water, 43
Zinc ferrite, 19
Zinc oxide (ZnO), 22, 97, 108, 122, 253, 298
 polymer hybrid fibers, 117
Zinc(II) octacarboxy phthalocyanine, 97
ZnS QDs, 99
Zwitterionic NC gels (Zw-NC gels),
 187, 232